ICHSF 2010

4th International Conference on High Speed Forming

Proceedings

March 9th-10th, 2010
Columbus, Ohio, USA

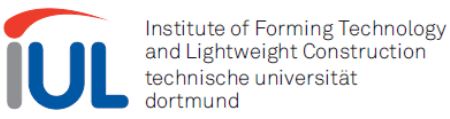

HIGH SPEED FORMING 2010

PROCEEDINGS OF THE 4th INTERNATIONAL CONFERENCE

MARCH 9th-10th, 2010
COLUMBUS,OHIO,USA

Edited by:

Glenn Daehn
Yuan Zhang
Kathleen Babusci
Christian Weddeling
Michael Marre
Erman Tekkaya

Table of Contents

Preface

The 4th International Conference on High Speed Forming was held on March 9 and 10 at the Blackwell Hotel on the campus of The Ohio State University. The initial meeting in this series was the brainchild of Matthias Kleiner with the previous meetings held in 2004, 2006 and 2008 at the Technical University of Dortmund, Germany. This meeting series is now being organized with the support of the International Impulse Forming Group (I^2FG) that was formed in October 2008 through the vision of Erman Tekkaya. His goal was to model this in many ways after the International Cold Forging Research Group which has been instrumental in taking cold forging from a laboratory curiosity to a technology that is widely practiced and used in the manufacture of every automobile transmission. The public face of this site will be at http://i2fg.org. Over time much useful information will be available at this location including the proceedings of all the ICHSF meetings.

The Columbus Meeting was well-attended and vibrant. The conference was truly international with 11 countries represented. 33 high quality papers were presented over a range of topics including impulse equipment, forming, welding and modeling. The papers in this collection have provided for examination of two referees and have been carefully peer reviewed. This collection of papers is noteworthy for its breadth, quality and timeliness. The audience for the meeting was diverse and came from academic institutions (28) industries (25) and research institutes (9).

One of the main goals of the I^2FG, is full dissemination of high-quality information in high velocity metal forming and working. Accordingly, this entire document is being made publicly available without copyright restriction; however, authors should be credited with their original contributions as they are referenced. Further, original slides and recordings of most of the presentations are available at http://omi.osu.edu/ichsf and https://eldorado.tu-dortmund.de/handle/2003/27022.

These works will also be available with a permanent archival 'handle ID' in the library at the Technical University of Dortmund.

Special thanks are due to Yuan Zhang, Kathy Babusci, Anupam Vivek and Aaron Washburn for compiling these materials. Despite the care that has gone into this project, neither the organizers, the I^2FG nor the Ohio State University can be responsible for any errors, omissions or infringements that may be part of this volume under any circumstances.

On behalf of the I^2FG and the organizing committee we hope you find these papers are useful and will consider these exciting techniques for application or research. If you find them useful, feel free to share these exciting works with your colleagues and friends. We have avoided copyrights to keep this kind of important exchange easy and legal.

We hope to see you at the next meeting in Dortmund in 2012.

Glenn S. Daehn
April 2010, Columbus, Ohio, USA

SESSION 1
INDUSTRIAL PROCESSES

A HISTORICAL REVIEW OF HIGH SPEED METAL FORMING

G. Zittel

Elmag, Inc., San Diego, CA, USA

Abstract

This paper will present a Historical Review of High Speed Metal Forming beginning with the first thought of forming metal by using an electromagnetic impulse to today, whereby High Speed Metal Forming is an accepted production process. Although this paper will briefly cover the basic physics of the process, it will not dwell on it. It will rather show how the industrial acceptance of High Speed Metal Forming is tightly connected to the knowledge acquired from many applications studies. These studies determined the main characteristics of the process and defined the requirements for reliable Forming Equipment. This paper will show where the process is most effectively used by presenting real industrial product applications and industrial forming equipment.

Keywords

Forming, Metal, Electromagnetic Metal Forming (EMF)

1 Introduction

High Speed Metal Forming (HSMF) refers to a forming process whereby the work piece material attains forming speeds in excess of 100m/sec. Although HSMF can be accomplished with explosives, it generally refers to Electromagnetic Metal Forming (EMF). The EMF process can further be categorized into three forming methods:

- The most widely used compression method; whereby round or tubular work pieces are compressed radially inward onto mating work pieces;
- The expansion method; whereby round or tubular work pieces are expanded into a mold or mating work pieces;
- Flat sheet metal forming; whereby electromagnetic pressure is applied to a flat sheet metal which then accelerates the material into a die or mold

Although for the last fifteen years, Professor Daehn and his team at Ohio State University have worked on flat sheet metal forming, most industrial applications of the

process involve compressing round or tubular work pieces, on mating parts. Therefore, the examples shown will be compression applications.

This paper will concern itself with the evolution of Electromagnetic Metal Forming (EMF). The basic theory of the EMF process is demonstrated with simple graphic models at the end of this paper.

2 Evolution of EMF Forming Process/Equipment

The phenomenon, that a force is exerted on a current carrying conductor when placed in a certain direction in an electromagnetic field or, when placed close to another current carrying conductor has been known for a very long time. In fact, this is the principle of the electric motor.

It was in the Twenties when attempts where made to use these forces to stress metals beyond their yield strengths and therefore to deform them permanently. However, to generate forces or electromagnetic pressures which exceeded the yield strengths of common industrial metals, electric currents and electromagnetic fields in the magnitude of several hundred kilo-Amperes and kilo-Gauss were needed. (To give the reader, who is not acquainted with electromagnetic fields, some idea of these magnitudes, one could compare the required field to the natural magnetic field of our earth, which is about 0.2 Gauss, and with the electromagnetic field of an electric motor, which is around 15 kilo-Gauss.) How then could such high fields and currents be generated? The experimenters in the Twenties tried short circuiting large rotating generators. It was hoped that the kinetic energy of the rotating machines could be used to produce the required high currents. These attempts failed because of various technical problems a discussion of which exceeds the intent of this paper. In any case, the experiments were discontinued and not much happened in this field until 40 years later.

In the early 1960's, General Atomic in San Diego, while conducting nuclear fusion research, experienced material failures caused by the forces between current carrying conductors. The extremely high temperatures required for fusion research were produced by compressing an ionized gas with a high-intensity electromagnetic field. The currents required to generate the high-intensity fields were produced by discharging many parallel-connected capacitors into a coil. Parallel copper bus bars were used to carry the capacitor currents to the coil. These currents could reach magnitudes from several hundred thousands up to around one million Amperes. The opposing forces generated between the parallel plates bus bar system therefore exceeded the yield strength of the material causing it to fail and the conductors to bulge apart, as shown in Figure 1 below.

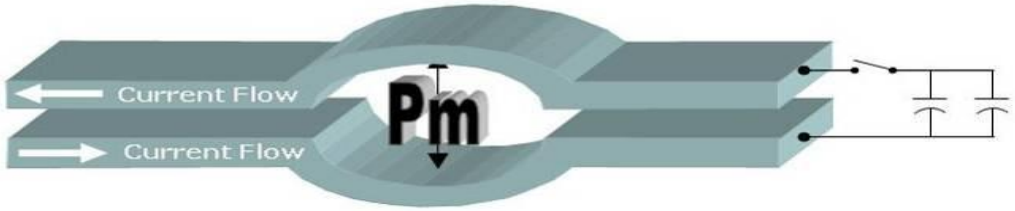

***Figure 1**: Bulges in parallel bus work due to electromagnet pressure*

Someone then had the idea of using these “undesired” forces to perform useful work. The bus bar system was transformed into a coil into which an electrical conductive

work piece would be inserted. The interaction of the field and induced current would exert pressure on the work piece. The set-up was primitive. However, the results of the following experiments were sufficiently encouraging to continue development of the process and equipment. This was the birth of what later developed into a widely applied new metal forming and assembly technology. The two pictures below, Figure 2a and 2b illustrate the concept of a typical coil with a work piece and one of the first coils with a re-enforcing case.

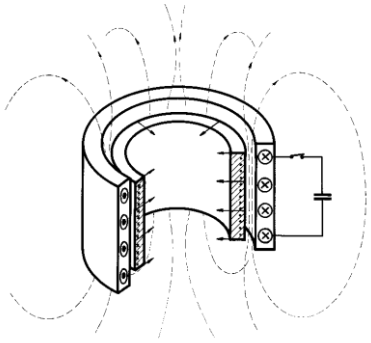

Figure 2a: *Concept of EMF Coil and Work Piece*

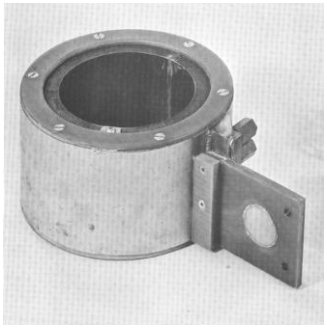

Figure 2b: *First Compression Coil with a re-enforcing Case*

The first introduction of EMF equipment in industry was in about 1964 at General Motors for the banding of neoprene boots onto automotive ball joints. The application and the machine are shown below in Figure 3 and Figure 4 respectively. The machine was technically primitive compared to today's equipment. However, it served well and for many years produced reliable components for the automotive industry. It was especially useful for manufacturing engineers to learn what can be done with EMF and for the equipment designer to learn what needed to be done to improve the process and equipment. Within ten years EMF equipment went through several design stages and was sufficiently improved to work reliably as part of a 28 station automated assembly line as shown in Figure 5.

Figure 3: *First industrial application used to shrink retaining rings onto neoprene boots. The above picture shows the ball joint before and after assembly.*

Figure 4: *A six kJ Electromagnetic Metal Forming machine built by General Atomic in the early 1960's and used by GM as a manually operated single station assembly machine.*

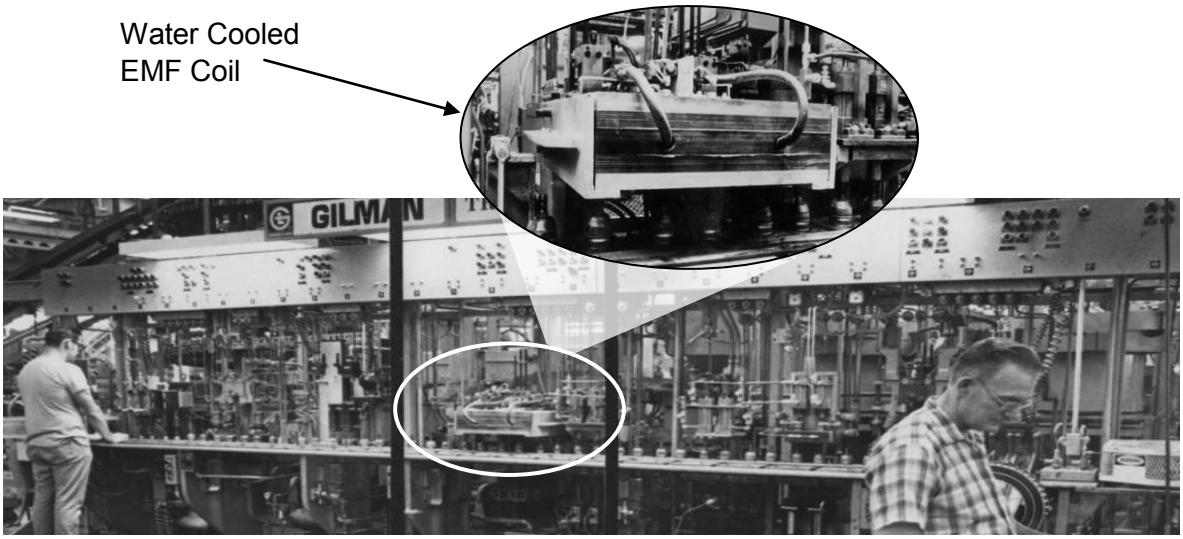

Figure 5: *A third Generation Electromagnetic Forming Machine used at General Motors for the final Assembly of Ball Joints. The machine was incorporated into a fully automated 28 station assembly line and produced several millions ball joint assemblies.*

3 Requirements To Make The EMF Process An Industrial Production Tool

From the early sixties to the present, several obstacles had to be overcome to make EMF technology an accepted production tool:

- Acquaint manufacturing engineers and product designers with the EMF process;
- For us, the promoters of the technology, i.e. initially GA, Inc. then MLI and since 1980 Elmag, Inc., to acquire practical application experience to define the key characteristics of the process and;
- Develop reliable, easy to use EMF production equipment.

3.1 Acquainting Industrial Engineers with EMF Technology

Initially, very few of the potential users of EMF equipment knew how the process worked and how it could be used most effectively. Therefore, almost all of the potential EMF applications were designed and intended for conventional metal working and assembling methods. This meant that before the EMF method could be successfully applied, all aspects of product design and manufacturing required review prior to adapting EMF technology. This included:

- Training of potential users of process, i.e. product designers and manufacturing engineers;
- Creation of graphic models to explain fundamental physics of the process;
- Publication and dissemination of technical papers and application evaluations;
- Industry specific Seminars and Trade shows

As time went on, product designers and manufacturing engineers also learned from colleagues and peers. Our experience has been that once one or more engineers in an industrial company became interested in the process, EMF equipment was introduced as a manufacturing tool.

3.2 Application Experience

We also had to learn about the practical and economic limitation of the process. In the early years, we as well as potential customers were so overly enthusiastic about this unique process that many times we attempted to solve problems with EMF which were just not suited for it. We simply had to learn to evaluate applications and not to pursue non-feasible applications. After years of studies and applied and basic research, we have acquired detailed knowledge of the basic properties and key characteristics of electromagnetic metal forming. This provided us the experience to efficiently evaluate the feasibility of most application inquiries. This experience also allowed us to summarize the Key Characteristics of the Process and disseminate them to potential users.

4 Key Characteristics of the Process

Although the EMF process is called a "metal forming process," it is mostly, but not exclusively used as an assembly process:

- The method works best with materials having relatively high **electrical conductivity**, such as copper, aluminum, and low carbon steel. The material resistivity is one of the parameters which determine the skin depth of the electromagnetic field and therefore the attainable electromagnetic pressure. For good practical results, the resistivity of the materials should be preferably less than 15 x 10^{-6} Ohm-cm which is the resistivity of mild steel. Materials with poor conductivity, such as stainless steel, can be formed by using a conductive driver, such as an aluminum band. A table showing the skin depth versa the range of electrical resistivity for copper, aluminum and mild steel at various discharge frequencies is presented in Figure 6.

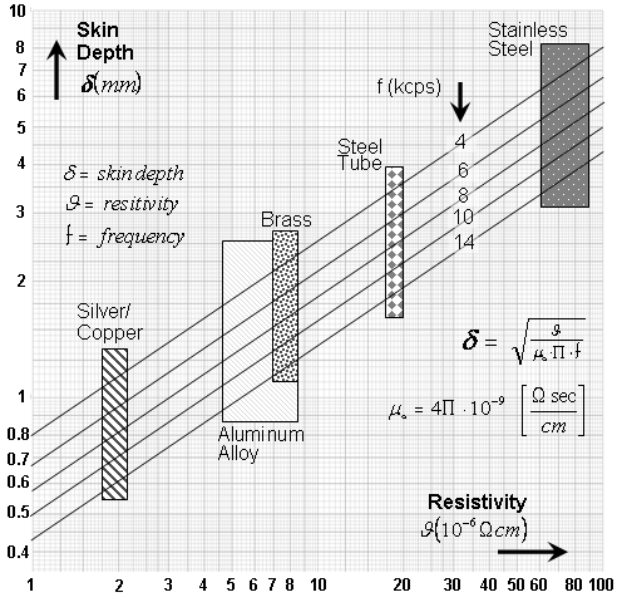

Figure 6: *Table shows skin depth vs. electrical resistivity of most common materials at various discharge frequencies.*

- In addition to being an electrical conductor, the work piece must provide a **continuous electrical path**. The current in a cylindrical work piece flows around the circumference. Therefore, if a cylindrical work piece were slit through its length, as shown in Figure 7a, the interference with the current flow would reduce and distort the forming forces. Figure 7b shows a tubular work piece containing some perforations. Such minor irregularities do

not seriously interfere with the current flow and are acceptable under many conditions. Deep slots at the end of tubes, such as those shown in Figure 7c, interfere with the current flow and produce uneven pressure on the work piece.

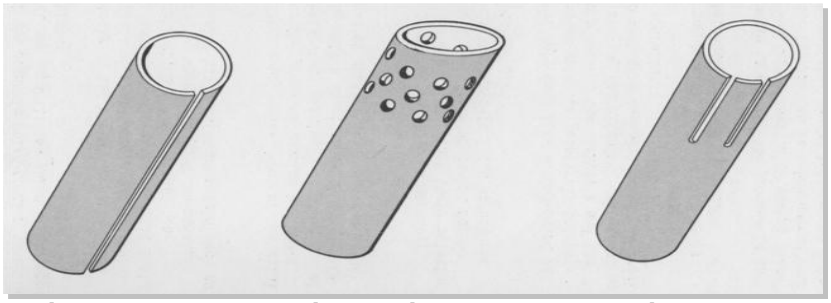

Figure 7a *The slot prevents uniform forming of the tube*

Figure 7b *The perforation produces only very minor distortion*

Figure 7c *The slots produce uneven forming*

- For efficient operation, the fit of the work piece to the coil should be considered. Efficiency is best when the gap between the coil and the work piece is at a minimum. However, sufficient clearance must be provided to allow space for insulating materials and to facilitate the loading and unloading operation.
- Forming is accomplished with no physical contact on the work piece. The pressure on the work piece is applied through the medium of a magnetic field. Since the magnetic field will pass through non-conductive materials, it is possible to work through a non-metallic coating or container. The picture below, Figure 8, shows an application for the Pharmaceutical Industry.

Figure 8*: Forming of a container in a clean room environment. The magnetic pressure is not diminished by the plastic bag*

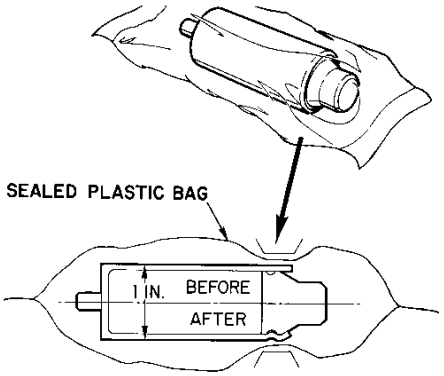

- Also, because there is no mechanical contact between forming tool and work piece, finishes can be applied to the work piece prior to the forming or assembly operation such as certain paints or anodized coatings as shown in Figure 9 and Figure 10.

Figure 9: *Aircraft Control Rod (Electromagnetic Compression Operation). The tubes have been anodized prior to forming. There is no surface damage to the anodized finish.*

Figure 10: *These anodized Platen for medical instruments were expanded with electromagnetic pressure into a mold.*

- Unlike the usual metal forming processes, most of the metal forming takes place after the pressure impulse has ended as the graph in Figure 11 indicates. During the pressure impulse, the metal is rapidly accelerated, gaining a large amount of kinetic energy thus reaching plasticity. The kinetic energy subsequently does much of the actual work of the forming. This results in intimate contact between parts in assemblies and precision conformance to dies in forming operations as shown in the cross section of the torque tube joints in Figure 12 below.

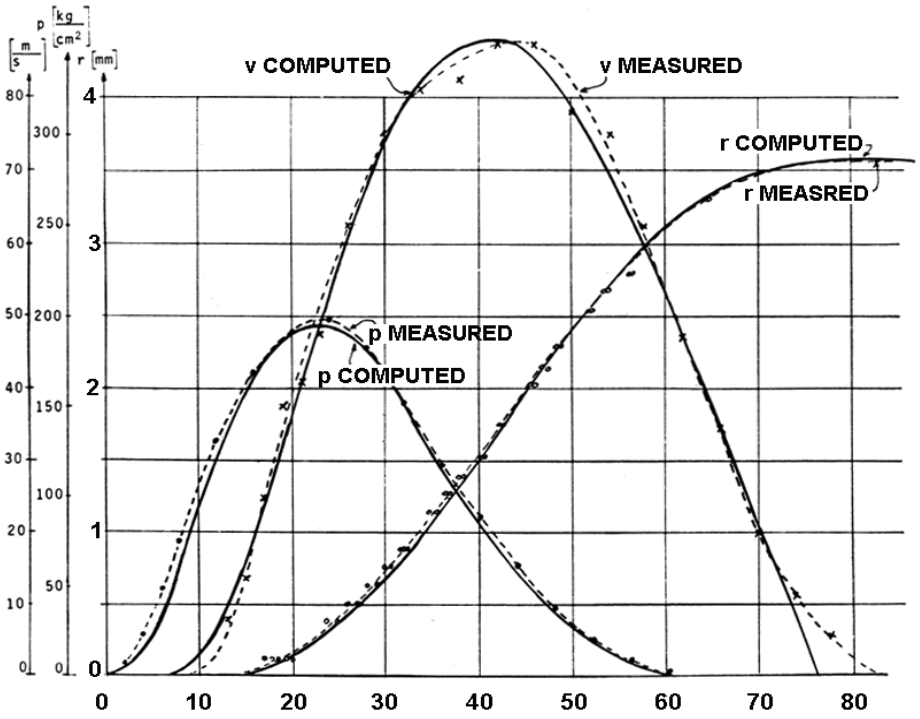

Figure 11: *This graph shows relative time delay between the magnetic pressure pulse, radial displacement and material velocity of material formed [1].*

Figure 12: Aircraft Torque Tubes. These Tubes were anodized prior to forming. The cross section shows the intimate contact of the tube to the steel fitting.

- Since the duration of the force is only in the area of 20 to 80 microseconds, the ratio of the masses of the pieces involved in assembly operations may be much more significant than their relative strength. Since no static forces are involved in the process, relatively light structures may be used for the support of dies;
- Being purely electromagnetic in nature, the process is not limited in speed by the mechanical inertia of moving parts. The timing of the magnetic impulse can be synchronized within tenth of a second precision and machines can be designed to repetition rates of hundreds of operations per minute. The strength of the magnetic pressure pulse can be controlled electrically with high precision;
- Unlike rolling or spinning, no friction is generated by the process; therefore, no lubricants are required. Consequently, no cleaning of the parts is required after the operation;
- Once a machine is set up, it can be operated by unskilled workers.

5 EMF Equipment Development

The first users of EMF equipment were R&D departments of larger companies, as well as technical institutes and universities who used it for research. Soon, however, the users of EMF shifted to the manufacturing companies who used the process in production. This required re-design and improvement of the early EMF forming devices to:

- Meet industrial safety and electrical machine tool codes;
- Be absolutely safe;
- Be able to be repaired by routine maintenance personnel in case of a break-down;
- Be easy operated by unskilled personnel;
- Be economical and be capable of running millions of cycles with minimal maintenance

These were severe requirements and could not be met by the first generation of EMF equipment which, in retrospect, was laboratory type machines adapted to manufacturing requirements. Major efforts and programs in research and development, material studies, and life testing were expended over years to design, build and test a line of EMF equipment which fulfilled these stringent requirements. Today's equipment is a seventh generation of EMF machines and incorporates over 40 years of practical industrial experience and improvements. They are compact, safe and built to stringent industrial safety codes and JIC standards. They are reliable and, if a breakdown should occur, have fault detecting devices to inform maintenance personnel of fault location.

6 Typical EMF Industrial Production Equipment

To use the EMF process and equipment effectively in manufacturing operations, it had to be married to work piece handling equipment and other production tools. A typical EMF assembly system consists of three major components-

- **The Energy Storage and Control** unit houses the energy storage bank with the discharge current switches; the high voltage power supply which charges the capacitor bank; the trigger circuits which initiate the capacitor bank discharge; and the control system with operator and diagnostic panel.

- The **Electromagnetic Forming Coil** (or actuator) converts the electrical discharge current into electromagnetic forming pressure. The field shaper adapts the forming coil to the specific size of the work piece.

- The **Work Station** inserts the work piece into the forming coil, holds it in position for the forming operation, and removes it from the forming coil. Depending on the customer's requirements, the work station can be something quite simple such as a manually operated positioning fixture as shown in Figure 14, or a semi-manually operated work station as shown in Figures 13 and 15, or it can be quite complex such as a fully automated turntable or assembly line as shown in Figure 5, 16, and 17.

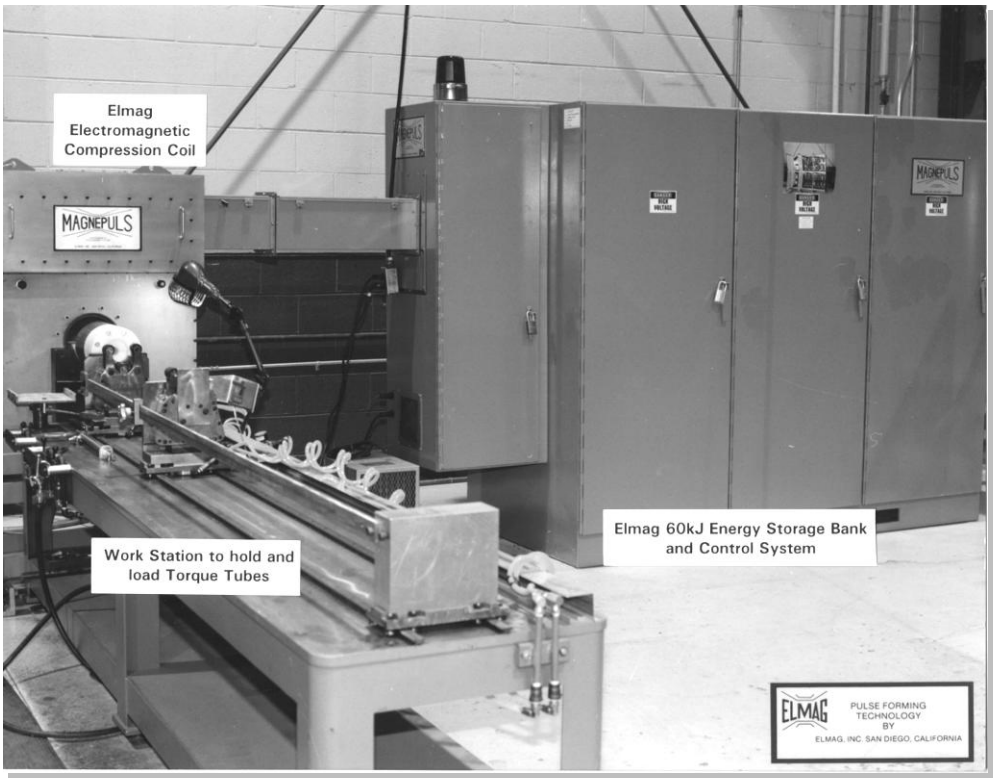

Figure 13: *Typical EMF Systems as used in the Aerospace Industry for the assembly of Flight Control Tubes shown in Figure 12*

Figure 14: *Simple Hold-Down Fixture mounted directly to the EMF Coil to assemble Electric Fuel Pumps.*

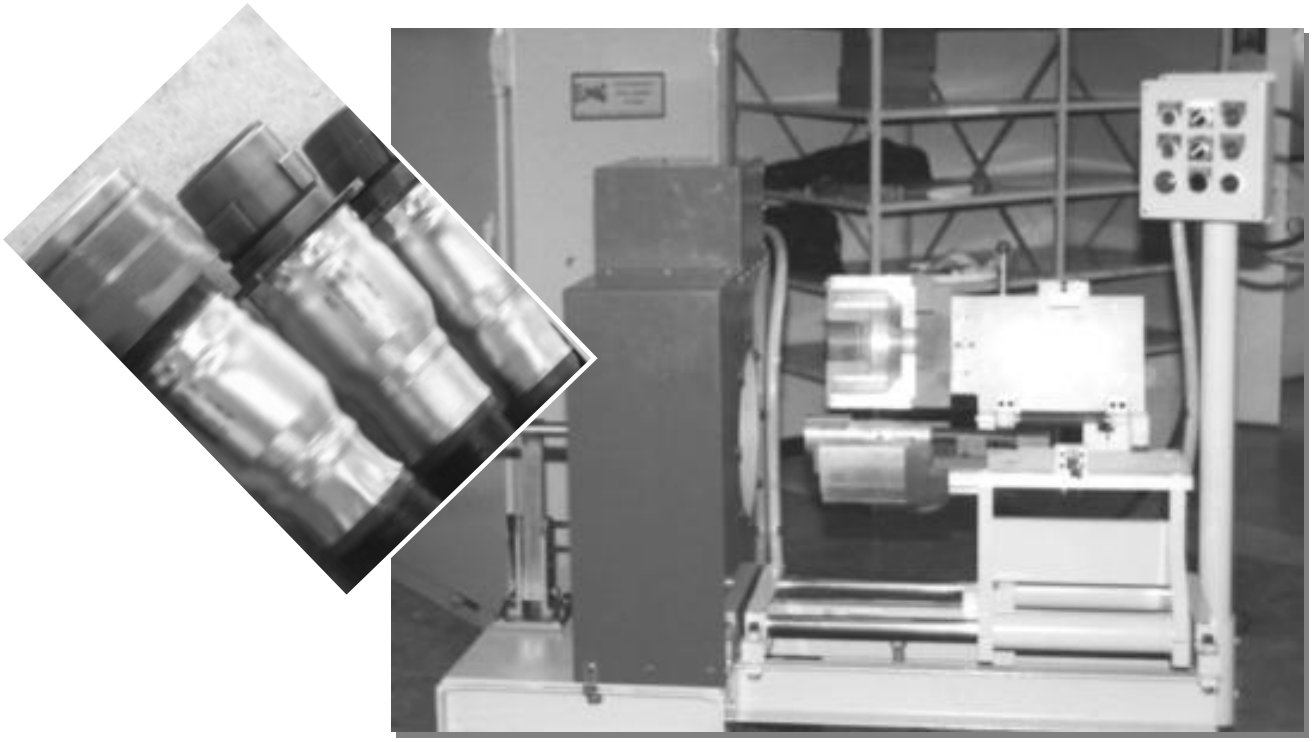

Figure 15: *EMF system with work station to assemble EMI-proof connectors. It required a split coil to accommodate the geometry of 15 different sizes connectors and cables.*

Figure 16: *Single station semi-manual operated work station (right) and an automated turn table (below) to assemble Oil Filters (center).*

Figure 17: *EMF systems with automated turntables to assemble worm gear components for automotive power steering.*

7 Limitation of the EMF process

There are some practical and economical limitations to the process. Although in principle, the pressure which can be generated by the magnetic pulse can be extremely high, in practice, the electromagnetic pressures used in forming operations are limited by the strength of work coil materials. The work coil material must be a relatively good electrical conductor and yet, have sufficient strengths to sustain the pressures required to form the work piece not only once but ideally millions of time. Thus, material fatigue must be considered in coil designs. The practical maximum pressures generated by industrial EMF equipment are therefore in the area of 30,000 to 40,000psi.

The size of the work piece generally determines the capital cost for the equipment. For instance, to form a 30-inch diameter tube would require a larger energy storage bank and physically larger coil than a one inch diameter work piece. The cost of the equipment may therefore not be economical.

Experience has shown that either the EMF capital equipment cost per part must be low enough to write off the equipment in a few years or that the process can do operations which cannot be accomplished with other methods. Successful applications are mostly assembly operations for components in the area of up to 10- inch diameter with wall thicknesses up to 0.10 inches.

8 Basic Principle of EMF

The following discusses briefly the basic theory of the EMF process. It uses the compression method as a model. However, the same principles can be applied to expansion and flat sheet metal forming methods.

Think of something simple first, like an electric motor!

In an electric motor, the interaction of a time changing electric field, B, with a current carrying conductor (I), creates a force (F), on the conductor. This is schematically represented in Figure 18. If the conductor is imbedded in a rotor, and if the arrangement of the rotor and field is properly positioned, the force on the conductor will cause rotation of the

rotor. The electromagnetic field density in a motor is somewhere around 15kG (fifteen thousand Gauss),

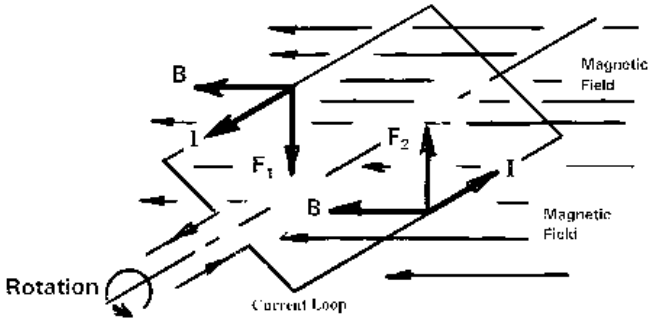

Figure 18: *Schematic presentation of the principle of an electric motor or, more general, of the Lorentz force. It shows the directions of the electromagnetic field, the current, and the forces which cause the loop to rotate*

In an electromagnetic forming device, we make use of the same principle except the generated force has to be sufficiently high enough to exceed the yield strength of the material to be formed. To generate such high forces, the required electromagnetic field needs to be as high as 300,000 Gauss compared to about 15,000 Gauss for an electric motor. The following shows how such high currents and field densities can be generated and how the device can be arranged to be useful as a manufacturing tool.

A basic electrical circuit of a **MAGNEPULS (TM)** machine is shown in Figure 19. A high voltage power supply charges a capacitor bank over a period of several seconds. When a preset voltage level is reached, Switch-1 opens and Switch-2 closes and the stored energy discharges into the load L, which represents the electromagnetic forming coil or actuator.

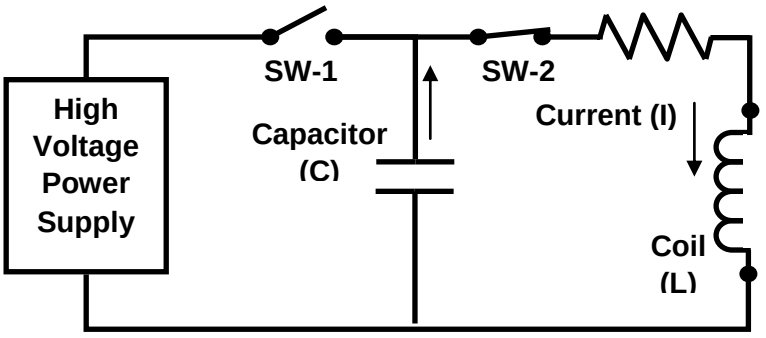

Figure 19: *Basic EMF Circuit*

The discharge current into the forming coil is a damped sinusoid as shown in Figure 20**.** For most industrial applications, the current is somewhere between 100kA and 500kA, and the period T about 100 micro-seconds. The current produces a uniform electromagnetic field in the coil as shown in Figure 21. However, if the work piece is an electrical conductor, e.g. an aluminum or steel tube as shown in Figure 22, then the electromagnetic field induces an azimuthal current in the work piece. This induced current prevents or reduces the field penetration through the work piece, increasing the field density between the coil and the work piece. The interaction between the high field density and the induced current generates an inward directed pressure pulse on the work piece. If the pressure pulse as shown in Figure 23 exceeds the yield strength of the work piece material, the work piece will be permanently deformed.

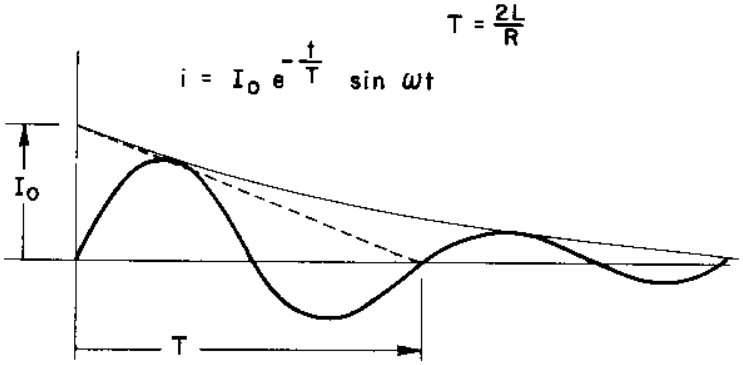

Figure 20 *Discharge Current into an EMF Coil*

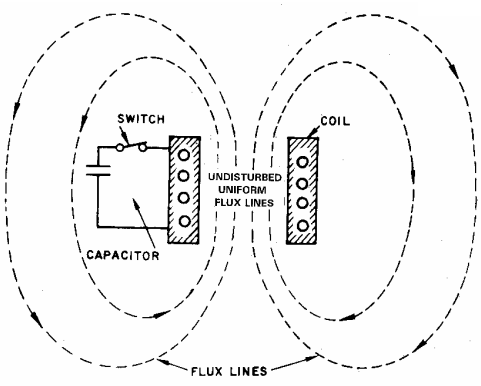

Figure 21: *Forming coil without a work piece. The discharge current produces a uniform electromagnetic field in the coil*

Figure 22: *EMF Forming Coil with an electrically conductive work piece inserted into the coil.*

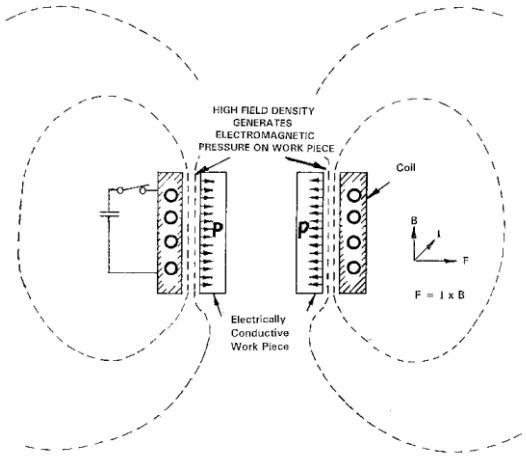

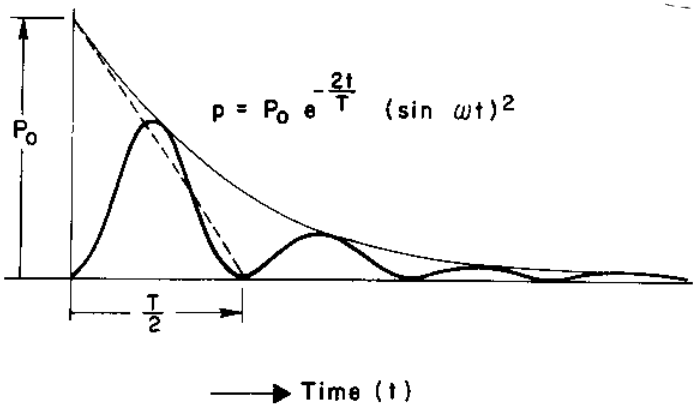

Figure 23: *EMF Pressure Pulse, typical T/2 is 25 to 50 micro-second. The pressure pulse is proportional to the square of the discharge current.*

Note there is no physical contact between the coil and the work piece. There are no moving tools which push, press, or move the work piece material. The pressure pulse imparts kinetic energy into the work piece. Consequently, it begins to move until all the kinetic energy is dissipated. The forces which resist this movement are those due to inertial energy and the energy of deformation. The final shape of the deformed work piece depends on a

combination of factors. These are the magnitude of the pressure pulse, the strength and geometry of the work piece, and the shape and geometry of a mating part such as a die or a mandrel, or a second work piece. Figure 24 shows a tube formed onto a fitting. Notice how the tube practically wraps itself around the contours of the fitting.

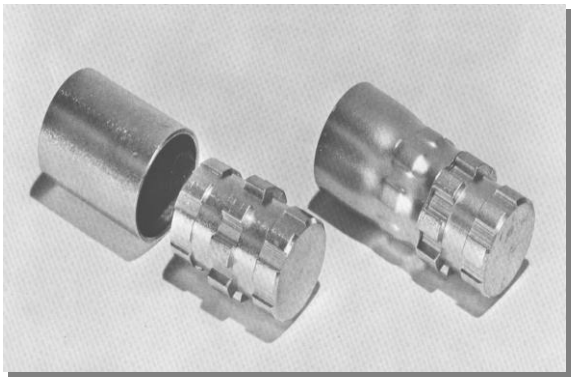

Figure 24: *Tube formed onto a fitting. Notice how tightly the tube wraps around the mating plug. This is because of the high forming speed which turns the material plastic.*

To adapt the coil to different work piece diameters and to concentrate the pressure pulse in particular areas, one makes use of a flux transfer member, also called a flux concentrator or a field shaper as shown in Figure 25.

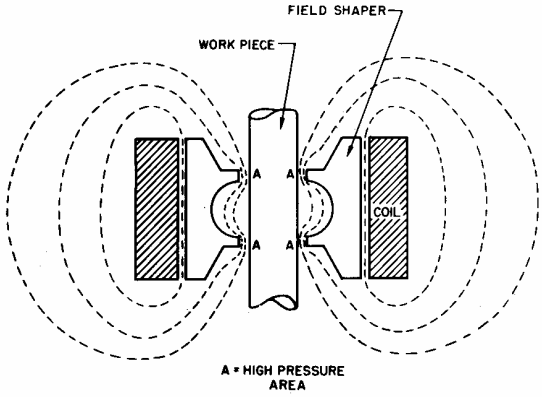

Figure 25: *This illustration shows a field shaper which concentrates the pressure in two areas, indicated as A.*

9 Conclusion

The foregoing has shown that as a result of an incidental nuisance, a known principle in physics found a new application in industry. With efforts in research and development, it was transformed into a unique and widely accepted manufacturing technology;

- The Acceptance by Industry of the EMF Technology was directly related to the improvement in reliability and safety of the EMF equipment;
- EMF Technology is unique and allows product designs which cannot be solved with conventional processes. Yet, it does not replace them but rather complements them.

Reference

[1] *Hansjorg Jansen*: Some Measurements Of The Expansion of A Metallic Cylinder With Electromagnetic Pulses. IEEE Transaction On Industry And General Applications. July/August 1968

Electromagnetic pulse forming technology. Keys for allocating the industrial market segment.

R. Schäfer, P. Pasquale

[1] PSTproducst GmbH, Alzenau, Germany

Abstract

The electromagnetic pulse forming technology (EMPT) provides substantial technological benefits with respect to tube forming and joining operations. However, in the past this technology was mainly adapted in academics, military production and small batch size productions. Establishing this technology in the world of civil-industrial mass production demands for several key prerequisites to be fulfilled. This report lists these requirements and moreover provides answers on ways for their completion.

Keywords

Industrial, Forming,Metal

1 Introduction

Even if the technological possibilities of a new production method apparently are overwhelming, the major key for adoption of this process in today's industrial mass production is the provision of economical benefits. A measure for the economics is the manufacturing costs per produced component.

The electromagnetic pulse technology (EMPT) today is mainly used in mass production for forming, joining and cutting of tubular structures or closed profiles. In this sector, the EMPT is in a strong competition to well established production processes, for example by hydroforming or by fusion welding processes. Substitution of these processes by the EMPT is only possible, if the conventional method suffers on one of the following disadvantages:

a) technical problems solvable only by major efforts
b) need for high priced semi finished products
c) quality problems by process instability
d) low production rate
e) maintenance intensive conventional production process underlying major wear problems
f) need for expensive quality insurance tests

g) the conventional production process does not match properly to the process chain
h) need for replacement of high priced production equipment

If at least one of the above mentioned problems is related to a conventional manufacturing process, EMPT can play its benefits.

2 EMPT system requirements for industrial mass production

The major factors, governing the economics of the EMPT process with respect to industrial mass production are the component life time of pulse generator and coil, the repeatability of the process and the system's control algorithms. Further, there are some technical aspects, being in strong relation to the EMPT system size and therewith to the prime costs.

2.1 Component life time

Industrial mass production means batch sizes of 100,000 to several million parts per year. The life time of the costly components of the pulse generator is therefore specified by the batch size per year. It should be at least in the range of a two year production. Costly components are the coil and the capacitors because of their purchase prize and even more because of the time which is essential for replacing those components. At a laboratory EMPT system, replacing the coil may be a task of some minutes. However, this changes if the system is integrated into a production line. Hence, coil life time is required to be in the range of some million pulses.

In the past, EMPT coils where commonly made of several windings of wire, embedded into an electrical insulator. This insulator was mainly made of plastics. The plastic insulator itself was surrounded by some metal or fiber reinforcement, enabling the coil to withstand the loads resulting from the magnetic pressure. This concept allows manufacturing multi-winding coils which can build up high magnetic pressure at relatively low discharge currents. This concept has one big pro but several contras:

The ratio of magnetic pressure to discharge current is high resulting in relatively small pulse generators and quite low electrical loads on all sensitive components, i.e. on capacitors and switches.

The biggest contra is the quite low coil life time. This is mainly due to the big discrepancy between Young's modulus of the electrical conductors and the insulating plastics which causes high strains in the conductors during the pulse. Young's modulus of copper is 115000 MPa, but that of fiber reinforced plastics is only round about 20000 MPa. The factor of 5.75 between the two material's elastic properties means, that under elastic conditions the plastic will reach the same stress as the copper at 5.75 times the strain. Hence, there is no real reinforcement effect of the insulator. Figure 1 illustrates the magnetic loading of a coil made of 4 wire windings. The wire is a Ø 10 mm copper wire. The coil bore is 40 mm in diameter. Inserted into the coil bore is a tubular workpiece, made of aluminium. The coil is loaded by an altering current of 100 kA amplitude at 10 kHz frequency. The maximum pressure acting on the coil in radial direction is ~75 MPa. This will cause an expansion of the coil. In vertical direction, there is magnetic pressure, too. This pressure component causes a compression of the coil in vertical direction.

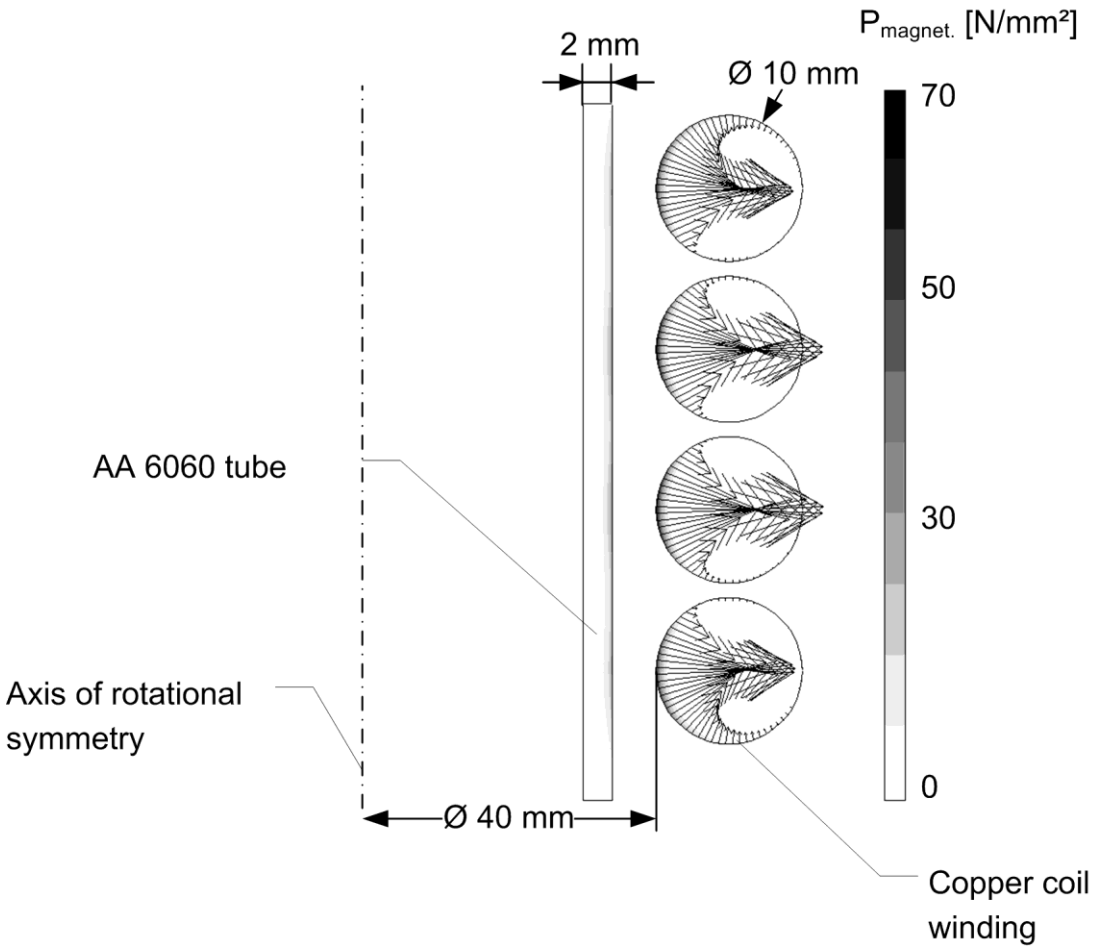

***Figure 1**: magnetic pressure loads at a 4 winding coil.*

The magnetic loading causes displacements inside the copper-insulation composite, resulting in fast ongoing micro fractures in the insulation. When the isolation is weakened by multiple cracks normally a shortcut between the coil windings or cracks in the electrical conductor will happen.

Building self reinforcing coils can help overcoming this problem. However, adding many windings to such a coil is more complex. Thus, self reinforcing coils normally are characterized by only some few windings, usually in the range between 1 and 5. As the number of windings is directly coupled to the magnetic pressure, these self reinforcing coils require elevated discharge currents. This disadvantage of the self reinforcing coils is more than balanced by their high life time, which is often 2 million pulses or even more [3].

Elevated discharge currents will lead to increased wear of cables, capacitors and switches. However, modern cables, capacitors and switches are capable to withstand electrical currents in the range of some 10 or 100 kA. Here, parallel use of these components helps to cope with currents in the range of some 100 kA to some 1000 kA. Proper component design leads to cable and capacitor life time of approx. 2 million pulses even with respect to pulse generators of the 100 kJ class [3]. The switch life time is above 200,000 pulses [3].

2.2 Matching system settings to the EMPT process requirements

As the price of the EMPT System significantly governs the economics of the process, choosing the proper system configuration is mandatory. The EMPT System is related to the following characteristics of the product:

a1. Cross-sectional dimensions of the tube or profile
a2. Workpiece material properties
a3. Magnetic pressure essential to accomplish the forming, cutting or joining operation
a4. Length of the pressure loaded area

The combination of these four aspects defines the characteristics of the EMPT System:

b1. Coil & field shaper
b2. Discharge current
b3. Discharge frequency

2.2.1 Choosing the appropriate discharge frequency:

For crimping and forming operations the discharge frequency is directly governed by the workpiece's wall thickness and its electrical conductivity. This correlation is caused by two mechanisms, based on the skin effect and the correlation between magnetic pressure build up and the magnetic flux density distribution at the inner and outer circumferential face of the tubular workpiece. The skin effect is the characteristic of altering currents to locate in a thin layer near the workpiece surface. The thickness δ of this layer is given by

$$\delta = \sqrt{\frac{1}{\chi \pi f \mu_0}} \tag{1}$$

In case of EMPT, χ denotes for the workpiece electrical conductivity, f for the discharge frequency and μ_0 for the magnetic permeability of the vacuum.

The dependency between the magnetic pressure and the difference of the magnetic flux inside and outside the tubular workpiece is given by the following equation:

$$P_{mag} \sim B_{inside} - B_{outside} \tag{2}$$

In case of a tube compression, equation 2 computes for the highest magnetic pressure, if there is no magnetic flux density at the tube's inner wall. This is roughly estimated true, when the skin depth is smaller than the tube's wall thickness. A skin depth exceeding the wall thickness of the workpiece, will cause significant losses in magnetic pressure. Figure 2 illustrates the numerically computed relation between frequency, skin depth and magnetic pressure build up for an Ø50 mm aluminium AA6061 tube with a wall thickness of 1 mm.

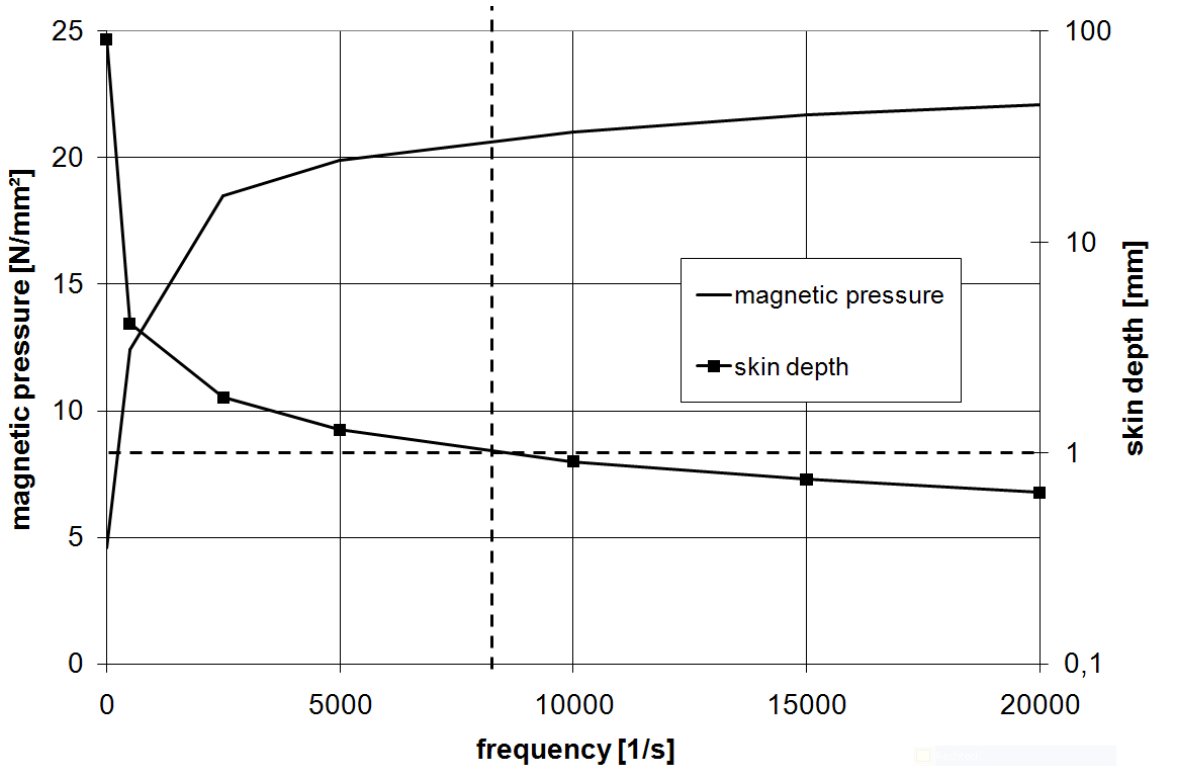

Figure 2: *numerically computed relation between frequency, skin depth and magnetic pressure build up for an Ø50mm aluminium AA6061 tube with a wall thickness of 1 mm.*

A rule of thumb for estimating the discharge frequency for sufficient build up of magnetic pressure is therefore given by:

$$f = \sqrt{\frac{1}{\chi \pi t^2 \mu_0}} \tag{3}$$

χ denotes for the workpiece electrical conductivity, f for the discharge frequency, μ_0 for the magnetic permeability of the vacuum and t for the workpiece wallthickness.

If the frequency is increased above the value computed by equation (3), no further significant pressure build up will be possible. However, an increase in discharge frequency boosts the velocity of the workpiece and therewith the strain rates. The strain rate influences the yield stress of the tube material. Herzig et. al. found that for steels, the difference between the yield strength under quasistatic conditions and at high strain rates differs by a factor of two, see Figure 3 [1].

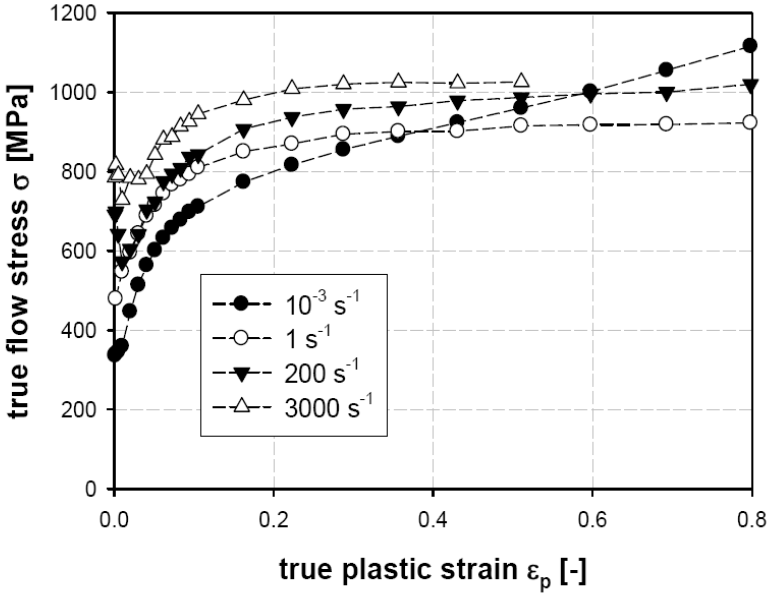

***Figure 3**: Flow stress behaviour of AISI 1045 steel at different strain rates [1].*

Increasing the discharge frequency also enlarges the tube accelerations and therewith the inertial forces. Hence, even if the correlation between strain rate and initial yield strength is negligible (i.e. for many aluminium alloys), a higher magnetic pressure will be essential when the forming result should be constant, but the discharge frequency is increased. An example for this is represented by the following described free compression experiment: An aluminium tube, diameter $Ø_{out}$ 50 mm, wallthickness 2 mm and tube length of 30 mm, material AA6082-T6 is compressed to a diameter of 40 mm. At 1 kHz discharge frequency a pressure about 50 MPa is essential for accomplishment of this. When increasing the frequency, the essential pressure for keeping the diameter reduction constant increases linearly. So at 20 kHz discharge frequency, the magnetic pressure amplitude required for decreasing the tube diameter to 40 mm is 130 MPa.

2.2.2 Coil

The inductance of a long coil (it's length must be significantly bigger than it's diameter) is approximately given by

$$L = 2\pi r \mu \frac{N^2}{l} \tag{4}$$

L denotes for the inductance, μ for the magnetic permeability, *r* for the coil's radius, N for the number of coil windings and *l* for it's length. The discharge frequency is given by

$$f = \frac{1}{2\pi\sqrt{LC}} \tag{5}$$

where C denotes for the capacity of the pulse generator, *L* for the inductivity of pulse generator and coil. Normally the inductivity of the pulse generator is far below that of the coil. Equation (4) shows, that an increase in coil diameter and the number of coil windings boosts the coil's inductance. However, according to equation 5 an increase in inductance decreases the ringing frequency.

On the other hand, the number of coil windings is directly related to the magnetic pressure. Hence, choosing the appropriate number of coil turns is some kind of optimization problem. However, the bigger the coil diameter, the less windings should be used, because of the therewith ongoing significant increase in inductance. Thus, often, in case of workpiece diameters above 100 mm the use of a single winding coil and a pulse generator, capable to supply high discharge currents is beneficial.

2.2.3 Field shaper

The field shaper focuses the magnetic pressure on the area to be deformed [4]. It is not a must for EMPT, however, it is beneficial because of several reasons:

- In case of changes in work piece diameter, only the field shaper and not the coil must be replaced
- The field shaper provides possibility to manufacture undercut joint geometries
- The field shaper locates the pressure on the workpiece. Hence, the coil is loaded with minor pressure than the workpiece, which results in improved coil life time.

When a field shaper is inserted into a compression coil, the coil induces surface currents in the outer circumferential face. These currents run via at least one slot of the field shaper to the field shaper bore. Figure 4 provides a schematic of a field shaper inserted into a coil.

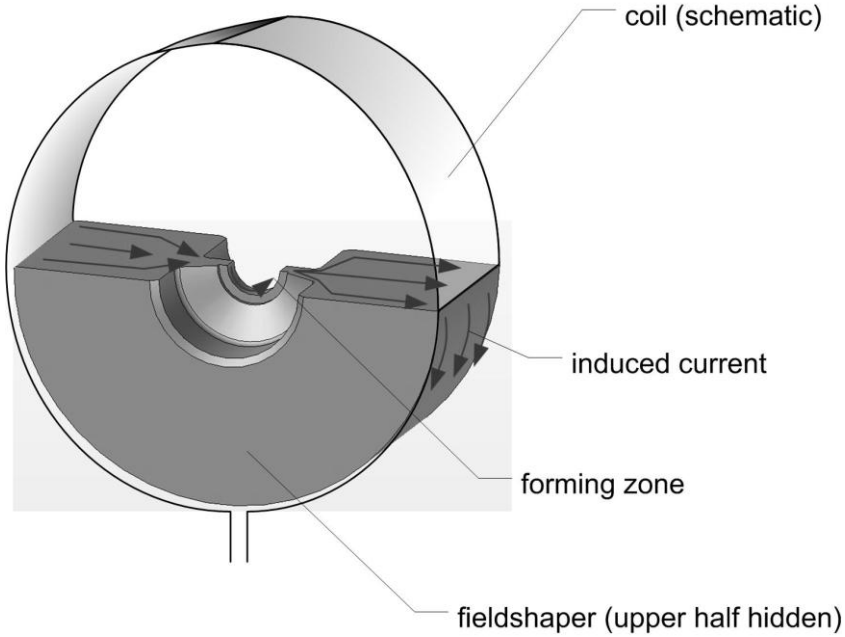

***Figure 4**: Schematic of a field shaper inside a compression coil.*

The bore length is usually smaller than the field shaper length. Hence, the current density is increased. This causes a local elevated magnetic pressure. Figure 5 illustrates the current density distribution at a field shaper half.

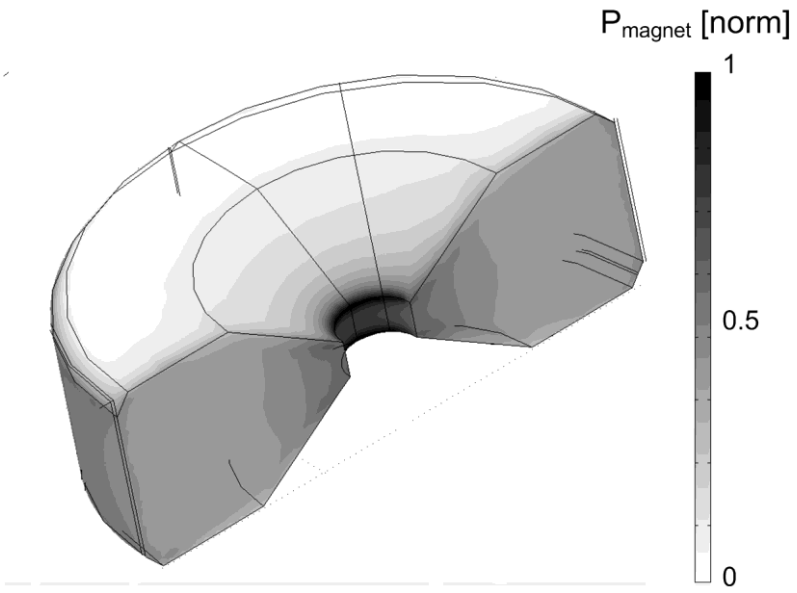

Figure 5*: Current density distribution at a field shaper half. Red colour denotes for high current density, blue for zero.*

2.3 Mjo coils: Increasing the production rate and the component life time, as well as decreasing the production costs

An appropriate chosen EMPT-System using field shapers is capable for economic forming cutting or joining of components up to medium batch sizes. However, in mass production situation it is often inevitable to increase the production rate. Adding a second EMPT system is not a choice because of the additional cost and the additional space requirements. Using one pulse generator to process several parts within one pulse is an option to increase the production rate at minor costs than by using several EMPT systems in parallel. This can be done best by use of a so called multiple joining coil (Mjo-coil). This coil is characterized by several bores, each usable for processing one part [2]. The current consumption of this coil is nearly the same as a single bore coil [2]. Hence, the EMPT process costs per manufactured part are divided by the number of parts manufactured within on pulse. Moreover, the maintenance interval is multiplied by the number of coil bores, too. If for example a Mjo coil is used, which can process two parts within one pulse, twice as much parts can be manufactured before the first system maintenance in comparison to a conventional single bore coil EMPT system. Figure 6 shows a Mjo coil for parallel processing of two workpieces.

***Figure 6**: Multiple joining coil for parallel processing of two work pieces (MJo2).*

2.4 Control algorithms

Today, economical mass production requires the application of online quality insurance systems. Often, these systems save relevant process data in a common database which provides possibility to retrieve information on any process, the manufactured part had undergone.

The result of an EMPT process is mainly related to the magnetic pressure applied to the specimen. So if there are only minor deviations of the material parameters within a workpiece batch, it is essential to keep the current and therewith the magnetic pressure constant. For this, on the one hand a constant charging voltage of the capacitors is essential, which is a question of the charging device's quality. On the other hand, parallel firing of all high current switches of the pulse generator within some nanoseconds is mandatory. Non parallel firing of the switches will result in deviations of the first current amplitude and the discharge frequency.

Additionally to this, a 100% control of the discharge current history of every pulse helps providing useful data for the quality insurance system. By monitoring the current amplitude and the frequency, the integrity of the machine is verified. In many cases these two characteristics can be even used to identify whether a workpiece is inserted in the coil bore or not.

Moreover, an appropriate pulse generator control algorithm can ensure the process stability by increasing the charging voltage, i.e. when one capacitor fails at the end of its life time. However, in case of a capacitor failure, the discharge frequency will also be changed. Hence, an automatic disconnection of the failed capacitor and an increase of the charging voltage for the working capacitors to reach the same discharge current as before the fail is not the appropriate solution. The better way is the use of a process window, which correlates discharge current and frequency to the result of the EMPT process.

Control algorithms for mass production EMPT systems should additionally provide the possibility for remote software maintenance and remote hardware diagnosis to minimize machine down times.

3 Conclusion

In mass production, EMPT is in a strong competition to conventional forming and joining processes. Hence, the technological benefits of EMPT will only be taken in account, if there are at least non economical benefits. However, in most of the cases, this new technique will only be adopted in mass production when technical and economical benefits are given.

For gaining economical benefits, EMPT system life time must be in the range of a two year component production. This can be accomplished by high quality switches, capacitors and cables. An additional use of multiple joining coils can further increase the maintenance interval and decrease the costs per manufactured component.

References

[1] *Herzig, N.; Bleicher, F.; Puschitz, F.; Dorn, C. et al*.: Collective Research for High Performance Manufacturing; 15th International Working Seminar on Production Economics, Innsbruck; 03.03.2008 - 07.03.2008; in: 15th International Working Seminar on Production Economic, p. 163 – 172, 2008

[2] *Pasquale, P*.: Mehrfachfügespule. German Patent application, 2007

[3] *Schäfer, R.; Pasquale, P.*: Die Elektromagnetische Puls Technologie im industriellen Einsatz. Whitepaper PSTproducts GmbH; http://www.pstproducts.com/downloads.htm, 2009

[4] *Winkler, R.:* Hochgeschwindigkeitsbearbeitung – Grundlagen und technische Anwendung elektrisch erzeugter Schockwellen und Impulsmagnetfelder. VEB-Verlag Technik, Berlin, p. 307-333, 1973.

Powder Forming Using Dynamic Magnetic Compaction

B. Chelluri[1], E. Knoth[1]

[1] IAP Research, Inc., 2763 Culver Avenue, Dayton, Ohio, USA

Abstract

Conventional powder forming of metals, ceramics and composites uses room temperature pressing approaches such as static uniaxial pressing, isotropic pressing - cold isostatic pressing (CIP) or elevated temperature hot isostatic pressing (HIP) methods. In this paper, description of a unique dynamic pressing approach for powder materials will be presented where very high pulse pressures (of GPa range) are applied for a short duration (of < 1 millisecond) on powders. Such a dynamic pressing offers the ability to form uniformly high density net shape parts with fine microstructures. The method can be applied to wide range of materials such as metals, ceramics, composites and soft and hard magnetic materials. A broad range of powder particle size distributions, from coarse micron size to fine nano size powders, can be used in the process. The principles of dynamic pressing method along with the summary of results on various powder material systems will be presented. The performance of parts made with dynamic method will be compared with conventional processes.

Keywords

Powder, Near net shape, Dynamic

1 Introduction

In the Powder Metal (P/M) industry there is a constant demand for producing high-density net shape parts at an affordable cost. In the commercial sector such as the auto industry, there is a need for close to full density parts such as power train gears for high performance applications. Currently such parts are machined from forged and wrought blanks. Due to high machining costs, these components are much more expensive than conventional press and sinter P/M parts. The conventional single press, single sinter process (including warm pressing) produces steel parts to low density of only about 6.9-7.4 g/cc. Similarly, high performance ceramics such as ballistic tiles are produced using

hot pressing (Pressure Assisted Densification- PAD) process or Hipping (HIP). Both PAD and HIP are batch processes, have low throughput and are expensive due to inherent time and secondary processes involved in producing the final tile shape. Various other powder materials such as permanent magnet powders for electric motor applications, thermoelectrics for efficient heating and cooling devices and nano structure powder materials with special microstructures require processing methods that preserve the properties of original powders while yielding high density and net shape for cost reduction.

This paper describes a high rate dynamic powder pressing approach that uses pulse magnetic pressures to compact the powders [1]. In dynamic magnetic compaction (DMC) processing, kinetic energy is imparted to powder material using magnetic fields in a sub millisecond time duration. DMC compaction pressures of a few GPa range on powders produces high green compact density. The development of DMC technique for ductile metallic materials has been demonstrated and implemented for net shape geometries such as gears [2] and cylinders. However, in the case of brittle ceramic powders, the compacted material can develop cracks during the release of internal strain energy during rebound. IAP Research, Inc. has developed an innovative design of a dynamic compaction system to control rebound energy and produce crack-free high performance ceramic parts [3]. In the following paragraphs, general process description along with selected examples of parts fabricated and their properties will be described.

1.1 Dynamic Magnetic Compaction (DMC) Process

The basic principle of the Magnepress™ DMC process is shown in Figure 1. In this method powders are filled in a conductive container (armature) placed in the bore of a high field coil. The coil is pulsed with a high current to produce a magnetic field in the bore that, in turn, induces currents in the armature. The induced currents interact with the applied magnetic field to produce an inwardly acting magnetic force that collapses the tube, thereby compacting the powder. The launched armature accumulates a large kinetic energy during compaction and is brought to rest by the powders within a few microseconds. The powders are pressed to full density via the transmitted impact energy with the entire compaction cycle occurring in less than one millisecond.

Magnetic forces have been used for over two decades in high rate metal forming [4] and powder compaction [5]. The same electromagnetic based pulse forces are used in DMC process to realize net shape powder consolidation. The powder pressing in DMC takes place through the transmitted impact energy analogous to driving a nail into a board with a hammer. Almost any material can be compacted to full density using a sufficiently large impact pressure. The important benefits of magnetic powder compaction are higher green (compaction) density, high aspect ratio (L/D) compacts when compared to die pressing and ability to preserve special microstructures.

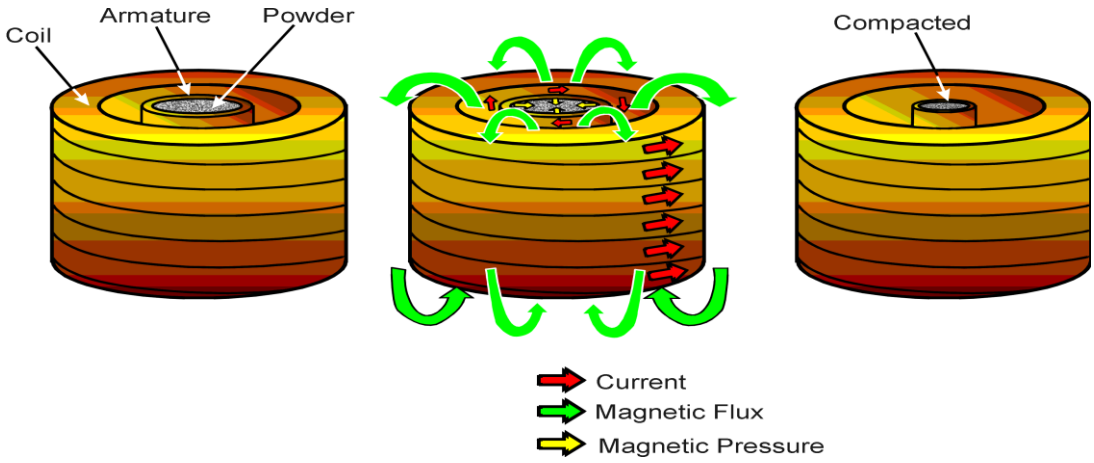

Figure 1: *Principle of DMC process*

The process steps of powder processing using DMC process are shown in Figure 2. These steps are similar to conventional P/M pressing which include tooling for compaction, powder filling, part extraction and sintering with the optional steps of sizing and finishing as required. In most commercial applications the powder filling and compaction are done in air at room temperature. The powder filling can be carried out in special environments such as in an inert gas or under other cover gases for special applications and can also be compacted at elevated temperatures with suitable system modifications.

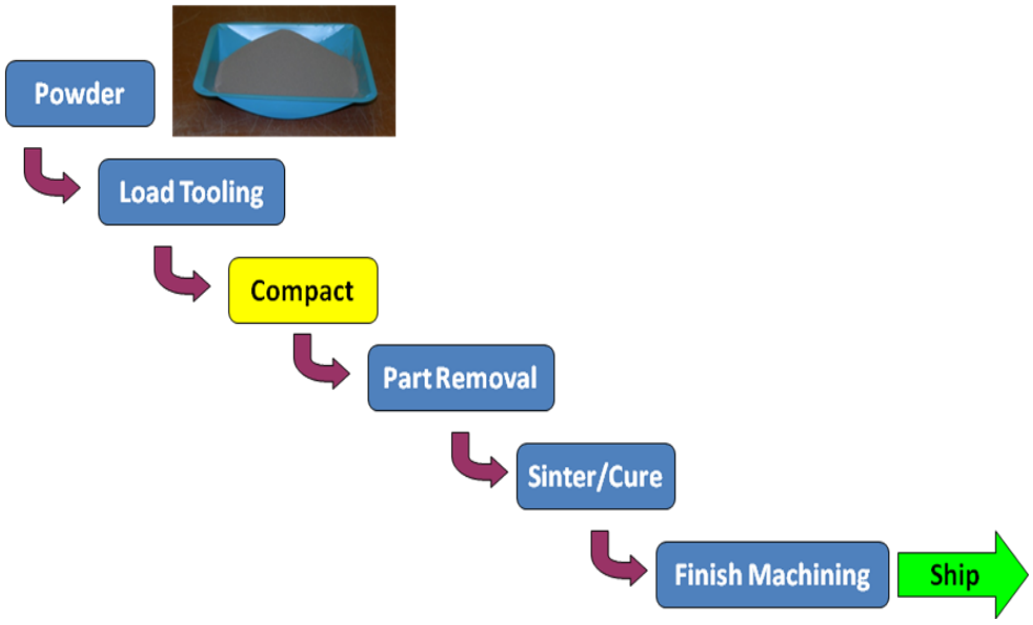

Figure 2: *Dynamic Magnetic Compaction processing steps*

2 Dynamic Magnetic Compaction Processing

2.1 Densities of ferrous and non ferrous alloys processed via DMC Magnepress™

Many different alloys of ferrous and nonferrous powders can be consolidated using magnetic pressing. Figure 3 shows the as pressed density achieved in various powder materials. No lubricants were added to any of these powders. In most steels, densities greater than 95% were achieved after DMC compaction.

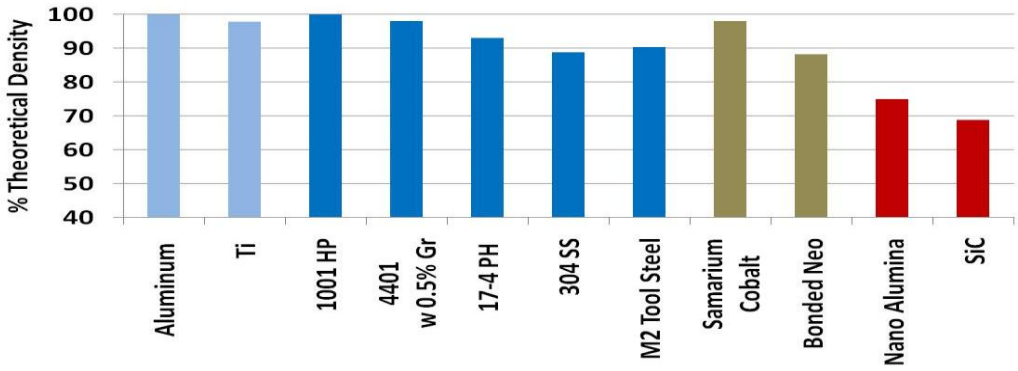

Figure 3: L*ist of materials compacted with the DMC process and the green density achieved*

In the 4405 alloy (4401 with 0.5%Graphite), the green density was greater than 97% of full density. The processes used for some alloys indicated in Figure 3 were not optimized and higher densities can be obtained with further development.

2.2 DMC Density Improvement Boosts Material Performance

The mechanical and microstructural properties of materials are positively affected by DMC processing.

2.2.1 Material Properties of DMC Processed 4405 Steel Alloys

A systematic evaluation of the material properties was carried out with 4405 steel powders. Rods were DMC compacted using 4405 powders at different pressures and sintered at 1180ºC (2156ºF) for 20 minutes in dissociated ammonia. The density and mechanical property measurements were made using ASTM standards. The measured mechanical properties such as transverse rupture strength, tensile, hardness and unnotched impact energy were measured and results were close to those of wrought material of the same composition. The transverse rupture strength of DMC green samples was higher than that of conventional pressed specimens as evident from Figure 4. In Figures 5 and 6, the tensile strength and ductility of DMC samples are summarized along with those of conventionally pressed P/M and malleable cast iron. Tensile and yield strength of DMC materials are higher than conventionally pressed material and closer to the properties of cast material. Tensile elongation of DMC material is 4-6 %, which is

similar to that of cast samples. The impact energy of (unnotched) DMC bars is 60 ft-lbs as shown in Figure 7.

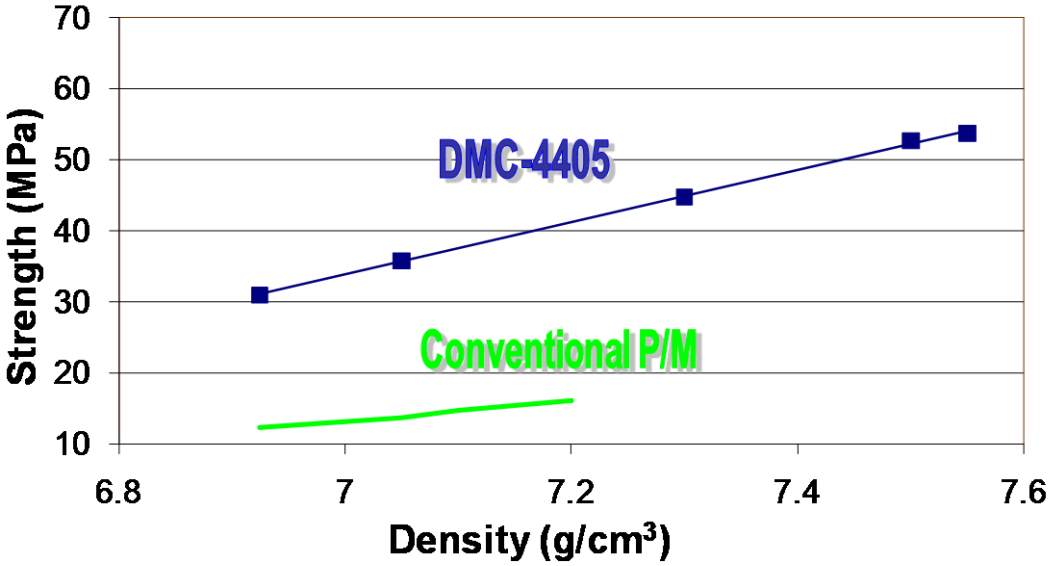

Figure 4: *Transverse Rupture Strength of DMC processed 4405 material compared to conventional P/M*

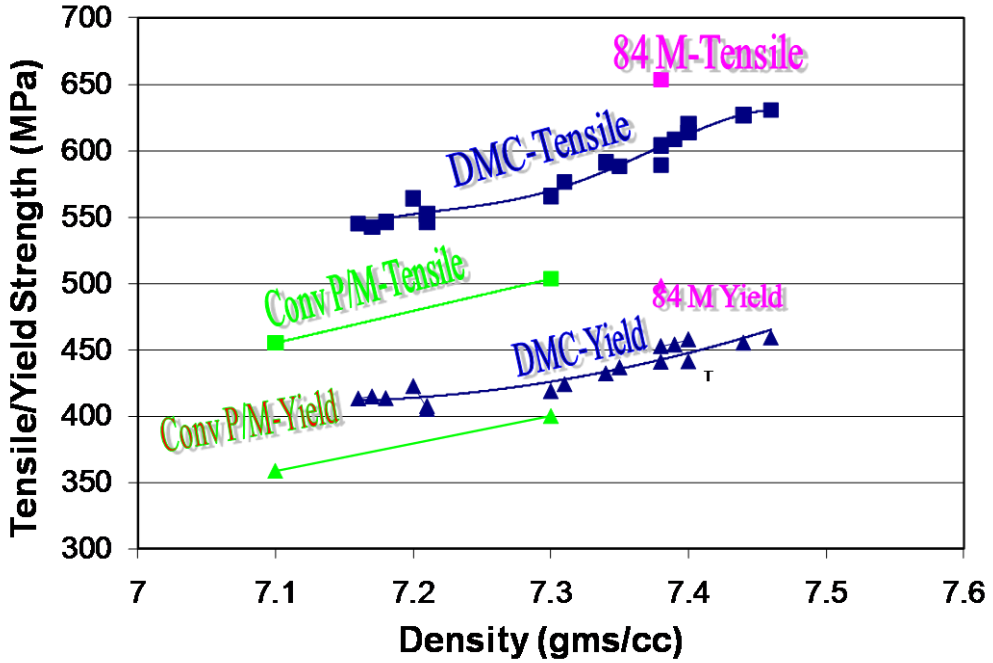

Figure 5: *Tensile and Yield strengths of DMC processed material as compared to 84M-malleable cast iron (2.5% nodular carbon)*

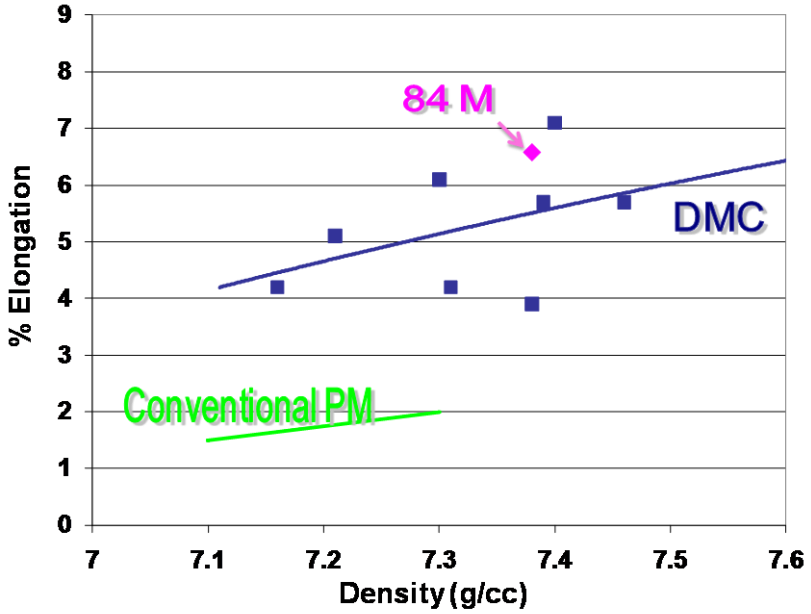

Figure 6: *Ductility of DMC processed 4405 alloy relative to conventional P/M 4405 and malleable cast iron (84M)*

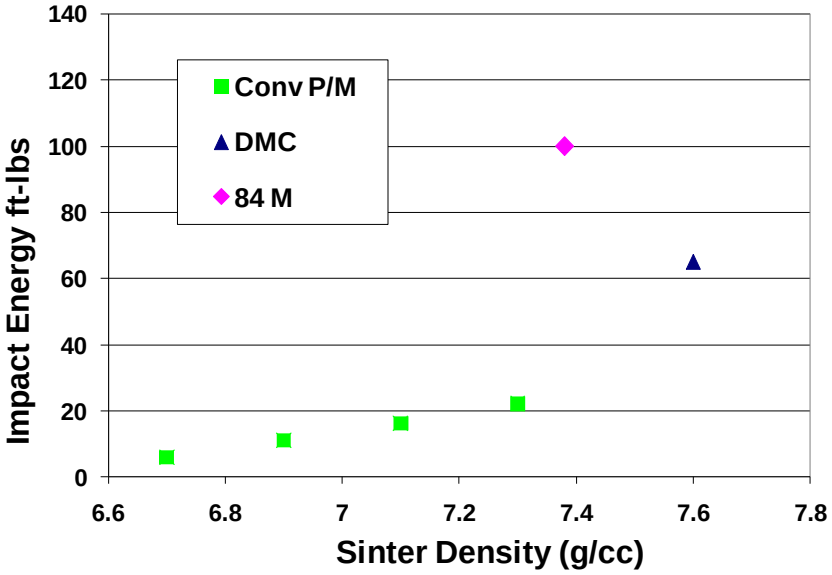

Figure 7: *Unnotched impact energy of DMC processed sample*

2.2.2 Microstructure of DMC Processed Materials

In addition to high density, the other benefits of DMC arise from its dynamic nature of sub-millisecond compaction. This feature aids in preservation of special microstructures including ultra fine grain size. One such example shown in Figure 8 where samarium cobalt magnetic powders (3-6 μm grain size) were compacted using two different compaction methods, cold isostatic press (CIP) and DMC magnetic pressing. Both of samples were subjected to the same sintering cycle side by side in the same furnace. Figure 8 shows the dramatic difference in microstructures in sintered CIP and DMC samples. The DMC sample retained the fine grain structure of the starting powders while the CIP samples showed increase in the grain size to 200 μm after sintering. The starting green density was 65% for CIP and 85% for DMC respectively. Similar results are

observed in processing of silicon carbide ceramics. The mechanism of retention of fine grain structure in DMC compacted sample is not fully understood and still under study.

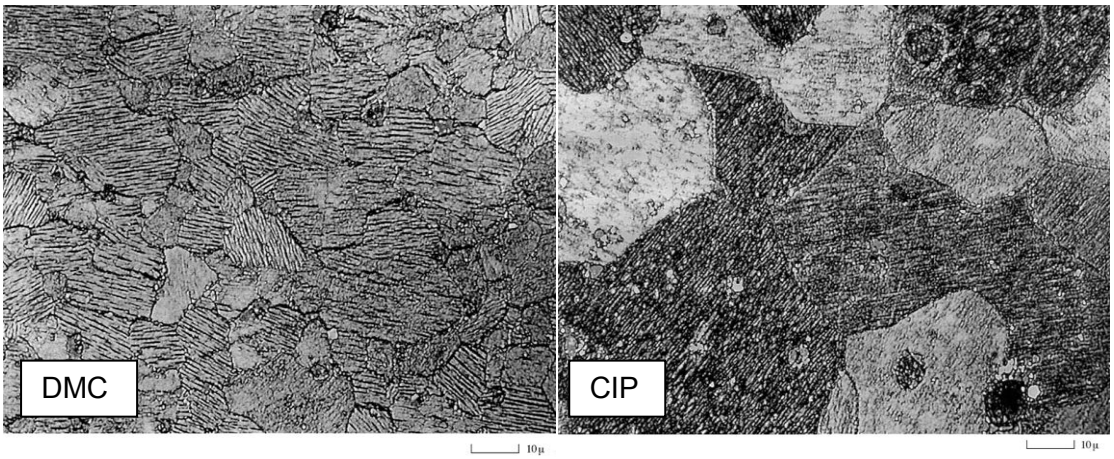

Figure 8: *Scanning electron micrograph of Samarium Cobalt powders compacted by DMC and CIP and then sintered under the same conditions*

2.3 Shapes and sizes of net shape parts via DMC

The radial DMC process is ideally suited to produce net shape parts with cylindrical symmetry, thin walled tubes, high aspect ratio (L/D) parts and parts with internal features. Shapes and sizes of the typical parts produced to date range from 0.5“ diameter x 3“ long to 5” diameter x 1“ long as shown in Figure 9. The helical ring gear, shown in Figure 9, achieved an AGMA 9 precision rating after sintering without any secondary operations on the teeth. A DMC system can produce flat parts such as rectangular parts shown in Figure 10.

Figure 9: *Typical shapes of the parts produced via radial DMC process*

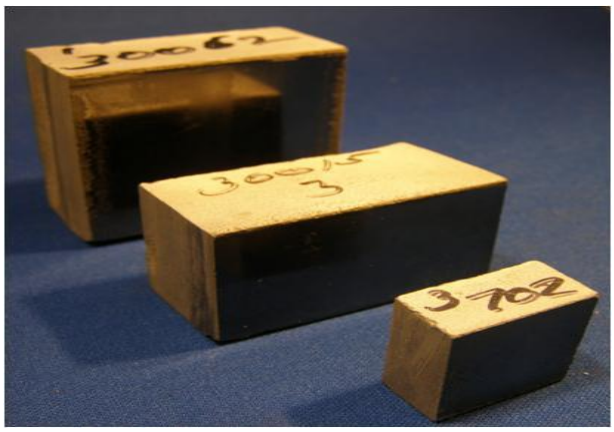

Figure 10: *Typical shapes of the silicon carbide parts produced via axial DMC process*

2.4 DMC Production Rates and Process Repeatability

Given a compaction cycle of the magnetic press at less than 1 millisecond, the production rate of five to fifteen parts per minute (ppm) can be achieved. The two factors that limit the production rates are the power supply charging time and the material handling rates such as insertion of powders and removal of part from the press. Our commercially available power supply module is rated for 15 discharges per minute. Power supply designs for faster than fifteen per minute are possible if required. Material handling rates are controlled by powder filling, part extraction, and transfer rates. DMC processing has demonstrated multi-part per pulse output for some parts.

The DMC process is highly repeatable. The amount of energy discharged into the part can be tightly controlled and measured for statistical control evaluation. The Magnepress™ DMC process also draws benefit of compacting different types of powders such as spherical, flakes, and coated powders without damaging special aspects of the starting materials. No binders or lubricants are required for compaction.

3 Conclusions

The Magnepress™ DMC process holds potential for expanding P/M markets into full density and high performance products. The process feasibility is demonstrated for various powders of ferrous, non-ferrous, ceramic and composites. The development of specific prototype parts with steel powders for automotive industry, electric motor parts and ceramic parts have been accomplished. Other product applications with different powder materials are being investigated.

References

[1] Chelluri, B., Barber, J.B., inventors. United States Patent Nos.: 5,405,574; 5,611,139; 5,639,797; 5,611,230.

[2] Barber, J.B., Bauer, D., Chelluri, B., Knoth, E., et.al. Dynamic Magnetic Compaction (DMC) for high power density helical gears. Proceedings of MPIF World Congress, Vancouver, BC, June 21-24 1999.
[3] Chelluri, B., Knoth, E., Schumaker, E.. Method for Producing SiC Armor Tiles of Higher Performance at Lower Cost. Proceedings of The 34th International Conference on Advanced Ceramics and Composites, Daytona Beach, Jan 24-29 2010, Daytona Beach, USA.
[4] Meyers, M.A., Murr, L.E., editors. Shock Waves and High Strain Rate Phenomena in Metals, Plum Press, N.Y. p. 913-1019.
[5] Gourdin, W.H., Dynamic Consolidation of Metal Powders. Progress in Materials Science, Vol.30, 1986, p. 39-80.
[6] Mamalis, A.G., Manolakos, D.E., Electromagnetic Forming and Powder Processing: Trends and Developments, Appl. Mech. Rev., July 2004, Vol. 57 N.4, p. 299-325

Agile Production of Sheet Metal Aviation Components Using Disposable Electromagnetic Actuators*

S. Woodward[1], C. Weddeling[1], G. Daehn[1], V. Psyk[2], B. Carson[3], and A. E. Tekkaya[2]

[1] Department of Materials Science and Engineering, The Ohio State University, 477 Watts Hall, 2041 College Rd., Columbus, OH 43210, USA
[2] Institute of Forming Technology and Lightweight Construction, Technische Universität Dortmund, Baroper Straβe 301, 44227 Dortmund, Germany
[3] Cutting Dynamics, Inc., 980 Jaycox Rd., Avon, OH 44011, USA

Abstract

Electromagnetic forming is a process used to produce high strain rates that improve the formability of sheet metal. The objective of this paper is to discuss the feasibility of the use of disposable actuators during electromagnetic forming of two aluminum components: an industry part whose main feature is a convex flange with two joggles, and a simple part with a one-dimensional curve throughout. The main forming complications after the parts were formed using conventional methods were the presence of wrinkles and excessive springback. The goal of this work is to use large, controlled electromagnetic impulses to minimize the springback of these components from a rough-formed shape, with the end result being a dimensionally correct part. The optimum test protocols for electromagnetic calibration of the components were determined by optimizing parameters such as design of the actuator, tool material, and capacitor discharge energy. The use of disposable actuators for electromagnetic calibration of the parts showed significant reductions in springback compared to the parts which were only preformed using conventional techniques (hydroforming and rubber-pad forming). Springback was decreased in the curved component by up to 87%. For the flanged component, the wrinkles were eliminated, the joggles were formed properly, and the average bending angle of the part was improved from 95.3° to 90.3°, very near the target bending angle of 90°. This study demonstrates that these forming techniques can be used to improve current sheet metal production processes.

---

* *The authors would like to thank Cutting Dynamics, Inc. for providing financial support, materials, and tooling for this study. Thanks to Geoffrey Taber for his support for the experiments. Thanks to the Martin-Schmeiβer Foundation for providing financial support for this study.*

Keywords

Forming, Aluminum, Agile

1 Introduction

Aircraft structures are quite complex, with an ever-increasing number of complicated, high strength aluminum sheet metal parts being used for their assembly. This makes these structural components extremely difficult to produce since conventional forming methods are reaching their limits. “Conventional forming” refers to any method using large static forces to accomplish the forming. Also, because production volumes are usually quite small for any given component, one-sided dies are typically used and it is not uncommon for a component to undergo several sub-processes during manufacturing. One example of a manufacturing process used in aircraft production is flexible-die forming, where a flexible tool half (such as a rubber pad or flexible diaphragm) applies pressure to form a blank around a solid tool half. This forming method is commonly used in the aviation industry to manufacture aluminum sheet metal parts [1].

This process, however, has some inherent problems that must be overcome to form the parts to specification. These problems can include wrinkling, crowning, and springback, and these cannot often be corrected within the flexible-die forming process. As a result, an annealing step must be performed prior to forming, which decreases the mechanical strength of the part but increases formability. If the desired shape can then be achieved, a second heat treatment step is necessary to re-strengthen the material. For parts that are especially difficult to form, a combination of multiple heat treatment steps and forming operations must be used to fabricate the required shapes. A costly manual calibration step is often required after the re-hardening due to the distortion of the part geometry as a result of the heating and subsequent cooling during the heat treatment process. It is desired that a high-impulse electromagnetic forming (EMF) process will make these heat treatment steps unnecessary, allowing parts to be formed to specification in the T6, or full-hard, condition.

It is expected that the use of electromagnetic forming will lead to lower part costs and shorter lead times. Without the time-consuming heat treatment steps the part manufacturer will be able to react with more flexibility regarding customer orders of parts manufactured with this process. This will contribute to an “agile” production process, meaning that it is simple and inexpensive to make low volumes of many different parts, each of which require different tooling.

In this paper two new methods to calibrate structural aluminum aviation parts using electromagnetic forming will be introduced. In contrast to past work, instead of using “traditional” actuators with durability for multiple discharges, within this work a concept of “disposable” actuators was used. These actuators are designed to only be able to withstand one discharge, but are inexpensively produced.

The purpose of this study is to demonstrate the feasibility of using electromagnetic forming with this kind of actuator in a production process. The forming process for two unique parts, a “flanged” component and a “curved” component, will be investigated using a combination of conventional and impulse forming techniques. This combination of quasi-static and impulse forming has been investigated for a deep drawing process in the work of Vohnout and of Psyk [2], [3]. Each part, shown in Figure 1, has characteristics inherent to a specific class of aviation sheet metal parts. The results of the investigation will then be compared to the results obtained using conventional forming techniques.

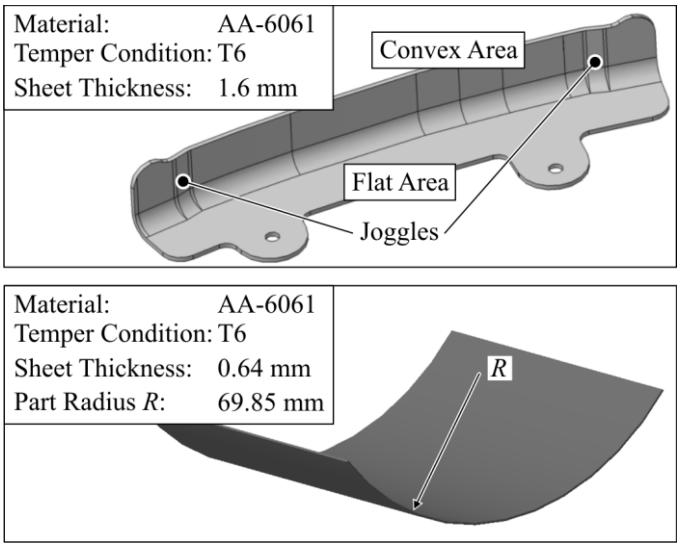

Figure 1: *Curved component and flanged component*

2 Electromagnetic Forming

2.1 Fundamentals

Electromagnetic forming uses the principles of magnetism and electromagnetic induction. A typical electromagnetic forming system consists of a discharge circuit and the components that are necessary for the operation of the system. A capacitor bank discharges a large current (with a peak on the order of 10^4-10^5 amps, depending on the parameters of the system) through an actuator using a high speed triggering mechanism. This results in a large damped sinusoidal current flowing through the actuator, which creates a powerful magnetic field around the actuator. This magnetic field induces eddy currents in the blank, which cause a magnetic repulsion between the actuator and blank. This results in large mechanical energy (high velocity/momentum) acting on the blank, which forces the blank away from the actuator. This forming energy can be adjusted by changing the energy to which the capacitor bank is charged. A larger charging energy will result in a larger magnetic pressure on the blank, and thus greater forming energy. Strain rates between 10^3/sec and 10^4/sec can be achieved with this process [4]. The principal limiting factor for this process is that the actuator and blanks must be made from a highly electrically conductive material such as copper or aluminum.

2.2 Disposable Actuators

To withstand the large and complicated impulse load cases experienced during EMF, traditional actuator concepts include large reinforcements that represent a large portion of the overall tooling costs. Since aviation parts are often low-volume, the tooling costs have a significant influence on the total cost per part. Thus the concept of “disposable” actuators was developed, wherein each actuator is only used to calibrate one workpiece and recycled afterwards. The basic idea of this concept is that the EMF actuator is manufactured out of thin, inexpensive sheet metal and placed on one side of the part. On the other side of the part is the solid tool, which contains the desired shape of the workpiece. The tool, workpiece, and actuator are pressed together into a rubber pad, which counteracts the electromagnetic forces that would otherwise repel the actuator away from the workpiece. The rubber pad also allows the actuator to follow the workpiece contour very closely. This results in a small gap between the actuator and part, which increases process efficiency [5]. In the following experiments AA-6061 aluminum is used

as the actuator material due to its relatively good electrical conductivity as well as its ability to be laser-cut, making production a simple and cost-effective process. After production, the actuators are covered with high voltage Kapton® insulation tape to provide the required electrical insulation between the actuator and the workpiece.

3 Curved Component

3.1 Experimental Setup

The first component to be investigated has only one feature: a circular curve across the entire length of the part, as shown in *Figure 1*. This component is representative of a class of parts, namely those with gradual one-dimensional curves where springback is the primary concern. A very simple un-optimized disposable actuator is used. Two variables were investigated in this work: the actuator design and the capacitor charging energy.

To set up the experiments, the flat blank and actuator were placed under the tool and the entire assembly was pressed into rubber using a hydraulic press. Thus, the blank was pressed firmly against the tool prior to electromagnetic forming, as shown in *Figure 2*B. Electromagnetic forming was then used to convert the elastic deformation of the part into plastic deformation, reducing residual strain and thus springback [6]. The capacitor bank is produced by Maxwell Magneform and has a maximum working voltage of 8.66 kV and a maximum energy storage of 16 kJ. The experimental setup can be seen in *Figure 2*A.

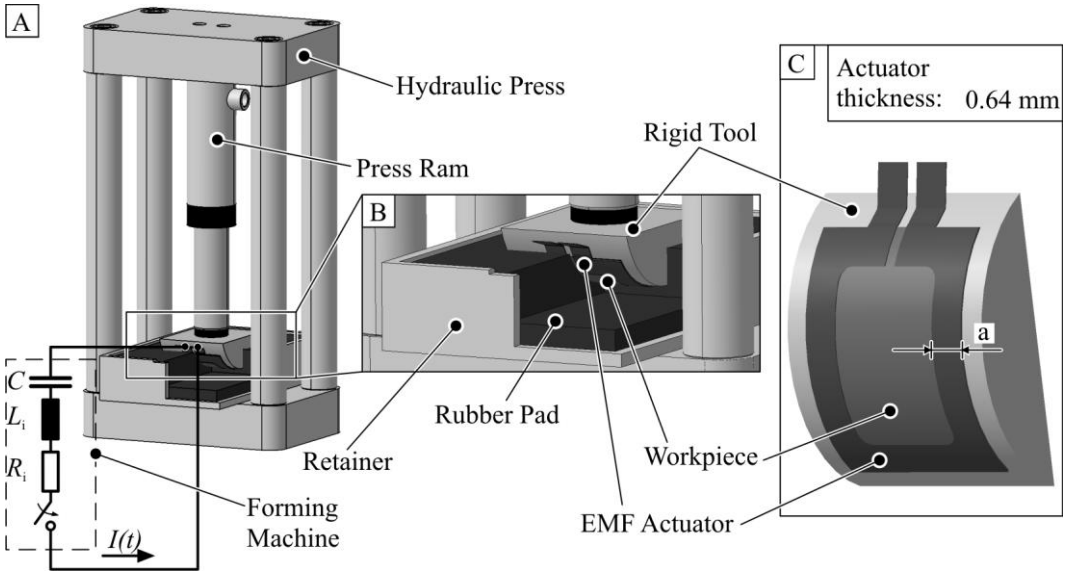

Figure 2: *A) Experimental setup for the curved component. B) Die and part setup in press. C) Actuator and part on die surface*

For this component, the actuator design is a thin single turn actuator that follows the edge of the blank. This design was chosen to allow an effective comparison between the actuator widths with a minimum of complicating variables. Two actuator widths (*a*) were investigated: 0.5 inch (12.7 mm) and 1 inch (25.4 mm). The actuator design can be seen in *Figure 2*C, where the 1 inch actuator is shown.

3.2 Effect of Actuator Width and Charging Energy

Experiments were completed at charging energies between 0.8 kJ and 5.6 kJ at intervals of 0.8 kJ. Output currents ranged from 75 kA to 160 kA for the 0.5 inch coils and from

95 kA to 210 kA for the 1 inch coils. *Figure 3*B and C show the parts formed with the two different actuator widths. These formed parts were compared to a part pressed into the rubber pad with a force of 12000 lbs with no electromagnetic forming, which is the bottom part shown in both figures. *Figure 3*D shows the target part shape with the correct radius.

To quantitatively compare the effects of changing the charging energy and actuator width, the radius of each part was determined. Since the radius decreases as the amount of plastic deformation in the part increases, a smaller radius is more desirable. The calculated radius was then compared to the applied charging energy for each actuator width. The resulting plot can be seen in *Figure 3*A.

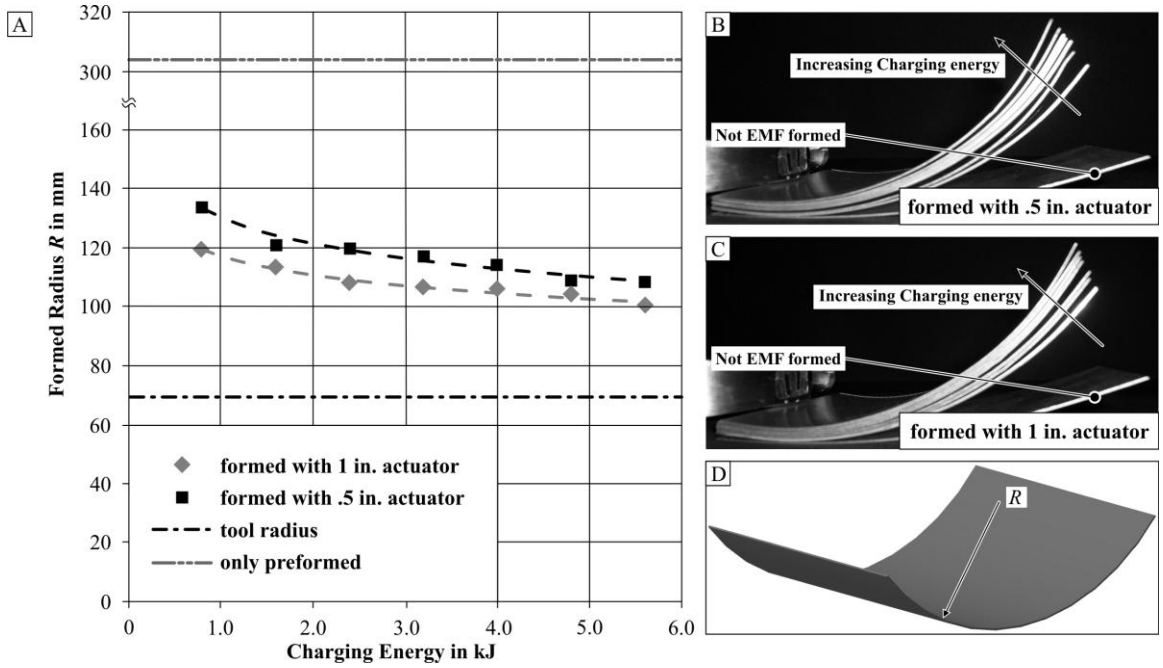

Figure 3: *A) Effect of charging energy on part radius B) Effect of 0.5 inch wide actuators on part shape C) Effect of 1 inch actuators on part shape D) Target part shape*

An increase in the charging energy as well as a decrease in actuator width will lead to an increase in the applied magnetic pressure. In the case of a greater charging energy the magnitude of the applied pressure is greater, while in the case of a smaller actuator width the magnetic pressure is concentrated on a smaller area. The plot shows that it is an increase in the magnitude of the magnetic pressure which primarily affects the formed radius. The average difference in radius between the parts formed with the 0.5 inch actuators and the 1 inch actuators was 9.4 mm. The decrease in the formed radius by increasing the charging energy from 0.8 kJ to 5.6 kJ was 18.9 mm for the 0.5 inch actuators and 25.3 mm for the 1 inch actuators.

3.3 Experimental Radii vs. Target Radii

Once the radii of all formed parts were determined, they were plotted against the target radius of the tool as well as the radius of a part formed only by rubber-pad forming. *Figure 3*A shows that, while the target radius was not achieved, electromagnetic forming significantly improved the formed radius. The use of electromagnetic forming resulted in an average decrease in the part radius of 196.7 mm, while the difference between the target radius and the average part radius was 43.3 mm, resulting in a springback decrease of nearly 82%. The maximum decrease in part radius, obtained using a 0.5 inch actuator and a charging energy of 5.6 kJ, was 209.1 mm. This was 30.9 mm greater than the target forming radius, meaning that over 87% of the springback was eliminated using

EMF calibration. The key parameters for an improvement in the formed radius were thinner actuators and higher charging energies. In future developments of this procedure, it would be beneficial to increase the number of turns in the actuator to increase the blank area exposed to magnetic pressure.

4 Flanged Component

The second example part investigated within this research work is a convex structural bracket with a changing radius at a few points along the flange (see Figure 1). It also contains two joggles along the radius, as shown in the figure. It is not possible to form this part in the T6 temper condition within the required tolerances by using quasi-static methods. *Figure 4* shows the defects resulting from the hydroforming step: wrinkles (*Figure 4*A and C), springback (*Figure 4*B), and crowning (*Figure 4*C).

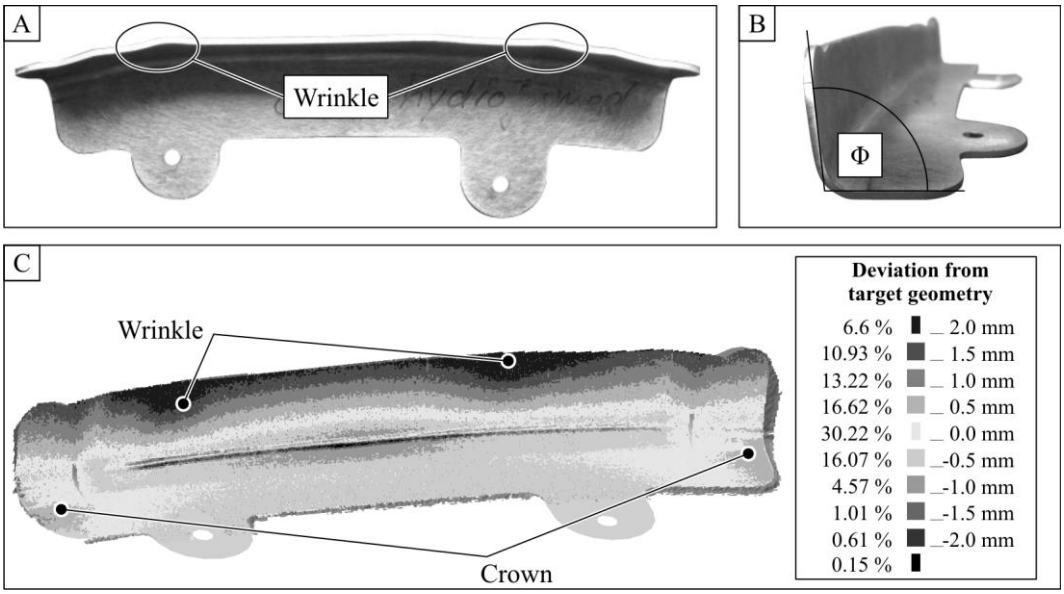

Figure 4: *A) Top view of a preformed part B) Side view of a preformed part with the bending angle Φ C) Deviation analysis of a preformed workpiece, by percentage of measured points*

4.1 Experimental Setup

The basic form of the actuator used for this application is a U-shape. The exact actuator shape is illustrated in *Figure 5*C. It was expected that the wrinkle and springback removal along the convex area of the part would require the highest magnetic pressure, while the removal of the crown along the flat area would require less pressure (see *Figure 4*C). To achieve the desired pressure distribution with respect to these forming tasks, the actuator had locally varied widths. A wider section of 0.6 inch (15 mm) was chosen to cover the workpiece area that has small crowns, on the flat face of the tool. For the section of the part with the wrinkles and joggles, a narrower branch of 0.5 inch (12.7 mm) was implemented.

The same hydraulic press and capacitor bank were used for this component as for the curved component. For the forming operation the actuator was bent around the die as shown in *Figure 5*C**.** On the flat side of the part, a steel blank-holder pressed the actuator against the part and inhibited its movement during the process. The curved part of the workpiece and the actuator were pushed into a rubber pad by the press. Thus the actuator was pressed securely against the part, resulting in an efficient forming process

when the capacitor bank was discharged [5]**.** *Figure 5*A shows the complete setup as used during the experiments.

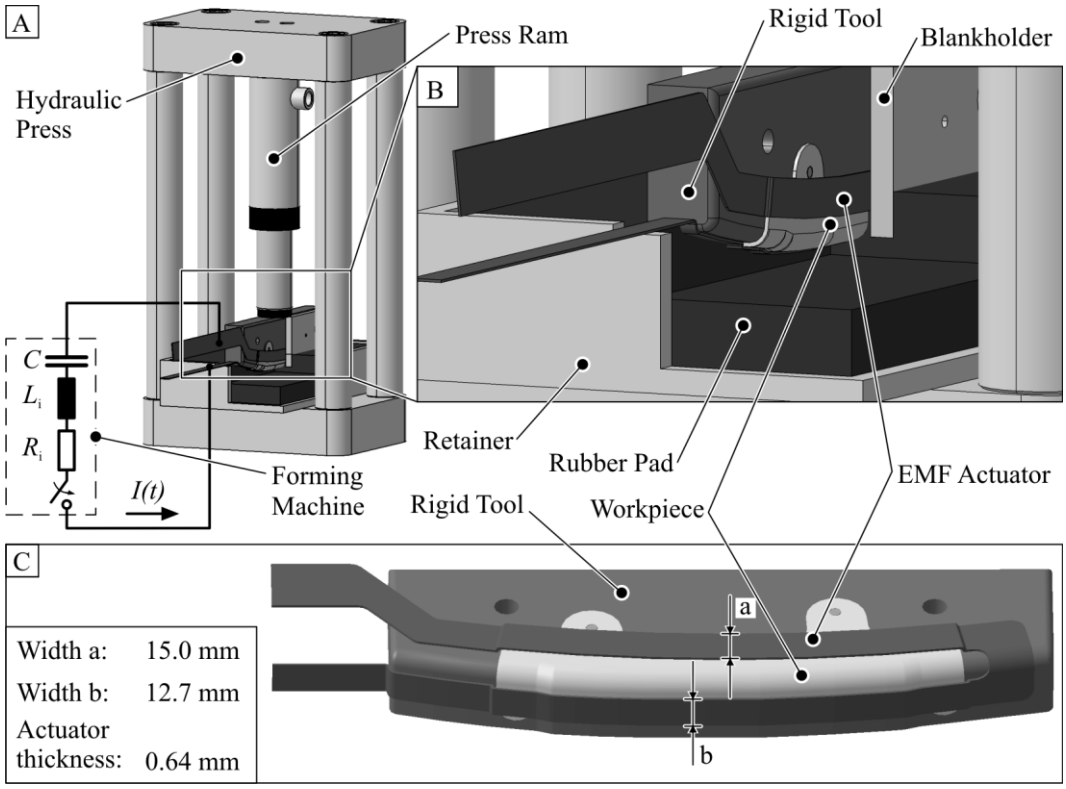

Figure 5: *A) Experimental setup for the flanged component B) Die and part setup in press C) Actuator and part on die surface*

The influence of two parameters was investigated during the experiments: charging energy and tool material. The goal was to find the optimal conditions for each parameter to form the part to specification. After the forming was completed, a laser scanner was used to digitalize the part shape. Distance analysis was then performed to obtain deviation plots showing the distance between matching points on the CAD model and the laser scans, as shown in *Figure 4*C.

4.2 Effect of Disposable Actuators

For disposable actuators it is necessary to consider if the actuator will fail when the capacitor bank is discharged during forming. In the case of the flanged component, it was typical for the actuator to fail during the forming process. The usual area of this failure was at the turn of the actuator. Due to the change in direction of the actuator, the current flow was concentrated close to the inside actuator edge. The higher current density at the inside edge led to increased Joule heating and higher temperatures in this region. As a result, the material strength of the actuator decreased and the magnetic forces caused the material to fail at this weak point. Evidence of the higher temperatures at the actuator turn were the partly melted edges of the inside radius. In most cases the Kapton® tape which covered the actuator withstood the heat and stayed intact. This actuator failure did not affect the finished quality of the formed part.

4.3 Effect of Charging Energy and Tool Material

In Section 2.1 it was described that for the same actuator geometry an increase of the charging energy leads to a higher magnetic pressure. For the electromagnetic calibration it is essential to know the optimum energy to form the desired shape and eliminate the wrinkles that are produced in the preforming step. The correlation of input energy with springback is also important. Since over-bending is the commonly used approach to compensate for springback this information is needed for the die design. Three charging energies were investigated: 4.0 kJ, 4.8 kJ, and 5.6 kJ. For these charging energies, the current through the coil varied between approximately 120 kA and 145 kA, with a frequency of 20 kHz. For these initial experiments the steel tool was used.

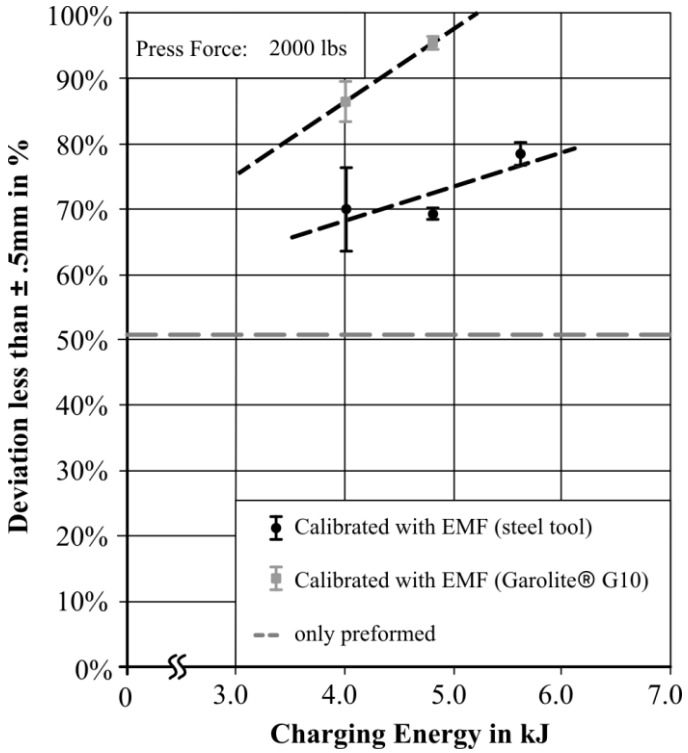

Figure 6: *Percentage of points of the scanned parts with a deviation from the CAD-model between -0.5 mm and 0.5 mm versus charging energy*

Figure 6 shows the relationship between achieved shape and applied charging energy. The quality of the shape is expressed by the percentage of scanned points from the distance analysis that are located within a maximum distance of ±0.5 mm from the target geometry. This is defined as the “deviation”. The dashed line in the diagram is the average value of the parts that were only preformed. The figure shows that an increase in charging energy, and thus an increase in magnetic pressure, will improve the part quality. The larger magnetic pressure was equivalent to a larger forming force, and resulted in a greater reduction in the wrinkles and better formation of the joggles.

Different tool materials could affect the achievable quality of small geometric features and the springback values due to their material properties, such as Young’s modulus, hardness, and damping characteristics. Therefore, knowledge about the influence of the die material is also important for the tool design. Three different tool materials were investigated: alloy 4140 steel which has high stiffness and low electrical conductivity, AA-6061 (T6) aluminum which has high conductivity and still relatively high stiffness, and Garolite® G-10/FR4, which is a glass cloth laminate with an epoxy binder; this material has no electrical conductivity and is by far the softest and best damping

material of the group. 4.0 kJ was chosen as the initial charging energy for these experiments.

Figure 6 shows the results of the realized part quality for the steel and Garolite® G-10 dies. The best results were achieved with the Garolite® G-10 die. Since this tool was relatively soft and its damping characteristics were desirable, it was able to dissipate the kinetic energy of the part quite well, and it is possible that this led to the better springback and rebound behavior as well as the improved shape accuracy which was observed compared to the metal tools. The poorer results of the aluminum tool and steel tool were very similar.

A deviation analysis of a part formed against the Garolite® G-10 die with an increased charging energy of 4.8 kJ is shown in *Figure 7*. This analysis shows that the wrinkling was eliminated, but also shows that humps were formed in the area of the bending radius at the extreme part edges or ends; these defects appear as darker areas in the figure.

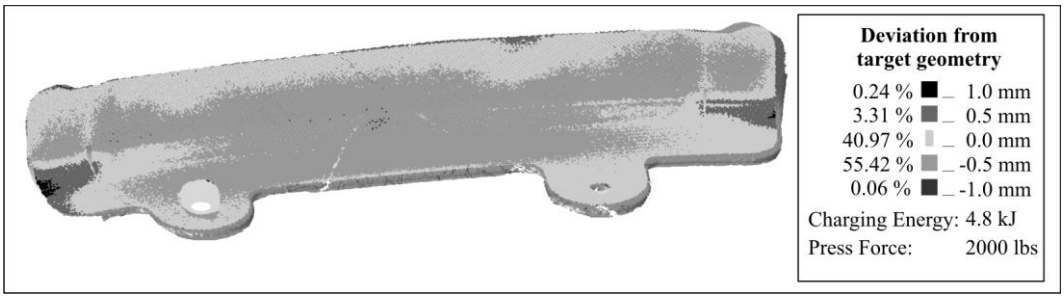

Figure 7: *Percentage of points of the scanned parts with a deviation from the CAD-model between -0.5 mm and 0.5 mm versus part shape*

*Figure 8*A shows the improvements due to the electromagnetic calibration. In this picture a workpiece that was only preformed is compared to a part which was calibrated with the new parameter setup of 4.8 kJ charging energy and the Garolite® G-10 die. This image shows the elimination of the wrinkles and the formation of the joggles along the flange.

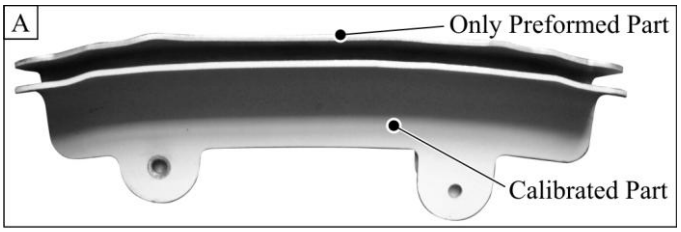

Angle measuring positions:

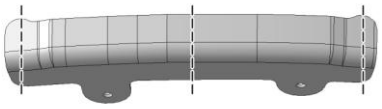

B Charging Energy: 4.8 kJ
Press Force: 2000 lbs

	Left side of the Part	Part center	Right side of the Part
Measured angle before EMF calibration in ° (average)	94	97	95
Measured angle after EMF calibration in ° (average)	90	92	89

Figure 8: *A) Comparison of a part that is only preformed with a part that is EMF calibrated B) Comparison of measured flange angles before and after EMF calibration*

Compared to the two metal tools the springback values of the parts calibrated with the Garolite® G-10 die were reduced significantly. *Figure 8*B shows springback angles measured at three positions along the flange, with an average reduction of the bending angle from 95.3° to 90.3°. The target bending angle was 90°.

4.4 Future Outlook – Exploding Foil Forming

A new method that is currently being explored to form the curved component is exploding foil forming. In this process a thin aluminum foil is connected to a thick copper actuator. When the capacitor bank discharges the current into the actuator, the resulting high current densities in the aluminum cause the foil to vaporize. This results in both a brief electromagnetic impulse as well as the release of a high-pressure shockwave, which serves as the primary forming mechanism.

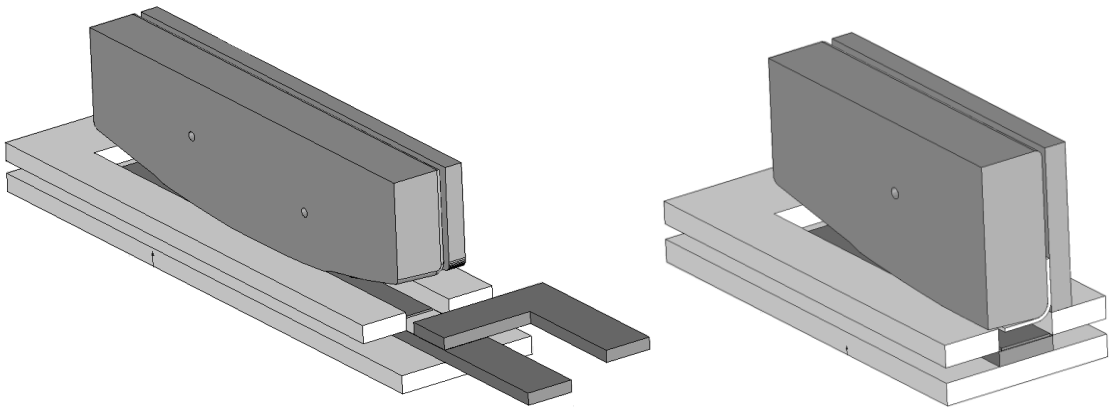

Figure 9: *Experimental setup for exploding foil forming (full and sectioned view)*

The setup for the exploding foil process can be seen in ***Figure 9***. A 0.032 inch (0.813 mm) thick aluminum flyer was used to transfer the pressure from the exploding foil to the part. It must be noted that the foil thickness has a significant role in the effectiveness of the exploding foil method. If the foil is too thin it will vaporize while the current is too low to generate the required shockwave, resulting in pressures that are too low to effectively form the part. If the foil is too thick it will not vaporize quickly enough and the principle forming mechanism will be due to electromagnetic impulse, resulting in a loss of planarity in the flyer and ultimately in a part that is not dimensionally correct [7]. As a result, an optimal coil thickness can be found that is a balance of the vaporization and magnetic impulse effects. Preliminary experiments indicate that the optimum coil thickness is 0.006 inch (0.152 mm), while higher charging energies appear to increase shape quality of the part. The foil and flyer are placed in a Garolite® G-10 channel which directs the shockwave and thus the flyer toward the part, increasing forming efficiency. The part and Garolite® G-10 tool are then pressed down on top of the actuator, foil, and flyer assembly.

The result of exploding foil calibration compared to a part that was only hydroformed can be seen in *Figure 10*. In addition to improvements over the preforming method, the use of the exploding foil process resulted in improvement of the flanged component shape over calibration from electromagnetic forming. The part formed using the exploding foil technique was completely within dimensional tolerances with all defects from the preforming (hydroforming) process removed, and produced comparable results to those achieved with the current production method. This process must be further investigated to determine optimal testing parameters, such as the optimal foil and flyer thickness and material, along with the optimal charging energy. The reliability and repeatability of this method must also be examined.

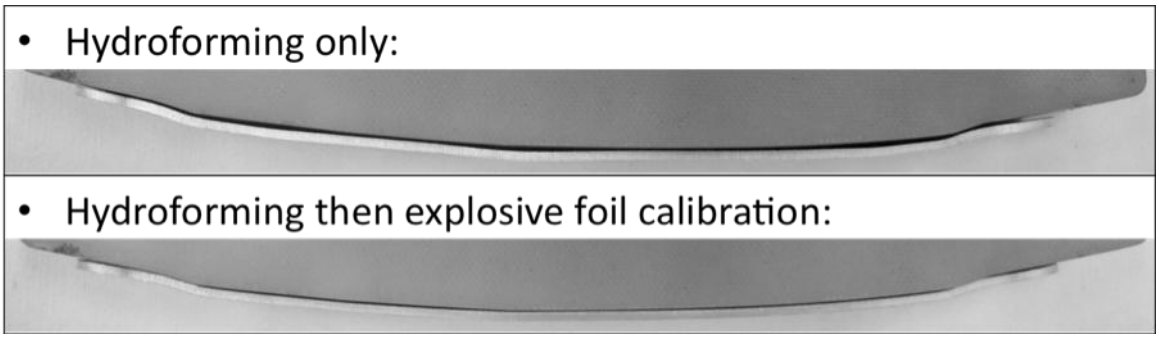

Figure 10: *Comparison of a part that is only preformed with a part that is explosive foil calibrated*

5 Conclusions

This work has shown that electromagnetic calibration with a disposable actuator approach is feasible and that current production processes of curved and flanged sheet metal parts can be improved. It was shown that good forming results were achieved with the EM actuators designed for both part classes. A simple disposable actuator with only one turn and a varied width to optimize the applied magnetic pressure appears to be an effective solution.

While the target radius of the curved component was not achieved, a significant improvement in the formed radius was achieved using electromagnetic forming along with the rubber-pad forming process. Increasing the discharge current or decreasing the actuator width decreased the formed radius of the parts regardless of the actuator design, but reducing actuator width had a limited effect because it only reduces the area affected by magnetic pressure. A maximum of 87% of the springback was eliminated from the part, while an average springback decrease of nearly 82% was achieved. In the future, results could be improved by developing more robust actuators that could achieve higher forming energies and, to a larger extent, by designing new actuators that applied forming force to the central region of the part as well as the edges. Also, the ability of the process to create a consistent curve across the whole part means that there is a possibility of using a die with a smaller radius than that which is desired for the part, and being able to form the part to specification after springback, much like over-bending using conventional forming techniques. Unlike conventional techniques, the careful control of discharge energy can provide an additional level of control on the springback reduction.

The wrinkling of the flanged workpiece resulting from the preforming step was eliminated. It was also possible to form the contour of the curved branch, including the joggles, within the required tolerances. The springback of the flanged part was significantly reduced as well. The complete removal of springback was not possible. Due to an actuator shape that was not completely optimized, there were some bulges at the ends of the best parts produced in this study. These dimensional defects were located at the bending radius. In this study, the best forming results were obtained by forming over a relatively soft Garolite® G-10 tool. The use of this tool material with exploding foil forming was demonstrated to be an improvement over this process. However, further work must be completed regarding this method to improve reliability and reproducibility of the results, as well as further optimization of the process parameters. Even with these challenges, the exploding foil process has shown that a dimensionally correct part can be formed fully in the T6 condition, and that parts formed using EMF or exploding foil techniques can be equivalent to or improve upon those produced using current production methods.

References

[1] *Hatipoğlu, H. A., Polat, N., Köksal, A., Tekkaya, A. E.*: Modeling flexforming (fluid cell forming) process with finite element method. Key Engineering Materials Vol. 344, 2007, 469-476.

[2] *Vohnout, Vincent J.*: A hybrid quasi-static / dynamic process for forming large sheet metal parts from aluminum alloys. Ph.D. thesis, The Ohio State University, 1998.

[3] *Psyk, V., Beerwald, C., Henselek, A., Homberg, W., Brosius, A., Kleiner, M.*: Integration of electromagnetic calibration into the deep drawing process of an industrial demonstrator part. Key Engineering Materials Vol. 344, 2007, 435-442.

[4] *Weimar, G.*: Hochgeschwindigkeitsbearbeitung III Umformung von Blechen und Rohren durch magnetische Kräfte. Werkstatt und Betrieb 96(12), 1963, 893-900.

[5] *Beerwald, C.*: Grundlagen der Prozessauslegung und -gestaltung bei der elektromagnetischen Umformung. Ph.D. thesis, University of Dortmund, 2004.

[6] *Kamal, M.*: A uniform pressure electromagnetic actuator for forming flat sheets. Ph.D. thesis, The Ohio State University, 2005.

[7] *Chau, H.H., Dittbenner, G., Hofer, W.W., Honodel, C.A., Steinberg, D.J., Stroud, J.R., Weingart, R.C., Lee, R.S.*: Electric gun: a versatile tool for high-pressure shockwave research. Review of Scientific Instruments Vol. 51, No. 12, 1980, 1676-1681.

Commercialization of Fuel Cell Bipolar Plate Manufacturing by Electromagnetic Forming *

J. Shang[1], L. Wilkerson[1], S. Hatkevich[1] and G. S. Daehn[2]

[1] American Trim LLC, Lima, Ohio, USA
[2] The Ohio State University, 2041 College Rd, Columbus, Ohio, USA

Abstract

The cost of manufacturing bipolar plates is a major component to the overall cost structure of a Proton Exchange Membrane (PEM) fuel cell stack. To achieve the commercialization of PEM fuel cells, a high volume and low cost manufacturing process for the bipolar plate must be developed. American Trim has identified high velocity electromagnetic forming as a suitable technology to manufacture metallic fuel cell bipolar plates, because of its low capital cost, flexible tooling and rapid prototyping capability. Through the support from the State of Ohio Third Frontier Fuel Cell Program, a group of collaborators consisting of American Trim, The Ohio State University and General Motors have developed a commercially viable prototype production process to manufacture metallic fuel cell bipolar plates in which electromagnetic coils and forming dies were integrated.

To manufacture fuel cell bipolar plates, a metal sheet is accelerated by electromagnetic force to impact against, and take the shape of, the forming die surface. A novel approach which introduces a compliant layer eliminates the need for expendable driver plates in order to reduce the production cost. This process enables continuous manufacturing of fuel cell bipolar plates in short-time cycles at very low cost, which demonstrates strong potential for commercialization.

This paper will introduce the electromagnetic forming process developed to manufacture metallic bipolar plates, and include a discussion of the preliminary results. The benefits of using this high velocity electromagnetic forming process over a traditional stamping press will also be discussed. To commercialize electromagnetic forming, coil life and die wear are being investigated. The results of some preliminary experiments involving coil durability and die wear will also be presented.

---

* *The authors would like to thank the State of Ohio Third Frontier Fuel Cell Program for its financial support.*

Keywords

Manufacturing, Sheet metal, Simulation

1 Introduction

Proton Exchange Membrane (PEM) fuel cells use hydrogen fuel and oxygen from the air to produce electricity, which is one of the most promising power sources in the near future to reduce our dependence on oil and lower harmful emissions [1]. A key component of PEM fuel cells is the bipolar plate, which separates reactant and coolant from one another. Each bipolar plate assembly has two plates known as the cathode and anode, which must be produced separately and joined together later. A fuel cell stack consists of about 500 bipolar plate assemblies. The volume requirements for PEM bipolar fuel cell plates are potentially very large.

The biggest barrier to PEM fuel cells becoming a mainstream technology is their cost. To reduce cost, each component of PEM fuel cells must be analyzed for cost savings potential. One study estimates that the bipolar plates make up about 41% of the cost of a typical PEM fuel cell stack, and the stack is the most costly part of the fuel cell system, at about 42% of the total system cost [2]. Therefore, to achieve the commercialization of PEM fuel cells, the cost of PEM fuel cell bipolar plates must be reduced, and a high volume and low cost manufacturing process for the bipolar plates must be developed.

American Trim, The Ohio State University and General Motors have developed a novel process to manufacture metallic PEM fuel cell bipolar plate by electromagnetic forming. The prototype manufacturing machine has been made, which proves this process is commercially viable. This paper will introduce the principles and the preliminary results of this manufacturing process, and also present the experiment results of the investigation on coil durability and die wear.

2 Background

2.1 Requirements for PEM Fuel Cell Bipolar Plates

PEM fuel cell bipolar plates need significant mechanical strength to maintain clamping forces without leaking. The serpentine channels on the face of plates should be deep and narrow to optimize fuel cell efficiency. Besides, the plates should be relatively thin to minimize mass. Therefore, the functional requirements for the bipolar plates are: (1) strong, light, thin; (2) corrosion resistant; (3) joinable; and (4) formable into complex shapes.

Currently, graphite composites draw lots of interests for PEM bipolar plate manufacturing for their low surface contact resistance and high corrosion resistance. But metals have higher durability to shock and vibration, and are more suitable for high volume and low cost manufacturing, when compared to graphite composites [3]. Among metals, stainless steels are considered as good candidate materials because of their high mechanical strength, good formability, easy manufacturability for complex shapes,

corrosion resistance, weldability and low cost. Therefore, in this development, stainless steel was chosen for bipolar plate manufacturing.

2.2 Possible Forming Methods

There are several methods that can be used to manufacture metallic bipolar plates: machining, hydro-forming, conventional stamping and high velocity electromagnetic forming. Machining bipolar plates from metal block has low production rate and much waste. Compared to hydro-forming, conventional stamping is more capable of high production rate required for high volume and low cost manufacturing process.

Electromagnetic forming is usually applied to accelerate metal sheet to high velocity at a very short period by non-contact electromagnetic forces. During electromagnetic forming, a large electric current pulse passes through a conductive coil by discharging a capacitor bank. The current pulse produces a transient magnetic field around the coil, which induces eddy currents in a nearby metal workpiece. Mutually repulsive forces between the stationary coil and the metal sheet cause the metal sheet to be accelerated toward and impact upon a nearby die surface at very high velocity.

Compared to conventional stamping, electromagnetic forming offers several advantages. First, only single-sided tooling is required, as opposed to a precisely machined matched punch and die set. As shown in Figure 1, the metal sheet impacts a tool only on one side and the other side only receives magnetic pressure [4]. Therefore, tooling cost and complexity are significantly reduced, and the need for precision alignment of upper and lower tools is eliminated. Furthermore, die changes and die modifications are greatly simplified.

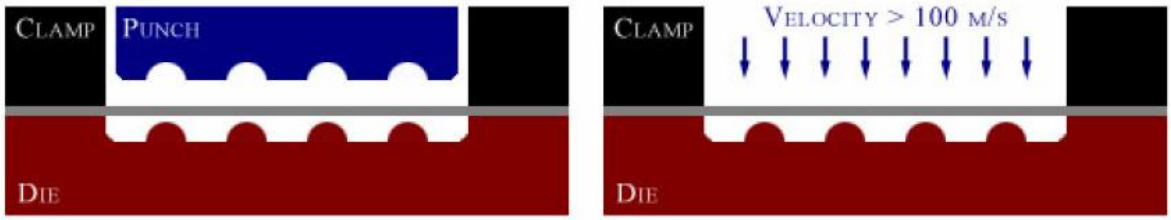

***Figure 1**: Schematic illustrations of conventional stamping (left) and electromagnetic forming (right) [4]*

The second advantage is that much lighter tooling and fixtures can be used in electromagnetic forming. In electromagnetic forming, the large pressure is generated only during high velocity impact between die and metal sheet. Therefore, the tooling and supports need only be sufficient to accelerate and decelerate a metal sheet, which typically has a low mass. The overall forming system can be a fraction of the size used in conventional press systems.

The third advantage is the improved formability. Electromagnetic forming is characterized by very high material velocity and deformation strain rates, which makes it fundamentally different from conventional sheet metal forming. At sufficiently high velocities and/or strain rates, stretching limits are not bounded by the restrictions of a traditional Forming Limit Diagram (FLD). Instead, ductility far beyond typical quasi-static forming limits can be achieved [5, 6]. Therefore, high velocity electromagnetic forming has the potential to improve material formability, and thus to expand the range of candidate materials for a particular application.

2.3 Compliant Layer Electromagnetic Forming

Manufacturing bipolar plate from stainless steel sheet by electromagnetic forming has two major challenges. The first challenge is the low electrical conductivity of stainless steel. Electromagnetic forming has high efficiency for metals with high electrical conductivity, such as Cu, Al alloys. For stainless steel, a secondary driver sheet/plate is needed to generate enough repulsive electromagnetic forces and drive stainless steel sheet to high velocity. This kind of driver plate is usually made of metals with high conductivity and placed between coil and metal sheet. The second challenge is the uniform pressure requirement for bipolar plate manufacturing. Bipolar plate has serpentine channels around the whole parts. This requires the whole stainless steel sheet impact onto the forming die at the same velocity, which needs the uniformly distributed forces on the whole sheet.

The flat spiral coil has a point without magnetic pressure at the center and can not directly provide a uniform pressure on the whole metal sheet [7]. The uniform pressure actuator developed in the Ohio State University can efficiently generate a uniform pressure on the entire metal sheet [7]. But for stainless steel bipolar plates, the uniform pressure actuator demands a thin driver sheet that impacts the forming die together with stainless steel sheet and then deforms together. This deformed driver sheet can not be reusable, which increases the manufacturing cost. American Trim developed a novel approach, compliant layer electromagnetic forming, to eliminate the need for expendable driver plates and also to enable the stainless steel sheet impact the forming die at the same velocity. Figure 2 is the schematic diagram illustrating this approach.

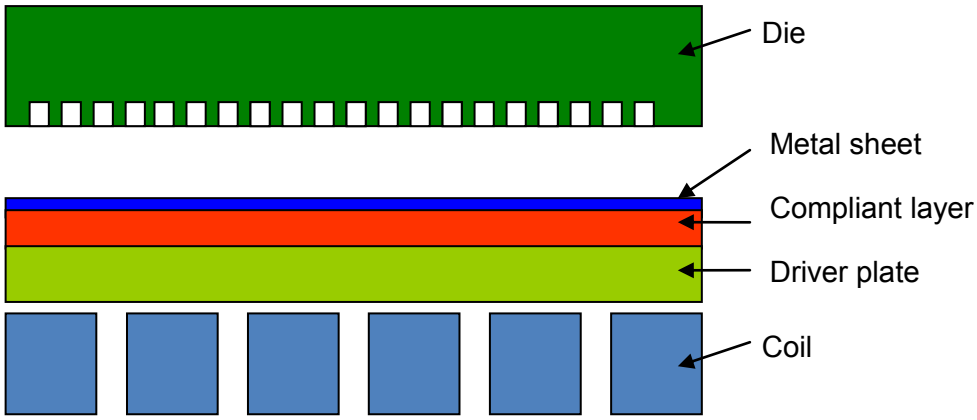

***Figure 2**: Schematic diagram of complaint layer electromagnetic forming*

In compliant layer electromagnetic forming, a thick driver plate made of high conductivity metal is positioned next to the flat spiral coil that is specifically designed according to the size of bipolar plate. A compliant layer made of elastomer materials such as urethane is placed between the driver plate and the stainless steel sheet. The forming die is above the steel sheet and there is a short distance between them. Upon discharge of the capacitor bank, the primary current in the spiral coil and the induced eddy currents in the driver plate produce the repulsive Lorenz force, which accelerates the driver plate together with compliant layer and stainless steel sheet to impact the forming die at high velocity. The compliant layer presses the stainless steel sheet into the die cavity, and also reduces the impact on the driver plate. After impact, the stainless steel sheet is formed to produce a bipolar plate. The driver plate and compliant layer retain their original shape and are ready for the next forming operation.

3 Commercialization of PEM Fuel Cell Plate Manufacturing

3.1 Prototype Machine for PEM Fuel Cell Plate Manufacturing

As described before, the potential volume requirements for bipolar plates are very large, which requires the automation of manufacturing process to improve the production rate. Compliant layer electromagnetic forming needs only single-sided tooling which remains stationary during the manufacturing process. This simplifies many aspects of the forming process, and eliminates considerations such as the alignment of matched tool sets, which makes it easy to apply automation for the manufacturing process. Figure 3 is the automation concept of bipolar plate manufacturing by electromagnetic forming. During the production, the stainless steel strip is fed continuously from one strip coil to the other strip coil, passing horizontally through the electromagnetic forming system that consists of capacitor bank, electromagnetic coil and forming die. In capacitor bank discharging, the strip stops, and the section of the strip between the coil and the forming die is deformed into a bipolar plate by electromagnetic forming. Then the deformed section moves away horizontally along the fixture, and another section of the strip moves in for next forming.

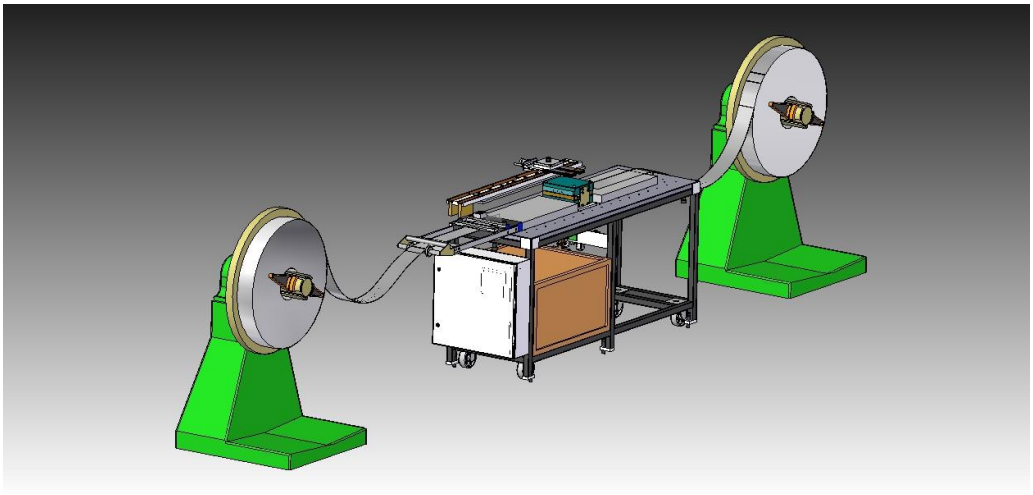

***Figure 3**: Automation concept of bipolar plate manufacturing by electromagnetic forming*

Based on the automation concept in Figure 3, American Trim has developed the prototype machine for sub-sized bipolar plate manufacturing by compliant layer electromagnetic forming. Figure 4 shows the photo of this prototype machine. In this machine, a capacitor bank is located in the left lower corner of the frame. And the flat spiral coil, the thick driver plate, the compliant layer and the forming die are placed at the upside section of the frame. The strip horizontal movement and the capacitor discharging can be all programmed to speed up the process. Using this prototype machine, the production rate reaches 5 seconds per plate, which demonstrates the commercial viability of this manufacturing process. Figure 5 is the bipolar plate strip formed by the prototype machine.

***Figure 4**: Prototype machine for bipolar plate manufacturing by compliant layer electromagnetic forming*

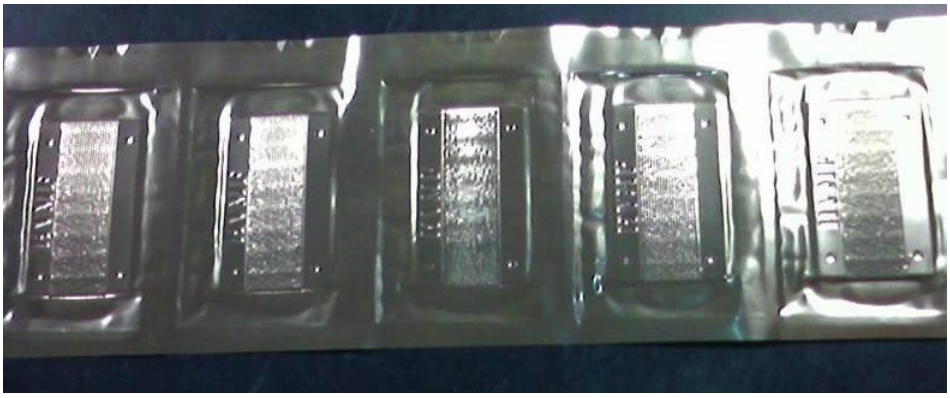

***Figure 5**: Bipolar plate strip formed by the prototype machine*

3.2 Preliminary Results

Compliant layer electromagnetic forming was applied to manufacture sub-sized bipolar plate. Figure 6 is the photo of the forming die used in bipolar plate manufacturing. The size of the die is 78.5mm x 63 mm. Figure 7 is the laser scan profile of the forming die along X line shown in Figure 6. The channel depth of the forming die was measured as 311 μm. Using this die and the compliant layer approach, a ferritic stainless steel 439 sheet with 0.1 mm thickness was deformed at 9 kJ energy input. Figure 8 is the laser scan profile of the formed bipolar plate along X line. The channel depth was measured as 260 μm, and reaches 87% of the channel depth of the forming die.

The energy input has large effect on the channel depth of the formed parts. The higher the energy input, the deeper the channel depth of the formed parts can reach. In the future experiments, an energy input larger than 9 kJ is planed to apply, in order to improve the channel depth.

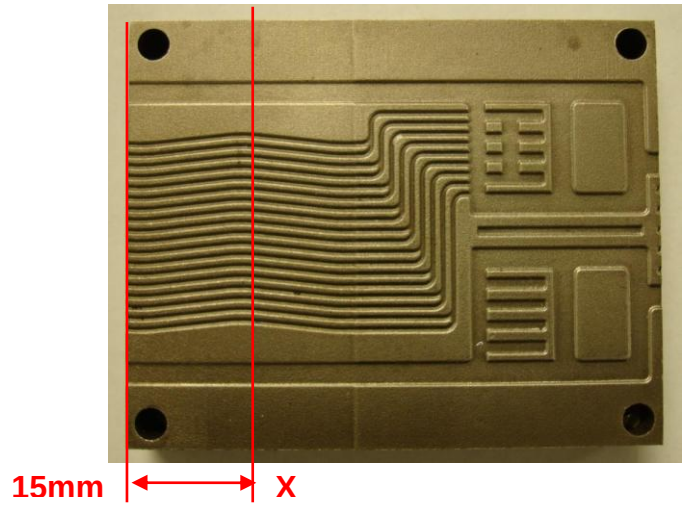

***Figure 6**: Photo of the forming die used in bipolar plate manufacturing (size: 78.5mm x 63mm)*

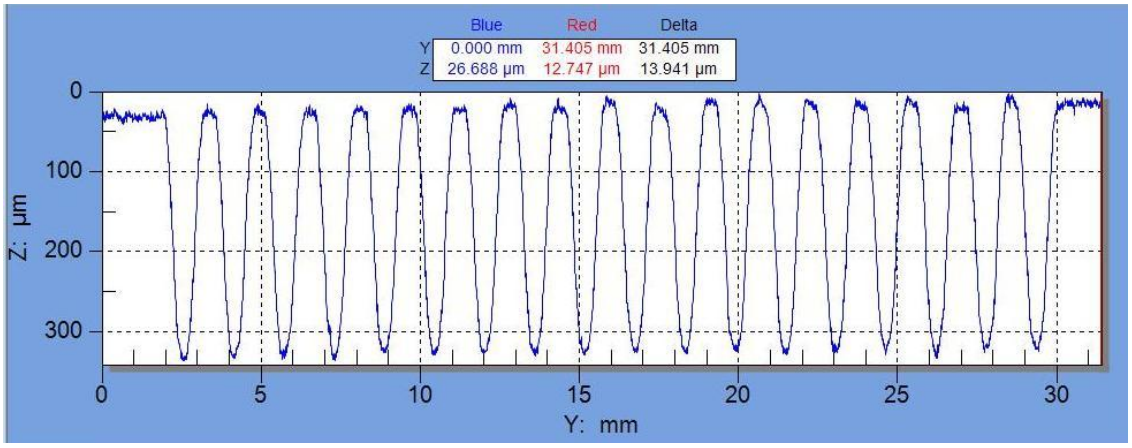

***Figure 7**: Laser scan profile of the forming die used in bipolar plate manufacturing*

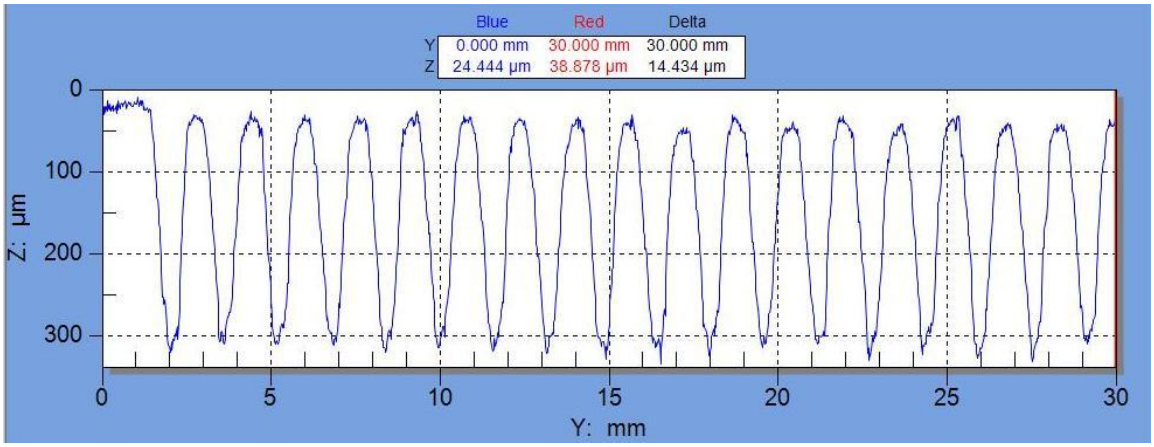

***Figure 8**: Laser scan profile of the formed bipolar plate by compliant layer electromagnetic forming (439SS with 0.1 mm thickness and 9 kJ energy input)*

3.3 Coil Durability and Die Wear

Besides of the production rate, the durability of forming system is important to the production cost and the commercialization of bipolar plate manufacturing. The electromagnetic coil and the forming die are two major components in the forming system. And their durability was investigated in this development.

During electromagnetic forming, repulsive forces are applied on the spiral coil and cause the coil to rebound from its initial position. Large deflections will reduce the coil life and affect the electromagnetic forces on the driver plate. The flat spiral Cu coil was applied in the compliant layer electromagnetic forming. The coil was embedded into a G10 Garolite block, and covered with a 1.0mm thick G10 Garolite sheet that serves as the insulation between the coil and the metal driver plate. Initially, the thin G10 sheet was flat. After over 500 electromagnetic forming operations, the flatness of the G10 sheet was checked by laser scanning along Y line shown in Figure 9. Figure 9 indicates that the maximum deflection is 0.24 mm, which is insignificant compared to the coil size (the coil thickness is 12.5 mm).

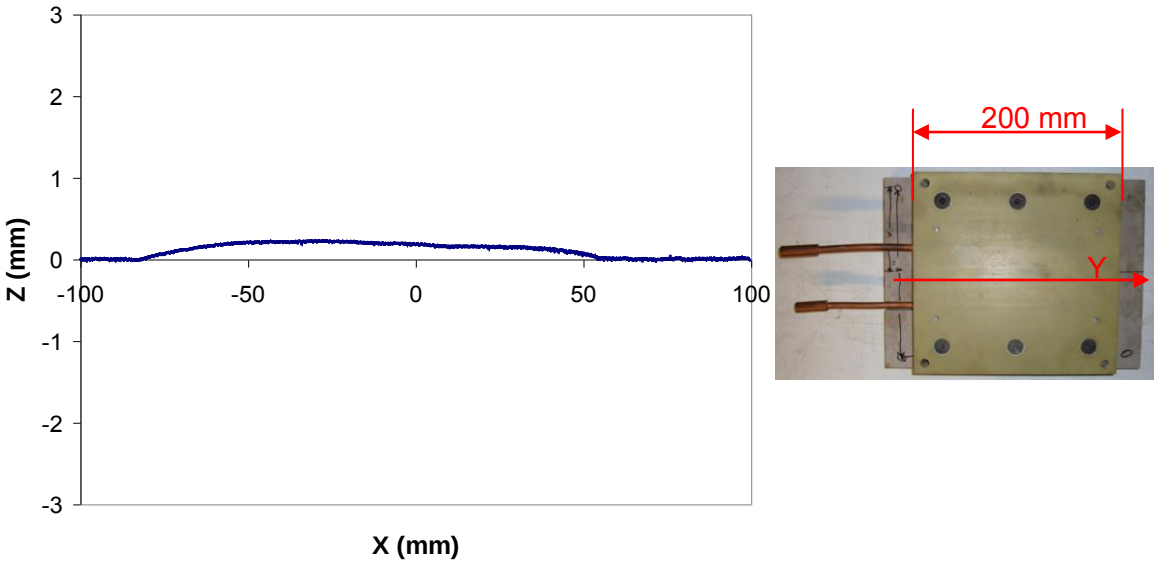

***Figure 9**: Laser scan profile of the top of the flat spiral coil along Y line after 500 hits*

For the forming die, the high velocity impact of stainless steel sheet onto the die will cause the die wear. Considerable die wear will make the dimension of bipolar plate inaccurate. In this development, the forming die was made of A2 tool steel. To investigate the die wear, the forming die was scanned by the laser profilometer before and after over 500 times of impact. Figure 10 is the comparison of the scanning results, which shows that there is no significant difference between these two scan profiles.

Above results indicate that there are no significant changes in the flat spiral coil and the forming die after over 500 electromagnetic forming operations. Therefore, the durability of the coil and the die wear are sufficient to commercialize the bipolar plate manufacturing.

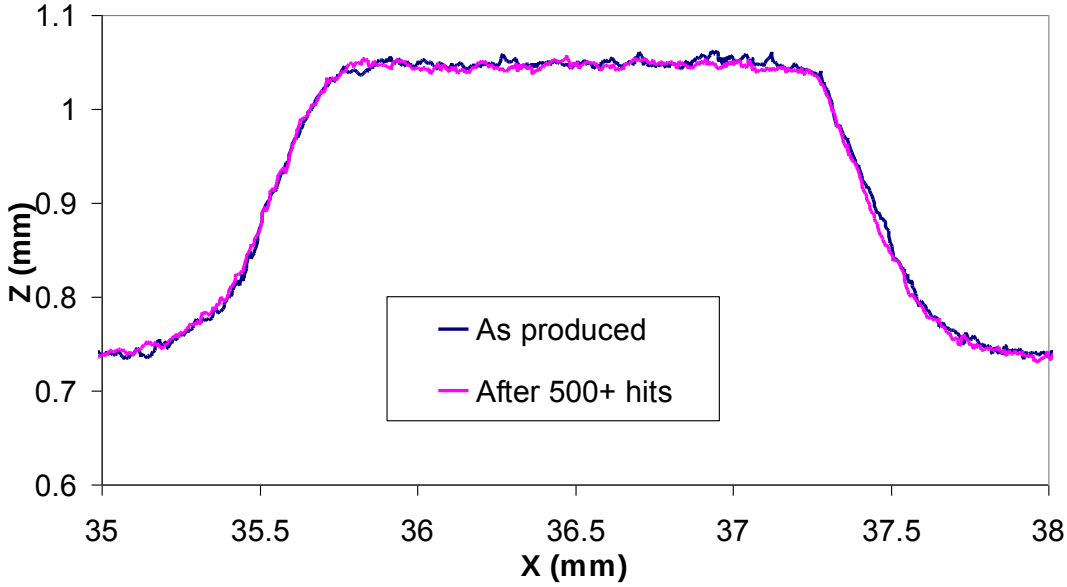

***Figure 10**: Comparison of laser scan profiles of one channel of the forming die*

3.4 Challenges of Electromagnetic Forming Commercialization

Overall, the preliminary manufacturing results and the durability investigation are encouraging. But there are still several challenges for the commercialization of bipolar plate manufacturing by electromagnetic forming.

(1) The prototype machine can be used to form the sub-sized bipolar plates. The process has to be scaled up for full scale bipolar plate manufacturing.

(2) More work is needed to improve the channel depth of the formed parts to reach the target channel depth, which includes the optimization of energy input, compliant layer properties, coil design, driver plate geometry and distance between stainless steel sheet and the forming die.

(3) Higher energy input and more electromagnetic forming operations are needed for the durability study on coil life, die wear and compliant layer life.

(4) Thermal management for the coil and the driver plate should be investigated, since the large currents in the coil and the driver plate generate resistance heat and then cause their temperatures increase.

4 Summary

A novel process, compliant layer electromagnetic forming, has been developed in American Trim to manufacture the PEM fuel cell bipolar plate. In this process, elastomer compliant layer and thick driver plate are introduced to eliminate the need for expendable driver plate and to accelerate the metal sheet to high velocity. A prototype machine was successfully developed to manufacture sub-sized PEM fuel cell bipolar plate by this process. By 9 kJ energy input, the channel depth reached 87% of the target channel depth. In addition, the 5-second cycle time was achieved using the prototype machine. The durability investigation shows that the coil life and the die wear are sufficient to commercialize the bipolar plate manufacturing process.

The preliminary results are encouraging, and demonstrate the above bipolar plate manufacturing process is commercially viable. To commercialize the full scale bipolar plate manufacturing, further development is required.

References

[1] *Wind, J.; Spah, R.; Kaiser, W.; Bohm, G.:* Metallic bipolar plate for PEM fuel cell, Journal of Power Sources, 105, 2002, p.256-260.

[2] *Kamarudin, S.K.; Daud, W. R. W.; Som, A. Md.; Takriff, M. S.; Mohammad, A. W.;* Technical design and economic evaluation of a PEM fuel cell, Journal of Power Sources, 157, 2006, p.641-649.

[3] *Tawfik, H.; Hung, Y.; Mahajan, D.:* Metal bipolar plates for PEM fuel cell – A review, Journal of Power Sources, 163, 2007, p. 755-767

[4] *Golowin, S.; Kamal, M.; Shang, J.; Portier, J. et al.:* Application of a uniform pressure actuator for electromagnetic processing of sheet metal, Journal of Materials Engineering and Performance, 16, 2007, p 455-460

[5] *Daehn, G. S.:* High Velocity Metal Forming, in ASM Handbook, Forming and Forging, 2006

[6] *Seth, M.; Vohnout, V.; Daehn, G. S.:* Formability of Steel Sheet in High Velocity Impact, J. Mater. Process. Technol., 168, 2005, p 390–400

[7] *Kamal, M.:* A Uniform Pressure Electromagnetic Actuator for Flat Sheet Forming, Ph.D. Dissertation, The Ohio State University, 2005

SESSION 2
ELECTROHYDRAULIC FORMING

Investigation of the Electrohydraulic Forming Process with respect to the Design of Sharp Edged Contours*

W. Homberg[1], C. Beerwald[1], A.Pröbsting[1]

[1] Chair of Manufacturing and Forming Technology (LUF), Paderborn University, Paderborn Germany

Abstract

The overcoming of design constraints with respect to forming of sharply contoured sheet metal workpieces made of high strength steel or other materials which are difficult to form is an important aspect in sheet metal part production. One interesting solution to extend existing forming limits can be the use of electrohydraulic forming as single forming operation or in combination with quasi-static hydroforming. Apart from promising results regarding the feasible part geometries this process allows a quite efficient production due to its potential to reduce equipment expenses.

Current research work at the Chair of Forming and Machining Technology (LUF) at Paderborn University deals with a comparison of investigations on both processes, quasi-static and high speed hydroforming. Recent results show an adequate comparison of achievable edge radii using an oblong die geometry and sheet metal made of thin stainless steel. It can be seen that when using electrohydraulic forming an increase of discharge energy leads to smaller radii than achievable by quasi-static hydroforming.

An additional potential can be seen in the process characteristic itself because the very short pressure pulse allows a significant reduction of locking forces using only the inertia of the tooling mass.

Keywords

Hydroforming, near net-shaped contouring/radius, high-speed hydroforming

---

* *This work is based on the results of a cooperation with the Poynting GmbH; the authors would like to thank the Poynting GmbH for the substantial support.*

1 Motivation

Requirements regarding the part design and the necessity of an economic realization lead to high demands on multifunctional parts with very complex geometries. Especially the demands regarding surface quality, producibility of sharp contours, and accuracy are difficult to meet by conventional forming processes like deep drawing. This becomes a serious problem when using high strength materials. A promising solution could be the use of special processes like (conventional) quasi-static hydroforming, high speed forming, or a combination of both. Conventional hydroforming allows the production of complex workpieces with favourable properties even when high strength materials are used [1]. Unfortunately, there is a high working media pressure necessary for the forming of sharp contour elements which increases with material thickness and strength. Consequently, very high expenses regarding the machine and tools are necessary [1]. On the other hand, high speed forming processes allow the manufacturing of complex geometries even when high strength materials are used because of a better use of the material formability or the special process characteristics [2]. But high speed processes have some constraints e.g. regarding the production of large scale components (electrohydraulic forming), security (explosive forming), or the material (electromagnetic forming) [3-8]. So a promising solution could be the combination of quasi-static and high speed forming processes. That is why comparative research work regarding a combination of conventional and high speed hydroforming processes is performed at the LUF at Paderborn University. The basis of this research work is a detailed analysis of the properties of the single processes.

2 Experimental setups

2.1 Hydroforming

Conventional quasi-static hydroforming was used as reference process for the comparison of conventional and high speed hydroforming processes. Therefore, a tool setup consisting of a die, intermediate plate, and pressure intensifier (p_{max}<400 MPa) was used (**Figure 1**). The tool was mounted inside of 8000 kN hydraulic press for applying the necessary locking force.

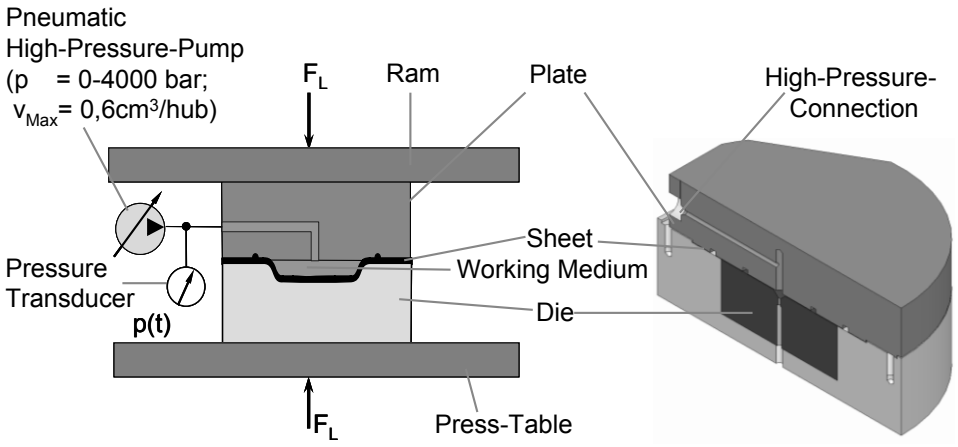

***Figure 1**: Experimental Setup for the hydroforming of thin sheet metals*

2.2 High-Speed-Hydroforming Setups

After a detailed analysis and valuation of principles for the generation of short pressure pulses for the deformation of sheet metal parts four promising methods were selected.

These methods were subject of intensive research work regarding course and result of the forming process, feasibility, achievable part properties, and expenses. Therefore, two different electrohydraulic experimental setups, one electromechanical and one pneumomechanical, have been realized (**Figure 2**).

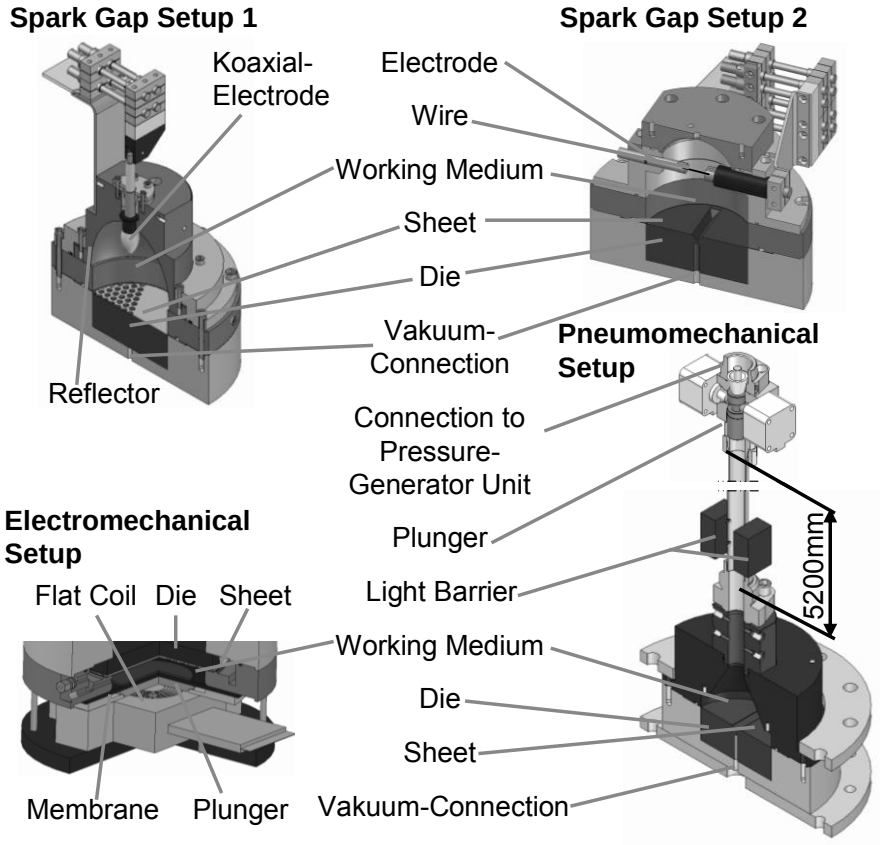

Figure 2: *Assortment of experimental setups for the generation of pressure pulses in a working medium*

The electrohydraulic setups consist first of all of a capacitor, a switch, and an underwater spark gap which was mounted inside of a closed container or tool. The maximal charging energy was 5.6 kJ. The difference between the two setups is the use of a thin wire for easier ignition in the second setup (**Figure 3**) and the use of a reflector for focussing the shockwave in the first setup.

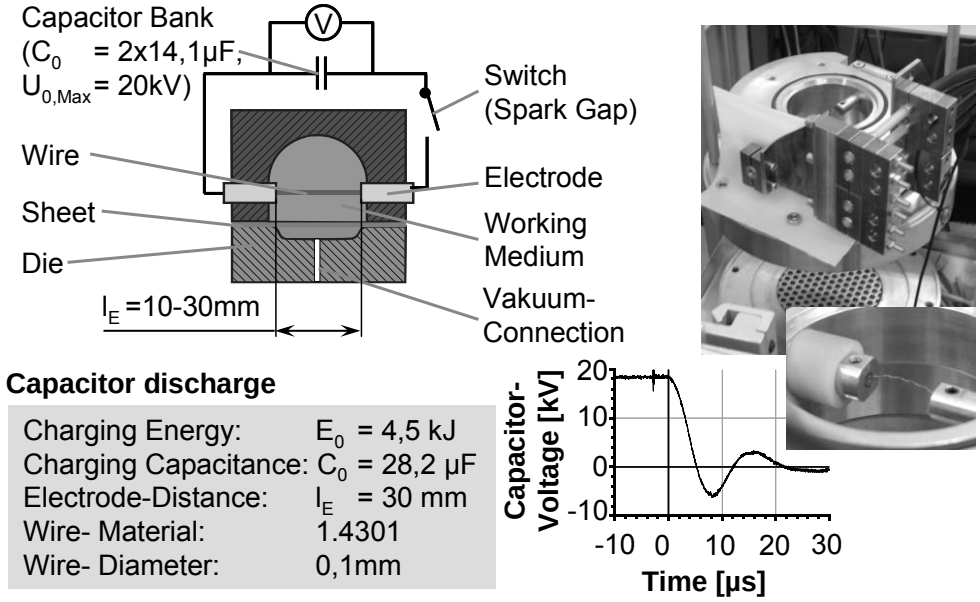

Figure 3: *Basic process cycle of the electrohydraulic forming process*

The electromechanical setup uses a flat coil (connected with a high current switch and a capacitor) to accelerate a plunger (**Figure 4**). The plunger movement causes a pressure pulse suitable for the desired forming operation. The maximal charging energy in this setup was 1.5 kJ.

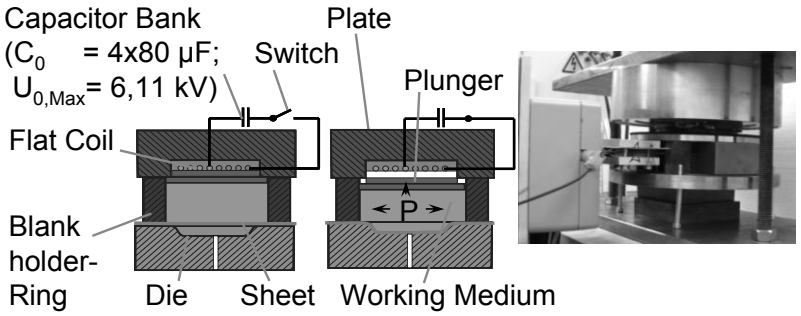

Figure 4: *Experimental setup with an electromechanical generated pressure pulse*

The fourth experimental setup which has already been investigated is a pneumomechanical setup where the pressure pulse is generated by the impact of a pneumatically accelerated plunger into a working media reservoir (**Figure 5**) [9], [10]. The experiments were conducted on the setup shown in **Figure 5** which had an acceleration tube made of steel with a length of 5200 mm, an outer diameter of 38 mm, and an inner diameter of 33 mm. The maximum energy that can be achieved with this setup is currently limited to 1.4 kJ.

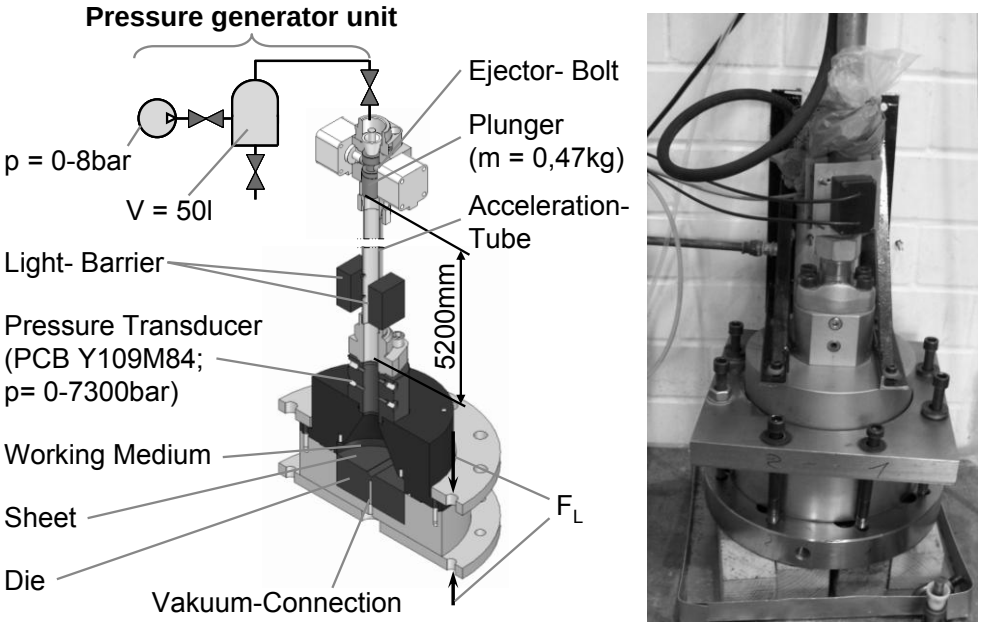

***Figure 5**: Pneumomechanical setup*

3 Technological Research Work

Focus of the technological research work concerning a comparison of conventional and high speed hydroforming was first of all the examination of pressure distribution and effects on the workpiece during the process. After that, the forming of strongly contoured workpieces with difficult geometrical details was subject of intensive research work. As demonstrator geometry a v-shaped groove with a wall angle of 90° and a width of 15 mm was selected. This geometry was chosen being comparable to a sharply contoured geometry element of body in white structures. To realize the desired sharply edged bottom radius with only small acceptable geometry deviations is a demanding forming task. A production using conventional deep drawing processes is extremely difficult and only possible with high expenses. A better solution is the use of hydroforming processes which allow the manufacturing of such parts at a better quality. But there are strong differences of workpiece behaviour and forming result using high speed or quasistatic hydroforming processes. During the according experiments workpieces made of aluminum, mild steel, and stainless steel were produced using the electrohydraulic, the pneumomechanic, and the conventional hydrofoming process. Therefore, within the scope of the series of experiments the sheets were deformed by increasing the pressure or energy from experiment to experiment. Subsequently, the geometry of the workpieces was measured.

The experiments showed that the manufacturing of sharply contoured workpieces is most conveniently feasible using electrohydraulic processes (**Figure 6**). The results of the quasistatic hydroforming experiments show that an increasing fluid pressure leads to a decreasing radius as expected. The minimal radius which could be realized by quasistatic hydroforming experiments was 1.75 mm. The required pressure of the working media was 2600 bar. The results of the electrohydraulic forming process show that the increasing charging energy leads to decreasing radii. Here, a much smaller radius of 0.8 mm could be achieved by a discharge energy of less than 6 kJ. Thus, with the help of this process e.g. the manufacturing of workpieces with smaller edge radii was possible compared to conventional hydroforming.

The experiments proved that high speed forming processes require dramatically smaller expenses for machines and equipment. So, for the conventional quasistatic hydroforming process a locking force of up to 6200 kN was necessary compared to 200 kN for high speed hydroforming. A disadvantage at this time was the occurrence of geometry deviations (edge radius and workpiece height) over the groove length. The reduction of those deviations is subject of current research work using improved process strategies.

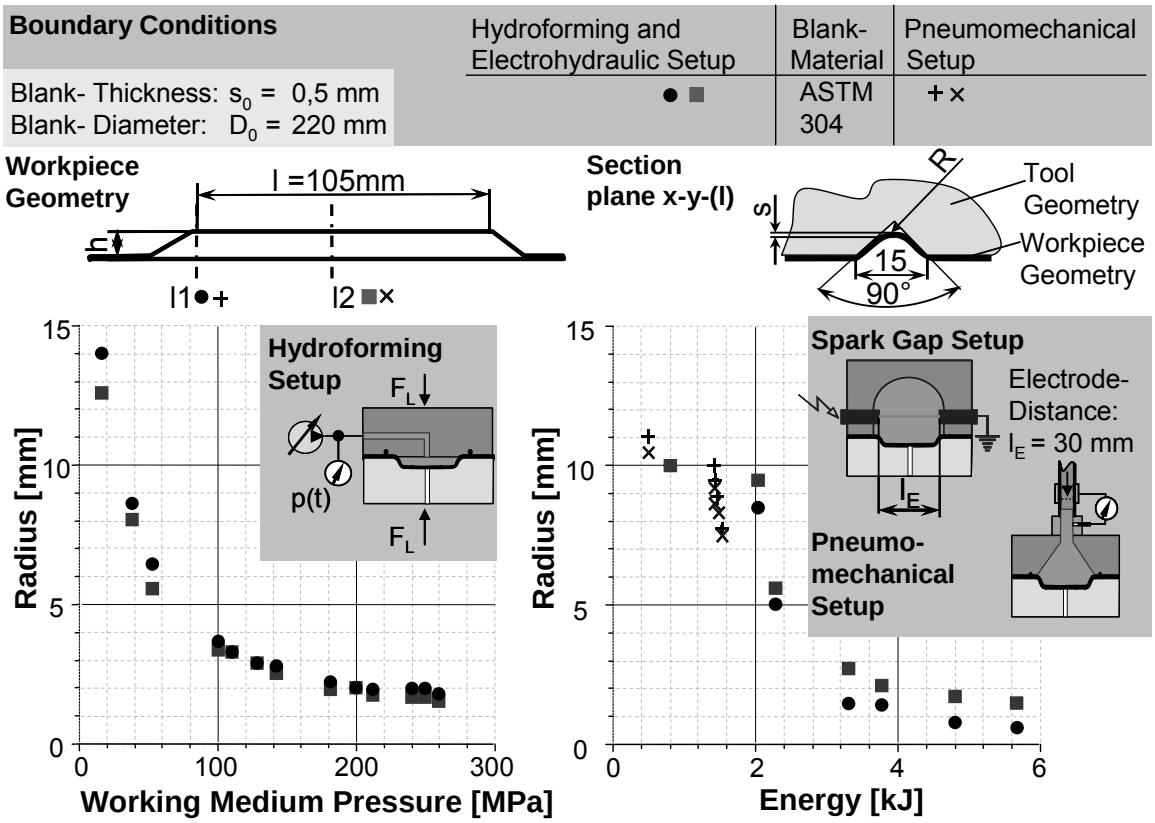

Figure 6: *Main influence on the achieved radii depending on increasing pressure and energy*

References

[1] *Kleiner, M.; Beerwald, C.; Homberg, W.:* Machine Tools and Process Strategies for Sheet Metal Hydroforming. Proc. of the 9th int. Conf. On Sheet Metal, 2-4 April 2001, Leuven, Belgium

[2] *Neubauer, A.; Schmicker, H.; Schmidt, E.:* Investigations to the influence of temperature at explosive sheet metal forming. CIRP Annals, Volume 39, Issue 1, 1990, p. 257-261

[3] *Winkler, R.:* Hochgeschwindigkeitsbearbeitung – Grundlagen und technische Anwendung elektrisch erzeugter Schockwellen und Impulsmagnetfelder. VEBVerlag Technik, Berlin, p. 307-333, 1973

[4] *Daehn, G. S. Balanethiram, V. S.:* Hyperplasticity: Increased Forming Limits at High Workpiece Velocity. Scripta Metallurgica et Materiala 30 (1994) 4, p. 515-520. ISBN/ISSN: 0956-716X

[5] *Cole, R.H.*: Underwater Explosions. Princeton University Press, 1948

[6] *Suzuki, H.*: Forming Process by Combustion, Electric Discharge and Electromagnetism (Japanese). Met. Technol. 56 (1986) 7, p. 56-62

[7] *Kleiner, M.; Beerwald, C.; Homberg, W.:* Analysis of Process Parameters and Forming Mechanisms within the Electromagnetic Forming Process. CIRP Annals - Manufacturing Technology, Volume 54, Issue 1, 2005, Pages 225-228

[8] *Woetzel, M.; Löffler, M.J.; Spahn, E.; Ritter, H.:* Preliminary examination of high-velocity metal-shaping with electrical wire explosion. 1st Euro-Asian Pulsed Power Conference, 18.-22.09.06, Chengdu, China, 2006

[9] *Tominga, H.; Takamatsu, M.:* Hydropunch, a pneumatic-hydraulic-forming machine. 2. International Conference of the Center for High Energy Forming, Estes Park, USA 1969

[10] *Kosing, O.E.; Skews, B.W.:* The use of liquid shock waves for metal forming. 21st International Symposium on Shock Waves, Great Keppel Island, Australia, 1997

Pressure heterogeneity in small displacement electrohydraulic forming processes

V. J. Vohnout[1], G. Fenton[3] and G. S. Daehn[2]

[1] Bemidji State University, 1500 Birchmont Dr., Bemidji, Minnesota, USA
[2] Ohio State University, 2041 College Rd, Columbus, Ohio, USA
[3] Applied Research Associates.,4300 San Mateo Blvd.,Albuquerque, New Mexico, USA

Abstract

Electrohydraulic (submerged arc discharge) forming of sheet metal parts has been used as a specialized high speed forming method since the 1960's. The parts formed generally had a major dimension in the 5 to 25 cm range and required gross metal expansion in the centimeter range. In the descriptions of this process found in the literature, the pressure front emanating from the initial plasma generated by the arc is considered to be uniformly spherical in nature. At least one commercial system used this model to design hardware for pressure front focusing to optimize the forming process[1] and it has been the subject of continued research [2].

Recently, there has been commercial interest in adopting the electro-hydraulic method for the production of much smaller parts requiring very high die contact pressures but little gross sheet expansion. The forming of these small shallow parts required only a few kilojoules but proved to be problematic in other terms. The process development clearly showed indications of random patterns of large pressure heterogeneity across distances in the millimeter range. The apparent pressure heterogeneity produced unacceptable small scale variation in the part geometry.

A test program was designed to verify and quantify this effect using a target (die) consisting of a flat plate having small closely spaced holes. This 50 mm diameter target proved very effective in clearly showing the extent of the heterogeneity as well as the approximate local pressures. Various discharge energies were investigated along with different chamber shapes and pressure transfer mediums. The pressure heterogeneity across the target face was a common feature to all experiments. These test results indicate that a uniform pressure front model can be seriously in error for the electro-hydraulic process as implemented to date. The results of a qualitative hydro-code model of the test system including the discharge event are presented. The model results are similar enough to the experimental to imply that the coaxial electrode's inherent off center discharge is a primary suspect among potential explanations for the observed heterogeneity in terms of asymmetric shock interaction. The absence of this phenomena in the earlier electrohydraulic forming literature is also discussed.

Keywords

Forming, Pressure, Electro-hydraulic

.

1 Introduction

High Speed Forming, (also referred to as High Rate Forming) of sheet metal parts has been in limited use by various industries since the 1960's. The advantages of the different methods of High Speed forming are well know and published. The advantages include extended formability and high level of surface detail replication. In the United States, early electrohydraulic systems for High Speed Forming lost favour among the user community possibly due to the added complexity of the fluid medium of pressure transfer and or problems with inconsistent results. The simpler and cleaner Electromagnetic process of High Speed Forming became the dominate method especially for axisymmetric crimping and swaging. More recently, electromagnetic High Speed Forming has been demonstrated to be an effective means of generating larger parts, up to automotive body panel scale, of aluminium with difficult geometry [3,4]. A common characteristic of these aluminium parts is a large plastic deformation requirement, for which High Speed Forming has a known advantage. However, there is a large class of smaller parts that require only modest plastic deformation but a high level of small scale detail such as small radii and surface embossing. High Speed forming has known advantages for this class of parts also. Unfortunately, the less gross deformation required, the greater the need for a uniform pressure distribution generated by the system "actuator" method. In the electromagnetic process, traditional coil design can generate undesirable witness marks of the high pressure areas on the part immediately over the coil path. This coil image is not entirely washed out by subsequent plastic deformation as it would be for large deformation parts. A solution to this problem, called a uniform pressure actuator was developed by one of the authors at the Ohio State University [5]. The uniform pressure actuator however shares the major short coming of all electromagnetic driven High Speed Forming which is the requirement for a work piece of acceptable electrical conductivity. Many high value parts with small features and specific surface finish are also of materials of low conductivity such as stainless steel and titanium. The use of a high conductivity flyer plate (sheet) can be used to advantage for these parts but practically only for low production custom parts. This situation was a major impetus for a re-examining of a hydraulic method of High Speed Forming. These methods have no work piece conductivity requirements while being well capable of generating the requisite forming pressures. Pressure distributions were generally assumed to follow from an assumed spherical wave front generated by the expanding plasma bubble. This assumption has been shown useful in the general practice to date.

An electrohydraulic method for a manufacture process program for a small medical device made of a titanium alloy was considered a good application. It was during this process development effort, that the extreme pressure heterogeneity was identified [6]. Perhaps this is a rediscovery but a search of the available literature on electrohydraulic forming did not uncover any discussion of the phenomena. This paper presents the results of a short investigation to further illuminate the nature, origin and possible amelioration of the undesirable pressure heterogeneity.

2 Description of the test system and process.

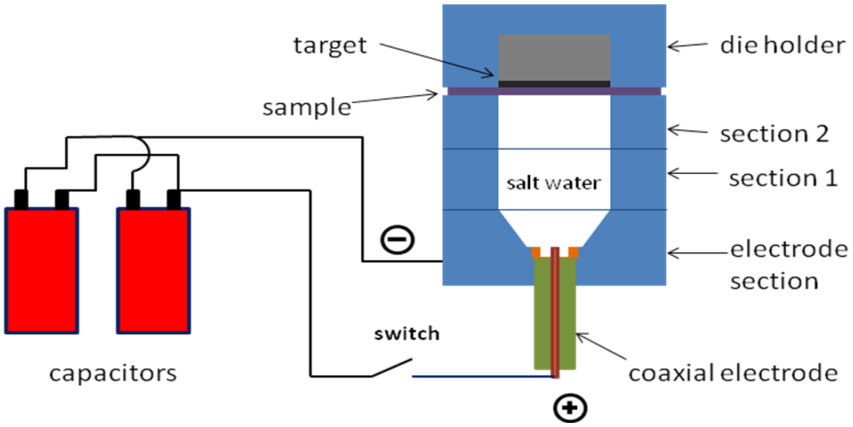

Figure 1: *Electrohydraulic test system schematic: chamber sections 1 & 2; 58mm inside diameter x 38mm long*

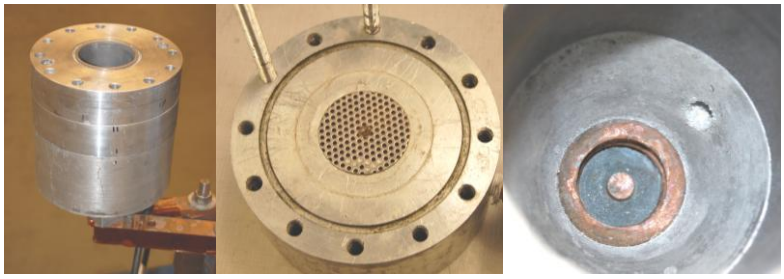

(a) (b) (c)

Figure 2: *The electro hydraulic test system , a) without target section, b) target section, c) coaxial electrode*

The coaxial electrode provided an arc length of 6.4mm which in the salt water medium reliably generated an arc at potential voltages of 5.0 kilovolt. The voltage was kept below 7 kilovolt for these experiments to minimize insulation breakdown problems. Note a coaxial electrode's arc is always off center. This was not initially considered an issue.

The target grid of Figure 2b is a piece of commercial perforated stainless steel sheet with 2.4 mm diameter holes on 3.8 mm centers. Not allowing deformation of the sample except at the grid holes proved to be a very inexpensive and effective means of recording the pressure distribution across the target face as can seen in Figure 3. The sample material is 6016-T4 , 1.0 mm thick aluminium sheet having an average yield strength of 123. MPa and an average ultimate strength of 223. MPa. The lower bound estimate of the pressure required to generate the hole can be found using equation (1) based on a simplified punch piercing relation from reference [7]

$$\text{Pressure} = P = S\pi Dt/(\pi D^2/4) = 4St/D \qquad (1)$$

Where: S= material shear strength t= material thickness, D=hole diameter

The minimum pressure at the sheared out grid holes, for the sample material, is given by eq. 1 as 227 MPa (33 ksI).

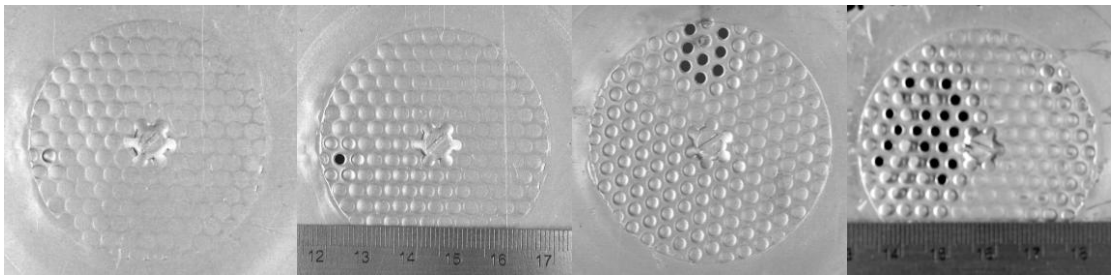

(a) (b) (c) (d)

Figure 3 Four test samples at four discharge energy levels a) 1.5 KJ(@120 µF*), b) 3 KJ(@120* µF*), c) 4.5 KJ(@120* µF*), d) 6 KJ(@240* µF*),*

Experiments were conducted at 1.5, 3.0, 4.5 and 6.0 KJ with bank capacitance of either 120 or 240 µF (one or two capacitors). The current-time traces followed the typical logarithmically damped sine function having a first half wave amplitude that varied from 40KA to 70KA with a rise time of 7-10 µsec. Experiments were also conducted using an insert which changed the conical volume of the electrode holder section into a 25 mm diameter right circular cylinder 25 mm long. Notable in Figure 3 is that the pressure distribution at 1.5 KJ had a lower peak pressure but not significantly more uniform than the higher discharge energies.

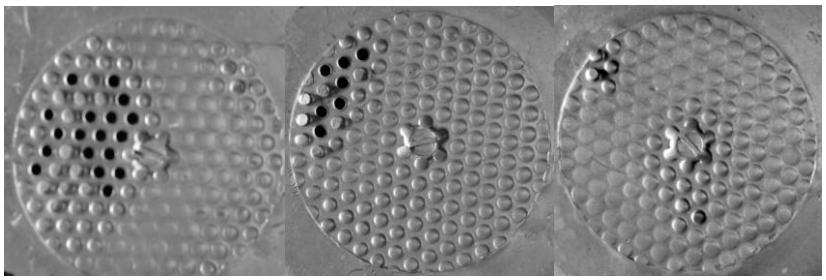

(a) (b) (c)

Figure 4: *Effect of chamber geometry change at constant 6KJ (@240* µF*) discharge; a) one spacer, b) two spacers, c) two spacers and electrode section, cone insert.*

Figure 4 qualitatively illustrates a pressure distribution variation with gross chamber geometry variation for a constant discharge energy. The basic variability of the pressure distribution for fixed process parameters is shown in Figure 5. All four samples resulted from 3KJ discharges using a two section chamber.

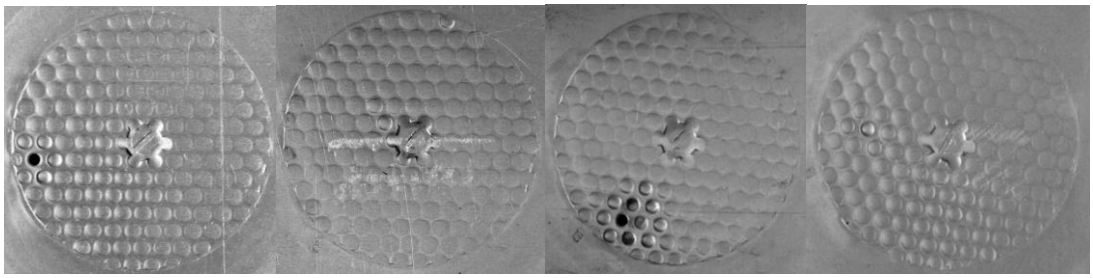

Figure 5: *Samples from four experiments using 3 KJ (@120* µF*) discharge energy in the two section chamber*

Figure 5 indicates that pressure “hot spots” can occur in a seemingly random manner under seemingly constant process parameters. Comparing Figure 5 with Figure 4 reveals that the extent of the “hot spot” generally increases with discharge energy. However, the localized nature, seen in the abrupt change from slight dimpling to shear-out, is evident at 3 and 6 KJ discharge levels. The experimental results of Figures 3 to 5 are consistent with those for the medical device component process reported in reference [6].
In addition, reference [6] provided evidence of an arc streamer from the electrode to the sample which was also seen in the experiments of this paper as shown in Figure 6.

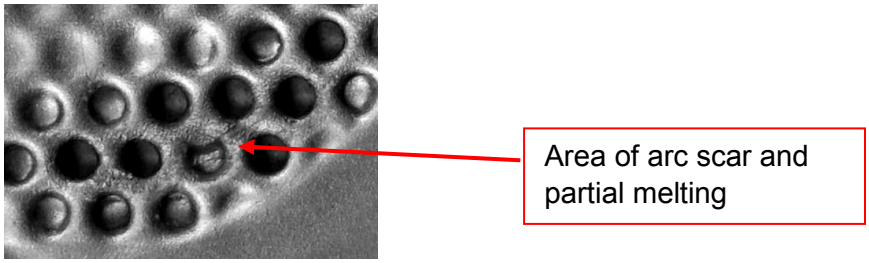

***Figure 6**: Evidence of arc streamer contact with sample*

A 25mm thick natural rubber plug was placed in the chamber such that it contacted the sample. The plug was closely fit to the chamber internal diameter but not otherwise constrained. The plug served to eliminate the very high pressure localizations but did not entirely eliminate the observable asymmetric pressure variations as seen in Figure 7

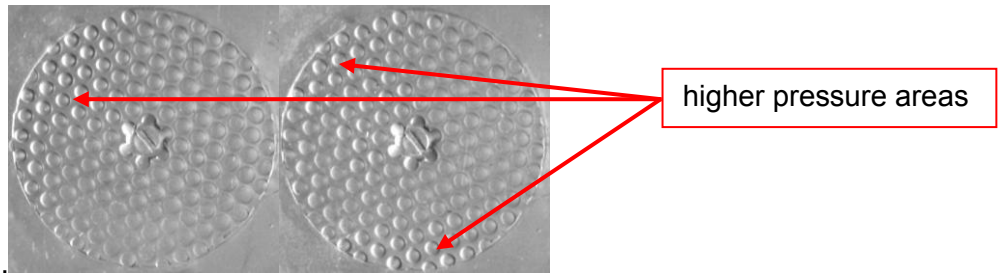

***Figure 7:** Two samples subjected to 6 KJ(@240 μF) discharge with an intervening 25 mm thick natural rubber pad.*

The nature and pattern of the pressure heterogeneity displayed in the results of theses experiments and those reported in reference [6] are certainly consistent with well known effects of the interactions of reflected shock waves. A simple numerical model of the test apparatus was used to investigate the influence of chamber geometry and the radial location of the discharge event in relation to the central axis of the chamber.

3 Numeric model of the experimental system

The model employed a multi-material, large deformation, strong shock wave, solid mechanics code called CTH**,** developed at Sandia National Laboratories. CTH has models for multiphase, elastic-viscoplastic, porous, and explosive materials. CTH numerically solves the partial differential equations describing the conservation of mass, momentum,

and energy. It does this in a structured Eulerian mesh fixed in space and uses equations of state (EOS) to close the coupled system of equations. CTH is capable of predicting cavitation in fluids as the result of events such as the submerged arc discharges of the experiments presented in this paper.

3.1 Numerical Model Geometry

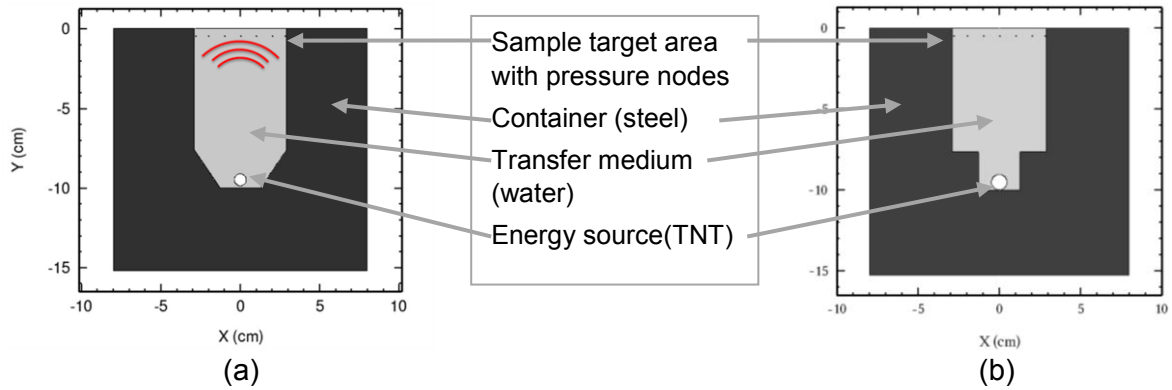

Figure 8: *Schematic of the CTH model geometries and component materials, (a) original, (b) with electrode section insert*

For simplicity, the energy source was modelled as a small mass of TNT that would release about 3 KJ of energy when ignited. The main difference between an explosive shock pulse and the electrically generated shock is the shape and duration of the generated pulse. The explosive completes its detonation burn within ~1.0 μsec. compared to the average electric arc pulse rise time of 8.5 μsec. The model input was about 3/4 of a gram of TNT which has an energy density of 4184 J/g. Compared to the arc discharge the explosive will generate a less dispersive shock wave. A higher amplitude, but shorter duration shock providing the same energy input is generated. The intent of the explosive is to provide a shock in lieu of an electric spark. The shock structure will be different and this difference has effects on the target end, but is useful in a qualitative sense. The main focus is to illustrate how the shocks interact within the structure in terms of qualitative effects not quantitative levels or values.

Two chamber geometries were modelled. The original two section chamber shown in Figures 1 and 8a and a second where the truncated cone volume at the electrode bottom end was replaced by a simple cylindrical volume of the same diameter as the electrode (~ 25mm), Figure 8b. Each geometry was run with two discharge location inputs. One at the bottom center of the chamber and another with the discharge off center by 6 mm. The charge offset represented the nominal center location of an arc generated in the annulus gap of the coaxial electrode shown in Figure 2c. The centered discharge case was run as a 2D axisymmetric model whereas the offset discharge case required a full 3D model.

3.2 Numerical model results

Graphical results of the CTH model solutions are presented in Figures 9, 10 and 11 Comparison of Figure 9 with Figure 10 clearly shows a significant pressure distribution asymmetry due to the 6mm offset of the discharge event.

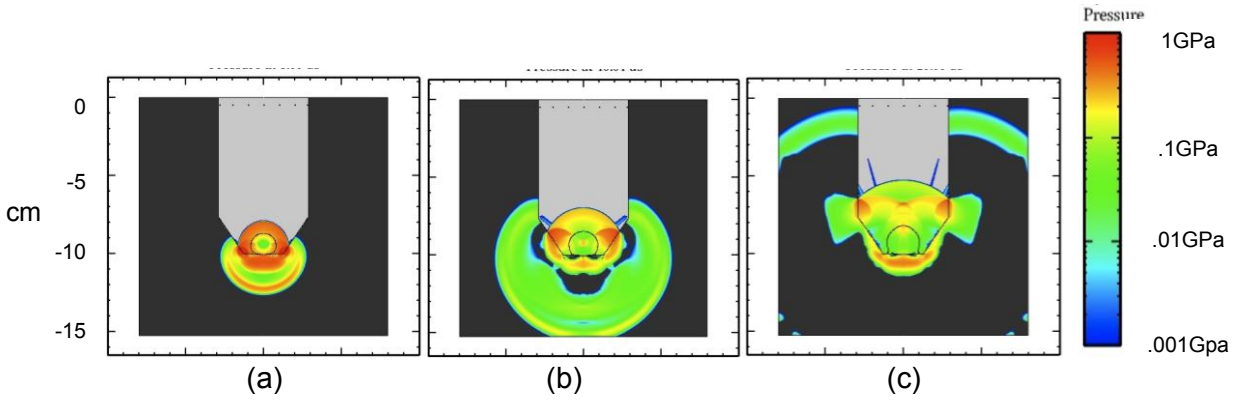

Figure 9: *Pressure – time history for symmetric case ; a) 5 µsec, b) 10 µsec c) 20 µsec*

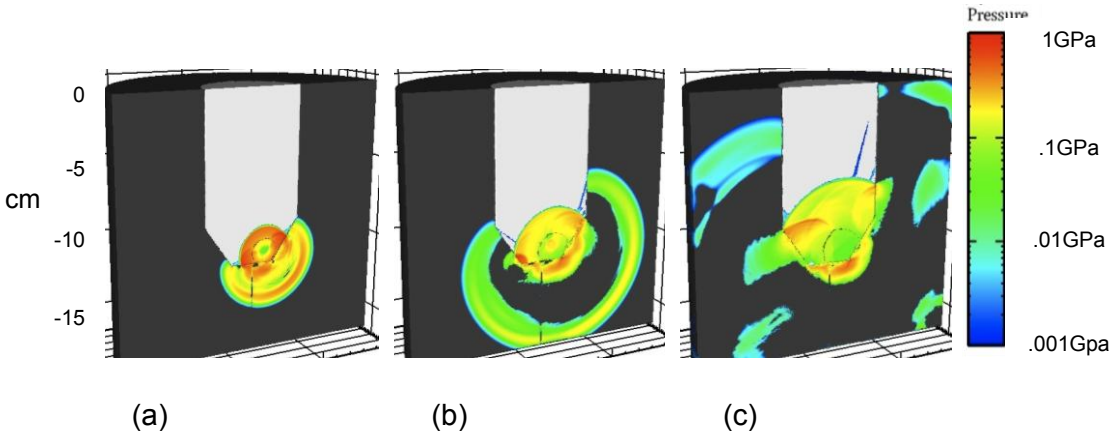

Figure 10: *Pressure – time history for asymmetric case ; a) 5 µsec, b) 10 µsec c) 20 µsec*

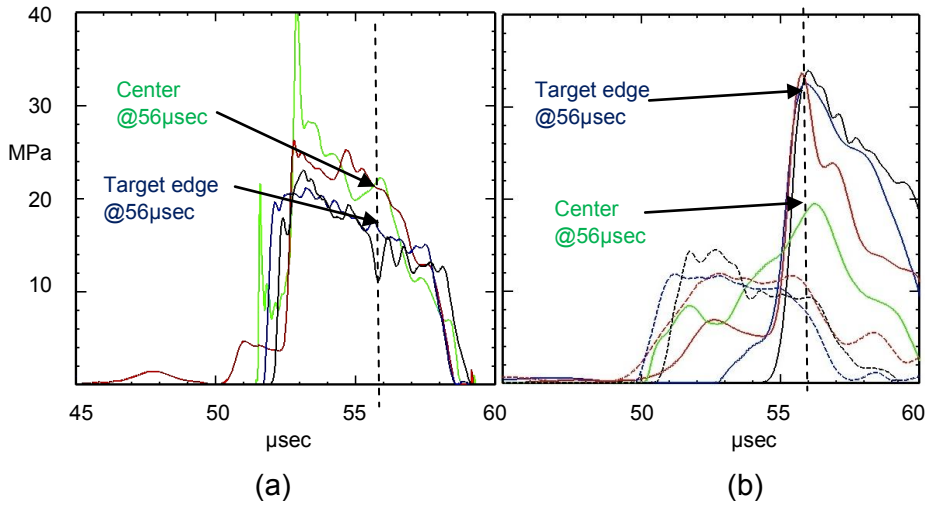

Figure 11: *Pressure-time histories at the model tracer nodes, a) symmetric case, b)asymmetric case*

The second model geometry simulated the effect of the straight cylindrical volume at the electrode end of the chamber. The simulation results are presented in Figure 12. Inspection of the graphs in the figure reveals a generally lower and more uniform pressure distribution for the asymmetric discharge in comparison to the original chamber geometry. The higher pressures change sides during the asymmetric shock impingement event

(Figure 12b). The left side pressures being greater than the right side up to 55μsec and the right hand node pressures are considerably greater than the left side beyond 60μsec. Figure 12a, the symmetric case displays a series of high pressure spikes at the center node at 60μsec which are considered to be cavitations. No evidence of cavitations was seen in the asymmetric simulations or in the experiment samples.

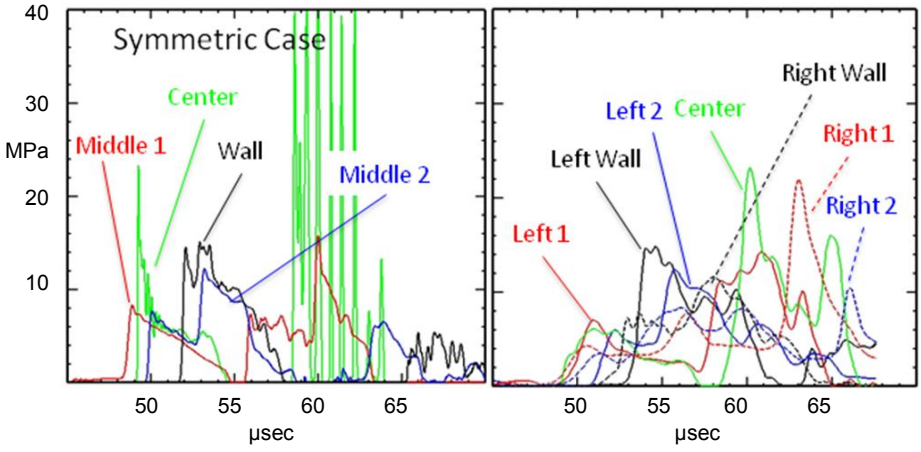

(a) (b)

Figure 12: *Pressure-time histories at the model tracer nodes in the second chamber geometry, a) symmetric case, b)asymmetric case*

The two samples shown in Figure 13 were generated at 4.5 and 6 KJ using the chamber geometry described by Figure 8b e.g. two chamber sections and a cylindrical volume at the electrode.

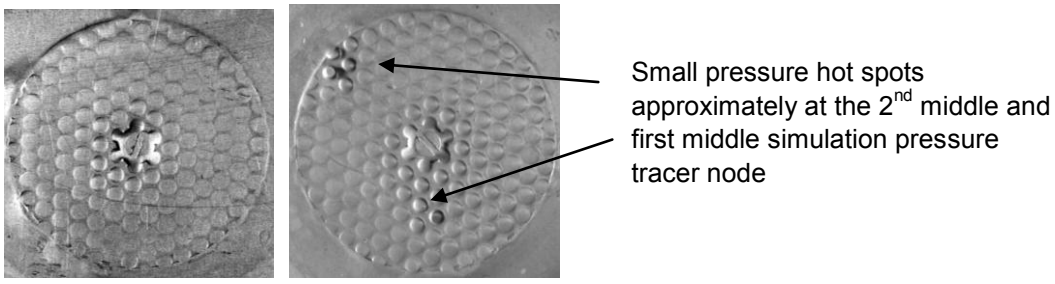

(a) (b)

Figure 13: *Two samples generated using Figure 8b chamber geometry using a) 4.5KJ (@120* μF*) discharge and b) 6 KJ (@240*μF*) discharge.*

Figure 13 appears to corroborate the results of the simulation of the second chamber geometry. With the exception of the small hotspots, the pressure distribution is more uniform than for the 6KJ samples from the original geometry chamber which is also consistent with the simulation results. Whether this agreement would be maintained for a larger sample size is an unanswered question in this investigation.

4 Summary and Conclusions

This investigation into extreme pressure heterogeneity in electrohydraulic pulse forming replicated the results described in Reference [6]. Specifically areas of a 50 mm diameter sample experienced pressures in excess of that required to shear out the 2.4 mm target grid holes (>230 Mpa) while adjacent areas, a millimetre or two away experiences pressures sufficient only to raise a slight bump at the target grid holes. This effect, to a greater or lesser degree, persisted over a span of discharge energy levels from 1.5 to 6 KJ and for chamber depths of 25, 63 and 100 mm.
The introduction of a 25mm thick natural rubber plug attenuated the heterogeneity considerably. Similar results were obtained by changing the chamber geometry at the electrode from a truncated cone diffuser geometry to a cylinder of the same height and a diameter just sufficient to accommodate the coaxial electrode.

A simplified numerical model of the experiment was built using the CTH code from Lawrence Livermore Labs with the intent of obtaining qualitative insights into the prime cause of the pressure heterogeneity. The results from the simulations were qualitatively consistent with the experimental results. From the simulation output it was seen that the original geometry was quite sensitive to off center discharges in terms of generating heterogeneous pressure distributions. The main culprit in the process appears to be the coaxial design of the electrode. Coaxial electrodes are sturdy and have good erosion properties but can not practically generate a centered discharge. Experiments and simulation results using the smaller cylindrical discharge volume at the electrode end of the chamber indicate that a extended variation of this geometry having a greater aspect ratio may be effective in reducing the pressure heterogeneity to acceptable levels. The other alternative is, of course, to design an electrode system that can reliably generate the discharge arc at the center line of the chamber without disturbing/occluding the initial arc plasma bubble. It may also prove productive to seek both chamber and electrode designs that can produce an appropriately uniform pressure front at the work piece. Additional changes to the system, which were not investigated were degasification of the water and inverting the chamber. Electrohydraulic systems with the fluid and electrode above the work piece has been utilized without reports of the pressure heterogeneity described in this paper. However, the complex nature of the shock wave nucleation and interaction with reflections from the chamber geometry should be acknowledged in all cases. These shock interactions clearly may render a system utilizing only fluid as the pressure transfer medium inherently too heterogeneous in terms of target pressure distribution unless large plastic deformation is the goal. For parts requiring only modest plastic deformation but high definition, a system wherein any pressure heterogeneity is absorbed and smoothed by an intervening elastomeric since that material does support cavitations. The experimental results shown in Figure 7 using the natural rubber insert provide evidence that this may be another productive approach.

The principal impetus behind this investigation is the desire to harness the advantages of high speed forming for materials ill suited to electromagnetic methods utilizing the main component of electromagnetic forming; the capacitor bank. The electrohydraulic approach used in these experiments and those of [6] have the potential advantages of relative low cost, compactness and shared capital equipment with electromagnetic methods. However, the observed extreme pressure heterogeneities reported in this paper will need

to be controlled or eliminated before the method can be productively applied to the targeted class of parts. e.g. high definition, low gross deformation parts of low electrical conductivity. That the results reported here are not explicitly available in the previous literature on high speed, electrohydraulic forming can be attributed to the simple fact that large plastic deformation was the goal of the early work. Large deformation would tend to obliterate any initial pressure heterogeneity especial after die contact.

5 References

[1] *Cadwell, G. C*, Electro-hydraulic metal working, Proc. 2nd International Conference of the Center for High Energy Forming, Estes Park, Colorado, June 23-27,1969

[2] Hasebe,T., Takenaga, Y., Kakimoto,H., Imaida, Y., High strain rate forming using an underwater shock wave focusing technique, Journal of Material Processing Technology, Elsevier 1999

[3] *Vohnout,V. J. ; Daehn, G. S.; Shivpuri*, *R. ,* A hybrid quasi-static-dynamic process for in creased limiting strains in the forming of large sheet metal aluminum parts", Proc. 6th Internation. Conference on Plasticity Technology, Nuremburg, Germany, Sept. ,p.19-23, 1999

[4] *Daehn, G.S. ; Shang, J; Vohnout, V.J:* Electromagnetically assisted sheet forming: enabling difficult shapes and materials by controlled energy distribution" in Energy Efficient Manufacturing Processes, *Fourth MPMD International Symposium on Global Innovations*, I. Anderson, T. Marechaux, and C. Cockrill, editors, TMS San Diego, p. 117-128, (2003).

[5] *Kamal, M.; Daehn, G.S.,* A uniform pressure electromagnetic actuator for forming flat sheets. J of Manuf. Sci. and Eng.*,* **129**, pp. 369-379, (2007).

[6] Johnson-Morke, L, Presentation at IIFG meeting in Bilbao, Portugal, May, 2009

[7] Mielnik, E. M.: Metalworking science and engineering. McGraw-Hill , New York, 1991, pg 707

Measurements of Pressure Fields with Multi-Point Membrane Gauges at Electrohydraulic Forming

M.K. Knyazyev, Ya.S. Zhovnovatuk

National Aerospace University "KhAI" named after M.Ye. Zhukovskiy, Kharkiv, Ukraine

Abstract

Success of electrohydraulic forming (EHF) process depends on coincidence of the needed pressure field with the field generated by discharge chamber at sequent stages of sheet blank deformation.

Impulse loading at high-voltage discharge has a very complicated character and involves many phenomena: direct shock waves, hydraulic flows, quasi-static pressure of gas bubble, reflected shock waves, cavitation, secondary shock waves, etc. Also internal shapes of a discharge chamber, design and location of electrodes have a great influence on pressure distribution along blank surface. Because of these features, the simulation of EHF processes is very complicated task to be solved for chambers equipped with single electrode pair. And difficulties are increased greatly for simulation of multi-electrode discharge blocks (MDB). First of all, reliable data on pressure distribution at various discharge conditions are necessary to reveal and describe influence of each factor of impulse loading.

Multi-point membrane pressure gauges (MPG) give an opportunity to obtain pressure maps with high resolution at relatively low cost. By design MPG typically consists of body plate with large number of small holes and sensitive element – metallic membrane. Deformation of membrane in each point (hole) can be measured and recalculated into pressure. Totality of many pressure points allows plotting a pressure map. MPGs are better suitable for measurement of shock-waves pressure. For this purpose the holes diameter and membrane thickness should be specified in such a manner that membrane is sensitive only to shock waves.

Combination of MPG measurements with piezoelectric sensors can give full information about pressure map changing in time. These data could be a good basis for simulation of impulse loading with approximation formulas and also could be used as a check data for the simulation programs based on theoretical relationships.

Initially the method based on MPG application was designed for investigations and improvements of discharge chambers with various forms of internal (reflecting) surfaces, electrodes position and their shapes, influence of design features on pressure distribution.

Vast experimental investigations were carried out with MPG application for typical single-electrode-pair discharge chambers (conical and parabolic) and multi-electrode discharge blocks.

Keywords

Impact Forming, Measurement, Distributed Pressure, Sheet metal, Membrane Pressure Gauge

1 Introduction

Simulation of processes of electrohydraulic impact forming (EHF) needs experimental determination of fields of impact loading along sheet blank surface with regard to its change in time.

Creation of models based only on theoretical description of loading impact often gives results inadequate to real loading conditions. In order to obtain more exact results the mathematical model should be corrected with the experimental data.

Application of piezo-electric sensors gives information about parameters of shock waves in time that is very essential for modeling the processes of impact loading and deformation of sheet blanks. But for obtaining the detailed loading map along large area the large quantity (several hundreds and even thousands) of piezo-electric sensors is needed. Complexity of organization of measurements with large quantity of sensors, high cost of piezo-electric sensors and measurement instruments result in impracticability of such experimental task.

Multi-point membrane pressure gauges (MPG) well suit to the task of measurement of pressure fields along large area. They are characterized by design simplicity and low cost. By design MPG typically consists of body plate with large number of holes and sensitive element – metallic membrane. However, by its nature, MPGs record integral action of all factors of impact loading generated by high-voltage discharge in a liquid: shock waves, hydraulic flows, quasi-static pressure of vapor bubble in closed discharge chambers. Action of pressure impact is recorded in the form of membrane deflection (residual plastic deformation) on places (points) of holes in a gauge body. Deformation of membrane on each point can be measured and recalculated into pressure. Totality of many points allows plotting a pressure map. Magnitude of membrane deflection is proportional to maximum (peak) value of a pressure impact, its duration and membrane parameters. That is, membrane gages give information about pressure impact combined in one parameter – membrane deflection.

Initially MPGs were applied for estimation of energy portions in blank deformation delivered by shock wave, hydraulic flow, quasi-static pressure, as well as for determination of maximum capabilities and pressure distribution for discharge chambers of various design.

This work has a purpose to develop method for making membrane-gauge tests and results processing that will allow describing a process of impact pressure loading with time increments.

Deformation of membrane under the action of all various energy-force factors of an underwater discharge has very complicated character. But shock waves have a leading role in deformation process. For the first approach the distribution of only shock waves pressure was specified for measurement. In the book [1] it is shown that, if time of membrane plastic deformation is much less than characteristic time θ of pressure impact, the membrane deflection will be proportional to the pressure amplitude. Time of plastic defor-

mation τ_{pl} is determined from the famous R. Cole's formula

$$\tau_{pl} = \frac{\rho c (d/2)^2}{4\sigma s}\ , \qquad (1)$$

where ρ and c – density of transmitting medium and sound velocity in it, respectively; d and s diameter and thickness of membrane, respectively; σ – average value of strength and yield limits.

Thus, selecting proper values of membrane diameter and thickness one can "tune" membrane pressure gauge to a measurement of shock wave pressure.

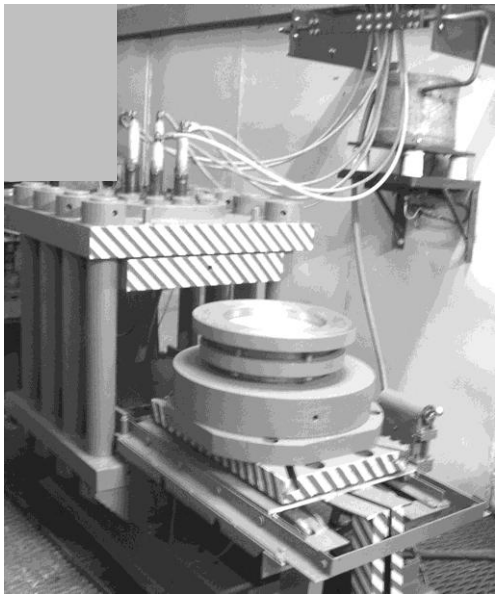

***Figure 1**: General view of technological block of UEHSH-2 installation*

2 Analysis of previous investigations results

One of the first vast investigations of pressure fields with MPG application is submitted in the dissertation [2]. Impact loading was created by multi-electrode discharge block (MDB) of experimental electrohydraulic installation UEHSH-2 (Figure 1).

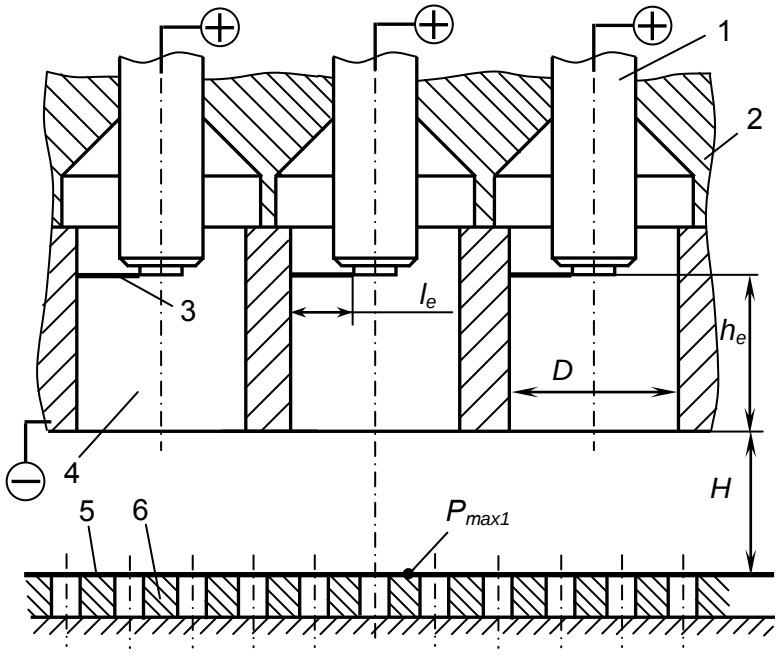

***Figure 2**: Test diagram for MPG measurements of pressure fields [2]: 1 – insulated electrode; 2 – MDB body; 3 – electric discharge channel; 4 – guide hole in opposite electrode-plate; 5 – membrane; 6 – MPG plate; l_e – spark gap length; h_e – axial coordinate of electrode; D – guide hole diameter; H – distance between MDB and MPG; P_{max1} – maximum pressure generated by one electrode pair*

When making tests the loading was mainly performed at the following parameters: charge voltage V_0 = 25 kV, capacity of one discharge circuit C = 16.6 microfarad, distance between MDB and membrane gauge H = = (50–130) мм (Figure 2), axial position of electrodes h_e = 95 mm, spark gap l_e = 30 mm. Mechanical properties of metallic membranes are: steel 08kp – ultimate tensile strength σ_u = 379 MPa, yield limit σ_y = 234 MPa, percentage elongation δ = 18 %; aluminum alloy AK4-1 – σ_u = 325 MPa, $\sigma_{0.2}$ = 290 MPa, δ = 6 %. Thickness of steel mem-

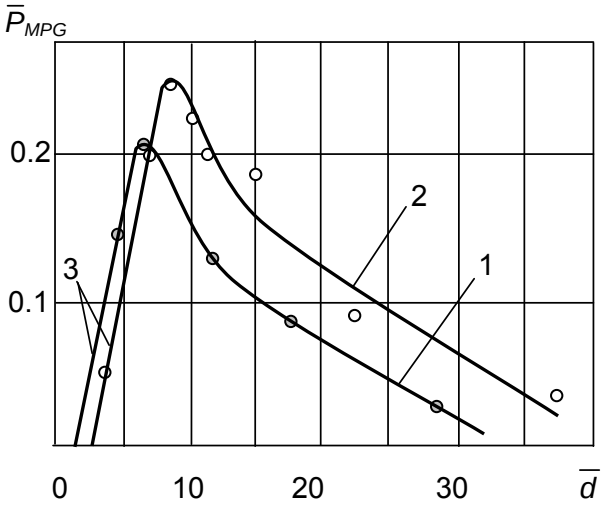

***Figure 3**: Relationship between normalized equivalent static pressure and relative diameter of MPG holes at constant discharge-circuit parameters [1]: 1 – membrane of steel 08kp, s = 0.8 mm; 2 – membrane of aluminum alloy AK4-1, s = 0.6 mm; 3 – straight segments of curves*

branes varied in the range of 0.6 to 0.8 mm, of the aluminum ones – 0.6 mm.

In the test diagram submitted in the Figure 2 the diameter of gauge holes was selected equal to 6 mm in order to register a pressure only from shock waves.

Investigations results [2, 3] showed that at some definite combination of geometric, mechanical and physical properties of membrane and parameters of pressure impact, membrane, as a sensitive element of gauge, registers only action of shock waves. Deformation of membrane occurs during characteristic time θ or less. Value of membrane deflection is linear proportional to peak value P_m of shock wave pressure in a definite range of ratios $\bar{d} = d/s$, where d is holes diameter, s – thickness of membrane (Figure 3). Approximately this range can be defined as $\bar{d}$ < (6…8). Here "equivalent static pressure" is adopted as a parameter for estimation of impact loading. It is calculated from the known Laplace formula for spherical element with the measured deflection (residual deformation) of membrane. In Figure 3 pressure is submitted in normalized form $\bar{P}_{MPG} = P_{MPG} / P_m$, where P_m is maximum (peak) pressure of direct shock wave.

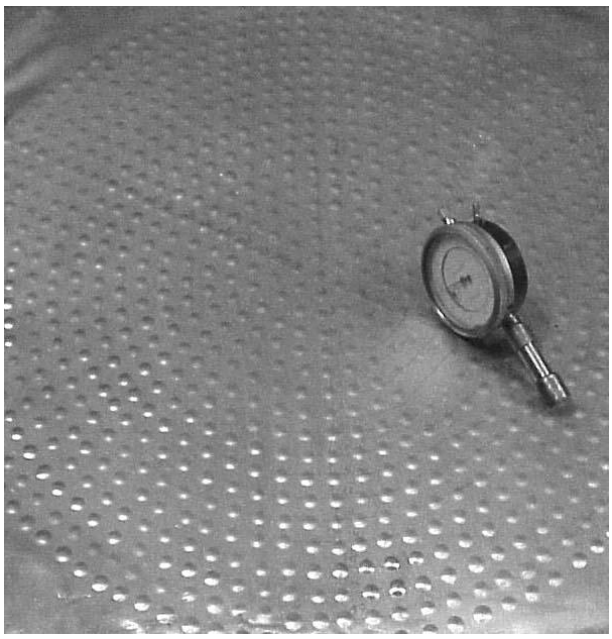

***Figure 4**: Membrane after impact loading and dial indicator for measurements of membrane deflections at the places of MPG holes*

Linear dependence between parameters $\bar{P}_{MPG}$ and $\bar{d}$ means that membrane deformation occurs during time of shock wave action. This proves correctness of the formula (1). With increase of parameter $\bar{d}$ value $\bar{P}_{MPG}$ reaches its maximum and begins to decrease. This proves that other factors of impact loading (hydraulic flows, cavitation, etc.) are involved in the process of deformation. It is worth to mention that dependence $h = f(\bar{d})$ has a similar form.

Typical metallic membrane after impact loading on the membrane gauge with 6-mm holes in the UEHSH-2 installation with 7 working electrodes is shown in Figure 4. Measurements of deflection (dimples height h) were performed with a dial indicator and special

adaptor with accuracy of 0.01 mm.

Results of MPG measurements showed peculiarities of shock-wave pressure fields generated by discharge chambers of certain design (Figure 5). Such maps are very useful for analysis and improvement of discharge chamber design, electrodes positions in order to obtain pressure fields of desired distribution.

For example, one of peculiarities of loading with a single electrode located in the MDB hole was displacement of high-pressure area to the side opposite to position of discharge channel (see Figure 5). Probably this peculiarity could not be revealed only with a theoretical model.

Loading with several simultaneous discharges has a more complicated character because of non-linear effects of interaction of several shock waves propagating at different angles respect each other. On the surface of wall they generate zone of interactions with maximum pressure greatly exceeding simple sum of shock-wave pressures. Interaction of 2 shock waves is easier for analysis. In Figure 6 interaction zone is located be-

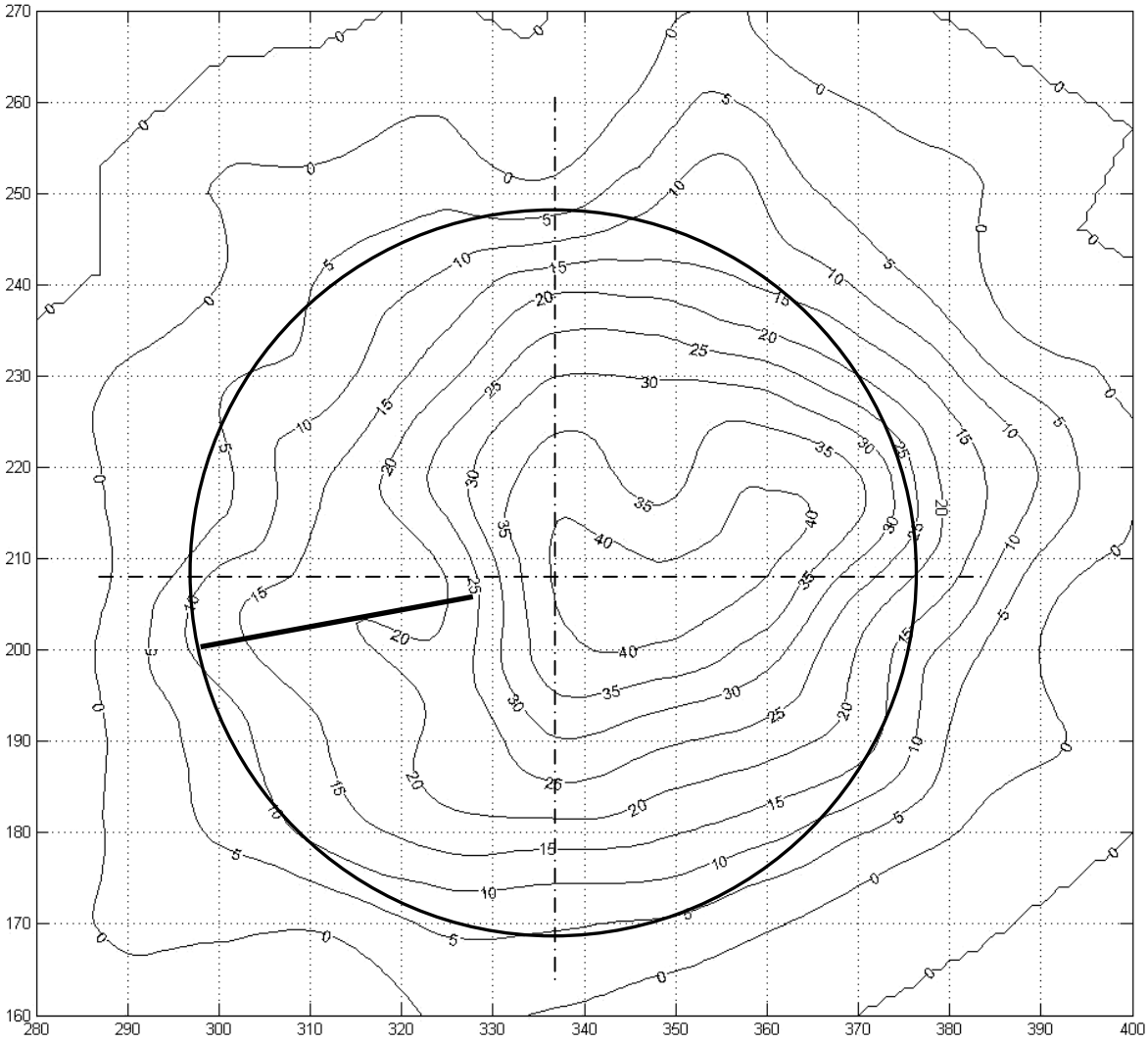

Figure 5*: Map of shock-wave pressure field generated by discharge in one electrode pair of multi-electrode block (see Fig. 2): round circle shows contour of exit hole D; thick straight line shows discharge channel. Pressure is given in MPa, coordinates – in mm*

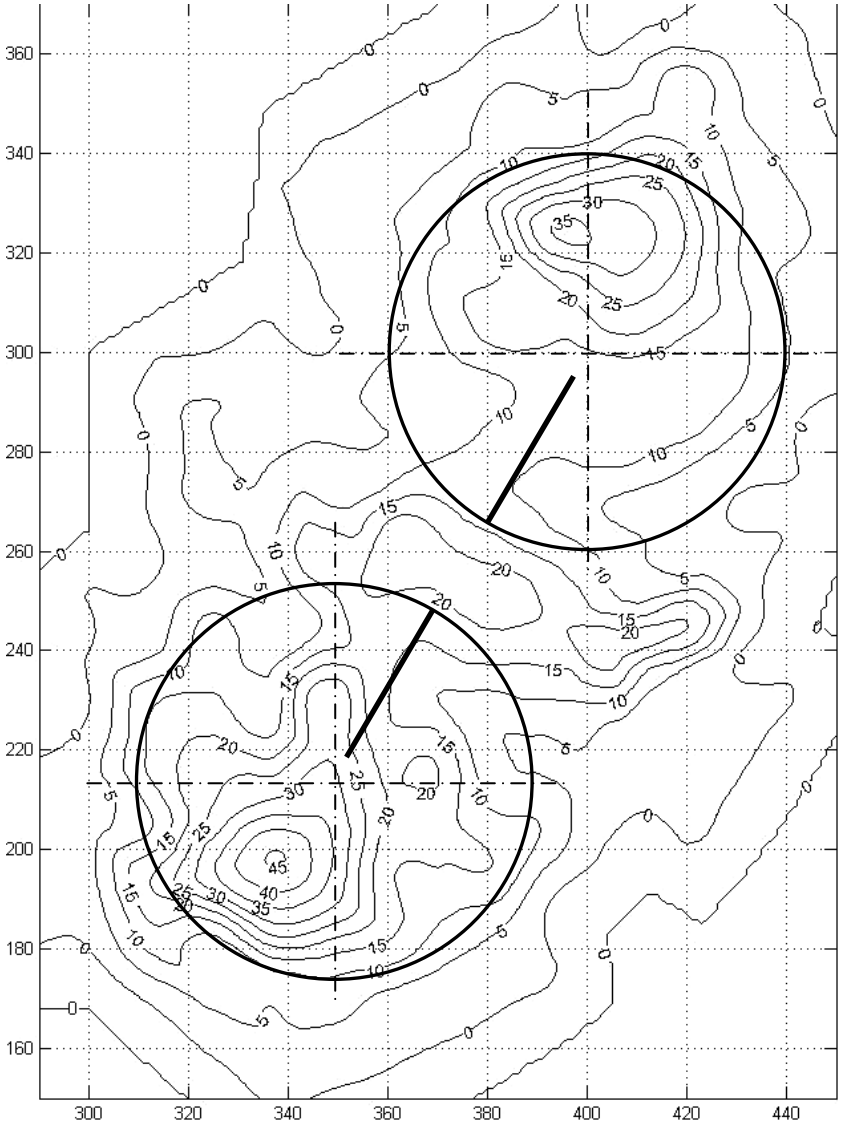

***Figure 6**: Map of shock-wave pressure field generated by discharges in two MDB electrode pairs (see Fig. 2): round circles show exit holes D; thick straight lines show discharge channels. Pressure is given in MPa, coordinates – in mm*

tween 2 circles (symbolizing 2 exit holes in MDB discharge plate) and determined by expanded isobar of 5 MPa with maximum pressure of 25 MPa and more in the center. In comparison with single-electrode loading (see Figure 5) total maximum pressure in the interaction zone increased approximately 25 times of sum of maximum pressures created by 2 shock waves.

Interaction of larger quantity of shock waves results in further strengthening of non-linear effects. Pressure maps generated by 3, 5 and 7 electrodes have more complicated character [4].

3 Method for tests carrying-out and results processing

Proposed method includes several stages.

The first stage has a purpose to find function for conversion of pressure values measured with a membrane gauge P_{MPG} into values of shock-wave peak pressure P_m. This is performed by several tests with various energies of discharges. Measurements are performed by single-point membrane gauge of apt hole diameter and membrane thickness (to register only shock wave, see Fig. 3) and piezo-electric sensor to register the P_m values at the same conditions. Thus, function $P_m = f(P_{MPG})$ will be obtained. It is assumed that this function will be linear. Also application of function $P_m = f(h)$ is possible, where h is deflection of membrane under the action of pressure impact. Hence, at this stage calibration of membrane gauge is performed.

The second stage is measurements of pressure fields with multi-point MPG under the discharge chamber to be investigated. Here the real pressure distributions are obtained in the form of data matrix (h_i; x_i; y_i), where (x_i; y_i) are coordinates of points (holes) of membrane-gauge plate. With aid of function $P_m = f(P_{MPG})$ (or $P_m = f(h)$) the data are converted into the matrix (P_{mi}; x_i; y_i). But this is a static distribution of peak values of shock-wave pressure.

At the third stage in order to obtain pressure parameter changing in time it is necessary to find characteristic time θ_i in the formula for each point *i*

$$P_i = P_{mi} \cdot e^{-\frac{\tau}{\theta_i}} . \qquad (2)$$

The θ_i values can be calculated from the known formulas [4, 5]

$$\theta = \tau_{0.1} / ln\,10 ; \quad \tau_{0.1} = 0.74 \tau_1 \bar{r}^{1/8} ; \quad \bar{r} = r \cdot \left(\frac{\rho\, I_e}{V^2 C^2 L} \right)^{1/4} , \qquad (3)$$

where τ_1 is a duration of the 1st half-period of discharge current; V, C, L – voltage, capacitance and inductance of discharge circuit respectively; ρ – density of transmitting medium (water).

Results of computations performed for the specified conditions showed the value θ_{com} = 30.3 microseconds, while experimental data gave the value θ_{exp} = 26 microseconds. Relative error of computations equals 16.5 % that is quite good for the first approach. Of course, application experimental θ_{exp} values obtained at the first stage will improve accuracy of the method.

At the fourth stage the moments $\Delta\tau_i$ when shock waves reach the wall (membrane) are determined from geometric formulas taking into account the design of considered discharge chamber or block. Here $\Delta\tau_i$ is a time delay when front of shock wave propagates from discharge channel to the point *i* on the membrane surface.

Performing all the works of specified stages one can restore the picture of loading that changes in time.

4 Conclusions

Peculiarities and advantages of measurements of pressure fields with multi-point membrane pressure gauges at impact forming have been analysed

The method for organisation of measurements with MPG and piezo-electric sensors, processing of measurements data has been proposed.

The results of MPG measurements and their processing could be a good basis for simulation of impulse loading with approximation formulas and also could be used as a check data for the simulation programs based on theoretical relationships.

Further improvement of the method based on MPG application should take into account other factors of impact loading (hydraulic flows, quasi-static pressure) and phenomenon of cavitation. For this purpose the application of MPG with larger holes is planned with respective correction of the data processing algorithms.

References

[1] *Vagin, V.A.; Zdor, G.N.; Mamutov, V.S.:* Methods for investigations of high-rate deformation of metals. – Minsk: Nauka and Tehnika Publishers, 1990. – 207 p. (in Russian)

[2] *Kyazyev, M.K.:* Research, development and introduction of manufacturing processes of electrohydraulic forming with application of multi-electrode discharge blocks / Dissertation ... of candidate of technical sciences. – Kharkiv: Kharkiv aviation institute, 1995. – 223 p. (in Russian)

[3] *Antonenko, A.A.; Chebanov, Yu.I.; Kyazyev, M.K.:* Investigation of processes of electrohydraulic forming in installations with multi-electrode discharge blocks // Eastern-European Journal of Enterprise Technologies, 2004, No. 1(7), p. 23-32.

[4] *Knyazyev, M.K.:* Optimisation of Pressure Fields with Multi-Electrode Discharge Blocks at Electrohydraulic Forming of Aircraft Components // Proceedings of the 4th International Conference “Supply on the Wings”, Frankfurt-am-Main, November 3-5, 2009. – 16 p.

[5] *Kryvytsky, E.V.; Shamko V.V.:* Transient processes at high-voltage discharges in water. – Kyiv: Naukova Dumka Publishers, 1979. – 208 p. (in Russian)

[6] *Shamko, V.V.:* Integral characteristics of plasma of underwater spark discharge // Journal of Technical Physics. – 1978. – 48. – Issue 5. – p. 967-971. (in Russian)

SESSION 3
WELDING/JOINING

Joining of Copper to Brass Using Magnetic Pulse Welding [*]

K. Faes [1], T. Baaten [1], W. De Waele [2] and N. Debroux [3]

[1] Belgian Welding Institute, St-Pietersnieuwstraat 41, Ghent, Belgium
[2] Laboratory Soete, Ghent University, St.-Pietersnieuwstraat 41, Ghent - Belgium
[3] CEWAC, Rue bois St-jean, 8, Liège Science Park, Ougrée, Belgium

Abstract

In magnetic pulse welding, electromagnetic pressure is used to deform, accelerate and weld workpieces. The process is mostly used for tubular specimens.
In this study, experiments were performed in order to investigate the weldability of copper tubes to brass solid workpieces. The tubes had an outer diameter and wall thickness of 25,0 mm and 1,5 mm respectively. A multi-turn coil with 5 windings in combination with a field shaper was used to focus the electromagnetic flux and thus realize the high pressures needed for welding.

The process parameters for joining these materials were optimised for maximum weld length. The parameters taken into account were the position of the field shaper relative to the workpieces, the width of the air gap between the tube and the internal workpiece and the energy level. The weld quality was verified based on metallographic examinations, scanning electron microscopy and hardness measurements.

Keywords

Magnetic Pulse Welding, Copper, Brass

---

[*] *This work is based on the results of the collective research project "SOUDIMMA" (Belgium). The authors would like to thank the Walloon region (DG06) for its financial support.*

1 Introduction

In magnetic pulse welding, a very high energy current is discharged through a coil. The high and extremely fast current discharge creates electromagnetic forces between the coil and the outer tubular workpiece, which accelerates the latter towards the inner workpiece. A high-pressure collision is then created between the two surfaces of the metals to be joined [1]. Under precisely controlled conditions a solid-state weld can be realised.

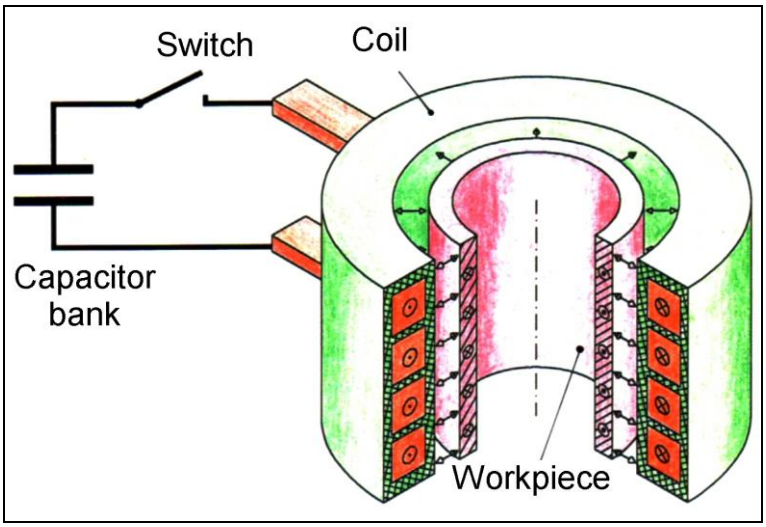

Figure 1: *Principle of magnetic pulse welding*

As in explosive welding, during the process a jet is created between the two surfaces to be joined. This jetting action removes all traces of oxides and surface contaminants, allowing the impact to plastically deform the metals for a very short time and to drive the mating surfaces together. This allows the contact of two virgin surfaces, stripped of their oxide layers. The surfaces are pressed together under very high pressure, bringing the atoms of each metal into close contact with each other, thereby allowing the atomic forces of attraction to come into play. There are a number of explanations for the precise mechanism at the collision point, but all agree that the metals momentarily behave like liquids, even though they remain solid [2].

2 Overview of the welding experiments

In this study, a total of 81 magnetic pulse welding experiments were performed in order to investigate the weldability of copper tubes to brass solid workpieces. The tubes had an outer diameter and wall thickness of 25,0 mm and 1,5 mm respectively. The properties of the materials are summarised in Table 1.

	Copper	Brass
Designation	EN 12449 Cu-DHP R290 (Mat. No.: CW024A)	EN 12164 CuZn39Pb3 (Mat. No.: CW614N)
Chemical composition (wt%)	Cu: 99,9 %	Cu: 57 - 59 % Pb: 2,5 - 3,5 % Zn: rest
Yield stress (MPa)	min. 250	min. 250
Tensile strength (MPa)	min. 290	min. 430

Table 1: *Overview of materials used*

The experiments were performed using a Pulsar model 50/25 system with a maximum charging energy of 50 kJ (corresponding with a maximum capacitor charging voltage of 25 kV) and a discharge circuit frequency of 14 kHz. The total capacitance of the capacitor banks equals 160 µF. The pressure resulting from the magnetic flux induced by a multi-turn coil is concentrated over the processing area using a field shaper with a width of the workzone equal to 15 mm (see Figure 2).

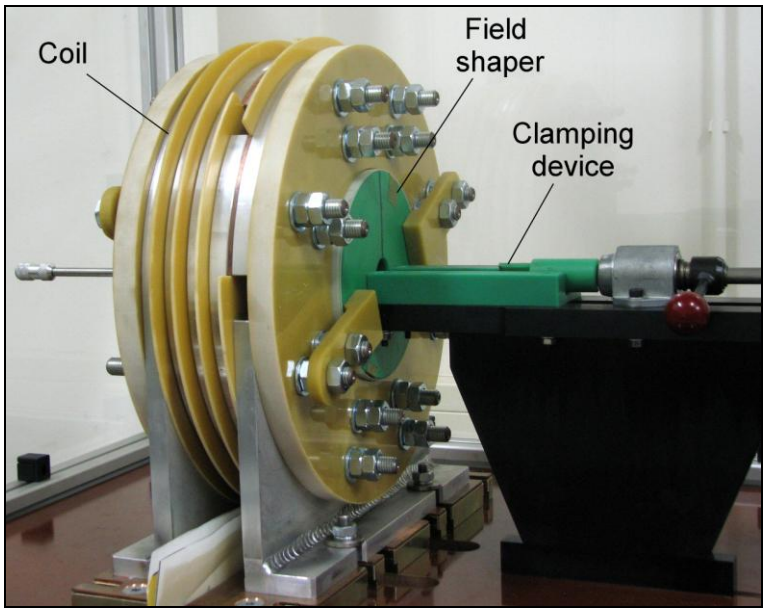

Figure 2: *Multi-turn coil used in the experiments*

The workpieces were positioned inside the field shaper in the overlap configuration. Various settings of the process parameters were used: the width of the air gap between the tube and the internal workpiece (s in Figure 3), by changing the outer diameter of the internal workpiece, the position of the field shaper relative to the workpieces (l_{FS} in Figure 3) and the charging voltage of the capacitors, determining the energy level. The overlap distance of the tube and internal workpiece and the discharge current frequency were kept constant.

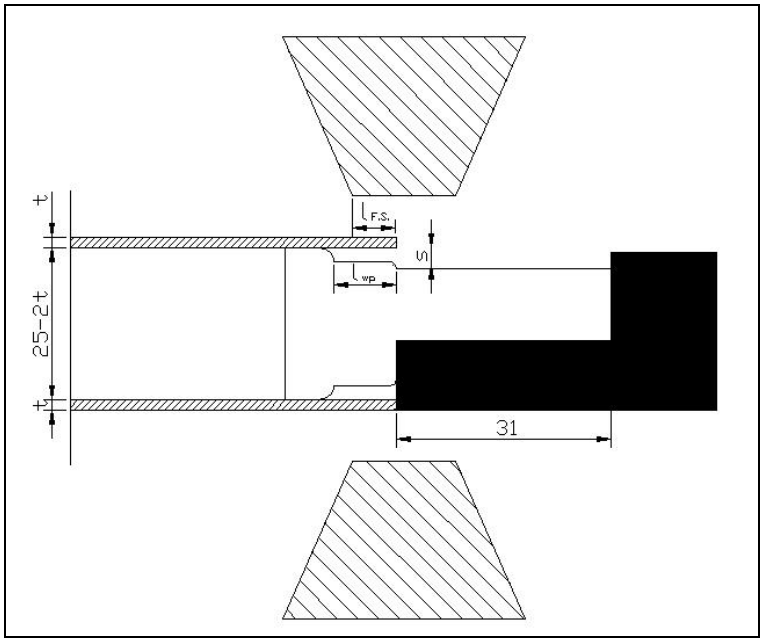

Figure 3: *Experimental test setup*
(l_{FS}: tube end position in the field shaper
s: air gap widt
l_{wp}: overlap length of the workpieces)

3 Parameter optimisation

The process parameters for joining the copper tubes and the brass solid workpieces were optimised experimentally. The parameter ranges used in the various experiments are summarised in Table 2. The optimisation was performed based on the measurement of the length of the welded zone. The weld length was defined as the average value of the weld lengths measured at two sides of a metallographic specimen (see Figure 5). The weld lengths which were encountered were maximum 7 mm.

Parameter	Setting range
Tube end position in the field shaper	Centre of field shaper + 0,5 up to + 5,5 mm
Air gap width	0,8 - 2,5 mm
Capacitor charging voltage **Energy**	12 - 20 kV 11,5 - 32 kJ

Table 2: *Overview of the parameter variations used*

During the welding experiments, it was observed that the tube end position in the field shaper is of high importance, characterising the overlap of the field shaper with the outer tubular workpiece. It was found that for different air gap widths, good weld quality is obtained for different ranges of tube end positions. This means that the field shaper overlap has a serious influence on the impact velocity and/or the impact angle. The zone

subjected to magnetic pressure increases with increasing field shaper overlap. This means that the total force will be higher, which will influence the impact velocity. However, also a maximum allowable overlap of the field shaper exists. As the impact velocity will be large enough for larger overlaps, the impact angle must have reached values outside the possible range for welding. This indicates that the field shaper overlap also influences the impact angle.

Further, it was demonstrated that no bonding occurred when using an air gap smaller than 1,0 mm or larger than 2,0 mm. The optimal air gap width was found in the range of 1,0 to 1,5 mm for all welding experiments. An overview of suitable process parameters for an air gap width of 1,0 mm is shown in Figure 4. The optimal position of the tube end equalled 2,5 mm out of the centre of the field shaper and the minimum required energy level was equal to 26 kJ.

The overlap distance of the tube and internal workpiece and the discharge current frequency were kept constant

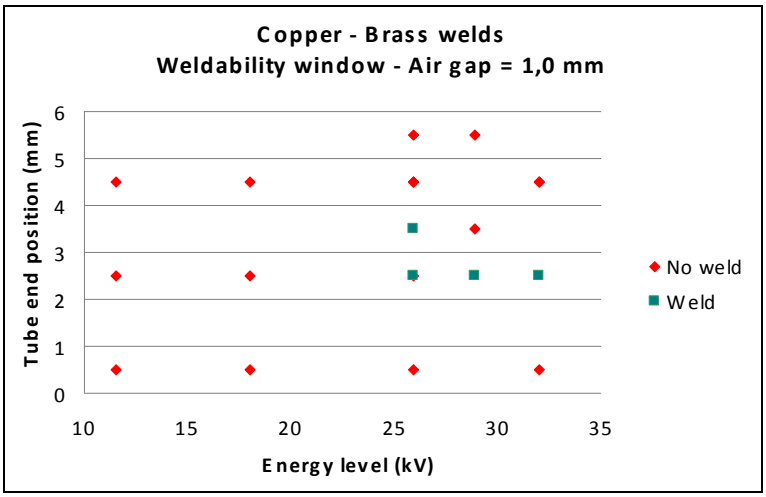

Figure 4: *Suitable parameters for joining copper to brass when using an air gap of 1,0 mm*

4 Metallographic observations

The weld quality has been assessed visually by means of metallographic examination. Hereto, the welded zone of each workpiece was isolated and cross-sectioned. After embedding in epoxy, the specimens were prepared by standard metallographic procedures; mechanical polishing down to 3 µm and chemical etching. The samples were etched by ammonia activated with hydrogen peroxide, during 20 seconds and finally examined by optical microscopy.

4.1 Macroscopic observations

The weld joint can be divided in 3 zones, which are shown in Figure 5. Actual welding of the materials will only occur in the middle part of the working zone. As the tube will impact

the solid workpiece from left to right in this figure, the zone on the left without weld is called the run-in zone and the right zone is called the run-out zone. No clear correlation was found between the lengths of the run-in and run-out zones and the settings of the process parameters.

At the end of the run-out zone, the tube makes a certain angle with the internal workpiece. This angle was measured for all experiments. It was noticed that the angle increases for a higher energy level. The overlap distance of the tube and internal workpiece and the discharge current frequency were kept constant for experiments with a higher energy level and for experiments with a longer overlap of the field shaper with the outer tube.

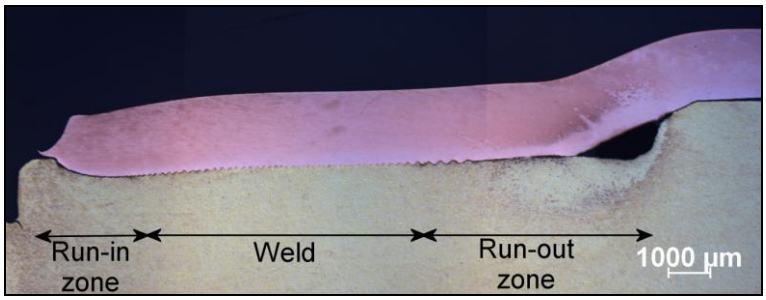

Figure 5: *Metallographic section of a typical weld*

In general, the inner workpieces were severely deformed during the impact. The most pronounced deformation occurs at the run-in zone, where the inner workpiece is compressed in a narrow zone. From there on, the deformation of the inner workpiece declines gradually towards the end of the weld (from left to right in Figure 5). This experimental observation proves that the impact of the tube occurs first at the run-in zone. The indentation in this zone was found to be between 0,5 and 1,0 mm. At a lower energy level and a smaller air gap width, the deformation decreases. The width of this severely deformed zone increases for a longer overlap of the field shaper. These high deformations show that in case a tube is used as internal workpiece, a mandrel should be applied to prevent deformation.

4.2 Weld interface morphology

The weld interface showed a typical wavy pattern (see Figure 6), similar as observed in joints realised by explosion welding. This transition zone between the dissimilar materials is believed to be caused by mechanical mixing, intensive plastic deformation and/or local melting. Temperature increase at the weld interface occurs due to Joule heating, the collision of the two pieces and the jet formation. Because the process takes place in a short lapse of time, heating is not enough to generate a temperature rise in a wider area, so there is no significant heat affected zone, as also has been stated before [3].

The dark zones in Figure 7, located in the brass material, are the result of severe plastic deformation. The size and orientation of the microstructural components in this zone have changed due to the impact. The Pb-particles have grown because of local melting.

The wavelength and amplitude variation along the weld interface was measured. The wave amplitude remains fairly constant along the weld interface and was approximately equal to 15 µm. The wavelength was found to increase towards the end of the weld (right in Figure 5) and varied between 50 and 160 µm.

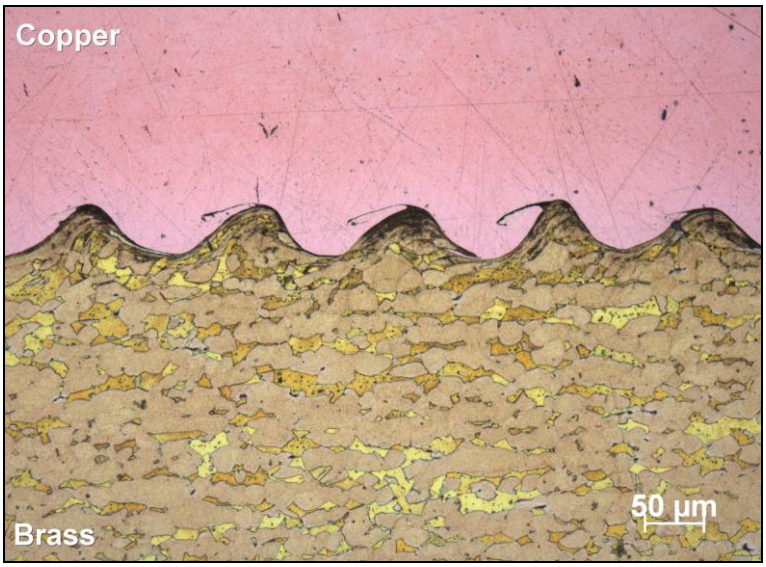

Figure 6: *Interface morphology of a copper – brass weld*

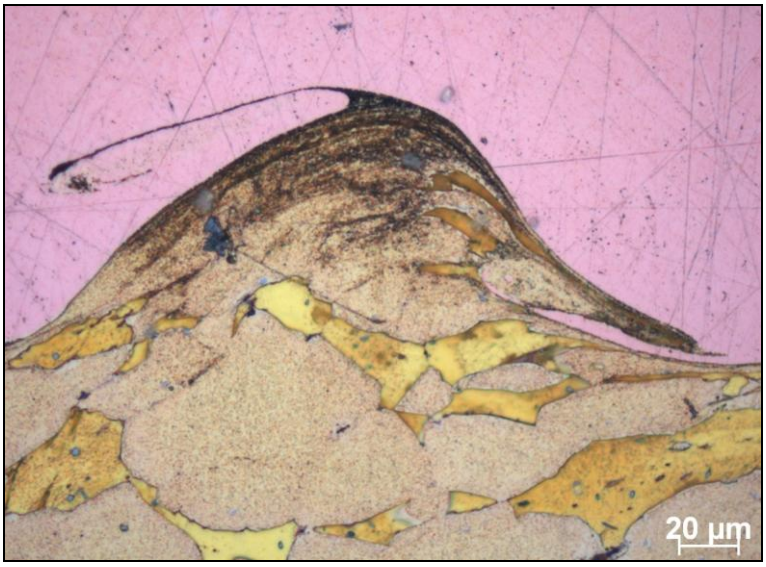

Figure 7: *Detail of Figure 6*

4.3 Microstructural observations

In some welds intermetallic layers were observed (see Figure 8). Such interface layers may support two possible mechanisms of bond formation: bonding as a result of solid-state processes based on accelerated mass transfer due to intensive plastic deformation

at very high rates, and bonding as a result of solid-liquid interaction and based on the formation of a thin layer of molten metal between the components [3].

These layers were analysed using scanning electron microscopy. It was demonstrated that the interlayer becomes copper-enriched: the chemical composition of the layer shown in Figure 8 consisted of 75,6% Cu, 22,1% Zn and 2,3% Pb.

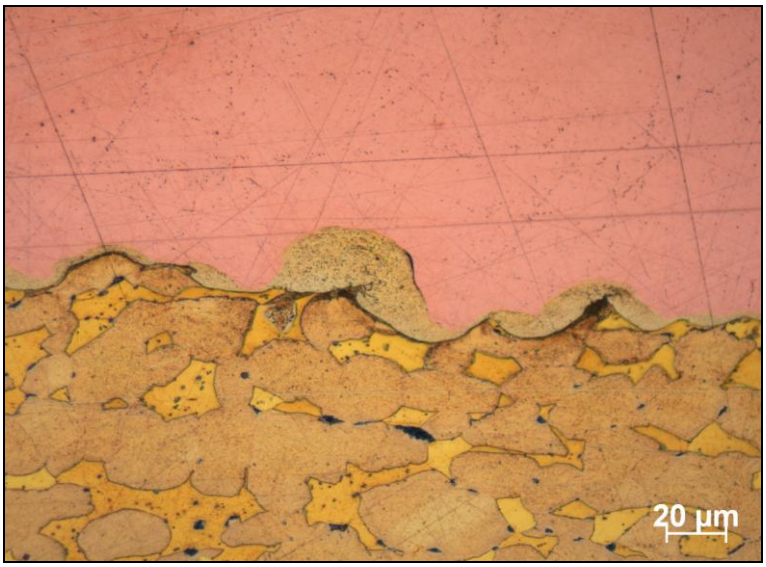

Figure 8: *Intermetallic layer observed in a copper-brass weld*

The intermetallic layers are susceptible for cracking, as shown in Figure 9 and Figure 10. In some welds, the interlayer was not able to withstand the residual stresses in the outer tube.

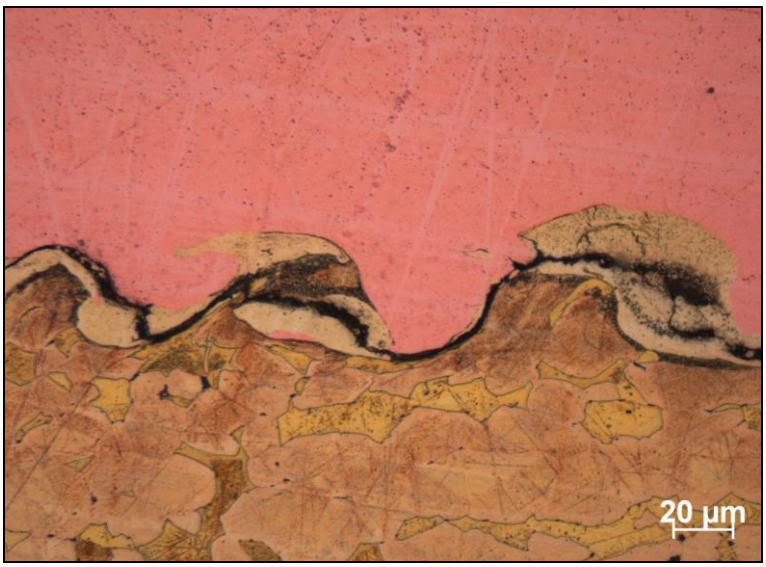

Figure 9: *Cracks in the intermetallic layer*

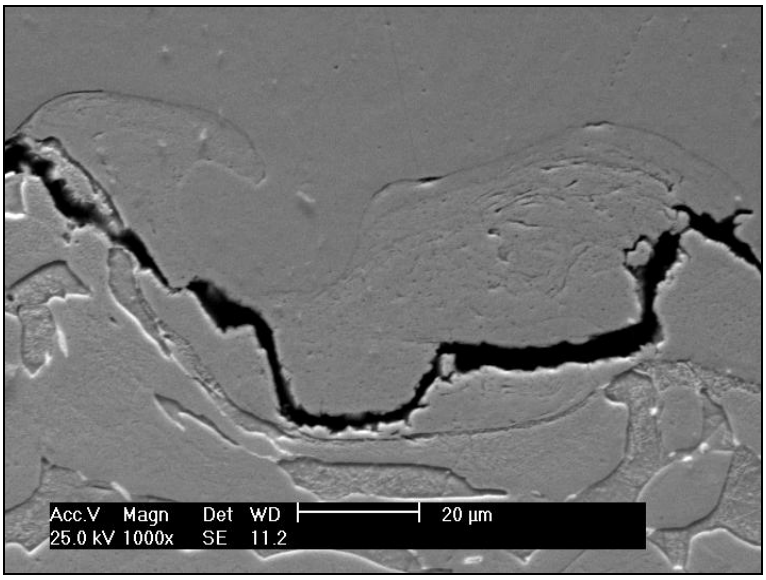

Figure 10: *Scanning electron microscopic analysis of a crack in the intermetallic layer*

4.4 Melting phenomena

In some welds, cracks in the intermetallic layers were observed which are the result of local melting and rapid solidification. A typical example is shown in Figure 11. This indicates that the temperature rise must have been higher than the melting temperature of copper and brass (1083 and 930°C respectively). The observed melt zones reached thicknesses up to 50 µm.

Zones which were molten were found in several samples, but not all of them were located in the welded area itself. Often, evidence of melting was found in the run-in or run-out zone (see Figure 13 and Figure 14). The molten zones were also analysed using scanning electron microscopy (see Figure 12 and Figure 14).

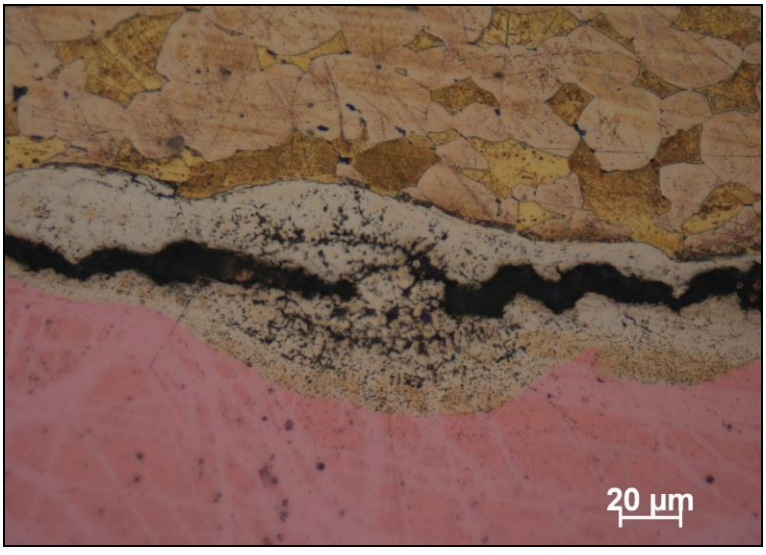

Figure 11: *Molten zones with cracks along the weld interface*

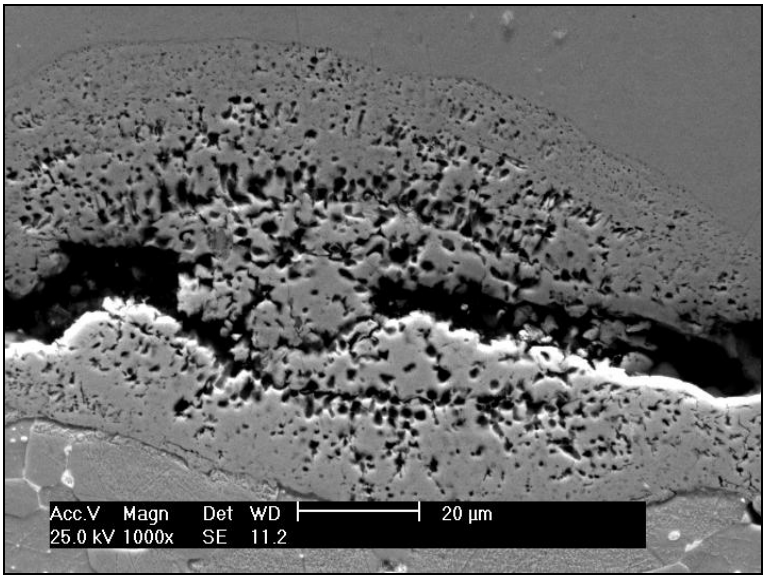

Figure 12: *Scanning electron microscopic analysis of a molten zone*

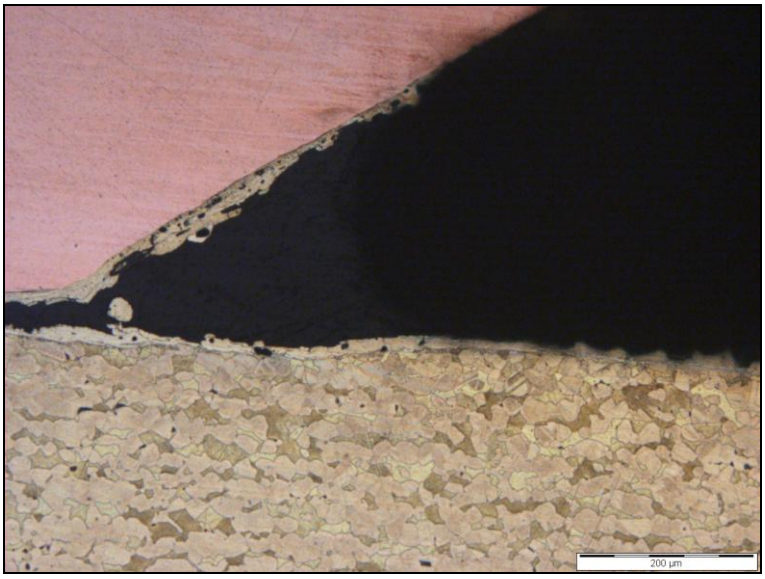

Figure 13: *Molten material in the run-out zone*

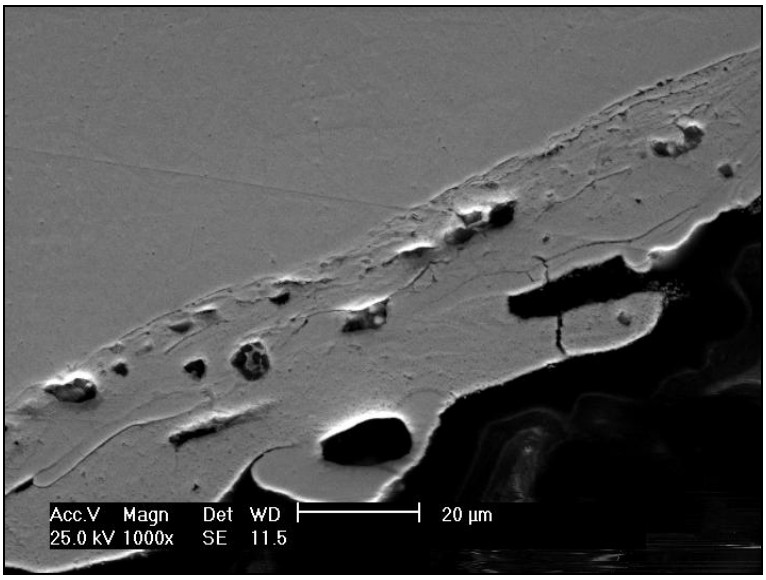

Figure 14: *Scanning electron microscopic analysis of the molten material in the run-out zone (detail of Figure 13)*

Most probably the observed cracks are caused by residual stresses in the outer tube and by shrinkage of the material during solidification. It was concluded that there is a considerable risk for melting during the magnetic pulse welding process. The sharp transition zone which is observed is typical for melting and rapid solidification [4]. A literature survey of both magnetic pulse and explosive welding confirmed that continuous molten layers or melt pockets can occur. Also the presence of pores due to the turbulent jet and the rapid solidification have been mentioned before [4]. Melting has generally been considered as a disadvantage due to the intermetallic compounds it can generate. These compounds can form a hard and brittle interlayer that is generally susceptible to cracking. In a recent paper, the jet has been found to be the main source for heating of the materials, apart from the heating due to the collision itself [4]. The temperature of the interface will increase due to the jet, which is dependent on the impact angle, the impact energy and the impact velocity. Therefore melting can be avoided by either decreasing the energy level or by decreasing the impact angle.

5 Hardness measurements

In order to investigate the hardness of the interlayers, Vickers hardness measurements were performed using a Struers Duramin A300D automatic hardness tester with a test load of 1,961 N (corresponding to HV0,2) and an indentation time of 12 sec. A hardness traverse across the weld was performed. The hardness as a function of the location is shown in Figure 15.

The hardness of the copper and brass base materials were measured well outside the weld zone, and were found equal to respectively 104 and 146 HV0,2. The interface layer shows an increase in hardness relative to the base materials. This can be attributed to the severe plastic deformation or to a new fine-grained microstructure produced by melting and rapid solidification of the weld interface.

As the width of the welded interface is in the order of 10 to 30 µm, precisely measuring the hardness of this area with a HV0,2 test is very difficult. The average hardness based on 5 measurements was equal to 183 HV0,2.

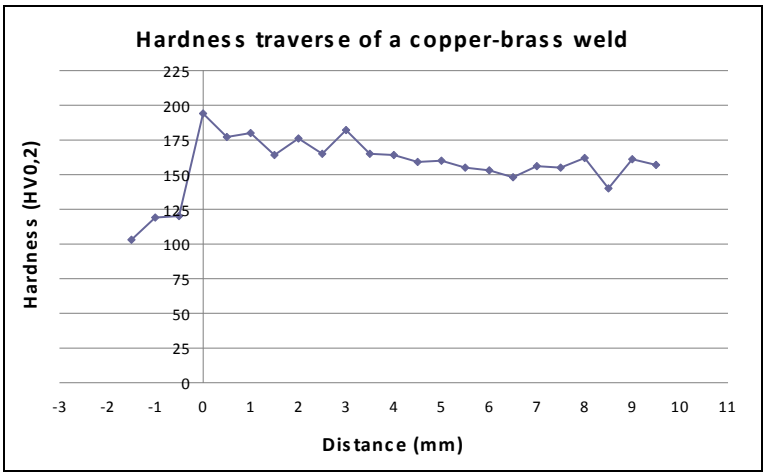

Figure 15: *Hardness traverse*

6 Conclusions

In this study, magnetic pulse welding experiments were performed in order to investigate the weldability of copper tubes to brass solid workpieces. In the experiments, the pressure resulting from the magnetic flux induced by the multi-turn coil is concentrated over the processing area using a field shaper with a width of the workzone equal to 15 mm. The tubes used in the experiments had an outer diameter and wall thickness of 25,0 and 1,5 mm respectively.

The following process parameters have been varied: the width of the air gap between the tube and the internal workpiece, the position of the field shaper relative to the workpieces and the charging voltage of the capacitors. The overlap distance of the tube and internal workpiece and the discharge current frequency were kept constant.

The weld quality was visually assessed by means of metallographic examination. It was observed that a considerable risk exists for melting during the process, which can impair the weld quality.In some welds intermetallic layers were formed, as a result of local melting and rapid solidification. The presence of cracks parallel to the weld interface was attributed to residual stresses in the outer tube and solidification shrinkage. The hardness increase of the interlayer was however moderate. After parameter optimisation, defect-free welds could be realised. The length of the welded zone was maximum 7 mm. A weld interface with a wavy pattern was created, similar to an explosion weld joint, showing severe plastic deformation and microstructural redistribution.

References

[1] *Schribman, V.* Magnetic pulse technology for improved tube joining and forming. Tube & Pipe Technology, nov./dec. 2006, p. 91-95.

[2] *Schribman, V.* Magnetic Pulse Welding. Proceedings of the BIL/NIL Welding Symposium, Belgian Welding Institute, Brussels, 18/10/2007.

[3] *Shribman, V. Stern, A., Livshitz, Y. and Gafri, O.* Magnetic pulse welding produces high-strength aluminium welds. Welding Journal 81, April 2002, p. 33–37.

[4] *Ben-Artzy, A., Stern, A., Frage, N. and Shribman, V.* Interface phenomena in aluminum-magnesium magnetic pulse welding. Science and technology of welding and joining, 13(4): p. 402-408, 2008.

Impact Welding in a Variety of Geometric Configurations [*]

Y. Zhang[1], S. Babu[2] , and G. S. Daehn[1]

[1] The Ohio State University, 2041 College Rd, Columbus, Ohio, USA, 43210
[2] The Ohio State University, 1248 Adams Drive, Columbus, Ohio, USA, 43221

Abstract

Magnetic pulse welding is an electromagnetically assisted high strain rate impact welding technology. The physical principle is similar to explosive welding and it also belongs to solid state impact welding. This high velocity oblique impact welding has been applied to various lap joint configurations. Three different geometric configurations on plate-to-plate welding were studied in this paper. They are direct lap joint, pre-flange lap joint, and lap joint with embedded wires. All of the three welding configurations have been used to provide metallurgical bonds between both similar and dissimilar metal pairs. The welded materials include copper alloy, aluminium alloy, and steels. The plates are centimeter or more thick and often centimeter in extent. The critical welding process parameters were instrumentally investigated by Rogowski Coil and Photon Doppler Velocimetry. Metallographic analysis of the welded interface showed refined grain structure. The mechanical properties of the welded plates were studied by lap shearing, peeling and nano-indentation tests. The test results showed that the impact welded interface has a much greater micro-hardness and fracture toughness than the base metals.

Keywords

Impact welding, Magnetic pulse welding, Welding configuration

---

[*] *The authors would like to thank American Welding Society for its financial support on magnetic pulse welding technology since 2007.*

1 Introduction

There is a growing recognition that optimal lightweight structures for automobiles, aircraft and even bicycles are often created from multi-material assemblies. Joining dissimilar high-strength light alloys has therefore been of significant and growing interest. One of the most elegant ways to accomplish dissimilar metal welding is by impact welding. The outstanding advantage of impact welding is that it can minimize the formation of continuous intermetallic phases while chemically bond dissimilar metals [1]. The impact welding does not result in heat affected zone or distortion near to the welded region. Therefore, more attention has been obtained for solid state impact welding on dissimilar materials joint. This paper studied one of the solid state impact welding processes, magnetic pulse welding (MPW). Since 1969, MPW has been successfully applied for tube to tube impulse welding but typically required fairly high electrical energies to be stored in capacitor bank with typical values in the range of 20~100 kJ [2]. With the recent development of MPW, the geometry of the welding workpiece could be cylindrically symmetrical [3] or asymmetrical [4-6]. Studies by Aizawa's group (2005) in Tokyo and Date's group (2007) in Mumbai have developed MPW seam linear welding [4, 5]. These methods tend to use much less energy than those for tube welding. For example, the reported energy to weld aluminium alloy plate about 1 mm in thickness to SPCC steel plate is only about 1.4 kJ [6]. Very rapid rise times (time for actuator to reach maximum primary current) in the capacitor discharge circuit are largely responsible for this efficiency.

The objective of this paper is to investigate the different configurations for MPW. MPW process completes within microsecond and does not involve hazard explosion, and thus it is more industrial acceptable. Three configurations for plate-to-plate welding were introduced with the instrumental measurement of the impact velocity and impact angle. The joint strength was examined by lap shearing, peeling, and nano-indentation tests. The welded interface microstructure was also studied by transmission electron microscopy.

2 Principles of Magnetic Pulse Welding

MPW is closely analogous to explosive welding and it is necessary to have a slight impact angle to form a jet along the mating surface [6]. However, rather than explosives, it uses electromagnetic force to accelerate the flyer plate. Therefore, MPW can be safely and reproducibly used in production environments controlled by an electric power supply. The fine adjustment to parameters is straightforward. With proper design, the energy is fairly efficiently used for accelerating the flyer plate rather than heating or melting the materials.

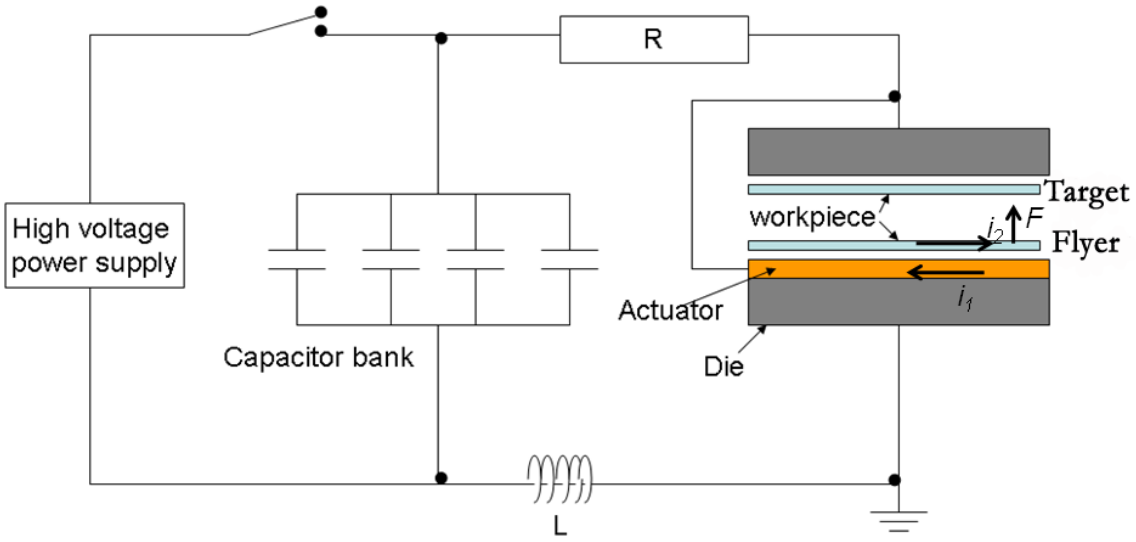

Figure 1 Schematic diagram of MPW system.

As shown in Figure 1, the MPW system includes a capacitor bank, an actuator, and workpieces. The capacitor bank simply consists of an inductance-capacitance circuit and an actuator of some impedance. Both the flyer plate and the target plate were supported by insulated layers with certain standoff distance between them. The electromagnetic actuator was connected to the capacitor bank. When capacitors are discharged, the current with high density flows through the conductive actuator, which is regarded as primary current. If there is a closed current path, the associated electromagnetic field induces a strong secondary current through the nearby metal workpiece (flyer plate). Therefore, the flyer plate carries current and stays in the electromagnetic field. Since the primary current and the secondary current generally travel in opposite directions, their interactions result in a strong repulsive force, which is the Lorentz force. As shown in Figure 2, the flyer plate is repelled from the actuator and accelerates with sufficient velocity for impact welding. MPW uses an electromagnetic field, and thus the flyer plate must be electrically conductive and plastically deformable, or coupled to a conductive driver.

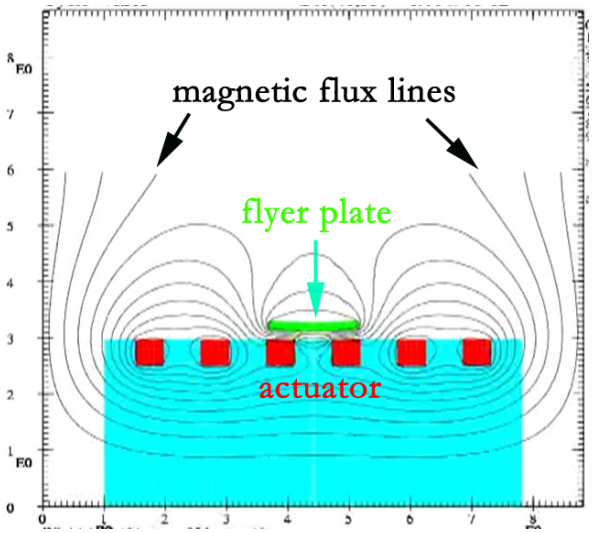

Figure 2 Illustration of magnetic flux lines during impact welding process [7]. The abscissa and the longitudinal axes is the length scale and the unit is millimetre.

3 Configurations for MPW on Plate-to-Plate Joint

3.1 Direct lap Joint

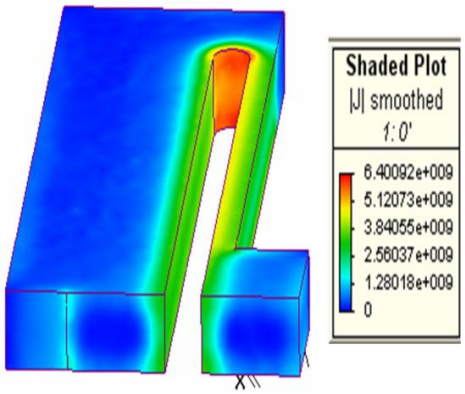

(a) Magnet® simulated current density (unit: A/m^2)

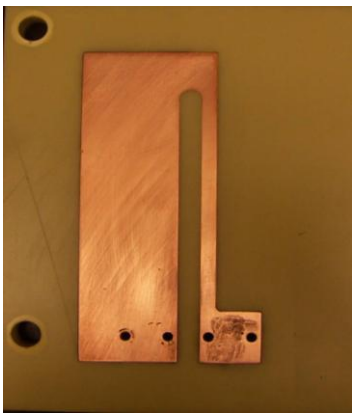

(b) Real actuator for lap joint

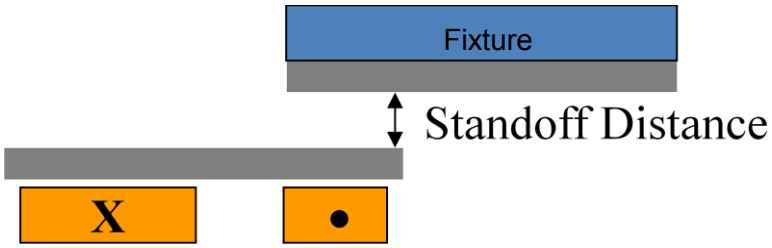

(c) Illustration of welding system (Some of the supporting blank holders are ignored in the figure.)

Figure 3 Schematic of the first generation flat bar actuator.

The direct lap joint was carried out on one asymmetrical 'Ո' shape flat bar actuator. The actuator material is half inch thick copper alloy C2C18150. As shown in Figure 3, the narrow leg and the wide leg have different current densities and the current is condensed on the narrow leg. Hence the being welded region is set right above this narrow leg.

In order to study the impact angle and impact velocity effects for lap joint, the second generation flat bar actuator was designed as shown in Figure 4. They can offer different initial launch angles. Figure 4(a) presents the actuator which is assembled into the die. The narrow leg has a chamfered angle and four through holes with 2.54 mm diameter. The holes are used to assemble the laser beam probes for impact velocity measurement at different locations. The chamfered angle determines the initial launch angle as shown in Figure 4(b). The narrow leg has been chamfered into 5º, 10º, 15º, 20º and 30º angles. Accordingly, the being welded flyer plates were bent to such angles which were regarded as the initial launch angles. The impact angles should be no larger than the initial launch angles.

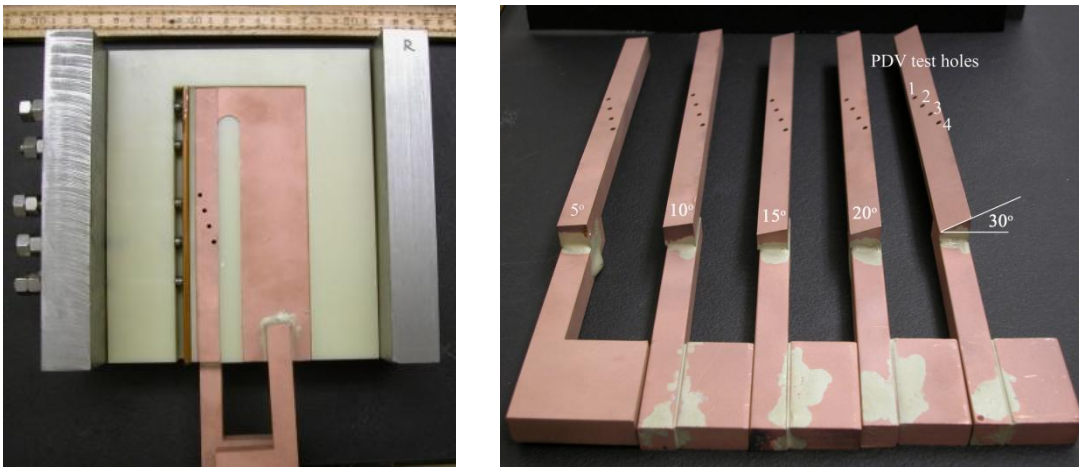

(a) Second generation of the flat bar actuator (b) Narrow leg with different chamfered angles

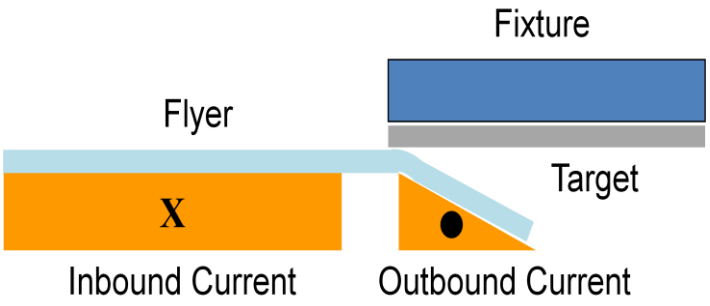

(c) Illustration of welding system

Figure 4 Second generation of the flat bar actuator.

3.2 Pre-flange Lap Joint

MPW was also conducted to flange and weld workpieces together by the pre-flange configuration as shown in Figure 5. The pre-flange actuator can be regarded as a bar actuator, however the inbound leg and outbound leg are not in the same plane. The being welded plate was bent and inserted beneath one of the actuator legs with certain pre-flanged angle. Once the primary current goes through the actuator, the Lorentz force from the outbound leg will push the flyer down against the target and weld them together with high impact velocity. Therefore, with such built in impact angle, the flyer plate undergoes flanging and welding at the same time.

Figure 5 Pre-flange actuator with workpieces. The inbound and outbound currents were labeled onto the actuator. (The supporting blank holders are ignored in this figure.)

3.3 Lap Joint with Embedded Wires

The uniform pressure (UP) actuator developed by Daehn, Kamal and Banik [8, 9] has been used for electromagnetically assisted forming process. Recently, it was applied for wire embedded plate-to-plate welding. The impact welding was conducted with embedded wires between the flyer and the target plates. The embedded wires are attached to the target plate prior to welding. These wires were used to make the flyer contact onto the target with certain impact angle. If there is no wire between them, the UP actuator accelerates the flyer plate against the target plate parallel but no joint can be formed after such parallel impact. As shown in Figure 6(a), UP actuator is a solenoid actuator with several turns. The flyer plate is loaded onto the outer channel. And it undergoes approximately uniform pressure from the inner actuator during the impact process. In order to fix the target plate during impact process, a top die is put onto the target plate and the welding system is then clamed down with 5000 psi pressure to avoid the top fixture moment as shown in Figure 6(b). One of the welded samples was shown in Figure 6(c). The welded plate materials were AA6061 and the embedded wire is steel. The thickness of the plate is 0.254 mm and the wire diameter is 0.25 mm.

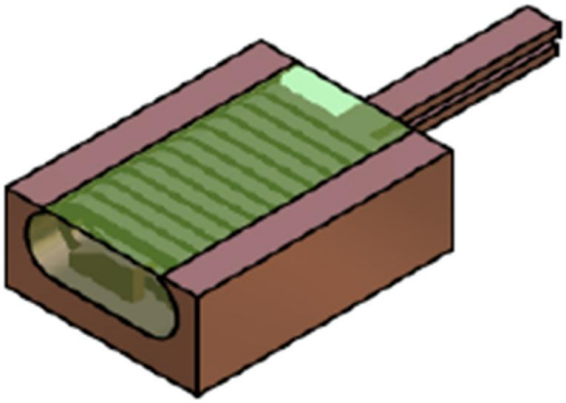

(a) Illustration of uniform pressure actuator[8]

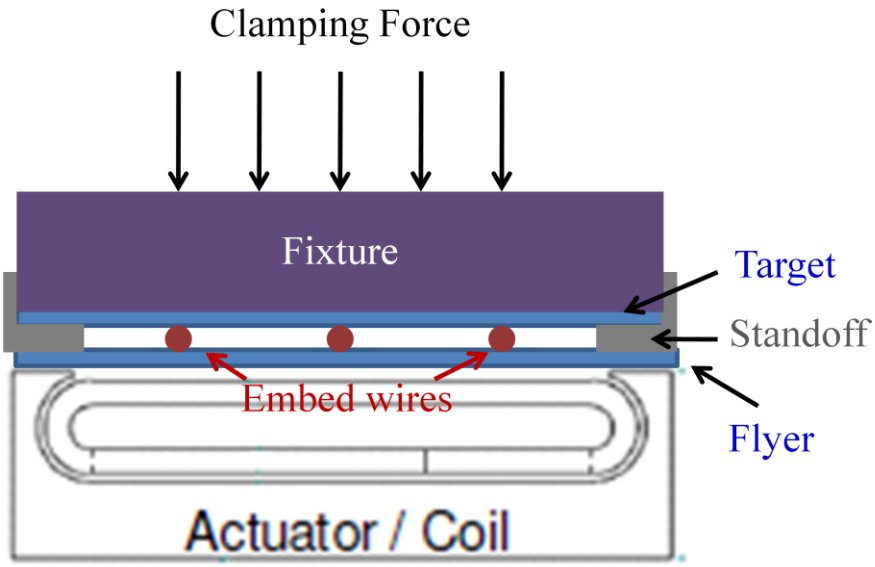

(b) Welding system with uniform pressure actuator

(c) Welded sample with embedded wires

Figure 6 Uniform pressure actuator applied for plate-to-plate welding with embedded wires.

4 Impact Velocity and Impact Angle Measurement

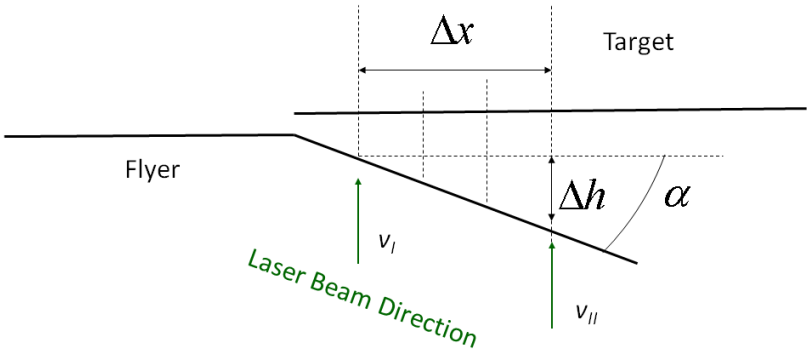

Figure 7 Schematic of impact angle measurement. (In order to measure the moving flyer plate velocity, the laser beam direction needs to be perpendicular to the flyer plate, which is very difficult in real experiment. In this study, two individual laser beams were used to measure the specific point velocity rather than the moving surface velocity. Hence, the beam direction is not perpendicular to the flyer plate.)

During impact welding process, the fiber optic laser beams aim at the flyer surface and capture its entire movement. A subroutine for Matlab program has been developed which is capable to analyses the raw PDV data into the impact velocity versus time profile directly. PDV probes can be used to measure multiple velocities at different specific locations. As shown in Figure 7, two individual laser beams were used to measure the specific point velocities at position *I* and position *II*. During impact welding, the flyer plate collides onto the target plate forming an initial welding line and this welding line moves along the being welded interface. Due to the oblique impact, the flyer plate travels in shorter distance to collide the target plate at the position of the initial welding line, than at the position of the final welding line. Assuming the flyer plate is rigid before collision and deformable after collision, the impact angle can be calculated as Equation (1~2).

$$\alpha = tg^{-1}\frac{\Delta h}{\Delta x} \tag{1}$$

in which, Δh is the travelling distance difference and Δx is the distance between the two measured positions. The travelling distance difference can be calculated as:

$$\Delta h = \int v_2 dt_2 - \int v_1 dt_1 \tag{2}$$

v_1 and v_2 are the velocities at the positions *I* and *II*, t_1 and t_2 are the total travelling times for the impact process at position *I* and position *II*. The welding map for Cu-Cu joint on the second generation flat bar actuator was measured and shown in Figure 8. For 0.254 mm thick Cu plate-to-plate welding, the welded velocity was larger than 250 m/s and the impact angle was in the range of 2°~7°.

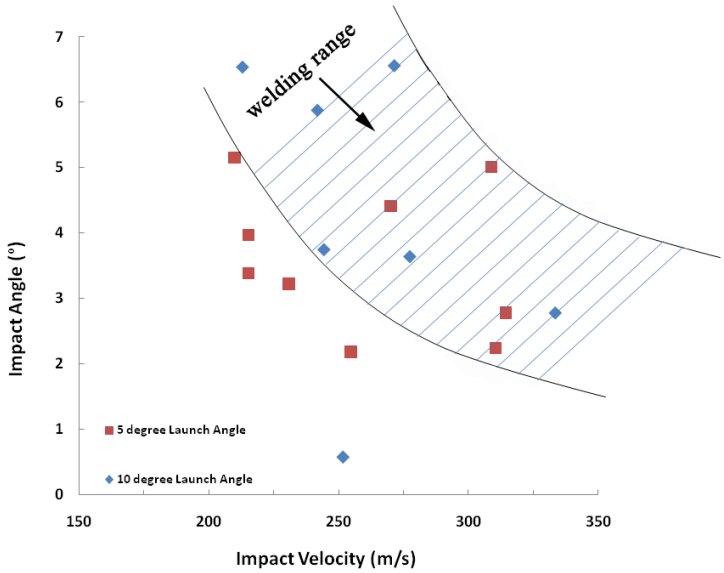

Figure 8 Weldability map for Cu110 joints of 0.254mm thick plates.

5 Joint Mechanical Property

The direct lap joint samples were studied by lap shearing, peeling and nano-indentation tests. For both AA6061 and Cu110, the fracture of the lap shearing test was out of the welded region and broke at base metals. AA6061 joints did not show elongation before fractured whereas Cu110 joint had obvious elongation. For dissimilar materials joint, the peeling test results exhibited base metals fracture before the joints were fully pulled apart. Lap shearing and peeling tests qualitatively suggested the impact joint was stronger than the base metals. Nano-indention test quantitatively presents the joint strength as shown in Figure 9. The joint hardness values increased significantly. The strengthened region across the welded interface was quite narrow for AA6061 joint, about 20 μm wide totally. And the impact hardened region was symmetrical with regard to the welded interface, whereas for Cu110 joint, the strengthened region did not show symmetrical pattern, and it was about 30~40 μm wide. The asymmetrical hardening patter may come from different hardening mechanisms or the variation between each indentation. More study is needed to understand this behaviour.

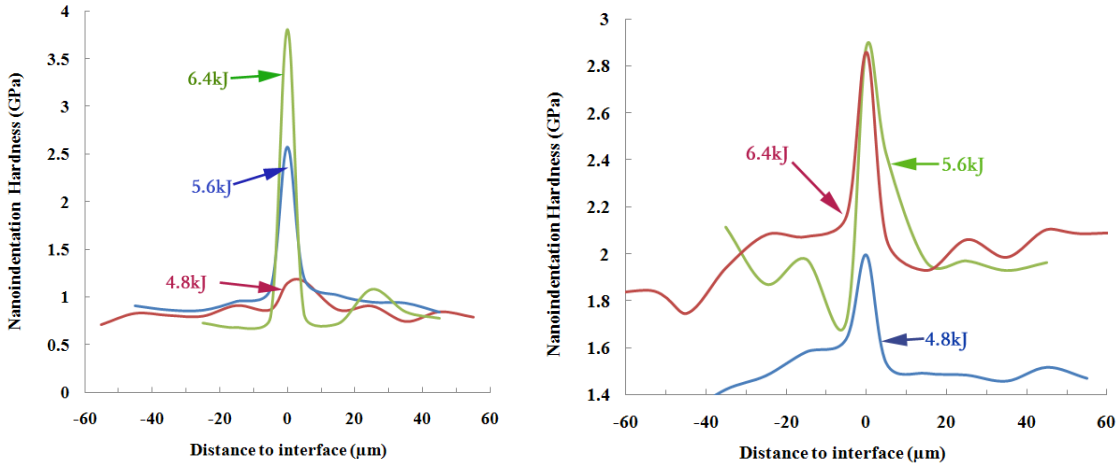

(a) AA6061 joints *(b) Cu110 joints*

Figure 9 Nano-indentation test results from MPW joints.

6 Joint Microstructure Characterization

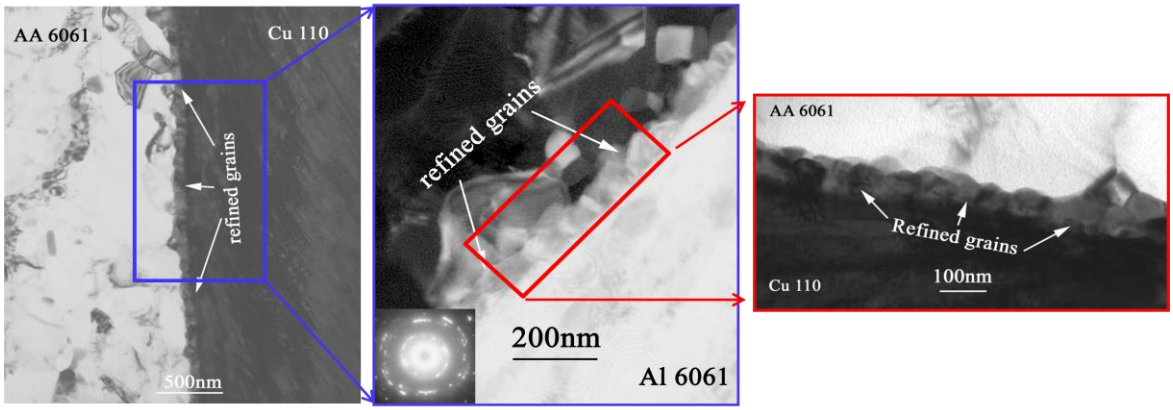

Figure 10 TEM images from Cu-Al joint showing grain refinement after high strain rate deformation. (All images are TEM BF image.)

The high strain rate deformation induced from MPW led to interface grain refinement and final equiaxed nano-crystalline structures despite the different strain paths [10]. The welded interface exhibited ultrafine grain structure, which was of several decade nanometers in diameter as shown in Figure 10. The TEM image was from 5.6 kJ welded Cu-Al interface, which clearly showed that the grain size decrease to nanometer in the impact interface with diffraction pattern changing from spot to ring patter. The interfacial grains transformed into essentially equiaxed nano-crystalline structures by adiabatic heating. As a result, the interfacial grain refinement was attributed to the interface strength increasing, which is in confirmation with the Hall-Petch relation. TEM observation showed the grain size changed from nanometer scale to micrometer scale in a continuous manner from interface to base metal. Such grain size gradient was caused by strain and strain rate gradients from high speed impact welding process. And the ultrafine grains were surrounded by high angle boundaries with the angles larger than 15˚. It was also noticed that the submicron grains near to the impact welded interface were

elongated along the impact direction. These high angle boundaries impeded the dislocation motion and strengthened the joint interface.

7 Conclusion

This paper studied the variety of the actuator configurations for magnetic pulse welding on plate-to-plate welding. Three types of configurations: direct lap joint, pre-flange lap joint, and embedded wire lap joint were applied onto plate-to-plate welding. The impact welding was applied onto both similar and dissimilar materials. The impact velocity and impact angle were measured by Photon Doppler Velocimetry. One welding map for Cu-Cu plate was developed. The joint strength was examined and the results indicated interface had greater strength than the base metal which could be explained by the interfacial grain refinement.

References

[1] *Psyk, V., Gershteny, G., Demir, O.K., Brosius, A., Tekkaya, A.E., Schaper, M., Bach, F.W.*, Process Analysis and Physical Simulation of Electromagnetic Joining of Thin-Walled Parts. in 3rd International Conference on High Speed Forming. 2008. Dortmund, Germany.

[2] *Khrenov, K.K. and V.A. Chudakov*, Magnetic pulse welding of butt joints between tubes. Automatic Welding Ussr, 1969. **22**: p. 75.

[3] *Tamaki, K. and M. Kojima*, Factors affecting the result of electromagnetic welding of aluminum tube. Trans. Jpn. Weld. Soc, 1988. **19**(1): p. 53-59.

[4] *Aizawa, T., Kashani M., and Okagawa K.*, Application of Magnetic Pulse Welding for Aluminum Alloys and SPCC Steel Sheet Joints. Welding in the World, 2005. **49**(9): p. 212-222.

[5] *Kore, S.D., Date P.P., and Kulkarni S.V.*, Effect of Process Parameters on Electromagnetic Impact Welding of Aluminum Sheets. International Journal of Impact Engineering, 2007. **34**: p. 1327-1341.

[6] *Lee, K.-J., Shinji, K., Takashi, A., Tomokatsu, A.,* Interfacial microstructure and strength of steel/aluminum alloy lap joint fabricated by magnetic pressure seam welding. Materials Science and Engineering A, 2007. **471**: p. 95-101.

[7] *Fenton, G., Daehn, G., Vivek, A., Johson, J., Taber, G.,* Electromagnetic ring expansion for high strain rate tensile testing. in TMS 2008. New Orleans, LA,USA.

[8] *Banik, K.,* Factors affecting electromagnetic flat sheet forming using the uniform pressure coil, in Materials Science and Engineering. 2008, The Ohio State University: Columbus,OH.

[9] *Kamal, M.,* A uniform pressure electromagnetic actuator for forming flat sheets, in Materials Science and Engieering. 2005, The Ohio State Univeristy: Columbus,OH.

[10] *Zhilyaev, A.P., Swaminathan, S., Gimazov, A., McNelley, T., Langdon, T.,* An evaluation of microstructure and microhardness in copper subjected to ultra-high strains. Journal of Materials Science, 2008. **43**(23): p. 7451-7456.

Modelling Pulse Magnetic Welding Processes – An Empirical Approach

E. Uhlmann[1], A. Ziefle[1]

[1] Institut für Werkzeugmaschinen und Fabrikbetrieb (IWF), Technische Universität Berlin, Germany

Abstract

In recent years pulse magnetic welding technology gained an ever increasing attention. The process was known for over 40 years, yet the poor knowledge of process parameters as well as the difficulties concerning the calculability of the process due to lack of adequate software, performance and appropriate material models hindered the application of the technology. In the past, some simulations treating the process of explosive welding were conducted. There, the assumption was made to define a friction condition to the boundary regions which was reasonable due to similar conditions in the collision region during the process. However, at pulse magnetic welding processes, the contact forces are highly transient and have big gradients over the geometry.

In this paper a new empirical approach is presented, which gives the possibility of modelling the welding process by parameter-controlled bonding at the welding interface. The pulse magnetic forming process was simulated by loose coupling of electromagnetic and mechanical FEM software with the commercial code ANSYS. As geometry the joining of a duct with an internally positioned conical bolt was chosen. The material used for both duct and bolt was EN AW 6063. First of all the influences of heat generation were analyzed. Therefore, the additional thermal simulation was coupled with the electromagnetic and the mechanical simulation. The heat generation caused by the plastic deformation was considered. As the resulting temperatures were below the melting temperature of the material, further simulations were carried out without thermal simulation. In order to calibrate the welding model, a set of relevant parameters were defined. It included the cumulative plastic work, the plastic deformation in collision direction, the normal and the tangential components of the collision velocity and the collision angle between the two parts. By comparing the simulation with experiments carried out at the same specific process parameters, it was possible to reduce the set of parameters to the normal collision velocity and plastic deformation. Based on their distribution, the parameter control of the bonding condition could be adjusted. Further experiments gave a high accordance to the simulations carried out with the parameters found for this model.

Keywords

Finite element method (FEM), pulse magnetic welding, parameter controlled bonding

1 Introduction

The process of pulse magnetic welding was already applied in the 1970s [1], when it was used for solid state welds between the fuel pin cladding and a tapered end plug insert. However, the poor knowledge of process parameters as well as the difficulties concerning the calculability of the process due to lack of adequate software, computing performance and appropriate material models hindered a wide acceptance for applications of the technology. Recently, the development of software as well as hardware made sufficient progress which capacitates to model shock-forming processes. Regarding explosive welding, some simulations treating the process of explosive welding were conducted by Akbari-Moussavi. There, the assumption was made to define a friction condition to the boundary of the joining regions which was reasonable due to similar conditions in the collision region during the process [2]. Though the forming process and the pressure distribution were modelled, no information was obtained whether welding occurred nor where it occurred. The aim of the investigations in this paper is to provide a method in order to be able to predict welding as well as the location during pulse magnetic welding processes, validated by experiments.

2 Experiments

The geometry chosen for the experiments was a tube of 1mm thickness and an outer diameter of 18 mm and a bolt with a conical join-region using an angel of 4°, as can be seen in Figure 1.

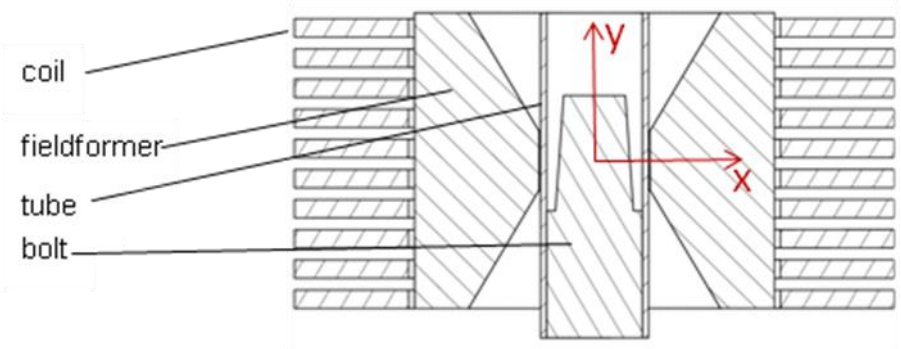

Figure 1: *Description of the Setup*

To guarantee a sufficient welding result, the tube needs a certain distance in order to sufficiently accelerate. Therefore a gap of 2 mm was set between the tube and the beginning of the cone. By pulse magnetic forming the tube was compressed and clashed on the conically turned surface. The chosen material was the aluminium alloy EN AW 6063, which properties are shown in Table 1.

Property	Value
specific resistance ρ	3,3 10^{-8} Ω m
thermal conductivity λ	201 W $m^{-1}K^{-1}$
specific heat capacity C_W	898 J kg^{-1} K^{-1}
thermal expansion coefficient α_W	23,5 10^{-6} K^{-1}

permeability μ	1 μ_0 = 1,2566 10^{-6} H m^{-1}

Table 1: Material properties of EN AW 6063

The experiments were carried out with a pulse magnetic forming machine (ELMAG), using a capacity of C = 240 µF with a loading voltage of U = 7,6 kV to 9,1 kV which equals a discharge energy of E_{EL} = 7 kJ to 9 kJ. The inductance of the machine for the used configuration is L_i = 0,36 µH, and the inductance of the coil is L_{coil} = 1,930 µH. This parameters of the RLC-circuit lead to a frequency of f = 7,3 kHz. For the experiments, a coil with 10 windings was used together with a fieldformer.

3 Simulations

3.1 Sequential Coupling of Electrodynamic and Mechanical FEM

The forming process is driven by the Lorentz force, which is generated due to inducted currents in the workpiece. According to [3] the skin effect has to be considered for high-frequency currents. In dependence of the conductivity of the material and the frequency of the discharge, the current experiences more resistance, the more it penetrates the material. Therefore the skindepth d is defined as:

$$d = \frac{1}{\sqrt{\kappa \mu \pi f}} \tag{1}$$

It is the length towards the inside direction of the material at which the current is reduced to 36 %. In this equation κ is the electrical conductivity, μ the permeability of the conductive material and f the frequency of the current. For the carried out experiments the skindepth can be calculated to d = 1,07 mm. Taking this into account, it can be assumed, that the current generating the Lorentz forces is flowing only at the outer surface of the tube. Thereby, the concept of the magnetic pressure applied to the surface of the tube can be developed. Together with the assumption, that at the inside of the workpiece the magnetic flux density is neglectable, the magnetic pressure p_{MAG} can be calculated for tubes [4]:

$$p_{MAG} = \frac{B^2}{2\mu} \tag{2}$$

where B is the magnetic flux density. The magnetic flux density is highly dependent on the geometry and additionally transient. At the beginning of the forming process, the tube acts like a faraday cage, forcing the magnetic flux in the gap between tube and coil. As soon as the shape of the tube is being compressed, the flux is much less concentrated, which leads to a significant drop of the magnetic pressure. Whereas in previous publications a loose coupled approach was used [5], a sequential coupled simulation model is now necessary in order to involve the change of geometry in the calculation of the Lorentz force. At the conducted simulations this was achieved by use of ANSYS APDL.

3.2 Empirical Model

Explosive welding and pulse magnetic welding are very similar concerning the bonding process [6]. It is common agreement that the welding process works as follows: a collider sheet metal plate clashes onto another plate with the inclination of the collision angle α. Due to the sudden shear strain at the collision point high pressures are generated. Therefore the material within the collision point switches to a quasi-viscous state and a material jet is generated, heading towards the free angle between the two workpieces and moving with the collision point, see Figure 2.

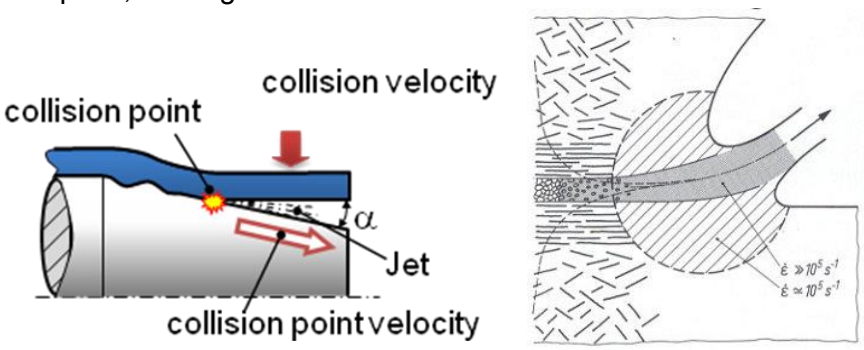

Figure 2: Welding process (left), formation of Jet (right, [7])

This way it is possible to form a thin interface layer of a few micros thick between the two workpieces. Kreye et al [7] and Koch [8] state, that the two materials approach to molecular distance and build intergranular bounds. Nevertheless the influence of the temperature should not be completely neglected. The wavy bounding structures found at experiments with pulse magnetic welding as well as explosion welding near the welding interface are comparable. Though the bounding process works similarly, there are differences between the two processes: Due to the high burning velocities of the explosives, the pressures as well as the collision velocities are usually higher than by use of pulse magnetic welding. Also, at pulse magnetic welding there is neither similar pressure nor similar deformation over the geometry of the tube. The whole welding process involves phase changes, chemical interaction and friction. A correct implementation of all effects would be either very complicated or entirely impossible due to lack of measurement data. In order to determine where welding effectively took place, a contact model has to be designed, which involves all relevant physical parameters dependent on which the contact elements will bond or continue having friction. In the literature, the weldability is very often set into relation to the collision angle, the collision velocity and the collision point velocity [5], because these parameters are measurable in experiments. As conclusion a model was implemented that can apply bonding at contact elements depending on the defined parameters.

$$B_{Bond} = f(\alpha, v_{\perp}, v_{cp}, P_{PL}, \varepsilon) \tag{3}$$

In this model B_{Bond} is a Boolean type with 1 equals to bonded and 0 equals to not bonded, α is the inclination-angle, $v_{\perp}$ the collision point velocity, v_{cp} the collision velocity, P_{PL} is the plastic work and ε is the deformation. The model does not consider cracking. After an element was bonded, it cannot be loosened any more.

3.3 Influence of the Temperature

As earlier stated, the influence of the heat generation also needs some consideration. In order to determine the influence of the heat generation due to plastic deformation and joule heating, the thermal simulation was additionally carried out after each time step of the sequentially coupled electrodynamic-mechanical simulation, sharing the same geometry. Due to the very thin welding region, the grid needed to be meshed especially in the contact region with a significantly higher definition, which led to a considerably longer calculation.

Figure 3 shows the temperature development at the inner side of the tube during the welding process. It can be seen, that the temperature never rises above 350 K, which is approximately 38 % of the melting temperature and 8 % of the required temperature difference. According to simulations the heat generated by friction, deformation and joule heating have a low influence on the welding process, the simulation of the heat generation was neglected for the further simulations.

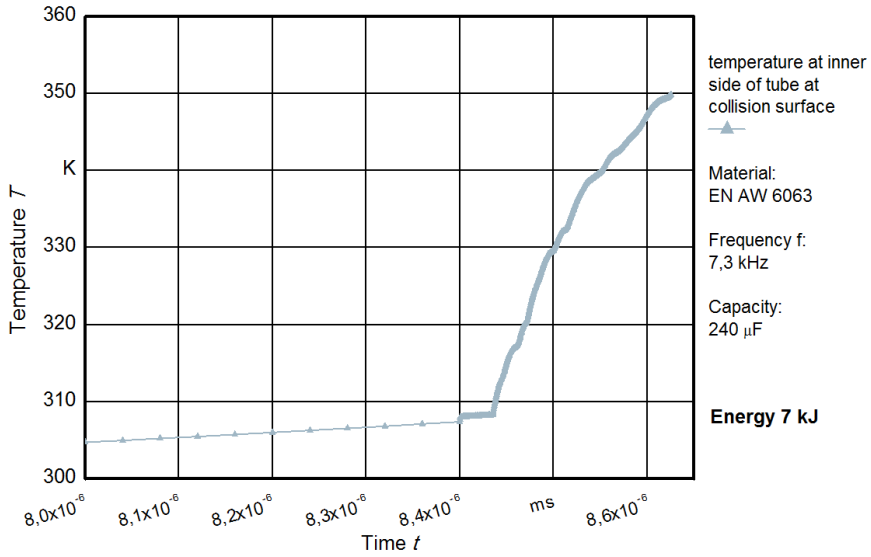

Figure 3: *Diagram of simulated Temperature of a contact element at the inner side of the tube*

4 Model setup

As a next step, the generic welding model had to be calibrated. Therefore, experiments with the later mentioned configuration were carried out, using 7 kJ and 9 kJ. At the same time simulations with the same parameters were carried out. In the interface region, a friction boundary was used. In Figure 4 the measured and simulated currents are plotted against each time for the case of 8 kJ. Though the simulation ended before the time the current had its first peak due to overdeformed elements in the bonding zone, the forming process was almost completed at this time, see Figure 5.

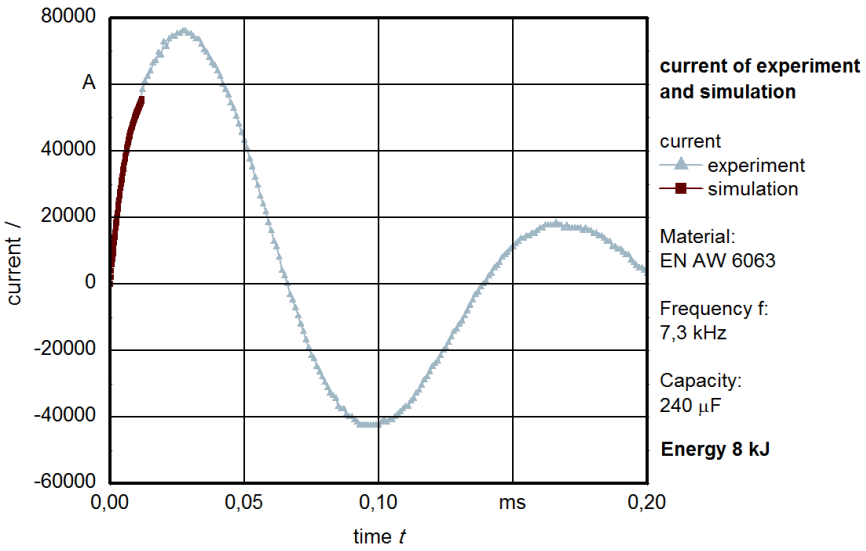

Figure 4: *Current distribution of the electromagnetic simulation and measurement*

In Figures 6 a.) to g.) each in Equation (3) defined entity is plotted over the y-coordinate of the joining zone at collision time. The collision time is the time when a node of an element of the tube collides with the surface of the bolt. As the collision is a gradual process, the collision time varies for every element. Origin and direction of the y-coordinate can be seen in Figure 1. Due to the impact of the collision there can be observed some instabilities and oscillations in the diagrams. For better data, in some cases also the diagrams of the same entities four time steps before to one time step behind the collision time are shown. The welded domains drawn as hatched areas into Figures 6 a.) to g.) show the geometrical y-position of the welds in the analogical carried out experiments. Therefore the welded probes were cut axially and polished.

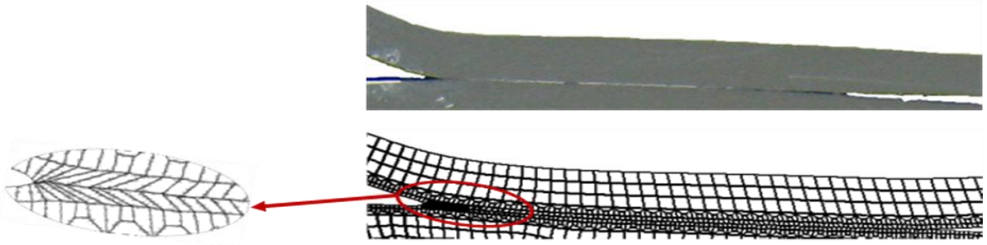

Figure 5: *Deformation of elements in the bonding region*

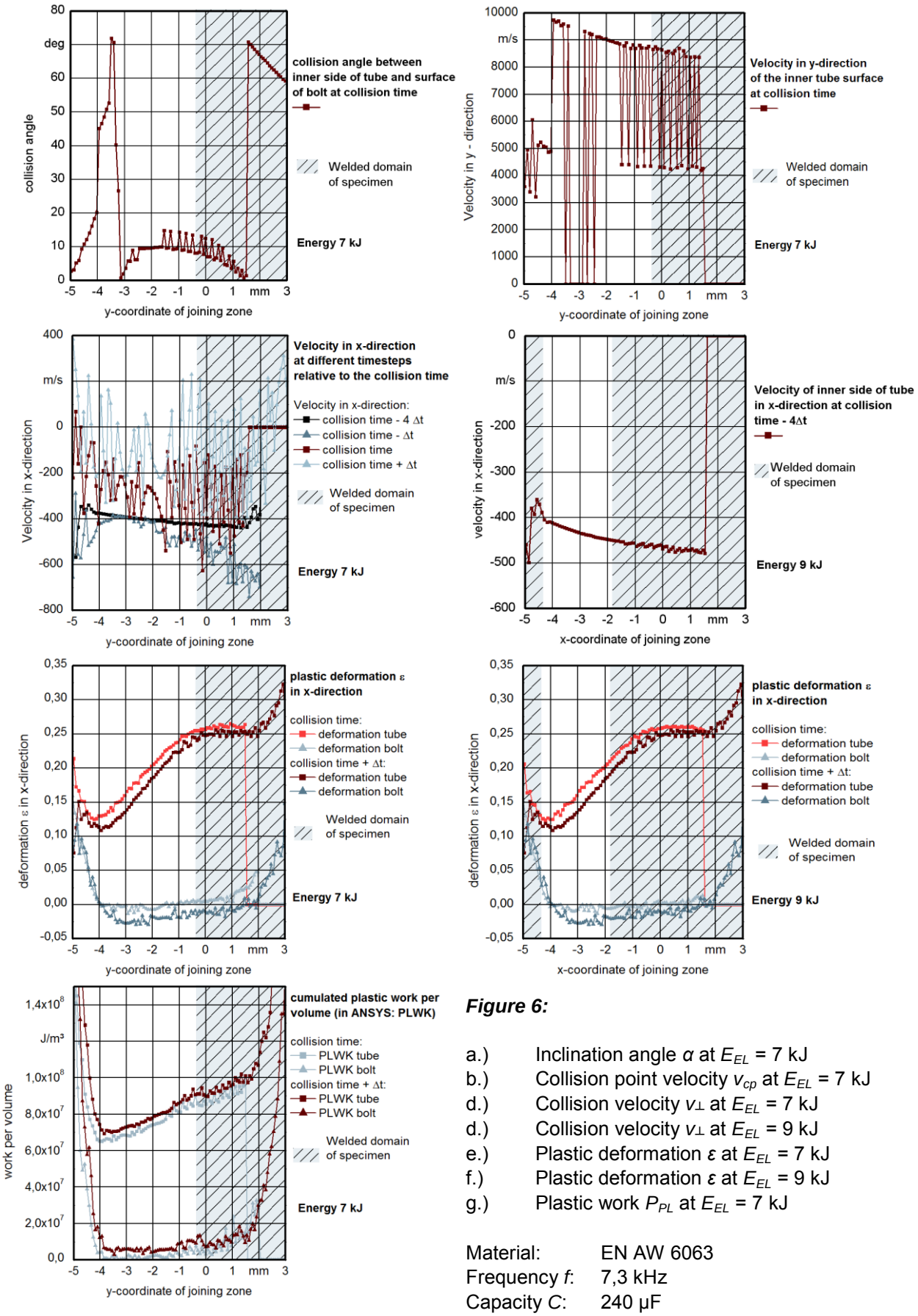

Figure 6:

a.) Inclination angle α at E_{EL} = 7 kJ
b.) Collision point velocity v_{cp} at E_{EL} = 7 kJ
d.) Collision velocity $v_{\perp}$ at E_{EL} = 7 kJ
d.) Collision velocity $v_{\perp}$ at E_{EL} = 9 kJ
e.) Plastic deformation ε at E_{EL} = 7 kJ
f.) Plastic deformation ε at E_{EL} = 9 kJ
g.) Plastic work P_{PL} at E_{EL} = 7 kJ

Material: EN AW 6063
Frequency f: 7,3 kHz
Capacity C: 240 µF

Figures 6 a.), b.), c.) and g.) show that the data of the entities inclination-angle α, plastic work P_{PL}, and collision point velocity v_{cp} cannot be used for the model due to difficulties to obtain a stable course of the values. In Figures 6 e.) and f.) the plastic deforma-

tion of the tube with a loading energy of 7 kJ (left) and 9 kJ (right) is shown. The diagrams are quite stable over the y-axis at both energies. Also, there are only little oscillations in the graph. Unfortunately this is not the case for Figure 6 g.), where especially at the transition between welded and not welded zone oscillations of the plastic work occur. However the diagrams show that the deformation alone is not sufficient to describe welding. Therefore, the collision velocity was selected as an additional parameter. In Figures 6 c.) the collision velocity is plotted at several time steps relatively to the collision time. It can be seen that the courses at collision time, as well as one time step before and after it, are not smooth due to shockwaves induced by the impact earlier. However, using the course four time steps before collision time gives a smooth curve in the relevant region, see Figures 6 c.) and d.). It is shown, that welding can only occur after surpassing a decent particular value of collision velocity. The big step on the left side is due to the ending of the simulation, because the elements couldn't bear the steep deformations occurring at the boundary. As a result there have been defined two thresholds that have to be surpassed in order to enable welding at contact, namely a deformation of ε = 0,2 and a collision velocity of $v_{\perp}$ 420 m/s.

5 Results

For validation an additional simulation was carried out by use of the values obtained in the model setup with a discharge energy of E_{EL} = 8 kJ. In Figure 7 the results of the simulation were compared with the experimental results. The weld domain measured in a corresponding experiment is in high accordance with the weld domain in the simulation.

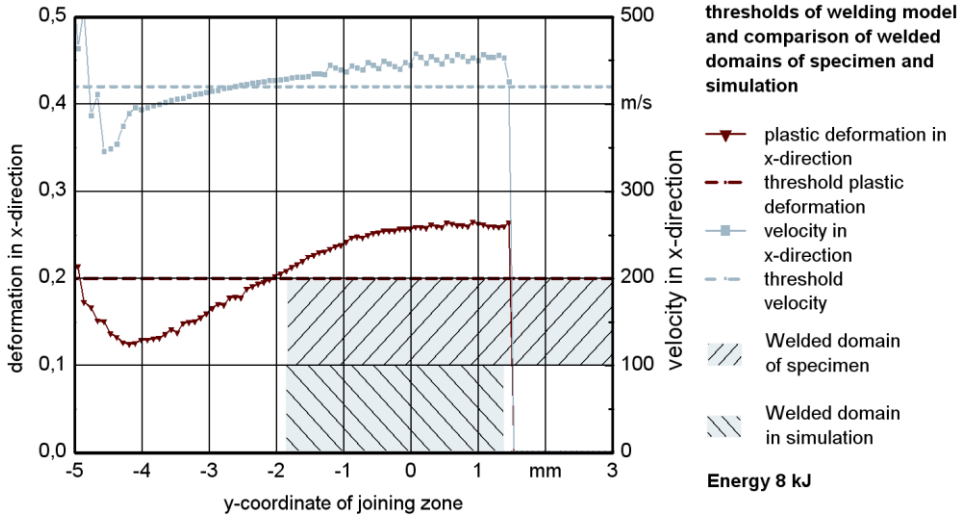

Figure 7: *Comparison of welded domains in model and simulation at E_{EL}= 8 kJ*

6 Conclusions

In order to model the process of pulse magnetic welding a fully sequential coupled simulation incorporating thermal, electrodynamic and structural simulation was implemented. Thereby the Lornetzforces could be directly calculated with the magnetic flux density, which includes all geometry related effects. Considering the material heating due to plastic deformation and joule heating the simulation showed low influences. Therefore the simula-

tion of thermal effects was neglected for the further cases. By comparing the simulation with experiments carried out at the same specific process parameters, the set of parameters was reduced, leaving the collision velocity and plastic deformation. Based on their distribution, the parameter control of the bonding condition could be adjusted. The validation experiment carried out using a discharge energy of 8 kJ gave a high accordance to the simulations carried out with the parameters found for this model. With this paper an empirical approach was presented to help determine the location of welds produced at pulse magnetic welding by means of simulation. Nevertheless it must be pointed out, that the found thresholds are only valid for the used material as well as the used rotational symmetric geometry. Further validation is necessary in order to expand the extent of validity as well as the usability for additional materials. Furthermore, the used model-parameters can not be obtained through experiments but only by the combination of simulations and experiments. Loosening and Cracks were not part of the Model either, not taking into account rebound effects.

References

[1] *Brown, W.; Bandas, J.; Olson, N.:* Pulsed Magnetic Welding of Breeder Reactor Fuel Pin End Closures. Reprinted from Welding Journal, June 1978.

[2] *Akbari-Mousavi, S.A.A.; Barrett, L.M.; Al-Hassani, S.T.S.:* Explosive welding of metal plates. Journal of Materials Processing Technology 202, 2008, p.224-239

[3] *Winkler, R.:* Hochgeschwindigkeitsbearbeitung – Grundlagen und technische Anwendung elektrisch erzeugter Schockwellen und Impulsmagnetfelder. VEB-Verlag Technik, Berlin, 1973.

[4] *Hahn, R.:* Werkzeuge zum impulsmagnetischen Warmfügen von Profilen aus Aluminium- und Magnesiumlegierungen. Dissertation, Uhlmann, E.(Editor) Berichte aus dem Produktionstechnischen Zentrum Berlin, 2004

[5] *Ziefle ,A.; Uhlmann, E.:* Lösungsansätze zur Darstellung des impulsmagnetischen Schweißprozesses mittels gekoppelter FEM – Simulation. Proceedings of Berliner Runde 2009.

[6] *Cramer, H.; Zech, F.; Appel, L.:* Metallographic Investigation of MPW Interfaces. Proceedings of “The first technical Conference on Industrialized Magnetic Pulse Welding & Forming”, Munich, 2008

[7] *Kreye, H.; Hammerschmidt, M.; Granz, U.; Woidneck, C.-P.:* Über den Bindemechanismus beim Explosivschweißen. Schweißen und Schneiden 37, vol. 7, 1985, p 297-302.

[8] *Koch, W.:* Vorgänge beim Explosivschweißen metallischer Werkstoffe. Dissertation, Fakultät für Bergbau und Hüttenwesen der Rheinisch-Westfälischen Technischen Hochschule Aachen, 1965.

Fundamentals of EMPT-Welding*

A. Elsen[1], M. Ludwig[1], R. Schaefer[2] and P. Groche[1]

[1] Institute for Production Engineering and Forming Machines, Darmstadt University of Technology, Darmstadt, Germany
[2] PSTproducts GmbH, Alzenau, Germany

Abstract

A well-suited solid state welding process for treatment of tubular structures is the electromagnetic pulse welding technique (EMPT): A pulsed magnetic pressure loads the structure to be welded within a few microseconds and accelerates one of the both contact partners (the so called "flyer") onto a stationary one. When the flyer strikes the stationary contact partner, contact normal stresses far above 1000 MPa act on the interfacial zone between flyer and stationary part. As a result of these high interfacial loads, a layer of several micrometers thickness next to the interface is severely plastically strained. Hence, the oxide layers covering both contact partners are cracked. These chipped oxide particles are blown out of the joining area by a so called "jet". This jet is caused by the air between the two joining partners being compressed and accelerated due to the movement of the flyer. The result of both phenomena –the oxide chipping by severe plastic deformation of the interfacial zone and the particle blow out caused by the jet– is a pure metallic interfacial zone, loaded by contact normal stresses. The conjunction of the highly reactive metallic surface and the contact normal stresses establishes a metallic bonding, whose strength equals at least the strength of the weaker contact partner.

This report presents the results of a collaborative research project between the Institute for Production Engineering and Forming Machines (PtU) and PSTproducts GmbH. Experimental welding analysis is accompanied by numerical work for the study of the underlying mechanisms of solid state welding with respect to interfacial plastic deformation and contact loads. Additional metallographic work gives insight into the microscopical structure of the interfacial joint zone.

Keywords

Welding, Interface, Waviness, Finite element method (FEM)

---

* *The authors would like to thank the German Federal Ministry of Economics and Technology for financial support*

1 Introduction

The electromagnetic pulse welding (EMPW) process allows for the integral joining of conductive metallic components without the addition of thermal energy [1]. For this the components to be joined are accelerated towards each other by a pulsed high-energetic magnetic field to form a solid state cold weld. Unlike thermal welding processes no influence on the microstructure due to heat effects occurs. Moreover the EMPW process offers the potential to join dissimilar and conventionally non-weldable material combinations, such as aluminum and steel, thus enabling the application of light and robust material combinations.

The electromagnetic pulse technology (EMPT) physically bases upon the utilization of electromagnetic body forces (Lorentz force) [2]: Alternating currents in a coil induce a current in a second coil in vicinity of the live coil. The induced current creates a corresponding magnetic field that strongly repels that of the live coil. Hence a tubular conductive part functions itself as a single-winded coil. High currents (> 100 kA) generate a strong force between the tube and the outer coil, which can overcome the yield strength of the work piece. With the help of magnetic field concentrators (“field shapers”) the repelling force can be directed to create permanent deformation of the component to a desired shape.

Regarding welding processes, a flyer tube is accelerated by electromagnetic pressure to impact with a tapered base insert at an adequate impact angle (Figure 1). The high impact pressure sweeps off the surface oxide film and forms an atomic bond between flyer and base tubes [3].

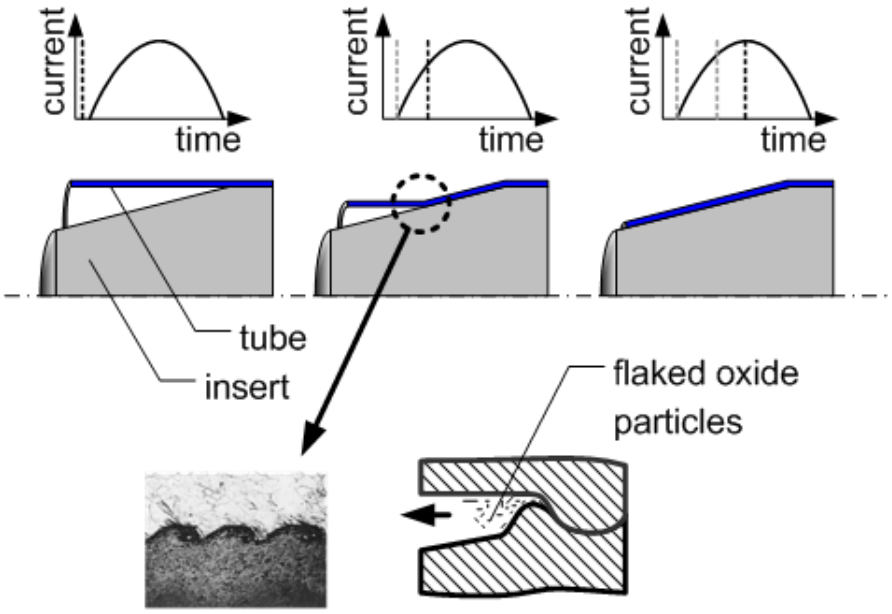

Figure 1: Schematic illustration of electromagnetic pulse welding

2 Experiments

Several experiments have been carried out to identify the influencing parameters on the evolution of the adhesively joined bonds and the characteristic waviness of the interface. A capacitor bank is discharged at a current of 930 kA and a frequency of 14 kHz through a

coil. Based on the geometry of coil and workpieces, this results in a magnetic pressure of 400 MPa onto the surface of the flyer. The material for the cast and machined insert and the outer extruded tube is EN AW-6061-T6 (AlMg1SiCu) (see Table 1 for mechanical properties and Table 2 for the chemical composition).

Alloy	$R_{p0.2}$ [N/mm²]	R_m [N/mm²]	A [%]
EN AW-6061 T6	240	260	9

Table 1: Mechanical properties of Al 6061 T6

Alloy	Si	Fe	Cu	Mn	Mg	Cr	Zn	Ti
EN AW-6061 T6	0.40-0.8	0.7	0.15-0.40	0.15	0.8-1.2	0.04-0.35	0.25	0.15

Table 2: Chemical composition of Al 6061 T6

The experimental setup consisting of a coil, a split field shaper and a specimen holder, which allows for aligning tube and insert inside the coil, can be seen in Figure 2. The capacitor bank is not displayed.

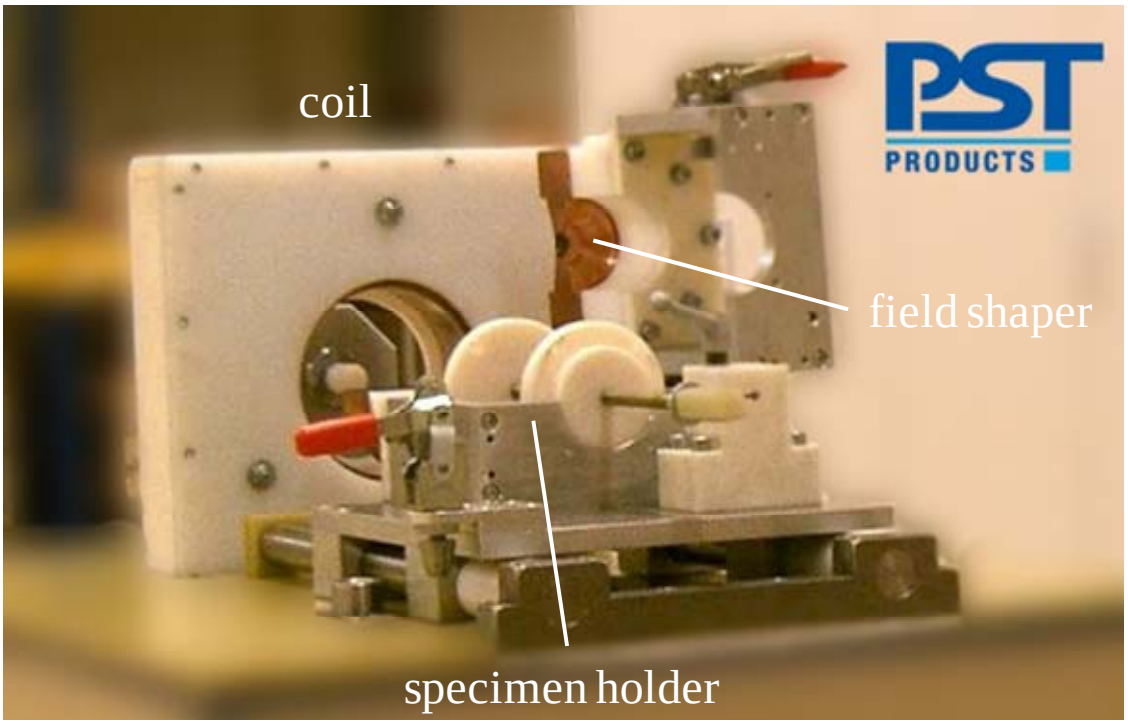

Figure 2: Experimental setup

The geometries and schematic alignment of tube and insert are shown in Figure 3. The aluminum tubes have an outer diameter of 50 mm and wall thicknesses of 1.5 mm, 2.0 mm or 3.0 mm, respectively. The section of the insert that is placed inside the tube has a length of 25 mm and a diameter of 50 mm less twice the wall thickness of the corresponding tube. After 5 mm there is a bevel of either 1 mm or 3 mm (“offset”) at an angle of 30°. Inlet and outlet are rounded down to R1 and R0.5. The actual effective area

for the welding process is the tapered part of the insert, angled at either 5°, 7.5° or 10° in the different experimental series.

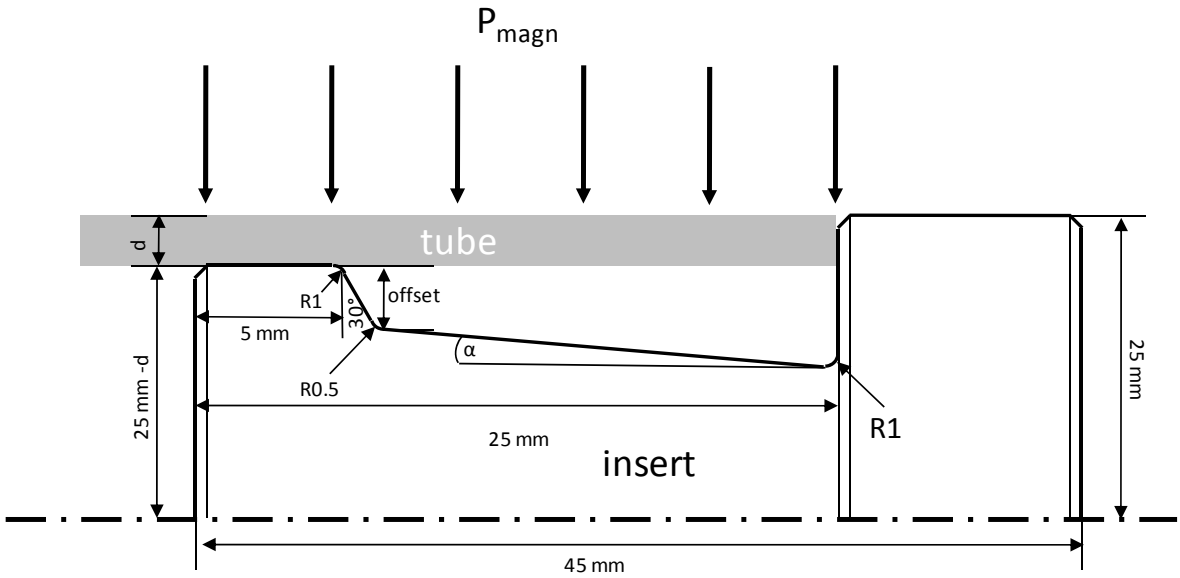

Figure 3: Schematic setup of the welding experiments

Each specimen has been cut through the longitudinal axis to examine the resulting welding length. The plots of the welding lengths in dependency of the wall thicknesses of the outer tubes in Figure 5 show a direct relationship between these parameters and the resulting welding length.

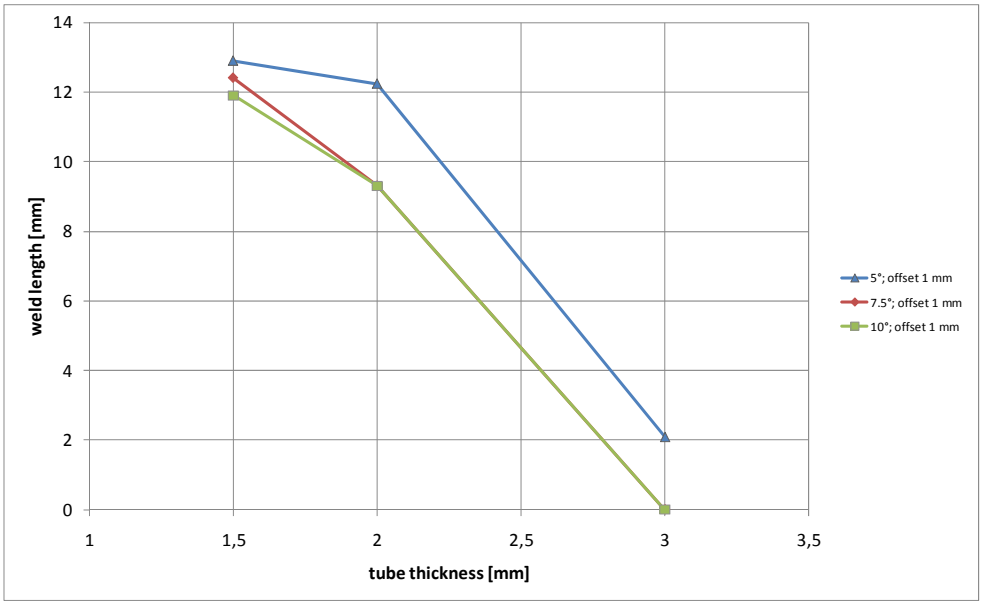

Figure 4: Welding length in dependency of the tube thickness for an offset of 1 mm

In general, the length of the welded joint decreases with increasing wall thickness of the tube. As the deployed magnetic energy is constant for all experiments, an increasing wall thickness results in a lower contact pressure between tube and insert as more energy is

consumed for the compression of the outer tube and the mass inertia of a heavier flyer tube is higher. Due to the velocity of the line contact being subject to the trigonometrical relation $v_{welding} = v_{impact} / \tan(\alpha)$, the lower impact velocity of the flyer results in a lower velocity of the line contact. The angle of the tapered section, which determines the contact angle of flyer and insert, has in this test series only minor influence on the resulting welding length, as the angles of 5°, 7.5° and 10° are already empirical values for sound welding results obtained from previous experiments. Noticeable is the fact that the experiments with an offset of 3 mm and a contact angle of 5° (Figure 5) did not result in a bond no matter the wall thickness. However, the specimen with 7.5° and 10° did weld with tubes of a wall thickness of 1.5 mm and 2.0 mm, while a wall thickness of 3 mm and an offset of 3 mm did not induce a bonding in any variation of the angle. Further investigations of the samples lead to the insight that the flyer tube had bounced off the insert at the low contact angle of 5°. Though the contact pressure was sufficient the contact angle did not result in a continuous line contact and thus in a weld joint.

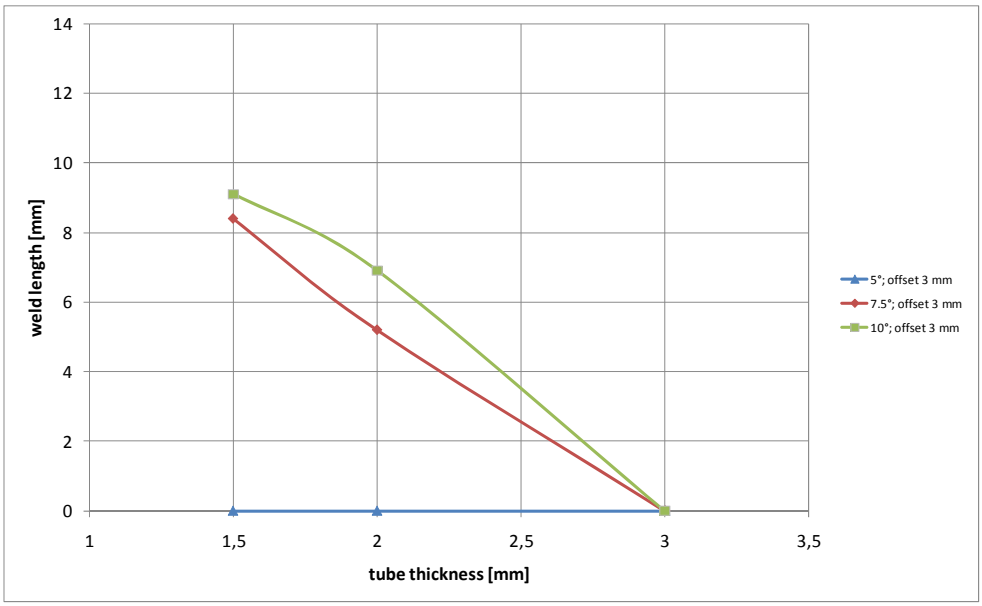

Figure 5: Welding length in dependency of the tube thickness for an offset of 3 mm

3 Metallographic Examination of the Welded Interface

For the investigation of the welded interface, metallographic microsections have been made by embedding the specimen in epoxy resin and subsequently grinding and polishing down to a graining of 0.25 µm. Etching with 1% hydrofluoric acid uncovers the grain boundaries and the welding interface. Figure 6 shows a weld interface with characteristic waviness.

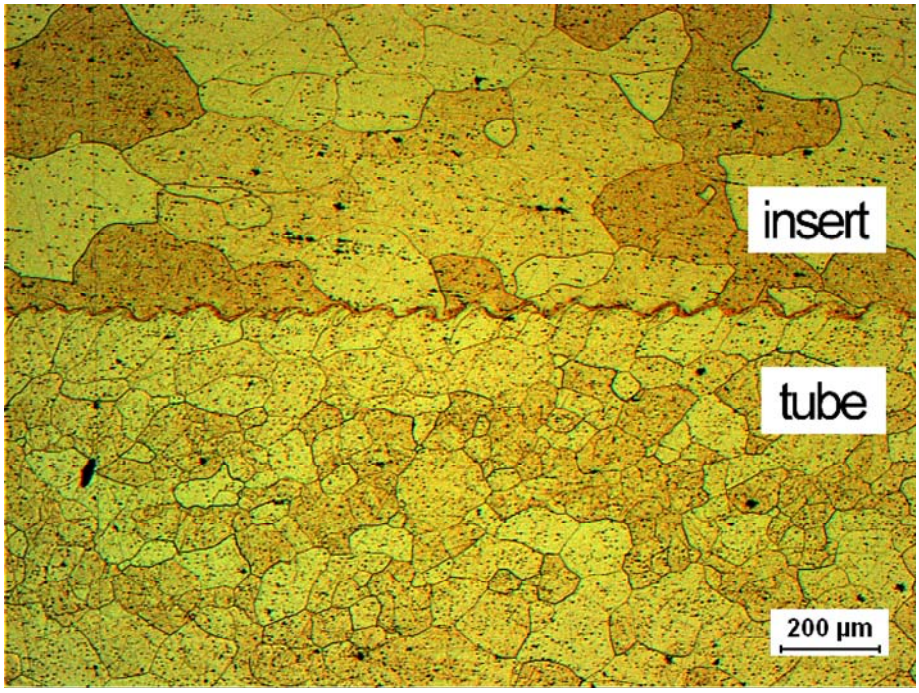

Figure 6: Weld interface with characteristic waviness

The insert exhibits a typical cast structure with large grains compared to the microstructure of the drawn tubes. Within the welding zone the grains are to some extend severely deformed in direction of the advancing line contact (see Figure 7). These specimens have been treated with Weck's etching solution to obtain a color contrast between grain boundaries and the welding interface.

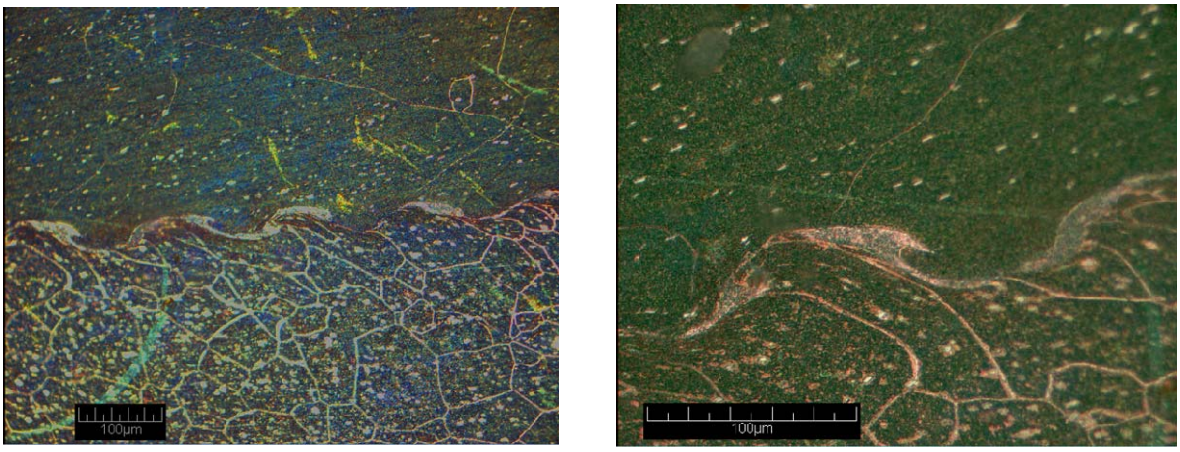

Figure 7: Welding Zone of Al6061-Al6061

Among others a theory based on the Kelvin-Helmholtz instability mechanism in fluid dynamics describes the wave formation as a result of flow velocity discontinuities across the interface [4]. Immediately after impact instabilities close to the severely deformed interface occur, caused by the different velocities of the interacting parts. Material close to the interface has to move faster across the wave hump than material more distant. According to Bernoulli's principle the pressure above a wave is lower than in the vicinity as a consequence of the higher velocity of the surrounding fluid. Hence there is a force that

pulls the crest upwards. The fluids nearby the wave trough behave analogously. Material yields more slowly across the surface of a wave trough than in its proximity, therefore the pressure is locally increased causing the wave trough to be pressed downwards. Refer to [5] for further details on this theory on the wave formation.

In Figure 8 a numerical simulation of a spatial Kelvin-Helmholtz-instability is compared to a microsection of a weld interface. Periodic sequences of sinusoidal waves and turbulent vortices can be observed in both the numerical simulation and the microsection of the specimen. This indicates that the theory of wave formation being an effect similar to the turbulent flow in fluids moving at different speeds is plausible.

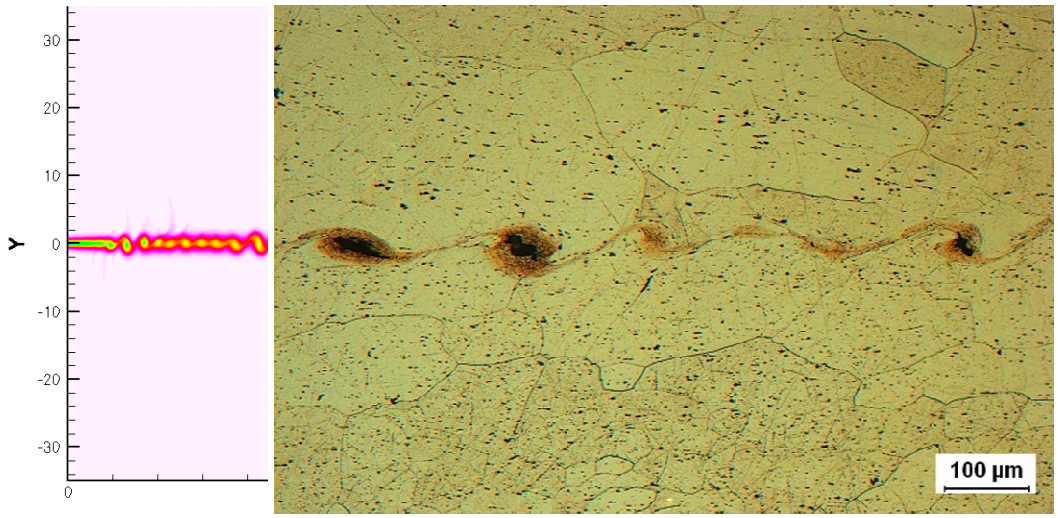

Figure 8: Numerical simulation of a spatial Kelvin-Helmholtz-instability (left) compared to a microsection of a weld interface of Al-Al (right)

4 Numerical Simulations of the Impact Zone

The finite element discretization of the EMPT-process is very challenging. Especially in the welding zone where very high strain rates occur the elements in the contact are underlying great distortions. However, with the help of adaptive meshing in this zone the process can be simulated. Figure 9 shows the setup of the simulation model.

The simulation is an explicit analysis with no mass scaling possibility because of the mechanical inertia effects in the forming process. 2D plane strain finite elements with a linear approach for the shape function and with reduced integration are used to model the welding process. A surface-to-surface contact with a penalty penetration method and a finite sliding formulation is chosen for the simulation. The friction formulation is also a penalty method with a coulomb friction coefficient of μ=0.15. Adaptive remeshing is executed with 20 sweeps per increment. The simulated process is velocity-driven at a velocity of 300 m/s. Adiabatic heating effects due to the temperature increase caused by the high inelastic deformations are included in the simulation model. A specific heat per unit mass of $c = 5 * 10^8$ $J(tK)^{-1}$ and a conductivity of $\lambda = 50$ $W(mK)^{-1}$ with an inelastic heat fraction of 0.9 have been assigned to the elements. Due to the high forming velocity the material parameters have to be adjusted to represent the correct material flow behavior. Therefore the plasticity model of Johnson and Cook [6] with a bulk modulus $E = 70000$ N/mm², a poisson ratio $\upsilon = 0.3$ and a material density $\rho = 2.7 * 10^9$ t mm^{-3} is chosen. In Johnson-Cook constitutive equation, the von-Mises yield stress is given as

$$\sigma = (A + B\varepsilon^n)\,(1+C \ln \dot{\varepsilon}_p)\,(1 - T^{*m}) \quad (1)$$

where ε is the equivalent plastic strain, $\dot{\varepsilon}_p = \dot{\varepsilon} / \dot{\varepsilon}_0$ is the dimensionless plastic strain-rate for $\dot{\varepsilon}_0$ = 1.0/s, T^* is the homologous temperature $(T - T_{room}) / (T_{melt} - T_{room})$, and T is the absolute temperature for $0 \le T^* \le 1.0$ [7]. The five constants are A, B, n, C, and m with the expression in the first set of brackets giving the stress as a function of strain for $\dot{\varepsilon}_p$ = 1.0 and T^* = 0 and the expressions in the second and third set of brackets representing the effects of strain rate and temperature [7].

The applied Johnson-Cook parameters are listed inTable 3.

Alloy	A	B	n	C	m	E_0
EN AW-6061 T6	275	500	0.3	0.02	1	1

Table 3: Johnson-Cook parameters for Al 6061-T6

The magnification of the contact zone in Figure 9 indicates that the elements close to the contact zone are subject to large strains and high strain rates. Due to the applied Johnson-Cook plasticity model the materials in these locations behave like viscous fluids, resulting in the familiar wavy interface.

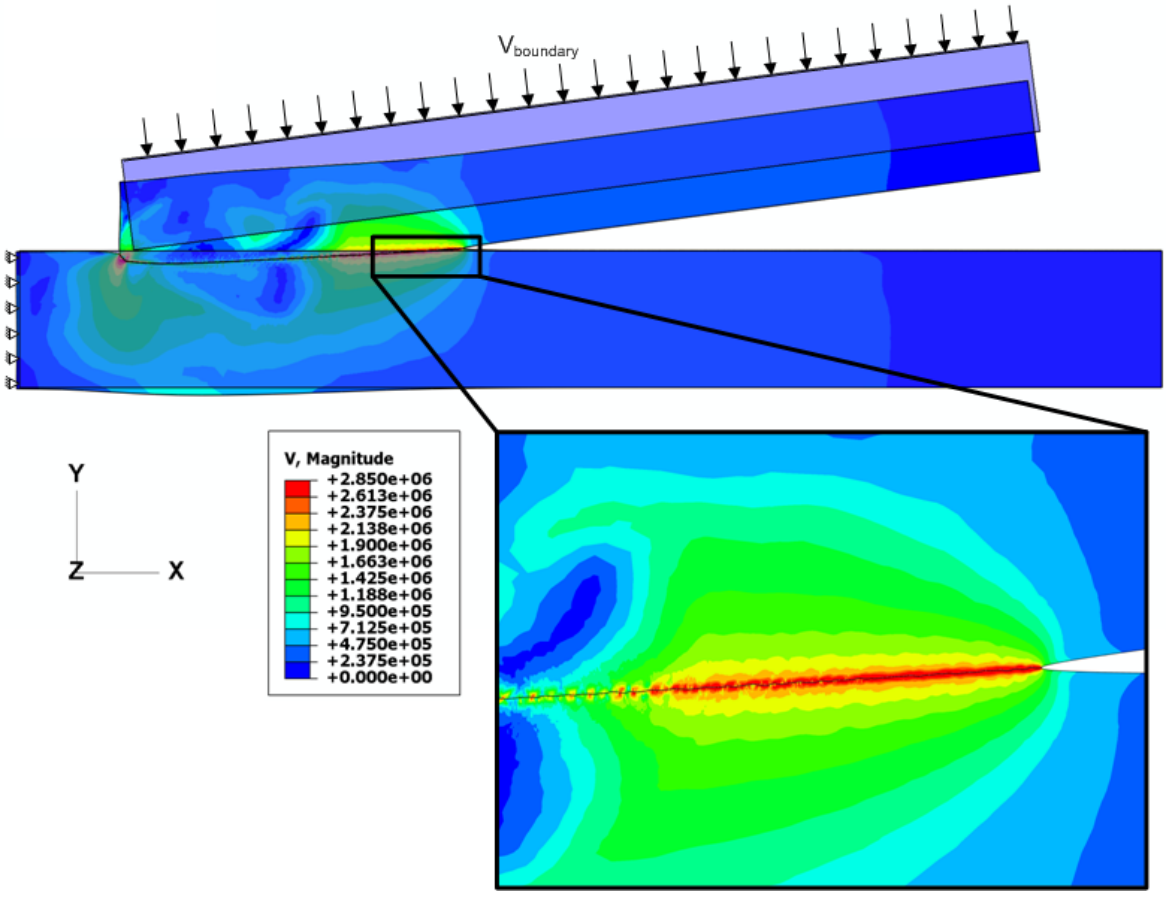

Figure 9: Setup and forming zone of the Finite-Element-model

Results from the numerical simulations of the welding zone are summarized in Figure 10. The welding velocity directly correlates to the impact velocity as indicated by the trigonometrical relation. Regarding wavelength of the interfacial waves, a slight

dependency on the impact velocity can be observed. However, the amplitude of the waves is subject to large variances due to the characteristics of the wave formation mechanism and is highly depending on the mesh properties of the impacting parts.

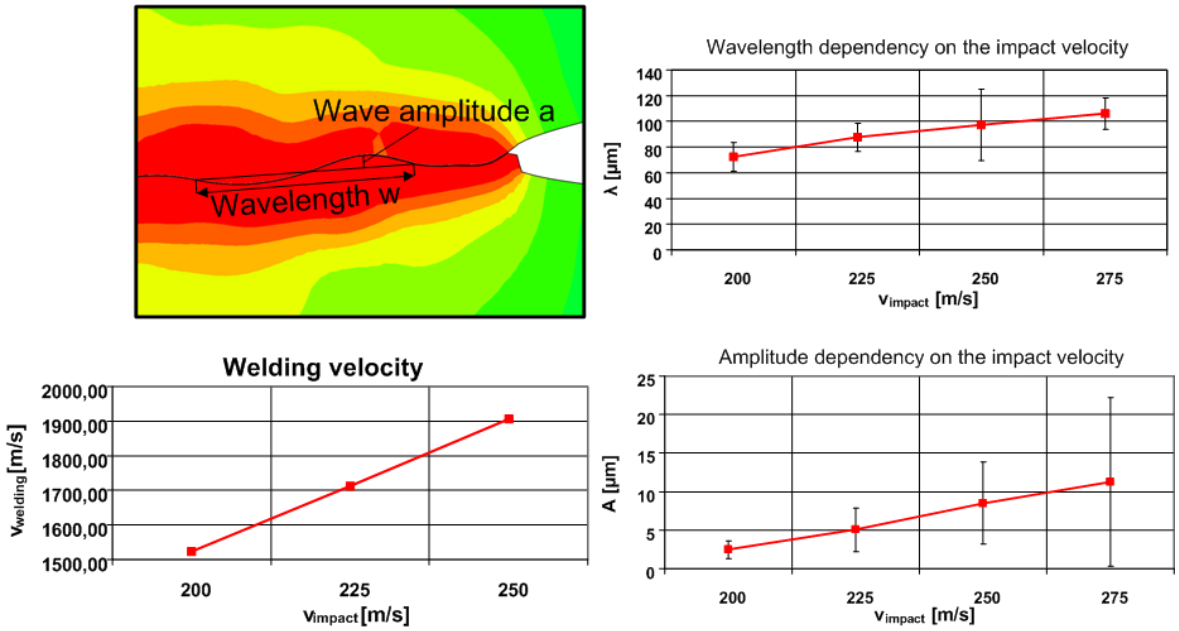

Figure 10: Welding velocity, wavelength and amplitude dependency on the impact velocity

5 Conclusions

In this work experiments have been carried out to identify the process parameters that govern the development of a solid state cold weld in impact welding processes. The impact angle and velocity of the line contact resulting from the trigonometrical relation between the impacting parts and the external pressure have been identified as important parameters for the formation of a welded joint. Metallographic examinations that show a characteristic wavy interface indicated that the material behavior of the surface layers involved is similar to the Kelvin-Helmholtz instability mechanism in fluid dynamics. This material behavior could be mapped in finite element simulations by applying the Johnson-Cook plasticity model.

6 Outlook

The experimental work will proceed in testing further material combinations of aluminum, steel and stainless steel concerning the technological parameters that influence the wave formation and its properties. SEM-imaging and electron microprobe analysis of the interface will be used to give information, whether there appears some kind of mixture or diffusion of the involved materials. These analyses can only be carried out reasonably using dissimilar materials.

The numerical simulations are currently not able to determine whether a bond is likely to occur. Future aspects of the simulative work will focus on contact algorithms that prevent the materials from separating, once threshold values for contact force and strain are exceeded.

References

[1] Aizawa, T.; Kashani, M.; Okagawa, K.: Application of Magnetic Pulse Welding for Aluminium Alloys and SPCC Steel Sheet Joints, Welding Journal, 2007, 86 (5), pp. 119-124

[2] Belyy, I. V.; Fertik, S. M.; Khimenko, L. T.: Electromagnetic Metal Forming Handbook. A Translation of The Russian Book: Spravochnik po Magnitno-impul'snoy Obrabotke Metallov.
Translated By M. M. Altynova, Material Science and Engineering Dept., Ohio State University, 1996

[3] Zhang, P.: Joining Enabled by High Velocity Deformation, Dissertation, Ohio State University, 2003

[4] Robinson, J. L.: The Mechanics of Wave Formation in Impact Welding, Philosophical Magazine, 1975, 31 (3), pp. 587-597

[5] Ben-Artzy, A.; Stern, A.; Frage, N.; Shribman, V.; Sadot, O.: Wave Formation Mechanism in Magnetic Pulse Welding, International Journal of Impact Engineering, 2010, 37, pp. 397-404

[6] Johnson, G. R.; Cook, W. H.: A Constitutive Model and Data for Metals Subjected to Large Strains, High Strain Rates and High Temperatures, Proc. 7th Int. Symp. on Ballistics, The Hague, The Netherlands, 1983

[7] Akbari Mousavi, A. A.; Al-Hassani, S. T. S.: Numerical and Experimental Studies of the Mechanism of the Wavy Interface Formations in Explosive/Impact Welding, Journal of the Mechanics and Physics of Solids, 2005, 53, pp. 2501-252

Insights into intermetallic phases on pulse welded dissimilar metal joints*

G. Göbel[1], J. Kaspar[1], T. Herrmannsdörfer[2], B. Brenner[1], E. Beyer[1,3]

[1] Fraunhofer Institute for Material and Beam Technology, Dresden, Germany
[2] Forschungszentrum Dresden-Rossendorf (FZD), Dresden, Germany
[3] Institute of Surface and Manufacturing Technology, Technical University Dresden, Germany

Abstract

The Magnetic Pulse Welding (MPW) process has been developed to an industrially used joining method which is considered to be a fast, noncontact, clean and "cold" solid state welding process. Unlike fusion welding, the absence of direct heat during the welding cycle makes it possible to join dissimilar metals, for instance aluminium to copper or copper to steel, without noticeable detrimental metallurgical defects. This is very desirable, as today's industry lacks technologies to join often not fusion-weldable dissimilar materials effectively. However, current metallographic studies show that for many material combinations the formation of intermetallic seams in the joint region of magnetic pulse welds can not be completely avoided.
Modern technical equipment for MPW is used to join aluminium with copper in order to study the microstructure and the intermetallic phases formed in the weld region in dependence of the processing parameters. The welds are analysed by means of metallographic and electron microscopic (SEM) methods. Relations between the parameters and the microstructures formed within the weld joints are shown. Based on the obtained results conclusions will be drawn with respect to the intermetallic phase formation process and the optimization of the weld microstructure and properties.

Keywords

Welding, Interface, Analysis

* *The authors would like to thank the European Regional Development Fund (ERDF) and the State of Saxony for its financial support*

1 Introduction

When joining dissimilar metals with fusion welding techniques, the formation of brittle intermetallic phases is usually considered as the biggest challenge and the primary obstacle to obtain a high-quality weld. To overcome the problem of intermetallic phase formation Magnetic Pulse Welding (MPW), which is generally considered as a "cold" high-speed welding technique, is regarded as an appropriate joining technology.

MPW can be used for applications where a high strength and temperature stable joint is needed. It is not as widely used as Electromagnetic Forming (EMF) due to its higher demands on the electromagnetic equipment.

Like explosion welding (EXW), MPW relies on the dynamic effects when the two joining partners collide at high impact speeds. It is generally agreed that a certain minimal impact velocity v_I and certain collision angle γ is required to start the welding process, and that the partners are welded by a continued movement of the initially joined contact line across the parts. Since the behaviour of the interface during and shortly after the welding front determines the quality of the weld it is regarded as the most important process of MPW and EXW. In order to understand the interface behaviour, to clarify its dependence on process parameters and to optimize the welding process an extensive amount of research has already been conducted by many authors leading to sometimes contradictory conclusions and theories. The present paper is not aimed to review and discuss these theories in detail. Instead, it intents to

- gain information from own experiments and literature about interface behaviour and bonding mechanisms particularly with respect to the formation of wavy structures, intermetallic phases and defects.
- draw conclusions how to set up welding parameters to avoid detrimental effects.

Although the paper deals primarily with MPW, it tries to incorporate the knowledge available from EXW research, if appropriate.

2 Interface effects in shock-welded joints

2.1 Theoretical background

The behaviour and velocity of the moving front in high speed welds has been studied by many authors for EXW and MPW. The materials are bonded by the high transient pressures which are produced by the oblique collision at high velocities. Typical collision point velocities v_C range between 1000 and nearly 4000 m/s. The formation of a so called jet between the surfaces during joining is considered as an important prerequisite for a sound weld, as it strips the surfaces of unwanted surface contamination and oxides and enables them to create a metallurgical bond. Its presence is not in question by most authors and it has even been photographed [1, 2]. However, the reasons for the formation of the wavy interface between the surfaces that follow the jet zone are still in discussion. Prominent theories of the wave formation process are the "Indentation mechanism" [3], the "Karman vortex street analogy" [4], the "Helmholtz instability mechanism" [5], the "stress wave mechanism" [6] and the "mechanism of vibration in the plastic state" [7]. A comprehensive discussion of these theories is e.g. given by Mousavi and Al-Hassani [8]. As an understanding of the interface formation is helpful for the optimization of the weld

joint and its properties, essential parts of these theories will be included in the discussion of the results.

2.2 Known detrimental interface effects and relevant parameters

Many researchers have examined metallurgical and geometrical effects along the interface line of EXW and EMP welds and discussed the possible impact on the mechanical behaviour. Relevant elements are: wave and intermetallic phase formation, pockets and films of molten and re-solidified material and inclusions of oxides. Also the formation of cracks, voids and pores, spallation effects, incomplete welding zones, strong plastic deformation as well as recrystallization zones are discussed.

Although many of these effects were analyzed in detail primarily for EXW, they are probably also relevant for MPW. Therefore it is important to know possible relations to the process parameters. Parameters that are often discussed in this regard are:

- Material combination
- Material assignment to flyer/base element
- Thickness of flyer and base material
- Impact velocity v_I
- Collision angle γ (as a function along the weld) [9]
- Collision point velocity v_C (as a function along the weld)
- Pressure (function over time)
- Temperature (e.g. preheating)

As all these parameters must be considered during a process setup, the aim of the following chapters is to examine MPW joints and discuss the findings from experiments and literature with respect to the process setup.

3 Metallographic investigation of weld interfaces

MPW experiments were conducted in cooperation with the High Magnetic Field Laboratory of the “Forschungszentrum Dresden Rossendorf”. The experiments were aimed to create different joint geometries and qualities. They were used as a basis to analyse the already discussed metallurgical and geometrical effects in detail.

3.1 Specimen and methods

A 1.5 millimetre thick Aluminium tube (diameter: 25mm) was electromagnetically joined onto a Copper cylinder with a rim, using different process parameters (Figure 1). Metallographic sections were prepared longitudinal and perpendicular to the cylinder axis. The longitudinal and cross sections were chemically etched, mechanically or ion polished and analyzed by means of optical microscopy, scanning electron microscopy (SEM) and energy dispersive X-ray analysis (EDX). The structural analysis concentrated on the characterization of the structural changes taking place in the welding zone, especially with respect to detrimental effects like cracking or massive intermetallic phase formation.

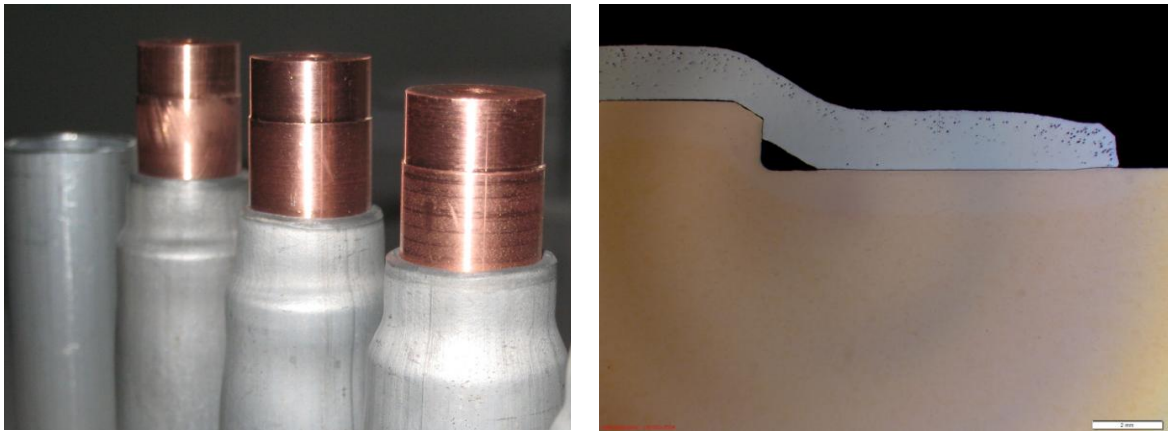

Figure 1: *Test parts made by MPW of a 25 mm diameter aluminium tube onto a copper cylinder, left: welded specimen (and an unwelded tube), right: longitudinal section*

3.2 Experimental Results

Based on the longitudinal and cross sections of different Al-Cu welds the following results, assessments and conclusions should be emphasized:

- The quality of the weld is changing strongly along the interface from start to end for all welds in this configuration. Generally, the start and end zones of the welds exhibited no or only limited bonding. In contrast, the middle section of the welds showed good bonding. The insufficient bonding at the start and the end of the weld zone is a typical feature of MPW cylindrical parts and according to literature not critical for many applications [10, 11]. However, the not connected sections can act as a very strong notch pointing at the weld, which would be very detrimental under cyclic load or corrosive environment.
- The process of wave formation along the interface strongly depends on sample geometry and to a lesser extent also on the process parameters (Figure 2). Using massive copper cylinders and relatively low pulse energies the wave formation was nearly totally inhibited. Contrary, applying hollow copper cylinders and high pulse energies pronounced waves were visible, especially in the middle section of the welds. This geometrical influence is in accordance with findings in [10]. It is important to note that the wave formation process is not mandatory for a good bonding. It is furthermore worth mentioning that to some extent wave formation could also be observed in regions without bonding.
- For the sample geometries and process parameters applied, the formation of intermetallic phases at the welding interface can not be avoided. The composition, arrangement and extent of the intermetallics formed depend on the process parameters chosen and is partly connected with the structure of the interface. If the interface shows a wavy appearance, the intermetallics mainly concentrate in so called “melt pockets”, which are mostly located at the crests of the waves (Figure 3). If EMP produces a waveless interface, the intermetallic phases form a film of varying thickness (Figure 4). It is pointed

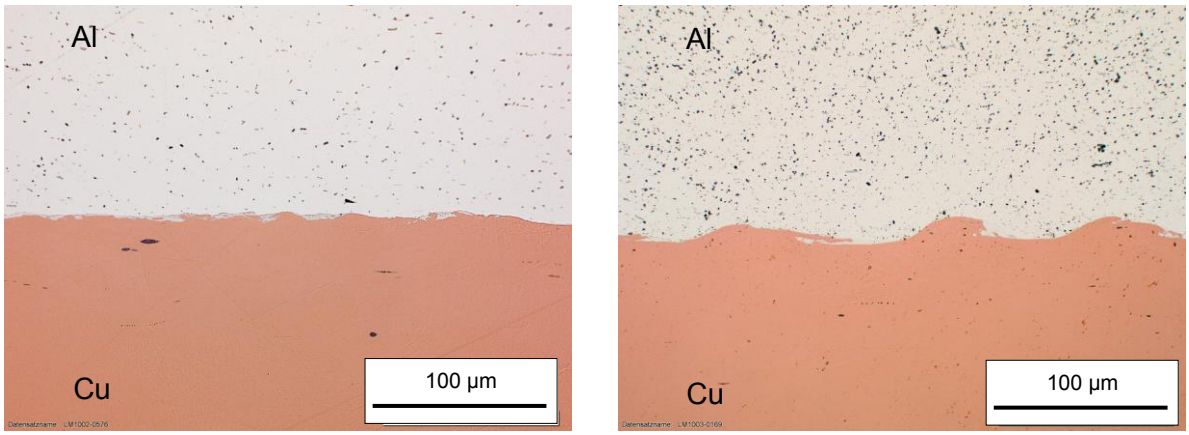

Figure 2: *Cross section details of welds with different interface morphology: (left) nearly waveless interface; (right) wavy interface. Peak pulse current I_{max}=66kA*

out that the phase film appears to be interrupted by regions without any intermetallics. Up to now it is not clear, whether this is true or if the intermetallic film in these regions is too thin to be detected by metallographic methods. For this reason TEM investigations of the weld interface are planned in future work.

- The tendency to intermetallic phase formation rises with increasing pulse energies (Figure 4). For low pulse energies a relatively thin intermetallic phase film is formed. Even if the maximum thickness of the intermetallic film is 5 microns a very good bonding can be achieved. For higher pulse energies the maximum thickness of the intermetallic phase film can increase above 25 microns. Comparing similar bonding conditions, the intermetallic phases are usually thicker if the interface exhibits a wavy appearance.
- The structural and chemical composition of the intermetallics strongly depend on their thickness and hence on the processing parameters chosen (Figure 4 and 5). For a thickness below 5 microns the intermetallics contain rarely any cracks, voids or pores.

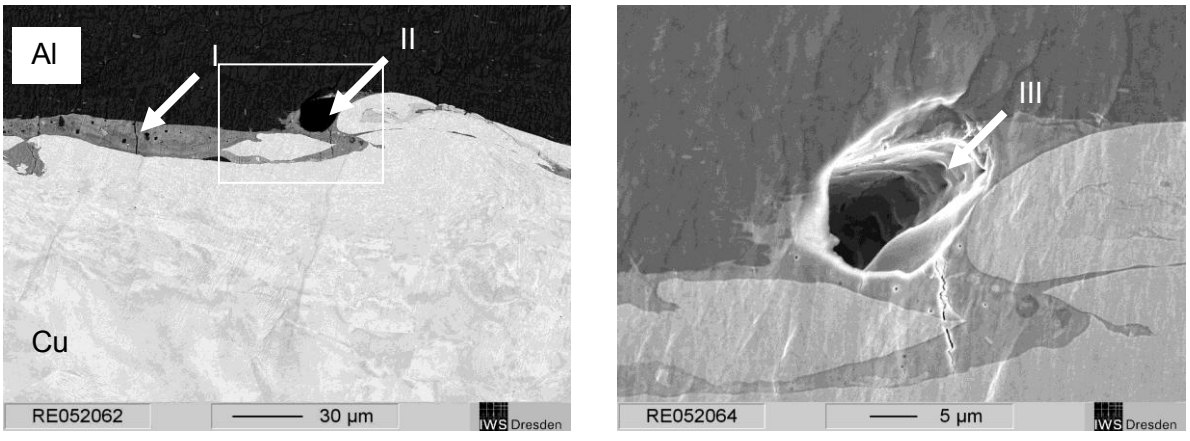

Figure 3*: Details of welds exhibiting typical wavy interface and intermetallics at so called "melt pockets" (SEM micrographs). Left: Note the cracks (I) and voids and pores (II), right: The view into the pore reveals characteristics of a molten and re-solidified surface (III).*

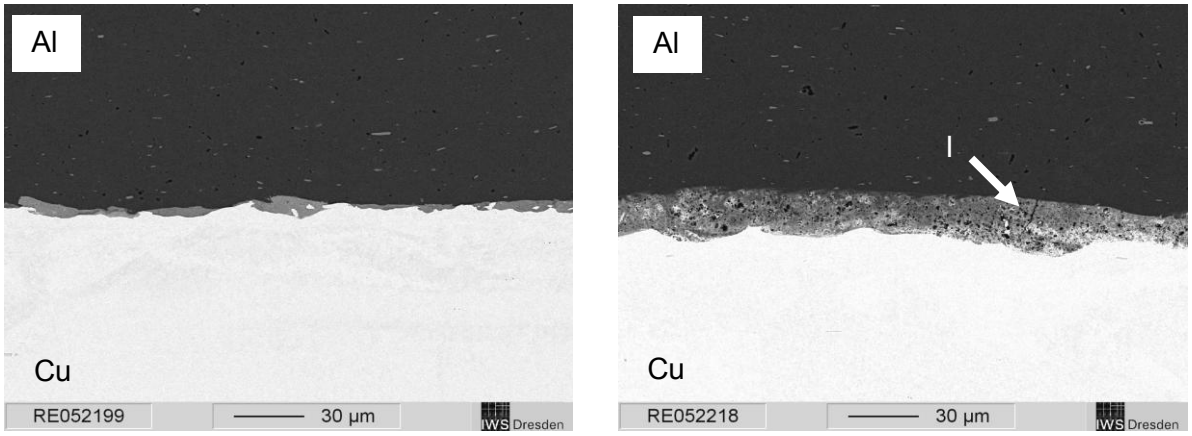

Figure 4: *Details of welds exhibiting waveless interface with intermetallics phase films of different thickness and structural composition (SEM micrographs: z-contrast).*
Left: thin phase film without major defects, I_{max}=66kA;
Right: thick phase film containing numerous pores and some cracks (I), I_{max}=76kA

- With increasing thickness the intermetallics reveal some voids and cracks running perpendicular to the weld interface. Above a thickness of 10 microns the intermetallics additionally contain numerous pores. Even severe cracking taking place parallel to the weld interface was observed in these samples. EDX analysis (Figure 5) revealed that the thin intermetallic films produced by low energy MPW are generally rich in aluminium containing only between 10 and 20 at.% copper. In contrast, the Cu content of the thicker intermetallics formed during higher pulse energy EMP varies more widely in the range from 10 to 50 at.% copper. Thereby the transition in composition is rather stepwise indicating that different intermetallic phases have formed.
- According to the EDX analysis, the phases identified with SEM cannot be directly linked to the complex phase diagram Al-Cu. Generally only Al-rich phases with a Cu content ≤ 50 at.% have formed. On the Al-rich side of the phase diagram however, only the phases Al_2Cu (θ, 33at.% Cu) and η_2 (50at.% Cu) exist and the Al crystal cannot dissolve significant amounts of Cu under equilibrium conditions. From this it is concluded that the generated Al-rich phases have formed under strong non equilibrium conditions. From the sharp and stepwise transition in chemical composition between the two parent metals and the formed intermetallic phases it is in accordance with Carpenter and Wittman [12] who deduced that solid state diffusion is not involved as active bonding mechanism in the process of MPW aluminium to copper.
- The absence of any diffusion layers leads to the assumption that local melting is mainly involved in the phase formation and bonding process along the interface. As for low pulse energies the intermetallic phases consist primarily of aluminium, it is deduced that solely aluminium but not copper was molten during low energy MPW. In contrast, higher pulse energies which produce thicker intermetallic phase films and so called “melt pockets” enable to exceed the melting temperature of copper locally as well as leading to a higher copper content in the formed intermetallic phases.

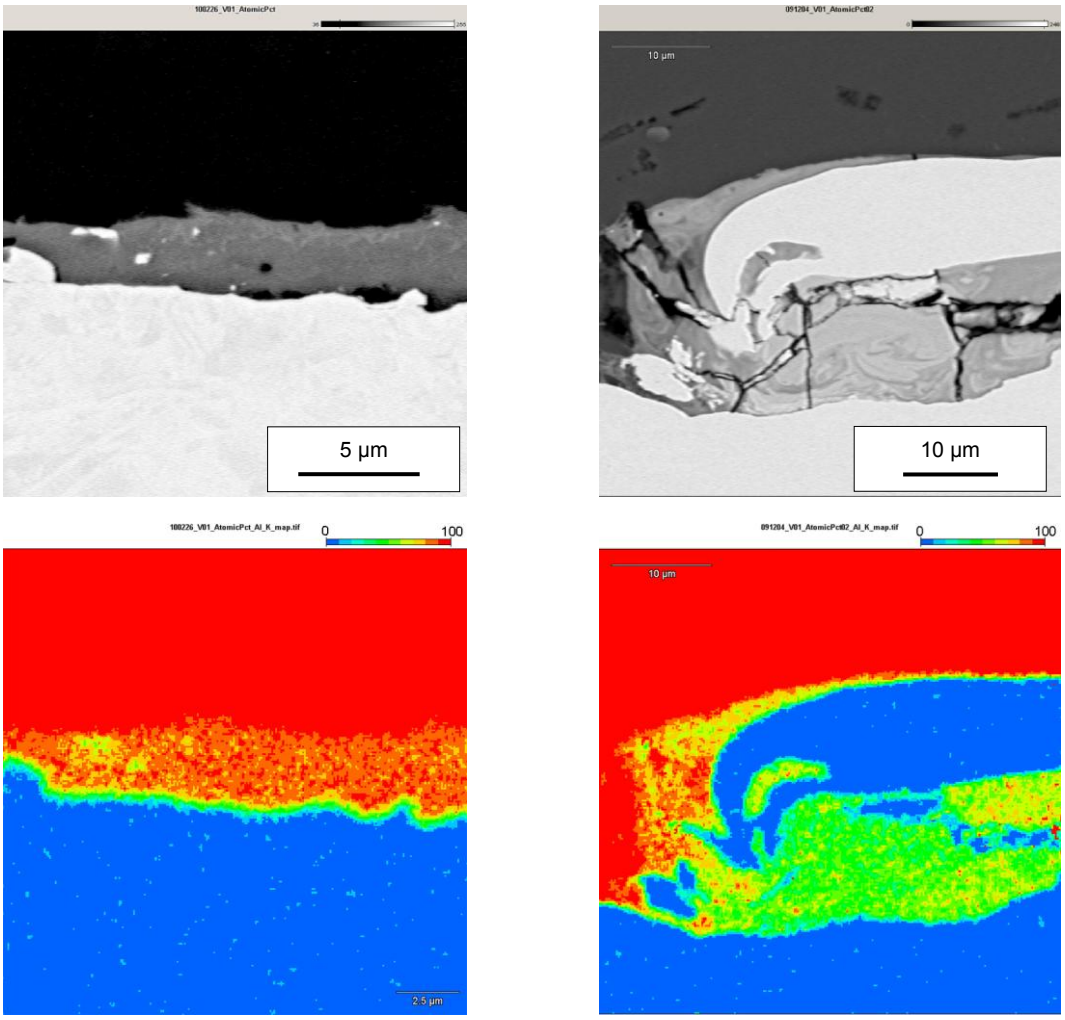

***Figure 5**: EDX-analysis of welds exhibiting different Interface morphology (top) SEM micrographs: z-contrast; (bottom) EDX-map: Al content in at.% (left) waveless interface with thin phase film, I_{max}=66kA; (right) wavy interface with "melt pockets", I_{max}=76kA;*
Note the different magnifications of the images: (left: 5000:1), (right: 2000:1)

- At both sides of the weld, i.e. in the Al- und Cu parent material, a strongly plastically deformed region exists in the vicinity of the interface. On the Al-side the plastic deformation causes an extensive grain elongation in the welding direction. Whereas on the Cu-side the strong plastic deformation leads to dynamic recrystallization resulting in an ultrafine grained structure (Figure 6). Adjacent to the recrystallized zone the copper grains show considerable distortion. The plastically deformed zones on both sides of the weld interface extend to maximum width of 500 microns.
- Although MPW is often discussed as a cold welding process [13, 14] the extreme plasticized regions as well as the common formation of intermetallic phases at the weld interface provide evidence for a localized short-time thermal loading. This can, in principle, lead to similar detrimental effects as in fusion welding, especially when phase films exceed certain thickness limits. Neither the formation of larger melt pockets and thicker intermetallic phase films nor wavy appearances of the weld interface are regarded as prerequisites for high-quality bonds between aluminium and copper. On the contrary,

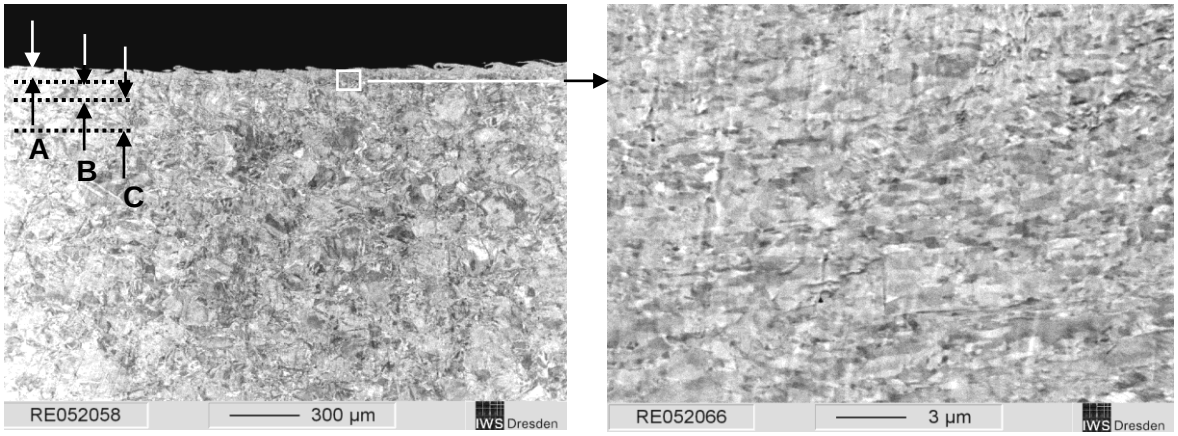

Figure 6: *Details of the structural changes taking place within the Cu adjacent to the weld interface (SEM micrographs: z-contrast). Left: Overview with marked zones; Right: detail of the recrystallized zone, I_{max}= 76 kA*
Regions: A = ultrafine recrystallized grains: 20-40µm, B = strongly distorted grains: 30-40µm, C = slightly distorted grains: 200-400µm

the best weld quality is achieved if a very thin intermetallic film, whose thickness does not exceed 5 microns, is formed. Especially in the welds without wavy interfaces perfectly bonded zones exist without any detrimental disturbances and defects.

4 General recommendations

The following conclusions can be drawn from literature and the experiments in regard to an optimal process setup:

- The collision angle is a critical parameter for the initiation of the weld. According to literature, angles between 5° and 20° between the flyer and the base material are regarded as appropriate (e.g. [11, 15]).This is in accordance with our results, where the best welding quality was achieved with a collision angle of approx. 11° at the start of the joint. However it has to be taken into account that, unlike in standard EXW, in typical MPW configurations the collision angle changes continuously from the start to the end of the weld. As a consequence it is difficult to attain uniform weld quality and bonding along the interface. In order to overcome this drawback, future work should try to compensate the unwanted effect by tailoring the geometry of the welding partners or the process parameters [16].
- In order to predict optimum welding conditions for EXW a so called “welding window”, i.e. a plot of appropriate combinations of collision angle and collision point velocity was very successful (e.g. [12, 17]). Although this approach was also suggested for MPW [13], it is unclear if the same concept can be easily assigned and adapted to MPW. Especially the comparability of the processes regarding parameters like pressure, temperature and the variation of these parameters with time are often unknown.
- Literature discussion concerning the importance of wave formation for the weld quality is controversial for both EXW and MPW. Several authors claim that the formation of a wavy interface is compulsory in order to achieve sufficient bonding and high strength welds [12, 14]. This view is not shared by Inal and co-workers [18]. According to these authors, the wavy interface is directly connected with the formation of localized “melt pockets” and thus with harmful intermetallics and cracking. This view is supported by

our results which show that the best weld quality and minimal intermetallic phase formation is obtained if the chosen process parameters result in a straight rather than a wavy interface.

- From literature and our own experiments it is not entirely clear if the formation of intermetallic phase during MPW of aluminium to copper can be completely avoided. We suppose that this is not possible, because localized interfacial melting seems to be a prerequisite for a successful bond. Nonetheless it could be clearly demonstrated that the extent, the structural and chemical composition and the arrangement along the interface can be controlled by the processing parameters. This is of much importance since as soon as the intermetallic phase film exceeds a critical thickness of about 5 microns voids, pores and extensive cracking considerably worsen the weld quality and strength. As seen by the experiments, a reduction of intermetallic phase formation can be directly reached by decreasing the effective impact energy.

5 Conclusion

In the present paper the results of the detailed structural investigations on MPW Al-Cu joints were presented. Based on the results and the conducted literature survey the following conclusions can be drawn:

- The formation of intermetallic phases can not be completely avoided during MPW of aluminium to copper. To confine detrimental effects on the mechanical properties of the joints the thickness of the formed intermetallics should not exceed 5 microns. Above this critical thickness the intermetallics are susceptible to cracking and spallation.
- The variety and chemical composition of the created intermetallics depend on the pulse parameters chosen. This behaviour is attributed to different temperature-time regimes of the process leading to varying amounts of melting of the two base materials.
- Best welding results concerning bond and weld quality can be archived applying relatively low pulse energies. Under these conditions the extent of intermetallic phase formation can be minimized to an uncritical level.
- The formation of a wavy interface is no prerequisite for an effective bonding during MPW

References

[1] *Bergmann, O. R.:* The Scientific Basis of Metal Bonding with Explosives. “High Energy Rate Fabrication – 1984”, The 8th Int. ASME Conf., 1984, p. 197-202.

[2] *Watanabe, M.; Kumai, S.*: Interfacial Morphology of Magnetic Pulse Welded Aluminium/ Aluminium and Copper/Copper Lap Joints. Materials Transaction 50, 2009, p. 286-292

[3] *Bahrani, A. S.; Black, T.J.; Crossland, B.:* The Mechanics of Wave Formation in Explosive Welding. Proc. of Royal Society Series A 296, 1976, p. 23.

[4] *Cowan G. R.; Bergmann O. R.; Holtzman A. H.:* Mechanics of Bond Wave Formation in Explosive Cladding of Metals. Metallurgical Transactions 2, 1971, p. 3145.

[5] *Hunt, J. N.:* Wave Formation in Explosive Welding. Philosophical Magazine 17, 1968,
p. 669-680.

[6] *El-Sobky, H.; Blazynsky, T. Z.:* Experimental investigation of the mechanism of explosive welding be means of a liquid analogue. Proc. 5th International Conference on “High Energy Rate fabrication”, Denver, Colorado, 1975, p. 1-21.

[7] *Patwardhan, W. D.:* Mechanism of wave formation at explosion bonded metal surfaces. Tran. of the Indian Institute of Metals, Vol. 36, 1983, 407-409.

[8] *Mousavi, A. A.; Al-Hassani, S. T.:* Simulation of wave and jet formation in explosive/impact welding. Proc. of the 7th Conference on “Engineering Systems Designs and Analysis”, Manchester, U K., 2004, p. 265-274.

[9] *Botros, K. K.; Groves,T. K.:* Characteristics of the wavy interface and the mechanism of its formation in high-velocity impact welding. J. Appl. Phys. 51, 1980, p. 3715-3721.

[10] *Ben-Artzy, A.; Stern, A.; Frage, N. ; Shribman, V.; Sadot, O.:* Wave formation mechanism in magnetic pulse welding. International Journal of Impact Engineering 37, 2010, p. 397-404.

[11] *Marya, M.; Marya, S.; Priem, D.:*On the characteristics of electromagnetic welds between aluminium and other metals and alloys. Welding in the world 49, 2005, p. 74-84.

[12] *Carpenter, S. H.; Wittman, R. H.:* Explosive Welding. Annu. Reviews Mater. Sci. 1975.5, 1975, p. 177-199.

[13] *Shribman, V.:* Magnetic Pulse welding for dissimilar and similar materials. Proc. of the 3rd International Conference on High Speed Forming, Dortmund, 2008, p. 13-22.

[14] *Uhlmann, E.; Damavandi, K.; Rautenstrauch, A*: Hochdynamischer Aufprallvorgang beim Magnetimpulsschweißen. Geesthacher Schweißtage ’06: „Festphasen Fügeverfahren“, GKSS 2006 / 15, 2006, p. 23-33.

[15] *Kojima, M.; Tamaki, K.; Furuta, T.:* Effect of Collision Angle on the Result of Electromagnetic Welding of Aluminum. Trans. Jap. Weld. Soc. 20, 1989, p. 36-42.

[16] *Psyk, V., Gershteyyn, G., Demir, O. K., Brosius A., Tekkaya, A. E., Schaper, M., Bech, F.-W.:* Process analysis and physical simulations of electromagnetic joining of thin walled parts. Proc. of the 3rd International Conference on High Speed Forming, Dortmund, 2008, p. 181-190.

[17] *Sartangi, P. F.; Mousavi, A. A.:* Experimental investigations on explosive cladding of cp-titanium / AISI 304 stainless steel. Materials Science Forum 580-582, 2008, p. 629-632.

[18] *Inal,O. T.; Szecket, A.; Vigueras, D. J.; Pak, H-R.* : Explosive welding of Ti-6Al-4V to mild-steel substrates. J. Vac. Sci. Technol. A 3, 1985, p. 2605-2609.

Development of design principles for form-fit joints in lightweight frame structures*

C. Weddeling[1], S. Woodward[3], J. Nellesen[2], V. Psyk[1], M. Marré[1], A. Brosius[1], A. E. Tekkaya[1], G. S. Daehn[3], W. Tillmann[2]

[1] Institute of Forming Technology and Lightweight Construction, Technische Universität Dortmund, Dortmund, Germany
[2] Institute of Materials Engineering, Technische Universität Dortmund, Dortmund, Germany
[3] The Ohio State University 2041 College Rd, Columbus, Ohio, USA

Abstract

Based on fundamental technological investigations, alternative joining strategies using electromagnetic forming (EMF) for the flexible production of lightweight frame structures are developed in the collaborative research project SFB/TR10. The results of these investigations will also be used to create general design principles for the joining process itself as well as for the joining zone. The focus of this article will be on dominating form-fit joints of aluminum frame structures and the parameters which have a significant influence on the strength of those joints. For the development of design principles regarding the joining zone, the groove geometry of the connection elements was varied in terms of size and shape, and the influence of those variations was analyzed. In terms of the joining process itself the effect on the joint strength of different forming pressures for a given groove geometry was also investigated. In the first step these experiments were performed on solid mandrels. In order to reduce the weight of the structure, experiments were then performed with hollow connection elements and similar groove geometries to analyze how the reduced stiffness of those elements affected the strength of the joints.

Keywords

Lightweight frame structures, joining, electromagnetic forming

1 Introduction

A current goal of the automotive industry is the reduction of the CO_2 emissions and increase of the fuel efficiency. To achieve this goal, the focus is currently on the

* *This paper is based on investigations of the Transregional Collaborative Research Center SFB/TR10, which is kindly supported by the German Research Foundation (DFG). In the scope of the DFG project INST 212/209-1 FUGG, the high-performance microfocus computer tomography system used in this work could be purchased, which is gratefully acknowledged as well.*

optimization of the powertrain as well as the reduction of a car body's weight. A successful approach to reduce the total weight of a car is the implementation of lightweight strategies in the design process, such as by using light weight materials [1]. The economic production of high strength joints is a major challenge for the manufacturing of a car's frame structure made from extruded aluminum profiles. An interesting alternative to conventional welding and riveting processes is joining by electromagnetic forming since the achievable joint strength is within the range of the strength of the weakest joining partner [2].

2 Fundamentals of joining by electromagnetic compression

2.1 Fundamentals of electromagnetic forming

Electromagnetic forming (EMF) is a noncontact high velocity process using pulsed magnetic fields to deform materials with high electrical conductivity, such as copper and aluminum alloys [3]. Depending on the setup, the tool coil geometry and the work piece, electromagnetic forming can be used for sheet metal forming operations or for the compression as well as the expansion of hollow profiles [4]. The forming process is typically finished after 100 microseconds. This means that a compression speed of 300 m/s can be achieved, which is equivalent to a strain rate of 10^3/s to 10^4/s [5]. A typical setup of work piece, tool coil and forming machine for the electromagnetic compression is shown in Figure 1.

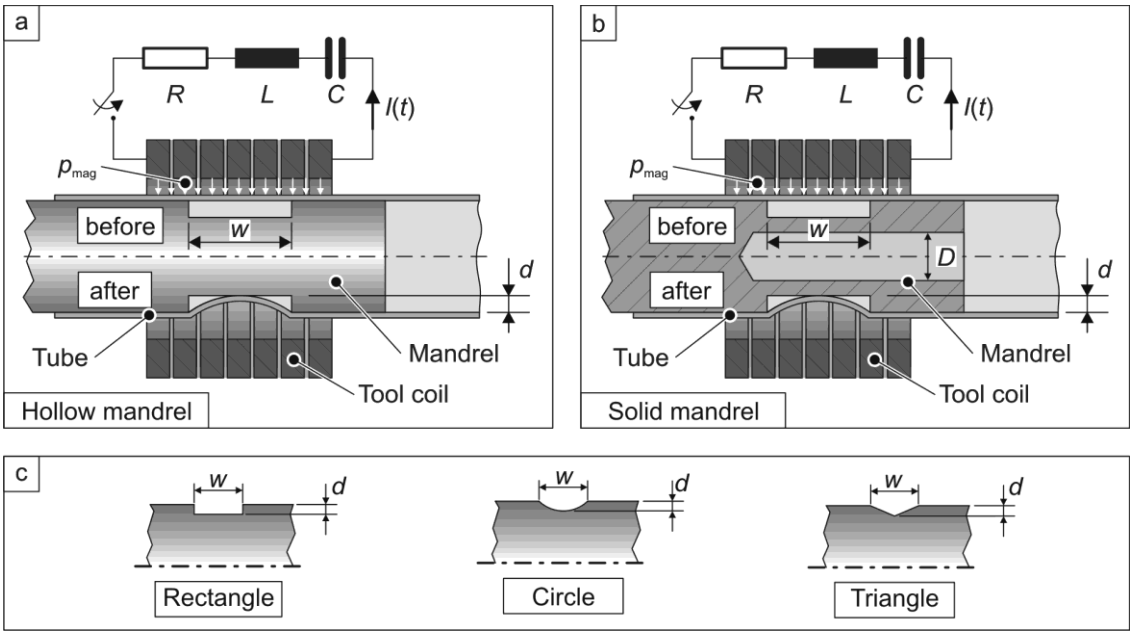

Figure 1 *a) Setup for the experimental investigations on solid mandrels and b) hollow mandrels. c) The different groove shapes (triangle, rectangle, circle) with width w and depth d used within this investigation.*

In the equivalent circuit diagram of this resonance circuit the forming machine is symbolized by the capacitance C, the inner resistance R_i and the inner inductance L_i. The work piece and the coil can be seen as a consumer load. Due to a sudden discharge of the electricity stored in the capacitor, a damped sinusoidal current $I(t)$ runs through the coil

(see Figure 1). The current, which typically ranges from 10 to 1000 kA, generates a magnetic field *H(t,r,z)* around the tool coil. According to Lenz's law, this magnetic field induces eddy currents in the work piece. They are directed opposed to the coil current and they shield the magnetic field from the inside of the work piece. The energy density of the magnetic field represents a pressure *p(t,r,z)* which acts orthogonally on the work piece [4]. Once the stresses in the work piece due to this pressure reach the yield stress of the material, plastic deformation of the tube starts. If the work piece movement is neglected, the magnetic pressure can be calculated by the following equation [6, 7 and 8]:

$$p(t,r,z) = \frac{1}{2}\mu \cdot \left(\frac{n \cdot I(t)}{l_{coil}} \cdot k_H(z)\right)^2 \quad (1)$$

Within this equation μ represents the permeability, n the number of turns of the coil and l_{coil} the length of the coil. The factor $k_H(z)$ determines the axial distribution of the magnetic field [9].

2.2 Joining by electromagnetic compression

Joining of tubular work pieces by electromagnetic compression is the most frequently used EMF application. The manufacturing of those joints does not require additional joining elements, such as screws, rivets, adhesives or auxiliary wire. According to the most dominating mechanism against an external load, joints manufactured by electromagnetic forming can be classified into interference-fit joints, form-fit joints and welded joints. Interference-fits are manufactured by a plastic deformation of one and an elastic deformation of the other joining partner so that interference stresses result [2]. For a form-fit joint, the material of one joining partner is formed into an undercut (e.g. a groove) of the other joining partner (see Figure 1). As a result, the joint is locked against an external load. In the case of very high impact velocities of the electromagnetically driven part it is possible to produce welded bonds between the joining partners. This application is called magnetic pulse welding. Furthermore, the resistance against an external load can be a result of a combination of each of those mechanisms. Typically, the loads which can be transferred by a dominating form-fit or welded connection are higher than those which can be transferred by an interference-fit joint. Compared to form- and interference-fit joints, welded connections usually require a much higher energy to be manufactured. Since similar joint strengths can be achieved by form-fit as with magnetic pulse welded connections, this kind of joint shall be investigated in the following. The factors which influence the strength of a connection formed by electromagnetic compression shall be analyzed.

Very detailed studies on the influence of different groove parameters on the joint strength of form-fit connections were done by Bühler [10 and 11], Golovashchenko [12] and Park [13]. In their work Bühler and Golovashchenko investigate the influence of the groove width *w* and depth *d* on the achievable joint strength for electromagnetically compressed form-fit joints. For their investigation, they varied the acting magnetic pressure in such a way that the tube wall just touched the groove base. They found that an increase of the groove depth as well as a decrease of the groove width lead to higher joint strengths. In contrast to Bühler and Golovashchenko, Park used a constant forming pressure in his work. He also found an increase in the joint strength with an increase of the groove depth. But he observed an increase of the joint strength with an increase of the groove width. This can be explained by the constant forming pressure Park used in his experiments. The pressure required to form a tube into a groove so that its wall just

touches the groove base decreases with increasing groove width. This is a result of the lower stiffness of the tube wall covering the groove [11]. Therefore, a constant forming pressure leads to an enlarged contact area at the groove base for wider grooves. As a result of the compressive forming, residual hoop stresses are generated in the contact area. Due to these stresses, an interference-fit is generated, and its effect on the overall joint strength grows with an increase of the contact area and therefore with wider grooves [13]. Park also investigated the influence of the groove edge radius on the joint strength. He found that up to a certain point a smaller edge radius leads to higher joint strength. But a decrease of the radius also causes an increase of shearing at the groove edge. As a result of these opposing effects, an optimal groove edge radius exists for a given groove depth [13]. All three research works also showed that the strength of a form-fit connection can be increased significantly by using multiple grooves.

3 Motivation

The results of the previous studies introduced above were applied for the design of form-fit joints for the lightweight frame structure shown in Figure 2 b). But the resulting joint strengths were much lower than expected from those studies. For weight reduction purposes, the inner joining partners were designed as hollow aluminum parts, which led to a much lower stiffness than the mandrels used by Bühler, Golovashchenko and Park for their experiments.

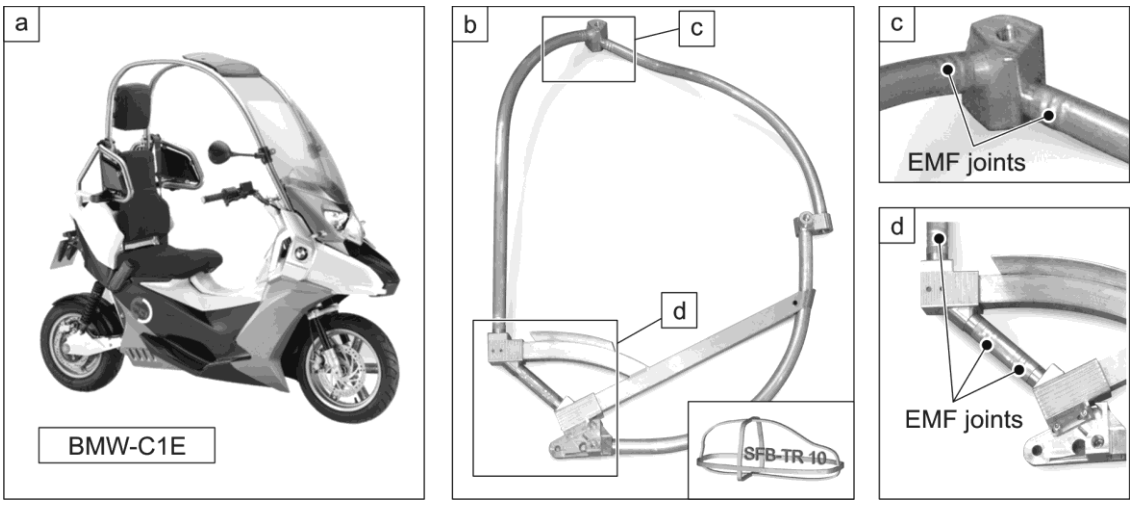

Figure 2 *a) BMW-C1E. b) Alternative frame structure for the BMW-C1E manufactured within the collaborative research center SFB/TR10. c) and d) EMF form-fit joints*

To determine the reason for the significant drop in joint strength and to develop joining strategies for those lightweight frame components, an investigation was carried out, the results of which are presented in the following. This development of joining strategies includes a study regarding the influence of different groove shapes on the joint strength. This parameter is especially important in terms of corrosion aspects. In case of a rectangular groove design, cavities are generated at the groove edges. These cavities are potential starting points of corrosion. By using circular grooves, these hollow spaces can be avoided. But this groove shape might lead to a different joint strength than the rectangular groove geometry.

4 Experimental investigation of the joining zone characteristics on the joint strength

Fundamental experiments were performed to indentify the parameters which affect the strength of form-fit joints for lightweight frame structures. The basic setup of the experiments carried out within this work is displayed in Figure 1 a) and b). For the experiments, solid and hollow mandrels with an outer diameter of 36 mm were used. The charging energy during the joining experiments was adjusted in order to apply the minimum amount of magnetic pressure that was required to cause contact between the tube and the bottom of the groove. This was defined as “filling” the groove, similar to the approaches of Bühler and Golovashchenko [10, 11 and 12]. The drilled hole in the hollow inner joining partners had a diameter of 24 mm. This diameter was chosen to ensure that, for all groove depths, the smallest annulus area of the mandrel was bigger than the annulus area of the tube. As a result, the tube was always the weaker joining partner. For the investigation of the influence of the groove shape, rectangular, circular and triangular grooves were machined into the mandrels (see Figure 1 c)). These grooves had three different widths *w* (12, 16 and 20 mm) as well as three different depths *d* (1, 1.5 and 3 mm). This variation was done to obtain a complete understanding of the parameters influencing the joint strength. To minimize an additional possible interference-fit between the joining partners, the same material, namely EN AW-6060 (F22), was chosen for the tubes and the mandrels [14]. For the same reason, there was no gap between the joining partners. The outer diameter of the tubes was 40 mm and the wall thickness 2 mm. To generate the magnetic pressure pulses, a Maxwell Magneform machine (Series 7000) was used. The relevant machine parameters were a capacitance *C* of 362 µF, an inductance L_i of 78 µH and an inner resistance R_i of 5.4 mΩ. As EMF actuator, a compression coil with an inner diameter of 40 mm and 10 turns distributed over a coil length of 60 mm was used.

4.1 Determination of the forming pressure

As mentioned above the forming pressure was selected in dependence on the groove dimensions width and depth. To find the proper forming pressure an analytical-experimental approach was used. In the first step the pressure p_{min} required to initiate the plastic deformation of the tube into the groove was determined. Therefore, the following equation developed by Bühler was used [11]:

$$p_{min} = \sigma_y \left[3 \cdot \left(\frac{s}{w} \right)^2 + \frac{s}{R} \right] \tag{2}$$

Within this equation σ_y represents the yield stress of the tube material, *s* the wall thickness and *R* the outer radius of the tube. The groove width is represented by *w*. The result of this analytical model provided an approximate starting point for the second step in the approach (see Figure 3). To determine the exact pressure required to fill a groove of any desired dimensions experimental data were used. The objective of these experiments was to determine the correlation between magnetic pressure and the resulting depth of forming into the channel. For these tests, two greased steel cylinders were inserted into an aluminum tube. They were connected by a threaded rod to adjust their distance. The cylinder gap width *w* was matched with the three groove widths for the mandrels: 12, 16, and 20 mm. The tubes were then electromagnetically formed into the gap between the steel cylinders using charging energies between 2.4 kJ and 6 kJ, at intervals of 1.2 kJ.

The measured discharge currents varied between 55 kA for 2.4 kJ and 90 kA for 6 kJ of charging energy. The rise time of the discharge was approximately 22 µs. After the removal of the cylinders, a ZEISS PRISMO VAST 5 HTG coordinate measurement machine was used to determine the maximum forming depth *d*. Figure 3 shows the resulting depth versus the respective magnetic forming pressures. The calculation of these pressures was based on the applied discharge current, using Equation 1. Upon plotting the magnetic pressures versus forming depths it could be seen that, for each gap width *w*, the resulting forming depth *d* rises linearly with the applied magnetic pressure. Figure 3 also shows that increased forming depths or decreased gap widths require a higher forming pressure.

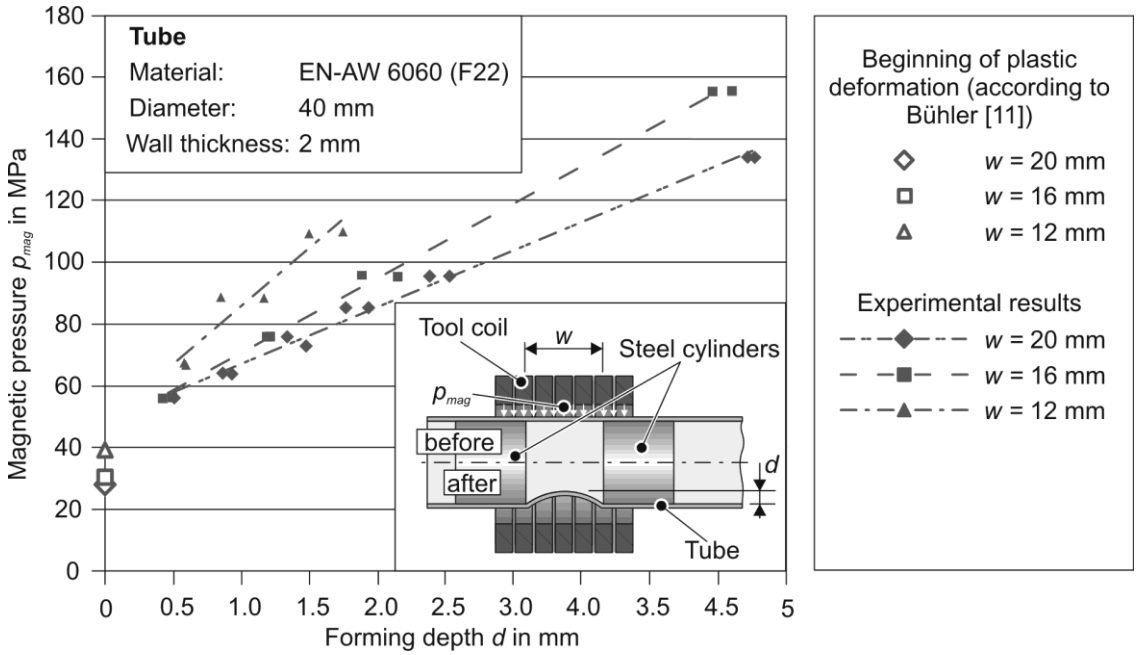

Figure 3 *Influence of the magnetic pressure on the achieved forming depth d for different groove widths w.*

By substituting a specific groove depth into the equation of the corresponding trend-line, the required magnetic pressure to fill a groove can be determined with a high degree of accuracy. The calculated pressure for each parameter set was multiplied by a safety factor of 1.1 to ensure filling. This factor accounts for the differences between the steel cylinders in the pre-tests and the aluminum mandrels used to create the joints. It also accounts for any possible inhomogeneities in the tube material.

4.2 Influence of the groove dimensions and shape on the joint strength

In order to analyze if the determined magnetic pressures were accurate and the tube wall touches the groove base, X-ray radioscopy and micro computer-tomography measurements were performed after the joining process. Another reason for these studies was to detect a possible shearing or thinning of the tube wall at the groove edges. A high-performance computer tomography system equipped with two X-ray tubes (directional microfocus and tube with transmission target) was used to carry out those measurements. The machine is equipped with a 7-axis manipulator and a large-sized flat-panel detector with an active area of 409.6 x 409.6 mm², containing 2048 x 2048 square pixels (see

Figure 4 a)). The X-rays which are emitted from the focal spot on the target of the microfocus tube penetrate the specimen and are attenuated due to interaction processes with matter. Since the X-rays diverge, the specimen is projected onto the detector plane with a magnification given by the ratio between the focus-detector-distance and the focus-object distance. Figure 4 shows the specific parameters which were used for the non-destructive 2D inspection and tomography. The joint of the specimen was mapped with maximum magnification onto the detector plane. This resulted in a reconstructed tomogram containing roughly 2000 x 2000 x 1000 voxels with a voxel edge length of 22 µm. An algorithm developed by Feldkamp [15] was used for the reconstruction.

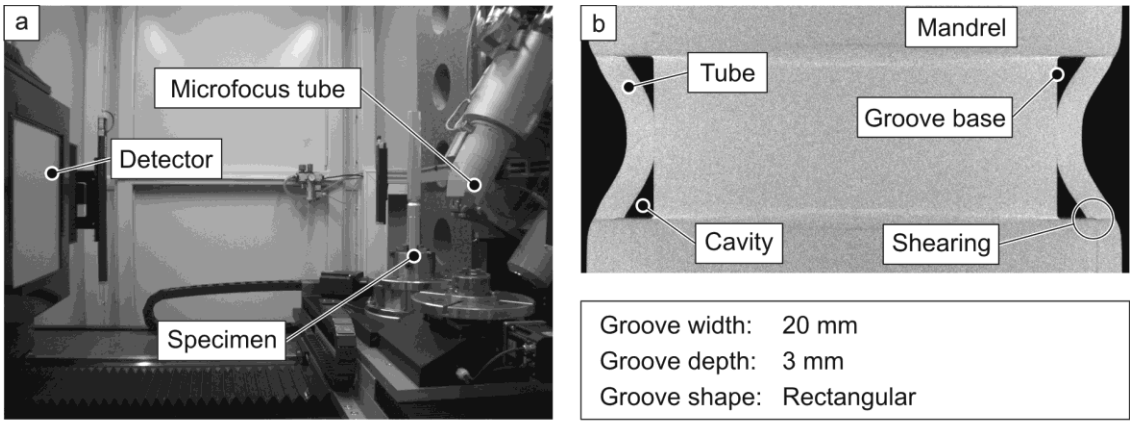

Computertomography (CT) Parameters

Acceleration voltage U_B:	230 kV	Magnification *m*:	~ 9.2
Tube current *I*:	100 µA (120 µA)	Geometry:	Cone Beam
Prefilter:	0.5 mm Cu	Number of Angular Position:	2200 (1440)
Focus-Object-Distance *FOD*:	131 mm	Angle Increment:	~ 0.164° (~ 0.25°)
Focus-Detector-Distance *FDD*:	1200 mm		

( ) = if parameters varied for the hollow mandrels

Figure 4 *a) Setup of the radioscopic and computer tomography (CT) measurements. b) CT image of a form-fit joint with a rectangular groove of 20 mm width and 3 mm depth.*

In Figure 4 c) a xy-slice of the joining zone is displayed. It can be seen that the tube wall makes contact with the groove. The tube wall lies against the deepest point of the groove (groove base) but cavities above and below the plane containing the groove base can also be observed. To determine the quality of the generated joints, pull-out test were performed afterwards. For these experiments a universal testing machine Zwick SMZ250 was used. A pull-out rate of 0.05 mm/s was chosen. Figure 5 a) shows a typical pull-out curve which was obtained by these tests. The force F_J was defined as failure criterion of the connections. At this force, the first relative movement between the tube and the mandrel occurred. Its value was indicated by a change in slope of the load-extension curve (see Figure 5 a)). This criterion was chosen in accordance with the work of Bühler [10]. In Figure 5 b) the two different failure modes which were observed during tensile testing are displayed: pull-out of the tube from the groove and tearing of the tube at the leading groove edge. Both failures occurred shortly after the connections reached their ultimate pull-out force. The tearing of the tube was observed when higher forming energies were applied to deeper and/or narrower grooves. This could be attributed to the tube being partially sheared at the groove edges as it was formed into the grooves at

higher magnetic pressures. For these joints the F_J as well as the ultimate pull-out force was higher than for those connections which failed by pull-out of the tube. Furthermore, the joints failing by tearing of the tube failed more suddenly due to a lower plastic deformation of the connection before the final separation of the joining partners.

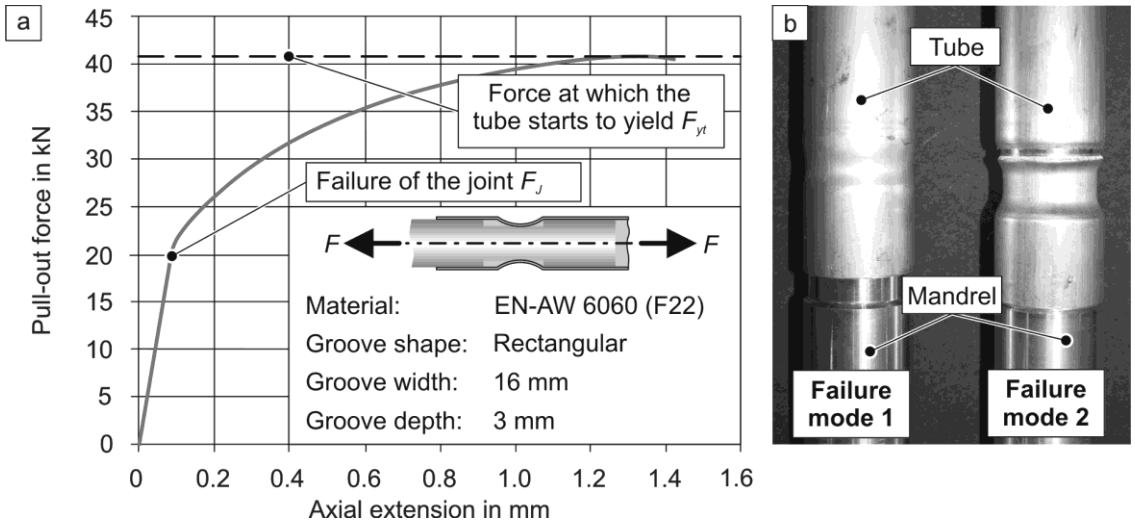

Figure 5 *a) Typical pull-out curve of the joint specimens. b) The two failure modes observed within this work: pull-out (left) and tearing (right) of the tube.*

The forces at which the joints failed were plotted versus the groove depth for different groove width and shapes (see Figure 6 a) and b)). The values of F_J were normalized with respect to the yield force of the tube itself, F_{yt}. Figure 6 a) shows that an increase of the groove depth as well as a decrease of the groove width leads to an increase in joint strength.

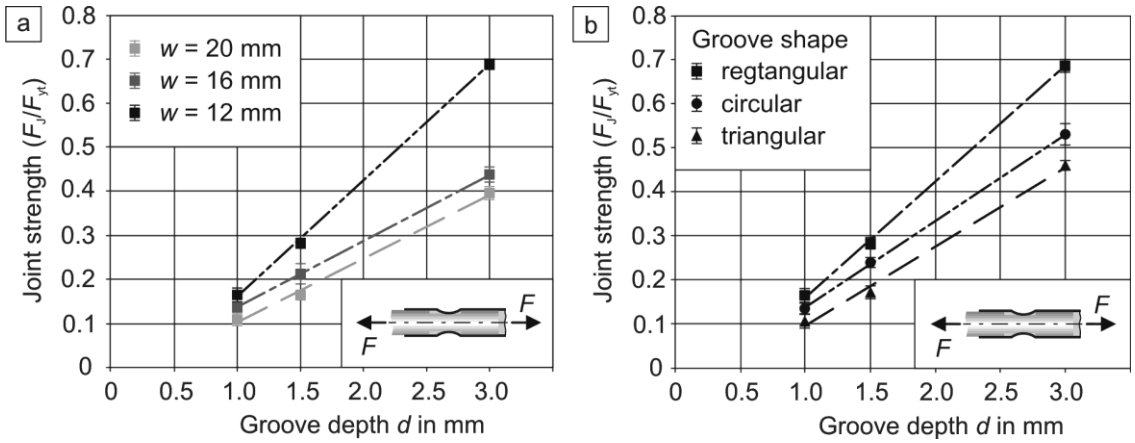

Figure 6 *a) Joint strength with respect to groove depth d and groove width w for solid mandrels with a rectangular groove shape. b) Joint strength with respect to groove depth d and different groove shapes for 12 mm wide grooves.*

This could be attributed to the fact that the resulting angle α (see Figure 7 b)) decreases with deeper or narrower grooves, which increases the incremental degree of deformation at the groove edge and thus requires a larger pull-out force. For all three grooves, the distribution of the data points suggested a linear relationship between the

depth of the groove and the pull-out. An upper limit of this linear relationship is expected due to the partial shearing of the tube at the groove edge, as shown in Figure 7 b). Eventually, the thinning of the tube due to shearing at the groove edge will weaken the joint more than the strength increase observed when forming the tube into a deeper/narrower groove, causing the overall joint strength to decrease. In the next step of this study the influence of the groove shape on the connection strength was analyzed. Figure 6 b) shows the normalized pull-out forces with respect to the depth of the groove for a constant groove width of 12 mm. For each groove shape, the point distributions again show a linear relationship between groove depth and pull-out force. Figure 6 b) shows that, for each individual groove depth, the joints formed with rectangular grooves always exhibit the highest joint strength, while the joints formed with triangular grooves are always the weakest.

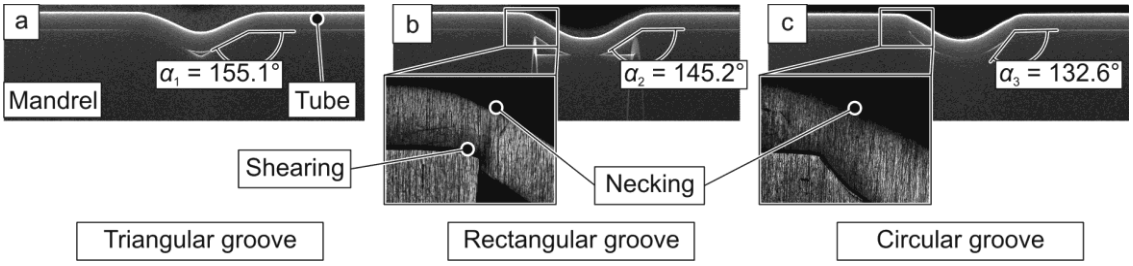

Figure 7 *Measurement of the angle α at the groove edge in radioscopic pictures of 3 mm deep and 12 mm wide grooves with different groove shapes.*

This could be attributed to the fact that the resulting angle *α* of the tube wall at the edge of the triangular geometry is greater than those of either the circular or rectangular grooves (see Figure 7). Therefore, the degree of deformation at the edge of the groove is lower and a smaller tensile force is required to initiate pull-out. Although Figure 7 displays that the joints generated with circular grooves have a smaller resulting angle *α* than the joints formed with rectangular grooves, the use of rectangular grooves results in a larger pull-out force for each parameter set. This can be explained by the fact that the amount of shearing at the groove edge is higher for the rectangular grooves than for the circular ones (compare Figure 7 b) and c)). Due to the greater partial shearing, the rectangular groove locks the tube in place more firmly than when formed into the circular groove, and thus requires a greater pull-out force. This is further supported by the fact that, as Figure 6 b) shows, the use of mandrels with rectangular grooves causes failure by tearing at the leading groove edge for groove depths of both 1.5 and 3 mm, whereas the failure of the connections with circular grooves was caused by tearing of the tube only for the 3 mm deep grooves. The fact that joints with rectangular grooves exhibit this failure mode at a shallower groove depth suggests that the effects of shearing play a more prominent role in the strength of this groove geometry, and it is possible that this accounts for the larger required pull-out forces.

4.3 Effects on the strength of joints with hollow inner joining partners

As mentioned above, the reduction of weight is a very important goal for the automotive industry, which means that the frame structure of a vehicle has to be as light as possible. Therefore, the joining behavior and the achievable joint strength for connection including hollow inner joining elements were also investigated. Figure 8 a) shows the achieved joint

strength for different groove depths with respect to the width of the grooves. The results in terms of the relationship between connection strength and groove depth/width are similar to the experimental findings for the solid mandrels. But especially the grooves with a width of 12 mm showed a significant drop in strength of up to 20% compared to joints which were formed onto solid mandrels with equivalent groove geometry. This could be attributed to a significant deformation of the mandrel, which is shown by the tomography image in Figure 8 b). This deformation led to an increase of the angle α at the groove edge. As described above, this decreases the incremental degree of deformation at the groove edge and thus requires a lower pull-out force. Due to the deformation of the mandrel the tube wall also did not touch the groove base. As a result, there was no interference-fit generated in this area. Whereas, without a deformation of the mandrel, this additional interference-fit would occur because, during forming, the plastic deformation in the tube creates a small amount of elastic deformation in the mandrel.

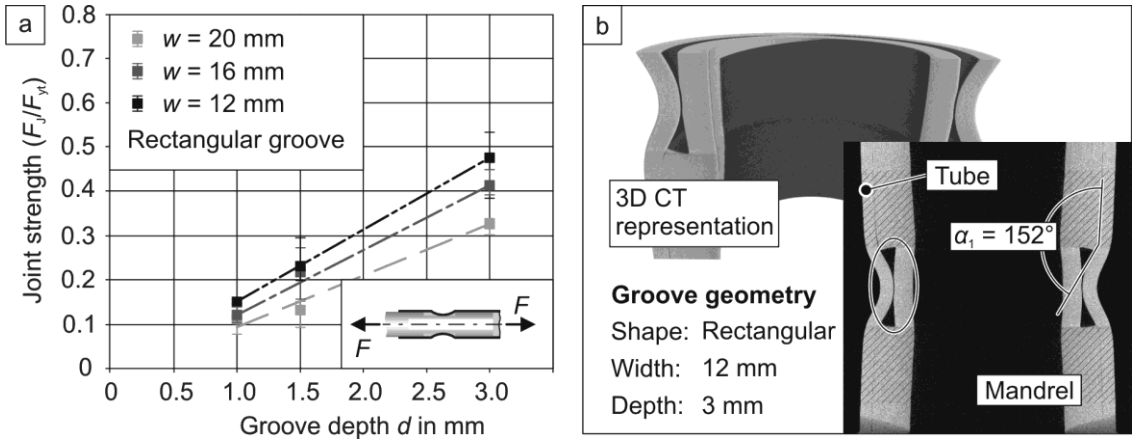

Figure 8 *a) Joint strength with respect to groove depth d and groove width w for hollow mandrels. b) Form-fit joint with a hollow mandrel as inner joining partner; upper left: 3D representation of the tomogram of the joint; lower right: 2D CT image (yz-slice) of the joint.*

When the forming process ends, the mandrel would be unable to release this elastically stored energy due to the plastic deformation in the tube, which would result in interference stresses at the contact surface between the tube and mandrel. This interference stress would resist tube pull-out during tensile testing, thereby increasing joint strength. Although there was no interference-fit generated at the bottom of the groove, an interference-fit was produced at the areas next to the groove (see hatching in 2D CT image Figure 8 b)). Since the same material was used for both joining partners, the additional joint strength created by this interference-fit was too low to compensate the losses due to the weaker form-fit joint [14]. The joints with a groove width of 16 or 20 mm showed only a very small deformation of the mandrel. This explains why they had almost the same joint strength as connections with equivalent groove geometry and solid mandrels. The larger deformation of the mandrels with a groove width of 12 mm resulted from the higher magnetic pressure used to generate these joints compared to those with wider grooves and an equivalent depth (see Figure 3).

A strategy to avoid the deformation of the inner joining partner and the resulting drop in joint strength is the usage of a support mandrel which is placed in the hole of the mandrel during the joining process. Since this support tool shall be removed after the joining process, an interference-fit between the mandrel and the support element has to be avoided. Therefore, a material which has a lower elastic recovery than the mandrel has

to be used for the support tool. This can be achieved by using a material with a higher Young's modulus or a lower yield stress than the mandrel material [14]. Within this study, a steel support mandrel with a Young's modulus three times higher than EN AW-6060 was used. Figure 9 a) shows the achieved pull-out strength for the connections formed with a support element compared to the strength of those which were joint without a support tool. It was possible to increase the joint strength with this setup significantly. The achieved increase was about 15% which means that the pull-out strength level of the joints with solid mandrels was almost reached. Figure 9 b) shows that the deformation of the inner joining partner was reduced significantly which led to the observed increase in joint strength.

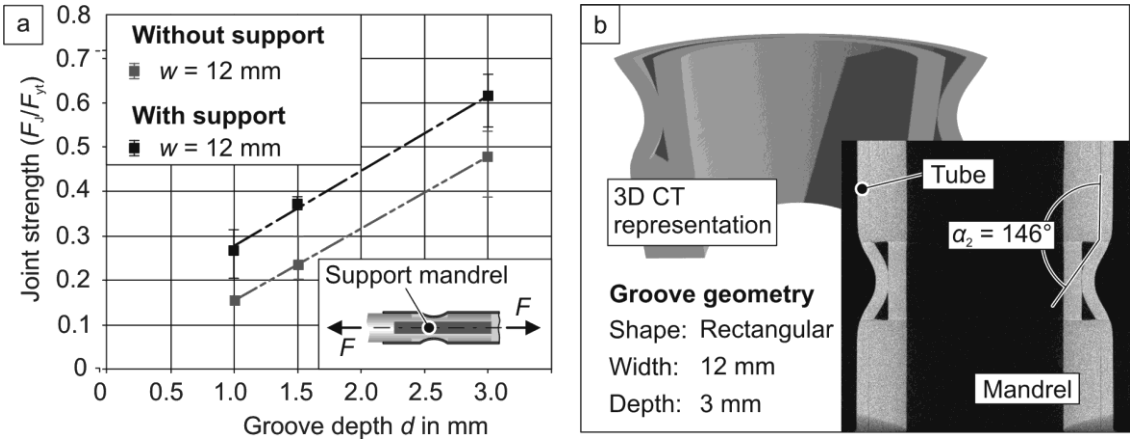

Figure 9 *a) Comparisons of the achieved pull-out strength between a joint generated with and one without the usage of a support mandrel. b) Form-fit joint which was supported by a stainless steel mandrel during the joining process; upper left: 3D representation of the tomogram of the joint; lower right: 2D CT image (yz-slice) of the joint.*

5 Conclusion

The results of this work have shown that the joining of extruded aluminum profiles by electromagnetic compression is a feasible approach to create lightweight frame structures. Due to a decrease of the angle α at the groove edge and the resulting increase of the degree of deformation during pull-out at this edge, the joint strength increases with deeper and narrower grooves. The results of the experimental investigations also showed a significant influence of the groove shape on the achievable joint strength. The highest connection strengths were observed for the rectangular grooves due to the presence of partial tube shearing at the groove edges. This shearing locked the tubes into place, requiring a larger pull-out force to cause failure. Although the partial shearing of the groove edge increased the quasi-static strength of the joints, it can be assumed that it is very problematic for connections which are exposed to cycling loads. Since the location of the shearing is a starting point for the formation of a crack, it has to be avoided for joints under cycling loads. It can be assumed that a rounded groove edge would reduce the formation of such a crack. But further investigations are necessary to determine the precise influence of the groove edge radius on the joint failure and the transferable loads.

The joining experiments with hollow inner joining partners have shown that the applied forming pressure in relation to the stiffness of the mandrel has a significant influence on the achievable joint strength. If the magnetic pressure required to "fill" the

groove exceeds the stiffness of the inner joining partner, a deformation of this element occurs. As a result the angle α at the groove edge is increased, which will lead to a decrease in joint strength. Therefore, it is important to consider the mandrel's stiffness with respect to the applied pressure during the design process of the joining elements. The deformation of the mandrel can also be avoided by using a support mandrel during the joining process. By placing this additional tool in the hole of the inner joining partner it was possible to achieve pull-out strengths similar to those achieved for connections with solid mandrels.

References

[1] Kleiner, M., Geiger, M., Klaus, A.: Manufacturing of Lightweight Components by Metal Forming. Annals of the CIRP "Manufacturing Technology". 53rd General Assembly of CIRP Vol. 52, Issue 2 (2003). Montreal, Canada, pp. 521 – 542.

[2] Marré, M., Brosius, A., Tekkaya, A. E.: Joining by Compression and Expansion of (None-) Reinforced Profiles. Advanced Materials Research: Flexible Manufacture of Lightweight Frame Structures - Phase II: Integration, Vol. 43. (2008), pp. 57 – 68.

[3] Daehn, G. S.: High-Velocity Metal Forming. ASM Handbook Vol. 14B, Metalworking: Sheet Forming. ASM International (2006), pp. 405 – 418, ISBN 0-87170-710-1.

[4] Bruno, E. J.: High Velocity Forming of Metals. Dearborn, Michigan, ASTME (1968).

[5] Weimar, G.: Hochgeschwindigkeitsbearbeitung III Umformung von Blechen und Rohren durch magnetische Kräfte. Werkstatt und Betrieb Vol. 96, Issue 12 (1963), pp. 893 – 900.

[6] Winkler, R.: Hochgeschwindigkeitsbearbeitung. VEB Verlag Technik, Berlin (1973).

[7] Mühlbauer, A., von Finckenstein, E.: Magnetumformung rohrförmiger Werkstücke. Bänder Bleche Rohre Vol. 8, Issue 2 (1967), pp. 86 – 92.

[8] Kleiner, M., Beerwald, C., Homberg, W.: Analysis of Process Parameters and Forming Mechanisms within the Electromagnetic Forming Process. CIRP Annals – Manufacturing Technology Vol. 54, Issue 1 (2005), pp. 225 – 228.

[9] Beerwald, C.: Fundamentals for Process Dimensioning and Design of Electromagnetic Forming (in German). Dr.-Ing. Thesis, Universität Dortmund (2004).

[10] Bühler, H., v. Finckenstein, E.: Fügen durch Magnetumformung. Werkstatt und Betrieb 101 (1968), pp. 671 – 675.

[11] Bühler, H., v. Finckenstein, E.: Bemessung von Sickenverbindungen für ein Fügen durch Magnetumformung. Werkstatt und Betrieb 104 (1971), pp. 45 – 51.

[12] Golovashchenko, S.: Methodology of Design of Pulsed Electromagnetic Joining of Tubes. Proceedings of the TMS Symposium "Innovations in Processing and Manufacturing of Sheet Materials". New Orleans, Louisiana, United States of America (2001), pp. 283 – 299.

[13] Park, Y., Kim, H., Oh, S.: Design of axial/torque joint made by electromagnetic forming. Thin-Walled Structures Vol. 43 (2005), pp. 826 – 844.

[14] Marré, M.: Grundlagen der Prozessgestaltung für das Fügen durch Weiten mit Innenhochdruck. Dr.-Ing. Thesis, Technische Universität Dortmund (2009), Shaker Verlag Aachen, ISBN: 978-3-8322-8361-2.

[15] Feldkamp, L. A., Davis, L. C., Kress, J. W.: Practical cone-beam algorithm. Journal of the Optical Society of America Vol. 1, Issue 6 (1984), pp. 612 – 619.

SESSION 4
METAL FORMING AND CUTTING

Impulse Hydroforming Method for Very Thin Sheets from Metallic or Hybrid Materials

C. Beerwald, M. Beerwald, U. Dirksen, and A. Henselek

Poynting GmbH, Dortmund, Germany

Abstract

Forming of very thin metallic and hybrid material foils is a demanding task in several application areas as for example in food or pharmaceutical packaging industries. Narrow forming limits of very thin sheet metals as well as minor process reliability due to necessary exact tool manufacturing (small punch-die clearance), both, causes abiding interest in new and innovative forming processes.

In this contribution a new method using high pressure pulses will be introduced to form small geometry elements into very thin metal foils or into hybrid polymer-metal foil. It will be shown how the acting pressure pulse will be generated by electromagnetic acceleration of a certain mass, which initiates a pressure wave within a working media. The effect of different pulse lengths has been compared and evaluated by the forming result. Finally, an outlook concerning suitable pulse power equipment and its industrial capability will be given.

Keywords

Manufacturing Equipment, Sheet Metal, Impulse Hydroforming

Introduction

New and more demanding forming tasks as well as the search for innovative forming methods, which extend or complement the number of conventional production processes, caused a steadily growing interest in high speed forming processes during the last years. Especially, Electromagnetic Forming (EMF) is actually on the way from laboratory use to industrial mass production.

Another group of high speed forming processes also using discharge impulses from a pulse power generator is the group of Electrohydraulic Forming (EHF) processes. In that process typically the sudden discharge through an underwater spark gap with or without ignition wire is used to initiate a pressure wave in a working media. This pressure wave acts on a tubular or sheet metal workpiece which is located in a certain distance to the spark gap (pressure source).

For both processes, EMF and EHF, the similar type of pulse generator can be used, but typically not with the same electrical parameters. Both processes have benefits and drawbacks related to the possible application spectrum: for example, EMF is easier to handle because no additional working media is required, on the other hand it is limited to workpiece material with good electrical conductivity. Other reasons to prefer the use of an acting fluid can be the workpiece accessibility or limiting workpiece properties, like a diameter which is too small for electromagnetic expansion or a wall thickness which is too thin for EMF, and so on. There is a lot of potential of EHF, quite similar to the benefits of "conventional" hydroforming processes.

Actually, the main application of underwater shock waves is in the area of kidney stone lithotripsy or other direct medical application. As part of a forming process they are not commonly used, but from time to time applications arise such as surface cleaning of casted parts [1] or calibration of preformed sheet metals [2].

Motivation and Demands of a Forming Example

Forming of very thin metallic and hybrid material foils is a demanding task in several application areas as for example in food or pharmaceutical packaging industries. An example of a typical aluminium blister for pharmaceutical packaging is shown in Figure 1: The material is a multilayer foil consisting of some plastic layers and a 45 µm aluminium layer in between which is an important barrier to light and gas diffusion.

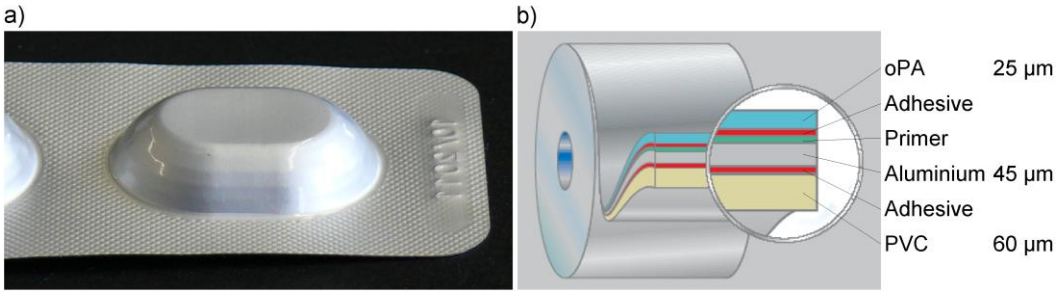

Figure 1: *a) Conventionally formed aluminium blister for pharmaceutical packaging b) composition of the standard multilayer material [3]*

The die cavities are typically 3 to 5 mm deep, depending on their diameter, and produced by a multi-step deep drawing process. This process is very demanding due to narrow forming limits of the very thin sheet and a necessary exact tool manufacturing which is caused by the required small punch-die clearance. An improvement of this manufacturing process can be achieved by reduction of process steps as well as by increasing the cavity density and a corresponding reduction of blister dimension. This can be achieved by small gaps between the cavities, but most by realization of steeper sidewalls.

At the same time the requirements according to the cycle time in series production are high. Typically, production rate is in the range of 700 to 1300 per minute, which corresponds to an operation frequency of 10 to 20 Hz. Typically, high speed forming processes are used at much lower frequencies, although the forming rate is extremely high. Therefore a feasibility investigation has to include the potential of sufficient low cycle time. In case of pulse power equipment, it must be the intention to reduce load of all components significantly. This means, a strong reduction of discharge energy, discharge current, and if possible lower charging voltage are required.

Very first tests to form the above mentioned hybrid material foil have been performed by EMF due to the electrical conductivity of the aluminium layer. The skin effect and the extremely thin aluminium layer require a very high discharge frequency, resp. a very short current rise time. Figure 2 is shown that even with a discharge frequency of more than 100 kHz the material could not be formed because the aluminium layer is too thin. On the one hand depending on the skin effect the thickness is not enough to shield the magnetic field from diffusing through the workpiece, so that no pressure difference can be achieved. On the other hand the induced current causes a strong heating of the aluminium layer and melting of the plastic layer. These results lead to the development of a new method of pulse generation as described in the following.

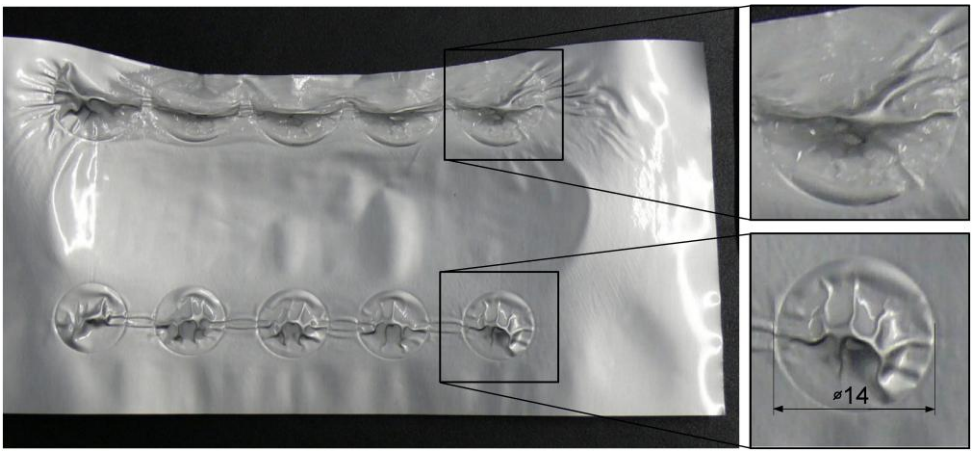

Figure 2: *First try to form aluminium blister foil by direct acting EMF with very short pulse duration (single turn coil, current rise time less than 3 µs)*

New Method of Impulse Hydroforming

Process Principle and Setup

With the intention to use high speed forming without induced current in the workpiece a kind of hydroforming process should be realized for the above mentioned forming task. As shown in Figure 3 a new method to initiate a pressure pulse in a fluid has been realized and tested. Different to EHF processes no spark gap is used, but the following setup:

A flat spiral coil is located below an aluminium or copper driver plate with a certain mass. This plate will be accelerated in vertical direction by electromagnetic forces of the sudden discharge of a pulse generator. It is fixed by a rubber membrane that allows the accelerated driver plate to move but brings it back into its initial position again. At the same time the membrane seals the water vessel above the plate. Workpiece and die are located in the water, but the vessel is “open”, with a free contact between water surface and the air above. There is no sealing required. However, the die cavity behind the workpiece must be evacuated as it is typical for high speed forming operations.

This setup was designed to show the feasibility of the method, but also to vary important process parameters, to exchange the die geometry, and to achieve accessibility for measurement systems. To get some information about the moving plate during the process an optical shadowing principle has been adapted to the setup. Therefore, a laser beam will be detected by an analogue position sensitive photodiode (PSD), when the driver plate moves so that a free distance h_{pl} between coil and driver plate is growing

linear with the vertical position of the plate. A second information is the discharge current which causes the very first acceleration forces acting on the driver plate (and on the coil as well). It will be measured by a kind of Rogowski coil in the HV output of the pulse generator / current input of the coil. The third aspect of investigation is the pressure impulse initiated in the fluid and acting on the workpiece. To detect the pressure wave at the workpiece position a PCB pressure transducer ICP M109B11 with a measurement range of 550 MPa and a rise time of 2 µs was integrated into a special die insert without cavity, see Figure 4d). In that way the pressure impulse will be measured instead of a forming operation. Therefore, the pressure signal does not include the interaction with the workpiece deformation. Finally, the workpiece deformation behavior over process time has been detected by a contact pin which could be mounted in the central die cavity and fixed in a certain distance to the workpiece. The time of contact at this certain distance was detected, in relation to the coil current over time.

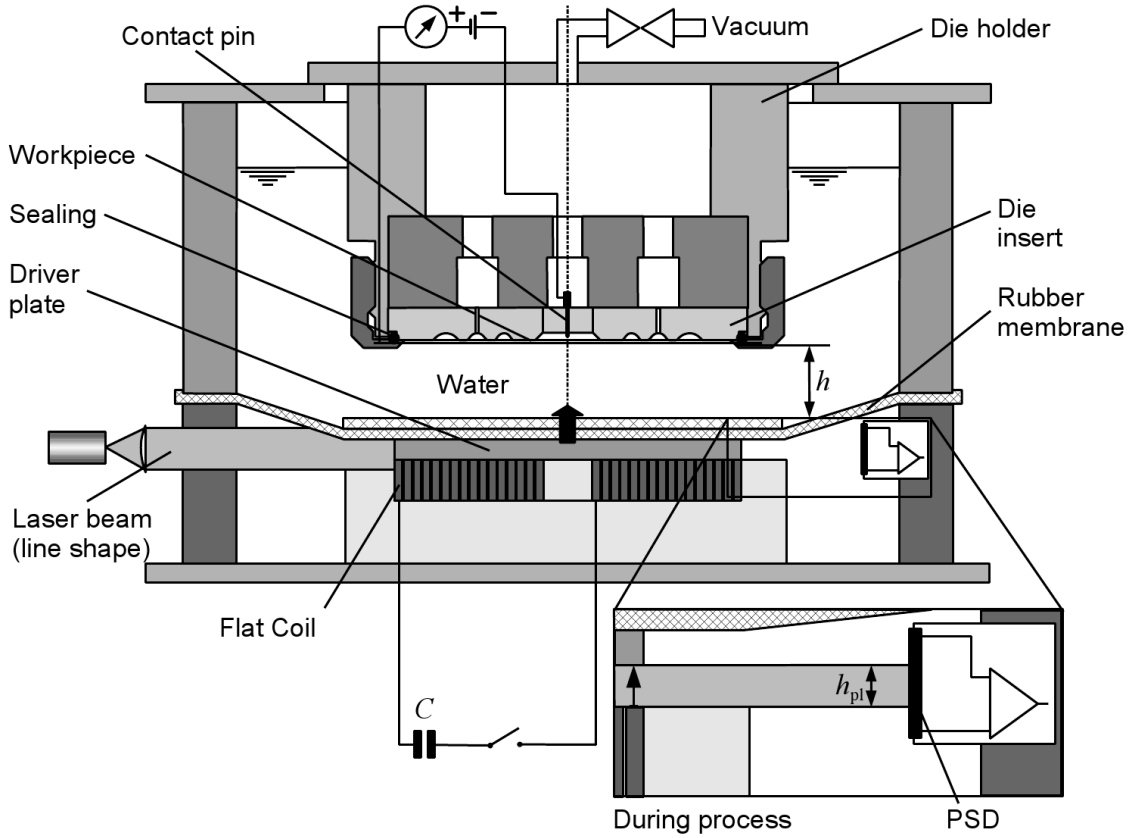

Figure 3: *Principle of new impulse hydroforming method*

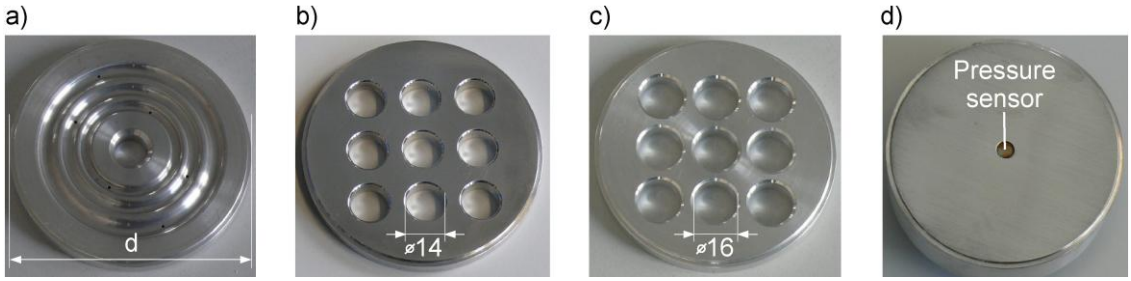

Figure 4*: Used die inserts (d= 90 mm) a) wavy cavity with 2 mm depth; b)-c) cavities for blister forming (depth is adjustable in range of 0 – 5 mm by additional inserts; d) position of pressure transducer in the centre of an insert without cavities*

Feasibility of Forming Pharmaceutical Packaging Foils

With the intention to introduce short and sharply rising pressure pulses in the water, the mass of the accelerated driver plate has been chosen as small as possible. On the other hand, the plate must not be deformed and should be reused over a lot of cycles. Finally, the weight of aluminium driver plate and rubber membrane was about 100 g. The water volume was kept constant 2.5 litres, as well as a distance h of about 10 mm between the moving bottom and the workpiece. Using this setup of the impulse hydroforming process the aluminium blister could be successfully formed, as shown in Figure 5.

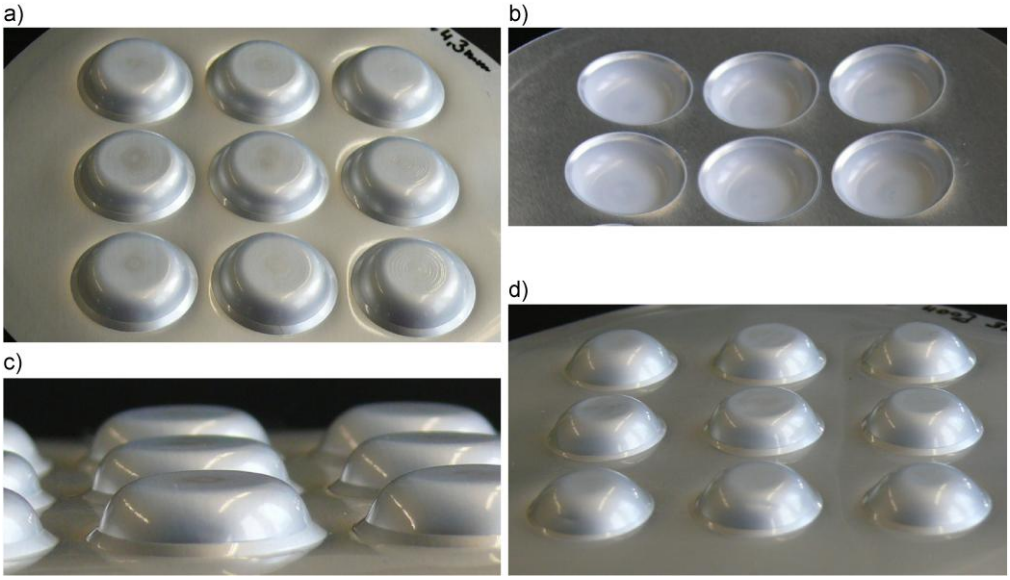

Figure 5: *Forming results for blister diameters d= 16 mm (a)-c)) and d= 14 mm (d)); discharge energy of 450J at 3.2 kV*

By the use of a 26 turn flat coil and a 90 µF capacitor bank, the required energy could be reduced down to a few 100 J. At the same time the coil current is only 8 kA and the charging voltage of this existing pulse generator (SMU1500, Poynting) is 3.2 kV. The very promising forming results demonstrate that it is possible to form a depth of e.g. 4.3 mm without fracture at a cavity diameter of 16 mm, Figure 5a)-c), as well as of 14 mm, Figure 5d). Only one single forming step is needed. Also an improved angle of the sidewall can be realized and allows an increased number of cavities per cm^2 or a smaller size of blister pack when the number of cavities will be kept. The only undesired effect is that the polymer-layer of the backside becomes opaque from stretching as shown in Figure 5b). Failure, like cracking, occurs when the maximum draw ratio of the aluminium layer is reached, or in case of the examples in Figure 6, when the die cavities are not completely dry. Even very fine water droplets on the backside of the workpiece material can cause cracking as shown.

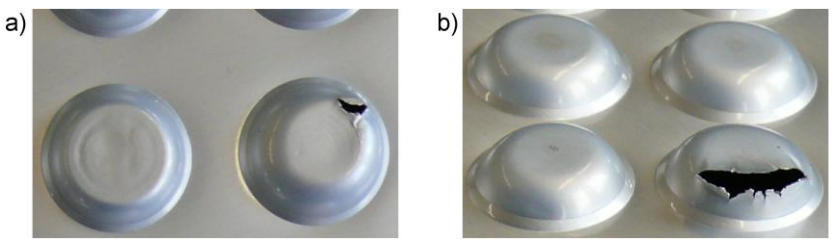

Figure 6: *Formed blisters with cracks caused by small water drops inside the cavities (a) blister diameter d= 14 mm, b) blister diameter d= 16 mm)*

Influence of Current Impulse Length

Due to the high mass of the driver plate it was expected that the current pulse should not be too short to work efficiently against mass inertia. This assumption comes along with the state of the art in electromagnetic riveting machines, as manufactured and described by Zieve et al [4]. The intention of Zieve also is to reduce costs of machine components by significant voltage reduction and longer pulse duration at the same time. In that case the impulse duration is in the range of milliseconds instead of microseconds, of course depending on the mass to be accelerated.

In order to find out which discharge time works best, first, the temporal interaction between coil current, membrane displacement and acting fluid pressure pulse had to be investigated. Exemplarily, in Figure 7 the measured curves for two typical experiments at 600 J discharge energy are shown.

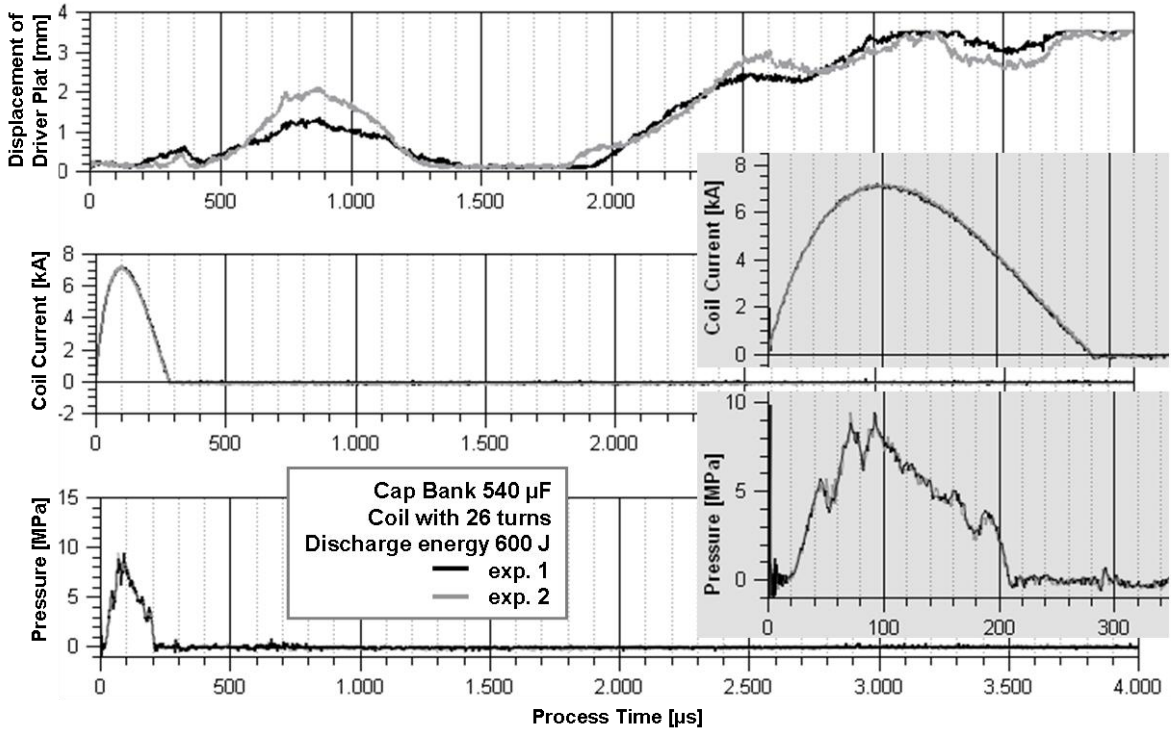

Figure 7: *Process- / Setup-specific time behavior of driver plate displacement, coil current, and pressure*

It can be seen that most of the aluminium driver plate displacement occurs a long time after the current pulse, but the fluid pressure acts only at the same time as the current discharge. This behavior was not expected but can be explained by the elastic membrane interacting with the “open” water volume obviously after the pressure pulse is finished. This comparable slow movement cannot cause a significant pressure because of the air above the water surface. So, the workpiece deformation can be achieved by the pressure pulse during the electrical discharge. A more detailed zoom into the time curves shows that the pressure rises after a short time delay. This delay depends on the distance between start position of the membrane and the position of the transducer, here h= 10 mm. If the distance will be decreased, the delay becomes shorter, with 0.7 µs/mm, which is in good correlation to the sonic speed in water.

To generate different current pulses at comparable amounts of discharge energy, the same setup has been used, but the capacitor bank has been changed [5],[6]. The charging voltage was adjusted for each setup to obtain the same discharge energy. In order to evaluate the process efficiency tin plated steel, 0.19 mm wall thickness, as it is used for can production for food packaging, has been formed into a die with wavy cavities of different width, Figure 4d). The measured current pulses and its forming results are shown in Figure 8. For experiment 4) a 16-turn coil was chosen instead of a 26-turn coil to further shorten the pulse length. In order to make the current curves comparable the current of the experiment 4) is normalized to a 26-turn coil. It can be seen that an optimum pulse length exist to form a workpiece with a sharp contour (experiment 3).

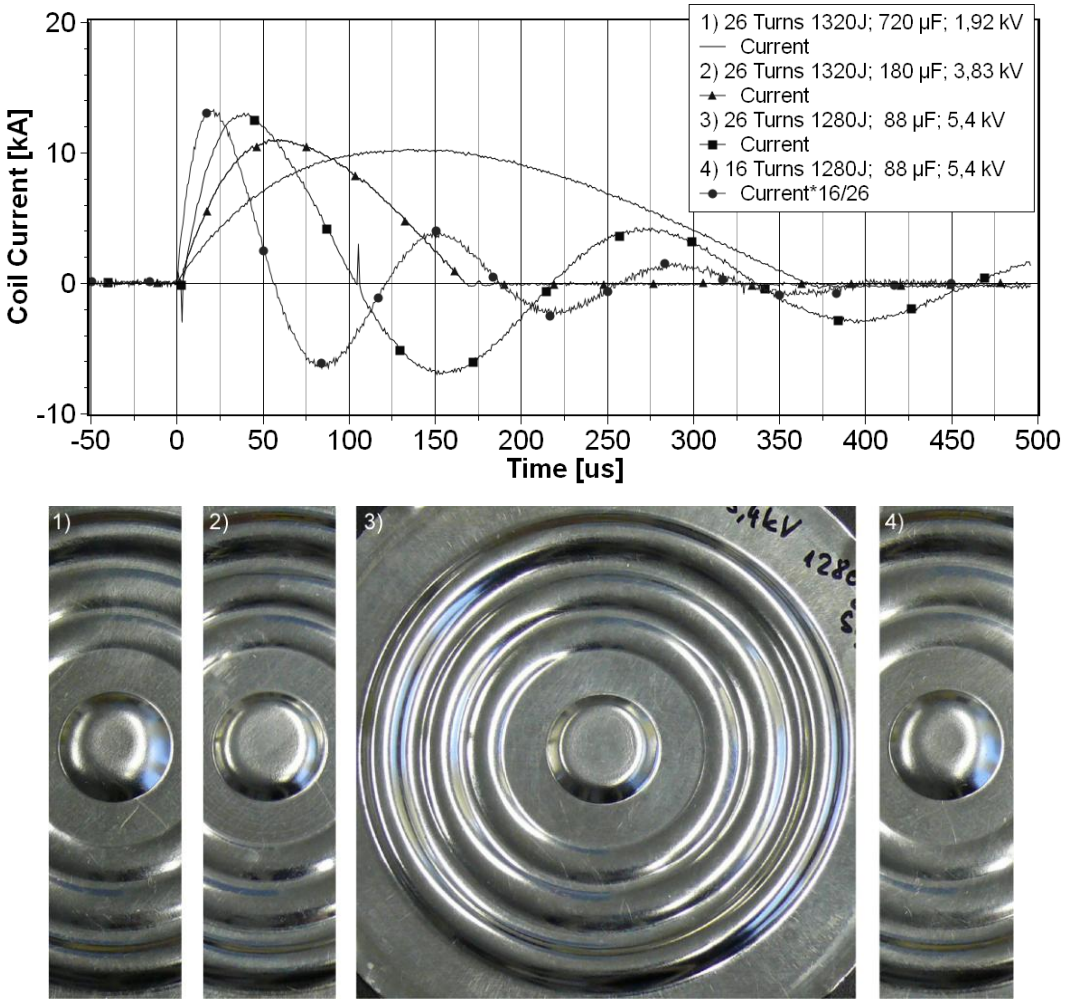

Figure 8: *Different current pulse lengths and corresponding forming results*

Additionally, the measurements with a contact pin in three distances to the sheet metal, 0.55 mm, 1.0 mm, and 2.0 mm, are shown as pictograms in the current over time graph, Figure 9, to give an impression of the sheet behavior related to the discharge pulse, whereas the first setup is the same as in experiment 3, Figure 8. This comparison shows the increased forming rate as advantageous effect of the more optimized capacitor-coil setup at experiment 3).

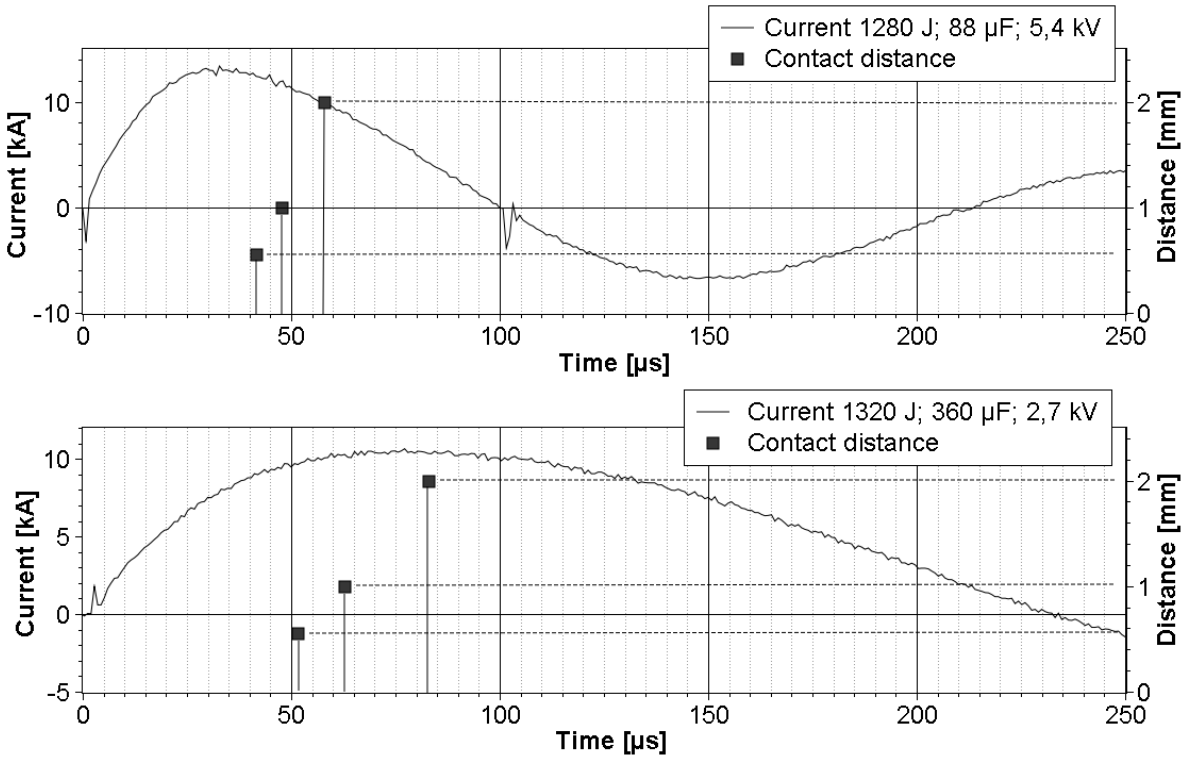

Figure 9: *Two setups with three contact pin measurements at different distances*

Outlook and Potential of the Impulse Forming Method

In this paper a new method for generating a pressure pulse in a kind of electrohydraulic forming process by using an electromagnetically accelerated driver plate is presented. This method is capable of forming very thin metallic and hybrid materials as used in pharmaceutical and food packaging industry [7]. In comparison to EMF the forming capability does not depend on the electrical conductivity of the workpiece material. An additional benefit comes along with the uniform pressure distribution caused by the use of an acting fluid. Especially, if the forming task means embossing of fine geometry details, most application geometries require the workpiece area to be uniform pressurized. Even with the un-optimized experimental setup blister packs can be manufactured in one step and with steeper sidewalls. This increases the usable area of the blisters and accordingly the packaging density. Additionally, the new process is more stable because it does not depend on such accurately manufactured tools as in a deep-drawing process.

In order to tap the full industrial potential of this impulse hydroforming process and to expand its application further development and a concrete design of the required equipment are necessary. Beside the suitability for forming very thin metallic and hybrid materials an additional intention is to keep the required energy and the coil current as low as possible to reduce load of the HV components, like capacitors and high current switches. The pulse generator, driver mass and the coil have to be optimized to minimize the required discharge energy down to only a few hundred joules. An application with e.g. 200 J discharge energy used at a production rate of 20 Hz would dissipate 4 kW. This would already be tolerable, but can be reduced again by recovering the swing back current by an additional circuit. The desired range of cycle time demands the use of long life components, which are usable for more than half a million discharges per day. One

step in the right direction is the application of coils with a lot of turns because this allows a reduction of the required coil current below 10 kA. With a current below 10 kA, a dI/dt below 1 kA/µs, and a voltage below 3 kV the durability of the components, especially of solid state switches, can be considerably increased. A lower current and voltage also makes the selection of capacitors easier. The described experiments have shown that the rate of current change dI/dt already is in a range, which allows us to use phase control thyristors. Not to exceed the 3 kV limit helps to avoid serial connection of such power switches to reduce components and assembly costs. Furthermore, it will be possible to replace the specialized pulse power components partially with standard components which will also significantly reduce the machine costs and the long term process costs.

For the blister pack manufacturing the magnitude of voltage and current are already in the mandatory process parameter range of below 3 kV, 10 kA and a moderate dI/dt. This is not the case for the investigated tin plate, yet, but the values are not far away and the existing optimization potential is not exhausted so far. With such an optimized process the machines and coils can be built with a components durability which will apply to necessary time cycles of 10 – 20 Hz with acceptable machine costs and long-term process costs. Finally, the next step must be the redesign of the experimental setup to the requirements of a continuously working production line. A principle solution is described in [7] including the workpiece and die handling as usual in state of the art mechanical blister pack production.

References

[1] *Winkler, R.:* Hochgeschwindigkeitsbearbeitung – Grundlagen und technische Anwendung elektrisch erzeugter Schockwellen und Impulsmagnetfelder. VEB-Verlag Technik, Berlin, p. 307-333, 1973.

[2] *Golovashchenko S. F.; Bessenov, N. M.; Ilinich, A. M.:* Two-step method for forming complex shapes from sheet metal. Journal of Materials Processing Technology, In Press, Corrected Proof Elsevier. http://www.sciencedirect.com/, available online, 2010.

[3] *N.N.:* The new generation aluminium blister pack. Alcan Packaging Singen GmbH, Singen. Document-Nr.: FORMING/E/02-05/SMD.

[4] *Zieve, P. B.:* Low Voltage Electromagnetic Riveter. Proceedings of SME FASTEC West '86, Anaheim, CA, Oct 21-23.

[5] *Kleiner, M.; Beerwald, C.; Homberg, W.:* Analysis of Process Parameters and Forming Mechanisms within the Electromagnetic Forming Process. Annals of the CIRP Vol. 54/1/2005, 22.-28.8.2005, Antalya (Turkey).

[6] *Henselek, A.; Beerwald, M., Beerwald, C.:* Design and Adaption of EMF Equipment – From Direct Acting Multi-turn Coil to separable Tool Coils for Electromagnetic Tube Compression. In: Proc. o. 1st Intl. Conf. on High Speed Forming ICHSH 2004, Dortmund, pp. 275-284, 2004.

[7] *Reichert, M.; Loecht, H.:* Vorrichtung und Verfahren zur Herstellung von Blisterverpackungen. Offenlegungsschrift DE 10 2005 028 371 A1, Robert Bosch GmbH, Stuttgart, 2006.

Warm Electromagnetic Forming of AZ31B Magnesium Alloy Sheet*

I. Ulacia[1], A. Arroyo[2], I. Eguia[2], I. Hurtado[1] and M.A. Gutiérrez[2]

[1] Mondragon Goi Eskola Politeknikoa, Mondragon Unibertsitatea, 20500 Mondragon, Spain
[2] Labein-Tecnalia Research Center, 48160 Derio, Spain

Abstract

Historically, electromagnetic forming technology has mainly been used to form parts from aluminium and copper alloys due to their excellent electrical conductivity and limited formability by conventional methods. However, little research has been carried out in high strain rate forming of magnesium alloy sheets. Therefore, in the current contribution electromagnetic forming experiments are performed for rolled AZ31B magnesium alloy sheet at different temperatures up to 250ºC.
Two forming operations are studied in this paper, i.e. drawing and bending operations. The final deformations achieved for the different conditions were measured and the effect of both temperature and discharged energy on deformation is shown. Bending experiments at room temperature were recorded by means of a high speed camera and the springback behaviour at high strain rates is evaluated.
In one hand, increasing the forming temperature the yield strength of the material decreases while on the other hand, the electrical conductivity and thus the induced forces are also decreased. It is observed that increasing the forming temperature, for a given discharged energy, the maximum height of the deformed part is decreased. However, increasing the discharged energy at warm temperatures, higher deformation values are achieved without failure. Additionally, bending experiments show that springback effect is also decreased at warm conditions. It is concluded that warm electromagnetic forming is a suitable procedure to manufacture magnesium parts.

Keywords

Electromagnetic Forming, Magnesium Alloy, Warm Forming

---

* *This work is based on the results of FORMAG II project; the authors would like to thank Basque Government for its financial support*

1 Introduction

In last decades there is a clear tendency of reducing the weight of vehicles in the automotive and aeronautic industry [1] due to both fuel economy and environmental concern. New materials with high specific strength, such as high strength steels or lightweight alloys, are being used in order to achieve such lightening. At the present, aluminium and steel are the most frequently employed functional materials in the production industry. However, magnesium alloys are approx. 30% lighter than aluminium and 75% than steel, being the lightest structural material. Therefore the use of magnesium alloys is increasing and it is expected to continue increasing (as reported by the USAMP [2]).

Despite these advantages, limitations such as unsatisfactory corrosion behaviour and a need of suitable forming technologies for magnesium sheets are inherent to magnesium alloys. The lack of formability at room temperature is related with the hexagonal close packed (hcp) crystal structure of Mg and the corresponding limited active deformation mechanisms. One way for increasing the formability of magnesium alloys is to increase the forming temperature owing to the activation of new deformation mechanisms such as non-basal slip systems (e.g. [3]). Therefore, conventional forming technologies are evolving to warm forming processes which owe to considerable increase of deformation as shown by Doege et al. [4] who obtained interesting limit drawing ratio (LDR) of 2.5 for AZ31 alloy.

Another way to increase the formability of magnesium alloys is to employ high speed forming technologies. Research in electromagnetic forming (EMF), despite having been in use since the early 1960's [5], was mainly focused in aluminum alloys (e.g. [6-7]). Very little research has been performed in the field of high speed forming of magnesium alloys. Nevertheless, they all agree that EMF is a promising technology for processing magnesium parts, even at room temperature. At room temperature, Psyk et al. [8] showed the increase of formability and the effect of alloying elements in compression experiments of extruded magnesium tubes. Revuelta et al. [9] performed electromagnetic sheet forming experiments at room temperature. Although they reported an increase of formability, unfortunately, they did not report any value of the deformation achieved. In a previous work by the current author [10] deformation values achieved in AZ31B alloy sheet by EMF were also shown to be higher than the FLC values obtained by conventional forming technologies.

First documented experiments of electromagnetic forming of magnesium alloys at warm conditions can be found in research performed in the former USSR according to [11]. The results show that for the investigated magnesium alloy an extreme increase of the formability was achieved at 200ºC. Uhlmann et at. [11-12] studied electromagnetic forming of magnesium alloys at warm conditions for tubular parts without any reference to the obtained final deformations. Recently, Murakoshi et al. [13] carried out warm EMF experiments for magnesium sheets and they stated that the height of the bulge increased with the increasing of forming temperature.

The electrical conductivity of the material plays an essential role in electromagnetic forming process. The conductivity of magnesium alloys is generally lower than that of aluminum alloys, although it depends on the alloying elements [14]. Nevertheless, the electrical conductivity values of magnesium alloys are adequate for electromagnetic forming process. The most important single factor affecting the electrical conductivity of a metal is the amplitude of the atomic vibration. This factor, in turn, is influenced by the composition of the metal and the thermodynamical variables, such as temperature or

pressure. Therefore, when considering warm electromagnetic forming, the decrease of the electrical conductivity of magnesium alloys must be considered since increasing the temperature the induced forces are lower for the a given discharged energy. Accordingly, increasing the temperature the yield stress also decreases at high strain rates as reported in [15] for AZ31B alloy, also employed in this study. Figure 1 shows the evolution of the electrical conductivity (σ_e) and stress values at $\varepsilon_{eps} \approx 0.01$ ($\sigma_{0.01}$) are plotted for different temperatures. Therefore, it is uncertain the effect of temperature on the final deformation for a given discharged energy.

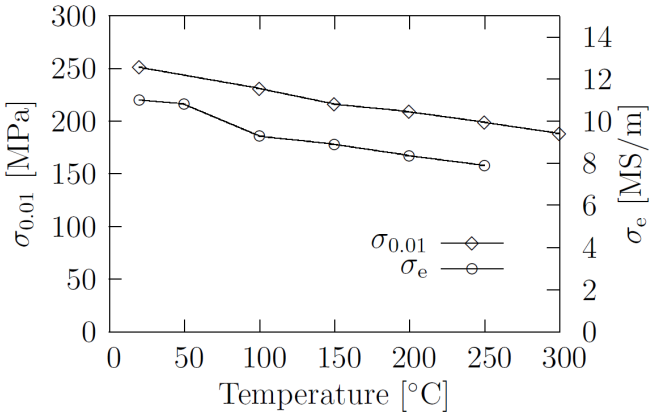

***Figure 1**: Effect of temperature on stress values (from Ulacia et al. [15]) and electrical conductivity values (from Avedesian and Baker [16]) for AZ31B magnesium alloy sheet.*

In the current contribution, warm electromagnetic forming experiments were carried out for AZ31B magnesium alloy sheets in order to evaluate the suitability of the technology. Drawing and bending operations are studied at different temperatures up to 250ºC. Finally, texture analysis is performed to show biaxial deformation mechanisms at high strain rates.

2 Experimental Procedures

2.1 Equipment and tooling

Electromagnetic forming experiments were carried out in the laboratories of Labein-Tecnalia. The experiments were conducted using a commercial Maxwell Magneform capacitor bank with a maximum stored energy of 60 kJ. The energy is stored in 30 capacitors, each of them with a capacitance of 60 µF, divided in four independent banks in order to adjust the discharging parameters. The four divisions of the banks are: one group of 3 capacitors (180 µF), 2 groups of 6 capacitors (360 µF) and one group of 15 capacitors (900 µF). The system has a maximum working voltage of 8.66 kV and the number of capacitors and the charging voltage is adjusted in order to control the discharged energy. The closing force between the die and the coil was achieved in all the experiments by means of a 40 Tn hydraulic press.

Photron FASTCAM-APX™ high speed camera was also used to record the deformation of the sample in the bending experiments at room temperature. The sampling rate was 37500 fps. Two different operations were studied in the EMF experiments carried out: drawing and bending operations. The coils and dies used for these experiments are shown in Figure 2.

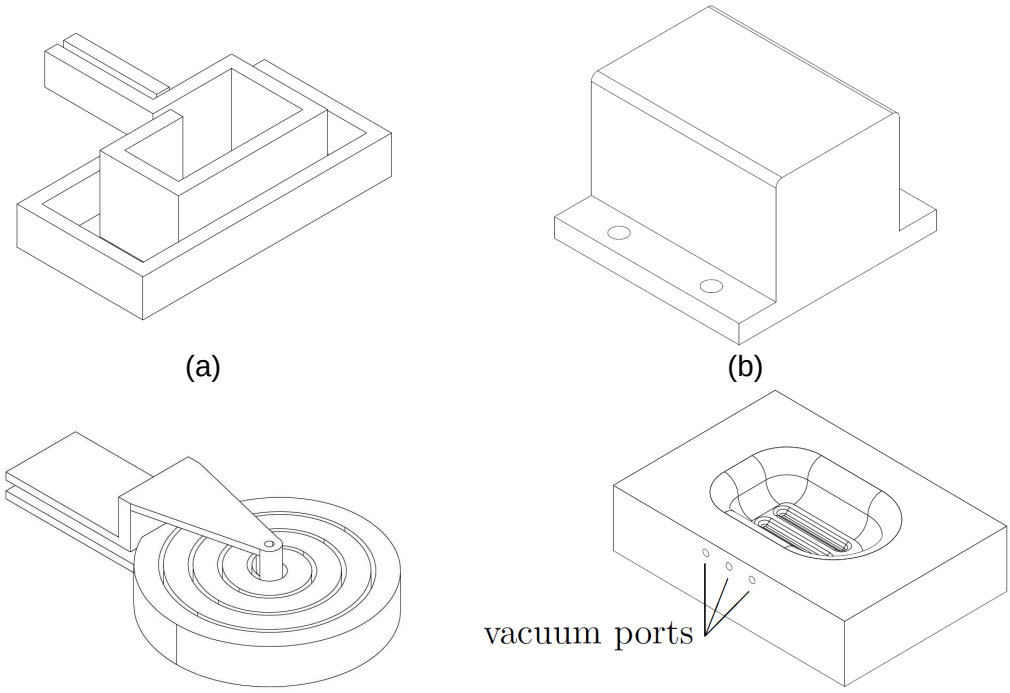

***Figure 2**: Coils and dies used for EMF experiments at different temperatures. (a)-(b) for the bending experiments and (c)-(d) for the drawing experiments.*

In the case of the drawing die, the dimensions were 75 mm width, 20 mm depth and the entry radii were 25 mm. The circular coil used in the experiments is shown in Figure 2(c). The workpiece dimensions were 250 x 175 mm^2. In the bending operation, the dimensions were 175 x 125 mm^2 with a flange of 45 mm. In electromagnetic forming experiments with close dies it is necessary to evacuate the air in the die cavity. Therefore, a vacuum pump is used connected to the vacuum ports of the drawing die (Figure 2(d)).

2.2 Heating Strategy

There are different ways to heat up the specimens that will be formed by means of electromagnetic pulses. One way could be heating up the workpiece in an electric furnace and translating it into the forming stage, taking into account the temperature decrease when contacting the tools. Another way could be to heat the part in the forming position. The coil employed for the forming operation can be used connected to a high frequency electric current pulse source (i.e. inductive heating furnace). This integrated induction heating and forming method allows further automation of the process. It was already patented in the 1960's [17] and also used for warm tube forming by Uhlmann and Hahn [11].

In the current electromagnetic forming experiments, the workpiece was heated by means of 800W electric resistance and it was then automatically transferred to the forming stage as it is shown in Figure 3. The heater is commanded with a PID control of the temperature measured by a thermocouple located on the surface of the heater. However, the temperature of the sample is lower than the one measured in the heater and therefore in the experiments the temperature achieved by the workpiece was measured in six different zones by means of thermocouples glued to the surface of the sheet.

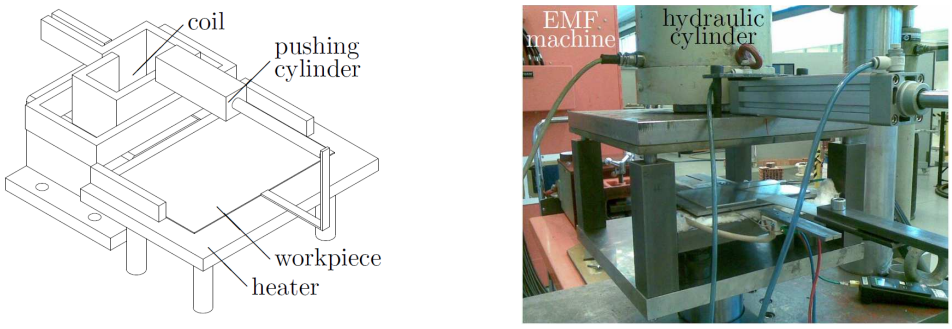

***Figure 3**: Heating strategy. (a) Schematic view and (b) set up of the device.*

The drop in temperature during positioning, closing and capacitor discharging is measured in order to identify the initial forming temperature. Results are shown in Figure 4. It can be noticed that the sheet is heated up to a temperature approximately 10ºC higher than the nominal temperature (i.e. 100ºC, 150ºC, 200ºC and 250ºC), maintained for 5 min and automatically moved to the forming position. However, the temperature during electromagnetic discharge was not measured by thermocouples (notice that in Figure 4 only the cooling during positioning is measured). One reason for not measuring the temperature with thermocouples is that the electric currents induced in the workpiece would flow through the thermocouples to the data acquisition system. Anyway, the response time of thermocouples is significantly higher than the EMF process time. Therefore, in each experiment the time spent for positioning and closing is measured (the average time was 6.5 s) and in this manner, knowing the elapsed time and the cooling curve for each nominal temperature, the initial forming temperature can be estimated for every experiment (and also for different positions). In the forming zone, the temperature was within $T_{nominal}$ ±5ºC in all the cases studied.

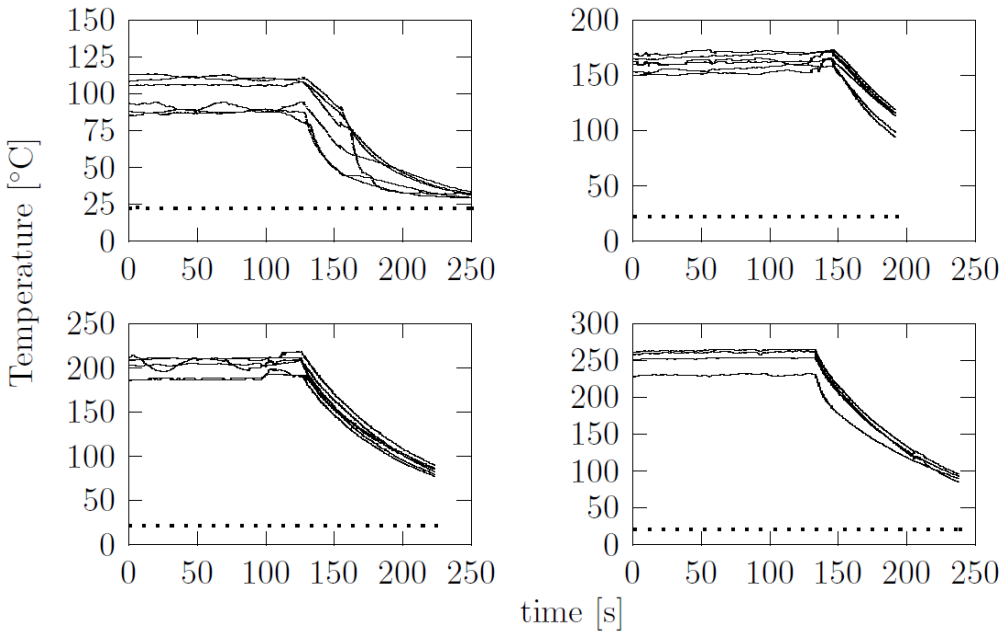

***Figure 4**: Measured heating and cooling curves for different nominal temperatures (dashed lines denote room temperature).*

3 Experimental Results and Discussion

3.1 Drawing operation

Figure 5 shows the influence of the forming temperature and discharged energy. It can be noticed that the maximum height achieved in EMF experiments is decreased when forming temperature is increased for a given discharged energy. The influence of the decrease in the electrical conductivity is slightly more significant than the decrease in yield strength for the temperature range tested. The results obtained in these experiments differ from the results recently reported in [13]. They found that increasing the forming temperature, the height is increased for a given energy (9.8 kJ). However, the material employed in those experiments was annealed at 250ºC for 1 h, whereas the material used in this dissertation was annealed at 400ºC for 2 h. Increasing both annealing temperature and time leads to an increase of grain size and thus, presumably, to a decrease of the electrical conductivity.

The effect of energy on the maximum height achieved is obvious, increasing discharged energy, the height increases for all the studied temperatures. Moreover, it should be remarked that at warm temperatures, a higher energy could be discharged without failure of the workpiece, obtaining better final results. For instance, at room temperature the sample is broken for energies higher than 9 kJ while at 250ºC 15 kJ were discharged without failure obtaining the workpiece completely filling the die cavity. Figure 6 shows the deformed parts obtained at different experimental conditions. It can be seen that the samples deformed at 100ºC (Figure 6(a) and Figure 6(b)) are broken for energies higher than 9 kJ, whereas the sample deformed at 250ºC (Figure 6(c)) completely fills the die cavity without failure. Therefore, warm forming is a suitable strategy for electromagnetic forming of this magnesium alloy because higher deformation degrees than obtained at room temperature can be achieved without a significant increase of discharged energies.

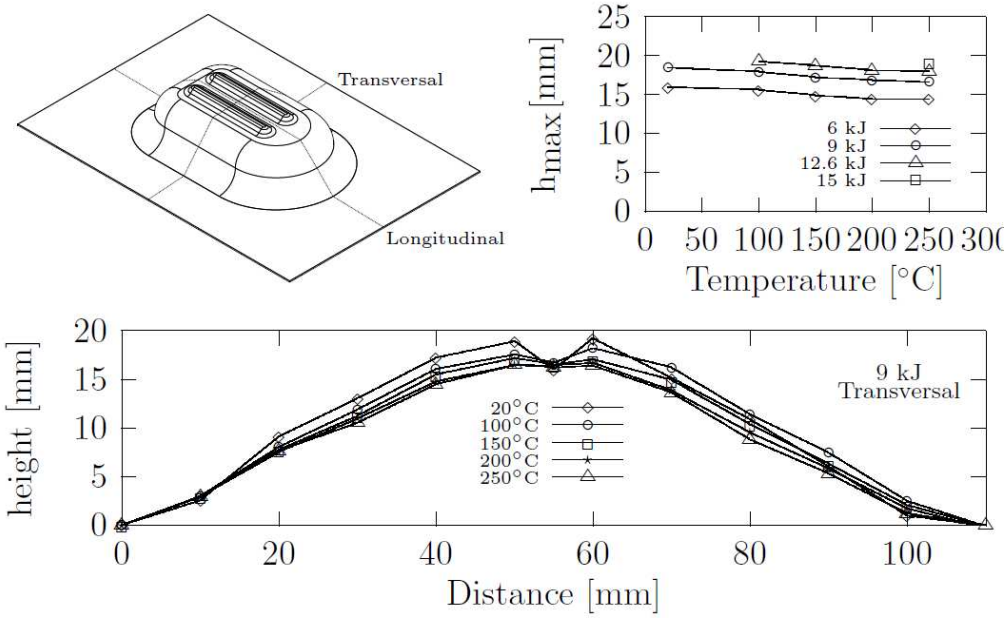

***Figure 5**: Effect of the forming temperature and discharged energy on the maximum height.*

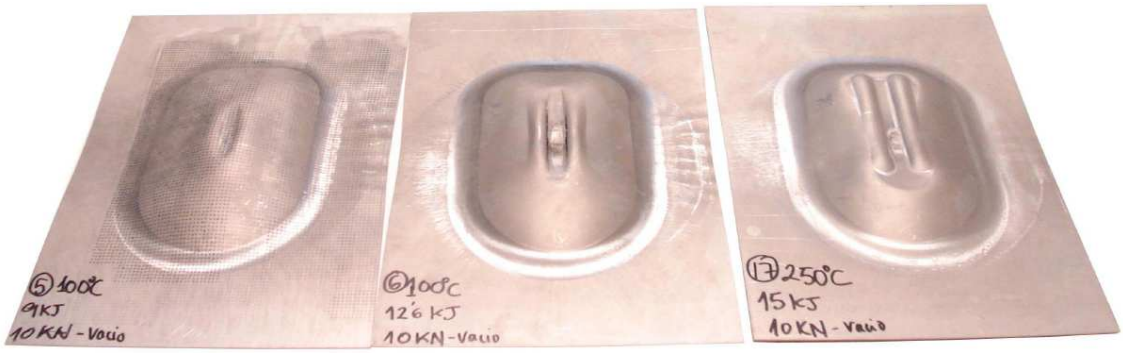

(a) (b) (c)

***Figure 6**: Deformed parts obtained by EMF at different conditions: (a) 100ºC – 9 kJ, (b) 100ºC – 12.6 kJ and (c) 250ºC – 15 kJ.*

3.2 Bending operation

Figure 7 shows the final results of the bending operation experiments for the different discharged energies and temperatures. When analyzing the results, it must firstly be remarked that the deformation achieved was not homogeneous in the whole flange due to the coil geometry and the induced forces for all the temperatures. The repeatability in the experiments was high. The measured angle corresponds to the difference between the final part and the target angle (90º) for an average section of the flange (Figure 7(d)).

At room temperature (Figure 7 (c)-(e)) it is shown that increasing the discharged energy the final angle is closer to the target angle, i.e. the difference is decreased. For the experiments carried out in the current research, it is shown a significant inflection point at a discharged energy of 3 kJ. Therefore, high speed camera was used in order to understand the evolution of the deformation during time at room temperature and different discharged energies (1 kJ, 2 kJ, 2.5 kJ, 3 kJ and 6 kJ). In Figure 8 some pictures of the key deformation states for different discharged energies are collected. The measured angle evolution during time is shown in Figure 9. The first conclusion is that the impact with the die is achieved for a discharged energy between 2.5 and 3 kJ (i.e. for 2.5 kJ discharge the workpiece almost hits the die and for 3 kJ an impact is already filmed). Therefore, the inflection point seen in the final angle at 3 kJ seems to be related with the impact of the flange and the die. Moreover, it can be seen that a springback effect is present in all the experiments. Increasing the discharged energy, the plastic deformation is higher, displacing the neutral fiber and therefore the springback is smaller, as previously seen by Iriondo [18].

Increasing the forming temperature, for a given discharged energy, the induced currents (i,e, forces) are decreased. Consequently, the acceleration of the workpiece will also be decreased and also the impact velocity. Therefore, from the previous results, one may incorrectly conclude that increasing the temperature the springback is decreased as a consequence of lower impact velocities. However, it is observed that the final angle is closer to the target angle (Figure 7(e)). This effect must be understood as a decrease of the springback, since the induced forces and therefore the plastic deformation of the part are expected (as seen in the drawing experiments) to be smaller with increasing the temperature. Springback is dependent on thickness-radius ratio (T/R), Young modulus (E) and yield strength (σ_y) [19]. In the experiments the die radius and the thickness of the sheet were kept constant. Meanwhile, increasing the forming temperature the yield

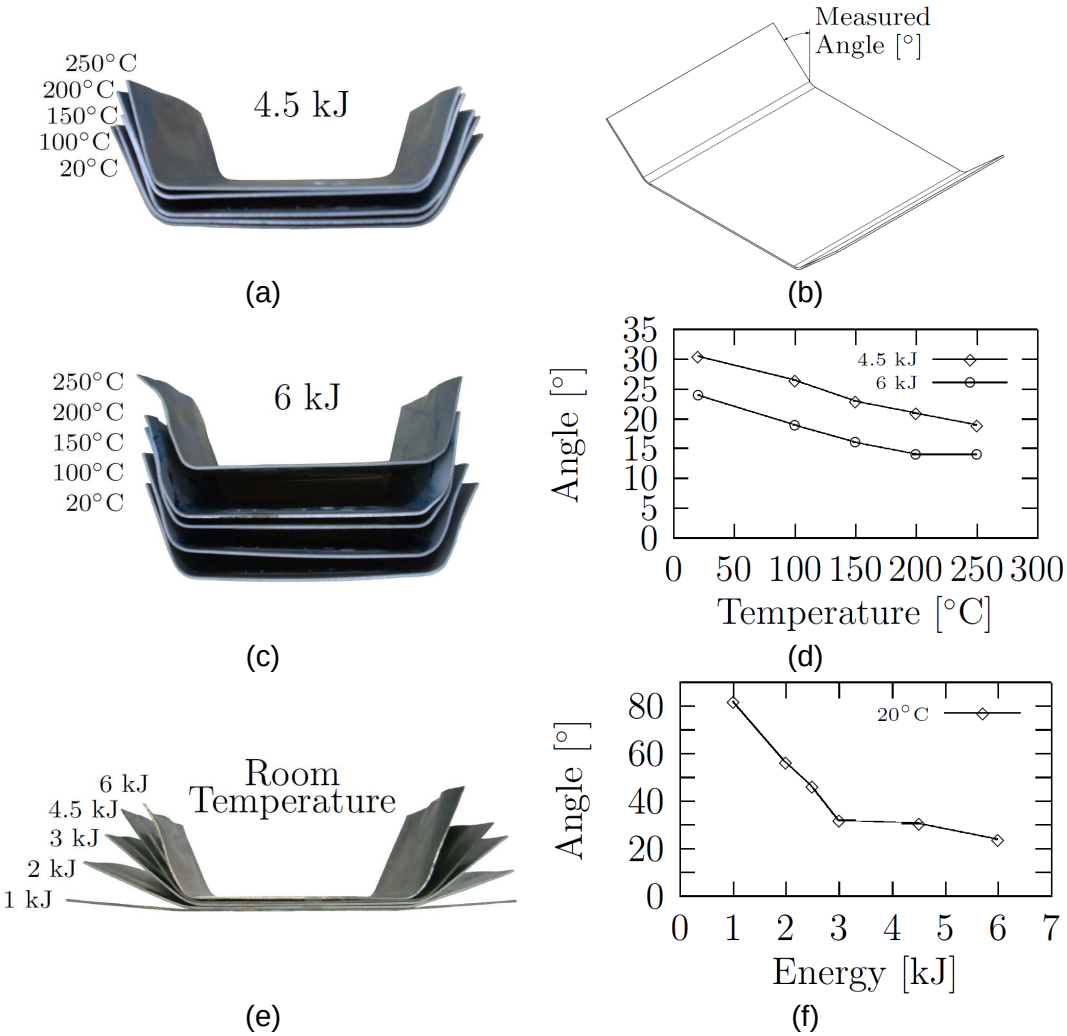

***Figure 7**: Effect of the forming temperature and discharged energy on the bending experiments: (a) different temperatures at 4.5 kJ, (c) different temperatures at 6 kJ (e) room temperature at different energies, (b) measured angle, (d) final angle vs. temperature and (f) final angle vs. discharged energy.*

strength is decreased (Figure 1) and therefore the decrease of the springback can be explained.

4 Conclusions

At warm conditions, the yield strength of the material is decreased while the electrical conductivity also decreases. Increasing the forming temperature, for a given discharged energy, the height of the deformed part is decreased. Therefore, the influence of the electrical conductivity in this type of deformation is more important than the decrease of flow strength. Furthermore, increasing the discharged energy at elevated temperatures, higher deformation values are achieved without failure. Therefore, it is concluded that warm electromagnetic forming is a suitable procedure to manufacture magnesium parts.

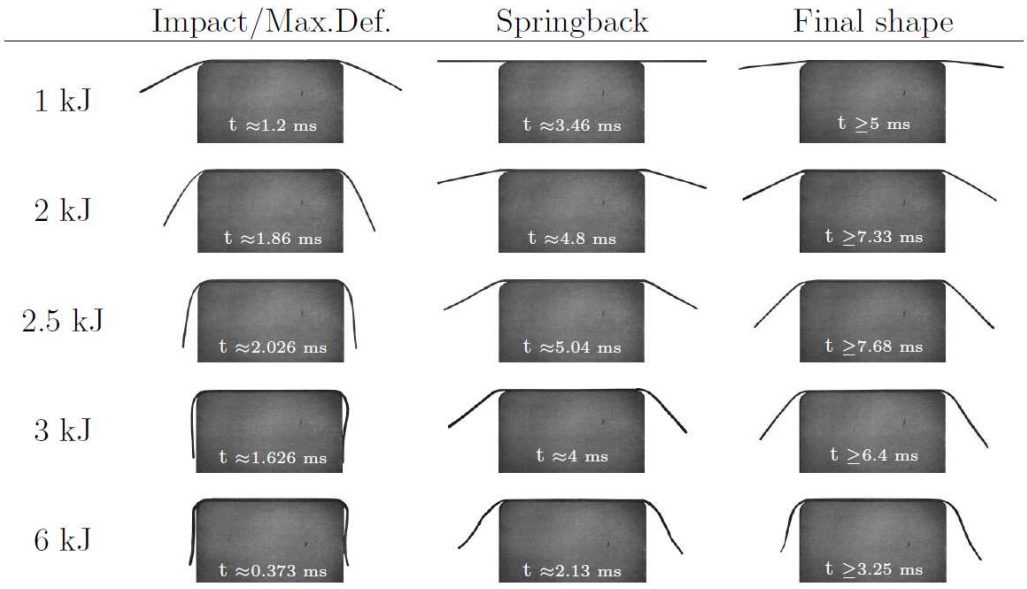

***Figure 8**: Room temperature bending by EMF filmed with high speed camera.*

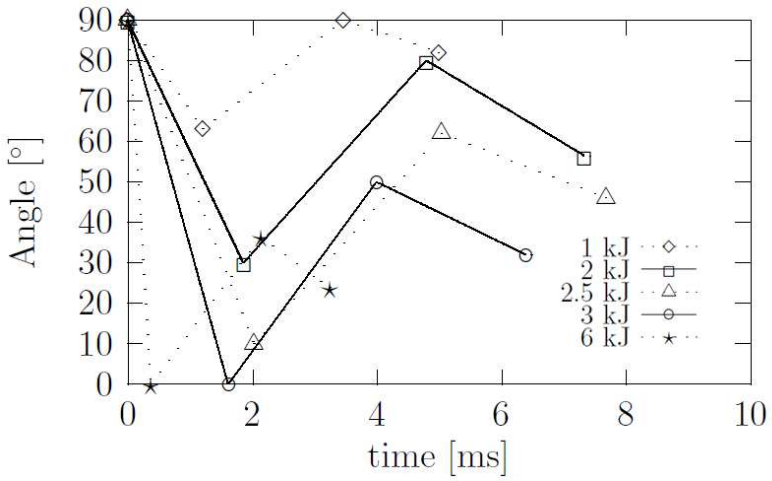

***Figure 9**: Evolution of the bending angle at room temperature (lines are drawn only to guide the eye).*

The springback behaviour at high strain rates is also studied. At room temperature, a decrease of the springback is observed in the samples which impact the die as a consequence of higher plastic deformation. The effect of temperature on the springback is also studied. The final angles achieved in bending operation at warm conditions are closer to the target angle. This can be explained as a reduction of the springback driven by the decrease of the yield strength with the increase of temperature.

In summary, it was observed that the effect of decreasing both yield stress and electrical conductivity with increasing temperature has dissimilar effects depending on the type of the forming operation. In drawing operations, the decrease of electrical conductivity has more influence while in the bending operations where springback is a major factor, the decrease of yield stress is more important.

References

[1] *Kleiner, M., Geiger, M., Klaus, A.:* Manufacturing of Lightweight Components by Metal Forming. 53rd CIRP General Assembly, Montreal, Canada, 2003, p.521-532.

[2] Magnesium Vision 2020: A North American Automotive Strategic Vision for Magnesium. USAMP report, 2007.

[3] *Agnew, S.R., Duygulu, Ö.:* Plastic anisotropy and the role of non-basal slip in magnesium alloy AZ31B. Int J Plasticity, 21, 2005, p.1161-1193.

[4] *Doege, E., Dröder, K.:* Sheet Metal Forming of Magnesium Wrought Alloys – formability and process technology. J Mater Proces Technol, 115, 2001, p.14-19.

[5] *Wagner, H., Boulger, F.:* High velocity metalworking processes based on the sudden release of electrical energy. Battle Memorial Inst. DMIC Rept, 1960.

[6] *Balanethiram, V., Daehn, G.:* Hyperplasticity: increased forming limits at high workpiece velocity. Scripta Metall Mater, 30 (4), 1994, p. 515 - 520.

[7] *Imbert, J., Winkler, S., Worswick, M., Golovashchenko, S.*: Formability and damage in electromagnetically formed AA5754 and AA6111. In: Proc. 1st Int. Conf. High Speed Forming. 2004. pp. 201 - 210.

[8] *Psyk, V., Beerwald, C., Klaus, A., Kleiner, M.:* Characterisation of extruded magnesium profiles for electromagnetic joining. J Mater Proces Technol, 177, 2006, p. 266-269.

[9] *Revuelta, A., Larkiola, J., Coronen, A.S., Kanervo, K.:* High Velocity Forming of Magnesium and Titanium Sheets. In: Proc. 10th ESAFORM Conference on Material Forming. AIP Conference Proceedings, 907, 2007, pp.157-162.

[10] *Ulacia, I., Hurtado, I., Imbert, J., Salisbury, C., Worswick, M., Arroyo, A.*: Experimental and numerical study of electromagnetic forming of AZ31B magnesium alloy sheet. Steel Res. Int. 80, 2009, p. 344 - 350.

[11] *Uhlmann, E., Hahn, R.:* Pulsed Magnetic Hot Forming of Magnesium Profiles. Prod. Eng. X/2, 2003, p. 87 - 90.

[12] *Uhlmann, E., Jurgasch, D.:* New Impulses in the Forming of Magnesium Sheet Metals, In: Proc. 1st Int. Conf. High Speed Forming, 2004, p. 229-241.

[13] *Murakoshi, Y., Katoh, M., Matsuzaki, K., Saigo, M.:* High velocity sheet bulge forming of magnesium alloy by electromagnetic forming. In: Proc 9th Int Conf Tech Plasticity (ICTP), 2008, pp. 1010 - 1015.

[14] *Westengen, H., Aune, T.:* Magnesium Technology. Metallurgy, Design Data, Applications. Springer, Ch. 5. Magnesium Cast Alloys, 2006, p. 160.

[15] *Ulacia, I., Dudamell, N.V., Gálvez, F., Yi, S., Pérez-Prado, M.T., Hurtado, I.*: Mechanical behavior and microstructural evolution of a Mg AZ31 sheet at dynamic strain rates, Acta Mater, 2010, doi:10.1016/j.actamat.2010.01.029.

[16] *Avedesian, M., Baker, H.:* Magnesium and Magnesium Alloys, ASM Specialty Handbook. ASM Int., Materials Park, OH, 1999.

[17] *Alf, F.:* Method of and apparatus for electromagnetically deforming metal. U.S. Patent No. 3,210,509, 1965.

[18] *Iriondo, E.:* Electromagnetically impulsed springback calibration. Ph.D. thesis, The University of the Basque Country, 2007.

[19] *Kalpakijan, S., Schmid, S.:* Manufacturing Engineering and Technology, 4th Edition. Prentice Hall, 2000.

Effects of Force Distribution and Rebound on Electromagnetically Formed Sheet Metal

J. Imbert[1] , M. Worswick[1] and P. L'eplattenier[2]

[1] Department of Mechanical and Mechatronics Engineering, University of Waterloo, 200 University Avenue West, Waterloo, Ontario, Canada, N2L-3G1
[2] Livermore Software Technology Corporation, 7374 Las Positas Road, Livermore, CA 94550

Abstract

Electromagnetic forming (EMF) is a high speed forming process that has been shown to increase the formability of aluminum alloys under certain conditions. Many authors have reported significant increases in formability; however, there is as of yet no complete understanding of the process. Obtaining a gain in formability is not the only factor that must be considered when studying EMF. The process rapidly generates significant forces which lead to the deformation of the material at very high rates. The applied forces depend on the shape of the electromagnetic coil used, which leads to force distributions that may not be ideal for forming a particular part. Once the sheet is accelerated it will travel at high speeds until it impacts the die. This high speed impact results in the sheet rebounding from the die. Both the force distribution and the rebound affect the final shape of the part. This paper presents the results of experimental and numerical study carried out to determine the effect of the force distribution and the rebound on samples of conical and "v-channel" geometry. It was found that both sample geometries are affected by the force distribution and the rebound, with the v-channel samples being considerably more affected. The results indicate that these effects must be carefully considered when EMF processes are designed.

Keywords

Metal, Forming, Electro-magnetic, High, Speed.

1 Introduction

Interest in electromagnetic forming (EMF) of sheet metal for automotive applications has been growing in recent years, due to its potential as a means of forming aluminum and other low formability materials. Forming of aluminum has been the main focus, due to its inferior forming characteristics relative to mild steel [1,2,3] and its relatively high conductivity.

Despite having been in use since the early 1960's [4], there is not yet a complete understanding of EMF. Progress has been made since the mid-1990's in this regard [5-13]; however, there is still not sufficient knowledge of this process to be able to properly design EMF processes for industrial sheet metal forming applications.

Obtaining the desired shape of a part within the specified tolerances is the goal of any forming operation. In conventional forming, the punch and die produce the final shape, with springback being the principal factor that may cause deviations from the desired final shape. Designers must account for spring back by modifying the design of the tools to achieve the desired part geometry. EMF differs significantly in that the punch is replaced by the forces induced on the sheet by the coil, which propel the sheet at high speeds into a die shaped in such a way as to provide the final part. Ideally, after the process is complete the material emerges with the final shape. Unfortunately, in EMF the force distribution generated on the sheet by the coil and the rebound caused by the impact of the sheet with the die can produce parts that deviate from the specified shapes. Imbert et al. [11] reported that samples formed with aluminum alloy sheets into a conical die, did not conform to the die shape. A step was generated on the part, which was attributed to the rebound of the sheet. Risch et al. [14-16] studied the effects of the rebound on axisymetric parts and suggested design changes in the part and die to alleviate the deformation caused by the rebound.

This paper presents the results of a study conducted on the effects of force distribution and rebound on the final shape of samples formed using EMF. Conical and open channel samples were formed from 1 mm sheet of AA 5754, which is an aluminum alloy in relatively widespread use in the automotive industry. These shapes were chosen since the cone has substantially greater geometric stiffness than the open channel geometry, which means that the conical shapes will be harder to deform. By using this approach, two extreme cases could be studied that would provide information on typical forming operations, since the response of typical manufactured parts will likely fall between those of these two geometries. The samples were formed using two different coils; the conical samples were formed with a spiral coil, while the open channel v-cross section samples were formed with a rectangular coil. The final shapes of the samples are presented to show the effects of the pressure distribution and the rebound. Numerical analysis was carried out to compliment and better understand the experiments. The analysis was carried out with a commercially available coupled code capable of simultaneously solving the electromagnetic and structural problem.

2 Experimental Procedure

2.1 Conical Samples

The conical samples were formed as part of the work described in [17], which provides details of the experimental procedures. Cones were formed with side angles of 34, 40 and 45°. The conical samples were formed using a 7-turn spiral coil with a nominal diameter of 100 mm and a maximum diameter of 115 mm. An IAP Magnepress [18] magnetic pulse generator with a storage capacity of 22.5 kJ at 15kV was used to form the samples. The material was clamped to the die and a vacuum drawn to remove the trapped air.

2.2 Open Channel Samples

The open channel samples were formed into a “V” shaped die (Figure 1). The side angle of 40° was chosen since it was the maximum angle reached with no failure for the conical samples [17]. The open channel samples were formed using a double pancake coil made from 4.6 mm (0.180 in) square copper rod, witch each side of the coil having six turns (Figure 2). The coil was connected to a Pulsar [19] MPW 20 – Research Edition magnetic pulse generator, which consists of a capacitor bank and a power supply to deliver the current to the capacitors at the required specifications. The power supply has a nominal maximum energy capacity of 20 kJ and charging voltage of 9 kV. The samples for this work were formed using 3 and 5 kV, which gave storage energies of 2.48 and 6.73 kJ respectively.

Figure 1: *Drawing of the stool used to form the v-channel samples, together with a schematic showing the coil position and a highly simplified pressure distribution over the area of the sample that deforms during the process.*

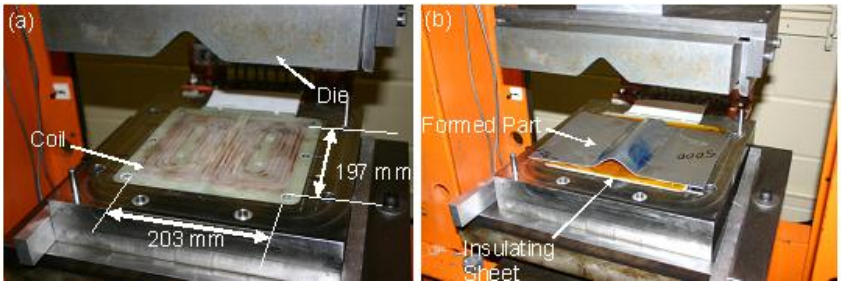

Figure 2*: Tooling used for the experiment a) coil and die and b) tooling with a formed part and insulating sheet****.***

The material tested was 1 mm AA 5754 in samples of 197 x 305 mm. The material was formed by placing over a coil that was connected to the pulse generator. The coil was encased in epoxy to provide insulation and structural strength. Additional insulation was provided by sheets of an insulating material (Kapton™). The insulating materials resulted in a separation between the sheet and the coil of approximately 1 mm. The sheet and die were held in place by the force provided by the hydraulic press.

3 Numerical Analysis

It is very difficult to measure experimentally the deformation history, the currents and the Lorentz forces induced on the sheet in EMF, due to the high speed nature of the process and the closed tools that are used. The experiments were modelled numerically to gain some insight on the parameters mentioned above. The numerical effort for this work was undertaken with a version of LS-DYNA which can model the EM and structural parts of the problem. The software performs the EM calculations by using both Finite Element Analysis (FEA) and the Boundary Element Method (BEM) to solve Maxwell’s equations in

the eddy-current approximation. FEA is used to solve the EM equation in the conductors (e.g. coil and workpiece) and the BEM is used to model the air. By using the BEM to model the air, the small and distorted elements that can result when small air gaps exist between the coil and workpiece are eliminated. The major drawback of this approach is that it is very memory and processor-time intensive. A detailed description of the method is provided in [20]. A study performed to validate the software is presented in [21].

The coil and workpiece were modelled using eight node hexahedral solid elements. Solid elements are required for both electromagnetic and structural calculations, to solve the induced currents and to capture the through thickness and shear stresses on the sheet during forming [11]. The sheet was modeled with an elastic-plastic piece-wise-linear plasticity model that is incorporated into LS-DYNA [22] with a quasi-static stress-strain flow curve (Figure 3). The details of this particular implementation are described in [17]. The coils were modeled as elastic materials. Tooling components were modelled as rigid bodies and their surfaces were discretised using shell elements for the structural calculation. The tool elements were ignored for the electromagnetic calculation. The mesh for the conical samples is shown on Figure 4 and for the v-channel on Figure 5.

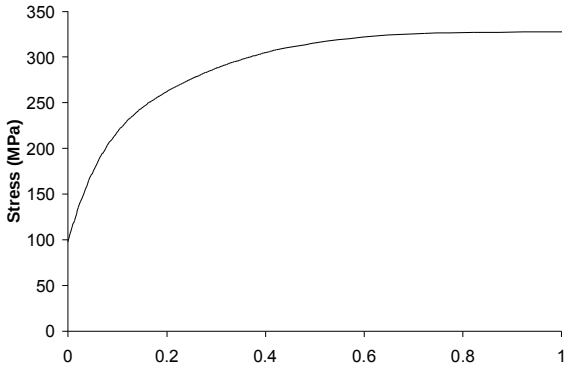

Figure 3: *Quasi-static true stress-strain data for AA5754 used in the numerical model.*

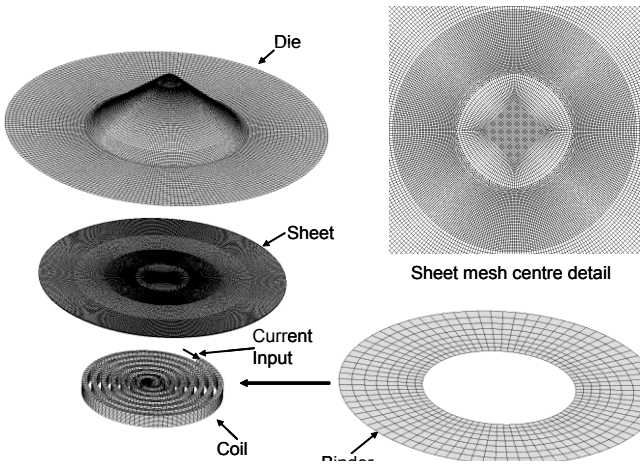

Figure 4*: Mesh for the conical sample models. The binder lies between the coil and the sheet and, together with the die, clamps the sheet. Neither the die and binder meshes are included in the EM calculations.*

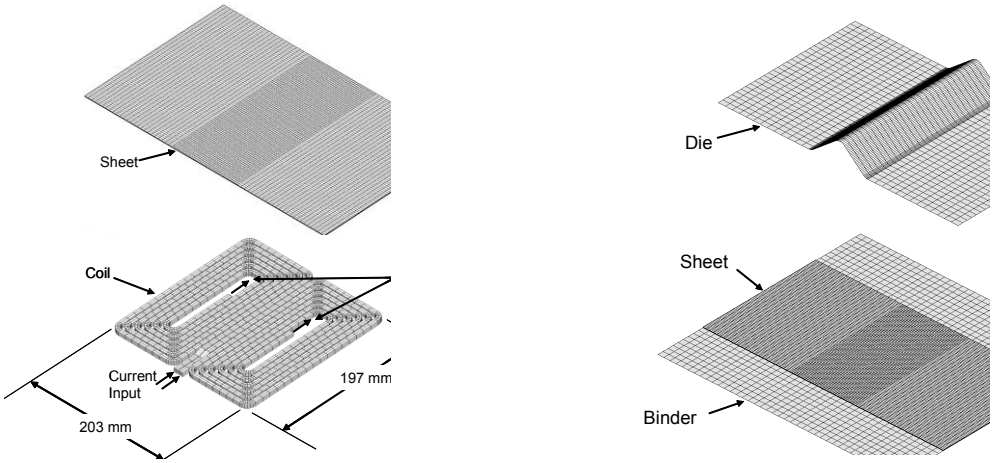

***Figure 5**: Meshes for the V-channel models. The binder and the die are uses to clamp the sheet in place.*

For the conical simulations, the sheet meshes were composed of 258,560 elements, while the sheet mesh for the v-channel simulations had 28,800 elements. The much larger number of elements for the cone mesh was needed to accurately capture the features found in the experimental results and to avoid erroneous predictions due to element geometry [17]. Utilizing more elements might have resulted in more accurate results; however, the memory limits of the computers being used was exceeded when more elements were used.

To reduce run times the EM part of the solver was not active for the whole simulation, it was deactivated after the induced forces became negligible. For the V-Channel models the run total time was 400 μs, with the EM module turned off after 50 μs. For the conical model the total run times were 200 μs and the EM module was deactivated at 25 μs.

The simulations captured the general behaviour of both forming operations. The observed discrepancies described below are believed to be caused by the material model, the coarseness of the sheet mesh (especially for the v-channel samples) and the imperfections of the coil that were not reproduced in the model.

4 Effect of Force Distribution

In EMF, the force on the sample is the result of the repelling magnetic fields of the coil and those of the induced eddy currents in the sheet. Since the path of the eddy currents will be opposite to the path of the current flowing through the coil, the eddy currents and the force distribution on the sample will be dictated by the shape of the coil. Practical limitations such as the provision of an adequate current path, ease of manufacture, structural strength and magnetic properties of the coil result in shapes that may not produce the ideal force distributions. Also, the sharp edges of the blank can produce current concentrations that will increase the induced force at the edges of the sample and consequently result in larger local deformations. The net result is a force distribution that may not be ideal for a particular forming process. The specimens studied in this work were formed using spiral (conical sample) and rectangular “double pancake” (v-channel) coils, which are illustrated schematically with approximate force distributions on Figure 6.

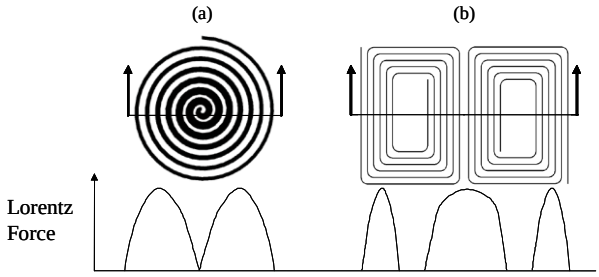

***Figure 6**: Schematic of a) spiral and b) rectangular "double pancake" coil with approximate force distributions along the centreline.*

4.1 Conical Samples

Figure 7 shows representative as-formed conical samples. The heights for the samples were 46.9 mm and 54.4 mm, for the 40° and 45° cones respectively. It can be seen that the parts do not form a perfect cone. A prominent feature present is the step that can be seen on both samples, in addition to distortion at the top of the cone. The step is attributed to the rebound and will be discussed below. The step can be used to visualize the uneven forming that is the result of the pressure distribution. It can be seen that the step for the 45° sample is not horizontal, which is a result of the force distribution. The 40° sample shown also has a non-horizontal step, but it is less prominent than the step of the 45° sample.

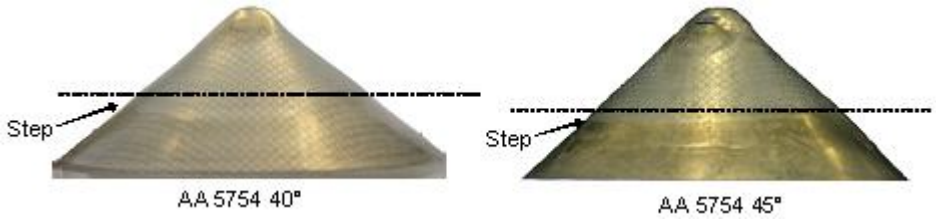

Figure 7**: Conical samples shoeing the step formed due to the rebound. Note that the step for the 45° samples is more inclined.**

The 40° conical sample experiments were modelled and the software was able to capture the expected behaviour for a sample formed using a spiral coil. The sample heights were very accurately predicted which was expected since the samples filled the die and did not vary drastically from the final shape. Figure 8 shows a comparison between the experimental and predicted heights for the conical and v-channel samples.

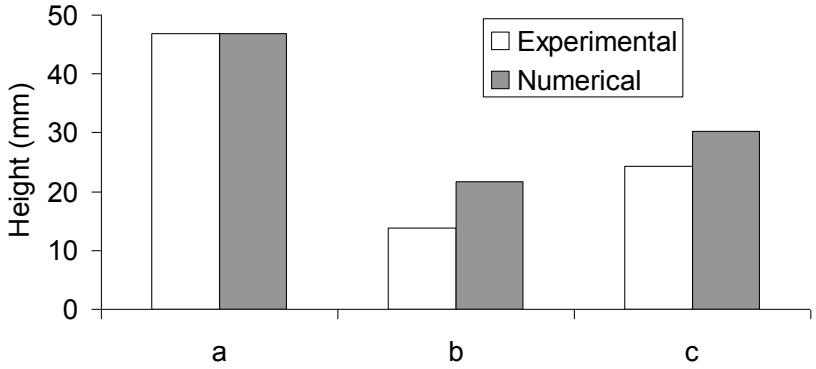

***Figure 8:** Experimental land numerical sample heights for a) the 40° conical samples, b) v-channel samples with no die contact and c) v-channel samples with die contact.*

Figure 9 shows the predicted force distribution produced on a sheet; which is characterized by a zone of zero induced force near the centre. Spiral coils are usually assumed be axi-symmetric in many analyses. Using this assumption they produce axi-symmetric current and force distributions, which is a simplification of the actual distributions. The result of the non-uniform force distribution is that the material fills the die unevenly producing a non-uniform strain distribution and surface features, as shown on Figure 10. The results for the 45° samples were not included due to the fact that failure was observed in the experiments and the numerical model was not able to capture the failure modes.

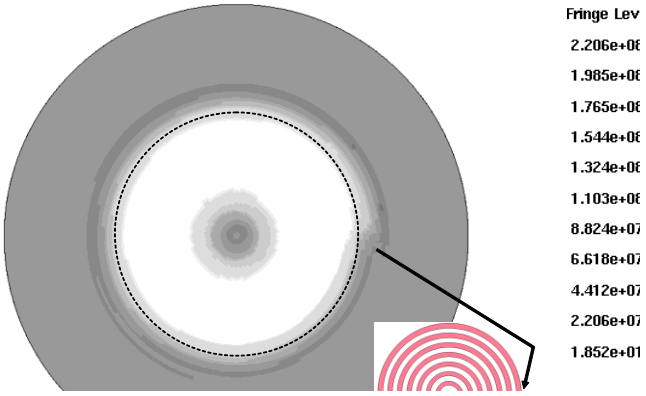

***Figure 9**: Predicted current density produced by a spiral coil on a flat sheet. The broken-line circle is placed to highlight the non-uniformity of the field. Fringe levels are of Lorentz force in μN.*

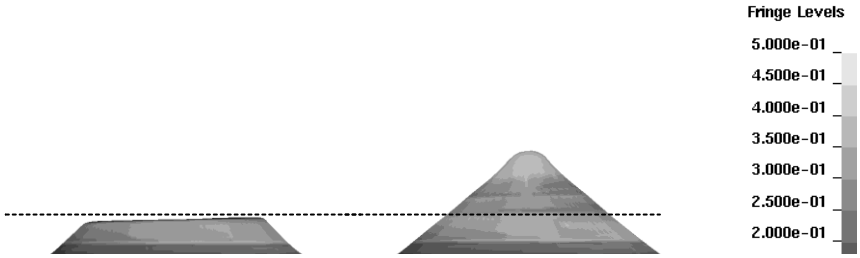

***Figure 10**: Conical die modelling results. The contours are of effective plastic strain.*

4.2 V-Channel Samples

Samples that did not make contact with the dies were formed using the v-channel apparatus to isolate the effects of the force distribution from the effects of the impact of the sheet with the die. A representative sample formed is shown on Figure 11. It can be clearly seen that the part does not have a uniform height. The final shape is the result of the non-uniform force distribution produced by the coil. It can be seen that the height varies along the length of the part, with the centre of the part being the highest point. The average height for three experimental samples is 13.8 mm. This height distribution is

consistent with the predicted force distribution shown on Figure 12. The right side of the sample is higher than the left, due to higher forces acting on that side of the sheet, which are the result of irregularities in the coil. These irregularities result in the coil being slightly more separated from the sheet on the side with the lower height. Towards the ends of the part there is a reduction in height which is consistent with the geometry of the coil and the predicted force distribution which will be discussed below. At the ends of the samples the height stops decreasing and increases at the very edge, this is likely due to the concentration of the current produced at the edges, which results in a local increase in Lorentz forces.

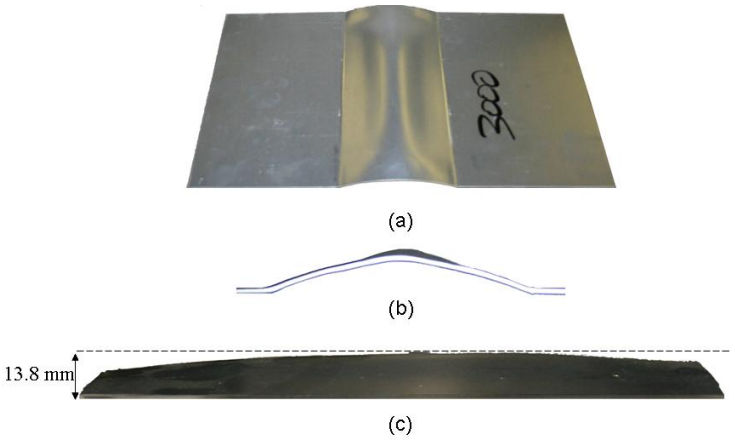

Figure 11: *Part formed using a charging voltage of 3000 volts and the double pancake coil, a) view from above and b) front view*.

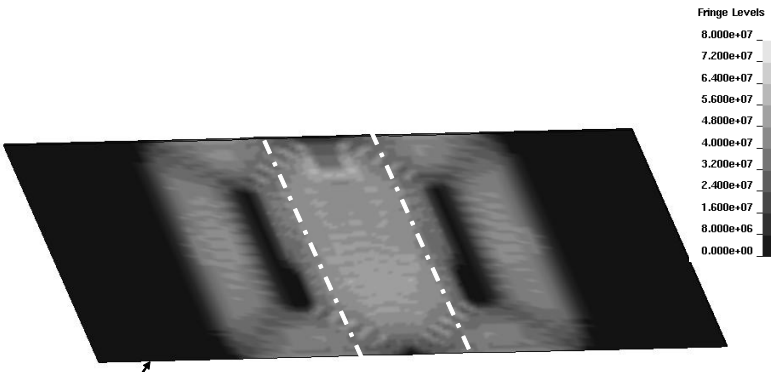

Figure 12*: Predicted force distribution on the sheet. Fringe levels are of Lorentz force in μN. The broken white lines indicate the approximate location of the die cavity*.

The predicted final shape for this experiment is shown on Figure 13. The maximum predicted height is 21.6 mm which is 38% higher than the actual height of the samples (Figure 8). This over prediction is likely due to the material model used and to the fact that the numerical coil has an ideal shape that does not take into account the imperfections of the actual coil. Thus, the coil is uniformly separated from the sheet, which results in higher induced forces when compared to the experiments. Another consequence of the numerical coils ideal shape is that the predicted shape is symmetric and does not exhibit the significant difference in height from one end to the other of the sample present in the actual samples. The models predict the raised edges which are observed in the actual samples. The predicted strain distributions are non uniform, which is an expected result given the force distribution.

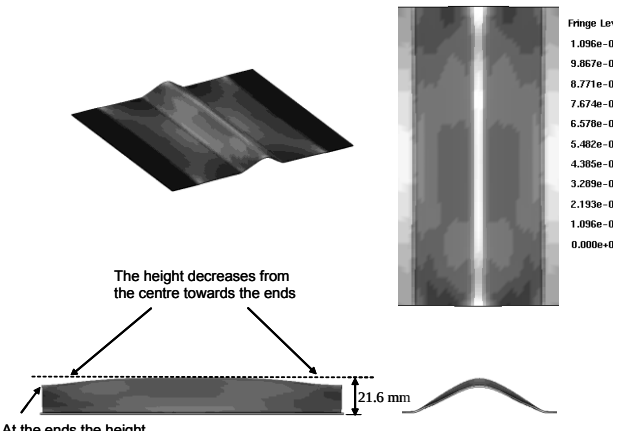

Figure 13: *Final predicted v-channel shape for a sample that makes no contact with the die (3000 V charging voltage). The general trends in the height are predicted by the model*.

5 Rebound of the Sheet

When the sheet impacts the die, not all of the kinetic energy results in plastic deformation, thus some of the energy is expended by causing the sheet to rebound off the die wall. The principal effect of this rebound is that the parts do no conform to the die shape. Both the conical and v-channel samples show clear evidence of this rebound, with greater rebound being observed in the latter due to its lower stiffness.

5.1 Conical Samples

The rebound in the conical samples causes a distinctive “step” which can be seen on Figure 7. Numerical models of conical samples formed using an axisymmetric pressure distribution predict the formation of a step, thus it is believed that the step is caused by the rebound. Although the step may not be a significant issue for some structural applications, it could be aesthetically unpleasing and render a part unfit if the appearance is an important criterion, such as a “class A” automotive surface. The steps present in the experimental samples were not usually horizontal. This was due to the uneven pressure distribution discussed above. Due to the more constrained nature of the conical parts and the more uniform pressure distribution provided by the spiral coil used in that work, the discrepancy between the final part and die were not as great as those that have been observed with the v-channel samples, which will be discussed next.

5.2 V-Channel Samples

A representative sample formed with the single cavity die is shown on Figure 14. Blue ink was applied to the surface of the die to confirm that the sheet impacted the die during the experiment. After forming, the samples showed clear indications of impact. The dark areas that can be seen on the part shown on Figure 14 are stains left by the ink from the die that indicate where the sheet contacted the tool. The rebound in the v-channel samples was significantly more pronounced than in the conical samples. It is clear that after impact the sheet rebounded from the die surface to form the final shape. In contrast

to the conical samples, the parts formed with the v-channel differ significantly from the shape of the die. The highest point on the samples was offset to the right of the die, as is shown on Figure 14**.** The average maximum final height of the samples was 24.3 mm.

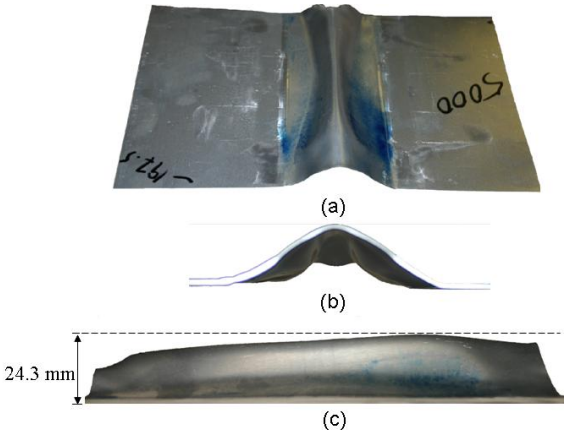

Figure 14: *Part formed using a charging voltage of 5000 volts, a) view from above, b) front view c) side view. The blue markings in a) indicate where the sheet made contact with the die.*

The rebound is predicted by the numerical analysis, although with less severity than is actually observed (Figure 15). This effect of the EM field is negligible for the impact event, since by the time the sheet impacts the die the EM forces are not significant. In fact, in the numerical simulations the EM solver is not active when the rebound occurs. The severity of the rebound will depend on the velocity, and thus the EM force that was induced on the sheet. Therefore, non-uniform force distributions will result in uneven rebound, which can be seen in the part shown on Figure 13. The model did not predict the exact height distribution seen on the samples nor the final maximum height (Figure 8). The final shape of the predicted samples showed an apparent reversal in the height distribution, with the highest points occurring towards the ends. This results from the sheet rebounding after impact. Figure 13 shows the sample geometry just before impact, and it can be seen that the height distribution is essentially the same as for the no-impact sample. The centre of the part is not only the highest point, but also the fastest moving. Therefore, when it impacts the die the rebound is greater than the ends of the part, and this effect was exaggerated in the numerical model. Finally, the effects of the edges are less evident in the model results, but are still present.

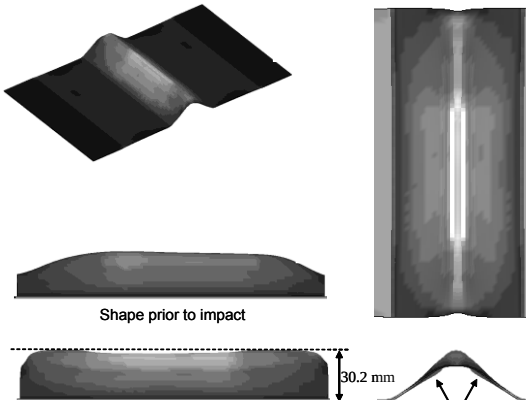

Figure 15: *Final predicted v-channel shape for sample with rebound present (5000 V charging voltage).*

6 Conclusions

Magnetic force distribution and rebound have a significant impact on the final shape of electromagnetically formed parts and must be considered when designing EM forming processes. One approach to eliminate the force distribution effects would be to use a coil that produces a uniform pressure distribution, like the one proposed by Kamal and Daehn [23]. If coils with non-uniform force distributions have to be used, the force distributions can be predicted from the shape of the coil using analytical approximations or they can be much more accurately determined from numerical analysis. Knowledge of this distribution can, in principle, be used to adjust the die and blank to obtain the desired final shape.

The rebound of the sheet can be a potentially more difficult challenge. Numerical models can be used to determine the general final shape of the part. However, to obtain an accurate solution reliable code and accurate material models are needed. The greatest challenge will be designing the coil, blank and die to try and minimize rebound. Some suggestions have been made in the literature, such as energy absorbing dies [14]; however, these solutions have significant practical challenges. Possibly the most significant amongst these challenges is how to make the dies economically feasible.

Both the force distribution and rebound can lead to final part shapes and surface conditions that could lead to parts that do not meet specifications. Understanding these effects is very important for the practical implantation of EMF. Further study is required to fully understand these effects.

References

[1] *Wilson, D.V.,* 1988. Aluminium versus steel in the family car-The formability factor", Journal of Mechanical Work Technology, 16, 1988, 257-277.

[2] *Miller W.S.; Zhuang L.; Bottema J.; Wittebrood A.J.; De Smet P.; Haszler A.; Vieregge A*., 2000. Recent development in aluminium alloys for the automotive industry. Material Science Engineering A280, 37-49.

[3] *Mori, T., Hino, M., Iwaya, J., Miyahara, M*., 1992. Press formability of aluminum alloy sheets for automobile parts", KOBELCO Technology Review, 14, 49-53.

[4] *Wagner, H.J., Boulger, F.W.,* 1960. High velocity metalworking processes based on the sudden release of electrical of electrical energy. Memorandum prepared by the Battle Memorial Institute for the Defense Metals Information Center.

[5] *Altynova, M., Hu, X., Daehn, G.S*., 1996. Increased ductility in high velocity electromagnetic ring expansion, Metallurgical and Material Transactions A, 27A, 1837-1844.

[6] *Balanethiram, V.S., Daehn, G.S.,* 1994. Hyperplasticity: Increased forming limits at high workpiece velocity. Scripta Metallurgica et Materialia, 30, 515-520.

[7] *Daehn, G.S., Vohnout, V.J., DuBois, L.,* Improved Formability with Electromagnetic Forming: Fundamentals and Practical Example. Proceedings of the TMS Sheet Metal Forming Symposium, San Diego, Ca., TMS, February 1999.

[8] *Oliveira, D.A., Worswick, M.J.,* 2003. Electromagnetic forming of aluminum alloy sheet", Journal de Physique IV, 110, 293-298.

[9] *Golovashchenko, S.F., Mamutov, V.S., Dmitriev, V.V., Sherman, A.M.*, 2003. Formability of sheet metal with pulsed electromagnetic and electrohydraulic technologies. In: Das, S.K. Proceedings of the TMS annual meeting, San Diego, Ca., TMS, pp. 99-110.

[10] *Golovashchenko, S.F.*, 2007. Material Formability and Coil Design in Electromagnetic Forming. Journal of Materials Engineering and Performance, 16, 314-320.

[11] *Imbert, J.M., Worswick, M.J., Winkler, S.L., Golovashchenko, S., Dmitriev, V.*, 2005. Analysis of the Increased Formability of Aluminum Alloy Sheet Formed Using Electromagnetic Forming . SAE Transactions, International Journal of Materials and Manufacturing. SAE paper number 2005-01-0082

[12] *Imbert, J.M.; Winkler, S.L; Worswick, M.; Oliveira, D.A. and Golovashchenko, S.,* 2005. The Effect of Tool/Sheet Interaction on Damage Evolution in Electromagnetic Forming of Aluminum Alloy Sheet. Journal of Engineering Materials Technology 127/1, 145-152.

[13] *Seth, M., Vohnout, V.J., Daehn, G.,* 2005. Formability of steel sheet in high velocity impact. Journal of Materials Process Technology, 168/3, p 390-400.

[14] *Risch, D., Beerwald, C., Brosius, A., Kleiner, M.*, 2004. On the Significance of the Die Design for Electromagnetic Sheet Metal Forming. In: Kleiner, M., Proceedings of the 1st International Conference on High Speed Forming, Dortmund, Germany, pp. 191-200.

[15] *Risch, D., Vogil, E., Bauman, I, Brosius, A., Beerwald, C., Tillman, W. Kleiner, M.,* 2006. Aspects of Die Design for the Electromagnetic Sheet Metal Forming Process. In: Kleiner, M., Proceedings of the 2nd International Conference on High Speed Forming, Dortmund, Germany, pp. 189-199.

[16] *Risch, D., Brosius, A., Kleiner, M.*, 2007. Influence of the Workpiece Stiffness on the Electromagnetic Sheet Metal Foming Process into Dies. Journal of Materials Engineering and Performance, 16, 327-330.

[17] *Imbert, J.,* 2005. Increased Formability and the Effects of the Tool/Sheet Interaction in Electromagnetic Forming of Aluminum Alloy Sheet. University of Waterloo M.A.Sc. thesis. http://etd.uwaterloo.ca/etd/jmsimber2005.pdf.

[18] IAP Research, 2006. Dayton, OH, USA, www.iap.com.

[19] Pulsar, 2006. Yavne, Israel. www.pulsar.co.il.

[20] *L'Eplattenier, P., Cook, G., Ashcraft, C., Burger, M., Shapiro, A., Daehn, G., Seth, M.,* 2006. Introduction of an Electromagnetism Module in LS-DYNA for Coupled Mechanical-Thermal-Electromagnetic Simulations. In: 9th International LS-DYNA Users Conference.

[21] *Imbert, J.M.; L'Eplattenier, P., and Worswick, M.*, 2008. Comparison Between Experimental and Numerical Results of Electromagnetic Forming Processes. In: Mindle, W., Proceedings of the 10th International LS-DYNA Users Conference 2008, Dearborn, Michigan, pp. 12-33-12-44.

[22] *Hallquist, J.*, 1998. *LS-DYNA Theoretical Manual*, Livermore software Technology Corporation.

[23] *Kamal, M. and Daehn, G. S.* , A uniform pressure electromagnetic actuator for forming flat sheets, Journal of Manufacturing Science and Engineering, Transactions of the ASME, v 129, n 2, p 369-379, 2007.

Simulation of Wrinkle Formation in Free Electromagnetic Tube Compression

O. K. Demir, V. Psyk, A. E. Tekkaya

Institute of Forming Technology and Lightweight Construction, Technische Universität Dortmund, Dortmund, Germany

Abstract

A 3-dimensional (3D) finite element (FE) simulation of free electromagnetic (EM) tube compression was performed with the aim of predicting wrinkle formation. Staggered coupling was applied between the EM and mechanical parts of the problem. The full 360° portion of the problem was modelled since the wrinkle formation does not represent any symmetry in circumferential direction. The initial geometric imperfections of the tube were measured and included in the model to trigger buckling. The deformed geometry with the wrinkles could be predicted accurately.

Keywords

Electromagnetic tube compression, Buckling, Finite element simulation

1 Introduction

EM tube compression is the reduction of tube radius due to the application of radial electromagnetic forces. The material may buckle under the increasing circumferential compression during the inward motion, which causes wrinkles on the final product. This does not only prevent the acquirement of the desired shape, but also complicates the prediction of the formed geometry. However, a tool that can predict wrinkle formation could be used to optimize process parameters to minimize wrinkles, or to demonstrate ways to avoid them, e.g. mandrel usage, or to reverse them, e.g subsequent hydroforming or EM expansion.

In a homogenously compressed body geometric or material imperfections trigger buckling. Because of that, researchers tried to predict wrinkles by simulations including the initial imperfections of the workpiece (WP). However, inadequacy of the simulation tools or harsh assumptions avoided good correspondence with the experimental results. The aim of the present study is to calculate wrinkles in free EM tube compression by a coupled 3D FE simulation.

2 State of the Art

In EM forming (EMF), a highly damped alternating current is sent through a coil in tens of microseconds. This current creates a counter current in the WP. The repulsive forces between the two currents form the WP. A tube is placed inside a solenoid for the EM compression.

Kirkpatrick and Holmes (1988) calculated wrinkling of tubes under radial explosive loading by means of FE method and shell elements. They showed the importance of including the correct initial geometrical imperfections in wrinkle prediction.

Min and Kim (1993) measured the magnetic flux during EM tube compression experiments and calculated the magnetic pressure vs. time from the flux. They applied this pressure uniformly on the outer wall and simulated the deformation with a 3D dynamic explicit FE method. The tube was modelled with solid elements, one in thickness direction. The initial imperfections were represented by an initial displacement perturbation given by

$$W(\theta) = \sum_{n=1}^{n_c} a_n \cos(n\theta + \phi_n), \tag{1}$$

where θ is the hoop angle, n is the mode number, a_n is the amplitude of the displacement perturbation, and ϕ_n is the phase angle. a_n was calculated with regard to roundness measurements, and random values were used for ϕ_n. The contribution of modes larger than a certain critical value of n_c was disregarded. 35 mm long Ø40 mm tubes were formed with coils longer then the tubes. The tubes were crushed and the resulting shapes were very complex to simulate accurately. The correspondence with the experimental results was better when a mandrel was used, especially at high energy values, when the tube was more ironed on the mandrel.

3 The Proposed Method

In order to predict the wrinkles due to EM compression accurately the initial imperfections must be included directly in the FE model and a simulation must be performed, in which the mechanical and the EM parts of the problem are coupled. The success of this method was demonstrated by comparing the simulation results with the experiment results in case of free compression of an aluminum tube.

4 Experimental Setup and Measurements

A 110 mm long, 2 mm thick Ø40 mm EN-AW 6060 tube in T6 condition was compressed. A 55 mm long copper coil with an inner diameter of 41.7 mm was used. The coil cross-section was rectangular with the dimensions: 13.7 mm width – 5.0 mm height. The resistivities of the tube and coil materials were measured as 2.94×10^{-8} Ωm and 1.79×10^{-8} Ωm, respectively.The compression was performed with a sudden release of 5 kJ energy stored in four capacitors with a total capacitance of 992 μF. The used machine had an inner inductance of 50 nH and an inner resistance of 3.3 mΩ.

Total current flowing through the coil during deformation was measured using a Rogowski coil, and is given in Figure 1a. The inner and outer contours of the unformed tube were measured using a 3D coordinate measuring device. The measurements were done at a single point along the axis. That is, the cross-sectional geometry was assumed to be uniform in axial direction. This was done depending upon the fact that the tubes were manufactured by profile extrusion. The measured initial contours are given in Figure 1c. According to those, the tube thickness changes between 1.95 mm and 2.07 mm. Data in Figure 1a and Figure 1c were then introduced as input to the simulations. The formed shapes were measured with a 3D digitizer to compare with the simulation results.

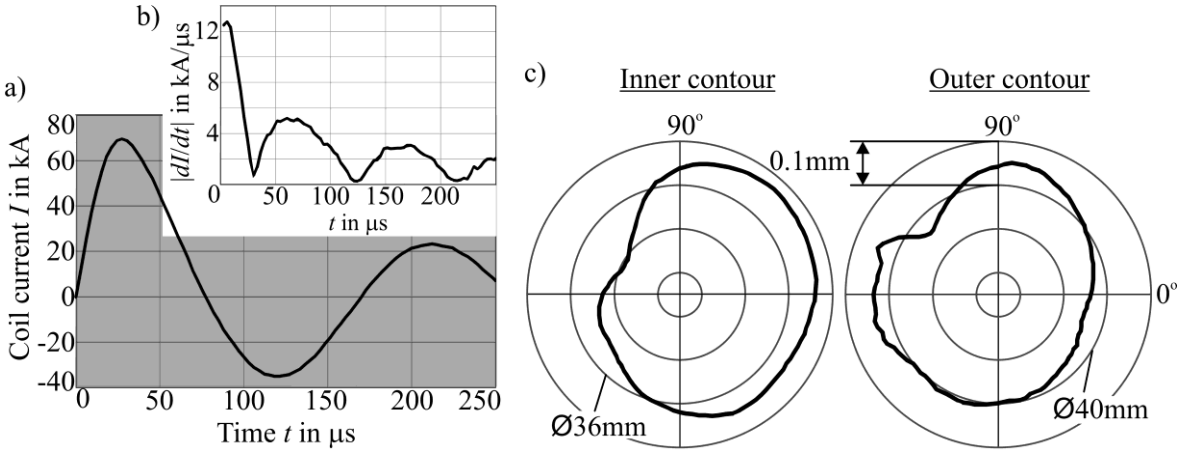

***Figure 1**: a) Measured coil current b) Slope of coil current c) Initial tube geometry*

5 Simulation of EMF

Before simulating the compression under EM forces, these forces must be calculated with a transient EM calculation. The thermal side of the problem was not taken into consideration in order to reduce the calculation time. That is, plastic heating and heating due to electrical resistance, and their effects on electrical resistivity and mechanical properties were neglected. In what follows, the principles of the EM and mechanical solutions, and the coupling between them are explained.

5.1 EM Problem

The EM problem consists of the four Maxwell Equations:

$$\vec{\nabla} \times \vec{B} = \mu_0 \left(\vec{J}_{tot} + \varepsilon_0 \frac{\partial \vec{E}}{\partial t} \right), \tag{2}$$

$$\vec{\nabla} \times \vec{E}_{ind} = -\frac{\partial \vec{B}}{\partial t}, \tag{3}$$

$$\vec{\nabla} \circ \varepsilon_0 \vec{E} = \rho_{tot}, \tag{4}$$

$$\vec{\nabla} \circ \vec{B} = 0. \tag{5}$$

Here, $\vec{B}$ is the magnetic field, $\vec{E}$ is the electric field, $\vec{J}_{tot}$ is the total current density, $\vec{E}_{ind}$ is the induced electric field, and ρ_{tot} is the total charge density. μ and ε are the magnetic permeability and electric permittivity, respectively. μ_0 and ε_0 are those of vacuum. $\circ$, $\times$, and $\vec{\nabla}$ denote dot-product, cross-product, and del operator, respectively.

According to Eq. 2 an electric current ($\vec{J}_{tot}$) and/or a changing electric field ($\partial\vec{E}/\partial t \neq 0$) produce a circulating magnetic field. In case of EMF the frequency of the excitation current (coil current) is too low to take the latter into account (low frequency assumption). This reduces Eq. 2 to:

$$\vec{\nabla} \times \vec{B} = \mu_0 \vec{J}_{tot} . \tag{6}$$

$\vec{J}_{tot}$ is the sum of conduction ($\vec{J}_{con}$), polarization ($\vec{J}_{pol}$), and magnetization ($\vec{J}_{mag}$) currents. Low frequency assumption neglects polarization ($\vec{J}_{pol} = \vec{0}$). $\vec{J}_{mag}$ emerges from the magnetization of the media under the application of a magnetic field. A media is magnetized to the extent of its permeability μ. If μ is used instead of μ_0 in Eq. 6, $\vec{J}_{tot}$ does not have to include $\vec{J}_{mag}$, since the magnetization effect is regarded by the parameter μ. Accordingly, Eq. 2 takes the form:

$$\vec{\nabla} \times \vec{B} = \mu \vec{J}_{con} . \tag{7}$$

The coil current in EMF is an alternating conductive current. By virtue of Eq. 7 it creates an alternating magnetic field. Eq. 3 reveals that an alteration in the magnetic field induces a circulating electric field ($\vec{E}_{ind}$). If a conducting material is present $\vec{E}_{ind}$ drives a circulating electric current according to:

$$\vec{J}_{con} = \frac{\vec{E}}{\rho} , \tag{8}$$

where ρ denotes the resistivity of the material. In EMF the conducting material is the WP, and the circulating currents are the so called eddy currents. Any charge moving in a magnetic field experiences Lorentz forces given by Eq. 9. Lorentz forces on the eddy currents are the triggering forces of EMF.

$$\vec{F} = \vec{J} \times \vec{B} . \tag{9}$$

Knowing the coil current for a certain time interval, the Maxwell equations can be solved for a given spatial configuration of the objects. The result is the $\vec{B}$ and $\vec{E}$ distributions with respect to time. Equations 8 and 9 give, then, the force distribution on the WP. This was accomplished by the commercial implicit FE code ANSYS/EMAG.

5.1.1 FE Model for EM Calculation

A quarter portion of the model is displayed in Figure 2, although the whole 360° was simulated. A ½ model was utilized owing to the mirror symmetry. The circumferential dimensions of the elements were 3° except in the core region. A time-step of 1 μs was used for the calculation after a sensitivity study of the total force on the WP.

The *skin effect* was taken into account while determining the mesh for the cross-section (z=0 surface) shown in Figure 2. The eddy currents whirl in such a manner that they oppose the *change* in the magnetic field created by the coil current. In other words, they resist the penetration of the magnetic field into the WP. The strength of this resistance is directly proportional to the *change* in the coil current, i.e., the slope of the current. Due to damping this slope decreases during the process (see Figure 1b). As a result, on one hand, at the beginning of the process no magnetic field can be seen except at the *skin* of the WP. On the other hand, towards the end of the process the magnetic field penetrates the WP, and even passes through it, reaching the inside of the tube. In order to calculate the magnetic field at the beginning of the process accurately, a finer mesh must be used at the outer regions of the tube's wall thickness. However, a very coarse mesh cannot be used at the inner regions and inside of the tube because of the penetration taking place towards the end of the process.

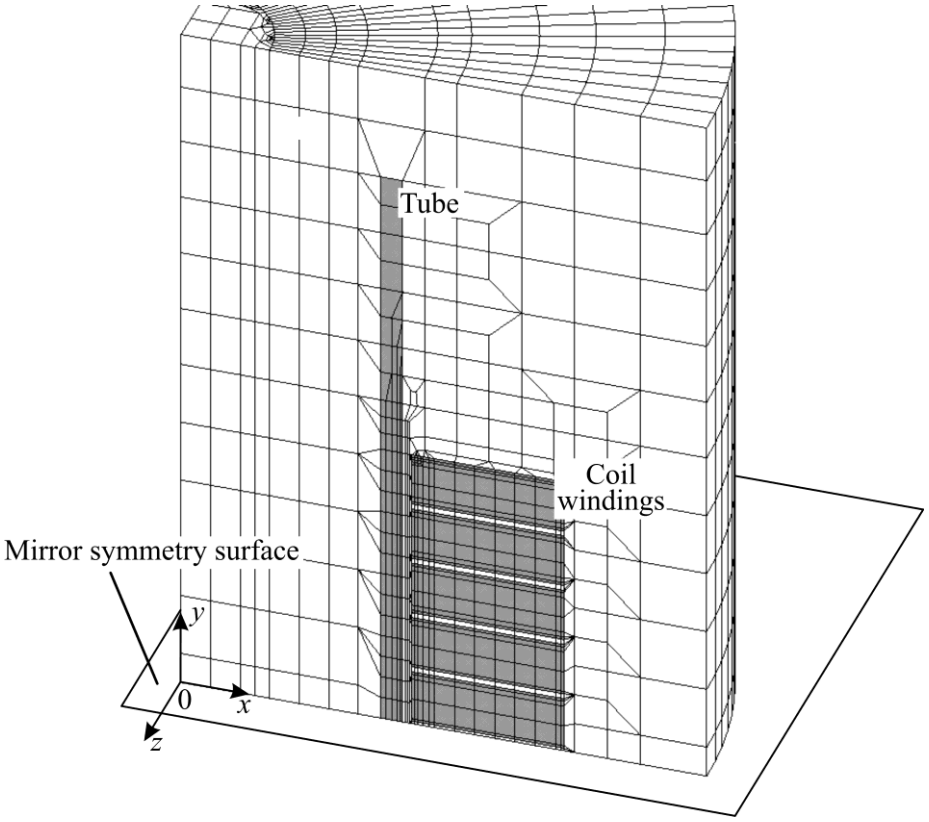

***Figure 2**: Quarter of the initial FE model for EM calculation*

This situation is valid also for the coils. The total current flowing through a winding is given as input (Figure 1a). However, the distribution must be determined by the FE calculation. Due to the skin effect the current tends to flow at the outer regions. Hence, a finer mesh is needed at the outer regions.

5.2 Mechanical Problem

After the EM solution for a certain time interval, the obtained nodal forces can be used for the forming simulation. This was accomplished by the commercial dynamic explicit FE code LS-DYNA. The tube mesh (3D continuum elements with 8 nodes) from the EM calculation was transferred to a mechanical model. Reduced integration scheme was employed. The strain rate dependent flow curve for the tube material was taken from [3].

5.3 Coupling

The EM forces on the WP are dependent on its spatial configuration, which is changing throughout the process due to deformation. Hence, the spatial configuration used for the EM simulation must be updated continuously during the calculation. This update is called the coupling of the EM and mechanical parts of the simulation. Such a simulation of EMF is called a coupled simulation. In the following the factors necessitating the coupling and the strategies to accomplish it are examined.

The effect of change of spatial configuration can be neglected in two cases. First, if the coil current that is creating the forces damps out before a significant WP move. This assumption was used in many early modelling efforts of EM sheet metal forming as stated by El-Azab et al. (2003) in their review paper on modelling of EMF. Second, if the calculation is going to be used only for small strains, for instance, in case of calibration processes. Iriondo (2007) simulated calibration processes uncoupled, owing to this assumption. Simulation of tube compression cannot be classified into both groups and demands a coupled calculation. Kleiner and Brosius (2006) showed that the correspondence with the experimental results show a significant improvement in case of coupling.

There are two coupling strategies. In monolithic coupling one set of equations is solved with degree of freedoms from both mechanical and EM problems. Excluding the work of Karch and Roll (2005) monolithic coupling could not find any application in EMF simulation yet, because of its difficulty and expense. In staggered (loose, weak) coupling EM and mechanical analyses are performed sequentially in a loop. This method has been applied by several researchers following Bendjima (1997) and Fenton and Daehn (1998). ANSYS/EMAG and LS-DYNA were coupled by Oliveira (2002) for 3D sheet metal forming.

In the present study, staggered coupling was utilized. In staggered coupling the EM simulation is interrupted regularly in order to update the WP geometry. A major difficulty emerges due to this interruption. The media between the conducting objects (air) must also be meshed in an EM FE simulation. When the WP geometry is updated the air geometry must also be modified accordingly. Oliveira (2002) accomplished this by including the air also in the structural simulation. He stated that the material properties selected for the air are very important for the air elements to keep acceptable aspect ratios throughout the simulation. In the present work the air mesh was morphed corresponding to the calculated tube deformation before every EM simulation.

A sensitivity study performed by Demir et al. (2009) showed that the converged result can be obtained when the interval for geometry update is selected as 2 μs.

6 Results and Discussion

Comparison of calculated and measured tube geometries are given in Figure 3.

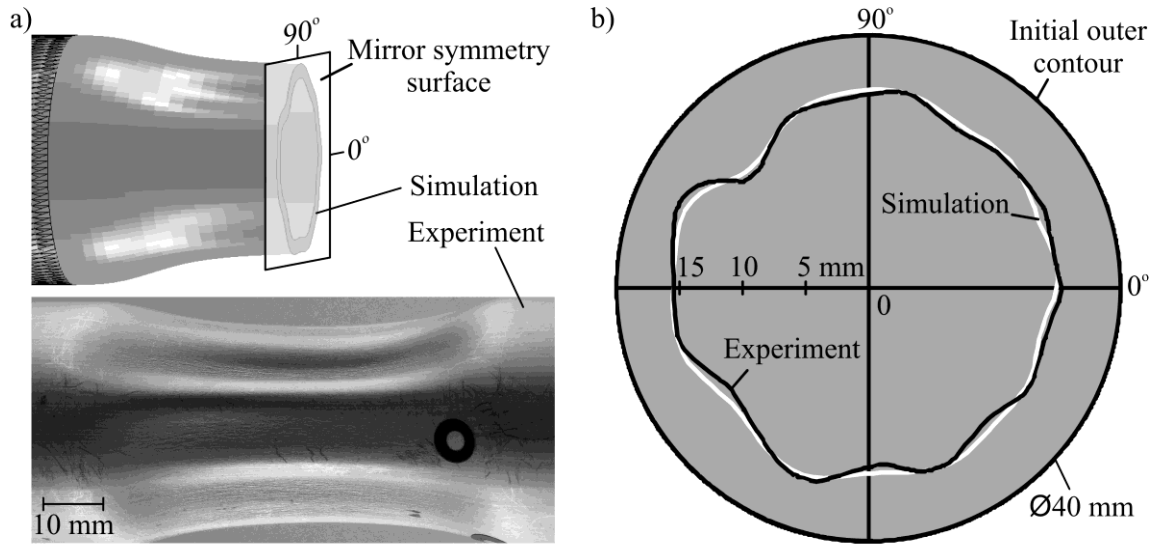

***Figure 3**: a) Simulated and measured tube geometries. b) Simulated and measured outer contours at the mirror symmetry surface*

Psyk et al. (2005) reported that the deteriorations of the initial tube roundness are intensified by the compression process. A comparison between Figure 3b and Figure 1b confirms this result. The compressed shape reflects the initial roundness. For instance, the gross wrinkle at approximately 135° is caused by the gross deterioration of the outer roundness at that region.

Figure 3a shows that the wrinkles' forms do not change in axial direction. Their intensity changes merely. So it is a justified assumption that the initial imperfections of the cross-section geometry are uniform along the axis. It is also reasonable to use mirror symmetry in the simulation.

The possible reasons for the slight discrepancy between the simulation and experimental results seen in Figure 3b are insufficient element partition in circumferential direction and thermal effects. The circumference was divided into 120 equal parts. A sensitivity study with respect to that parameter is yet to be performed. Kirkpatrick and Holmes (1988) showed that the geometry of the wrinkles can be better predicted when the number of elements per wrinkle increases. Thermal effects were neglected. Karch and Roll (2005) detected an approximately 90° increase in WP temperature (Ø40 mm EN-AW 6060 tubes) during EM compression by means of 2D axisymmetric simulations. This should change the electrical and mechanical properties of the WP. More accurate results can be obtained when the combined effect of temperature increase and high strain rate is taken into consideration.

7 Conclusion

The wrinkle formation in free EM tube compression can be simulated by a 3D staggered coupled EMF simulation. The initial geometrical imperfections must be included in the model in order to predict the final geometry accurately. The correspondence between the experimental and simulation results is acceptable, although the thermal effects were not taken into consideration. Other cases with varying geometries, materials, and process parameters must also be simulated to free the conclusion from being specific.

The simulation tool can be used for process design for a given exact initial geometry. However, it is not practical to measure the actual initial imperfections for every WP. This problem can be solved in two ways. First, seamless tubes coming from the same source (a combination of dies and process parameters) will have the same cross-section because of the steady-state nature of the profile extrusion process. A single measurement for a group of tubes will be adequate. Second, instead of the exact initial geometry, random imperfections, which are created according to the known geometry tolerances, can be taken into account. The simulation tool can also be used to decide on the allowable initial geometry tolerances to manufacture a given product.

Acknowledgements

This work is based on the results of the research group PAK343; the authors would like to thank the German Research Foundation for its financial support.

The EMF machine is a 7000 Series MAGNEFORM, manufactured by MAXWELL and modified by POYNTING. The 3D coordinate measuring device is from the company ZEISS. 3D digitizing was performed using the ATOS system from the company GOM.

References

[1] *Kirkpatrick, S. W.; Holmes, B. S.*: Structural response of thin cylindrical shells subjected to impulsive external loads. AIAA Journal, 26, p. 96-103, 1988

[2] *Min, D. K.; Kim, D. W.:* A finite-element analysis of the electromagnetic tube-compression process. Journal of Materials Processing Technology, 38, p. 29-40, 1993

[3] *Demir, O. K.; Psyk, V.; Tekkaya, A. E.*: Simulation of tube wrinkling in electromagnetic compression. Proceedings of ICAFT 2009, Chemnitz, Germany, p. 121-135, 2009

[4] *El-Azab, A.; Garnich, M.; Kapoor, A.*: Modeling of the electromagnetic forming of sheet metals: State-of-the-art and future needs. Journal of Materials Processing Technology, 142, p. 744-754, 2003

[5] *Iriondo, E.*: Electromagnetically Impulsed Springback Calibration. Ph.-D.-Dissertation, The University of the Basque Country, 2007

[6] *Kleiner, M.; Brosius, A.*: Determination of flow curves at high strain rates using the electromagnetic forming process and an iterative finite element simulation scheme. Annals of the CIRP, 55/1, 2006

[7] *Karch, C.; Roll, K.*: Transient simulation of electromagnetic forming of aluminium tubes. Advanced Materials Research, 6-8, p. 639-646, 2005

[8] *Bendjima, B.*: Finite element modelling of electromagnetic phenomena related to electromagnetic forming. Doctoral Thesis, University of Nantes, France, 1997

[9] *Fenton, G. K.; Daehn, G. S.*: Modeling of electromagnetically formed sheet metal. Journal of Materials Processing Technology, 75, p. 6-16, 1998

[10] *D. A., Oliveira*: Electromagnetic forming of aluminum alloy sheet: experiment and model. Masters thesis, University of Waterloo, Canada, 2002

[11] *Psyk, V.; Beerwald, C.; Homberg, W.; Kleiner, M.*: Extension of Forming Limits by Using a Process Combination of Electromagnetic Forming and Hydroforming. Proceedings of the 8th Int. Conf. on Technology of Plasticity (ICTP) 2005, Verona, Italy, 2005

Texture Evolution of AZ31 Magnesium Alloy Sheet at High Strain Rates*

I. Ulacia[1], S. Yi[2], M.T. Pérez-Prado[3], N.V. Dudamell[3], F. Gálvez[4] , D. Letzig[2] and I. Hurtado[1]

[1] Mondragon Goi Eskola Politeknikoa, Mondragon Unibertsitatea, 20500 Mondragon, Spain
[2] GKSS Research Center, 21502 Geesthacht, Germany
[3] Madrid Institute for Advanced Studies in Materials, IMDEA Materials, 28040 Madrid, Spain
[4] ETS Ingenieros de Caminos, Universidad Politécnica de Madrid, 28040 Madrid, Spain

Abstract

In the current contribution the mechanical behaviour at high strain rates of AZ31 magnesium alloy sheet is studied. Uniaxial deformation properties were studied by means of tensile split Hopkinson pressure bar (SHPB) at different temperatures. The influence of the strain rate and temperature on the deformation mechanisms was investigated by means of electron backscatter diffraction (EBSD) and neutron diffraction. It is shown that twinning plays an important role on high strain rate deformation of this alloy, even at elevated temperatures. Significant evidence of prismatic slip as a deformation mechanism is observed, also at warm temperatures, leading to the alignment of <10-10> directions with the tensile axis and to a spread of the intensities of the basal pole figure towards the in-plane direction perpendicular to the tensile axis. The rate of decrease of the CRSS of non-basal systems is observed to be slower than at quasi-static rates. Secondary twinning and pyramidal <c+a> slip were also outlined for some conditions. At warm temperatures, in contrast to quasi-static range, a generalized dynamic recrystallization is not observed. Moreover, the activation of rotational recrystallization mechanisms is reported.

Keywords

High strain rate, Magnesium Alloy, Texture

---

* *This work is based on the results of MAGNO2008 and MANUFACTURING 0,0 projects; the authors would like to thank Spanish Ministry and Basque Government for its financial support.*

1 Introduction

Magnesium alloys have been thoroughly studied in the last decades due to their low density and thus their potential to reduce weight of any structure. Even though large number of studies have been carried out on the plastic deformation behaviour of magnesium alloys, most of them have their focus on the materials response under quasi-static loading conditions (e.g. [1-10]). However, in some structural applications, components must be designed to operate over a broad range of strain rates and temperatures. For instance, the high strain rate behaviour is of great interest to automotive, aerospace and/or defence industries because some critical components should have the proper mechanical properties to work under severe loading conditions, such as crash or impact. Furthermore, in most metalworking processes, materials undergo large amounts of strain at different strain rate and temperature conditions. High strain rate deformations (in the order of 10^3 s^{-1}) are subjected to the materials in some innovative manufacturing methods such as in electromagnetic forming operations, owing to an increase in the forming limit as reported in [11] for Mg AZ31 alloy.

The mechanical behaviour and deformation mechanisms of magnesium and its alloys at low strain rates have been extensively investigated. Slip in hexagonal close packed (hcp) metals may take place along the <11-20> (<a>) direction, mainly on {0001} basal plane, but also on non-basal planes, such as {10-10} prismatic and {10-11} pyramidal planes. Additionally, second order pyramidal <c+a> slip has also been observed along {11-22} planes [2]. Deformation is also accommodated by twinning, mainly along {10-12} and {10-11} planes, so called extension and compression twinning respectively. Apart from single twinning, secondary twinning from a primary twin ({10-11} – {10-12}) was also reported in magnesium single crystals by Wonsiewicz and Backofen [4]. Recently, Barnett et al. [3] have also shown non-Schmid behaviour of this secondary twinning by EBSD and TEM investigations.

It is generally accepted (e.g. [2, 5, 6]) that at room temperature, slip on basal planes and {10-12} twinning are the main deformation mechanisms in uniaxial deformations at low strain rates. However, deformation temperature plays an important role in the activity of different deformation modes. The critical resolved shear stress (CRSS) for basal slip and {10-12} twinning is temperature independent [5]. Meanwhile, the CRSS for prismatic and pyramidal systems decrease with increasing temperature, even to smaller values than {10-12} twinning. Moreover, at temperatures higher than 200ºC dynamic recrystallization takes places simultaneously [7-9]. The activation of these additional mechanisms results in an increase of ductility and a decrease of yield and flow stress.

The low availability of independent slip systems makes Mg alloys highly dependent on texture [10]. It is further emphasized by the polarity of {10-12} twinning, which only allows shear in one direction (opposed to forward and backward shear in deformation by slip) [12]. When investigating rolled or extruded magnesium, as they develop strong texture during processing, the dependence of the initial texture on the deformation mechanisms and thus the mechanical properties is more pronounced. For example, a strong tension-compression asymmetry at low strain rates has been reported and related to texture.

The deformation behaviour of Mg alloys at high strain rates (10^3 s^{-1}) has not been thoroughly investigated yet [13-17]. Generally, it has been concluded that ductility increases with increasing the strain rate [13-15]. Additionally, twinning has been observed to significantly contribute to plastic deformation even at high temperatures, at which it is

mostly suppressed at quasi-static strain rates. However, most of the studies carried out to date mostly dealt with extruded or casted Mg alloys and predominantly under compressive loading. Above all, the influence of temperature, loading condition (tension-compression) and texture on the deformation mechanisms and flow stress at high strain rates is still unknown.

In the current study, the uniaxial mechanical behaviour of AZ31 sheet under dynamic conditions (10^3 s^{-1}) was analyzed and compared with that observed at low strain rates. AZ31 sheets have been tested in tension and compression using Hopkinson bar apparatus from 25ºC to 400ºC. Detailed microstructure and texture examination by electron backscatter diffraction (EBSD) and neutron diffraction has been carried out to elucidate the predominant deformation and recrystallization mechanisms.

2 Experimental procedure

2.1 Initial material. Microstructure and crystallographic texture analysis

The initial material used in this study was the commercial-grade Mg alloy AZ31. Two rolled and annealed sheets, 1 and 3 mm thickness, were used.

The microstructure and texture of the as-received material was analyzed by electron backscatter diffraction (EBSD) employing EDAX-OIM™ software in a Zeiss Ultra 55™ FEG-SEM scanning electron microscope. Sample preparation for EBSD included grinding up to 4000 SiC paper, mechanical polishing with a 0.05 µm silica suspension and final electro-chemical polishing for 90 s at 33 V using the AC2™ commercial electrolyte. The microstructure is presented by EBSD orientation maps and the texture by recalculated pole figures. Since EBSD only allows examination of the local texture, macrotexture measurements were also performed by means of neutron diffraction in the Stress-Spec instrument from FRM-II of the TU-Munich (Germany) with a beam size of 5 mm diameter.

The initial microstructures of the two AZ31 sheets of 1 and 3 mm thickness were formed of equiaxed recrystallized grains with average intercept sizes of 10 and 13 µm respectively (Figure 1). As generally observed in annealed AZ31 sheets, both sheets show strong basal type texture (i.e. crystallographic *c*-axes are aligned in the sheet normal direction). It can also be seen in the pole figure from Figure 1 that the <0001> fiber is not perfect and a spread of the basal poles toward sheet rolling direction (RD) is present. Neutron diffraction measurements were consistent with the EBSD measurements.

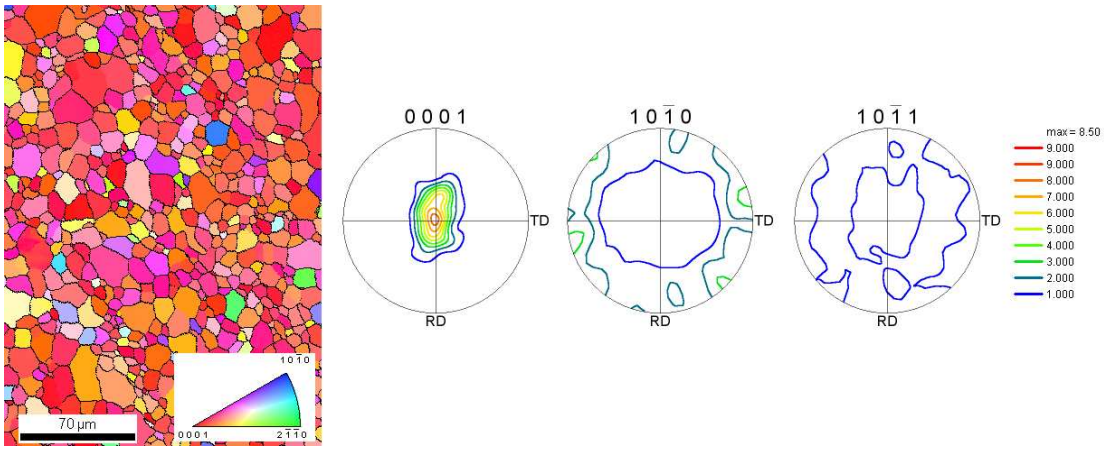

***Figure 1**: Microstructure and texture of the as-received AZ31 Mg alloy measured by EBSD (The colour code corresponds to the normal direction -ND- inverse pole figure).*

2.2 Mechanical testing

An exhaustive testing campaign was performed in order to compare high strain rate with quasi-static behaviour at different temperatures. Tensile tests were performed on the 1 mm thick sheet. The reader is referred to [18] for more detailed description of the testing procedures. High strain rate tests at 10^3 s^{-1} were carried out using a tensile split Hopkinson bar. A radiative furnace was used for testing at several temperatures. Thermocouples were glued to both surfaces of the specimens to measure the initial temperature of the sample. Quasi-static tensile tests were carried out using a conventional INSTRON-4206 testing machine equipped with a heating furnace. The specimens tested at low strain rates were machined according to ASTM E8 M-0 standard. At both high and low strain rates, tests were performed along RD at temperatures ranging from 25ºC to 300ºC (In-plane RD-TD anisotropy in tension can be seen in [19]). Compression testing was performed on the 3 mm thick sheet. High strain rate compression tests at 10^3 s^{-1} were carried out using a Hopkinson bar apparatus. At both high and low strain rates, tests were performed along RD and ND at temperatures ranging from 25ºC to 400ºC. The specimens compressed along RD were 3 x 3 x 4.5 mm while the samples compressed along ND were 3 x 3 x 3 mm cubes (See [19] for the ND-RD anisotropy in compression).

The microstructure and texture of the samples deformed in tension were examined by EBSD and also by neutron diffraction (procedure explained above). Microstructural analysis of the samples deformed in compression could not be performed because the specimens were smashed during testing.

3 Results and discussion

3.1 Mechanical behaviour at high strain rates

Figure 2 shows true stress - true strain curves comparing tension-compression behaviour at different strain rate and temperature conditions. It is observed that at room temperature the shape of the curves is concave down under tensile loading and concave up under compressive loading. The tension-compression asymmetry, generally observed at low strain rates and room temperatures, is maintained at high strain rates. These stress differences are consistent with the predominance of crystallographic slip in tension and {10-12} twinning followed by strain hardening in compression.

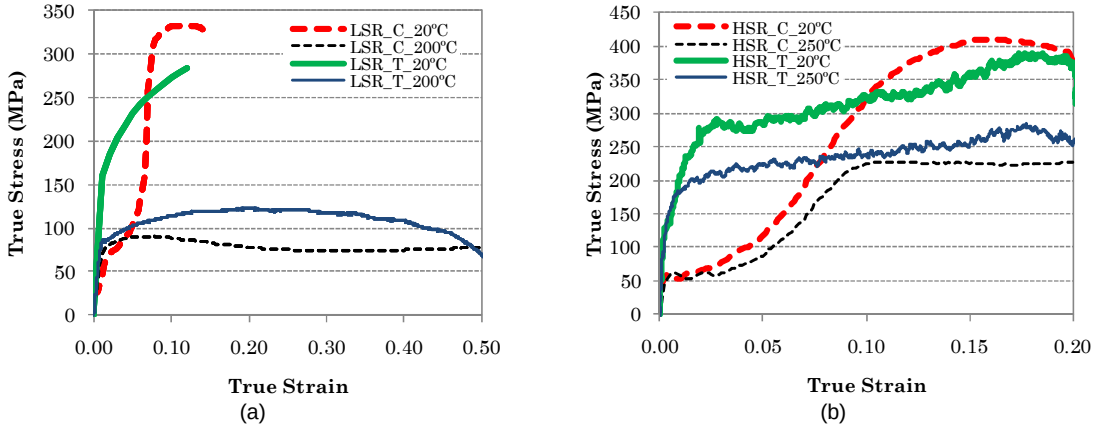

***Figure 2**: True stress – true strain curves showing tension-compression asymmetry at a) low strain rates (10^{-3} s^{-1}) and (b) high strain rates (10^3 s^{-1}).*

At elevated temperatures, at low strain rates, the tension-compression asymmetry is significantly reduced as a consequence of the activation of non-basal slip systems in combination with the dynamic recrystallization (DRX) in both loading conditions. However, at high strain rates the asymmetry is still observed and a strain hardening behaviour is observed in contrast to the softening behaviour seen at low strain rates. Moreover, concave up curves have been obtained when testing in compression along RD at temperatures as high as 400ºC. It can also be confirmed from compression tests along ND that the CRSS for {10-12} twinning is strain rate independent.

3.2 Microstructure and texture evolution at high strain rates

The microstructure and texture of the different tensile samples are shown in Figure 3. The sample deformed at RT shows elongated grains in the loading direction with some twins, while dynamic recrystallized microstructure is observed after the quasi-static loading at 250ºC. Interestingly, the strengthening of the texture component corresponding to the alignment of the <10-10> direction in the tensile loading direction is observed in both samples evidencing the activity of prismatic slip. The intensity of the <10-10> poles parallel to the loading direction is decreased significantly in the sample deformed at 250ºC in comparison with that in the room temperature sample as a consequence of the generalized DRX as it observed in the microstructure.

At high strain rates, an increase of the amount of twins is observed, in comparison with quasi-static samples. Neutron diffraction analysis also shows a new texture component in the (0001) pole figure at high strain rates, not observable at quasistatic strain rates. This new component was associated with the increase of {10-12} tensile twinning activity which causes the grain rotate ~86º. Secondary twins are also observed in EBSD orientation maps by analyzing the boundary characters (Figure 4) in a significantly higher amount than at quasi-static samples. Moreover secondary twins are also observed at high strain rate and elevated temperatures. Finally, a splitting of the intensities in the basal pole figure is observed at 250ºC. This texture type can be developed by the activation of <c+a> pyramidal slip as it was previously suggested [20]. Additionally, secondary twinning could also contribute to splitting basal intensities as shown in Figure 4.

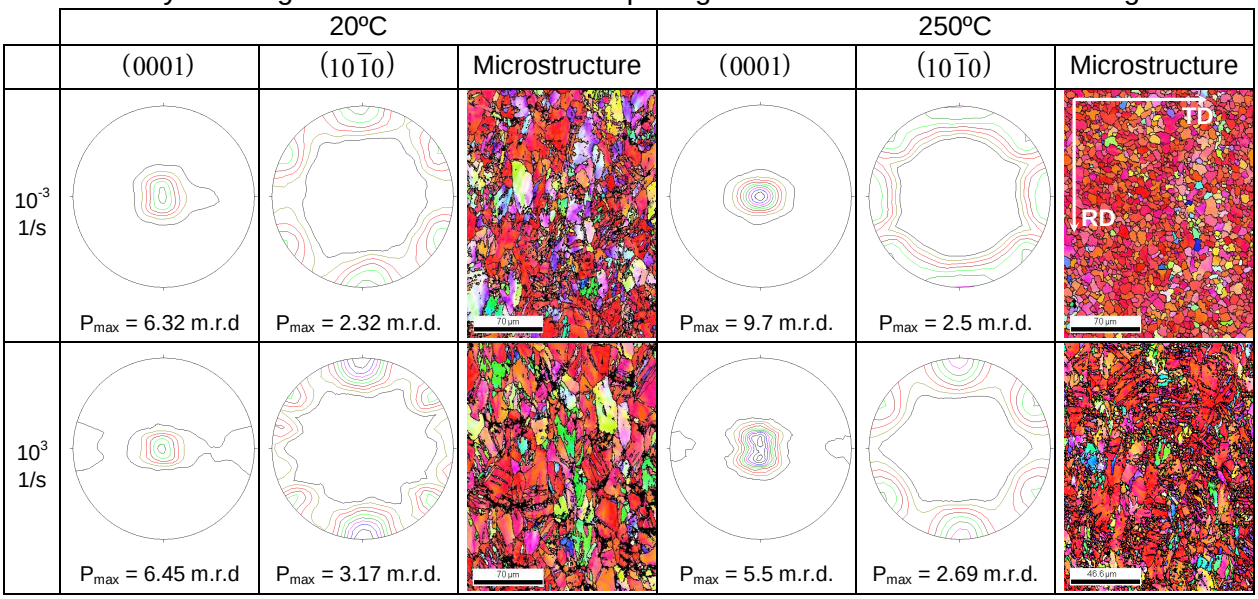

***Figure 3**: Microstructure measured by EBSD (The colour code corresponds to the ND inverse pole figure) and macrotexture of the different samples.*

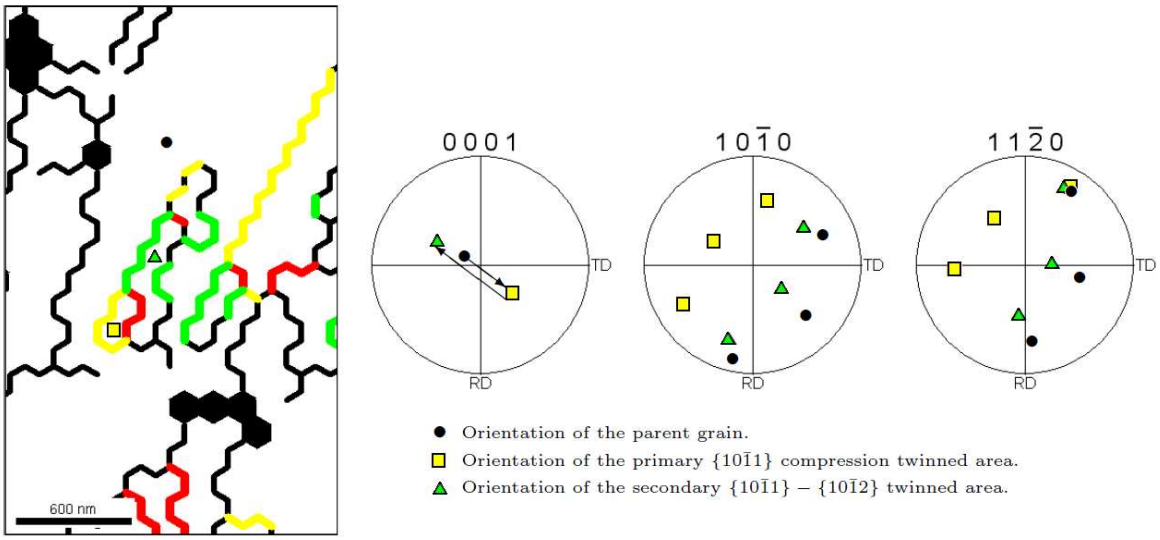

***Figure 4**: Example of a secondary twin formed and the orientations in the pole figures of the parent grain, primary compression twin and secondary tensile twin. The contribution of the secondary twinned area to the micro-textures with orientation between 0º and 90º towards the perpendicular of the loading direction (in this case RD) is visible.*

The dynamic recrystallization (DRX) mechanisms observed in Mg alloys can either be discontinuous (DDRX) or continuous (CDRX) [8, 21]. The first type consists on the nucleation of new grains and their growth and in the latter type new high angle boundaries are formed as a consequence of local lattice rotations by dislocation accumulation. Rotational dynamic recrystallization (RDRX) is a variation of the latter in which new grains are formed near grain boundaries due to increased dislocation activity as a consequence of intergranular strain incompatibilities [1, 8, 22]. Rotational dynamic recrystallization has been observed during high strain rate deformation of not only minerals [23] but also metals [24].

However, differentiating DDRX and RDRX mechanisms can be challenging, as in both cases the new grains usually develop near grain boundaries. For the particular case of rolled sheets of AZ alloys, it has been reported that recrystallized grains nucleated by DDRX usually possess a basal fiber [2, 25], whereas those formed by RDRX tend to have orientations in which *c*-axes are tilted away from the ND [22]. Results from the current study confirmed that when testing the AZ31 alloy in tension at 250ºC at low strain rates DDRX took place, as revealed by the development of basal fiber texture and strain free recrystallized grains (Figure 3). When testing at high strain rates and 250ºC, a small amount of recrystallized grains is observed in contrast to the generalized RX observed at low strain rates. In addition, clear divergences are observed in contrast to DDRX. Two observations suggest an increasing contribution of rotational recrystallization. Firstly, the KAM map in Figure 5 reveals that some small grains were not strain free. Secondly, in some small grains the *c*-axes were rotated away from the ND as it can be seen in Figure 5, where the orientation of several recrystallized grains is plotted using discrete pole figures. Finally, from these results, it is suggested that recrystallized grains may be formed by a combination of both DDRX and RDRX due to the limited time for diffusion.

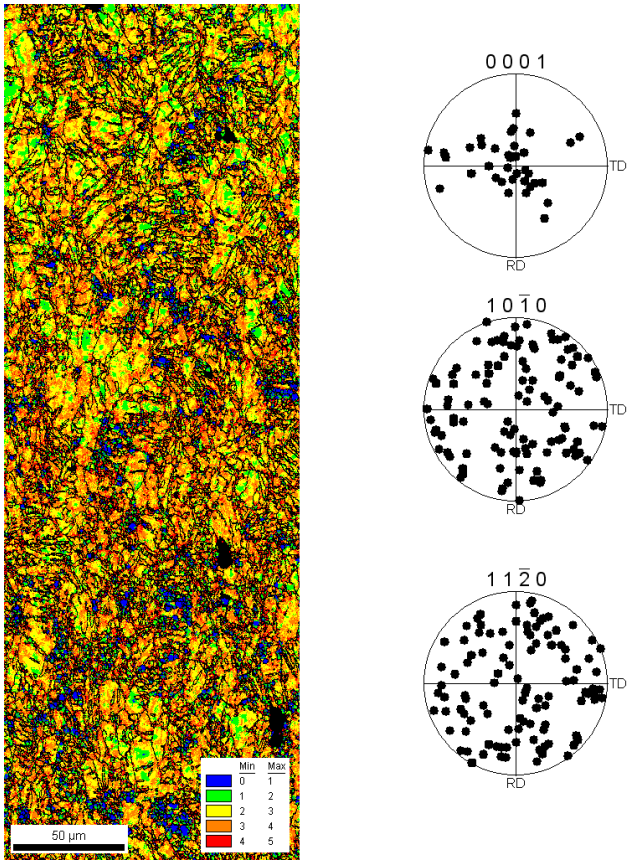

***Figure 5**: Kernel average misorientation (KAM) map and discrete orientations of the recrystallized grains of the sample deformed at high strain rates (10^3 s^{-1}) and 250ºC.*

4 Conclusions

The mechanical behaviour of AZ31 magnesium alloy has been investigated at high strain rates and compared to quasi-static data. Results from this study will be interesting to design parts for dynamic loading condition. The main conclusions are listed below:

1. With increasing temperature at low strain rates, the tension-compression asymmetry decreases and non-basal slip planes become active. However, at high strain rates, this asymmetry is retained at high temperatures and twinning remains active under these conditions.
2. Tensile twinning is enhanced at high strain rates compared with low strain rates. It remains being the predominant deformation mechanism during the early stages of deformation in compression tests even at elevated temperatures.
3. Alignment of <10-10> directions with the tensile axis was observed which evidences activity of prismatic slip at high strain rate deformation even at high temperatures.
4. {10-11} – {10-12} secondary twins were also observed in EBSD orientation maps in the sample deformed at high strain rates.
5. A splitting of the intensities in the basal pole figure is observed in the sample deformed at high strain rates and 250ºC. This texture type can be developed by the activation of <c+a> pyramidal slip. The importance of second order

pyramidal slip is not only because it can accommodate deformation along *c*-axis but also because on supporting 5 independent slip systems by itself.

6. A small fraction of recrystallized grains was observed in tensile samples deformed at high strain rates and 250ºC. It is suggested that rotational recrystallization is activated due to the limited time for diffusion at high strain rates.

Acknowledgements

Neutron diffraction measurements were supported by the EC under the 6th FP through the Key Action: Strengthening the ERA, Research Infrastructures. Contract no. RII3-CT-2003-505925. The authors would like to thank the vehicle interior manufacturer Grupo Antolin Ingeniería S.A. within the framework of the project MAGNO 2008-1028 CENIT funded by the Spanish Ministry.

References

[1] *Yi, S., Zaefferer, S., Brokmeier, H.-G.*: Mechanical behaviour and microstructural evolution of magnesium alloy AZ31 in tension at different temperatures, Mater. Sci. Eng. A, 424, 2006, p. 275-281.

[2] *Agnew, S.R., Duygulu, Ö.:* Plastic anisotropy and the role of non-basal slip in magnesium alloy AZ31B, Int. J. Plasticity, 21, 2005, p.1161-1193.

[3] *Barnett, M.R., Keshavarz, Z., Beer, A.G., Ma, X.*: Non-Schmid Behaviour of Secondary Twinning in a Polycrystalline Magnesium Alloy, Acta Mater., 56 (1), 2008, p. 5-15.

[4] *Wonsiewicz, B.C., Backofen, W.A.*: Plasticity of magnesium crystals, Trans. TMS-AIME, 239, 1967, p. 1422-1431.

[5] *Barnett, M.R.*: A Taylor model based description of the proof stress of magnesium AZ31 during hot working, Metall. Mater. Trans. A, 34, 2003, p. 1799-1806.

[6] *Agnew, S.R., Yoo, M.H., Tomé, C.N.*: Application of texture simulation to understanding mechanical behavior of Mg and solid solution alloys containing Li or Y, Acta Mater., 49, 2001, p. 4277-4289.

[7] *Ion, S.E., Humphreys, F.J., White, S.H.*: Dynamic recrystallisation and the development of microstructure during high temperature deformation of magnesium, Acta Metall., 30, 1982, p. 1909-1919.

[8] *Kaibyshev, R., Sitdikov, O.*: Dynamic Recrystallization of Magnesium at Ambient Temperature, Z. Metallkd., 85 (10), 1994, p. 738-743.

[9] *Galiyev, A., Kaibyshev, R., Gottstein, G.*: Correlation of plastic deformation and dynamic recrystallization in magnesium alloy ZK60, Acta Mater, 49, 2001, p. 1199-1207.

[10] *Gehrmann, R., Frommert, M.M., Gottstein, G.*: Texture effects on plastic deformation of magnesium, *Mater. Sci. Eng. A* 395, 2005, p. 338–349.

[11] *Ulacia, I., Hurtado, I., Imbert, J., Salisbury, C., Worswick, M., Arroyo, A.*: Experimental and numerical study of electromagnetic forming of AZ31B magnesium alloy sheet, Steel Res. Int., 80, 2009, p. 344-350.

[12] *Christian, J.W., Mahajan, S.*: Deformation twinning, Prog. Mater. Sci. 39, 1995, 1-157.

[13] *Mukai, T., Yamanoi, M., Higashi, K.*: Ductility enhancement in magnesium alloys under dynamic loading, Mater. Sci. Forum, 350, 2000, p. 97-102.
[14] *El-Magd, E., Abouridouane, M.*: Influence of strain rate and temperature on the compressive ductility of Al, Mg and Ti alloys, J. Phys. IV, 110, 2003, 15-20.
[15] *Ishikawa, K., Watanabe, H., Mukai, T.*: High temperature compressive properties over a wide range of strain rates in an AZ31 magnesium alloy, J. Mater. Sci., 40(7), 2005, p. 1577-1582.
[16] *Rittel, D., Wang, Z.G.*: Thermo-mechanical aspects of adiabatic shear failure of AM50 and Ti6Al4V alloys, Mech. Mater., 40(8), 2008, p. 629-635.
[17] *Tucker, M.T., Horstemeyer, M.F., Gullett, P.M., El Kadiri, H., Whittington W.R.*: Anisotropic effects on the strain rate dependence of a wrought magnesium alloy, Scripta Mater., 60(3), 2009, p. 182-185.
[18] *Ulacia, I., Salisbury, C.P., Hurtado, I., Worswick*, *M.J.*: Tensile characterization and constitutive modeling of AZ31B magnesium alloy sheet over a wide range of strain rates and temperatures, J. Mater. Proc. Tech., Manuscript submitted, 2009.
[19] *Ulacia, I., Dudamell, N.V., Gálvez, F., Yi, S., Pérez-Prado, M.T., Hurtado, I.*: Mechanical behavior and microstructural evolution of a Mg AZ31 sheet at dynamic strain rates, Acta Mater, 2010, doi:10.1016/j.actamat.2010.01.029.
[20] *Styzynski, A., Hartig, Ch., Bohlen, J., Letzig, D.*: Cold rolling textures in AZ31 wrought magnesium alloy, Scripta Mater., 50, 2004, p. 943-947.
[21] *Del Valle, J.A., Ruano, O.*: Influence of texture on dynamic recrystallization and deformation mechanisms in rolled or ECAPed AZ31 magnesium alloy, Mater. Sci. Eng. A, 487, 2008, p. 473-480.
[22] *Del Valle, J.A., Pérez-Prado, M.T., Ruano, O.*: Texture evolution during large-strain hot rolling of the Mg AZ61 alloy, Mater. Sci. Eng. A, 355, 2003, p. 68-78.
[23] *Humphreys, F.J., Hatherly, M.*: Recrystallization and related annealing phenomena, Oxford, Pergamon, 1995.
[24] *Andrade, U., Meyers, M.A., Chokshi, A.H.*: Constitutive Description of Work- and Shock-Hardened Copper, Scripta Metall. Mat., 30, 1994, p. 933-938.
[25] *Hutchinson, B., Barnett, M.R., Ghaderi, A., Cizek, P., Sabirov, I.*: Deformation modes and anisotropy in magnesium alloy AZ31, Int. J. Mater. Res., 100, 2009, p. 556-563.

Electromagnetic Forming of Longitudinal Strengthening Ribs in Roll Formed Automotive Profiles

I. Eguia[1], A. Mangas[1], R. Iturbe[2], and Mª A. Gutiérrez[1]

[1] Labein-Tecnalia, Edificio 700, C/Geldo, Parque Tecnológico de Bizkaia, 48160 – Derio, Bizkaia, Spain

[2] Antec, Ramón y Caja*l, 74, C.P: 48920, Portugalete, Vizcaya

Abstract

In the automotive industry, increasing ecological concerns and demands for higher performance have become lightweight construction a key aspect. Due to the gradual introduction of high strength materials on the one side, and greater consideration with regard to continuous manufacturing technologies on the other side, it is possible nowadays to address the demands that structural and complex automotive parts have to face, from the standpoint of lightweight manufacturing. Thickness, shape and impact conditions constitute the main aspects to consider for such parts and shape conditions in particular require from complex, costly and lengthy procedures, especially when discontinuous forming operations such as stamping and hydro forming procedures are selected. However, continuous forming operations like Roll Forming (RF) can prove to be advantageous and suited for scalable parts (e.g in length) and at the same time be economically reasonable. RF lines as well generally incorporate additional installations to perform multiple forming operations destined to imprint strengthening ribs perform punching operations or weld certain parts. It is in this context where the usefulness of the electromagnetic forming technology for completion of auxiliary operations can be proven, given its flexibility and reasonable investment costs.

* *The author would like to acknowledge and express heartfelt gratitude to the PROFORM project partners for giving permission to reproduce results of an ongoing investigation, in the field of the roll forming process. PROFORM (contract 026706-2) is funded by the European Commission under the Sixth Framework Program (Priority3).*

Electromagnetic forming (EMF) is a contact-free technique where large forces can be imparted to a conductive metallic workpiece by a pure electromagnetic interaction. The produced electromagnetic pressure can produce stresses in the workpiece that are several times larger than the material flow stress. Ultimately this can cause the workpiece to deform plastically and to be accelerated achieving high velocities. Once the velocity is imparted to the workpiece, the shape can be developed either by free or die forming.

The work described in this paper explores the potential of the EMF process to adequately form shallow longitudinal ribs or stiffeners in components previously formed utilizing an innovative concept called Flexible Roll Forming, developed at The Technical University of Darmstadt in Germany, by means of magnetic pulse forming, maintaining the integrity of the workpiece while trying to meet industry standard tolerances. Profiles exhibiting hat-like cross sections made of AHSS steels were subjected to localized impulses in order to achieve strengthening features in the roll formed part. ZStE340 steel alloy profiles were first roll formed and then inserted in the EM forming installation designed for the occasion. A high strength copper alloy (Cr-Zr-Cu) was used as a conductor for the single turn coil, placed opposite to the sidewall in the moment of the energy delivery. Formed specimens were subsequently measured to account for existing dimensional deviations.

Keywords

Profile, Finishing, Forming

1 Introduction

Shape, thickness and impact conditions are often referred as the main aspects to consider for structural automotive parts [1]. Shape conditions in particular require from complex, costly and lengthy procedures, compared to continuous forming processes. In a discontinuous process like the roll forming process, the bending occurs gradually in several forming steps from an undeformed strip to a finished profile. It constitutes a continuous manufacturing process for the production of arbitrary shaped profiles that can account for the standardization of the vehicle body components. Typical applications in the automotive industry are for example bumpers and door beams [2]. The possibility to change the length and size of the vehicle body are inherent to this process making it a very suitable technology for the new modular and adaptable concepts of the automotive (space-frame architecture) and a friendly technology for design changes.

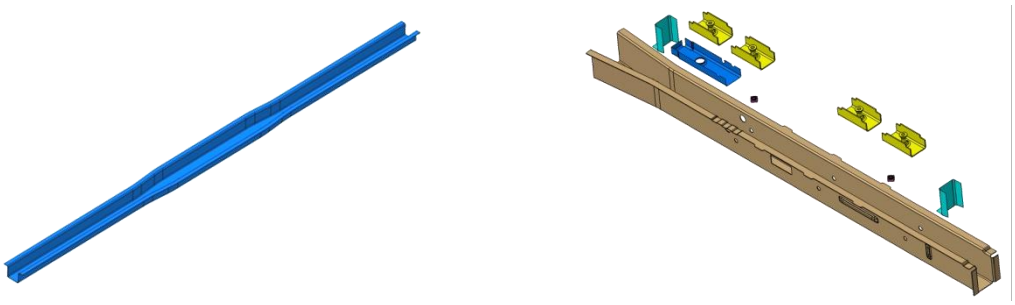

Figure 1: Example of a generic longitudinal beam (right) and a finished profile that underwent multiple complimentary operations (left)

In roll forming (RF), additional manufacturing steps needed in the components are often made in separate, independent forming cells. Stamping operations or bending operations of the extremities of the parts are required to meet functional demands in the part, and this is usually made using conventional technologies. The advantage of roll formed components could be enhanced if EMF is considered as a forming process that can produce equivalent deformation level and product variants from a pre-formed roll part, at an affordable cost, as can be observed elsewhere [3].

It is well known that with Electromagnetic Forming (EMF) large forces can be imparted to a conductive metallic workpiece by a pure electromagnetic interaction. The produced electromagnetic force can produce stresses in the workpiece that are several times larger than the material flow stress. Ultimately this can cause the workpiece to deform plastically and to be accelerated at high velocities.

The work described in this paper deals with the potential of the EMF process to impulse form stiffening features or strengthening ribs in the lateral walls of roll formed parts, made of high strength steels (ZStE340), in a continuous manner. For that, profiles with a variable cross section were first manufactured utilizing the flexible RF prototype line that was temporarily installed in Labein. The flexible Roll Forming Process concept utilized to obtain the parts was originally developed at the Technische Universität Darmstadt, and a 17 forming-stand prototype line incorporating an axis-control system was built during the course of the project in a coordinated effort by several members of the project consortium. The coil design process is then briefly described. The commercial finite element software Maxwell3D ® was used to ensure a proper magnetic field generation and concentration between coil and workpiece. The necessary energy being relevant, the coil manufacturing was undertaken to achieve an actuator that would last several shots. Experiments were carried out in Labein and results analyzed and discussed in subsequent paragraphs. Lastly, a discussion about the possibilities to integrate the technology is held and an alternative presented: a separate station comprising an electromagnetic forming device allowing for the forming of features while the main profile is being formed, at the preset line-speed. This alternative to conventional local forming could bring advantages such as reduced investment cost, derived from the lower costs of the tooling utilized versus the conventional tooling, as well as ease of integration and versatility of the process.

2 Sample preparation and coil design

2.1 Specimen preparation in the flexible roll forming line

Body in white components like transverse beams, roof beams, base side reinforcements or longitudinal beams are generally constructed on steel grades able to withstand elevated stress levels, and are generally designed taking into account crash requirements. The current study focuses on one of such materials, namely ZStE340, zinc coated micro-alloyed steel, with a thickness of 1.35 mm and mechanical characteristics illustrated in Table1. The variety of materials present in the structural frame can be variable; nonetheless all share the common property of being mechanically strong, while including the ability to absorb energy as deformation energy.

	σ_{Yield} (MPa)	σ_{UTS} (MPa)	σ_{Yield} / σ_{UTS}	εuniform (%)	E (MPa)	Poisson's Coefficient ν	Thickness (mm)
Zste340	270	355	0.76	38	210000	0.3	1.35

Table 1: Mechanical properties of ZStE340 grade

The procedure to form the strengthening ribs or stiffeners was then discussed. In conventional forming features in the longitudinal sense are stamped, creating an overall stiffening effect in the workpiece. In fact, with the EMF technology, it could be a possibility to impart energy in such a way that vertical grooves are formed in the lateral walls of the workpiece, broadening design possibilities as well as adding extra functionality. In that sense, the ability of the EMF technology to impart localized high pressure expands design possibilities, as it can be observed in other studies [4], [5].

Of all of the alternatives assessed (Figure 2) it was finally decided to proceed with the full design of an experimental setup to form a longitudinal groove, 130 mm in length, in the centre of the vertical wall. The width of the groove was set in 10 mm, setting the desired height in the order of one to two times the workpiece thickness.

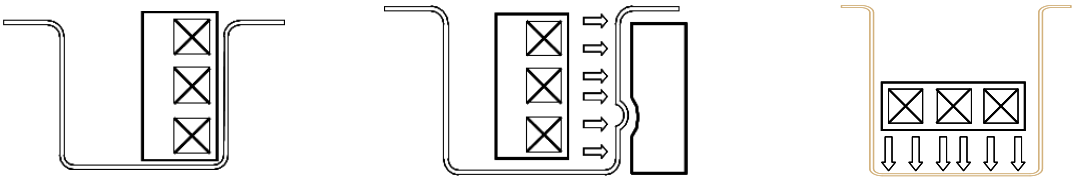

Figure 2: *Different alternatives for strengthening rib location*

The material formats were taken from a coil strip delivered by Daimler and inserted in the flexible roll forming line comprised of a laser cutting station, and several roll forming stands. The material is gradually bent with conventional rollers with the particularity that the so called flexible stands stretch-form the metal in certain areas, augmenting the size of the cross section in the central zone. The resulting workpiece is a profile with a length of 2000 mm with a variable cross section, like the one depicted in Figure 3.

Figure 3: *General view of roll formed profile (right) and close-up of the transition from narrow section to broad section.*

2.2 EMF coil design

It is well known that the material with which the magnetic actuator or coil is made must incorporate good current carrying properties as well as optimum mechanical properties [4]. It is then important the selection of a material that exhibits high conductivity while retaining considerable strength, that generally leads to a trade off in the balance of the properties. For the experiments performed in this study a Chromium-Zirconium-Copper alloy with a conductivity of 72% IACS and a tensile strength of 470 MPa was selected. It was expected that the reaction forces present during an EMF discharge be withstood by this alloy, maintaining the integrity of the coil during several discharges.

The target shape to form in the sidewall was defined afterwards. A longitudinal, strengthening rib, 130 mm long, 10 mm wide to be placed at approximately 20 mm from the bottom of the part. It was decided that the depth of such stiffener should be between 1 to 2 times the thickness of the base material, for this to be considered a proper stiffener.

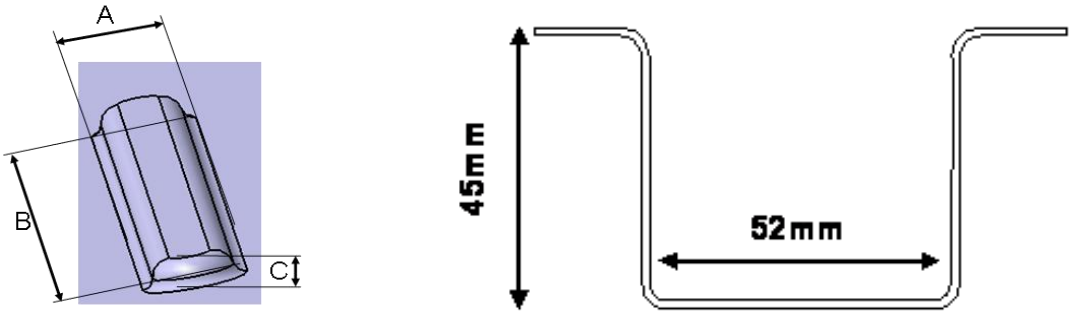

Figure 4: *Proposed shape for the stiffener (left), dimensions of the cross section in the narrow area of the workpiece*

For an actuator to emboss the described shape it was decided that a robust single turn coil was needed, that could account for the large counterforce expected in this kind of operations [6], [7]. Space limitations due to the size of the cross section were determinant in this choice too. The conceived shape is shown in Figure 5. For the validation of the proposed coil shape Maxwell 3D® was utilized. The mentioned FEM software allows for

the computation of an equivalent circuit connected to the FEM model comprised of coil and workpiece, simultaneously calculating discharge current and magnetic field values.

Figure 5 shows the calculated primary current for the preset discharge parameters, with the associated peak current. The simulation was run considering that the coil is attached to a bank charged at 30kJ. The electrical parameters of the coil material were obtained in the laboratory according to standard measurements, while the electrical parameters of the steel alloy were obtained from the literature. As a result of the discharge a peak current of approximately 700 kA was obtained being the time to peak 10 microseconds. The figure on the right side shows a plot with the achieved pressure distribution on the sidewall. The calculated pressure peak at peak time was 48MPa, which gave first indications that the needed energy would be significantly higher if direct forming was desired.

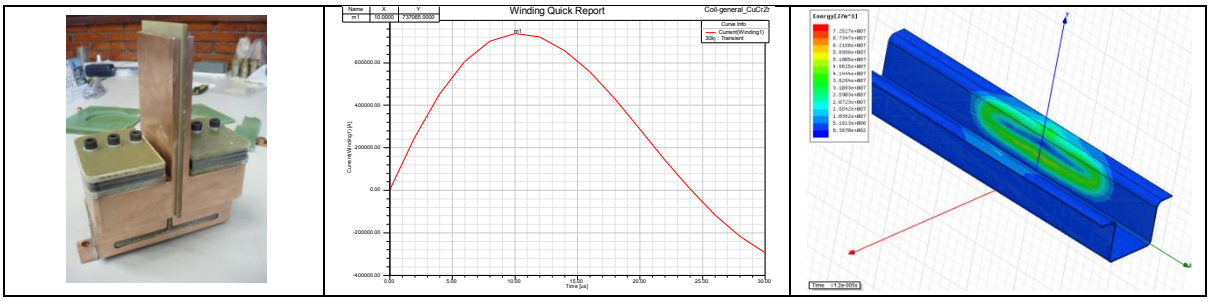

Figure 5: *Manufactured coil (left), computed discharge current (centre) and pressure distribution (right)*

Hence, the simulations validated the coil concept leading to the next step, the detailed design and manufacturing of the coil. The company Antec finished the design, manufactured the coil and reinforced it using fibreglass pre-impregnates giving the coil the desired robustness. Figure 5 (left) shows the delivered coil as it was tested at Labein's facilities.

3 EXPERIMENTAL PROCEDURE

3.1 Experimental Setup

The electromagnetic forming operation was performed using a 60KJ Magneform Energy storage control unit system where the actuator or coil is connected. The single turn coil describes a closed loop parallel to the vertical flange, being the width of the conductor of 10 mm along the direction of the groove (Figure 4). A die manufactured using Boehler's K390, heat treated and coated using a TiAlN layer to prevent premature erosion and die wear was utilized. Additionally, the die will exhibit good anti-spark properties, given the properties of the surface. If an accidental arcing occurred, the high temperatures present

whilst the discharge lasts would tend to melt and erode the surface of the die, in the absence of such coating.

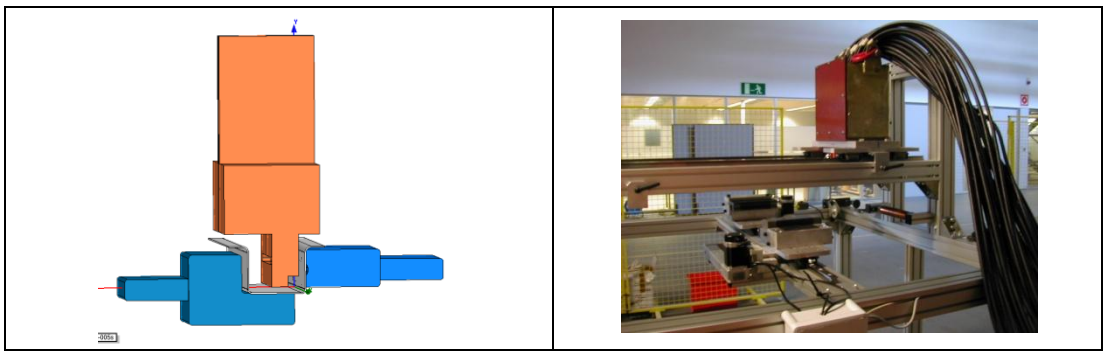

Figure 6: *Schema of the configuration of coils and dies (left), actual setup (right)*

Once the coil has been positioned, the entire assembly is attached to the pulse generator, and discharge parameters selected. The efficiency of the process is determined mainly by the confinement degree and the electrical properties of the workpiece. A low value of this parameter results in a poor energy transfer, as it is the case with the high strength steels. Generally, direct forming is not possible if the depth to be achieved is too high, and additional and more conductive materials are usually attached to the HSS in order to assist the forming. In this case, thin copper foil (0.5 mm thickness) was used in the experiments.

3.2 Implementation strategy

From the previous experiments it is concluded that the forming of features resembling stiffeners or strengthening ribs is feasible using the electromagnetic technology. Energy considerations apart, its versatility to imprint diverse features within intricate shapes could be valuable in terms of agile manufacturing. A variety of shapes can be formed, not only inside-out but also outside-in, vertical or horizontal, multiple or a sole feature with a single discharge. It certainly has proven to be a suitable technique for stringent conditions. Nonetheless, the success or failure of technologies does not solely depend on the intrinsic capabilities, but on the potential to be utilized in conjunction with other techniques. For example, one disadvantage of the roll forming process is the reduced freedom in cross-section design compared to metal extrusion; e.g. ribs within a closed profile. Results of the investigation have shown that EMF technology could be utilized or taken into consideration to emboss this shapes.

Integration, though, has to be addressed taking into account technical and economical aspects. Considering only technical factors an alternative for the EMF operation is presented, in a way that process combination is possible. The key aspect in this case is determined by the possibility to simultaneously form a feature in a moving profile, a profile that is being formed by means of forming rollers. A process lay-out like the one depicted in Figure 7 was designed and installed, where a separate forming stand comprising all necessary means to form the stiffener is installed. The profile is formed by the action of the rollers and at the same time the driven rollers would guide the profile

towards the EMF stand. Without motion interruption, the EMF operation can be executed once the profile reaches the specified point where the stiffener needs to be inserted.

This kind of combination strategy can constitute a real advantage over more conventional operations and can enhance the possibilities of process like the flexible roll forming.

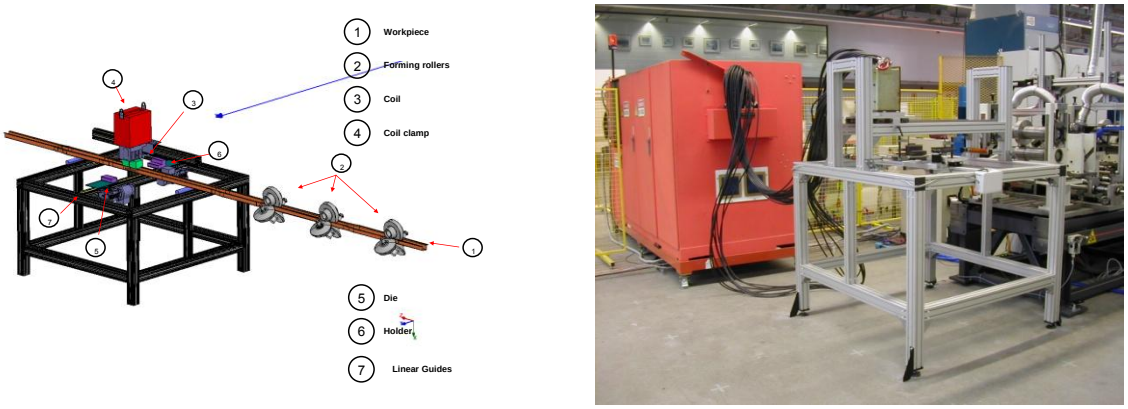

Figure 7: *EMF stand incorporating a coil that releases forming energy to moving workpiece (right)*

4 RESULTS

The experimental results obtained in the experimental try-outs are summarized in Figures 8 and 9, where the final formed configuration of a sample piece can be observed. Zste340 steel was formed using energies ranging form 21 to 45 KJ until the shallow rib was achieved in the vertical wall. Figure 8 shows a ZStE340 sample exhibiting a stiffener when a 45 kJ and an auxiliary driver were used.

Figure 8: *ZStE 340 profile with strengthening rib located in the central section*

The workpieces were then measured and compared against the theoretical geometry to account for significant deviations. It was noted that certain flange length located right above the affected area showed a deflection of 0.86mm. The defect arose as a consequence of the proximity of the coil to the flange, and insufficient blankholder-part adjustment. Even though the distance between coil and part is considerable in that area, the strength of the magnetic field is such that produces the mentioned effect.

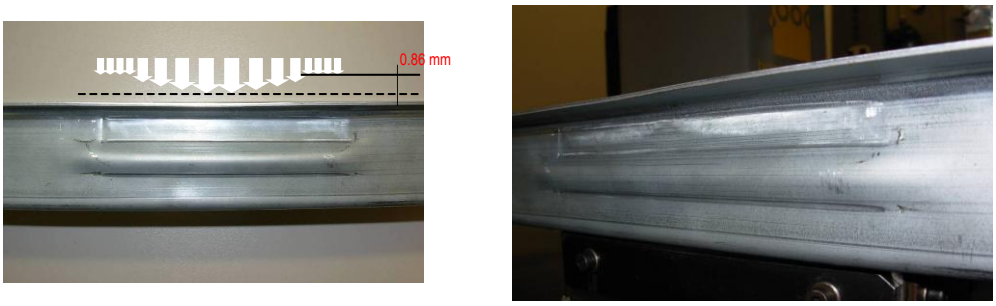

Figure 9: *Measured flange deflection (left) and close-up of stiffener (right).*

Three sections were defined in the middle zone in order to investigate the stiffener characteristics on the wall and to evaluate the geometrical deviation to reference cad data. Two different sides were scanned, the internal and external sides. The distance between the curves represents the component thickness. An average thinning of 8% was detected and a flange deflection angle varied from 0.1 to 0.3 mm.

The desired stiffener shape was achieved in the process keeping the stiffener dome height in the range of one to two times the thickness of the base material. It was observed that the cavity was not filled fully but nevertheless an approximate shape was obtained. Visual inspection of the affected areas showed slight roughness and surface quality affectation of the surface coating.

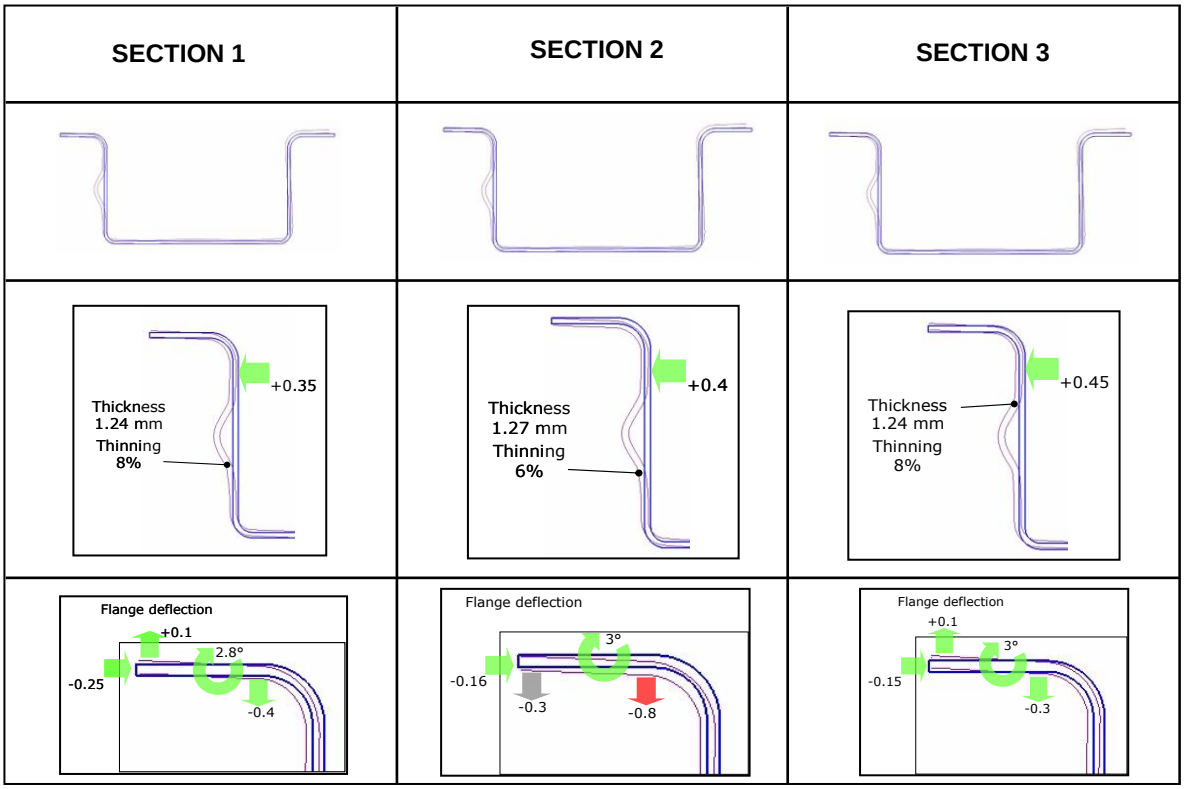

5 CONCLUSIONS

The forming of features resembling stiffeners or strengthening ribs is feasible using the electromagnetic technology. ZStE340 steel was formed using energies ranging form 21 to 45 kJ until the shallow rib was achieved in a vertical wall achieving the desired objective. The advantage of roll formed components could be enhanced if EMF is considered as a forming process that can produce equivalent deformation level and product variants from a pre-formed roll part. When considering implementation, the integration has to be addressed taking into account technical and economical aspects. In this case it is determined by the possibility to simultaneously form a feature in a moving profile, a profile that is being formed by means of forming rollers. An integration concept has been presented that can account for the manufacturing of scalable parts combining EMF and flexible roll forming technologies. This kind of combination strategy can constitute a real advantage over more conventional operations and could enhance the possibilities of process like the flexible roll forming.

REFERENCES

[1] *M. Kleiner, M. Geiger, A. Klaus*, “Manufacturing of Lightweight Components by Metal Forming”

[2] *Javad Marzbanrad, Masoud Alijanpour, Mahdi Saeid Kiasat*, “Design and analysis of an automotive bumper beam in low-speed frontal crashes”, Thin-Walled Structures 47 (2009) 902–911.

[3] *Kevin Sweeney, Ulrich Grunewald*, “The application of roll forming for automotive structural parts”, Journal of Materials Processing Technology 132 (2003) 9–15

[4] *C.S. Namoco Jr., T. Iizuka, N. Hatanaka, N. Takakura , K. Yamaguchi,* “Influence of embossing and restoration on the mechanical properties of aluminium alloy sheets”, Journal of Materials Processing Technology 192–193 (2007) 18–26.

[5] *Winfried Beisel, Ingo Oberste-Dommes*, “Precision embossing Alternative method of forming flat parts”, Journal of Materials Processing Technology 71 (1997) 18-24

[6] *Young-Bae Parka, Heon-Young Kimb, Soo-Ik Oh,* “Design of axial/torque joint made by electromagnetic forming”, Thin-Walled Structures 43 (2005) 826–844.

[7] *Józef Bednarczyk*, “Distribution of forces in the inductors used in metal processing in the pulse magnetic field”, Journal of material processing technology 133 (2003) 340-347

Microflanging of CuZn30 Specimens Using Electromagnetic Forming

R. VanBenthysen[1] and B. L. Kinsey[1]

[1]Mechanical Engineering Department, University of New Hampshire. Durham, NH, USA

Abstract

In this research, electro-magnetic (EM) forming was investigated as an alternative process to form microscale components. Both EM and quasi-static flanging experiments were conducted with CuZn30 specimens of 0.127, 0.508 and 1.588 mm thicknesses that were heat treated to achieve 2 and 10 grains through the thickness to assess this parameter. Results from the quasi-static tests showed that as the sample size decreased with a constant grain size through thickness ratio, the springback angle increased. For the 0.127mm and 0.508mm thickness specimens, the EM results showed that the flanging angle increased as the power input increased from 1.7 to 3.7 kJ. For 3.7 kJ energies and above, complete 90 degree flanging with no springback was achieved for the 0.508mm specimens. However, EM flanging could not be achieved for the 1.588mm case. Microhardness testing conducted on specimens of similar flanging angles yielded no observable change in deformation between the EM and quasi-static processes for the 0.508mm specimens.

Keywords

Forming, Miniaturization, Springback

1 Introduction

Recently there has been an increasing trend towards miniaturized systems, e.g., smart phones, mp3 players, personal computers, sensors, etc. An estimated 1.8 billion MEMS devices were shipped in 2005, with an anticipated growth of 11% through 2010 [1]. An increasing number of industries utilize these miniaturized systems including automotive, electronics, medical, defense and aerospace. With the increase in these systems comes the need to manufacture them in a more efficient, cost effective, and repeatable manner. Since macroscale manufacturing processes cannot be scaled down to produce these miniaturized components, alternative methods such as microinjection molding, micromachining, IC processing and microforming are used. Microforming is a high rate, cost effective process that involves plastically deforming components with at least two sub millimeter dimensions [2].

The inability to scale down conventional manufacturing processes stems from size effects, i.e. variations in material properties and process parameters as the grain size approaches the specimen feature size [3]. The results are anomalies in final part shapes, springback, increased data scatter, variations in frictional effects, etc. An example of a shape anomaly can be seen in Figure 1 as the pin with a coarse grain size of 211µm curves after being extruded from .76mm to .57mm [4]. This was caused by the size and orientation of a single grain in the material. A macroscale component generally consists of many grains through a thickness or part feature whereas a microscale component may consist of only a few grains and possible less than a single grain. Figure 2 demonstrates the effects of varying the number of grains through the thickness (φ) on yield strength during bending and tensile tests [5]. It can be seen that as φ is reduced from 10 to 1, there is a decrease in yield strength associated with an increased ratio of surface to volume grains [2]. As φ is decreased further, the yield strength increases due to the effect of individual grain orientation. In addition, a decrease in the φ also causes an increase in data scatter.

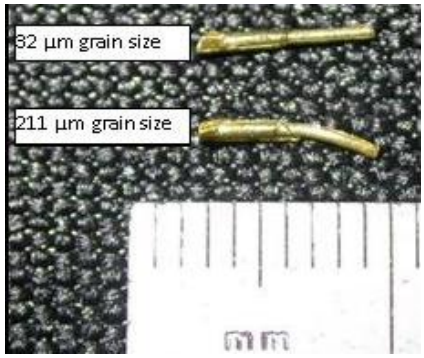

***Figure 1** : Shape anomaly due to miniaturization of micro-extruded pins [4]*

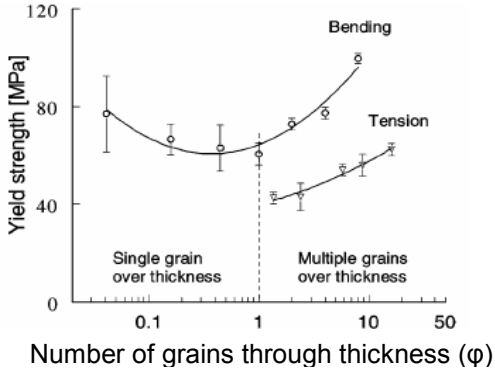

***Figure 2** : Effect of miniaturization during bending and tensile tests [5]*

For bending processes, springback and data scatter are of utmost concern. The inability to predict final part geometry would significantly reduce the consistency of manufacturing. Figure 3 demonstrates how springback is affected by miniaturization of the feature. In this case, a scaling factor λ is introduced to specify the geometry scaling [6]. Al 99.5 was used in the experiments and a λ of 1 corresponds to 200µm thickness. The three grain sizes presented all show the effect of an increased springback angle as the scaling factor is decreased.

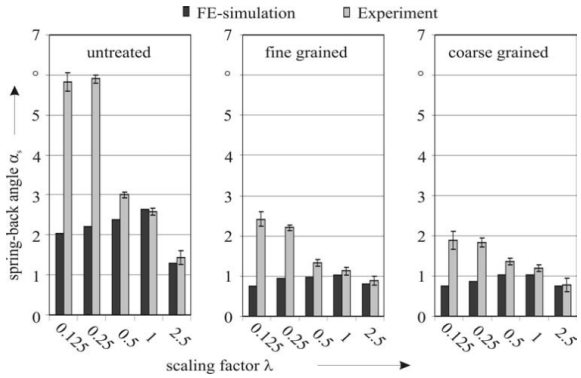

***Figure 3** : Effect of miniaturization on springback angle and data scatter during bending [6]*

In this paper, results from both EM and quasi-static flanging experiments are presented. As in past research, the springback angle increased with miniaturization for quasi-static experiments. The EM flanging process was able to achieve no springback (i.e. 90 degree flanging) for the 0.588mm and 0.127mm cases. The quasi-static case was unable to achieve 90 degree flanging due to springback and limitations of the die and punch setup. Microhardness measurements performed on both quasi-static and EM flanged specimens did not reveal any significant difference in deformation. Finally, simulations were conducted to design an EM flanging coil for future bending experiments.

2 Quasi-static Setup

The quasi-static and EM flanging processes utilized dies and punches with features that were a function of the specimen's thickness. CuZn30 specimens (0.127, 0.508 and 1.588mm thicknesses) were used. Figures 4 and 5 show schematics of the sample and tooling. To achieve a plane strain condition the sample width was ten time the thickness (10t). Sample lengths were twenty six times the thickness (26t) to assure contact between the sample and punch at full punch depth. Heat treatments were used to achieve a desired 2 and 10 grains through the thickness for all three specimen sizes (see Table 1). These values were chosen as it is estimated that size effects will arise when less than 15 grains through a feature size are present [7]. See [8] for further details and results related to the quasi-static experiments.

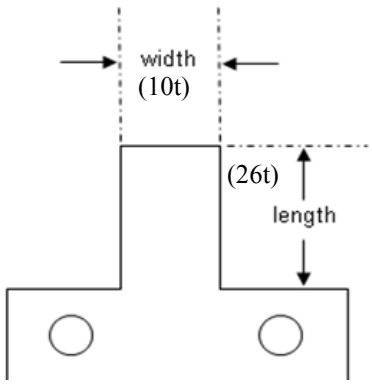

Figure 4 *: Schematic of Sample*

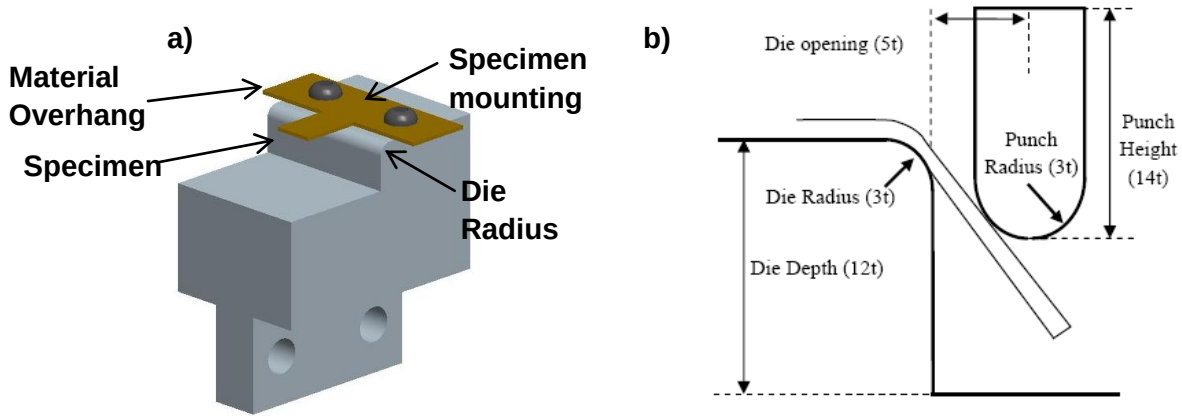

Figure 5 *: Schematic of a) Sample and Die combination and b) tooling features bases on specimen thickness*

Thickness (μm)	Target grains through thickness	Measured grain size (μm)	Measured grains through thickness	Heat Treatment (degrees C)	Duration (minutes)
1588	2	484.4	3.1	800	90
	10	127.5	11.8	665	90
508	2	208.3	2.4	700	60
	10	45.5	11	600	60
127	2	55.2	2.3	800	75
	10	15.0	8.5	600	60

Table 1 *: Heat treatment information and achieved grain sizes for various sheet thicknesses.*

3 Quasi-static Springback Results

For a similar number of grains through the thickness, the springback angle increased as the sample size decreased (see Table 2). This was measured optically using digital images and software. At the desired depth a picture was taken with the punch still in contact with the specimen. The punch was then removed and another picture was taken. These two images were then compared to determine the springback angle as can be seen in Figure 6.

a)

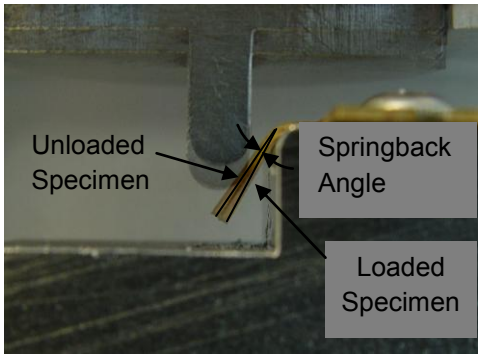

Figure 6 *: Springback in 0.508mm specimen*

b)

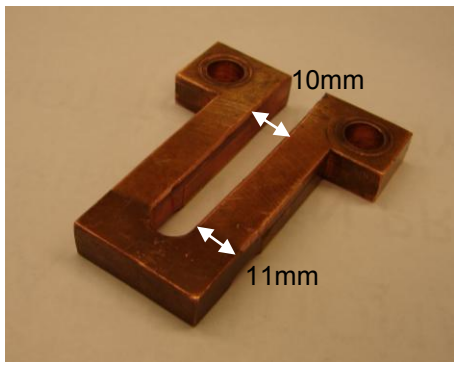

Figure 7 *: Cu101 coil*

sample #	Sample size (μm) / # of grains through thickness					
	127 / 10	127 / 2	500 / 10	500 / 2	1500 / 10	1500 / 2
1	4.6	4	3.3	2.3	1.8	2.9
2	3.3	4.4	4.4	1.4	1.6	1.8
3	2.9	4.4	3.8	2	1.8	2.2
4	5.4	3.7	3	2.2	2.2	1.4
5	4.6	4.1	3.1	-	2.9	1.6
average	4.16	4.12	3.52	1.975	2.06	1.98

Table 2 *: Springback angle values in degrees for various cases*

4 EM Flanging Experimental Setup

The dies used in the quasi-static process were also used for the EM flanging while the punch force is replaced by the force resultant of the magnetic field. A Cu101 coil for EM flanging was designed by Hirotec inc., a collaborator on this project. The coil and its location above the sample are shown in Figures 7 and 8 respectively. The specimen positioning on the die can be seen in Figure 5a.

The EM flanging setup is shown in Figure 9. The steel plates attached with bolts are to prevent unwanted deformation in the coil's leads, as the magnetic field that forms the specimen also affects the opposing lead of the coil. Kapton tape was used to prevent arcing between adjacent metal surfaces. The die is placed in a piece of G10 for easy positioning.

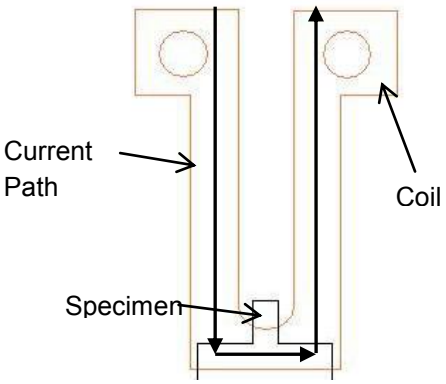

Figure 8 *: Position of sample under coil*

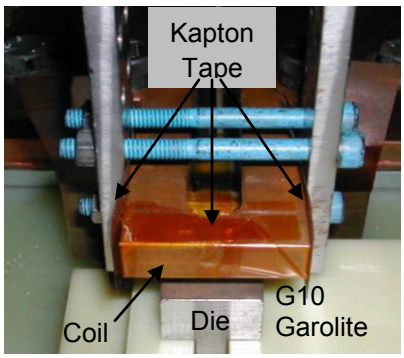

Figure 9 *: EM Flanging setup at Hirotec Inc.*

5 EM Flanging Experimental Results

For the 0.127mm and 0.508mm cases, the input energy level was varied in order to determine its effect on the flanging angle. The effect of the input energy on the 0.508mm specimens is shown in Figure 10 and Table 3. As expected, the flanging angle increases with increased energy input. Complete flanging was achieved for energy levels above 3.7 kJ. Since the distance between the coil legs (10mm, see Figure 7) is less than the 1.588mm specimen width (15.88mm), flanging was not achieved on the outer edges for this specimen (see Figure 11). This may be due to the repulsive eddy currents only being produced in the specimen's center as will be discussed in the section on coil design. Also, the energy level used may not have been sufficient for the deformation even if a wider coil width was used.

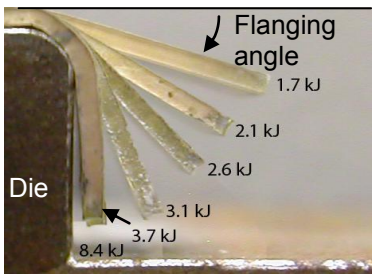

Figure 10 *: Effect of energy input on flanging angle for 0.508mm specimen*

Figure 11 *: EM Non uniform flanging of 1.588mm specimen.*

0.5 mm specimens		
Input energy setting (kJ)	Flanging angle in degrees	
	10 grains/thickness	2 grains/thickness
1.7	23.8	17.4
2.1	30.6	32.0
2.6	47.7	47.3
3.1	58.5	67.9
3.7	87.3	86.5
4.4	87.2	87.0
5.1	86.3	87.1
6.6	86.2	86.4
8.4	86.6	86.8

***Table 3** : Comparison of flanging angles and grain size ratios for various energy inputs*

Complete flanging of the 0.127mm specimen was also achieved with an energy level of 3.1kJ (see Figure 12). However, a driver material was required for the 0.127mm case which is in agreement with skin depth calculations performed to determine the minimum thickness required to achieve EM flanging (i.e., 0.328mm) [8]. Note though that the ends of the mounting strip (which were larger than the specimen and hung over the sides of the die; see Figure 5a) were flanged despite not having the driver material in this area. See Figure 12. Thus the effectiveness of flanging is affected by the area (length x width) as well as the thickness. This may be due to the eddy currents not being generated in the small specimen area of our workpiece. Effective design of a coil is needed to correct this concern.

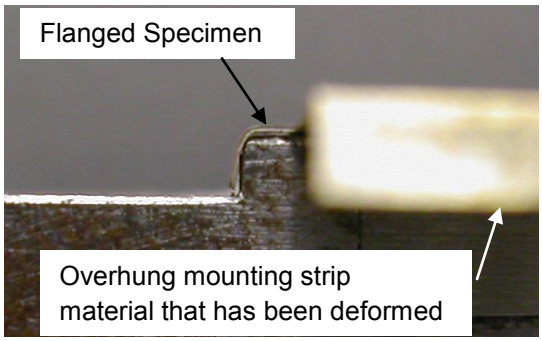

***Figure 12** : Complete flanging of 0.127mm specimen*

Hardness measurements through the thickness and along the bent region were obtained in order to observe any difference in the deformation mechanism inherent to each process. Since EM flanging was not achieved with the 1.588mm specimens and microhardness indentations are too large to produce sufficient data for the 0.127mm specimens, only hardness measurements on the 0.508mm specimens were conducted. An EM flanged specimen (3.1kJ) with a similar angle to the quasi-static case was chosen for comparison. Figure 13 shows the hardness contour plots for these cases. Hardness

measurements were also taken for the complete flanging case (3.7kJ). See Figure 14. The hardness profiles shown cover the whole bent region of the deformed specimens with a zero position along the length corresponding to the start of the die radius and the zero position through the thickness corresponding to the mid-plane of the sheet.

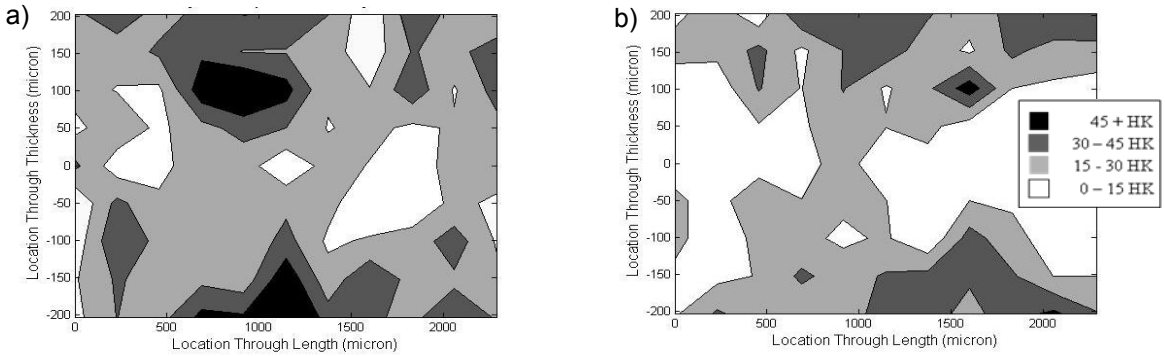

***Figure 13** : Contour plots for the a) quasi-static and b) EM processes, both 10 grains/thickness*

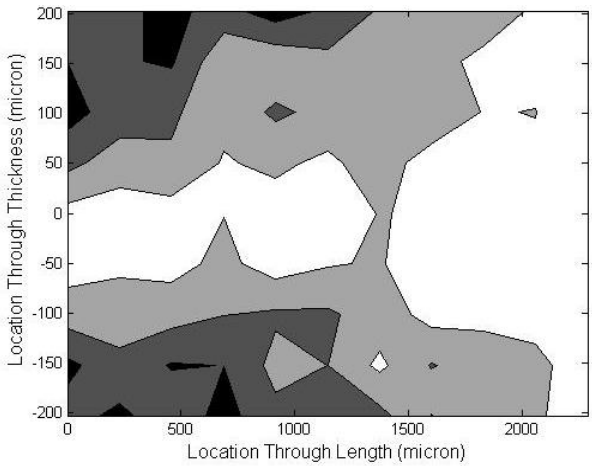

***Figure 14** : Hardness plot for 3.7kJ, 10 grains/thickness*

Comparing the quasi-static and 3.1kJ cases, there is no change in deformation present. The plots show a rough layered pattern with higher hardness at the surface of the sheet and lower hardness near the neutral axis. This rough pattern is due to only one set of measurements being taken. Only one sample was EM flanged for every thickness and grain size ratio; thus, obtaining an average plot is not possible. However, past three point bending research utilizing the same punches and dies with features based on the same specimen thickness ratio has shown an increased definition in hardness layering when an average plot is obtained. See Figure 15. An average of four samples (see Figure 15b) shows a much more defined hardness layering pattern than that of only one sample (see Figure 15a). The 3.7kJ case demonstrates more of a layered pattern due to the increased strain from a larger amount of deformation. Note that the plots in Figures 13-15 are the increase in hardness from the center region.

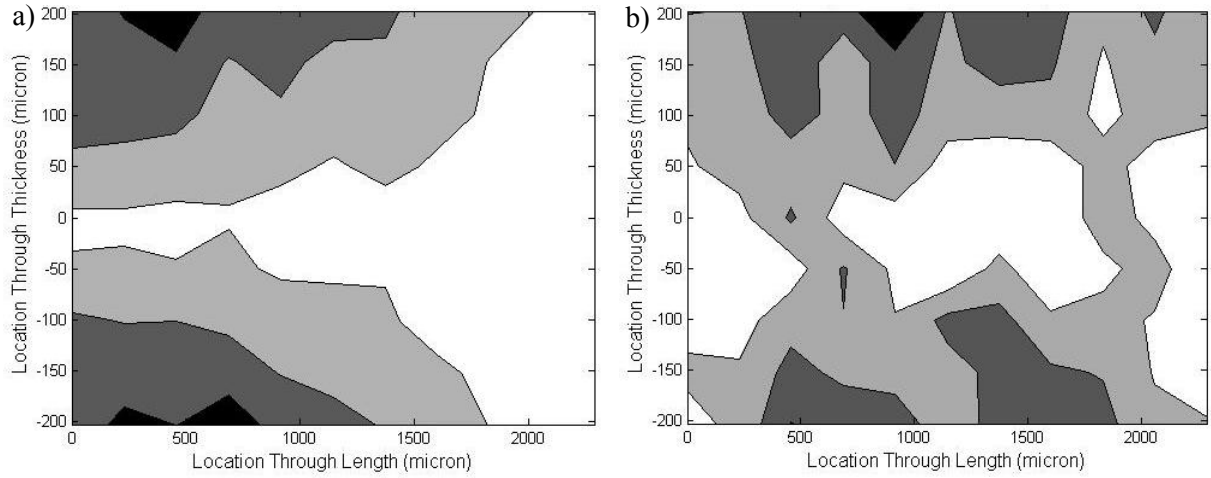

***Figure 15** : Results from past 3 point bending experiments. a) 1 set or measurements and b) an average of 4 sets*

6 Coil Design Simulations

In order to continue this research, a Magneform JA7000 series 12kJ machine, which is capable of producing a 400kA current with 6000V, was acquired. As the largest sample was unable to be uniformly EM flanged (see Figure 11), a coil for this specific specimen will be designed and fabricated. To avoid unwanted deformation of the coil legs, a single leg coil will be utilized (see Figure 16). Various designs were modeled in Magnet, an electromagnetic simulation package by Infolytica Corp. To compare magnitudes and uniformity of the magnetic fields, static cases were conducted. Of course, EM forming is a dynamic process; however, it was anticipated that these static cases would provide reasonable results with respect to the differences in coil geometries. Since only one leg of the coil is of concern, the model was a 2-D representation of the cross-section. See Figure 17 for the four different geometries. A current of 146kA was used due to an assumed rise time of 10μs. The coil material used is Cu101. The bottom face of the coil (19mm) was designed to be larger than the width of the large specimen (15.88mm). This is to assure that the specimen experiences a more uniform magnetic field. See Figure 17d for this length (L).

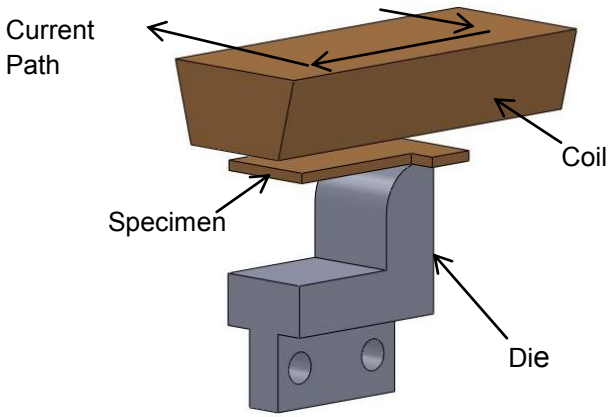

***Figure 16** : Schematic of single turn coil, die and specimen*

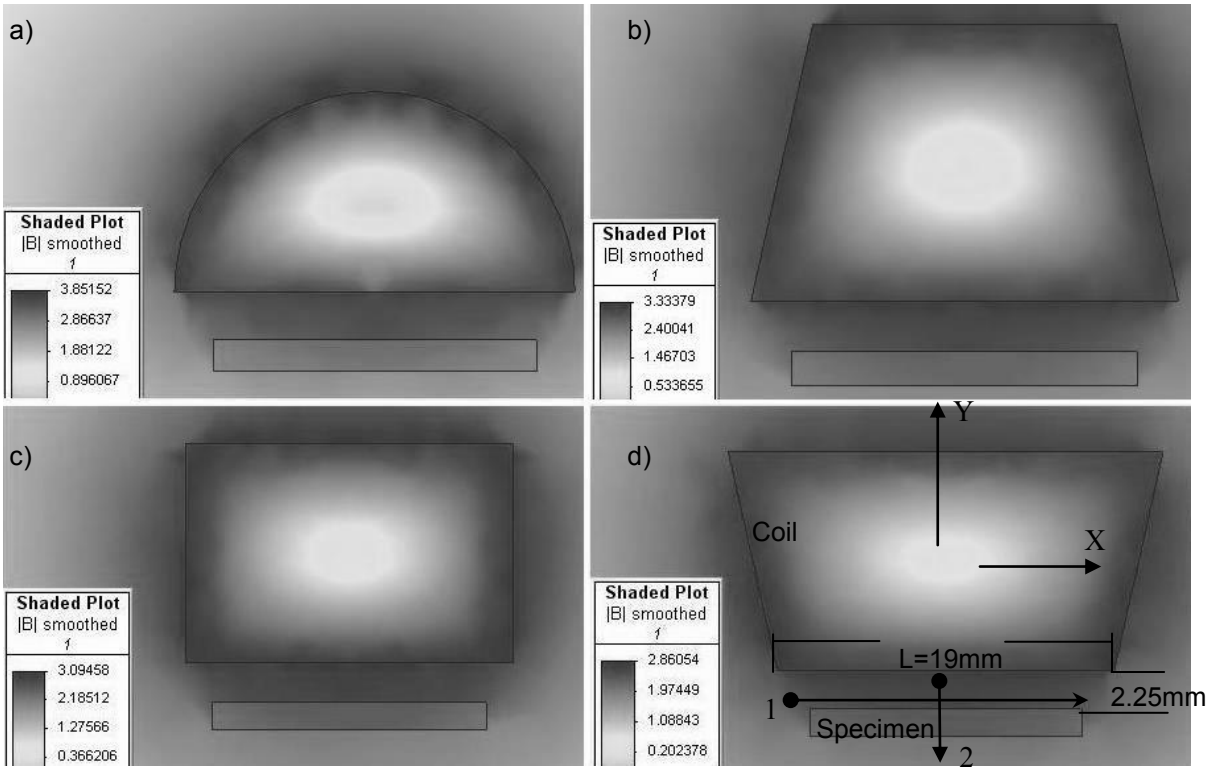

***Figure 17** : Different coil models for EM flanging; A) semi circular, B) inward 15º taper, C) rectangular and D) outward 15º taper. The units of B (the magnetic flux density) are Tesla.*

Line plots of the magnetic field were obtained for each coil design; 1) Along the width of the specimen at a distance of 2mm under the coil face and 2) from the bottom of the coil through the specimen thickness, at the vertical midplane of the coil (X=0). See Figure 17d for a visual representation of these two directions. Data for the 1 and 2 directions are shown in Figure 18. Figure 18b shows the effect of the specimen on the magnetic field's magnitude.

The coils were designed so the cross-sectional areas increase from geometry A to geometry D. Thus the current density is decreased and a lower magnetic field value (B) is predicted. However, lower B values also correlate to a more consistent magnetic field across the width of the specimen (see Figure 18a). This is desirable since a lower consistency may lead to non-uniform flanging, as was the case in past experiments with the largest specimen (1.588mm) (see Figure 11). Since previous experiments suffered from the lack of a uniform magnetic field, geometry D (outward taper) was chosen as it has the most uniform magnetic field across the width of the sample (from approximately -8mm < X < 8mm). Note the specimen may be located directly under the coil or may be offset. This will be adjusted to produce eddy currents that flow in a circular pattern in order to produce an optimal repulsive magnetic force for forming.

7 Conclusions

Increased springback was observed for a decrease in sample size with a similar number of grains through the thickness (φ) in our quasi-static microscale experiments. No change in hardness was observed for EM and quasi-static specimens of similar flanging angle. The

0.127mm and 0.508mm specimens experienced near complete flanging angles for power levels at approximately 4kJ. The 1.588mm specimen was unable to achieve a uniform flange due to the size of the coil in relation to the specimen's width. A new EM coil design for flanging of the 1.588mm thickness specimens was investigated.

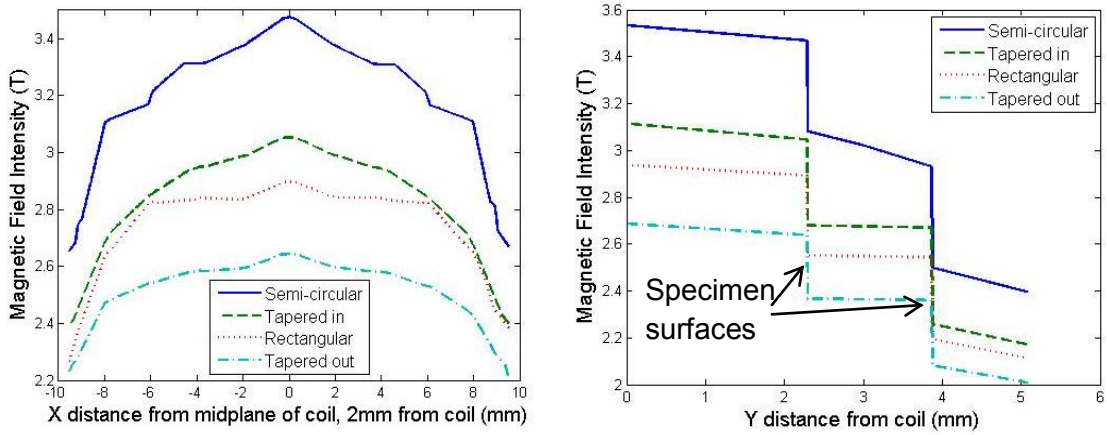

***Figure 18** : Plots of magnetic field intensity versus location a) along and b) perpendicular to the specimen for various coil geometries*

.Acknowledgments

Funding from the National Science Foundation (CMMI-0644705) and assistance with the EM flanging experiments from Hirotec America, Inc. are gratefully acknowledged

References

[1] In-Stat, "An Industry in Transition: 2006 MEMS Forecast", IN0603149ESCA, 2006.
[2] Geiger, M., Kleiner, M., Eckstein, R., Tiesler, N. and Engel, U., "Microforming", Keynote Paper, *Annals of the CIRP*, 50-2, 2001, 445-462.
[3] Armstrong R.W., "On Size Effects in Polycrystal Plasticity," *J. Mechanics & Physics of Solids*, 9, 1961, 196-199.
[4] Parasiz, S., VanBenthysen, R., and Kinsey, B.L., "Deformation Size Effects Due to Specimen and Grain Size in Microbending", *Journal of Manufacturing Science and Engineering*, 132, 2010, in press.
[5] Raulea, L.V., Goijaerts, A.M., Govaert, L.E., and Baaijens, F.P.T., "Size effects in the processing of thin metal sheets", *J. of Mat. Processing Technology*, 115, 2001, 44-48.
[6] Diehl, A., Engel, U., and Geiger, M., "Investigation of the spring-back behavior in metal foil forming", *Proceedings of the 24th IDDRG Conference*, Besancon, Frankreich, 2005.
[7] Hansen, N., "The effect of grain size and strain on the tensile flow stress of Aluminum at room temperature", *Acta Metallurgica*, 25, 1971, 863-869.
[8] VanBenthysen et al., "Comparison of Microscale Flanging Using Quasi-Static and Electromagnetic Forming Processes", *2008 International Manufacturing and Science Engineering Conference (MSEC),* Evanston, IL, Oct. 8-10, 2008.

SESSION 5
MODELING AND SIMULATION

MATHEMATICAL MODELING OF AN ELECTROMAGNETIC FORMING SYSTEM WITH FLAT SPIRAL COILS AS ACTUATOR*

E. Paese[1], M. Geier[1], J. L. Pacheco[1], R. P. Homrich[2], J. C. S. Ortiz[1]

[1] Grupo de Projeto, Fabricação e Automação Industrial – PROMEC – Universidade Federal do Rio Grande do Sul.
[2] Laboratório de Máquinas Elétricas, Acionamentos e Energia – DELET – Universidade Federal do Rio Grande do Sul.

Abstract

This study presents mathematical modeling and calculation procedure for problems of electromagnetic forming of thin circular metal sheets using flat spiral coil as actuator. The method focuses specifically on the calculation of the electromagnetic field generated by the flat coil and analysis of the circuit that models the electromagnetic forming system. The flat coil is approximated by concentric circles carrying the current discharge from the capacitors. The calculation of electromagnetic force and magnetic couplings between the coil and metal sheet are made to the initial time, before the plastic deformation of the sheet. The method is based on the Biot-Savart law, and the solution of magnetic induction integral equations is performed by numerical methods specifically with the use of Matlab commercial software. A routine calculation, which models the problem as a set of differential equations was implemented in the Matlab, this provides important information that serves as feedback for system design. Free bulging experiments were performed to demonstrate a good relationship with the mathematical model predictions for electrical discharge current in the coil and induced currents in the metal sheet, behavior of the transient electromagnetic force between coil and workpiece and, distribution of magnetic field and electromagnetic density force along the coil. Also, achieved results showed that there is a strong dependence of the back electromagnetic force with respect to plate

* This work is based partially on the results of the Master of Science Dissertation of Evandro Paese. The authors would like to thank the following persons: Eng. Michael S. Ertle from TDK-EPCOS for donating the capacitors; Eng. Augusto Nienow from Ensinger Engineering Plastics for donating of polyoxymethylene block; Eng. Eliseu Silveira Brito for milling the actuator coil and dies, and to Eng. Marcio Migliavacca from Rexfort for milling the spark-gap parts.

thickness for the system analyzed. The difference phase between the current induced in the coil and workpiece with higher negative peaks generate the back electromagnetic force.

Keywords

Mathematical, Forming, Electromagnetic forming of metal sheets

1 Introduction

An electromagnetic forming system is essentially a mutual induction system composed of an actuator coil and a conductive workpiece [1]. This process is based on a repulsive force generated by the magnetic fields opposite in adjacent conductors. The transient magnetic field induces eddy currents in the metal sheet, which create a magnetic field opposite. Intense and fast repulsive forces will act on the workpiece, accelerating it at high speed [2].

Several studies have started from this premise, but most involve specific situations for deformation of tubular parts by solenoid coils, while few studies have analysed sheet metal forming by planar coils [1].

The mechanical and electromagnetic phenomena of the process are strongly interrelated, and the deformation of the sheet metal affects the magnetic field and, consequently, the Lorentz forces developed. An approximate but more realizable approach is to treat the process as a loosely coupled problem, disregarding the influence of deformation of the workpiece in the evolution of the magnetic field, and then apply the forces generated by the electromagnetic field in the mechanical problem [2].

This work will show a mathematical model of the electromagnetic forming system and numerical methods for solving a specific problem at the initial time before plastic deformation of circular metal sheets by using a flat spiral coil. The method used approximates the flat spiral coil for circular and coaxial conductors, and the sheet metal is discretized in elementary segments of circular and coaxial conductors. The magnetic field produced can be calculated by applying the law of Biot-Savart. This discretization of the workpiece allows the calculation of the electromagnetic coupling between actuator coil and workpiece. The system to be represented by a set of differential equations where the electromagnetic problem is formulated in terms of the magnetic field and the electrical problem is a circuit with mutual inductances. Experimental results are also presented for different thicknesses of aluminum plates and the results are compared with numerical solution of mathematical model in Matlab software.

2 Description of the Electromagnetic Problem

A schematic model of the system analyzed is shown in Figure 1, which shows a circular clamped metal sheet is placed above a flat spiral coil connected to a charged capacitor. The calculations of the electromagnetic problem use a method based on discretization of the metal sheet in a number of circular elementary conductors for axisymmetric configuration.

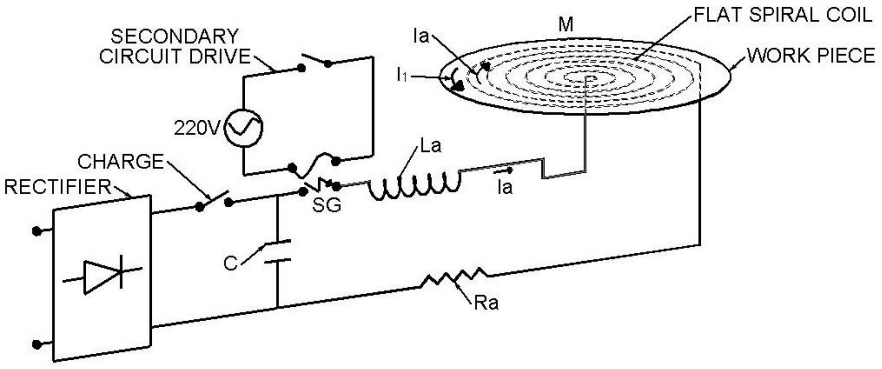

***Figure 1**: Scheme of the electromagnetic forming system.*

The transient electromagnetic problem can be separated in a RLC primary circuit coupled with secondary RL circuit [4], [5]. The discharge of the capacitor in the primary circuit can be written in differential equation:

$$\frac{d}{dt}\left(L_a \cdot I_a + M \cdot I_1\right) + R_a \cdot I_a + V_c = 0 \tag{1}$$

Where L_a, R_a and V_c are the self inductance, resistance of actuator coil and electric potential in capacitor bank. M is the mutual inductance between the actuator coil and workpiece. I_a and I_1 is the discharge current in actuator coil and the induced current in workpiece.

For secondary RL circuit the differential equation is obtained:

$$\frac{d}{dt}\left(L_1 \cdot I_1 + M \cdot I_a\right) + R_1 \cdot I_1 = 0 \tag{2}$$

Where L_1 and R_1 are the self inductance and resistance of workpiece.

This set of differential equations is solved by a resident function of the software Matlab after the discretization of the metal sheet in a finite number of conductive turns.

3 Magnetic Field

The magnetic vector potential produced by the actuator coil can be computed by applying the Biot-Savart law. The transient discretization in time is needed to evaluate the magnetic field, the density of current in the actuator coil and the workpiece and the electromagnetic forces acting on the workpiece to each variation of the time [6].

3.1 Law of Biot-Savart for Calculation of the Magnetic Field Produced by a Circular Loop at any Point in Space

Figure 2 shows a conductor with circular geometry carrying current "I". Applying the Biot-Savart law the values of magnetic induction at the points p(x,y,z) of the space can be determined mathematically by equations (3), (4) and (5) in Cartesian coordinate system.

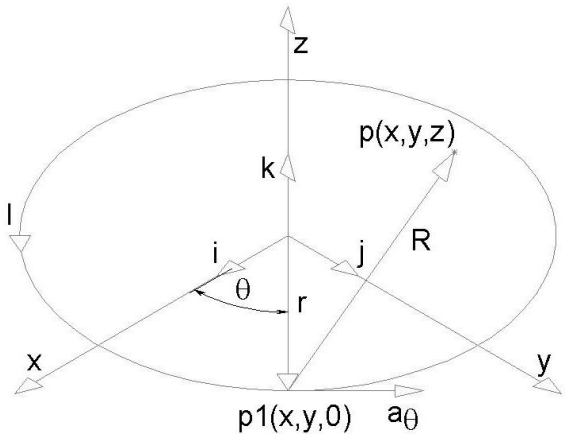

***Figure 2**: Representation of the circular conductor in cylindrical coordinates.*

$$Bx = \frac{\mu_0 \cdot I \cdot r \cdot z}{4 \cdot \pi} \cdot \int_0^{2 \cdot \pi} \frac{\cos\theta}{\left[x^2 + y^2 + z^2 + r^2 - 2 \cdot r \cdot \left(x \cdot \cos\theta + y \cdot \sin\theta\right)\right]^{3/2}} \cdot d\theta \qquad (3)$$

$$By = \frac{\mu_0 \cdot I \cdot r \cdot z}{4 \cdot \pi} \cdot \int_0^{2 \cdot \pi} \frac{\sin\theta}{\left[x^2 + y^2 + z^2 + r^2 - 2 \cdot r \cdot \left(x \cdot \cos\theta + y \cdot \sin\theta\right)\right]^{3/2}} \cdot d\theta \qquad (4)$$

$$Bz = \frac{\mu_0 \cdot I \cdot r}{4 \cdot \pi} \cdot \int_0^{2 \cdot \pi} \frac{r - y \cdot \sin\theta - x \cdot \cos\theta}{\left[x^2 + y^2 + z^2 + r^2 - 2 \cdot r \cdot \left(x \cdot \cos\theta + y \cdot \sin\theta\right)\right]^{3/2}} \cdot d\theta \qquad (5)$$

Or in cylindrical coordinate system:

$$Br = \frac{\mu_0 \cdot I \cdot z \cdot r}{4 \cdot \pi} \cdot \int_0^{2 \cdot \pi} \frac{\cos(\theta - \alpha)}{\left[x^2 + y^2 + z^2 + r^2 - 2 \cdot r \cdot \left(x \cdot \cos\theta + y \cdot \sin\theta\right)\right]^{3/2}} \cdot d\theta \qquad (6)$$

$$B_{\alpha} = \frac{\mu_0 \cdot I \cdot z \cdot r}{4 \cdot \pi} \cdot \int_0^{2 \cdot \pi} \frac{\sin(\theta - \alpha)}{\left[x^2 + y^2 + z^2 + r^2 - 2 \cdot r \cdot \left(x \cdot \cos\theta + y \cdot \sin\theta \right) \right]^{3/2}} \cdot d\theta \qquad (7)$$

$$Bz = \frac{\mu_0 \cdot I \cdot r}{4 \cdot \pi} \cdot \int_0^{2 \cdot \pi} \frac{r - y \cdot \sin\theta - x \cdot \cos\theta}{\left[x^2 + y^2 + z^2 + r^2 - 2 \cdot r \cdot \left(x \cdot \cos\theta + y \cdot \sin\theta \right) \right]^{3/2}} \cdot d\theta \qquad (8)$$

Where μ_0 is a magnetic constant equal to $4 \cdot \pi \cdot 10^{-7}$ [H/m].

$$\alpha = arctg\left(\frac{By}{Bx} \right) = arctg\left(\frac{y}{x} \right) \qquad (9)$$

Equations (6), (7) and (8) are used to calculate the three components of the vector density of magnetic field B at the point p in cylindrical coordinates. These equations can be solved analytically only for points located in the center of the circular geometry and p (0,0,z). This study uses resident functions in software Matlab for the numerical solution of the integral for equations above. Figure 3 shows the actual actuator coil and the simplified model with coaxial circular conductors.

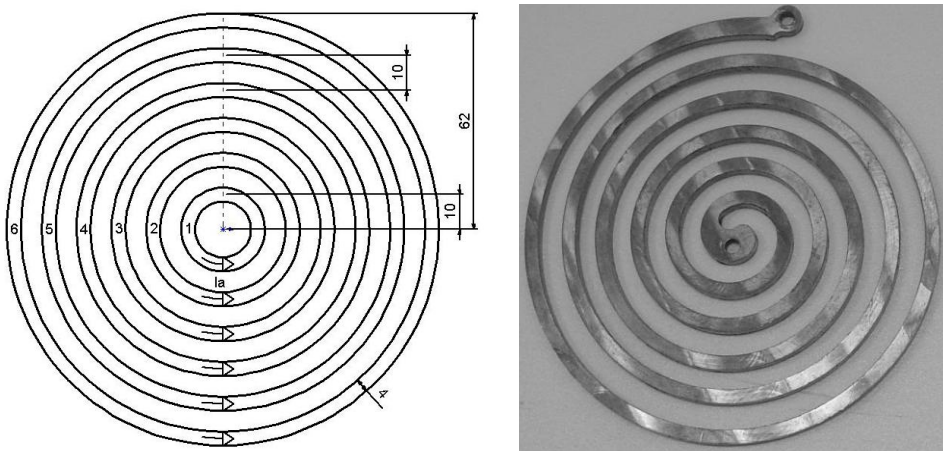

***Figure 3**: Simplified and actual model of the flat spiral coil used in this study*

Figure 4 shows the magnetic field generated by ampere in plane of the metal sheet in the radial direction. Considering the symmetry of the problem, these values are same at any radial direction.

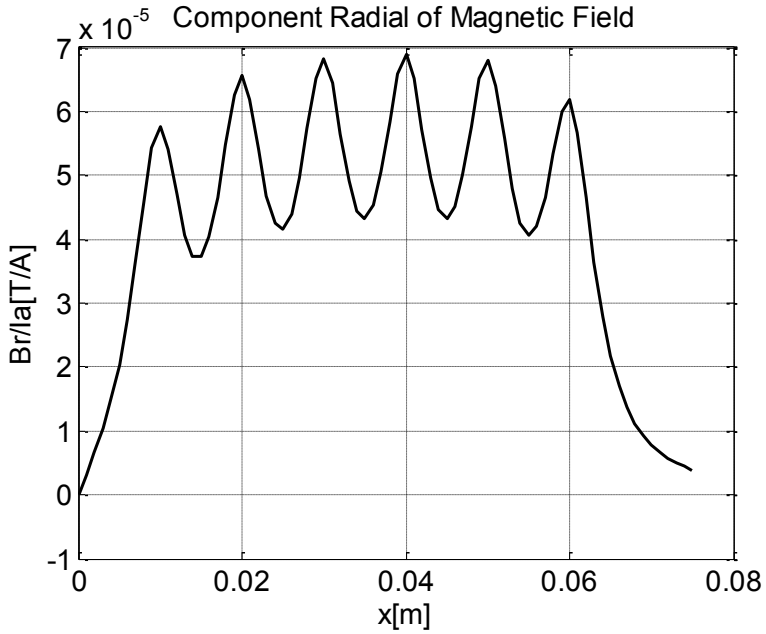

***Figure 4**: Component radial of magnetic field of different thickness.*

3.2 Calculation of the electromagnetic force

The metal sheet is discretized in coaxial circular elementary conductors (L1, L2...L12), where L1 and L12 are the outer diameter and inner diameter respectively. The greater the number of circular elementary conductors the more accurate the model is but more processing is needed. The electromagnetic force generated by each circular conductor can be calculated by:

$$F_n = Br \cdot I_a \cdot I_n \cdot C_n \tag{10}$$

Where F_n, Br, I_a, I_n, C_n are the force in circular conductor n of the workpiece, the magnetic field in radial direction, the discharge current in actuator coil, the induced current in conductor n of the workpiece and length of the circular conductor n of the workpiece.

4 Parameters of the Electromagnetic Forming System

With the aid of preliminary analysis using mathematical model, a system of electromagnetic forming was developed for deep drawing of thin circular metal sheets by using a flat spiral coil. More information about the characteristics of the system are shown in Figure 5 and Table 1.

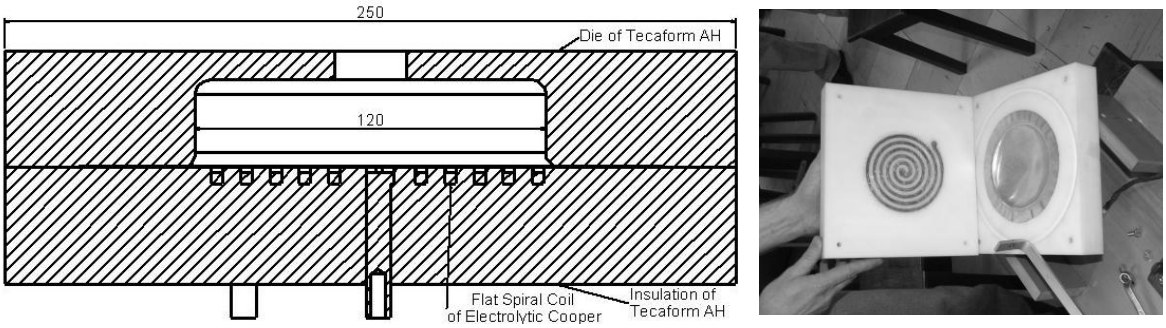

***Figure 5**: Die of electromagnetic forming device.*

Equipment	Parameter	Value
Actuator Coil of Electrolytic Cooper	Numbers of turns	6
	Outer diameter	120mm
	Pitch	10mm
	Section of the wire	4 x 4mm
	Self inductance (L_a)	1.0326μH
	Resistance (R_a)	1.4mΩ
Bank of capacitors	Capacitance	8400μF
	Maximum voltage	900V
	Maximum energy	3.4kJ
Metal Sheet	Material	Aluminium
	Thickness analyzed	0.3, 0.5 e 1mm
	Diameter of metal sheet	170mm
	Resistivity	$2.82 \cdot 10^{-5}\,\Omega$.mm
	Gap between actuator and metal sheet	1.5mm

Table 1: System parameters and working conditions.

5 Numerical Simulation and Experimental Results

The system of ordinary differential equations and integrates of magnetic field was solved with numerical method in software Matlab. The component in direction z of magnetic field is important to calculate the self and mutual inductances and the component in radial direction is used to calculate the electromagnetic force in direction z. The electromagnetic system shown schematically in Figure 1 with its parameters given in Table 1, has been simulated and some of the results obtained are shown in the following figures. Figure 6 shows the simulated current in the coil (Ia) and the induced current in the workpiece that is discretized in twelve circular coaxial conductors, being that the index one is the smallest conductor. Figure 6 shows only the induced current in the conductor eight (I8), which has the highest induced current and diameter equal to 80mm.

Figure 6 we can verify that the peak of electric current in the actuator remained almost constant for thicknesses of 0.3mm, 0.5mm and 1mm. The biggest changes occur in the induced currents in the elementary circular conductors of metal sheet, which shows fairly consistent, because the resistance of the elementary conductors of workpiece are strongly altered by the thickness. It is also observed that the different phase between the

current in the coil and in the metal sheet is higher for thinner sheet and that the discharge occurs more rapidly when decreasing the resistance of the workpiece by increasing the thickness of it.

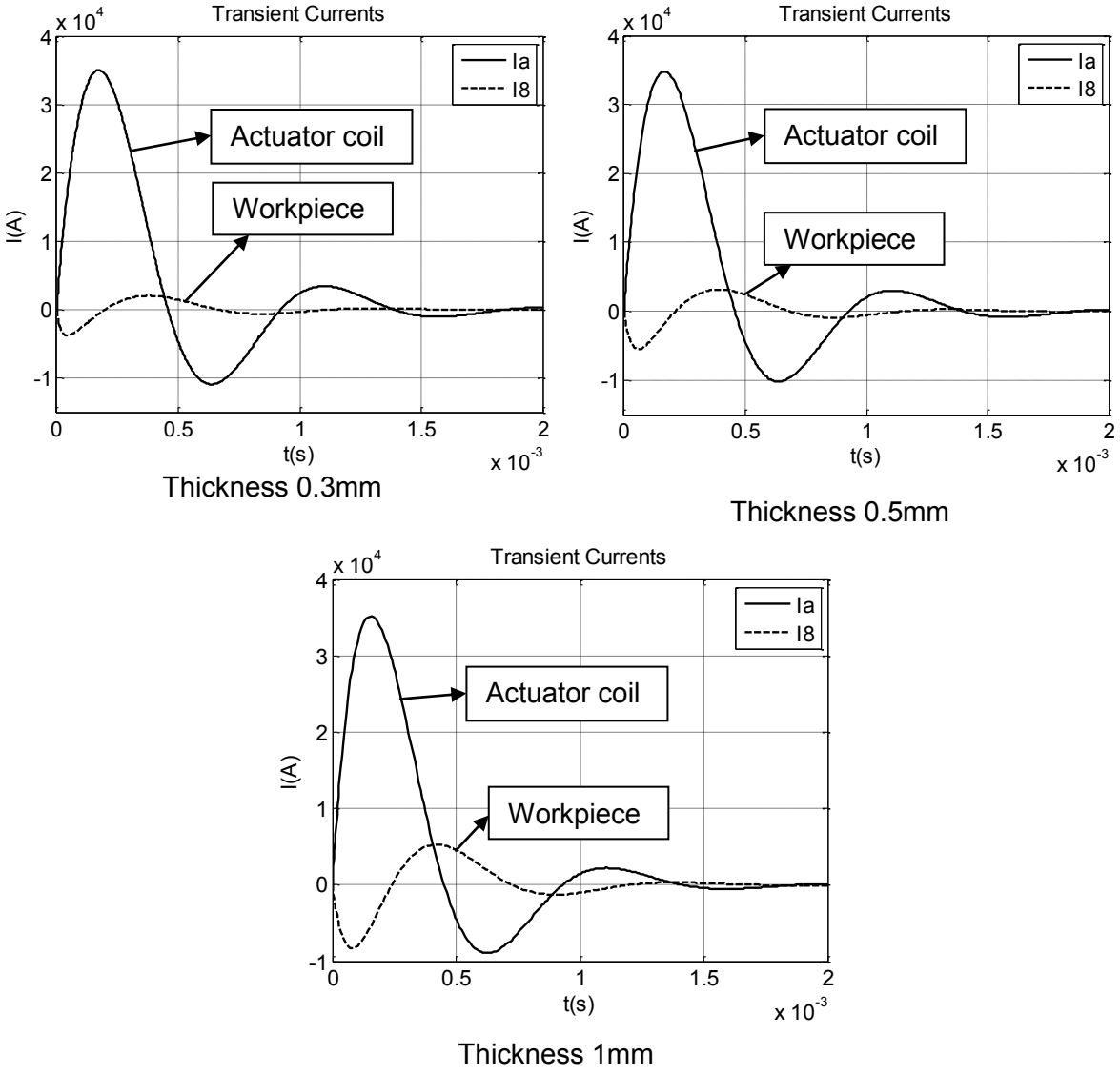

***Figure 6**: Simulated currents in the actuator coil and in the workpiece.*

The system behaves as a RLC circuit underdamped and the currents in the source coil and workpiece are opposite. The first peak of the induced currents are around -0.38kA, -0.55kA and -0.83kA. Figure 7 is shows the axial maximum transient electromagnetic force and we can see that considerable forces are developed in this process and that more difference phase between the current in the actuator coil and currents in workpiece causes a greater back electromagnetic force when it's compared with electromagnetic force of repulsion. This shows that back electromagnetic force is more in thinner metal sheets.

The energy for total deep drawing of plates analyzed by conventional methods is equal to 237, 503, 1582 Joules [7]. Comparing these values with the energy stored in capacitors shows that much of this available energy already is dissipated in the equivalent resistance of primary circuit.

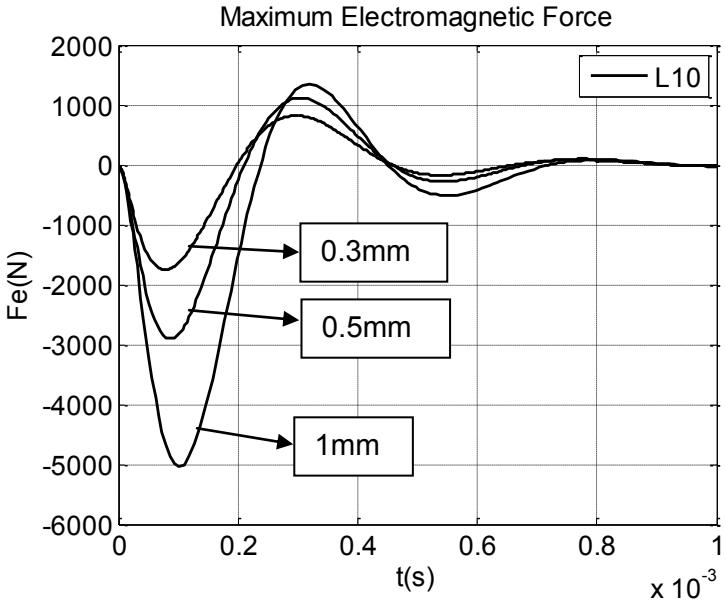

***Figure 7**: EM forces in the actuator coil and in the plate.*

Figure 8 shows the distribution of the peak repulsive force for axisymmetric problem. Figure 9 shows experimental results for different thicknesses.

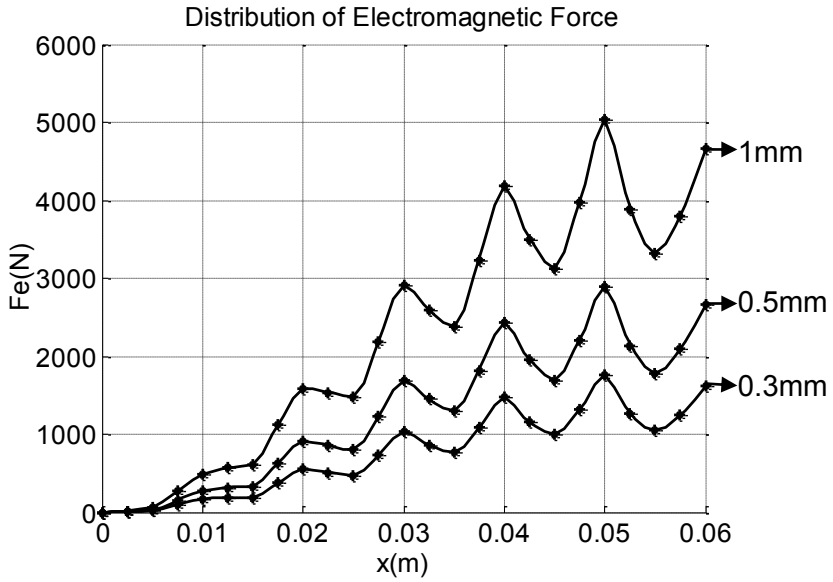

***Figure 8**: Distribution of the peak repulsive electromagnetic force.*

Thickness 0.3mm | Thickness 0.5mm | Thickness 1mm

***Figure 9**: Experimental results for different thicknesses.*

6 Conclusions

It can be observed in practical experiments that the back electromagnetic force in thinner metal sheets made it unable to form electromagnetically with the system proposed in this paper. This work developed a numerical method which can simulate the electromagnetic forming of metal sheets in initial time before plastic deformation. This algorithm was implemented in software Matlab. This mathematic model showed satisfactory results when compared with experiments, validating it and the method of numerical solution. In this algorithm the process parameters can be easily changed to obtain better results, and theories used in the construction of this algorithm are easily evidenced in it. This facilitates the understanding of the electromagnetic problem and results obtained are satisfactory and can be used for design flat spiral coils. This mathematical modeling was used as a basis for designing an experimental machine for electromagnetic forming.

References

[1] *Takatsu N., Kato M., Sato K., and Tobe T.:* High speed forming of metal sheets by electromagnetic force. J.S.M.E. International Journal, vol. 31, no. 1, p. 142-148, 1988.

[2] *Mamalis, A. G., Manolakos, D. E., Kladas, A. G., Koumoutsos, A. K., Ovchinnikov, S. G.*: Electromagnetic forming of aluminum alloy sheet using a grooved die: numerical modeling. The Physics of Metals and Metallography, Vol. 102, Suppl. 1, p. S90–S93, 2006.

[3] *Boutana, I., Mekideche, M. R.*: Simulation of aluminum sheet electromagnetic forming with several dies. Systems, Signals and Devices, 2008. IEEE SSD 2008. 5th International Multi-Conference on, p.1-6, July 2008.

[4] *Kamal, Manish*: A uniform pressure electromagnetic actuator for forming flat sheets. Dissertation of Graduate Program in Materials Science and Engineering School of the Ohio State University, 2005.

[5] *Shang, Jianhui*: Electromagnetically assisted sheet metal stamping. School of The Ohio State University, 2006.

[6] *Meriched, A., Feliachi, M., Mohellebi, H.*: Electromagnetic forming of thin metal Sheets. Magnetics, IEEE Transactions on, vol.36, no.4, p.1808-1811, 2000.

[7] *Lange, K.*: Handbook of Metal Forming. Michigan, Society of Manufactures Engineers (SME), 1994.

[8] *Paese, E.*: Electromagnetic Forming of Thin Metal Sheets: Technical Feasibility. MSc Thesis (in Portuguese), Universidade Federal do Rio Grande do Sul, Brazil, 2010.

[9] *Xu, W.; Fang, h.; Xu, W.*:Analysis of the Variation Regularity of the Parameters of the Discharge Circuit with the Distance Between Workpiece and Inductor for Electromagnetic Forming Processes. journal of materials processing technology 203 (2008) 216–220.

[10] http://www.epcos.com/inf/20/30/db/aec_09/B43456__B43458.pdf, last access on 02/23/2010.

Characterization and Simulation of High-Speed-Deformation-Processes*

M. Engelhardt[1], H. von Senden genannt Haverkamp[1], Y.Kiliclar[2], M. Schwarze[2], I. Vladimirov[2], D. Bormann[1], F.-W. Bach[1], S. Reese[2]

[1] Institute of Materials Science, Leibniz University Hannover, Hannover, Germany
[2] Institute of Applied Mechanics, RWTH Aachen University, Aachen, Germany

Abstract

The combination of the processes deep drawing and electromagnetic pulse forming is a promising way to cope with the ever higher complexity of new sheet metal designs. A cooperation between the Institute of Materials Science (IW) of the Leibniz Universität Hannover and the Institute of Applied Mechanics (IFAM) of the RWTH Aachen is investigating these processes both experimental and in simulation. Aim is the characterization of the combined process. Therefore the material properties of the investigated aluminum alloy EN AW 6082 T6 have to be determined quasi-static as well as at high speed. These properties are then used as a basic for the simulations. Anisotropic behaviors as well as dynamic hardening effects are investigated in the quasi-static state. Several experiments for analyzing "Bauschinger" respectively "Ratcheting effects" have been conducted resulting in a new measuring set-up for thin sheets. For the determination of high speed forming limit diagrams a novel testing device on the basis of the Nakajima-test has been developed allowing for strain rates of approximately 10^3 s^{-1}. Both testing methods are described in this paper; the results are then used to adapt the simulation models for the combined processes.

The high speed deformation process is simulated by means of finite elements using a material model developed at the IFAM. The finite strain constitutive model combines nonlinear kinematic and isotropic hardening and is derived in a thermodynamic setting. It is based on the multiplicative split of the deformation gradient in the context of hyperelasticity. The kinematic hardening component represents a continuum extension of the classical rheological model of Armstrong–Frederick kinematic hardening which is widely adopted as capable of representing the above metal hardening effects. To prevent locking

---

* *This work is based on the results of PAK 343 "Hochgeschwindigkeitsblechumformung"; the authors would like to thank the "Deutsche Forschungsgemeinschaft DFG" for its financial support*

of the simulated thin sheets a new eight-node solid-shell finite element based on reduced integration with hourglass stabilization developed at IFAM has been used. With these features it was possible to simulate the Bauschinger effect obtained by the previous experiments.

Keywords

deep drawing, simulation, material properties

1 Introduction

It is known that the processing limits of single processes can be enhanced through a combination of them [1] [2] [3]. Complex deep drawing geometries for example can be processed through a combination of superplastic forming above the recrystallization temperature with a subsequent cold forming process [1]. Superplastic forming allows for forming complex structures while the following conventional deep drawing process in conjunction with strain hardening gives the required mechanical properties. Experiments with pultruded tubes showed that a combination of electro-hydraulic pre-strain with further quasi-static forming can enhance the ultimate strains at lower yield stresses [4].

Throughout the last decades researchers have proven that the formability of all kind of materials can be improved due to high speed deformation processes [5]. El-Magd et al. tested light metals (Al-, Mg- and Ti-alloys) and steels at quasi-static and dynamic loading between 10^{-4} 1/s and 5 x 10^{3} 1/s and proved an increase in flow stress and formability at higher strain rates [6] [7].

For the characterization and simulation of this new field of combined quasi-static and high-speed-deformation-processes the determination of material properties for both processes is essential. The special mannerism of the combined processes investigated within this project is very complex thus not only dynamic and static properties, hardening behaviors and forming limits have to be specified but also the different load paths and strain rates have to be included. While re-loading a specimen on the same load path has no influence on the initial flow stress of a DC06 steel concludes the re-loading in opposite direction in a decrease of the initial flow stress [8]. An unbalanced loading ($\sigma_{mean} \neq 0$ MPa) for instance results in a summation of the realized strains [9]. These effects are called the „Bauschinger"- respectively the „Ratcheting"-effect.

With increasing availability of fast computer hardware the finite element method is used more and more effectively to predict and simulate material behavior. In order to reduce computational time, a new efficient finite element technology is developed. To simulate this, the use of a purely isotropic hardening model (expansion of the yield surface) is not sufficient. Therefore, a finite strain constitutive model which combines nonlinear kinematic and isotropic hardening, based on the multiplicative split of the deformation gradient, developed in a recent work by Vladimirov et al. [10], is used in this work. The papers Choi et al. [11], Dettmer & Reese [12], Hakansson et al. [13], Menzel et al. [14], Svendsen et al. [15], Wallin et al. [16] are dealing with this subject.

Beside the dynamic material properties an appropriate model has to consider forming limits for all appropriate load paths and, especially in this case, strain rates. Forming limit diagrams respectively the forming limit curves are normally used to describe the form-

ing limits of one material. Within this diagram it is possible to determine the maximum deformation a material can bear for a certain combination of major and minor strain, the load path.

2 Material characterization

The following paragraphs focus on the development of testing methods used for the material characterization within the scope of this project. Investigated were the evaluation of dynamic hardening effects and high-speed forming limits of thin sheet metals.

2.1 Dynamic material properties

For describing dynamic hardening and softening effects of metallic materials a variety of testing methods is available. Torsion or bending tests can be used to describe these effects with the possibility of testing thin sheet materials without the risk of buckling or the like. The problem with this type of testing is that the results have to be processed further to gain the material properties equivalent to the commonly used tensile testing method. While cyclic tension-compression testing gives the possibility to determine the Bauschinger and Ratcheting effect directly the experiment set-up has to be adapted to prevent buckling of the specimens whilst compressive loading. To circumvent the problem of buckling two different methods are used in recent years. The first possibility is to use guidings the second is to miniaturize the specimens. While the first requires adequate lubrication and tolerances of the guiding the latter puts high demands on the measuring method. For the testing of the thin rolled sheets of the Aluminum alloy EN AW 6082 T6 used within this project micro specimens together with a micro tension-compression testing device make Kammrath & Weiss have been used. The advantage of said device is the possibility of online testing inside the institutes SEM. The geometry of the used specimens and the testing device are shown in Figure 1.

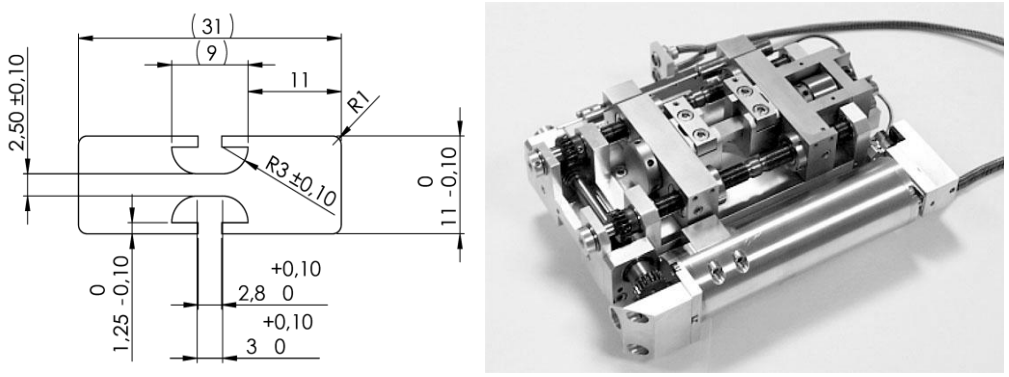

Figure 1: *Drawing and Dimensions of the specimens in mm (left) and picture of the testing device (right / Source: www.kammrath-weiss.com)*

To identify appropriate specimen dimension tests with measuring lengths of 10, 6 and 4 mm have been conducted. After inspection of the specimens only a measuring length of 4 mm showed adequate compression strains of up to 5 % without buckling. To ensure compression tests without buckling a measuring length of 3mm had been chosen for the following experiments.

After setting the specimen dimensions cyclic tension-compression tests inside a SEM were made. The testing inside the SEM was done due to the lack of a strain measuring device suitable for this kind of specimens. The device itself only has the possibility to measure the load and displacement of the clamps. While the calculation of the according stress is easy the conversion of the measured clamp displacement for getting the strain inside the specimen is not possible. Within the SEM it was possible to measure the actual strain by controlling the displacement of prominent areas on the surface of the specimen. A disadvantage of this method is that while the measurement is extensive the test has to be stopped for the time being. Thus the strains can only be determined incrementally. The resulting load-displacement plots of the testing device and the according stress-strain plots are shown in Figure 2. The first results have then been used for simulation of the dynamic behavior of the aluminum sheets in section 3.

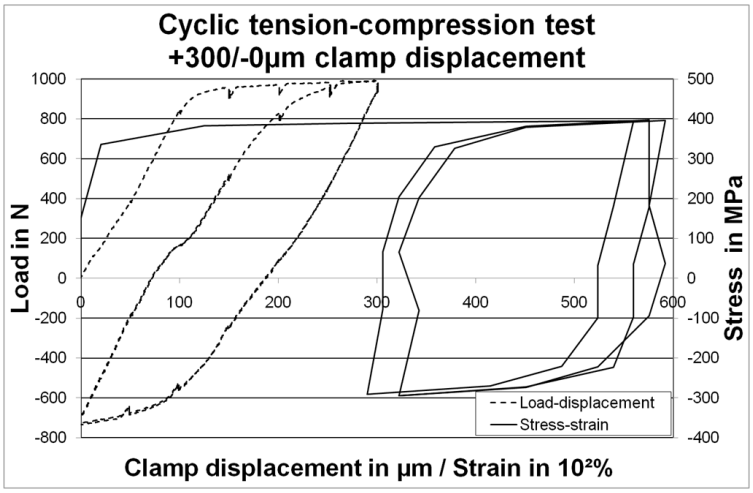

Figure 2: *Load-displacement and stress-strain curve of the testing inside the SEM*

Due to the lack of information needed for preparing the simulation between the SEM-measurements and the difficulties of getting an accurate measurement, a new method of measuring strains had to be looked for. In cooperation with the Laser Zentrum Hannover an electron speckle pattern interferometer was found as the best option for measuring strains online. The new experiment set-up is currently in the trial phase. The results of the new experiments will be published as soon as possible.

2.2 Investigations of high-speed forming limit diagrams

The knowledge of the formability of a material is a requirement for defining a production process. In sheet metal forming the forming limit diagram (FLD) is a means to characterize the maximum deformation a material can withstand prior to failure. Within the FLD the forming limit curve (FLC) depicts the maximum deformation to failure for different states of in-plane strains and stresses such as deep drawing, uniaxial state of stress, plain strain or plain state of stress. There are several procedures available for defining forming limit curves [17]. The most commonly used procedure is the Nakajima-test where a punch deforms a specimen clamped between a blank holder and the drawing die until fracture. The Nakajima-test is being standardized within the EN ISO 12004-2. The punch speed is defined at 1,5mm/s which is according to the hydraulic testing devices used. For defining

forming limit curves adapted to high-speed deformation processes new testing methods have to be developed.

To simulate deformation speeds equal to those at electro-magnetic pulse forming a punch speed of 100m/s or higher has to be applied. Recently published developments e.g. by Kim et al. report punch speeds of around 20m/s [18]. While these experiments already show a change in the FLDs for the tested materials, the punch speed still is at least one power of magnitude lower than is needed to simulate deformations equal to those in electro-magnetic pulse forming. Within this project it is anticipated to develop a novel testing device that is able to test at strain rates of $1000s^{-1}$ to $4000s^{-1}$ with the according punch speeds of 100m/s to 400m/s.

There are several possibilities to provide the energy needed to perform a Nakajima-test at these high speeds or strain rates like energy of rotation or hydraulic energy, as used for the experiments by Kim et al. [18]. While most of them are able to provide sufficient energy they require special equipment and machinery or big storage for saving the energy. A testing device (Figure 3) was developed within this project which increases deformation speed using conservation of momentum. A drop weight hits the impulse device and accelerates the punch until it hits the integrated stopper at the aimed penetration depth. Springback of the punch is not prevented but so far is to be considered as uncritical.

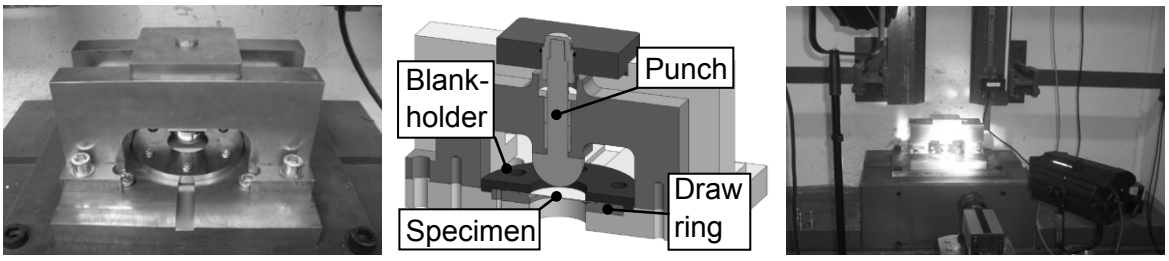

Figure 3: *Impulse device (left), CAD-model sectional view (middle) and test set-up (right)*

The testing was filmed via high-speed camera at 12500Hz to measure the punch displacement and the according speed as well as the occurring spring back. First tests with a drop weight of about 90kg and a drop height of 3m resulted in a max. punch speed of more than 90m/s. The impulse device and pictures of the high-speed camera are shown in Figure 4.

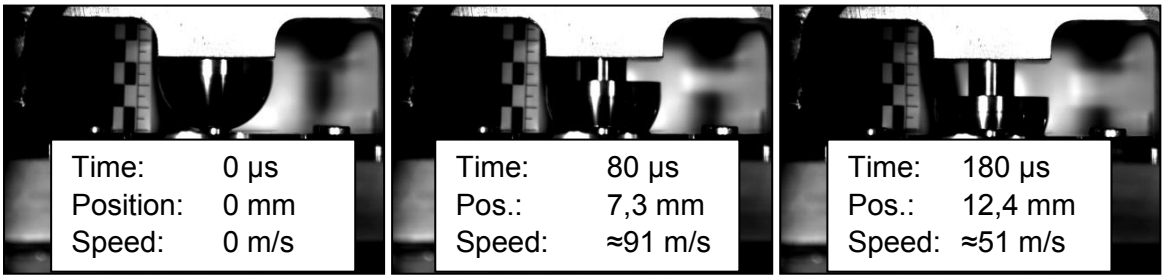

Figure 4: *Punch displacement of the impulse device during high speed forming*

According to EN ISO 12004-2, circular blanks with 100mm diameter in four different geometries were tested. The four geometries match the deformation states deep drawing ($\varphi 2 = -\varphi 1$), uniaxial tension ($\varphi 2 = -2\varphi 1$), plane strain ($\varphi 1 = 0$) and uniform stretch drawing ($\varphi 2 = \varphi 1$). Aluminum thin-sheets of the alloy EN AW 6082 T6 with 1mm thickness were

used. Additionally, hot rolled three-layer composite sheets made of EN AW 5754 with core layers of steel (1.4008) or titanium (grade 1) were used to examine the device's adequacy for testing more complex materials. Circular blanks were water jet cutted, the different specimen geometries were eroded afterwards. A single Teflon spray coating has been used to reduce friction between tool and specimen. The cracked specimens of the first experiments with four different geometries are shown in Figure 5.

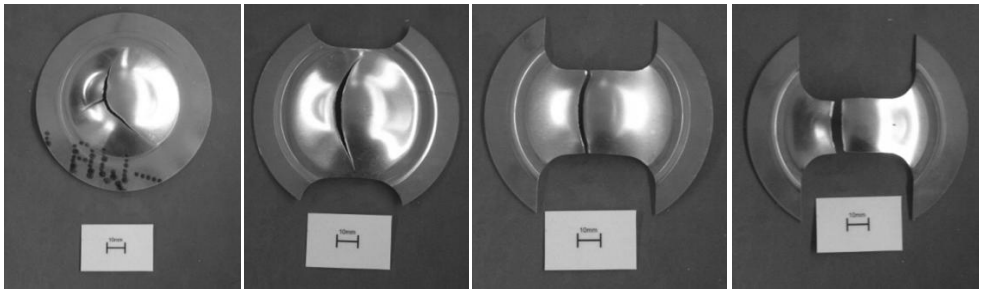

Figure 5: *Cracked specimens after testing*

The first step was to prove feasibility and to verify the demanded punch speeds. Evaluation of the optimal penetration depth of the tool in order to stop at beginning of crack opening as well as the strain analysis with an optical measurement system to deduce the forming limit diagrams will be subject of prospective investigations.

3 Simulation

The main goal is to build a new module for a realistic and numerically robust simulation with focus on contact modeling, the implementation of a plastic and a damage model and to demonstrate its applicability to simulate large deformations as the hardening behavior of materials e.g. the Bauschinger effect.

3.1 Material Modeling

The constitutive model is based on the multiplicative split $F_p = F_{pe}\, F_{pi}$ of the plastic deformation gradient into "elastic" and "inelastic" parts, $F = F_e\, F_p$ being the classical multiplicative split of F. As a result, a continuum mechanical extension of the classical rheological model of Armstrong-Frederick kinematic hardening [19] can be achieved.

The Helmholtz free energy per unit undeformed volume ψ is additively decomposed into the three parts $\psi = \psi_e(C_e) + \psi_{kin}\left(C_{pe}\right) + \psi_{iso}(\kappa)$. The first part ψ_e describes the macroscopic elastic material properties. The second term ψ_{kin} corresponds to the elastic energy stored in dislocation fields due to kinematic hardening and vanishes if the kinematic hardening is zero. The third term represents elastic energy due to isotropic hardening, where κ is the isotropic hardening variable. The Helmholtz free energy is a function of the elastic right Cauchy-Green tensor $C_e = F_e^T F_e = F_p^{-T} C F_p^{-1}$ and the elastic part of the plastic right Cauchy-Green tensor is defined as $C_{pe} = F_{pe}^T F_{pe} = F_{pi}^{-T} C F_{pi}^{-1}$.

Inserting this in the Clausius-Duhem inequality $-\dot{\psi} + S \cdot (1/2)\dot{C} \geq 0$ results in a relation for the second Piola-Kirchhoff stress tensor S.

The derivation of the material model is suitably carried out in the intermediate configuration. For the numerical implementation of the constitutive equations it is, however, more appropriate to work in the undeformed or reference configuration.

The set of constitutive equations of the model in the reference configuration is summarized below [20]:

- Stress tensors

$$S = 2F_p^{-1}\frac{\partial \psi_e}{\partial C_e}F_p^{-T},\ \ X = 2F_{pi}^{-1}\frac{\partial \psi_{kin}}{\partial C_{pe}}F_{pi}^{-T},\ \ Y = CS - C_pX,\ Y_{kin} = C_pX \tag{1}$$

- Evolution equations

$$\dot{C}_p = 2\dot{\lambda}\frac{Y^D C_p}{\sqrt{Y^D\cdot(Y^D)^T}},\ \ \dot{C}_{pi} = 2\dot{\lambda}\frac{b}{c}Y_{kin}^D\ C_{pi},\ \dot{\kappa} = \sqrt{\frac{2}{3}}\dot{\lambda} \tag{2}$$

- Yield function

$$\Phi = \sqrt{Y^D\cdot(Y^D)^T} - \sqrt{\frac{2}{3}}\left(\sigma_y - R\right),\ \ R = -Q(1-e^{-\beta\kappa}) \tag{3}$$

- Kuhn-Tucker conditions

$$\dot{\lambda} \geq 0,\ \Phi \leq 0,\ \ \dot{\lambda}\Phi = 0 \tag{4}$$

3.2 Finite element technology

Resent research focuses on the large deformation version of a new eight-node solid-shell finite element based on reduced integration with hourglass stabilization [21]. The major problem of low-order finite-elements used to simulate thin structures like sheet metal is locking, a nonphysical stiffening effect. Therefore in our recent solid-shell formulation the enhanced assumed strain (EAS) as well as the assumed natural strain (ANS) concept are implemented to circumvent locking. To cure transverse shear locking the corresponding transverse shear terms evaluated at locking-free sampling points are interpolated within the element domain. The same procedure applied to the transverse normal strain cures curvature thickness locking. For the EAS concept, the derivation is based on the well-established two-field variational functional

$$g_1(u, E_e) = \int_{B_0}\tilde{S}(E)\colon\delta E_c\ dV + g_{ext} = 0 \tag{5}$$

$$g_2(u, E_e) = \int_{B_0}\tilde{S}(E)\colon\delta E_e\ dV = 0 \tag{6}$$

which depends on the displacement vector u and the enhanced Green-Lagrange strain tensor E_e. In this enhanced strain tensor, the strain in thickness direction is enriched linearly. E_c is the compatible Green-Lagrange strain tensor. The EAS concept hence simplifies to a scalar equation, which leads to an efficient and robust element formulation.

Further important key points to improve the efficiency of the hourglass stabilization are different Taylor expansions with respect to the shell director.

The hourglass kernel C^{hg} depends on the material behavior in the integration point. The results of the following structural analysis carried out in ABAQUS have been obtained by means of this new eight-node-solid-shell element.

3.3 Uniaxial stress-strain test

As presented above, a large deformation elastoplastic material model with combined non-linear kinematic and isotropic hardening. It should describe the Bauschinger effect which belongs to the most characteristic phenomena of the hardening behavior of metals. The Bauschinger effect is defined by the fact that straining in one direction reduces the yield stress in the opposite direction.

Based on the experimental results of the Institute of Materials Science, Leibniz University Hanover, the model has been validated by fitting its parameters. A cycle of uniaxial tension/compression is shown in Figure 4, which depicts a good agreement between test and simulation data.

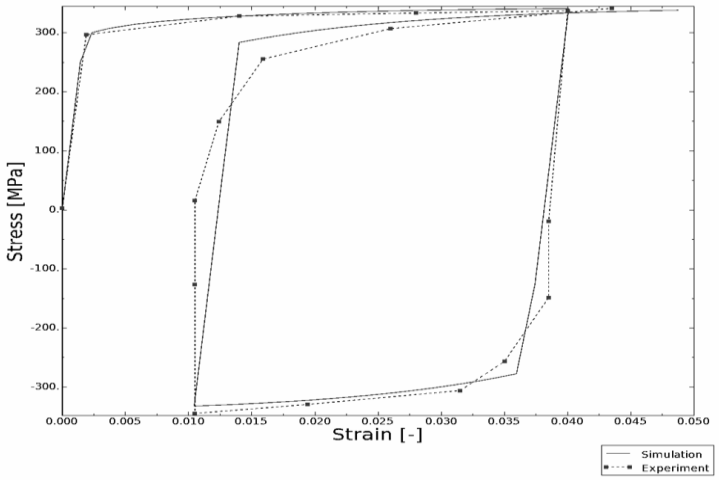

Figure 4: *Fit of material model for EN AW 6082 T6 sheet with thickness 1 mm, combined hardening*

According to the procedure used in [10], first the model is fitted based on the flow curve by using only kinematic hardening. This means, the isotropic hardening parameters β and Q are set equal to zero. At the second step, the fitting is performed by using only the isotropic hardening parameters. The kinematic hardening parameters (b and c) have in this case zero values.

Using this method, we obtain four "start" values for the hardening parameters. But as shown in Figure 4, only a combination of the four hardening parameters provides a good fit to the experimental data. The finally identified set of material parameters are: $\sigma_y = 296\,MPa,\ c = 2000\,MPa,\ Q = 11\,MPa,\ b = 70$ and $\beta = 200$.

Although a small deviation between experimental and simulation data is observed the correlation between the results can be considered to be very good. Certainly we need more complex (e.g. multiaxial) experiments to fully validate the model.

4 Discussion

The cyclic micro tension-compression tests beneath the critical unsupported length allow preventing buckling without any support. Any influence caused when using a support can be avoided. Main disadvantage is the small measuring length, which complicates mechanical or optical strain measurement on the specimens' surface. The first measurements of the Bauschinger effect using a SEM were problematic due to the lack of information be-

tween each measurement, a new method for measuring the strains using an electron speckle interferometer is tested right now. With this new measuring method together with the micro testing module it will be possible to realize the aimed compression-tension measurements at thin sheet metals.

The new device for high-speed Nakajima-testing enables punch speeds of 91m/s with the expected maximum speed being much higher. A disadvantage of this method is the strong springback of the punch. This causes a second impact of the tool on the tested sheet and may influence the results. More experiments are needed for verification. Testing of monolithic materials is possible. Composites are problematic for testing because failure mechanisms as delamination cannot be detected easily. The lubrication seems to be less important than in quasi-static testing but again more experience is needed for verification.

The simulation of dynamic effects shows good correlation with the experiments. The material model considering both kinematic and isotropic hardening works satisfactorily. Obviously, more experiments are needed to fully validate the model.

5 Summary and future work

The results of experiment and simulation can be referred to as follows:

- The modified cyclic micro tension-compression test is feasible for testing dynamic hardening effects
- The used measuring method needs to be optimized to gather more data
- The material model used for simulation allows to reproduce the experimental data satisfactorily but more experimental data is needed for further optimization
- The developed impulse device is capable of high-speed Nakajima-testing with punch speeds of 91 m/s and more
- The experimental setup works for monolithic materials; composite sheets cannot be tested satisfactorily due to their multiple failure mechanisms
- The lubrication seems to have less influence than in quasi-static testing, further experiments are needed for verification

Determination of forming limit curves and diagrams by means of optical measurement systems will be one focus of future investigations. The results of the simulation can only be improved with a better experimental data base thus more dynamic testing with improved strain measurements will be a further emphasis.

References

[1] *Siegert K.; Vulkan M.:* Superplastische Umformung von Aluminium-Blechen mit nachfolgendem hydromechanischem tiefziehen. In: 8. Sächsische Fachtagung Umformtechnik ISBN: 3-86012-158-8, S. 251-271, 2001.

[2] *Vohnout, V. J.:* A hybrid quasi-static / dynamic process for forming large sheet metal parts from aluminum alloys, Phd Thesis, Dept. of Industrial Systems and Welding Engineering, THE OHIO STATE UNIVERSITY, 1998.

[3] *Vohnout, V. J.; Daehn, G. S.:* Effect of quasi-static prestrain and eddy currents on limit strains in electromagnetic pulse forming of two aluminum alloys. IN: Aluminum 2002 – Proc. Of the TMS 2002 Annual Meeting, S. 19-26.

[4] *Fyfe, I. M.; Rajendran, A. M.:* Dynamic Pre-Strain and Inertia Effects on the Fracture of Metals. IN: Journal of Mech. Phys. Solids, Vol 28, pp. 17-26, 1980.

[5] *Wood, W.W.:* Experimental Mechanics at Velocity Extremes – Very High Strain Rates; Experimental Mechanics;1967, S. 441-446.

[6] *El-Magd, E.:* Abouridouane, M.: Einfluss der Umformgeschwindigkeit und -temperatur auf das Umformvermögen metallischer Werkstoffe; Zeitschriftenartikel; Zeitschrift für Metallkunde 94. Jg., Nr. 6, 2003.

[7] *El-Magd, E.; Abouridouane, M.:* Characterization, modelling and simulation of deformation and fracture behaviour of the light-weight wrought alloys under high strain rate loading; Zeitschriftenartikel; International Journal of Impact Engineering Vol. 32, No. 5, 2006.

[8] *Bouvier, S.; Gardey, B.; Haddadi, H.; Teodosiu, C.:* Characterization of the deformation-induced plastic anisotropy of rolled sheets by using sequences of simple shear and uniaxial tensile tests, J. Mater. Process. Technol.174, pp.115-126, 2005.

[9] *Khan, A. S.; Huang, S.:* Continuum theory of plasticity, Wiley, New York, 1995.

[10] *Vladimirov I.N.:* Anisotropic material modelling with application to sheet metal forming, Dissertation, Technische Universität Braunschweig, Aachen, 2009.

[11] *Choi, Y.; Han, C.S.; Lee, J.K.; Wagoner, R.:* Modeling multi-axial deformation of planar anisotropic elasto-plastic materials, part I: Theory, International Journal of Plasticity, 22, 1745-1764, (2006).

[12] *Dettmer, W.; Reese, S.:* On the theoretical and numerical modelling of Armstrong-Frederick kinematic hardening in the finite strain regime, Computer Methods in Applied Mechanics and Engineering, 193**,** 87-116, (2004).

[13] *Hakansson, P.; Wallin, M.; Ristinmaa, M.:* Comparison of isotropic hardening and kinematic hardening in thermoplasticity, International Journal of Plasticity, 21, 1435-1460, (2005).

[14] *Menzel, A.; Ekh, M.; Runesson, K.; Steinmann, P.:* A framework for multiplicative elastoplasticity with kinematic hardering coupled to anisotropic damage, International Journal of Plasticity, 21, 397-434, (2005).

[15] *Svendsen, B.; Levkovitch, V.; Wang, J.; Reusch, F.; Reese, S.:* Application of the concept of evolving structure tensors to the modeling of initial and induced anisotropy at large deformation, Computers & Structures, 84, 1077-1085, (2006).

[16] *Wallin, M.; Ristinmaa, M.:* Deformation gradient based kinematic hardening model, International Journal of Plasticity, 21, 2025-2050, (2005).

[17] *Lange, K.:* Handbuch der Umformtechnik. Bd. 3: Blechbearbeitung. Springer-Verlag Berlin, 1990.

[18] *Kim, S. B. et al.:* Forming limit diagram of auto-body steel sheets for high-speed sheet metal forming. in: Journal of Materials Processing Technology, Vol. In Press, Corrected Proof.

[19] *Frederick, Armstrong, PJ; CO:* A mathematical representation of the multiaxial Bauschinger effect, C.E.G.B. Report RD/B/N731, Berkeley Nuclear Laboratories, Berkeley, U.K. (1966).

[20] *Vladimirov, I.N.; Pietryga, M.P.; Reese, S.:* On the modelling of nonlinear kinematic hardening at finite strains with application to springback – comparison of time integration algorithms. International Journal for Numerical Methods in Engineering, 75, 1–28, (2008).

[21] *Schwarze, M.; Reese, S.:* A reduced integration solid-shell finite element based on the EAS and the ANS concept – geometrically linear problems. International Journal for Numerical Methods in Engineering, Vol. 80, 1322-1355, (2009).

Dimensional Control and Formability in Impact Forming

S. Srinivasan[1], H.Wang[1], G.A.Taber[1] and G. S. Daehn[1]

[1] Ohio State University 2041 College Rd, Columbus, Ohio, USA

Abstract

Electromagnetic forming (EMF) is a high speed forming technique that can be used for embossing fine surface features onto sheet metals. Here two coupled experimental and analytical studies show how interface conditions including rebound and friction affect the ability to create a component in impact forming. In the first part of this work high velocity is generated with the Uniform Pressure Actuator (UPA) and impact with a die emboss fine features in a nominally flat component. The primary objective of this work is to develop a modelling facility that guides experimental design nominally flat grooved components. Both shape fidelity and formability aspects are presently considered. In a second short study expansion of a round tube into a square hole is considered. Traditional modelling techniques solve a coupled system of equations with spatially varying electromagnetic fluxes controlling the dynamics of the plastic deformation. Because the magnetic pressure is spatially uniform, the flux equations are obviated from the coupled system rendering them computationally efficient. The calibration of contact mechanics that influence the rebound behaviour of the sheet metal remains as a difficult issue. The interfaces between various sheet metals and the metal die play a critical role in controlling the shape of the final product. The characterization of such an interface using appropriate calibrated friction coefficients is assessed. The role of magnetic pressure in reducing the sheet metal rebound is demonstrated via a comparison between results from mechanical and electromagnetic simulations. The influence of the channel geometry on final shape is illustrated through simulation and experiments.

Keywords

Electromagnetic forming, Numerical Simulation, Constitutive behaviour

1 Introduction

Electromagnetic forming uses the magnetic repulsion between two very large opposing currents to form sheet metal [1]. The punch is eliminated from the assembly and the sheet metal is driven into the die by its own inertia. Typical primary currents on the order of 100 kA with rise times of about 10μs are common and velocities within the range of 100-300 m/s are often achieved. The current investigation concerns high speed forming for the manufacture of grooved nominally flat plates. Understanding both the correspondence between the die shape and final part shape and ability to make the part without sheet rupture are paramount in a successful forming operation.
This study will consider two kinds of problems, first a more complex one dealing with the manufacture of a nominally flat plate with semi-circular grooves (Section 2). This will point out the need for simpler, more tractable problems. That motivates the much simpler, but still illuminating study of expansion of the proverbial round tube into a square hole that is considered in Section 3.

2 Impact Forming of Grooved Plates

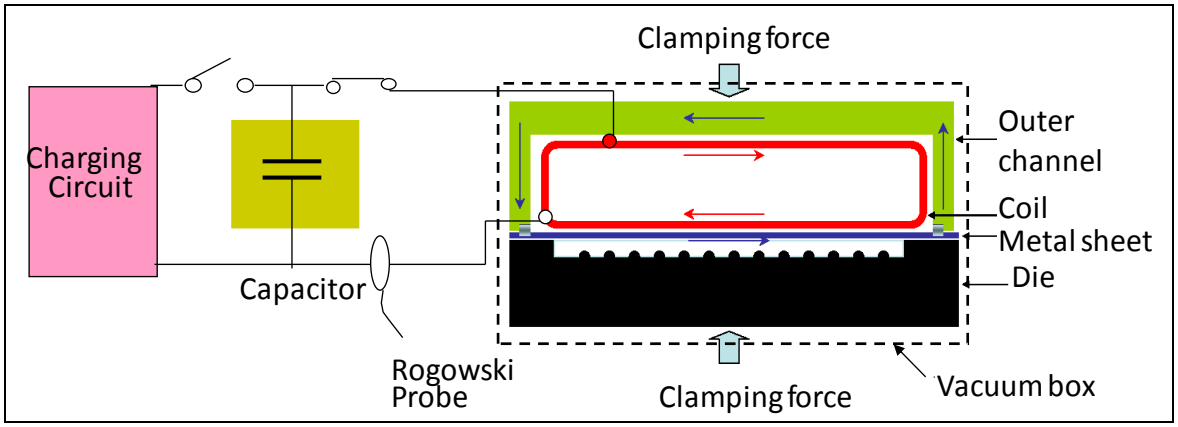

Figure 1: *Schematic of electromagnetic forming for grooved plates (Kamal & Daehn, 2007)*

2.1 Experimental Setup

The experiment system consists of a 16 kJ capacitor bank, helical copper coil, uniform pressure coil, a cylindrical casing, a flat box casing, a square metal die cavity (2.25 inches), aluminium rings of inner radius 24 mm, width 10 mm and thickness 1.3 mm. The primary copper coil is embedded inside the casing by cast tooling grade urethane. The ring or sheet specimen as the case may be, sits on the casing to complete the secondary circuit. The separation distance between the specimen and the die is 3 mm. Figure 1 shows that a high electrical discharge from the capacitor bank charges the primary circuit embedded in the coil box. The primary current induces a secondary current in the metal blank. The two currents being opposite in nature generate repulsion high enough to drive the ring into the die. A photon Doppler velocimeter system [2] is used to measure velocities of the accelerating specimen. The overall utility, design and behavior of this UPA forming system have been described by Kamal [1] and Banik [6] previously.

2.2 Constitutive Models

Titanium sheets of thickness 0.003" were formed into a steel die with fine semicircular channels with depths of the order of 0.015 inches as shown in Figure 2. A copper driver sheet of thickness 0.006" was used to complete the secondary circuit owing to its high electrical conductivity. The copper driver provides pressure to the titanium sheet during the forming process, accelerating it and co-deforming with the titanium. The forming is accomplished under vacuum to eliminate the resistance to forming due to compressed air. The strain distributions from the simulation model have been superimposed on the experimental measurements in Figure 2. The simplified Johnson and Cook (J-C) model [3] as shown in equation (1) was selected to characterize the material behavior. This form was chosen for its relative simplicity and the absence of a clearly better simple model [4]. For simplicity, the influence of temperature on the flow stress was neglected [5]. The J-C form is represented as:

$$\sigma_y = \left(A + B\,\varepsilon^n\right)\left(1 + c \ln \dot{\varepsilon}\right) \tag{1}$$

Where σ_y represents the flow stress (applied force per unit area), *A* is the yield stress (transition from elastic to plastic regime), *B* and *n* are parameters corresponding to the strain hardening law, *c* is the strain-rate parameter, ε is the effective plastic strain, and $\dot{\varepsilon}$ is the strain-rate. The simplified failure law of Johnson-Cook involves a characteristic parameter i.e. the effective (von-Mises criterion) plastic strain at fracture (ε_f) shown in (2). Numerically, this implies that if the average strain (von-Mises criterion) in any grid element is greater than fracture strain then the element is deleted from the simulation.

$$\bar{\varepsilon} \geq \bar{\varepsilon}_f \qquad at\ failure \tag{2}$$

The strain rate sensitivity was used as an optimization parameter and its values are tabulated in *Table 1*.

2.3 Simulation

Simulations are carried out in the fully explicit simulator LS-DYNA. The boundary condition for the simulation is set using the magnetic pressure on the driver plate. This magnetic pressure is calibrated using the velocity of the flyer measured from the experiments using the PDV system described in section 2.1.

Specimen	A (MPa)	B (MPa)	n	*c*
Copper driver	100	150	0.3	0.06
Titanium	200	700	0.22	0.06
Steel (Die)	20	550	0.05	0.05

***Table 1**: Johnson-Cook parameters for titanium specimen and copper driver*

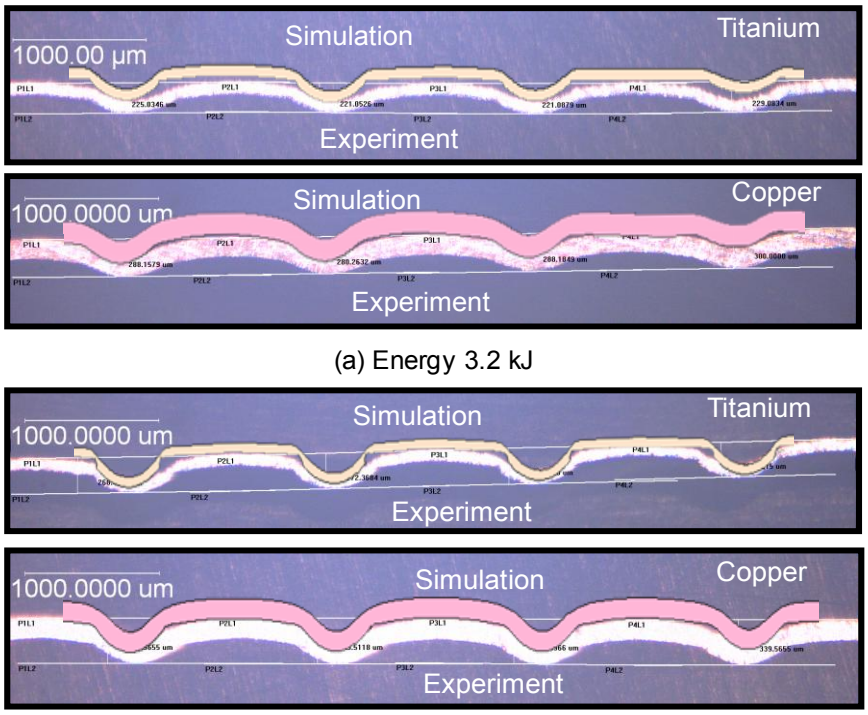

(a) Energy 3.2 kJ

(b) Energy 6.4 kJ

Figure 2: *Deformed specimens of titanium sheet and copper driver at two energies*

3 Effect of Friction on Quality of Formed Workpiece

3.1 Experimental Setup

The experiment system is identical to the one described in section 2.1. Experiments were conducted with austenitic stainless steels SS201 (instead of Titanium) and copper was used as a driver. *Figure 3* shows comparison between model and experiments for the SS201 sheets. The comparison for copper sheets is not shown. The same metal die described in section 2.1 was used. A lubricant such as boron nitride was used to study frictional effects on interfaces [6].

3.2 Mechanics

The contact interface between the two metal sheets and the die influences the impact dynamics and strongly affects local strain accumulation. It governs the efficiency of load transfer between components involved in the impact. Under normal conditions the frictional coefficient is high and ensures efficient load transfer between interfaces. This gives relatively uniform strain distributions. With the addition of lubricant, the friction coefficient is reduced and the propensity of relative lateral motion between the components is enhanced. This tends to cause strain localization at the die corners. Figure 3(b) shows that when lubrication is applied only between SS201 and the die there isn't very efficient transfer of energy between SS201 and the die. There is however good energy transfer between copper and SS201. This implies that a large proportion of the energy is absorbed by SS201 and thus there are 3 fractured zones. Figure 3(c) shows that when lubrication is applied on all surfaces large amount of the impact energy is absorbed

by copper driver (towards plastic flow and heating). A lower amount than in the cases of (a) and (b) is transferred onto SS201 or the die.

3.3 Simulation

The boundary conditions used in this model were identical to section 2.3. The pressure condition is calibrated against experimentally evaluated velocities (PDV system). The friction conditions in LS-DYNA factor in the contact cards that are used to describe the interface conditions. The CONTACT_AUTOMATIC_SURFACE_TO_SURFACE keyword was used to simulate all the interfaces (Details available in LS-DYNA manual 2006, http://lstc.com/manuals.htm). The Coulombic friction co-efficient was used in the simulation as shown in equation (3) below. The static and dynamic friction coefficients under normal conditions were 0.5 and that with lubrication were 0.05. The decay co-efficient was set to 0.1 for all cases.

$$\mu_{eff} = \left(\mu_{dynamic} + \left(\mu_{static} - \mu_{dynamic}\right) \bullet \left(e^{-\alpha \Box v_{rel}}\right)\right)$$

$$\mu_{eff} = \text{Effective frictional coefficient}; \alpha = \text{decay coefficient}$$

$$v_{rel} = \text{relative velocity between contacting bodies} \qquad (3)$$

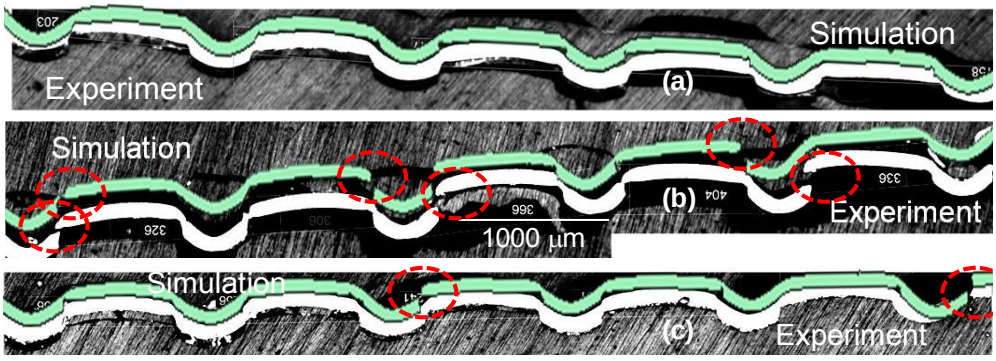

Figure 3: *Deformed specimens of SS201 sheet from simulation and experiment (Energy 4.8 kJ) (a) No lubrication (b) Lubrication between SS201 and Die (c) Lubrication on all interfaces*

Figure 3 only shows the comparison between experimental and model for austenitic steels SS201. The copper driver is not shown since SS201 is the product of concern. It is clear that the second case where lubrication is applied only between copper and SS201 has the maximum damage induced on the specimen. This is counterintuitive. The traditional expectation is that adding lubricants between interfaces prevents failure or damage and friction is often considered detrimental to the final product. However, under high speed conditions, it seems like the absence of friction is detrimental to the product shape and quality.

4 Constrained Ring Expansion

4.1 Objective

Experimental work in forming shallow pans with the UPA and similar driver systems has demonstrated that dimensional irregularities, failure and 'ghost lines' can often form away from the corners. A good example of this can be seen in [7]. Here a simple prototypical problem is considered and the numerical finite element model is validated against the experimental strain distributions and velocity measurements.

4.2 Experimental Setup

A circular aluminum ring was expanded into a steel square die. The experiment uses a 16 kJ capacitor bank (at maximum charging voltage of 8.66 kV), 5 turn helical copper coil, a cylindrical casing of outer radius 24 mm, a square metal die cavity (2.25 inches), aluminum rings of inner radius 24 mm, width 10 mm and thickness 1.3 mm. The primary copper coil is embedded inside the cylindrical casing by means of tooling grade urethane. The ring fits onto the casing to complete the secondary circuit. The standoff distance between the ring and the die cavity is 3 mm. Discharge from the capacitor bank charges the primary circuit embedded in the coil box. The primary current induces a secondary current in the metal blank. The two currents being opposite in nature generate repulsion high enough to drive the ring into the die.

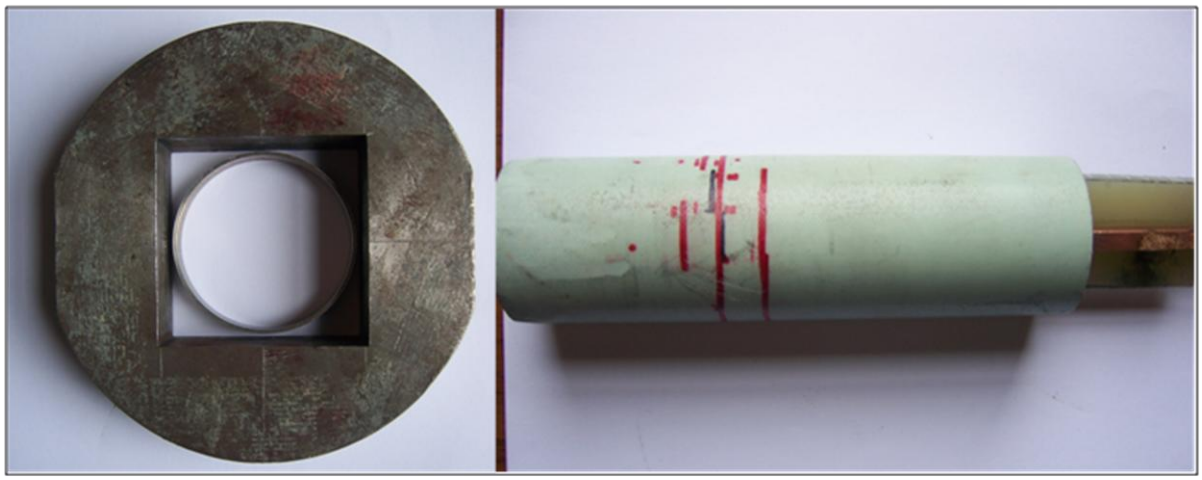

Figure 4: *Experimental setup of electromagnetic ring expansion (a) Square die (b) Helical coil*

4.3 Simulation

The traditional modeling algorithm [8] is divided into two coupled parts; electromagnetic flux equations and the mechanics governing plastic flow. The measured current from the capacitor bank sets the initial condition to the simulator. The entire system of equations is solved by the electromagnetic version of LS-DYNA [9]. In the subsequent cases, the electromagnetic component of the system of equations is excluded and a magnetic pressure boundary condition is applied to the ring. This method is identical to the sections described above. The pressure boundary condition is released at the onset of impact to let the ring flow plastically on account of its own inertia. The plastic strain at fracture as

described in equation (2) is inferred empirically from the relative change in cross sectional areas of the sheet metal specimen before and after impact. Two velocities were measured in the directions shown in *Figure 5* (b).

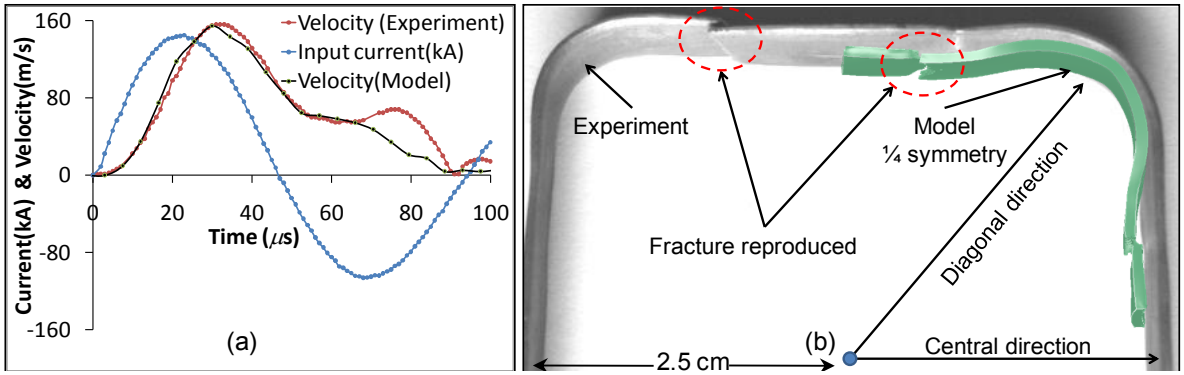

Figure 5: *(a) Input current and output velocity (b) Model vs. ring expansion experiments @ 5.6 kJ*

Figure 5 & *Figure 6* show the input current, the experimental and simulated impact velocities (along the diagonal direction only) and the comparison between the ring configurations after impact at two energies. The magnetic pressure (single constant value), inferred from the input current sets the input condition to the simulation. The impact velocities measured at two locations on the ring circumference in both the indicated directions help were used to calibrate the model. Both the simulations and experiment shows reduced propensity for failure at the higher impact energy. This is presumably because the sample strikes the die more uniformly [10]. Both the simulations and model show that there is a rebound phenomenon that produces a component that is far from square in the end and these rebounds drive the failure process.

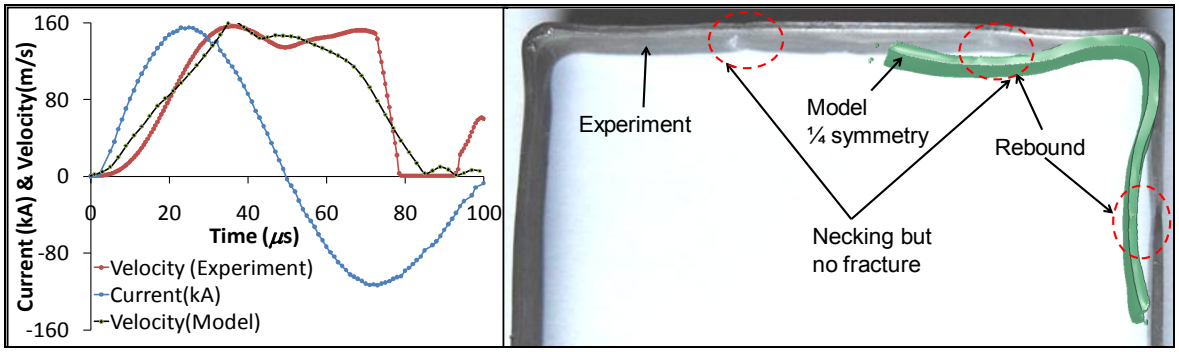

Figure 6: *(a) Input current and output velocity (b) Model vs. ring expansion experiments @ 7.2 kJ*

4.4 Results

In part (1) of *Figure 7*, as the ring strikes the square die, it rebounds and undergoes a rapid change in stress states (tensile to compressive in the circumferential direction). Meanwhile, the magnetic pressure causes the ring to advance in the diagonal direction. The intermediate region between the central and diagonal direction acts like a tensile

specimen. It necks and consequently fails under influence of a multiaxial stress states [11]. There is a complicated interaction between stress waves travelling towards each other as shown in *Figure 7*. In this process there is a strong interaction between the wave fronts subsequently followed by their energy dissipation (Part (2)). Part (4) shows the stress release upon fracture. The final shape of the product is not exactly the same as the square die. This is largely attributed to rebound of the ring from the edge of the die. There is a distinct similarity observed in the fracture paths from the simulation model and the experiments shown in Figure 8. Part of the kinetic energy of the ring has to be plastically dissipated in order to minimize the bounce-off.

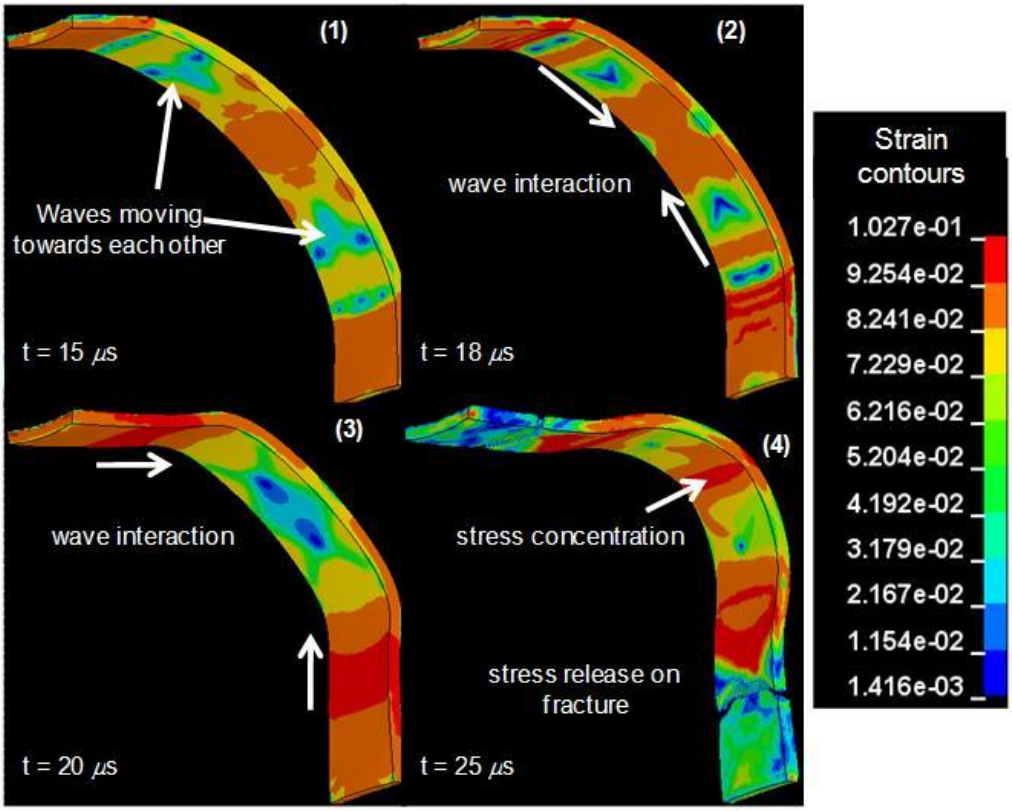

Figure 7: *Simulation results for the ring expansion (Effective von-Mises strain contours)*

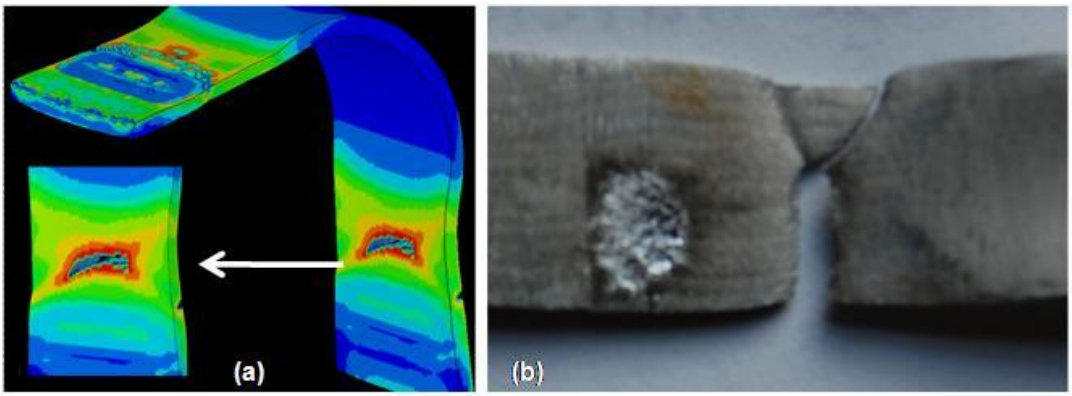

Figure 8: *X-shaped fracture patterns (a) Model (Effective von-Mises strain contours) (b) Experimental ring specimen*

4.5 Rebound Calibration

The rebound characteristics of sheet metal upon impact critically influence the shape conformity of the formed product. The qualitative comparison between the numerical model and formed specimens shown in Figure 5 reveal insights into the coupling between the electromagnetic and the mechanical process. The numerical model in general has higher rebound than the experimental product. This is because the pressure boundary condition is released upon contact to let the ring specimen fly on account of its own inertia. In reality, the specimen upon impact is stabilized against the square die by the magnetic pressure that prevents it from bouncing back. The measured velocity profiles in Figure 5 and Figure 6 show a trough followed by another peak in sync with the current profiles. The second peak is due to the magnetic pressure. The simulation model does not adequately portray this peak and shows a steady decline and manifests as a rebound. At low energy (5.6 kJ) the magnetic pressure begins its decline prior to the strike of the ring specimen (compare second peak in Figure 5 (a)). At 7.2 kJ, the second peak in velocity precedes that in current thus stabilizing the rebound effect and producing flatter parts. The magnetic pressure thus holds the part firmly against the die dissipating its kinetic energy into stress waves that traverse the circumference of the specimen.

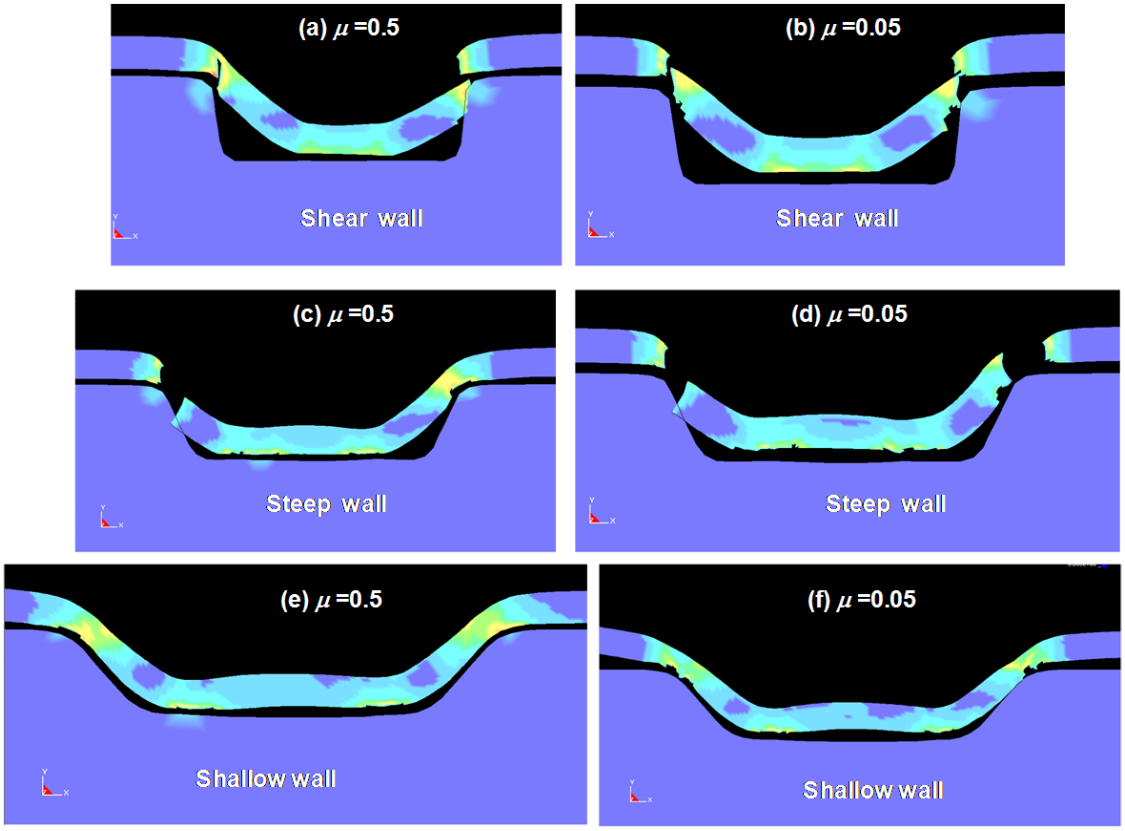

Figure 9: *Effect of entry wall angle and frictional coefficient (μ) on formed workpiece*

4.6 Effect of entry wall angle

The quality and shape of the formed sheet metal is highly dependent upon the entry wall angle of the die channels. A steeper angle increases the propensity for shear under high

speed impact. A shallower angle is beneficial for good shape conformity as shown in *Figure 9* (e) and (f). The effect of friction has been established from section 2.4. From *Figure 9* (c) and (d), it is evident that there is higher kinetic energy in the plate that causes material to flow into the cavity and consequently shear at the edges. For these cases, a secondary forming operation is essential to ensure better shape conformity.

5 Conclusions

1. In impact forming the shape of the component can vary significantly from the shape of the die upon which the sheet strikes. This is influenced by rebound of the specimen upon impact, friction between interfaces, geometry of the die (including the stiffness of the component produced) and the persistence of magnetic pressure after die strike. Rebound can be minimized by plastically dissipating the kinetic energy of the workpiece.
2. The ability to make a given shape with a specific material is closely related to frictional conditions in impact forming, as it is in traditional quasi-static forming. However, in impact forming high coefficients of friction are generally favored because draw-in is difficult in impact forming. The design strategy is to have each material segment maintain a path along its launch vector.
3. Failure mechanisms are attributed to interaction between stress and/or displacement waves, rapid change in stress states that lead into necking and consequent failure.
4. The entry wall angle plays a critical role in the shape conformity of sheet metal. For vertical shear walls, the formed shape is very different from the metal die shape. For steep angles a secondary forming operation is beneficial in improving the conformity.

References

[1] *Kamal, M. and G. S. Daehn.:* A Uniform Pressure Electromagnetic Actuator for Forming Flat Sheets." Journal of Manufacturing Science and Engineering 129(2): p.369, 2007

[2] *Strand, O. T., D. R. Goosman, et al.* Compact system for high-speed velocimetry using heterodyne techniques. Review of Scientific Instruments 77(8), p.083108., 2006

[3] *Johnson, G. R. and W. H. Cook*. Fracture characteristics of three metals subjected to various strains, strain rates, temperatures and pressures. Engineering Fracture Mechanics 21(1),p.31-48.,1985

[4] *Liang, R. and A. S. Khan*. A critical review of experimental results and constitutive models for BCC and FCC metals over a wide range of strain rates and temperatures. International Journal of Plasticity 15(9),p.963-980.,1999

[5] *Wang, Y. and Y. Xia*. Modeling of mechanical behavior of brass at high strain rates. Journal of Materials Science Letters 22(20),p.1393-1394.,2003

[6] *Banik, K. E.* Factors effecting electromagnetic flat sheet forming using the uniform pressure coil., Thesis, Ohio State University, 2008.

[7] *Kamal, M., J. Shang, et al.* Agile manufacturing of a micro-embossed case by a two-step electromagnetic forming process. Journal of Materials Processing Technology 190(1-3),p.41.2007

[8] *El-Azab, A., M. Garnich, et al.* Modeling of the electromagnetic forming of sheet metals: state-of-the-art and future needs. Journal of Materials Processing Technology 142(3),p.744.,2003

[9] *El-Azab, A., M. Garnich, et al.* Modeling of the electromagnetic forming of sheet metals: state-of-the-art and future needs. Journal of Materials Processing Technology 142(3),p.744.2003

[10] *Hu, X. and G. S. Daehn*. Effect of velocity on flow localization in tension. Acta Materialia 44(3),p.1021-1033.,1996

[11] *Imbert, J. M., S. L. Winkler, et al.* The Effect of Tool--Sheet Interaction on Damage Evolution in Electromagnetic Forming of Aluminum Alloy Sheet. Journal of Engineering Materials and Technology 127(1),p.145.,2005

An MPP version of the Electromagnetism module in LS-DYNA for 3D Coupled Mechanical-Thermal-Electromagnetic simulations

P. L'Eplattenier[1], C. Ashcraft[1], I. Ulacia[2]

[1] Livermore Software Technology Corporation, 7374 Las Positas Road, Livermore, CA 94551, USA.
[2] Mondragon Goi Eskola Politeknikoa, Mondragon Unibertsitatea, Loramendi 4, Mondragon 20500, Spain.

Abstract

LS-DYNA is a general multi-purpose explicit and implicit finite element program used to analyse the non-linear dynamic response of three-dimensional solids and fluids. It is developed by Livermore Software Technology Corporation (LSTC). A new electromagnetism module is being developed in LS-DYNA for coupled mechanical/thermal/electromagnetic simulations. One of the main applications of this module is Electromagnetic Metal Forming (EMF). The electromagnetic fields are solved using a Finite Element Method (FEM) for the conductors coupled with a Boundary Element Method (BEM) for the surrounding air/insulators. Both methods use elements based on discrete differential forms for improved accuracy.
Recently, a Massively Parallel Processing (MPP) version of the EM module was developed allowing sharing the CPU and memory between different processors and thus faster computations on larger problems. The implementation of the FEM and BEM in MPP will be presented.
Finally, the EM module will be illustrated on an actual EMF case. Experimental and numerical results will be compared and the speed-up of the MPP version will be studied.

Keywords

Modelling, Finite Element Method (FEM), Boundary Element Method (BEM)

1 Introduction

LS-DYNA is a general-purpose nonlinear finite element program that is capable of simulating complex real world problems [1]. The major development goal of Livermore Software Technology Corporation (LSTC) is to provide within LS-DYNA capabilities to seamlessly solve problems that require multi-physics, multiple-stages, and multi-

processing. LS-DYNA is suitable to investigate phenomena that involve large deformations, sophisticated material models and complex contact conditions. LS-DYNA allows running an analysis explicitly or implicitly and combining different disciplines such as coupled thermal analysis, fluid dynamics, fluid-structure interaction, SPH (Smooth Particle Hydrodynamics), EFG (Element Free Galerkin). Metal forming is one of LS-DYNA's main applications, with capabilities to simulate rolling, extrusion, forging, casting, spinning, ironing, super-plastic forming, sheet metal stamping, profile rolling, deep drawing, hydro-forming, multi-stage processing, springback, hemming [1].

An electromagnetism (EM) module is under development in LS-DYNA in order to perform coupled mechanical/thermal/electromagnetic simulations [2],[3],[4]. Electromagnetic Metal Forming (EMF) is the main application of this development, but other processes could also be simulated, where magnetic pressure induces mechanical stress and deformations and/or the Joule effect induces a heating process: magnetic metal cutting, magnetic metal welding, very high magnetic pressure generation, computation of the stresses and deformations in various coils, magnetic flux compression, induced heating and so forth. This module allows us to introduce some source electrical currents into solid conductors, and to compute the associated magnetic field, electric field, as well as induced currents. These fields are computed by solving the Maxwell equations in the eddy-current approximation. The Maxwell equations are solved using a Finite Element Method (FEM) [5] for the solid conductors coupled with a Boundary Element Method (BEM) [6] for the surrounding air (or insulators). Both the FEM and the BEM are based on discrete differential forms (Nedelec-like elements [7]).

The computation of the electromagnetic fields, and especially the BEM part, is very time consuming and requires a lot of memory. An MPP implementation [8],[9] allows reducing both the CPU time and the memory requirement by splitting them between different processors. An MPP version of the mechanical and thermal modules already exists in LS-DYNA. More recently, a Massively Parallel Processing (MPP) version of the EM module has been introduced, allowing coupled mechanical-thermal-electromagnetic simulations in MPP.

This paper is organized as follows: In part 2, we will present the physics of the EM part of the problem, its coupled finite element / boundary elements representation, and the respective solvers.

In part 3, the MPP implementation of the EM module will be presented, and in part 4, the MPP version will be illustrated on an EMF case. Numerical and experimental results will be compared and the speed-up of the MPP version will be studied.

2 Presentation of the model

In this section, we will present only the EM part of the model. For details on the Mechanical and Thermal parts, the reader should consult [1].

2.1 Presentation of the physics

Let Ω be a set of multiply connected conducting regions. The surrounding insulator exterior regions will be called Ω_e. The boundary between Ω and Ω_e is called Γ, and the (artificial) boundary on Ω at the end of the meshing region (hence where the conductors are connected to an external circuit) is called Γ_c. In the following, we will denote $\vec{n}$ as the

outward normal to surfaces Γ or Γ_c. The electrical conductivity, permeability and permittivity are called σ, μ and ε respectively. In Ω_e, we have $\sigma = 0$ and $\mu = \mu_0$.

We solve the Maxwell equations in the so called low frequency or "eddy-current" approximation, which is valid for good enough conductors with low frequency varying fields such that the condition $\varepsilon \frac{\partial \vec{E}}{\partial t} \prec\prec \sigma \vec{E}$, where $\vec{E}$ is the electric field, is satisfied. When using a vector potential $\vec{A}$ and scalar potential φ representation and using the Gauge condition $\vec{E} = -\vec{\nabla}\phi - \frac{\partial \vec{A}}{\partial t}$, we end up with the following system to solve [4],[10]:

$$\nabla \bullet \sigma \vec{\nabla} \phi = 0 \tag{1}$$

and

$$\sigma \frac{\partial \vec{A}}{\partial t} + \vec{\nabla} \times \frac{1}{\mu} \vec{\nabla} \times \vec{A} + \sigma \vec{\nabla} \phi = \vec{j}_S \tag{2}$$

Where $\vec{j}_S$ is a divergence free source current density.

2.2 The coupled Finite Element Method/Boundary Element Method

We use Nedelec "edge elements" [7] and call $W^0, \vec{W}^1, \vec{W}^2$, and W^3 the basis functions associated respectively with the 0, 1, 2, and 3-forms [11]. Equation (1) is projected against 0-forms basis functions and equation (2) against 1-forms to give, after using the appropriate Greens vector identities [11],[12],[13]:

$$\int_\Omega \sigma \vec{\nabla} \phi \bullet \vec{\nabla} W^0 d\Omega = 0 \tag{3}$$

$$\int_\Omega \sigma \frac{\partial \vec{A}}{\partial t} \bullet \vec{W}^1 d\Omega + \int_\Omega \frac{1}{\mu} \vec{\nabla} \times \vec{A} \bullet \vec{\nabla} \times \vec{W}^1 d\Omega = -\int_\Omega \sigma \vec{\nabla} \phi \bullet \vec{W}^1 d\Omega + \frac{1}{\mu} \int_\Gamma [\vec{n} \times (\vec{\nabla} \times \vec{A})] \bullet \vec{W}^1 d\Gamma \tag{4}$$

or equivalently after decomposing $\vec{A}$ and ϕ respectively on the 0-form and 1-form basis functions [4]:

$$S^0(\sigma)\varphi = 0 \tag{5}$$

$$M^1(\sigma)\frac{da}{dt} + S^1(\frac{1}{\mu})a = -D^{01}(\sigma)\varphi + Sa \tag{6}$$

Where we introduced the 0-form stiffness matrix S^0, the 1-form mass matrix M^1, the 1-form stiffness matrix S^1 and the 0-1 form derivative matrix D^{01}[13]. The last term of equation (6) which involves the "outside matrix stiffness" S is computed using a BEM [6]:
An intermediate variable "surface current" $\vec{k}$ is introduced. This surface current, defined on the boundary Γ is such that it produces the same vector potential (and thus $\vec{B}$ field) in the exterior regions Ω_e as the actual volume current flowing through the conductors [4],[14]:

$\vec{A}(x) = \frac{\mu_0}{4\pi} \int_\Gamma \frac{1}{|x-y|} \vec{k}(y) dy$ for all $x \in \Omega_e$ (and in particular for all $x \in \Gamma$). (7)

One then has:

$$[\vec{n} \times (\vec{\nabla} \times \vec{A})](x) = \frac{\mu_0}{2} \vec{k}(x) - \frac{\mu_0}{4\pi} \int_\Gamma \frac{1}{|x-y|^3} \vec{n} \times [(\vec{x} - \vec{y}) \times \vec{k}(y)] dy$$

for $x \to x_0 \in \Gamma$ (8)

When projecting these equations on the 1-forms basis functions for $\vec{A}$ and the "twisted" 1-forms $\vec{V}^1(x) = \vec{n} \times \vec{W}^1(x)$ for $\vec{k}$ one gets the following matrix equations [4]:

$$Pk = Da \tag{9}$$

$$Sa = Qk \equiv Q_S k + Q_D k \tag{10}$$

Where we introduced the BEM matrices

$$P_{i,j} = \frac{\mu_0}{4\pi} \iint_{\Gamma_x \Gamma_y} \frac{1}{|x-y|} \vec{V}_i^1(x) \bullet \vec{V}_j^1(y) d\Gamma_x d\Gamma_y \text{ , } D_{i,j} = \int_{\Gamma_x} \vec{V}_i^1(x) \bullet \vec{W}_j^1(x) d\Gamma_x \tag{11}$$

$$Q_{S\,i,j} = \frac{1}{2} \int_{\Gamma_x} \vec{W}_i^1(x) \bullet \vec{V}_j^1(x) d\Gamma_x \text{ ,} \tag{12}$$

$$Q_{D_{i,j}} = -\frac{1}{4\pi} \iint_{\Gamma_x \Gamma_y} \frac{1}{|x-y|^3} \vec{W}_i^1(x) \bullet \{\vec{n}_x \times [(\vec{x}-\vec{y}) \times \vec{V}_j^1(y)]\} d\Gamma_x d\Gamma_y \tag{13}$$

2.3 Domain decomposition

Contrarily to the FEM matrices, the BEM matrices P and Q_D are full dense and cannot be stored as dense arrays since the memory requirement would grow up very quickly with the size of the system. In order to limit the memory requirement, a domain decomposition is done on the BEM mesh, which splits the BEM matrices into submatrices. On the off-diagonal submatrices, a low rank approximation based on a rank revealing QR decomposition is performed [15],[16]. For submatrices corresponding to far away domains, the rank can be significantly smaller than the size of the submatrix, thus reducing the storage of the submatrix. We typically see reductions of by factors around 20 between the full dense matrix and the block matrix with low rank approximations. This low rank approximation also speeds up the matrix * vector operation used intensively in the iterative method to solve the BEM system (equation 9).

2.4 Solvers

The coupled FEM/BEM system is solved in an iterative way [4]:

$$Pk_{n+1}^{t+1} = Da_n^{t+1} \tag{14}$$

$$[M^1(\sigma) + dtS^1(\frac{1}{\mu})]a_{n+1}^{t+1} = M^1(\sigma)a^t - dtD^{01}(\sigma)\varphi^{t+1} + dtQk_{n+1}^{t+1} \tag{15}$$

until convergence on both k_n^{t+1} and a_n^{t+1}.

The dense system (14) is solved using a pre-conditioned gradient (PCG) method [15] where different preconditioners [17] can be used, such as a diagonal line or a diagonal block preconditioner. Other types of preconditioners are being developed. When successive systems have to be solved with the same matrix and different right hand sides (rhs), as it happens in time domain problems, the solution for a given rhs can be used as an initial solution for the next system. This is done when the successive rhs's are nearly parallel and the initial solution is then adjusted by the ratio of the norms of the two rhs. Starting with a good initial guess considerably reduces the number of iterations in the subsequent solves.

The sparse system (15) is solved using a direct solver [1].

3 MPP implementation

3.1 Introduction

The assembly and solve of the electromagnetic systems, and especially the BEM one which involves dense matrices are computationally expensive. The use of an MPP architecture [15],[16] allows sharing some of the computations between the different processors. It also allows sharing the storage of the different matrices between the processors, and thus gives an overall gain in memory and in computational time. We will now present how the electromagnetism systems are implemented in MPP. We will insist on the BEM implementation where the gains are maximal. In the following, we will call n_p the number of processor for a given simulation.

3.2 Implementation of the FEM part in MPP

The FEM part of the EM systems is handled in the same manner as the mechanical and thermal systems. For details, the reader should consult [1].
A domain decomposition with n_p domains is defined on the solid mesh. This is a serial operation performed on one processor. Each processor is assigned one domain. Associated with this domain is mesh data (node position and element connectivity) which largely stays local to each processor.

An FEM matrix is computed in parallel. Each processor creates elemental matrices for the elements it owns and the partial matrices on the processors are assembled and partitioned (an “all-sum” operation). The matrix-vector multiplies become sequences of serial computations followed by collective “all-sum” and “all-gather” operations.

3.3 Implementation of the BEM part in MPP

The BEM system deals with dense matrices and thus requires a lot of computational time, both for the matrices assembly and for solving the systems. A large gain can be made by using an MPP implementation. Unlike the FEM system where only one element is needed to compute an elemental matrix, the elemental BEM matrices involve double integrals over 2 elements, like in equations (11) and (13). The full BEM mesh (node position, BEM faces connectivity) is thus broadcasted to each processor.

3.3.1 BEM matrices: singular integration

The entries of a typical BEM matrix P are computed by integrating a kernel, smoothed by the basis functions between 2 faces, like in equations (11) or (13). Since the kernel is a negative power of the distance between the faces, these integrals can become singular or near singular for self or neighbour faces. Such singular integrations are based on Duffy transform which regularizes the kernel [18],[19]. The transforms depend on the type of face (quadrilateral or triangular) and on the type of singularity (self face, faces with common edges, faces with common nodes and so forth).
They require many integration points on each face and the evaluation of the kernel between these integration points and are thus numerically expensive.

In MPP, the pairs of neighbour BEM faces are classified based on a cut-off on the face separation parameter $p = \frac{dist(C_1, C_2)}{\max(R_1, R_2)}$

Where C_1 and C_2 are the centers of faces 1 and 2 respectively, and R_1 and R_2 their respective radii. The smaller the value of p, the more singular the pair (face 1, face 2) is and the more integration points are needed. The neighbour pairs are distributed among the processors to balance the singular integration work to compute P_S, the singular part of P.

3.3.2 BEM matrices: regular integration

A domain decomposition is performed on the BEM mesh with n_d domains ($n_d \succ n_p$). This domain decomposition allows decomposing any BEM matrix P as a block matrix:

$$P = \sum_{\Omega_1, \Omega_2 \in \delta} P(\Omega_1, \Omega_2) \tag{16}$$

Where $P(\Omega_1, \Omega_2)$ represents the submatrix of matrix P with the rows in Ω_1 and the columns in Ω_2.

For any 2 domains Ω_1 and Ω_2 we call the separation parameter:

$$p(\Omega_1, \Omega_2) = \frac{dist(C_1, C_2)}{\max(R_1, R_2)} \tag{17}$$

Where C_1 and C_2 are the centers of domains 1 and 2 respectively, and R_1 and R_2 their respective radii.

The n_d domains are partitioned between the n_p processors using the following method:

- n_p "center" domains are chosen so that they are as well separated as possible, i.e. so that their separation parameters (17) are maximized.
- Each center domain is assigned to a processor.
- The other domains are assigned to the processor whose center domain is closest, by keeping the number of domain per processor as uniform as possible.

We thus end up with a domain partition such that each processor owns its domain center plus all the surrounding domains. An example of such a domain partition is presented on figure 1.

The sum (16) is partitioned between the processors using the following method:

- $P(\Omega_1, \Omega_2)$ is computed either by the processor which owns Ω_1 or by the processor which owns Ω_2.
- The couples of domain are split between the processors in order to keep the same number of couples per processor.

The singular part P_S is then block partitioned with the same partition (16) used for the regular part of the matrix, and each singular block is added to the corresponding regular block in order to assemble the full matrix P.

All together, the amount of work to assemble the matrix is thus evenly split between the processors, as well as the memory needed to store the matrix.

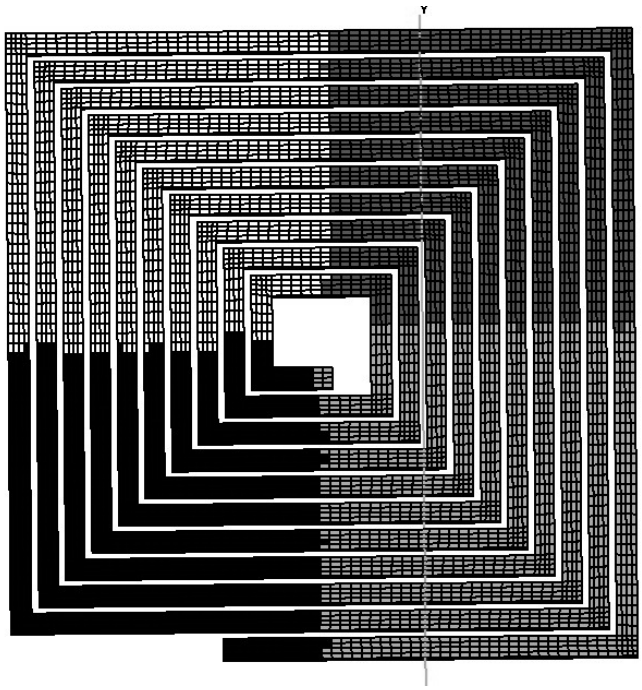

***Figure 1**: Example of a domain partition of a BEM mesh into 4 processors*

4 Results

4.1 Presentation of the EMF experiments and numerical models

The material used in this experiment was a commercial AZ31B magnesium alloy sheet for which the mechanical and microstructural evolution at high strain rate can be found in [20]. A square free forming operation is considered for the numerical study: The employed coil and die are shown in Figure 2. More details about the experiments can also be found in [21]. The selection of these operations is motivated by the fact that the deformation of the workpiece could be recorded by a high speed camera in the experiments and thus not only the final results but also their evolution in time can be compared.

A Photron FASTCAM-APXTM high speed camera was used to record the deformation at a sampling rate of 37500 fps. Moreover, in free forming operations, the influence of the die geometry in the final shape of the workpiece is less noticeable than in a close die forming operation and therefore it makes the numerical simulation more challenging, evidencing possible discrepancies with experiments.

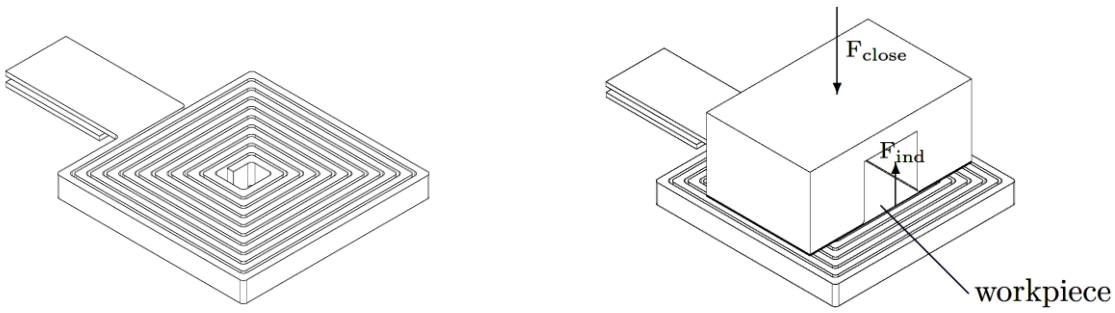

Figure 2: *Coil and die used for the square free forming case.*

The resistance, inductance and capacitance values of the equivalent RLC circuit used in the experiments are respectively R_0=0.956 mΩ, L_0=10 nH and C_0=180 μF. A charging voltage of 5.773 kV (i.e. 3 kJ) is used in the numerical simulations.

The clamping force is applied as nodal forces between the die and the blank holder.

The electromagnetic analysis is performed up to 300 μs with a time step of 1.5 μs and a recomputation of the BEM and FEM matrices every 10 steps. There thus are 200 electromagnetic time steps and 20 matrices reassembly in each simulation. The thermo-mechanical analysis is performed up to 300 μs with t_{therm}= 2 μs and t_{mech}= 30 ns respectively.

The main electrical parameter for non magnetic materials, such as non-ferrous materials like copper or magnesium alloys, is the electrical conductivity (σ_e). In the numerical models the temperature dependence of the electrical conductivity is taken into account whereas the influence of the plastic deformation is not considered. The temperature dependence of the electrical conductivity is modelled using a Burgess model [22] and also using linear interpolation between conductivity values at given temperatures. The evolution of the electrical conductivity of copper (i.e. the coil) with temperature is taken from [22] and the conductivity values for the AZ31B magnesium alloy (i.e. the workpiece) are taken from [23]. The die and the binder are considered insulators, so there is not current calculation in these bodies since the skin depth is usually small in EMF operations.

The die and the blank-holder are considered as rigid bodies made of steel (ρ = 7.8 g/cm^3; E = 210 GPa; ν = 0.33) in order to save computational time. The coil is modelled as an elastic material of very high strength to avoid any deformation, since the study is not focused in the coil but in the deformation behaviour of the workpiece. The assumption of the coil to work in the elastic domain is faithful when the resin in which it is embedded resists the reaction forces produced by the EMF discharges. In order to model the constitutive response of the workpiece, the flow stress is determined as a function of the plastic strain, the strain rate and the temperature using the constitutive equation given by Johnson and Cook [24]. The values employed in this paper are taken from [25].

The thermal properties considered in this study are the specific heat capacity (c_p), the thermal conductivity (κ) and the coefficient of thermal expansion (α). Data for oxygen free copper is taken from ASM Specialty Handbook for Copper and Copper alloys [26] and data for AZ31B magnesium alloy is taken from ASM Specialty Handbook for Magnesium and Magnesium alloys [23].

For the numerical study, different cases have been studied, with different coil mesh densities representing the same geometry. The model corresponding to Mesh1 is shown in Figure 3 and table 1 gives the statistics of the different meshes. All the cases have been solved with the same tolerances in the PCG method and with the same block-diagonal pre-conditioner.

Case name	Mesh1	Mesh8	Mesh16	Mesh32	Mesh64
# nodes	39504	63759	86537	131747	420478
# elements	28595	43568	62600	98744	343224
#BEM Pdofs	19851	36971	44279	62363	147843
#BEM Qdofs	39688	73920	88532	124688	295648

Table 1*: Statistics on the different meshes used for the numerical study.*

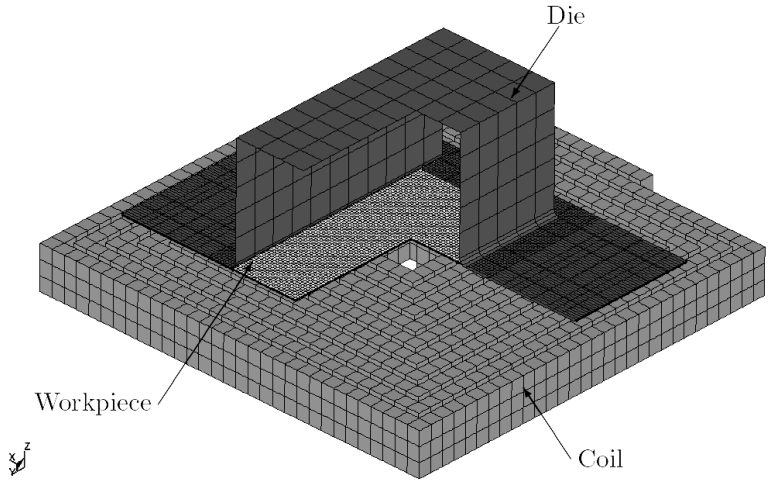

Figure 3: *Model corresponding to Mesh1 (a quarter of the workpiece and die is removed to show the coil).*

4.2 Numerical-experimental comparisons

The experimental and numerical final shapes of the workpiece showed a good agreement as pictured on figure 4. The numerical and experimental *Z* displacement versus time were also compared and showed a very good agreement as shown on figure 5. More details can be found in [21]. The numerical results given by the different meshes are fairly consistent with of course more details on the thinner meshes.

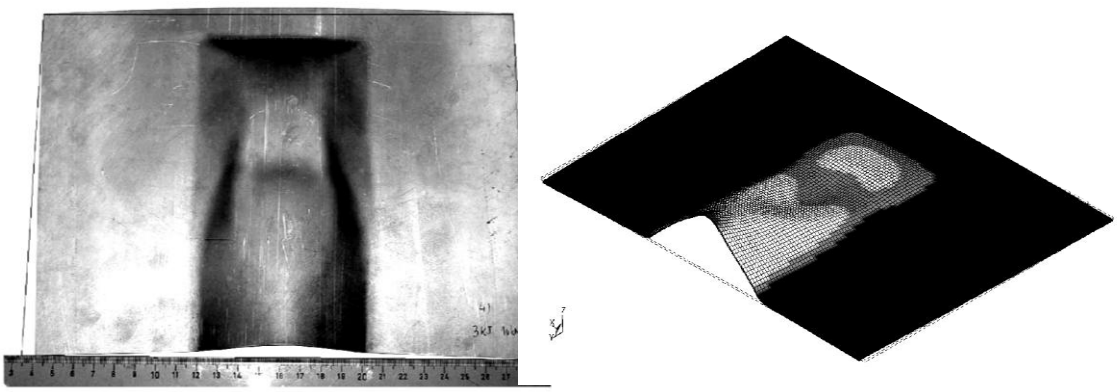

Figure 4: *Final shape of the workpiece: experimental (left) and numerical (right).*

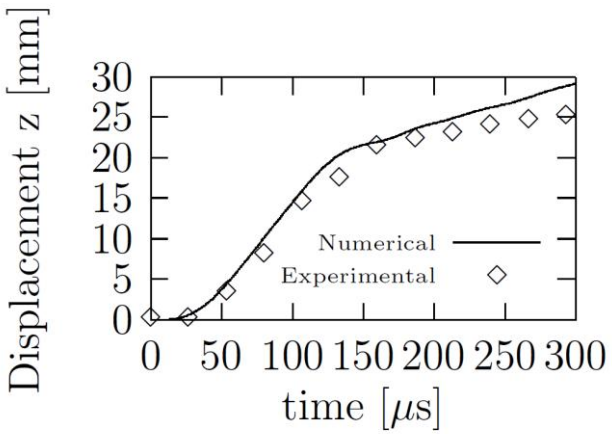

Figure 5: *Comparison between numerically predicted and experimentally observed time evolution of the maximum height of the workpiece.*

4.3 Study of the MPP speed-up

The different cases have been simulated using 1, 2, 4, 8, 16, 32, or 64 processors. Table 2 shows the total computational time versus the number of processors for the different cases and figure 6 shows the computational time vs the number of processors for mesh1 and mesh8. One can notice the large reduction in computational time for Mesh1 when going from 1 to 2 and then to 4 processors. This reduction is less dramatic when increasing even more the number of processor on such a small case. This is because for large numbers of processors, the communication between processors becomes very important compared to the work done by each processor. We looked in more detail at the two most time consuming parts of the computation, i.e. the BEM matrices assembly, which we will call “assembly” and the BEM solve using a PCG method which we will call “solve”. On both mesh1 and mesh8, the assembly time scales pretty well with the number of processors. The solve time does not scale as well, but represents a small fraction of the total time on these small cases.

The larger test cases, mesh16, mesh32 and mesh64 can only be run on larger number of processors due to the memory requirement. On these cases, doubling the number of processors shows a significant reduction in the computational time.

# processors	Mesh1	Mesh8	Mesh16	Mesh32	Mesh64
1	24:16	55:41			
2	12:16	27:42			
4	6:28	14:13			
8	3:56	8:49	12:14		
16	2:29	5:15	7:34	15:53	
32	1:36	3:07	4:22	8:57	42:16
64	1:09	2:01	2:46	5:32	26:31

Table 2*: Computational time (hours:minutes) versus number of processors for the different meshes.*

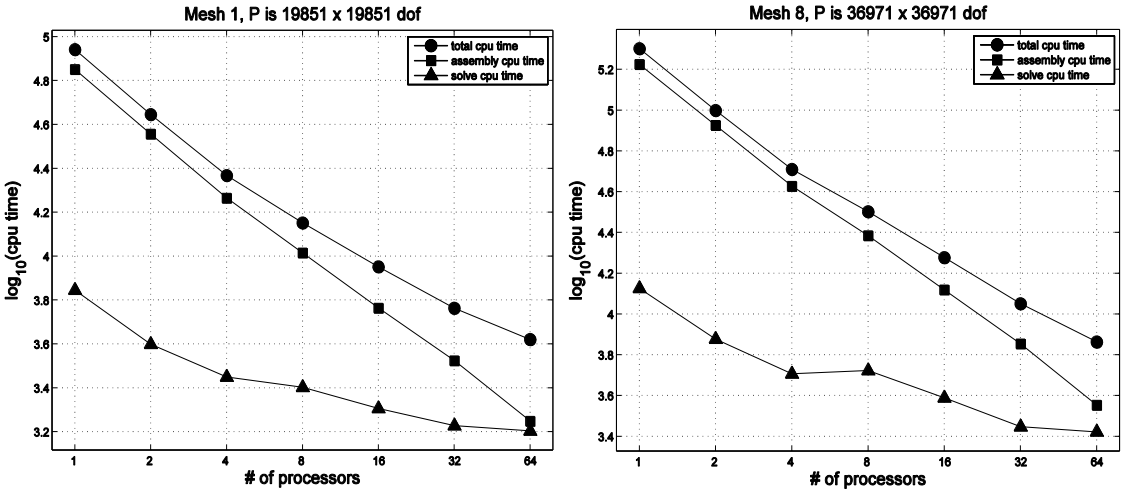

Figure 6*: Computational time (log scale) versus number of processors for Mesh1 (left) and mesh8 (right). The dots represent the total time, the squares the assembly time, and the triangles the solve time.*

In order to better compare the speed-up, we define the efficiency of a simulation performed with p processors compared to a reference simulation performed with p_0 processors ($p_0 \le p$ and $p_0 = 1$ whenever the total memory needed by the run makes it possible) as:

$$E_p = \frac{p_0 T_{p_0}}{p T_p}, \tag{18}$$

Where T_{p_0} is the computational time for p_0 processor, and T_p is the computational time for p processors. Ideally, we would like this efficiency to be equal to 1, and lower

values show time spent (“wasted”) in communication and synchronization. Figure 7 shows the total computational time versus the number of processors for all cases, as well as the efficiency versus the number of processors for all the cases. One can see that for the small cases, the efficiency falls down below 0.5 for large number of processors, but for the larger cases, it stays above 0.6 even at large numbers of processors. In the future, better pre-conditioners will be introduced in order to improve the solve efficiency and thus the overall efficiency.

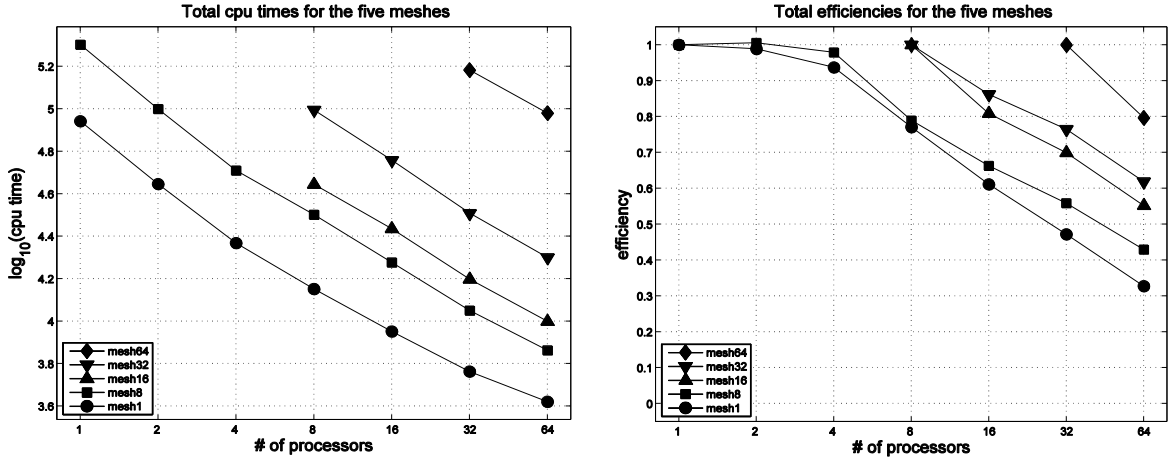

***Figure 7**: Total CPU time (left) and total efficiency (right) versus number of processors for the different cases: dots: mesh1, squares: mesh8, up triangles: mesh16, down triangles: mesh32, diamonds: mesh64.*

5 Conclusions

The newly introduced Electromagnetism module of LS-DYNA was presented. The electromagnetic fields are computed by solving the Maxwell equations in the eddy-current approximation, using a FEM for the conductors coupled with a BEM for the surrounding air and insulators. The implementation of the MPP version of the module was presented, and in particular, the BEM system part. Results were presented on an EMF test case, and the speed-up of the MPP version was presented. The MPP version allows much faster simulation and much larger cases due to the distribution of the memory between the different processors.

Further improvements on the speed-up are currently being addressed, such as the introduction of new pre-conditioners in MPP which could considerably improve the efficiency of the solve part.

More recent developments in the EM module include an induced heating and resistive heating capability, as well as a sliding contact capability for the electromagnetic fields which allows the simulation of rail gun like experiments. In the future, the EM module will be extended from hexahedral to tetrahedral and wedge solid elements as well as shell elements, and a mesh adaptivity capability will be introduced. Finally, other solvers than the eddy-current will be introduced, including a magnetostatics solver.

The EM module is integrated in the 980 version of LS-DYNA, which should be released sometime in 2010. In the mean time, it is available as a “beta version”.

References

[1] LS-DYNA Theory Manual, LSTC.

[2] *P. L'Eplattenier, G. Cook, C. Ashcraft, M. Burger, A. Shapiro, G. Daehn, M. Seith*, "Introduction of an Electromagnetism Module in LS-DYNA for Coupled Mechanical-Thermal-Electromagnetic Simulations", 9th International LS-DYNA Users conference", Dearborn, Michigan, June 2005.

[3] *P. L'Eplattenier, G. Cook, C. Ashcraft* , "Introduction of an Electromagnetism Module in LS-DYNA for Coupled Mechanical-Thermal-Electromagnetic Simulations", Internatinal Conference On High Speed Forming 08, March 11-12, 2008, Dortmund, Germany.

[4] *P. L'Eplattenier, G. Cook, C. Ashcraft, M Burger, J. Imbert, M. Worswick*, "Introduction of an Electromagnetism Module in LS-DYNA for Coupled Mechanical-Thermal-Electromagnetic Simulations", Steel Research Int. 80 (2009) no 5.

[5] *J. Jin*, "The Finite Element Method In Electromagnetics", Wiley, 1993.

[6] *J. Shen*, "Computational Electromagnetics Using Boundary Elements, Advances In Modelling Eddy Currents", Topics in Engineering Vol 24, Series Eds: C.A. Brebbia and J.J. Connor, Southampton and Boston: Computational Mechanics Publications, 1995".

[7] *J.C. Nedelec*, "A New Family of Mixed Finite Elements in R3", Num. Math, 50:57-81, 1986.

[8] *Marc Snir, Steve Otto, Steven Huss-Lederman, David Walker, Jack Dongarra*, "MPI, the complete reference, Volume I, the MPI core", Scientific and Engineering Computation Series, MIT press, 1998.

[9] *William Gropp, Ewing Lusk, Anthony Skjellum*, "Using MPI, Portable Parallel Programming with the Message-Passing Interface", Second Edition, Scientific and Engineering Computation Series, MIT press, 1998.

[10] *O. Biro and K. Preis*, "On the use of the magnetic vector potential in the finite element analysis of three-dimentional eddy currents", IEEE Transaction on Magnetics, 25(4)3145-3159,1989.

[11] *P. Castillo, R. Rieben and D. White*, "FEMSTER: An object oriented class library of discrete differential forms". In Proceedings of the 2003 IEEE International Antennas and Propagation Symposium, volume 2, pages 181-184, Columbus, Ohio, June 2003.

[12] *R. Rieben*, "A Novel High Order Time Domain Vector Finite Element Method for the Simulation of Electromagnetic Devices", Ph-D Thesis, University of California Davis, 2004.

[13] *R. Rieben and D. White*, "Verification of high-order mixed finite element solution of transient magnetic diffusion problems", IEEE Transaction on Magnetics, 42(1), 25-39, 2006.

[14] *Z. Ren, A. Razek*, "New technique for solving three-dimentional multiply connected eddy-current problems", IEE Proceedings, Vol. 137, Pt. A, No 3, May 1990.

[15] *G. H. Golub and C. F. van Loan*, "Matrix Computations", Third Edition, Johns Hopkins University Press, Baltimore, MD, 1996.

[16] *P. A. Businger and G. H. Golub*, "Linear least squares solution via Householder transformations", Numer. Math, volume 7, 269-276, 1965.

[17] *K.E. Chen*, “On a class of preconditioning methods for dense linear systems from boundary elements”, SIAM J. Sci. Comput. 20(2), 684-698, 1998.
[18] *D.J. Taylor*, "Accurate and Efficient Numerical Integration of Weakly Singular Integrals in Galerkin EFIE Solutions", IEEE Transactions on Antennas and Propagation, vol. 51, no 7, July 2003.
[19] *A. Frangi, G.Novati, R.Springhetti, and M.Rovizzi*, "3D fracture analysis by the symmetric Galerkin BEM", Computational Mechanics 28 (2002).
[20] *I. Ulacia, N.V. Dudamell, F. Gálvez, S. Yi, M.T. Pérez-Prado, I. Hurtado*, “Mechanical behavior and microstructural evolution of a Mg AZ31 sheet at dynamic strain rates”, Acta Mater, 2010, doi:10.1016/j.actamat.2010.01.029.
[21] *I. Ulacia, I. Hurtado, J. Imbert, C. Salisbury, M. Worswick, A. Arroyo,* “Experimental and numerical study of electromagnetic forming of AZ31B magnesium alloy sheet”, Steel Res. Int. 80, 2009, p. 344 - 350.
[22] *T. Burgess*, “Electrical resistivity model of metals”, Proc. 4th Int. Conf. on Megagauss Magnetic Field Generation and Related Topics, 1986, pp. 307 - 316.
[23] *M. Avedesian, H. Baker*, “Magnesium and Magnesium Alloys”, ASM Specialty Handbook. ASM Int., Materials Park, OH, 1999.
[24] *G. Johnson, W. Cook*, “A constitutive model and data for metals subjected to large strains, high strain rates and high temperatures”, Proc. 7th Int. Symp. on ballistics. pp. 541 – 547, 1983.
[25] *I. Ulacia, C.P. Salisbury, I. Hurtado, M.J. Worswick*, “Tensile characterization and constitutive modeling of AZ31B magnesium alloy sheet over a wide range of strain rates and temperatures”, J. Mater. Proc. Tech. Manuscript submitted for publication, 2009.
[26] *J. Davis*, “Copper and Copper Alloys”, ASM Specialty Handbook. ASM Int., Materials Park, OH, 2001.

Proposal for a Test Bench for Electromagnetic Forming of Thin Metal Sheets*

M. Geier[1], E. Paese[1], J. L. Pacheco[1], R. P. Homrich[2], J. C. S. Ortiz[1]

[1]Grupo de Projeto, Fabricação e Automação Industrial, Universidade Federal do Rio Grande do Sul, Brazil.
[2]Laboratório de Máquinas Elétricas, Acionamentos e Energia, Universidade Federal do Rio Grande do Sul, Brazil.

Abstract

This paper presents a proposal to build a test bench for electromagnetic forming processes. The project considers the analysis of the electrical circuit and forces involved in the system for selection of low voltage capacitors, resistors, buses, main discharge switch and material choice for actuator's insulation and rigidity, considering also the manufacturing process of actuators and dies. Among the aspects considered for the design, energy efficiency has been prioritized by the use of non-conducting material to the dies. Main switches by mechanical contact and spark gap types were used and its wear and functionality was assessed. Free bulging experiments were performed with aluminium AA1100 plates for a system configured with a flat coil actuator. Test measurements of electric currents in the coil actuator with and without the workpiece as the secondary circuit were performed, as well as an evaluation of wear and functionality of the system. It is observed that the main switch discharge is one of the most critical items of the system.

Keywords

High speed forming, Flat coil, Spark-gap

---

* *This work is based partially on the results of the Master of Science Dissertation of Evandro Paese. The authors would like to thank the following persons: Eng. Michael S. Ertle from TDK-EPCOS for donating the capacitors;* Eng. *Augusto Nienow from Ensinger Engineering Plastics for donating of* polyoxymethylene *block; Eng. Eliseu Silveira Brito for milling the actuator coil and dies, and to Eng. Marcio Migliavacca from Rexfort for milling the spark-gap parts.*

1 Introduction

In recent years, the electromagnetic forming (EMF) technique has been widely studied, especially with regard to the behaviour of materials under high strain rate, the potential for applications and numerical modelling of the process, with several works dedicated to these topics [1-12]. However, few studies have been presented for the design of EMF machines, whether for industrial or laboratorial applications [13].

Commercial solutions for EMF machines are very expensive and the user´s flexibility facing the choice of components with specific electrical properties is subjected to manufacturer´s availability. In laboratorial experiments, the electrical data are very important, as they help the understanding and identification of relevant parameters to the process while also allowing the development of numerical models to design actuators and dies, as well process analysis.

Given the importance of the machine, this paper presents an alternative proposal for a test bench for electromagnetic forming of thin metal sheets, prioritizing laboratorial application. The project considers the analysis of electrical components, development of a main switch like spark gap, choice of material and manufacturing process for insulation and rigidity of the actuator and dies, emphasizing the efficiency of the system. Free bulged tests results are presented with aluminium alloy AA1100 plates for an EMF system configured with a flat spiral coil as actuator, including discharge currents, wear analysis and systems functionality, providing more information for the design of EMF machines and the process itself.

2 The Electromagnetic Forming Process

In a simplified way, an electromagnetic forming system consists of a capacitor bank, an actuator coil, a main switch and the metallic workpiece to be deformed. The capacitor bank is connected to the actuator coil which is very close to the workpiece. When the main switch is closed, the energy previously stored in the capacitors is rapidly discharged through the coil as a high electric current pulse producing a transient magnetic field that induces opposite currents on the nearby conductive workpiece (Lenz's law). The electromagnetic repulsion between the currents flowing in opposite directions and in close proximity provides the deformation force (Lorenz law) to the workpiece [11].

2.1 Simplified Analysis of EMF Processes

The analysis of the EMF process is very complex because it responds to interaction of electric, magnetic, thermal and mechanical fields. This section presents a simplified way of examining the case to illustrate the basic principles of the process and its main parameters. Advanced information about the interaction of deformation and electromagnetic fields can be found in [14-18].

2.1.1 Analogy to Electrical Circuit

An electromagnetic forming system is a discharge circuit which consists of a primary RLC circuit coupled with a secondary RL circuit. Equations (1) and (2) describe the analogous electrical circuit of the system [19]:

$$\left(L_1\right)\frac{di_1}{dt}+\frac{d}{dt}\left(Mi_2\right)+\left(R_1\right)i_1+\frac{1}{C_0}\int i_1 dt=0 \tag{1}$$

$$\frac{d}{dt}\left(L_2 i_2\right)+\frac{d}{dt}\left(Mi_1\right)+R_2 i_2=0 \tag{2}$$

where, C_0 is the capacitor bank, L_1 and R_1 are respectively the total inductance and resistance of the primary circuit; M is the mutual inductance between the coil and workpiece, i_1 is the coil current, i_2 is the equivalent induced current in the workpiece, L_2 and R_2 are respectively the workpiece's equivalent inductance and resistance. The initial conditions for equations (1) and (2) are:

$$i_1=0,\quad \left(L_1\right)\frac{di_1}{dt}=V_0,\quad i_2=0 \tag{3}$$

with V_0 the initial voltage of the capacitor bank. The Mi_2 term is not constant, it varies significantly with the deformation of the workpiece (moves away from the actuator coil) and, to a lesser intensity with the penetration of the magnetic field in the workpiece.

2.1.2 Induced Magnetic Force and Magnetic Pressure Distribution

The resulting repulsive force between the magnetic field in the actuator coil and the induced magnetic field in the workpiece is typically referred to as the magnetic pressure. The induced magnetic force and pressure is given by equations (4) and (5) [9,11]:

$$\frac{F}{l}=\frac{\mu_0 I_1 I_2}{2\pi d} \tag{4}$$

$$P=\frac{\mu_0 H^2}{2} \tag{5}$$

Where F is force, P is pressure in Pascals, μ_0 is the permeability of free space, H is the electromagnetic intensity, d is the distance between the workpiece and the actuator.

The electromagnetic intensity H, which may be calculated by Biot-Savart law, is very dificult to determine because it depends on time, on the space location, on the applied current and geometry of the conductive media, in this case, the actuator coil and the deforming workpiece. Electromagnetic intensity distributions for idealized spiral coils have been analytically determined, but no general analytical solutions exist for sheet metal forming operations with flat coils [9,12].

2.2 Equipment

An electromagnetic forming machine may be treated as an RLC circuit, equation (1), and is basically composed of a high voltage DC power supply, capacitors, connecting lines, main discharge switch, actuator coil and other devices for operational safety and control. The most critical parts are the capacitors and the main discharge switch, which must be robust enough to withstand the high reverse voltage and current that may exceed 100 kA [13,20]. In addition to these characteristics, it is desirable that the resistance and inductance of the components are as low as possible in order to maximize the efficiency of the deformation process. Special attention should be given in the selection of connecting lines (buses), capacitors (capacity and internal resistance and inductance), the actuator coil design, and especially in respect to the main discharge switch.

3 Design Solution for an EMF Test Bench

The design for the test bench presented in this paper considered the above mentioned technical aspects and an economic alternative when compared to a commercial solution, as the total budget for purchasing and manufacturing the required components, excluding monitoring and data acquisition devices, amounts $2500.00 with all parts being made in Brazil. The following sections provide further detail on all the components used to build the machine. *Warning: readers interested in following the assembly and operation of the presented machine need to use individual protection equipment and take special care when handling with high voltage. Also, the reader should know that a high voltage (DC) power supply is needed to charge the capacitor bank and so make the machine operational. It is also recommended at least two persons to operate the machine, where one controls the charging procedure and the other the trigger circuit (main discharge switch).*

3.1 Capacitors

The energy stored (*U*) in a capacitor is determined by the following equation:

$$U = \frac{1}{2} C V^2 \tag{6}$$

Commercial EMF machines exploit this relation by using capacitors of low capacitance and high voltage (thousands of Volts). This is possible due to the highly insulating material (dielectric) which these capacitors are made from.

For this bench test, low voltage capacitors were selected on the basis of cost, market availability and operational safety. Based on these criteria, EPCOS electrolytic pulse capacitors of 450 V and 5600 µF (±20%) with screw terminals were chose. More detailed information about these capacitors may be found in the reference [21].

3.2 Main Discharge Switch

The main discharge switch needs to be efficient in the transmission of the high currents and provide operational availability, i.e., it needs to resist to the wear. Discharge switches

based on terminal contacts are not efficient in the transmission of high current, much less wear resistant and in some times, resulting in the undesired welding of the terminals [11-13]. Two possible switches without contact are the spark-gap and the thyratron valve, both are electronic controlled high voltage switches (hundreds of kV) and support high peak currents (kA). The solution was the development of a non automated spark-gap (SG) of easy construction and implementation (Figure 1). In this system a secondary circuit is used to form plasma between the electrodes and thus driving the main switch without mechanical contact. The secondary circuit consists of a small wire diameter, which is evaporated by short circuit from its own, forming plasma between the electrodes and thus conducting the high current pulse [12].

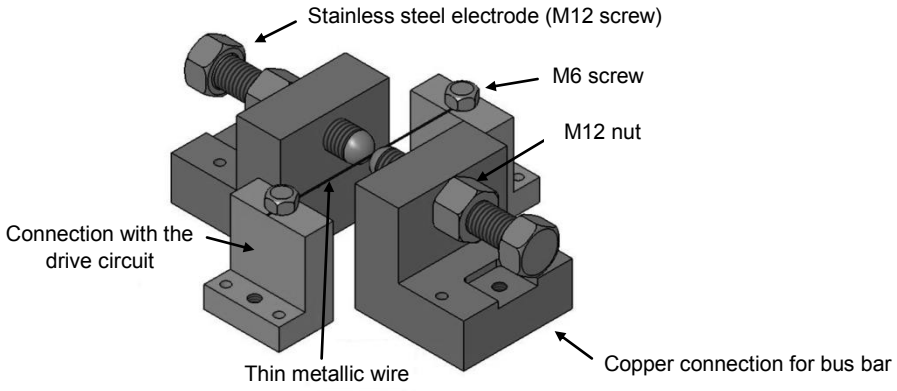

Figure 1: *Main discharge switch without mechanical contact (Spark-gap) [12].*

3.3 Actuator Coil and Dies

For this project, a flat spiral coil actuator was selected (Figure 2). The coil was modelled on CAD and then machined on a CNC machine from a 150 x 150 x 15 mm copper plate. A cavity in the shape of the coil was machined with a 0.1 mm gap in a polyacetal block providing rigidity and insulation. The upper die has a circular cavity. The coil and the upper die were fixed by screw connections (M6). Table 1 presents more detailed information.

Coil	Material	Electrolytic copper
	No. of windings	6
	Radius of outer ring	60 mm
	Pitch	10 mm
	Cross-section area	16 mm^2
	Electrical resistivity	1.2396 mΩ (ohmmeter-D05 Cropico)
	Self inductance	1.2 μH (LCR meter Minipa MX-1001)
Die mould	Material [22]	Tecaform AH (Polyoxymethylene)
	Ultimate yield strength	60.7 MPa
	Hardness	86 HRM
	Dielectric strength	19.7 kV/mm
	Cavity diameter	Ø=120 mm
	Cavity depth	30 mm
	Blank diameter	Ø=180 mm

Table 1: Coil and die parameters

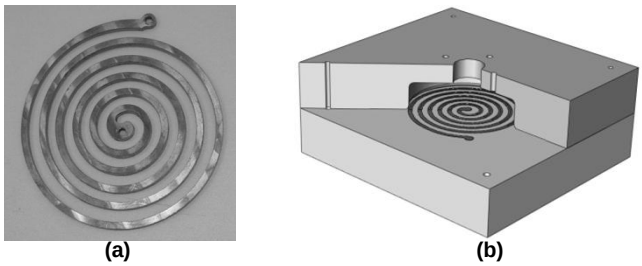

Figure 2: *Machined flat spiral coil of electrolytic copper (a) and a sectioned view of the dies (b).*

3.4 Connecting Lines

Usually, a coaxial configuration for the connecting lines is used, as this will minimize the inductance. As this type of solution is expensive, simple copper bus bars were used. The bars should have a lower electrical resistivity, in other words, it must have no more than the same electrical resistivity than the actuator coil installed on the machine. Commercial copper profiles of 15.87 x 3.17 mm meets the desirable requirements with a cross section area of 48.8 mm^2 and sufficient width to maximize the contact area with the terminals of the previously selected capacitors. Copper flexible connectors, with an equivalent cross section area of 36.4 mm^2 were also used.

3.5 Electrical Circuit Configuration

With all major components defined, it is now important to sketch the electrical circuit configuration to assist the assembly process. Figure 3 shows a schematic electric circuit for the EMF system.

The capacitor bank C_0 shown on figure 3 consists of six capacitors, arranged as a series-parallel circuit (Figure 8). In this configuration it is possible to apply up to 1000 V and the maximum energy storage, which is calculated by applying the equation (6), gives 4.3 kJ. The circuit presented on Figure 4 has 10 kΩ resistors between the capacitors terminals. These resistors equalize the applied voltage and also serve to discharge the capacitors when the power is not used for electromagnetic forming.

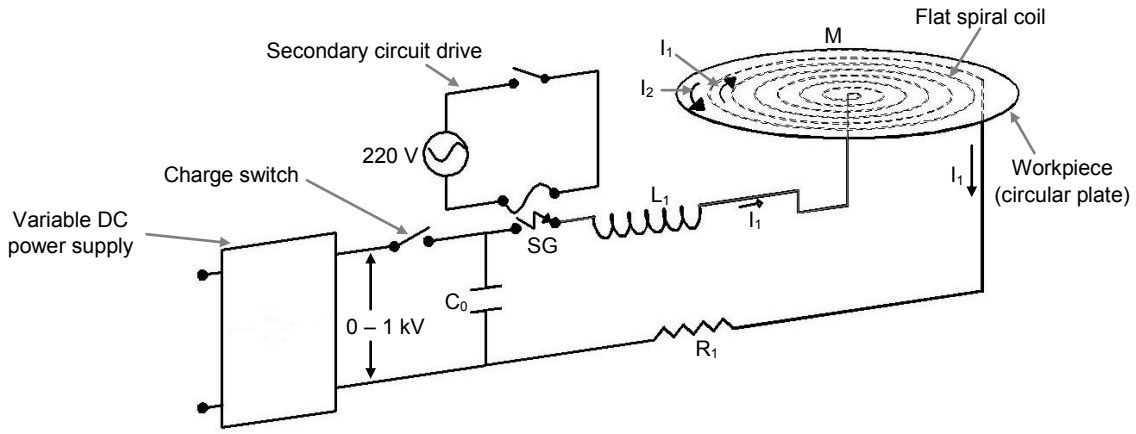

Figure 3: *sketch of the electrical circuit.*

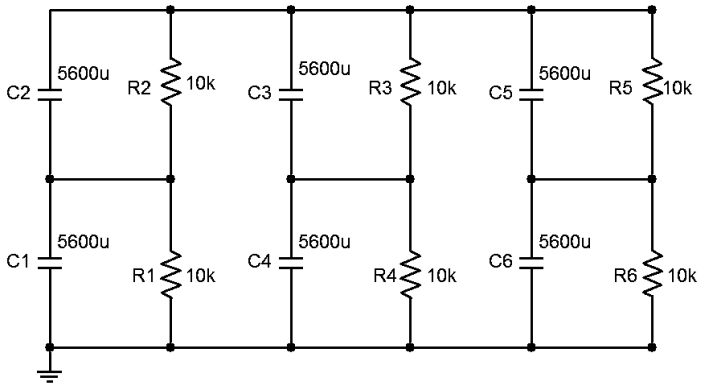

Figure 4: *circuit of the capacitor bank with 5600 µF capacitors and the 10 kΩ resistors.*

3.6 Test Bench frame

All components were mounted over medium-density fibreboard, fixed with screws and nuts. Figure 5 shows the completed EMF machine with all monitoring and data acquisition devices.

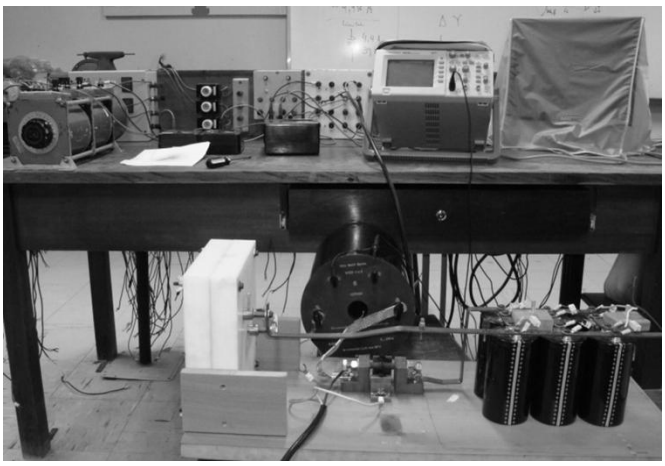

Figure 5: *Test bench for electromagnetic forming of thin metal sheets at LMEAE/UFRGS.*

3.7 Procedures for operation of the test bench

The steps to prepare the machine for an EMF operation consist of: checking if the system is energized and then disconnect and/or discharge it if necessary, positioning the sheet on the die/closure and fixation of the dies with butterfly nuts and place the thin metallic wire on the trigger circuit (secondary circuit). Setup of the monitoring and data acquisition devices and start charging the capacitor bank with the desirable energy. Once the charge is complete, the DC power supply must be disconnected from the capacitor bank and then the trigger circuit may be fired. Again, users are warned to beware of the risk of electric shock and fire by short circuit. The authors recommend installing voltmeters on the charging and trigger circuits to ensure that it is not energized. If necessary, wait a moment for the 10 kΩ resistors to dissipate the previously stored energy. Always use individual protection equipment and a voltmeter to check the voltage of the circuit before touching it.

4 EMF Analysis procedure

The experimental procedures consisted of free bulging tests of aluminium alloy AA1100 sheets. A voltmeter, a 1 mΩ shunt resistor and an oscilloscope were used for data acquisition and monitoring (Figure 5). Table 2 presents system parameters and working conditions.

Circuit conditions	Capacity of condenser bank Energy (maximum)	8400 μF 4.3 kJ @ 1 kV
Workpiece	Material Electrical resistivity [23] Thickness Diameter Gap distance	AA 1100 $3 \cdot 10^{-8}$ Ω·m 0.8 and 3 mm 180 mm 1 mm

Table 2: System parameters and working conditions

5 Results and Discussion

The machine showed satisfactory results with the electromagnetic forming deformation imposed to the workpiece. On Figure 6 it is possible to see the final deformed sheets of 0.8 mm and 3 mm thick.

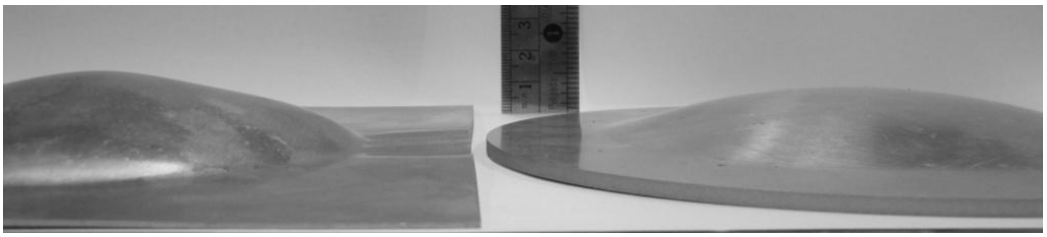

Figure 6: *Electromagnetic forming results for AA1100 sheets with 0.8 (0,9 kV) and 0.3 mm (1 kv).*

Discharge current and voltage tests showed that the spark-gap switch has great efficiency (Figure 7) where it is also possible to note that the spark-gap switch allows current and voltage reversion. Workpiece thickness has influence on current peaks: a thin sheet has a small area relative to the induced currents flow, thus a higher electrical resistivity.

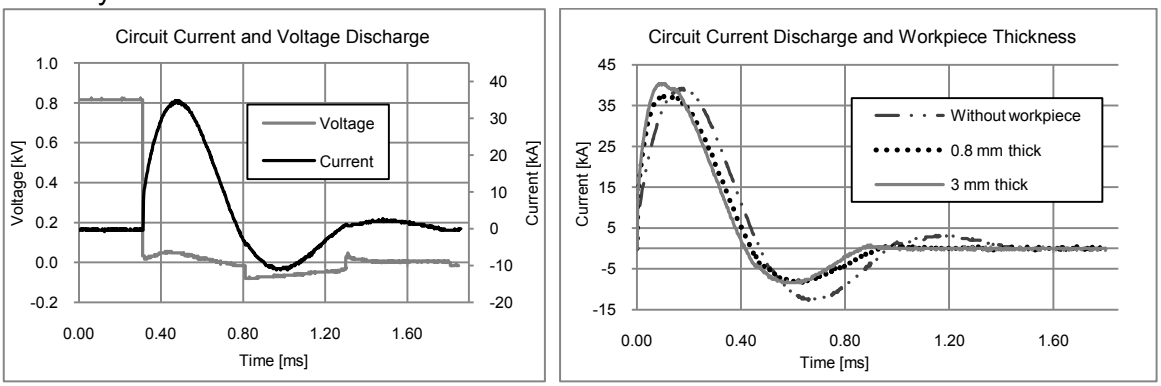

Figure 7: *Acquired voltage and current curves for the spark-gap and circuit current discharge curves situations with and without the aluminium sheet plate charge.*

Data from the experimental results confirmed the high current and reverse voltage that the machine components are subjected. Upon completion of over 50 experiments, the machine is still operational. However, wear its noticeable in the spark-gap, in the flexible copper connections and in the actuator coil, Figure 8, due to the high current discharges.

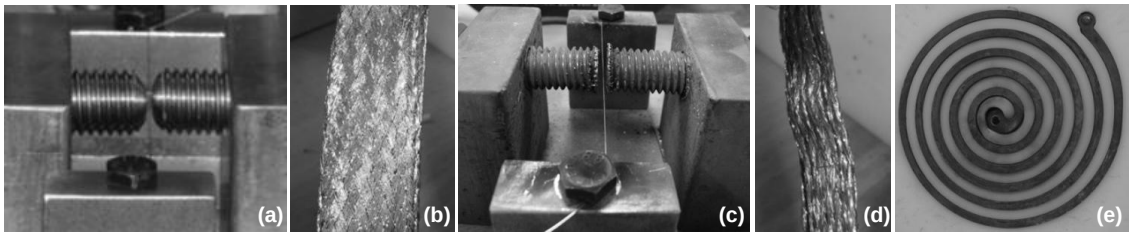

Figure 8: *initial state of the spark-gap (a) and copper flexible connector (b). Noticeable wear after over 50 highly energized pulses: spark-gap (c), copper flexible connector (d) and actuator coil (e).*

6 Conclusions

The paper presents a proposal of a test bench for electromagnetic forming of thin metal sheets for laboratorial experiments. The presented design solutions are simple, functional and feasible. Aluminium sheet plates of up to 3 mm thick (Table 1) were successfully deformed by the presented EMF machine confirming that this concept serves as test bench and also as a reference for the construction of more powerful and robust machines and with higher degree of automation. Acquired data for discharge current and voltage helped to identify process parameters and its influences, assisting in the development of other areas such as numerical modelling, die design and materials, and finally to the dissemination of this technique.

References

[1] *Marré, M.; Brosius, A.; Tekkaya A. E.*: New Aspects Of Joining by Compression and Expansion of Tubular Workpieces. Int J Mater Form (2008) Suppl 1:1295 –1298.

[2] *Marré, M.; Ruhstorfer, M.; Tekkaya, A.E.; Zaeh, M.F.*: Manufacturing of Lightweight Frame Structures by Innovative Joining by Forming Processes. Int J Mater Form (2009) Vol. 2 Suppl 1:307–310.

[3] *Unger, J.; Stiemer, M.; Schwarze, M.; Svendsen, B., Blum, H.; Reese, S.*: Strategies for 3D Simulation of Electromagnetic Forming Processes. journal of materials processing technology 199 (2008) 341–362.

[4] *Mamalis, A. G.; Manolakos, D. E.; Kladas, A. G.; Koumoutsos, A. K.; Ovchinnikov, Daehn, S. G*.: Electromagnetic Forming of Aluminum Alloy Sheet Using a Grooved Die: Numerical Modeling. The Physics of Metals and Metallography, 2006, Vol. 102, Suppl. 1, pp. S90–S93.

[5] *Meriched, A.; Feliachi, M.; Mohellebi, H.*: Electromagnetic Forming of Thin Metal Sheets. Magnetics, IEEE Transactions on, vol.36, no.4, pp.1808-1811, 2000.

[6] *Haiping Yu, Chunfeng Li, Zhiheng Zhao, Zhong Li.*: Effect of Field Shaper on Magnetic Pressure in Electromagnetic Forming. Journal of Materials Processing Technology 168 (2005) 245–249.

[7] *Golowin, S.; Kamal, M.; Shang, J.; Portier, J.; Din, A.; Daehn, G. S.; Bradley, J. R.; Newman, K. E.; Hatkevich, S.*: Application of a Uniform Pressure Actuator for Electromagnetic Processing of Sheet Metal. JMEPEG (2007) 16:455–460. Doi: 10.1007/s11665-007-9085-4.

[8] *Zhang, P.*: Joining Enabled by High Velocity Deformation. School of The Ohio State University, 2003.

[9] *Boyd, J. M. S. I.*: Increased Formability and the Effects of the Tool/Sheet Interaction in Electromagnetic Forming of Aluminum Alloy Sheet. Master of Applied Science thesis, University of Waterloo, Ontario, Canada, 2005.

[10] *Motoasca, E. T.*: Electrodynamics in Deformable Solids for Electromagnetic Forming. Ridderprint Offsetdrukkerij B.V. The Netherlands, 2003.

[11] *Kamal, M.*: A Uniform Pressure Eletromagnetic Actuator for Forming Flat Sheets. School of The Ohio State University, 2005.

[12] *Paese, E.*: Electromagnetic Forming of Thin Metal Sheets: Technical Feasibility. MSc Thesis (in Portuguese), Universidade Federal do Rio Grande do Sul, Brazil, 2010.

[13] *Martel, D.; Bultman, Jim*. Electromagnetic Metal Forming Machine. Lawrence Technological University, 2007.

[14] *Fosdick, R.; Tang, H.*: Electrodynamics and Thermomechanics of Material Bodies. J Elasticity (2007) 88:255–297.

[15] *Xiao, J.*: Equations for the Interaction between Deformation and Electromagnetic Field. PIERS ONLINE, VOL. 3, NO. 6, pp 808-811, 2007.

[16] *Hachkevych O. R.; Solodyak, M. T.; Ivas'ko, R. O.; Ya Boichuk, V.*: Modeling Of The Influence Of Electromagnetic Fields On The Thermomechanical Behavior Of Deformable Bodies. Materials Science, Vol. 45, No. 1, pp 41-56, 2009.

[17] *Woodson, H. H.; Melcher, J. R.*: Electromechanical Dynamics. 3 vols. (Massachusetts Institute of Technology: MIT OpenCourseWare). http://ocw.mit.edu (accessed 02 10, 2010). License: Creative Commons Attribution-NonCommercial-Share Alike.

[18] *Maugin, G. A.*: On modelling electromagnetomechanical interactions in deformable solids. Int J Adv Eng Sci Appl Math pp 25–32, 2009.

[19] *Takatsu, N.; Kato, M.; Sato, K.; Tobe T.*: High Speed Forming of Metal Sheets by Electromagnetic Force. J.S.M.E. International Journal, vol. 31, no. 1, 1988.

[20] *Xu, W.; Fang, h.; Xu, W.*:Analysis of the Variation Regularity of the Parameters of the Discharge Circuit with the Distance Between Workpiece and Inductor for Electromagnetic Forming Processes. journal of materials processing technology 203 (2008) 216–220.

[21] http://www.epcos.com/inf/20/30/db/aec_09/B43456__B43458.pdf, last access on 02/23/2010.

[22] http://www.ensinger.com.br last access on 02/23/2010.

[23] http://matweb.com last access on 02/23/2010.

SESSION 6
CONSTITUTIVE EFFECTS

Dynamic Characterization of Powdered Ceramics*

G. Fenton[1]

[1] Applied Research Associates, 4300 San Mateo Blvd., A-220, Albuquerque, NM 87110

Abstract

The dynamic behavior of powdered materials such as granular silica (sand), technical ceramics, and porous geological substances has importance to a variety of engineering applications. Structural seismic coupling, planetary science, earth penetration mechanics, and the performance of ceramic armors are just some of application areas. Although the mechanical behaviors of sand and other granular ceramics have been studied extensively for several decades, the dynamic behavior over a range of strain rates and pressures of such materials remains poorly understood. This paper describes how instrumented electromagnetic tube compression driven by capacitive discharge can be used to measure compaction of porous materials at moderate pressures and controlled strain rates. The technique relies on electromagnetically crushing a powder-filled conductive tube. By measuring the current as a function of time and the tube displacement through Photon Doppler Velocimetry (PDV) sufficient data can be obtained to reveal the behavior of the porous material. The method will be described in detail and example data will be shown for compaction of silica sand.

Keywords

Dynamic, Compression, Ceramic

1 Introduction

Compression of powdered ceramics falls into a field of science, which has been studied extensively, using both quasi-static and dynamic methods to characterize these materials.

---

* *The author gratefully acknowledges Glenn Daehn and his team at OSU for lab use and experimental work, as well as Tracy Vogler of Sandia National Laboratories for his technical inputs and guidance. Without the financial support granted under Contract PO 208726 from Sandia National Laboratories this effort would not have been possible.*

In this discussion dynamic characterization is obtained through the use of a high-rate technique that does not use an impacting shock wave as the primary consolidation mechanism. This work has similarities to the work of Johnson et al. [1], where expanding materials were investigated.

Investigators have recognized for many years that most materials do not behave the same under static conditions as they do in a dynamic environment. The difference between static and dynamic behavior of powder materials is nicely detailed by Vogler et al. [2]. Scientists have used many different approaches to evaluate the mechanical properties of powder materials under rapid loading. High-quality experimental data is needed for the development of computational models of dynamic material events along with the need to improve our general understanding of dynamic powder material physics.

Dynamic compactions of powder materials typically use shock wave techniques such as explosives or high velocity impactors. This paper describes how instrumented electromagnetic tube compression driven by capacitive discharge can be used to measure pressure-volume relationships for model materials at high and controlled strain rates. By measuring the driving current as a function of time and the tube displacement through Photon Doppler Velocimetry (PDV) based on Strand et al. [3,4], the behavior of the porous material can be revealed. The electromagnetic compression technique affords the investigator symmetric loading, repeatability, and precise energy input which is why this technique is being used to obtain high rate low-pressure data [5]. This data is used to validate the P-λ equation-of-state [6] for describing the compaction of porous granular media at the continuum level.

2 Experimental Concepts

2.1 Traditional Methods

The traditional methods used to dynamically compress porous materials usually involve explosives and/or high velocity drivers where direct and intense shock waves achieve compression. These methods while effective at compression can have undesirable attributes associated with them. For example, the methods can be time consuming to perform and usually require expensive testing to obtain accurate and reproducible data. In addition, it is difficult to control the delivery of the compacting energy and maintain the reproducibility of the energy delivery to the material sample over a sequence of experiments.

2.2 An Alternative Method

The Photon Doppler Velocimetry is an enabling technology for porous material compression testing, as velocity is a key parameter in modeling. A heterodyne velocimetry system based on the work of Strand et al. [2,3] was constructed for channels of velocity data at peak velocities under 1000 m/s. The system was used successfully to measure velocities of electromagnetically compressed axisymmetric samples. The low cost methodology illustrated in Figure 1 has contributed useful data to determine material properties under high strain rates and benchmarks for numerical analysis of porous material compaction.

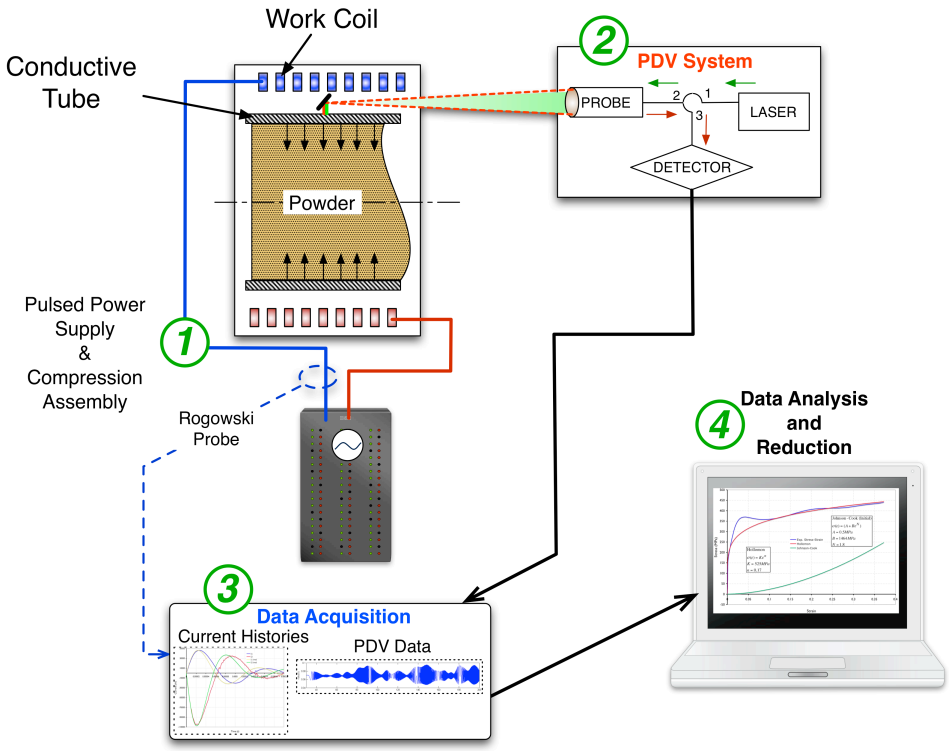

***Figure 1**: Electromagnetic compression system for porous material compaction.*

The compression system shown above, consists of four main components: 1) Power supply and work coil; 2) PDV system; 3) Data acquisition; and 4) Data analysis software. A specimen is placed in the work coil and a high frequency electrical discharge is released into the coil to dynamically compress the specimen at high strain rates $(10^2 s^{-1}$ to $10^4 s^{-1})$ within an axisymmetric strain field. The high strain rates are achieved due to the intense interaction of opposing Lorentz forces acting between the conductive tube and the work coil. The interacting Lorentz forces can create magnetic pressures, which may reach upwards of 500 MPa for this test configuration.

3 Mechanics of Alternative Method

This section describes the mechanics of the EM technique, which are needed to perform analysis of the data obtained from the EM compression experiment. The required information consists of material information about the conductive tube, initial bulk density of the sample material, resistance-inductance-capacitance (RLC) values about the capacitor system (this can be resolved from the time-history waveform of the driving current and are assumed to remain constant during the experiment), and lastly the velocity time history of the conductive tube (this is determined from the processed data signal obtained by the PDV system).

To gain understanding of the system operation, the system can be described as a capacitive discharge unit connected to a coil. The coil delivers the magnetic energy to the sample tube. This configuration mimics a series RLC circuit mutually coupled to an RL circuit. Figure 2 illustrates this coupled circuit concept. Kirchhoff loop laws may be applied to the circuits in Figure 2 to obtain ordinary differential equations, which relate the external circuit to the changing sample tube circuit.

Primary current (I_1) induces an Eddy current (I_2) in the tube. The interactions of the currents cause a repulsive force (F_m). The mutual inductance governs the electromagnetic coupling and the magnetic force generated (F_m).

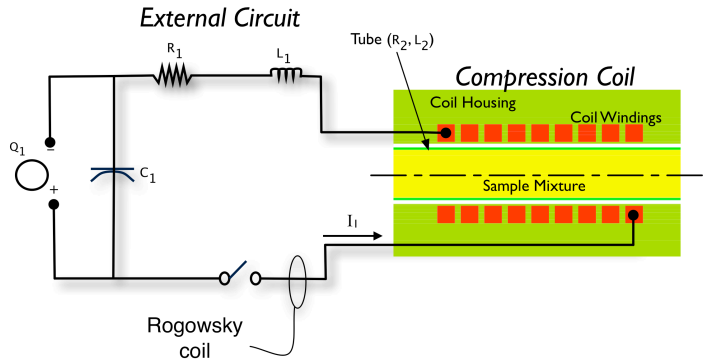

***Figure 2**: Compression system circuit schematic. Consists of two mutually coupled circuits, the external driving circuit plus the compression coil (subscript 1) and the sample tube (which will be subscript 2 in further reading).*

Kirchoff's loop rule was used to sum the voltages across the elements in the coupled circuit shown in Figure 2. The loop law yields the ordinary differential Equations 1 and 2.

$$\frac{d}{dt}\left(L_1 I_1 + M I_2\right) + R_1 I_1 + \frac{Q_1}{C_1} = 0 \tag{1}$$

$$\frac{d}{dt}\left(L_2 I_2 + M I_1\right) + R_2 I_2 = 0 \tag{2}$$

Equation 1 is the sum of the voltages around the primary circuit (external circuit + coil). Equation 2 is the sum of the voltages around the secondary circuit (tube). According to Lenz's Law the induced current in the tube is always in a direction as to oppose the cause that produced it. Hence, a plus sign results in front of the MI_2 and the MI_1 terms found in the two differential Equations 1 and 2. To obtain the total time derivatives of the currents I_1 and I_2 the product rule of differentiation and Cramer's rule were used. This resulted in two total time derivatives of current in the coil,

$$\dot{I}_1 = \frac{\dot{M}\left(L_2 I_2 - M I_1\right) + L_2\left(\frac{Q_1}{C_1} + R_1 I_1\right) - M I_2\left(R_2 + \dot{L}_2\right)}{M^2 - L_2 L_1} \quad , \tag{3}$$

and the tube,

$$\dot{I}_2 = \frac{\dot{M}\left(L_1 I_1 - M I_2\right) + L_1 I_2\left(\dot{L}_2 + R_2\right) - M\left(R_1 I_1 + \frac{Q_1}{C_1}\right)}{M^2 - L_2 L_1} \quad . \tag{4}$$

An energy balance between the two circuits exists, which allows for an expression of the magnetic force (F_m) acting between the coil and the conductive tube,

$$F_m = \frac{1}{2}\frac{dL_2}{dr} I_2^2 + \frac{dM}{dr} I_1 I_2 \quad . \tag{5}$$

The mutual inductance term M and the self-inductance L_2 of the tube are critical items for properly calculating the motion of the tube wall. The self-inductance and the mutual inductance of the tube are assumed to follow the induction relations from Rosa and Grover [7].

Looking only at the sample tube for now, the sample tube can be considered to be a thin walled structure with flow strength and magnetic pressure (P_m) acting on the outside of the tube, as well as resistive compaction pressure (P_c) from the granular material acting on the inside of the tube. This concept allows for the development of a free-body-diagram of forces acting on a differential element of the conductive tube. Figure 3 illustrates the pressures involved in relation to the geometry of the sample tube, which leads to the free body diagram also shown in Figure 3.

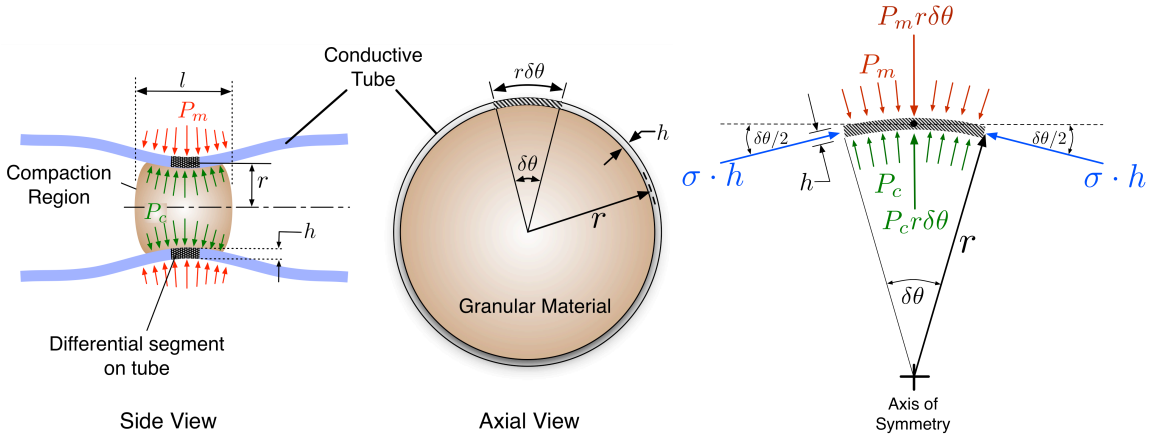

***Figure 3**: Pressure acting on sample tube and the assumed tube geometry with a free body diagram of forces acting on a differential element of the tube.*

Summing the radial forces acting on the differential element of the tube provides an equation of motion for the tube element. Equation 6 is the tube radial equation of motion. P_m and P_c are the magnetic and compact pressures acting on the tube. σ is the material flow stress of the tube, which is assumed to be a known relationship to the radial strain in the tube. ρ is the tube material density. Variables h_o and r_o are the tube initial wall thickness and initial wall radius respectfully. $r(t)$ is the radial location of the tube as a function of time. The radial motion of the tube wall is measured by the PDV system, which is how $\ddot{r}(t)$ and $r(t)$ is determined for inclusion into Equation 6.

$$\ddot{r}(t) = \frac{(P_m - P_c) r(t)^2}{\rho\, h_o r_o^2} - \frac{\sigma}{\rho\, r(t)} \quad . \tag{6}$$

The primary current history (I_1) is measured using a Rogowski probe. Given the radial velocity, and therefore the radial displacement as well as I_1 are all measured as a function of time, the magnetic pressure between the coil and the tube is solvable.

$$P_m = \frac{\frac{1}{2}\frac{dL_2}{dr} I_2^2 + \frac{dM_{12}}{dr} I_1 I_2}{2\pi\, r(t) l} \tag{7}$$

Equation 7 gives the magnetic pressure; the radial equation of motion can be turned around and solved for the nominal compact pressure at the interface of the granular material and the conductive tube. Equation 8 gives the nominal compact pressure,

$$P_c = P_m - \frac{h_o r_o^2}{r(t)^2}\left(\rho\, \ddot{r}(t) + \frac{\sigma}{r(t)}\right) \quad . \tag{8}$$

The data obtained from a compression test consists of the primary current recorded by a Rogowski coil and the free surface velocity of the tube measured by Photon Doppler Velocimetry (PDV). Figure 4 illustrates a typical data set obtained from a compression experiment. The top plot in Figure 4 is raw PDV data. The middle plot is a Fourier reduced signal from the raw PDV data, which renders a radial velocity history of the tube outer wall. The bottom plot in Figure 4 is the primary current which is the driver of the compression test. With the primary current measured and applying assumptions about the inductance of the experimental setup the magnetic pressure can be calculated from Equation 7. The velocity of the tube wall is measured over time, which means we can differentiate and integrate the PDV data to provide radial acceleration and radial location of the tube. Using an assumed flow stress model for the tube material, the calculated magnetic pressure, the radial location, the radial acceleration, and the nominal compact pressure within the powder material can be computed through the use of Equation 8.

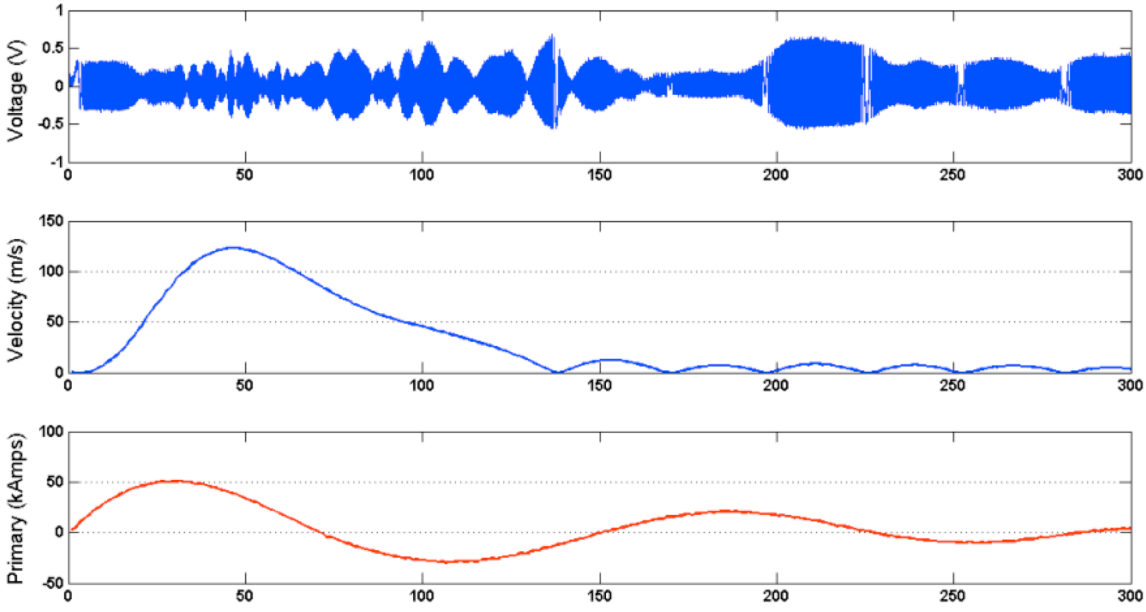

***Figure 4**: Typical data obtained from EM compression experiment.*

4 Equation of State Model

Numerical methods have proven extremely effective in computing the detailed dynamic deformation of materials in a wide variety of different geometries and under many different loading conditions. As such they are ideally suited for the detailed study of stress wave interactions during and after the consolidation of porous materials. We have chosen the CALE code, a two-dimensional (2D) Arbitrary Lagrangian Eulerian (ALE) wave interaction computer program [8] due to its unique capabilities for modeling magneto hydrodynamics and mechanical deformation in a coupled manner.

A number of computational models have been developed to treat the dynamic compaction of porous media. However, predicting the response of a heterogeneous mixture of materials, which most powders constitute, is difficult. The constitutive response of solids is commonly decomposed into the equation-of-state (volumetric) and strength response (deviatoric). Microstructure properties such as grain size, porosity, and multiple phases play an important role in the strength of porous materials. Not commonly recognized is that the same microstructure properties can also influence the volumetric response of powders leading to volumetric hysteresis and dissipation. The purpose of the P-λ equation-of-state is to only encompass the volumetric response. Our approach is focused on the dynamic response of a mixture of materials (including porosity) with wide disparities in density, strength, and compressibility. The model is intended to be robust for both computational and analysis applications. Above all, the model is intended to provide a first-order dynamics response of the material with relatively few material properties. This follows the philosophy of the P-α model, described by Herrmann [9] and, by Carroll-Holt [10].

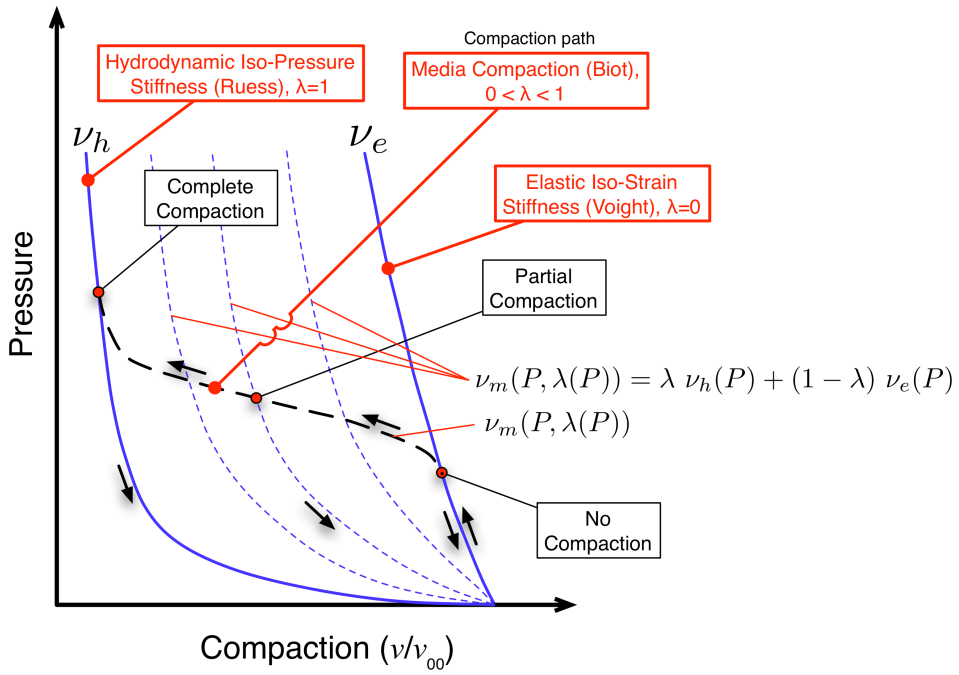

***Figure 5**: The P-λ model illustrated in P-V space.*

Figure 5 illustrates the P-λ computational model, which was developed for describing the compaction of heterogeneous media (in this case a mixture of silica and air). The P-λ material equation-of-state [6] is suitable for distended mixtures of powdered

solids (base material) and interstitial fluid (matrix material) such as water, air, or vacuum. It is intended to model compaction behavior under extreme pressure loadings. It is based on the superposition of specific volume,

$$\text{Compaction of mixture}(P) \equiv \frac{v_m(P)}{v_{oo}} = \lambda(P)\ \frac{v_h(P)}{v_{oo}} + (1-\lambda(P))\ \frac{v_e(P)}{v_{oo}} \tag{9}$$

where $v_h(P)$ and $v_e(P)$ are elastic compression relations for the fully compacted solid media (iso-pressure curve) and the initially distended media (iso-strain curve), respectively. The parameter λ is a pressure dependent function ranging from "0" for the initial un-compacted media to "1" for the fully compacted material. The functional form (Equation 10) currently used for λ is based on a Weibull statistical strength of materials concept, where σ and n are compaction parameters in this representation,

$$\lambda(P) = 1 - e^{-\left(P/\sigma\right)^n} \tag{10}$$

and P is the pressure or stress. The σ parameter is related to the strength of the mixture at a granular level, which roughly controls the point of departure from iso-strain behavior. The n parameter represents the homogeneity of compaction which relates to the abruptness of the transition to iso-pressure behavior. The effects of the parameters are illustrated in the Figure 6.

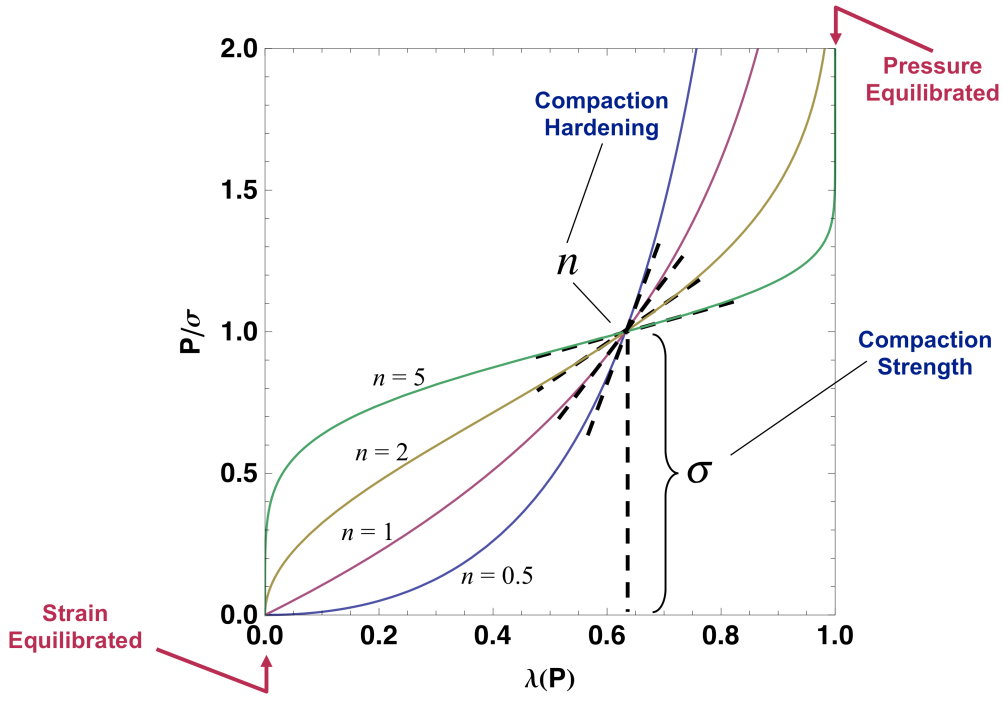

***Figure 6**: Compaction parameters of the exponential P-λ model.*

The specific values of σ and n are obtained through a least squares regression of the compression data and it is assumed you know some characteristics of the components of the powder mixture, specifically the granular volume fractions, densities, sound speeds, and the slopes of the linear $U_s - u_p$ Hugoniot equation of state.

5 Results

A sand compaction simulation was performed in CALE [8]. The P-λ equation-of-state for the sand was taken from the investigative work performed by Brown et al. [11]. In this work they performed a number of high velocity gas gun experiments, which resulted in a locus of Hugoniot data points from which a P-λ model was derived. The P-λ model parameters (as seen in Equation 10) were determined to be a $\sigma = 0.115$ GPa and $n = 0.3$. This model was implemented in CALE and run with a poloidal magnetic field option, which compressed the sample tube. Results of the simulation and experiment are shown in Figure 7.

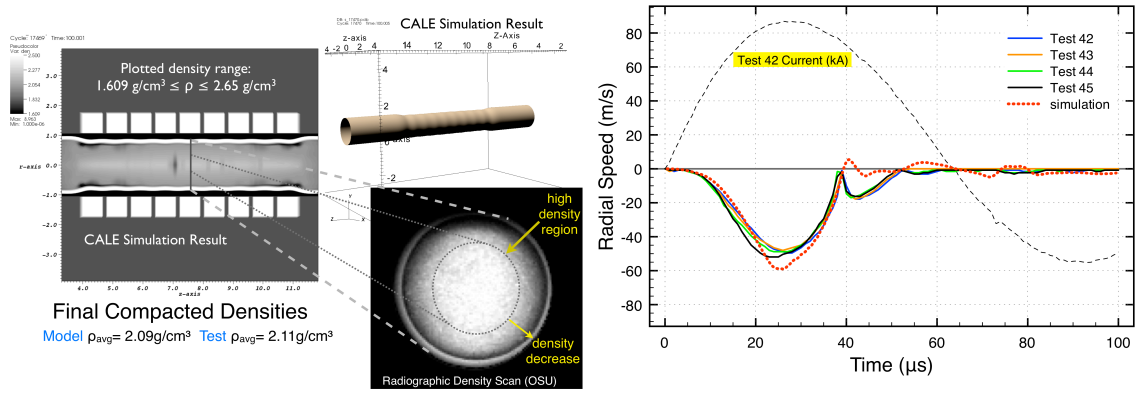

***Figure 7**: Computational and experimental results of a compression test.*

Velocity data taken from the PDV system is plotted in Figure 7 for several tests. These tests were conducted at the same initial bulk packing density and the same driving current. The primary current from Test 42 is shown in units of kilo-amps to illustrate the relative timing of the driving current as compared to the velocity of the compressing tube wall. Figure 7 also shows the apparent reproducibility of data from test to test, as well as the good agreement between the experimental and the simulated tube velocity. Figure 7 illustrates how well the P-λ model aids in describing the dynamic response of the sand filled tube.

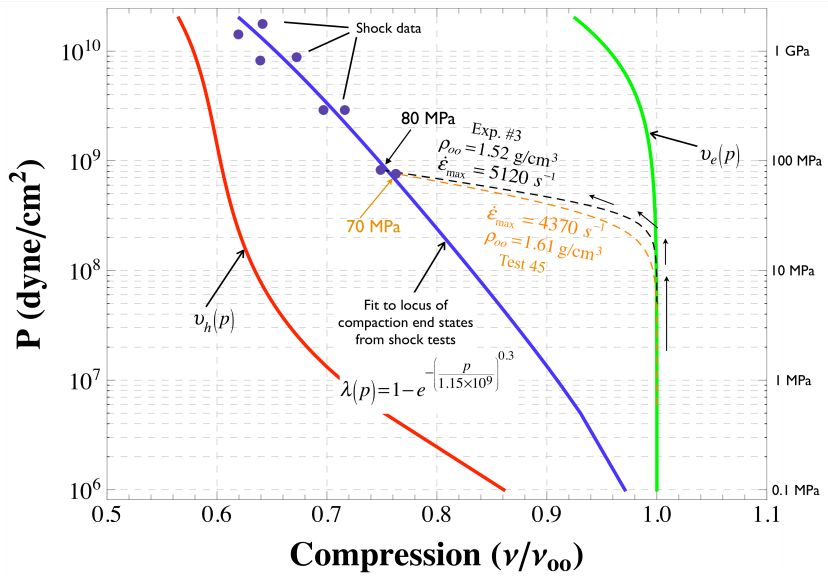

***Figure 8**: Pressure vs. Compression plot for silica sand.*

Figure 8 portrays a lot of information about the compression of dry silica sand. The pressure levels displayed span many decades from very low to moderately high. The black and orange dashed curves are overlaid results of two EM compression tests. These curves represent compaction paths as well as final compaction end states for the sand. The end points of the EM compression curves fall very close to the extrapolated shock data fit. The orange and black curves were two separate and unique experiments on the same material. The fact that the end points from the EM compression tests are nearly the same, suggests that the test technique has invariance to sample configuration.

6 Conclusions

Both experimental and computational studies of the compaction of silica were explored. The PDV technique was used successfully to measure compression velocities of EM compressed samples. This method has contributed useful validation data of mixture compaction under high strain rates and benchmarks for numerical analysis of porous material compaction. The EM technique has proved to be successful in determining low pressure Hugoniot response of mixtures showing simulation and experiment agree well with each other.

References

[1] *Johnson, J.R.; Taber, G.; Vivek, A.; Zhang, Y.; Golowin, S.; Banik, K.; Fenton. G.K.; Daehn, G.S.; Coupling Experiment and Simulation in Electromagnetic Forming Using Photon Doppler Velocimetry, Steel Research Int., 80, 359-365, (2009).*

[2] *Vogler, T.J.; Lee, M.Y.; Grady, D.E.; Static and Dynamic Compaction of Ceramic Powders, Int. J. of Solids and Struct., 44, 636-658 (2007).*

[3] *Strand, O.; Berzins, L.; Goosman, D.; Kuhlow, W.; Sargis, P.; and Whitworth, T.; In 26th International Congress on High-Speed Photography and Photonics, edited by D. Paisley, (SPIE, Alexandria, VA), Vol. 5580, p. 593, (2004).*

[4] *Strand, O.; Goosman, D.; Martinez, C.; and Whitworth, T.; Rev. Sci. Instrum. 77, 83108, (2006).*

[5] *Fenton, G.; Caipen, T.; Daehn, G.; Vogler, T.; Grady, D.; Shock-less High Rate Compaction of Porous Brittle Materials, AIP Conference Proceedings, SHOCK COMPRESSION OF CONDENSED MATTER, Volume 1195, pp. 1337-1340 (2009).*

[6] *Grady, D.E.; Winfree, N.A.; Kerley, G.I.; Wilson, L.T.; Kuhns, L.D.; Computational Modeling and Wave Propagation in Media with Inelastic Deforming Microstructure. Journal de Physique IV 10, 15–20, (2000).*

[7] *Rosa E. B. and Grover F. W., Formulas and Tables for the Calculation of Mutual and Self Induction," [Revised], Bulletin of the Bureau of Standards, Vol. 8, No. 1, 1911, p. 122.*

[8] *R. E. Tipton; A 2D Lagrange MHD Code. In 4th Int. Conf. on Megagauss Magnetic Field Generation and Related Topics, page 299, New York, 1987. Plenum Press.*

[9] *Herrmann, W.J.; Appl. Phys., 40, 2490-2499 (1968).*

[10] *Carroll, M.M. and A.C. Holt; J. Appl. Phys., 43, 1626-1635 (1972).*

[11] *Brown, J.L.; Vogler, T.J.; Grady, D.E.; Reinhart, W.D.; Chhabildas, L.C.; Thornhill, T.F.; Dynamic Compaction of Sand, AIP Conference Proceedings, SHOCK COMPRESSION OF CONDENSED MATTER, Volume 955, pp. 1363-1366 (2007).*

Influence of different process parameters on deformation velocity in laser shock forming*

H. Wielage, F. Vollertsen

BIAS - Bremer Institut für angewandte Strahltechnik GmbH, Klagenfurter Str. 2, 28359 Bremen, Germany

Abstract

In laser shock forming TEA-CO_2-laser induced shock waves are used to form metal foils, such as aluminum or copper. The process utilizes an initiated plasma shock wave on the target surface, which leads to a forming of the foil. Several pulses can be applied at one point in order to achieve a high forming degree without increasing the energy density beyond the ablation limit. During the process, pressure peaks in range of MPa can be achieved. In this article, the dependence of deformation velocity in laser shock forming on various materials as well as laser pulse intensities was determined experimentally for a laser shock bending process. In order to categorize these influences a theoretical model for deformation velocity based on the energy balance is proposed, which allows the evaluation of the influencing variables.

Keywords

High speed forming, Laser shock forming, Shock wave, Strain rate

---

* *The presented work is part of the project VO 530/38-2 "Hochgeschwindigkeitsumformen durch laserinduzierte Schockwellen" and SFB 747 – B1 "Formänderungsvermögen". The authors would like to thank the Deutsche Forschungsgemeinschaft for their financial support within the project.*

1 Introduction

Due to an ongoing trend towards function compaction, miniaturization becomes more and more important in industrial production. With increasing miniaturization, so-called scaling effects occur [1], which inhibit a further increase in miniaturization. However, scaling to smaller parts also enables the application of new processes. Such a new micro production process is the laser shock forming process, which operates as a high speed forming process based on TEA-CO_2-laser induced shock waves.

In former publications laser shock forming was already presented as a process which can be used for deep drawing of copper and aluminum foils [2]. For the forming process the pulsed laser focus is positioned on the specimen surface and creates a plasma which initiates a shock wave propagating into the material. This shock wave forms the sample. A more detailed process description of laser shock forming is already presented in various publications, i.e. [3] and [4]. The laser induced shock waves reach pressures in range of MPa with a pulse intensity of 0.8 GW/cm². In [2] it was determined, that the maximum of measured shock wave signal has a rise time of 5 µs. In this article, the influence of various laser pulse energies and various materials on the deformation velocity of laser shock forming is investigated for a single bending process. In order to categorize these influences a theoretical model for deformation velocity based on the energy balance is proposed. This model will allow the evaluation of the effect of the influencing parameters.

2 Methods

2.1 Experimental Set-Up

In this article, laser shock forming is applied to single bending in order to investigate the material behavior. Fig. 1 displays a sketch of the bending tool and the geometrical process parameters: bending angle α, bending radius R_N, sample overlap length x_L and focus position on the sample. The forming process was recorded by a high speed camera (Vision Research Phantom V 5.1) at a frame rate of 95000 fps and a resolution of 64 x 32 pixels in order to visualize and measure bending angle over time as a basis for calculating bending velocity over time. For bending angle, a 45° angle was chosen. For sample overlap length 5 mm was chosen. To determine an appropriate bending radius, the minimum formable radius was estimated. With a uniform elongation ε_u of 14 % for the used 50 µm thick Al99.5 foil, a lower boundary for the bending radius $R_{N,min} > 0.2$ mm was calculated given by following formula, which is valid for small bending angles [5]

$$\varepsilon_{pl} = \ln(\varepsilon + 1) = \ln\left(\frac{\frac{S_0}{2}}{R_N + \frac{S_0}{2}} + 1\right) \tag{1}$$

$$\Leftrightarrow R_{N,\min} > \frac{\frac{S_0}{2}}{e^{\varepsilon_u}} - \frac{S_0}{2}$$

where R_N is the drawing die radius, s_0 is the thickness of foil, ε_{pl} is the true strain and ε is the engineering strain. For manufacturing reasons a bending radius of 0.5 mm was used for the 45°-bending angle. The focus size was 2.6 mm x 2.6 mm. The focus centre is positioned at the end of the specimen (see Fig. 1) in order to ensure a uniform and highly reproducible movement of the strip. For determination of deformation velocity of various materials aluminum as well as copper in thicknesses of 20 µm and 50 µm with overlap lengths of 5 mm were investigated. In Fig. 2, the temporal evolution of a typical laser shock bending process is given. Tool environment in this assembly with laser pulse intensity of 0.8 GW/cm² relate to shock wave pressures of approximately 2.3 MPa according to our shock wave measurements. The video was taken at a sampling rate of 95.000 fps. It displays that bending angles can be determined very well.

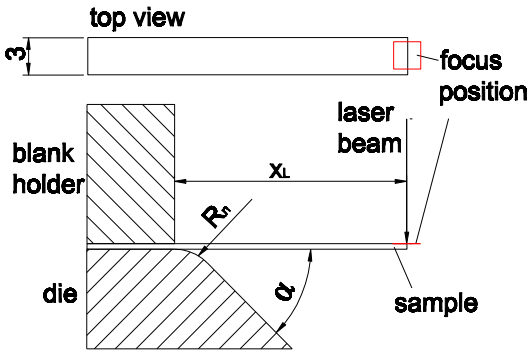

Fig. 1 Single bending tool for laser shock forming (x_L: sample overlap length, R_N: bending radius, α: bending angle)

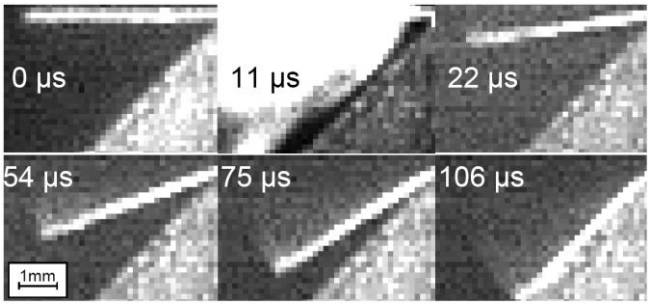

Fig. 2 Laser shock bending (laser pulse intensity: 0.8 GW/cm², pulse duration: 100 ns, laser focus size: 0.07 cm², shock wave pressure: 2.3 MPa, material: Al99.5, thickness 50 µm, overlap length x_L 5 mm)

2.2 Estimation of strain

In order to evaluate workpiece deformation velocity of laser shock bending, the bending angle was obtained from high speed video data. On the basis of a determination of the bending angle for each frame using image evaluation code, workpiece deformation velocity v_d was calculated using the temporally changing bending angle α.
The current workpiece deformation velocity v_d was calculated by virtual circular arc of specimen edge per second:

$$v_d = \frac{x_L \cdot \Delta\alpha}{\Delta t} \tag{2}$$

where x_L is the specimen overlap length, α is the bending angle and t is the time.

3 Model for deformation velocity

A theoretical model for deformation velocity is proposed in order to describe the dependency of the deformation velocity v_D on the material and the laser pulse energy. For this model, the energy balance of the bending process is made. By comparison with the experimental results, an efficiency factor c_{eff} for the laser pulse can be obtained, describing the proportion of effective laser pulse energy. The laser pulse energy E_{pulse} is mainly attributed to kinetic energy E_{kin}, bending energy E_{bend} and aerodynamic drag energy E_{cw}

$$c_{eff} \cdot E_{pulse} = E_{kin} + E_{bend} + E_{cw} \tag{3}$$

The kinetic energy E_{kin} of a strip with strip width b, thickness s_0, sample overlap length x_L and material density ρ is given by i.e. [6]

$$E_{kin} = \frac{1}{2}\int_0^{x_L} \rho b s_0 v^2 dx_L = \frac{1}{2}\int_0^{x_L} \rho b s_0 (x_L\dot{\alpha})^2 dx_L = \frac{1}{2}\rho b s_0 \dot{\alpha}^2 \frac{x_L^3}{3}$$
$$\Leftrightarrow E_{kin} = \frac{1}{6}\rho b s_0 v^2 x_L \tag{4}$$

The bending energy of the single bending process is given by the acting moment M at the shock wave application point (i.e. the focus point of the laser spot) over the bending angle α. Thus, with the given true stress $k_f(\varepsilon_{pl})$ and a bending angle α, the bending energy E_{bend} is given by [7]

$$E_{bend} = \int_0^{\alpha} M d\alpha = \frac{1}{4} \cdot k_f(\varepsilon_{pl}) \cdot b s_0^2 \alpha \tag{5},$$

where true strain ε_{pl} is calculated out of formula (1).
Finally, the aerodynamic energy E_{cw} of the strip with aerodynamic drag c_w can be written as [6]

$$E_{cw} = F_{cw} \cdot s = \frac{1}{2}\int_0^{x_L} c_w b \rho_L x_L (x_L\dot{\alpha})^2 dx_L$$
$$\Leftrightarrow E_{cw} = \frac{1}{8} c_w b \rho_L v^2 x_L^2 \tag{6}$$

with density of air ρ_L.
Thus, for the velocity v_E of the end of the strip we find

$$v_E = \sqrt{\frac{c_{eff} \cdot E_{pulse} - \frac{1}{4} \cdot k_f(\varepsilon_{pl}) \cdot bs_0^2 \alpha}{\frac{1}{6} \rho b s_0 x_L + \frac{1}{8} c_w b \rho_L x_L^2}} \tag{7}$$

4 Experimental Results

4.1 Influence of specimen material on deformation velocity

Fig. 3 illustrates the time-related characteristics of bending angle for different materials. It is obvious that the bending velocity is quite constant for aluminum 20 µm and 50 µm as well as for copper 20 µm over the whole bending process. Only for copper 50 µm, the 45° bending angle was not be achieved, and a decrease of deformation velocity was observed. As an assumption, a deformation velocity v_D independent of time can be obtained for the specimens aluminum 20 µm, aluminum 50 µm and copper 20 µm as slope of a linear data fit. For the specimens copper 50 µm a deformation velocity v_D independent of time can be obtained by the same linear approximation up to the bending angle of 15°.

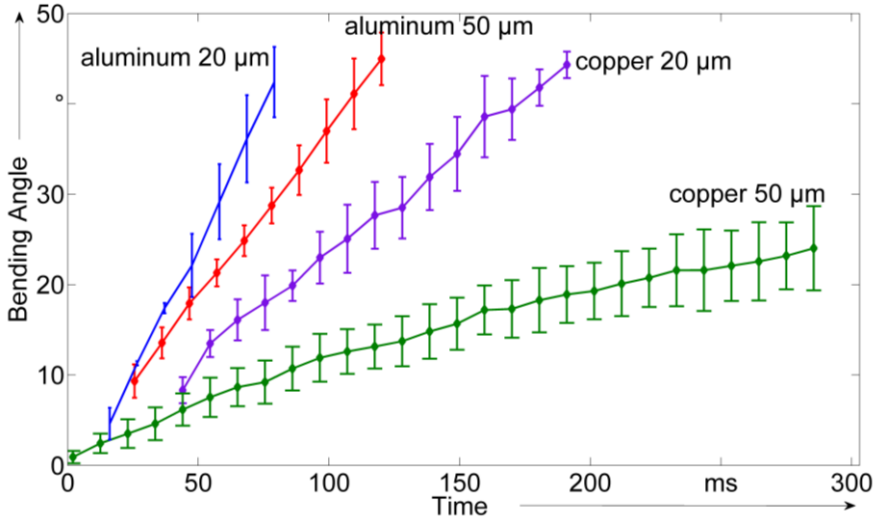

Fig. 3 Bending angle versus time for Al99.5 and copper with thicknesses 20 µm and 50 µm (pulse intensity: 0.8 GW/cm²; shock wave pressure: 2.3 MPa; x_L = 5 mm)

Fig. 4 displays the deformation velocity approximated accordingly by linear fit for all materials and thicknesses investigated. Velocities between 8.5 and 48 m/s were reached. It can be inferred that with increasing foil thickness the deformation velocity decreases. Furthermore, as expected, the deformation velocity is material-dependent and decreases with increasing density and yield stress.

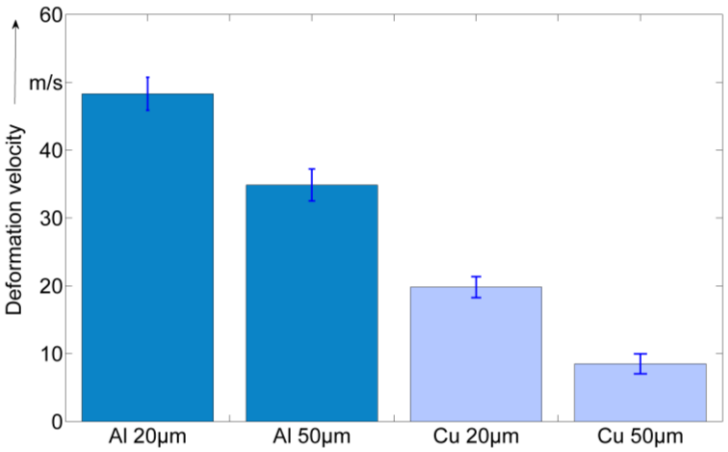

Fig. 4 Deformation velocities for Al99.5 and Cu with thicknesses 20 µm and 50 µm (pulse intensity: 0.8 GW/cm²; shock wave pressure: 2.3 MPa; x_L = 5 mm); for copper 50 µm linear approximation up to bending angle of 15°

4.2 Influence of pulse energy and pulse intensity on deformation velocity

In order to determine the influence of pulse energy and pulse intensity on deformation velocity, aluminum and copper specimens with thickness of 50 µm and overlap lengths of 5 mm were applied with different pulse energies and deformation velocities were determined. Fig. 6 and Fig. 7 display the results for aluminum and copper specimens. The copper specimens reached not more than 3° bending angle for the lowest laser pulse energy. Furthermore, the deformation velocities were not constant over time for copper 50 µm specimens (see Fig. 3). Thus, the mean deformation velocity was calculated for all laser pulse energy steps between 0 and 3° bending angle. In case of aluminum and copper, an obvious decrease of deformation velocity with decreasing pulse energy and intensity was observed.

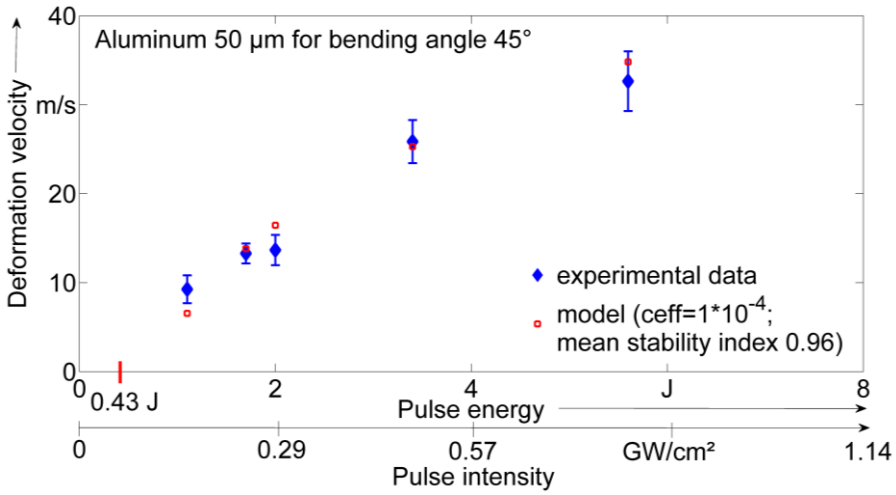

Fig. 5 Experimental and theoretical results of deformation velocity at various laser pulse energies for 50 µm thick Al-sample (shock wave pressure: up to 2.3 MPa; x_L = 5 mm)

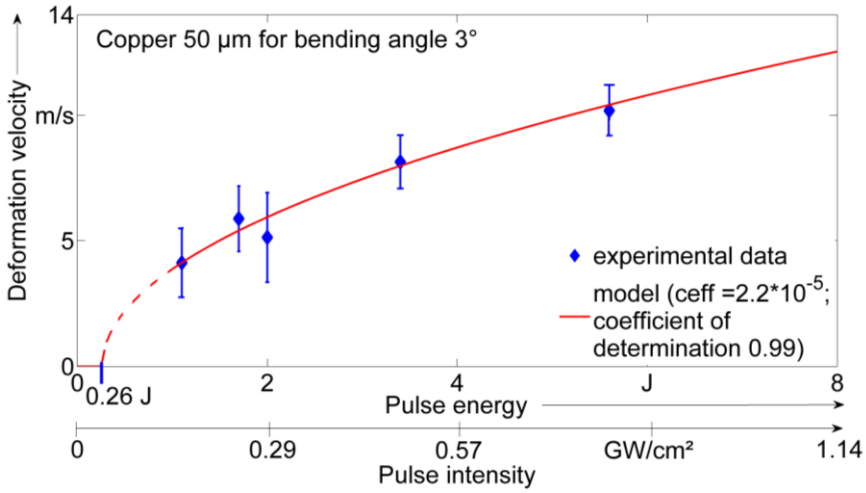

Fig. 6 Experimental and theoretical results of deformation velocity at various laser pulse energies for 50 µm thick Cu-sample (shock wave pressure: up to 2.3 MPa; x_L = 5 mm)

5 Comparison of experimental results and theoretical model

In order to describe the influence of laser pulse energy and the material on the deformation velocity, the base model in section 3 based on the energy balance of the process was used. A closer view on the contribution of the components of the energy balance for the exemplary case of an Al99.5 foil with a thickness 50 µm and various laser pulse intensities investigated in this study is given in Fig. 7. This illustrates that for higher energy the kinetic energy is 0.3 mJ (75 %) higher than the other energies. By decreasing laser pulse energy, an approximation of kinetic and bending energy is observable.

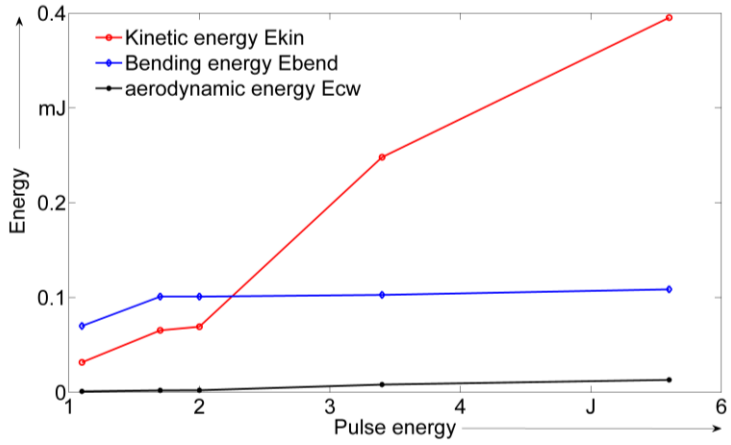

Fig. 7 Calculated kinetic, bending and aerodynamic energy versus pulse energy for aluminium foil with a thickness of 50 µm

The efficiency factor c_{eff} was fitted on the basis of all experimental data for various laser pulse energies depending on the respective material. The resulting values for c_{eff} are $1 \cdot 10^{-4}$ for 45° bending of aluminum, $5.5 \cdot 10^{-5}$ for 3° bending of aluminum and $2.2 \cdot 10^{-5}$ for 3° bending of copper. Besides of the material, the efficiency factor depends on the spatial

restriction on the shock wave (change in effective pressure on the specimen) i.e. by the tool and the bending angle. Earlier estimations of the process efficiency by means of pressure measurements for stretch forming using a blank holder amounted to $6 \cdot 10^{-4}$ to $7 \cdot 10^{-4}$ for aluminum 50 µm [8]. This shows that the pressure wave is more effective in forming a circular specimen surrounded by a blank holder than in bending without any restriction on the spatial propagation of the shock wave.

For comparison of experimental data and theoretical model in Fig. 5 and Fig. 6 the material-dependent efficiency factors of $1 \cdot 10^{-4}$ for 45° bending of aluminum and $2.2 \cdot 10^{-5}$ for 3° bending of copper, measured true strain $k_f(\varepsilon_{pl})$ and material density ρ from literature were taken. True strain was calculated based on the realized bending radius. The results in Fig. 5 and Fig. 6 illustrate a good correlation with coefficient of determination of 0.96 for aluminum and 0.99 for copper. Thus, the significant decrease of deformation velocity with decreasing laser pulse energy can be properly described by the energy balance incorporating kinetic energy, bending energy and aerodynamic energy.

Furthermore, it is obvious that laser pulse energy of 0.43 J is the theoretical lower limit required for plastic bending of 45° for aluminum 50 µm in this set-up. It is a theoretical value, since laser shock forming causes high speed forming and this always integrates kinetic and aerodynamic energy. For plastic bending of 3° of copper 50 µm, a laser pulse energy of 0.29 J is calculated as the required lower energy limit with the set-up and tooling used.

In Fig. 8 the experimentally determined deformation velocities for the materials from Fig. 4 are compared to the deformation velocities predicted by the model. The model for copper is calculated with angle of 3°, with the efficiency factor determined for bending of copper of 3°. The tolerance markers at the model bars indicate the sensitivity of the calculated deformation velocity taking into account the uncertainty of the model parameters yield stress k_f and material density ρ. Based on our measurements for the yield stress k_f a variation up to 13 %, for the true stress $k_f(\varepsilon_{pl})$ a variation up to 8 % and for the material density ρ an assumed variation of 5 % was used for the sensitivity analysis. This sensitivity analysis Δv_E showed that the material density has a bigger influence on the deformation velocity than the yield stress of the material:

$$\Delta v_E = \sqrt{10^{-15} \Delta k_f^{\,2} + 10^{-5} \Delta \rho^2} \tag{10}$$

The comparison of experiment and model in Fig. 8 displays a good correlation for the 50 µm thick aluminum and copper specimens. The comparison of experiment and model for the 20 µm thick copper samples demonstrates less correlation, which is not clarified yet. However, the range of the deformation velocity matched quite well with experimental results.

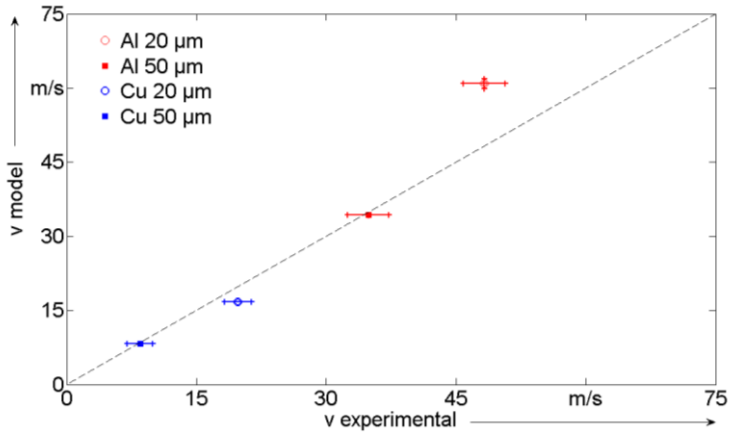

Fig. 8 Deformation velocities from theoretical model vs. deformation velocities from experimental data for Al99.5 and Cu with thicknesses 20 µm and 50 µm (pulse intensity: 0.8 GW/cm²; shock wave pressure: 2.3 MPa; x_L = 5 mm)

6 Conclusions

The dependence between deformation velocity of laser shock bending and laser pulse intensity was determined experimentally and investigated by a theoretical model based on the energy balance incorporating kinetic energy, bending energy and aerodynamic energy. It was established that the kinetic energy is up to 75 % higher in high energy case, and therefore it has a larger influence than the other energies. The efficiency factor c_{eff} was estimated depending on the respective material. The resulting values are $c_{eff} = 1 \cdot 10^{-4}$ for 45° bending of aluminum and $c_{eff} = 2.2 \cdot 10^{-5}$ for 3° bending of copper with a laser pulse intensity of 0.8 GW/cm² (shock wave pressure: 2.3 MPa). The model showed a good correlation for single bending with a shock wave, which is initiated in an open environment without any surrounding tool. The theoretical minimum laser pulse energy for plastic bending by laser shock bending was determined by the model.

References

[1] *Vollertsen, F.:* Categories of size effects, Production Engineering - Research and Development, Volume 2, Number 4, 2008, p. 377-383

[2] *Wielage, H.; Schulze Niehoff, H.; Vollertsen, F.:* Forming Behaviour in Laser Shock Deep Drawing, International Conference on High Speed Forming 2008, ICHSF 2008, Proceedings, Universität Dortmund, Institut für Umformtechnik und Leichtbau, Dortmund, Germany, March 11-12 2008, p. 213-222

[3] *Vollertsen, F.; Schulze Niehoff, H.; Wielage, H.:* On the acting pressure in laser deep drawing, Production Engineering - Research and Development, Volume 3, Number 1, Springer-Verlag, Berlin/Heidelberg, März 2009, p. 1 – 8

[4] Schulze Niehoff, H.; Hu, Z.; Vollertsen, F.: Mechanical and Laser Micro Deep Drawing, SheMet 2007, Trans Tech Publications, CH-Zürich, 2007, p. 799-806

[5] *Doege, E.; Behrens, B.-A.:* Handbuch der Umformtechnik – Grundlagen, Technologien, Maschinen, Berlin, Springer, 2007, p. 56

[6] *Beitz, W. (Hrsg.) ; Grote, K.-H. (Hrsg*.): Dubbel : Taschenbuch für den Maschinenbau, 20. Aufl. Berlin, Springer, 2000

[7] *Lange, K. (Hrsg.):* Umformtechnik – Handbuch für Industrie und Wissenschaft, Band 3: Blechbearbeitung, Springer-Verlag, 1990

[8] *Wielage, H.; Vollertsen, F.:* Investigations of forming Behaviour in Laser Shock Deep Drawing, steel research international 80, No. 5, Düsseldorf, 2009, p. 323 -328

Constitutive relation development through the FIRE test

J. R. Johnson, G. A. Taber, and G. S. Daehn

Ohio State University 477 Watts Hall, 2041 College Rd, Columbus, Ohio, USA

Abstract

The importance of well-developed constitutive models for predicting deformation behavior of materials at high strain rates cannot be overstated. The study and development of these constitutive models is pertinent to several fields, yet the test methods utilized to probe this high strain-rate realm are limited in both number and standardization. In an effort to augment current high rate tests, new technologies have been leveraged to revive an old, under-utilized test method – the axisymmetric expanding ring. The combination of Photon Doppler Velocimetry (PDV) and one of several ring launch techniques allows the successful testing and instrumentation of samples loaded in tension without wave effects at strain rates exceeding 10^4 s^{-1}. Design and construction of the embodiment of this test at OSU, dubbed the Fully Instrumented Ring Expansion (FIRE) system, will be discussed. The key difficulties to implementation of the test are examined, along with our efforts to overcome them and preliminary results.

Keywords

High Strain-Rate, Tensile Test, Ring Expansion

1 Introduction

The ring expansion test is an interesting technique that has undergone several revisions since its inception many decades ago. Inherently this method does not suffer from end effects, and has the unique ability to test samples in uniform simple tension at very high rates of strain. Other high rate tests are typically limited to some extent by the unavoidable limit of plastic wave propagation velocity, given by the Von Karman velocity, v_{VK}:

$$v_{VK} = \sqrt{\frac{\partial \sigma / \partial \varepsilon}{\rho}} \tag{1}$$

The relation determined by Theodore Von Karman is effectively a general case solution to the simpler issue of elastic wave velocity, and incorporates dissipative effects associated with plastic flow. For conventional tensile testing, the Von Karman velocity represents a critical threshold – above which localized fracture occurs near the loaded end. This effect arises because each portion of the sample has inertia, and the end closest to the load has the largest amount of sample to pull along with it. Hence the

stresses here reach the failure point first; following fracture a release wave propagates through the material and unloads the rest of the sample before additional deformation can be accomplished. In the case of real materials, this critical tensile impact velocity takes on values from less than 10 m/s for metals like lead and bismuth, to values approaching 200 m/s for high strength steels and superalloys [1].

The critical impact velocity does not represent the same type of threshold for all cases of one dimensional loading. While the simple tension test with one fixed & one moving crosshead is limited by flow localization near the loaded end for crosshead velocities greater than v_{VK}, compressive loading is instead limited by buckling in long geometries, and shear banding in cases with large frictional end effects. Buckling is actually less of an issue at high test velocities due to inertial effects, while shear banding is exacerbated at high rates due to adiabatic effects. Adiabatic effects can also plague high rate torsional tests, by causing runaway thermal softening which promotes heterogeneous deformation (also note that torsion is equivalent to biaxial balanced tension/compression, not as simple as 1-D tension or compression).

One way to realize materials deformation at high rates while avoiding the effects of abrupt one dimensional loading is to apply strain through a uniform velocity gradient. It is possible to establish such a gradient by expanding (or contracting) any surface of revolution about its axis. Uniformity of the velocity gradient is ensured if all angular segments have the same velocity at any given time, since the gradient in this case is due solely to the rotation of the outward facing surface normal. For such expanding surfaces of revolution with constant radius (tubes and rings), the entire problem thus reduces to a single dimension – coincident with the radial dimension of the test. This type of test, called the axisymmetric expanding ring test is therefore capable of testing ring shaped samples of material in uniform, simple tension at arbitrarily high strain rates.

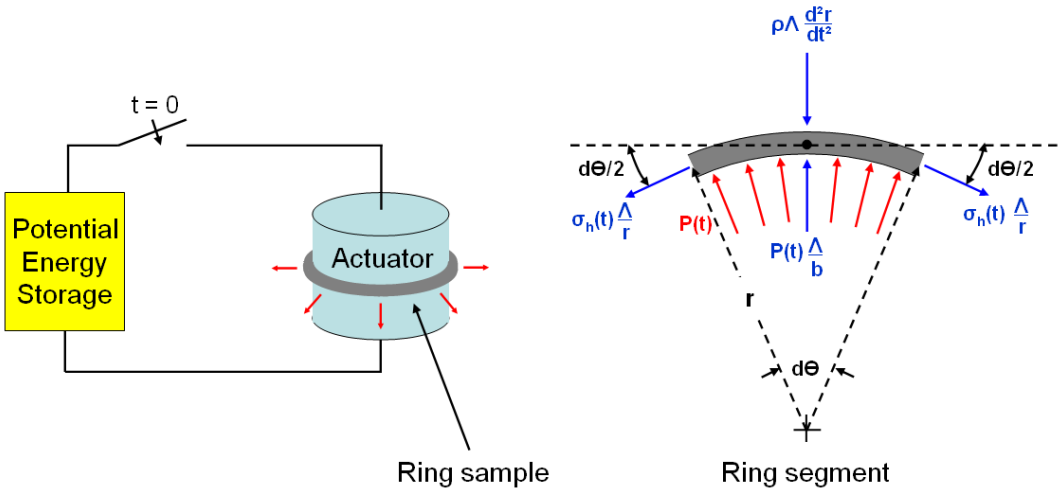

Figure 1: *Left – simplified schematic of a ring expansion experimental setup. Right – free body diagram for an angular ring segment; t is time, P(t) is the time varying pressure exerted by the actuator, r is the current ring radius, Θ is the included angle, $\sigma_h(t)$ is the hoop stress as a function of time, ρ is material density, and Λ is the volume of the differential segment (given as Λ = (b*h)*rdΘ with h and b denoting current ring height and thickness respectively).*

Upon examination of the free body diagram, one can see that initially the outward driving force (P(t)rdΘ) is balanced by the sum of the hoop tension σ_h and the inertial forces ($\rho\Lambda * d^2r/dt^2$, where d^2r/dt^2 is positive since the sample is accelerating). If P(t) goes to zero at some time greater than t = 0, the term d^2r/dt^2 goes through zero and becomes negative such that the outward force is subsequently produced only by the sample's inertia. In this case, called the *freely* expanding ring, the deceleration is caused solely by the flow stress of the ring. Thus if a suitable method of measuring d^2r/dt^2 is employed, the flow curve of the ring material can be unambiguously identified. These results can be summarized mathematically as shown below in equations (2) through (4). Please note that small dΘ and conservation of volume have been assumed in the formulation of the following:

$$\rho\Lambda\frac{d^2r}{dt^2} = P(t)\frac{\Lambda}{b} - \sigma_h(t)\frac{\Lambda}{r} \quad \text{; in which:} \tag{2}$$

$$\Lambda = bhrd\theta \tag{3}$$

$$\sigma_h(t) = -r\rho\frac{d^2r}{dt^2} \quad \text{; For P(t) = 0.} \tag{4}$$

Additionally, since the ring sample is continuous in the direction of tensile stress there are no end effects. The only wave effects that are encountered are through the thickness direction and are correspondingly small. Furthermore the stress state can be adjusted from plane stress for a short ring (cross section aspect ratio of approximately 1), to plane strain in the case of a very tall ring or tube sample. This effect is due to the axial inertia of the sample – as the relative amount of material above and below a given segment increase, so does the constraint along the axial direction. In the limit of long tubes (cross section aspect ratio >>1), very little strain is accomplished in the axial direction and a state of plane strain can be assumed as in Figure 2.

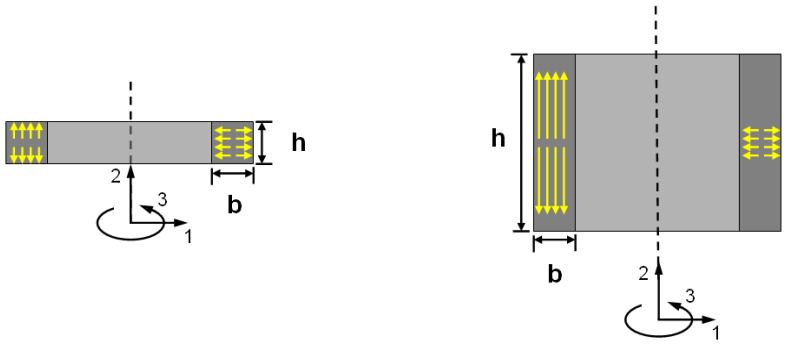

Figure 2: *Left - ring sample with small aspect ratio, a state of uniform plane stress exists in the sample; i.e. $\varepsilon_1 = \varepsilon_2 = -\varepsilon_3/2$. Right – tube sample with aspect ratio > 1, inertial constraint (denoted with yellow arrows) causes ε_2 to decrease such that in the limit of very long tubes a state of plane strain is achieved; i.e. $\varepsilon_2 = 0$, $\varepsilon_1 = -\varepsilon_3$.*

Another inertial effect arises in the expanding ring test that is the source of some debate in the literature concerned with the effect of multiple necking on ductility [2]. From a strictly academic point of view, uniform elongation is not improved in the expanding ring geometry; i.e. the strain accumulated up to the point of instability remains very close to what would be observed in a quasi-static situation. However, instability propagation occurs at a finite speed and so as a result multiple necks can be formed in a sample – each necked region still participates in accomplishing post uniform elongation, and as a result the total elongation to failure is seen to increase monotonically with expansion velocity [3].

Significant work in the field of fragmentation has been done with the expanding ring as a research tool [4]. As a general rule these studies are fairly qualitative, with the number and mass distribution of fragments as primary interests. Fragmentation of rings with defects has been studied also (though to a much lesser extent) [5]. The idea of purposefully introducing notches or holes into the ring sample could also potentially be used to establish fracture toughness as a function of strain rate. This however, is a much more quantitative and difficult task than fragmentation studies – much like developing high rate flow curves. The success of such quantitative ring expansion testing hinges on two aspects of the experimental setup: accurate high speed velocimetry capabilities and precise, repeatable actuators.

2 Enabling Technologies

2.1 Velocimetry Equipment

Early efforts focused on determining the acceleration history (d^2r/dt^2 vs. t for the entire experiment) by using high rate framing cameras or streak photography. These methods present the difficulty of double differentiating displacement data in the temporal domain. Since the time scales for these experiments are so short (typically less than 30 μs) any error in velocity difference will be magnified when normalized by time. It is therefore desirable to eliminate one or both differentiation steps to enhance accuracy and repeatability.

Revisions of the ring expansion test in the 1980's by Gourdin [6] tackled this issue through the use of the Velocity Interferometer System for Any Reflector (or VISAR). While this was an important step forward, VISAR systems were and remain to be very difficult and finicky beasts to build and operate successfully. As such, the improved ring expansion test was still left as an academic curiosity. While a comparatively small amount of work happened on the issue of ring expansion in the following two decades, a vast amount of technology was being developed and proliferated for the telecommunications industry. In 2004 individuals working with VISAR systems for other high rate projects hit on the idea of utilizing cutting edge telecomm technology to create a new velocimetry system that is more robust, less ambiguous and easier to use than the VISAR predecessors [7]. This new system is commonly referred to as Photon Doppler Velocimetry, or PDV.

Since that time, PDV has been adopted for the resurrected ring expansion test, both at The Ohio State University and the University of Texas [8]. The OSU team's PDV setup is an example of a compact, portable system with a minimalist set of components. Details may be found elsewhere [9] on the component selection for this system, but the overall capabilities include direct velocity measurement for speeds of up to approximately 1 km/sec, temporal resolution on a nanosecond scale and spatial resolution on the order of microns. This is coupled with the ability to simultaneously measure up to 4 channels, each

corresponding to the velocity history of a single point on a target's surface (actually an area of ~0.01 mm^2 is interrogated by the probe, from which multiple velocities and/or a velocity distribution can be extracted). Typical data analyses will processes the raw PDV data with a fast Fourier transform, and frequency information from the signal is then directly converted to velocity data, as in the following spectral density surface plot obtained with the *spectrogram* command in MatLab.

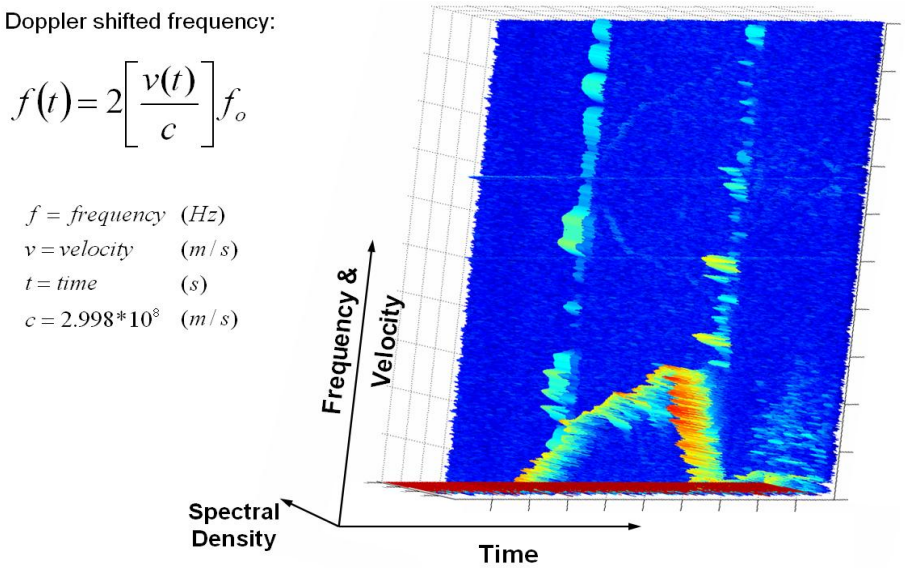

Figure 3: *Example spectral density surface plot generated with MatLab's "spectrogram" function. The plot is essentially a color indexed Short Time Fourier Transform (STFT) of the raw PDV data. The dominant signal component can be extracted from a plot such as this and converted directly into a velocity history.*

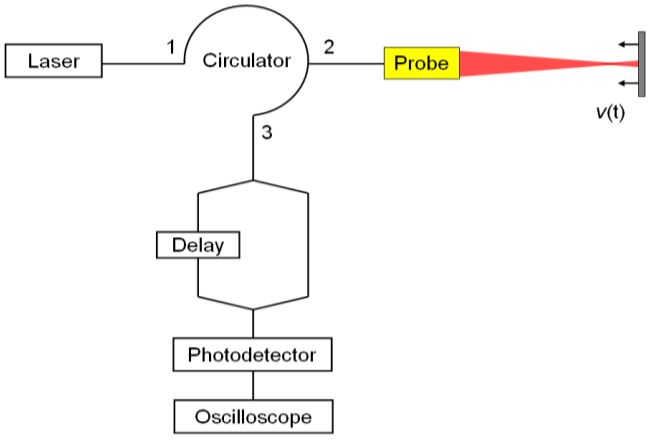

Figure 4: *PDA concept. Probe must be a non-back reflecting type, i.e. -60 dB return loss. The delay is provided by a known length of fiber optic cable, and patched into the optical path with two 50/50 splitters as shown. In this fashion, Doppler shifted light from time t is mixed with shifted light from time t-t_{delay}. The resultant beat frequency is then indicative of the difference in velocity at the two times.*

A promising new technique that leverages the same technology as traditional PDV has emerged very recently. Initially discussed at the 4th International PDV conference in

2009, the idea of utilizing PDV with appropriate fiber optic delay lines to measure acceleration directly has been dubbed the Photon Doppler Accelerometer, or PDA (the name PDVISAR has been suggested too, due to the similarity of the techniques). The concept is schematically illustrated above in Figure 4.

2.2 Actuators

The actuator is the active element that is used to drive a ring or tube sample to high radial velocities. Several variants have been demonstrated, these can largely be separated into categories including electromagnetically launched systems, explosively driven setups (both chemical explosives and exploding wire), and devices utilizing an incompressible media and high speed piston. Any of these techniques may be used in some cases with a driver or backing ring, and in other cases used directly to drive the sample ring. The first two cases are found to be the most useful so far and are illustrated below in Figure 5.

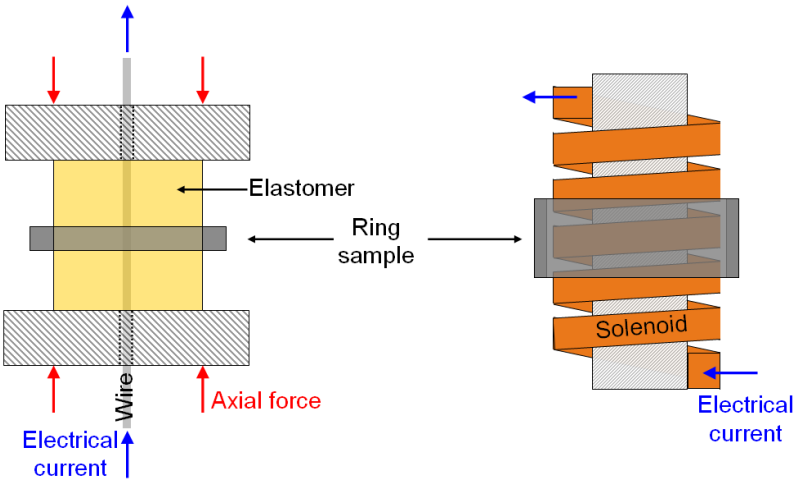

Figure 5: *Schematic representation of the two main types of actuator, the Exploding Wire (EW) style – left, and the Electro-Magnetic (EM) style – right. EW actuators are capable of driving nearly any sample, while the EM type requires samples that are good electrical conductors (or the addition of a conductive driving ring). Not shown are optional catcher rings for stripping of driver ring from sample.*

The Electro-Magnetic (EM) actuator has been in fairly wide use both in the manufacturing arena and elsewhere, including electromagnetic metal forming and induction heating. As such, the physics that accompany the design of solenoids and similar coils are well established. The basic incarnation of an EM actuator is a simple helical solenoid, though other geometries exist as well [10]. Materials that are highly conductive can be directly driven quite efficiently with an electromagnetic actuator; other materials require a conductive driver ring. The resulting composite sample can be analyzed by subtracting the effects of a well characterized driver, or by using an oversized driver that can be stripped away from the sample by catcher rings. In the latter case, a freely expanding ring analysis may be used, while the former requires a more sophisticated reduction technique. This is due to the fact that magnetic pressures are highly sensitive to small variation in geometric factors of the actuator and sample – resulting from the rapid change in mutual inductance with these dimensional variations.

Exploding Wire (EW) type actuators typically consist of a disposable elastomeric pressure medium, concentrically surrounding a sacrificial wire. Passage of large electrical

currents through the wire cause it to vaporize very rapidly and the expanding vapor/plasma pocket is harnessed to do work on the ring or tube sample. As the expanding gases take the path of least resistance, it is important to provide axial confinement on the pressure medium in order to ensure high velocity radial deformation. EW actuators are generally only utilized to produce a freely expanding ring. Here detailed knowledge of the time varying pressure P(t) is not always possible, hence the focus on the less demanding analysis route. EW actuators have the further advantage of possessing no definite upper limit for their power density capabilities. This is in contrast to an EM actuator, which has a definite limit on the amount of energy it can process in a given time frame without failure. Typical rigid EM actuators experience the same pressure as the sample or driver ring does (at a minimum), placing a further restriction on their ability to expand materials of high strength. The cost of overcoming these issues with EW actuators is primarily associated with their disposable nature.

2.3 The FIRE System

With the above discussion points in mind, a modular, multi-purposed Fully Instrumented Ring Expansion (FIRE) system has been developed at OSU. The central component in the system is a pulse discharge capacitor bank made by Maxwell Magneform. This source can supply up to 16 kJ of energy while discharging its 480 μF capacitance into the actuator at currents of up to 200 kA. Interchangeable EW and EM actuators have been designed for ring and tube sizes from 0.25” to 2” inside diameter, and heights from 0.04” to 12”. The actuator components are housed inside a safety chamber which provides shrapnel protection and electromagnetic shielding for test energies of up to at least the rated 16 kJ. Concentrically located with the actuator are provisions for 1 to 6 radial PDV or PDA channels (separated by 60°), each independently adjustable in axial height and angular alignment. Machine tool accuracy has been maintained throughout the construction of all components, maximizing repeatability and accuracy.

One important feature of the FIRE system is the symmetric ground path. This 3-bar design, as shown below in Figure 6 provides balanced magnetic forces on the wire and plasma channel of an EW actuator, and also minimal disturbance of the field surrounding an EM actuator. The primary current path and nearly all of the other conductive components have been machined from C18150, a copper-chrome-zirconium alloy with excellent electrical and mechanical properties (Cu plus 1 wt% Cr, 0.15 wt% Zr; C18150 exhibits conductivity greater than 75% IACS while maintaining a yield stress of at least 400 MPa) [11]; alloy 304 stainless steel was chosen for most of the remaining components. Another feature of the present design is the use of periscope probes – where the focusing probe body is placed outside of the blast guard (shining straight up into the chamber through a small hole) and the light is subsequently redirected through 90° via a first surface mirror inside the chamber to the expanding ring target. In this setup, the relatively expensive probes are out of harm’s way.

Also included in the current suite of instrumentation is measurement of the real-time current and voltage provided by the capacitor bank. This is done with a Rogowski type current probe and capacitive voltage divider (Tektronix p6015a). A reconfigurable port into the blast chamber also offers the option of adding other optical, thermal or magnetic transducers to the list of possible setups for data acquisition. This will become important in the near future, when elevated temperature testing capability is added to the FIRE system.

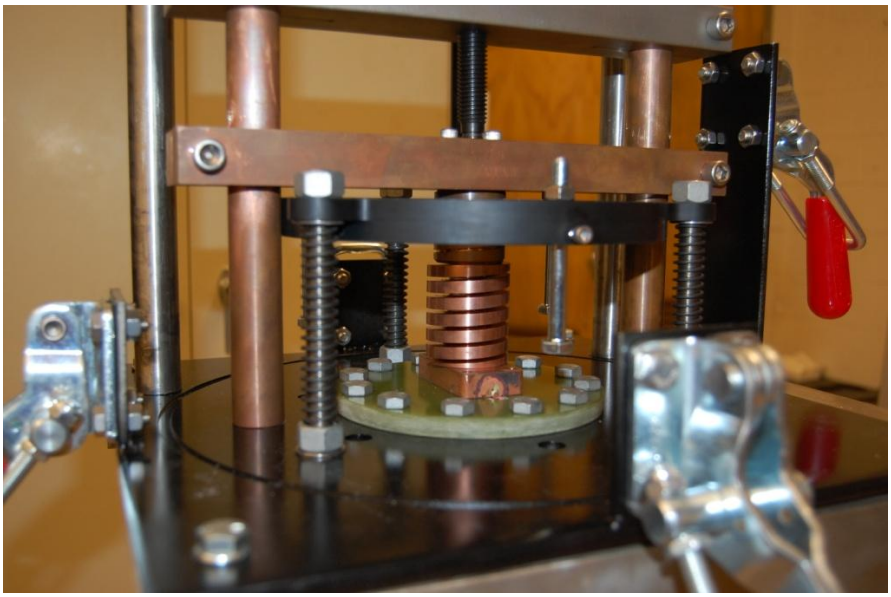

Figure 6: *View of the FIRE system with the cover open. All visible copper is C18150, electrical feedthrough plates (center) are machined from high strength composite (G-11), and the PDV probe support ring is black acetal polymer. Not shown is the 12" diameter cylindrical stainless steel blast cover (above), or high current busbars and secondary PDV support fixturing (below).*

3 Experimental results

3.1 Polycarbonate

Polymers lack the highly ordered structure common to crystalline substances. While their long molecular chains may indeed exhibit in some cases a degree of crystallinity, the structures are relatively open in comparison to their close packed counterparts and they generally posses a lower degree of symmetry. However, unlike amorphous ceramics and metals the glass transition temperature of most engineering polymers is sufficiently low enough to promote ductile deformation at room temperature. In contrast to the deformation of crystalline solids, much of the "plastic" strain can be recovered since the strain is often accommodated through entropy driven anelastic processes [12]. Also, polymer structures and the associated deformation barriers change rapidly with temperature (due primarily to changes in free volume). This often makes the high rate behavior of polymers very interesting and/or counterintuitive.

To demonstrate a ring expansion technique appropriate for non-conductive materials such as polymers, an EM type actuator was used to indirectly expand polycarbonate rings. Rings were obtained by machining short segments of extruded polycarbonate tubing. Samples were cut from 2" inside diameter clear polycarbonate tube to provide a square cross section of 0.12" x 0.12". The actuator consisted of a 4.5 turn spiral stripline type coil [10], having an outside diameter of 1.5" and height of 1.25", potted inside a high strength biaxial fiber composite tube (G-10) with an outside diameter of 1.875". Half inch tall driver tubes were machined from an extruded 6061-O aluminum tube of 2" outside diameter and 0.049" wall thickness. Sample rings were then lightly press fit onto the drivers. Also at this point small squares of retro-reflective tape (made by 3M) were placed on the surface of the polycarbonate sample rings to maximize PDV return

signal (the tape did not come off during the experiment). Focusing probes of 10 cm focal length and -15 dB return loss were utilized to generate velocity histories.

Results from six shots are shown below in Figure 7; these represent two shots at each of 3 energy levels – 3.2, 4, and 5.6 kJ. One shot at each energy corresponds to a bare driver ring, and the other to the response of the composite driver and sample. Peak strain rates in the polycarbonate samples are 1500, 2165, and 3150 s^{-1}, respectively. All polycarbonate samples remained intact, even to the largest strains of 0.4. Deconvolution of the velocity data to stress-strain information is quite involved for this case, since P(t) is significant throughout the duration of the experiment, and due to the fact that rings are being expanded with a driver. However, even this relatively qualitative comparison demonstrates both the excellent high rate properties of polycarbonate and the ability of a FIRE type system to rapidly compare material behavior under varying dynamic conditions.

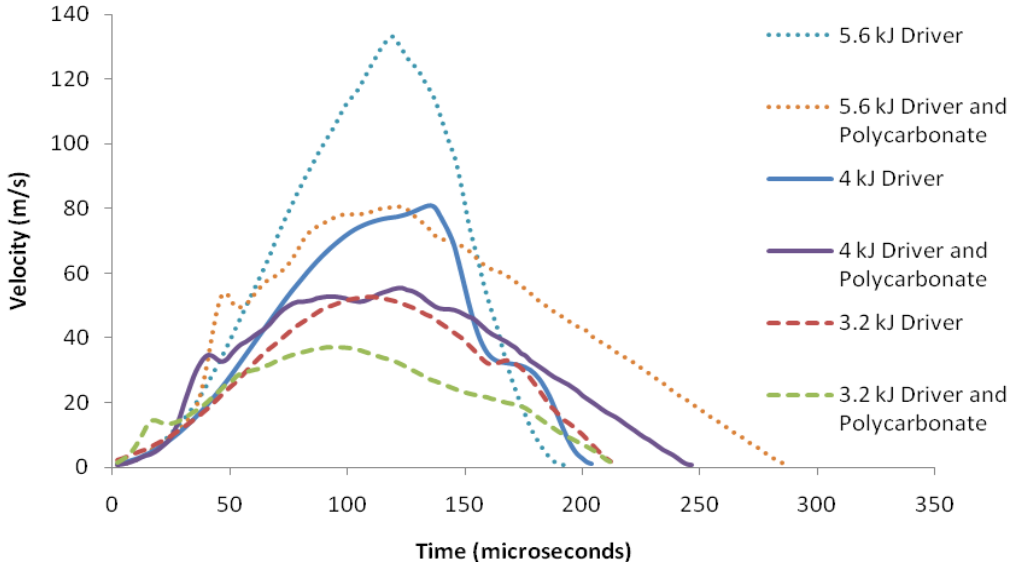

Figure 7: *Radial velocity histories for bare drivers and drivers loaded with polycarbonate ring samples.*

3.2 AISI 4130 Steel

Much of the EW actuator technology here at OSU has been developed in the interest of expanding rings made from high strength materials. Here such an example is shown for expansion of a HSLA steel ring cut from a seamless DOM tube. The as received tube was 1.027” inside diameter with 0.049” wall thickness; the sample was obtained by cutting a 0.375” length of tube by parting on the lathe. The slight radial gap of 0.013” between the polyurethane and the steel ring is easily taken up by the polyurethane actuator when the confining axial force is applied to the pressure medium.

The EW actuator used for this experiment was constructed with a 1” outer diameter, 1” length of extruded polyurethane round stock with a hardness of 80 Shore A. The wire utilized was a 3 inch length of 1100 series aluminum welding wire with a diameter of 0.060”. The wire was vaporized with a 6.4 kJ capacitor discharge which produced a non-ringing electrical oscillation with 20 μs rise time and 70 kA peak current. Again a focusing type probe was used with -15 dB return loss, but here a 30 cm focal length was used. The PDV data from the shot is presented below in Figure 8, following this is the corresponding

stress-strain plot is depicted in Figure 9. Free flight of the ring starts around 25 μs and fracture of the sample occurs at approximately 45 μs. The release wave from fracture imparts a tangential momentum to the fragment of interest which causes rotation and a subsequent increase in velocity along the radial direction. This can be thought of much like cracking a whip, where the tip attains a velocity much greater than the driven end due to geometrical factors (plus conservation of momentum).

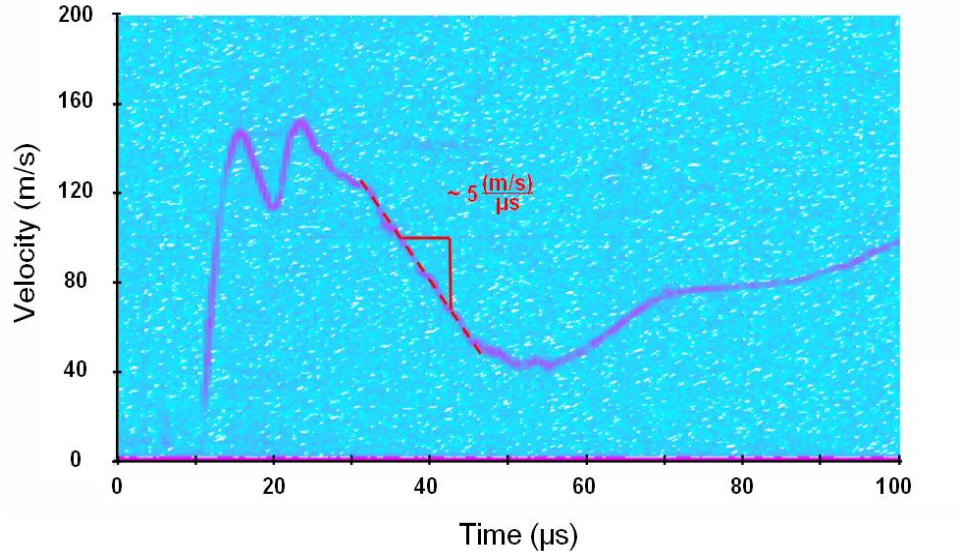

Figure 8: *Velocity history spectrogram used for construction of Figure 9. A constant deceleration is assumed throughout the region marked with the red dotted line – this is the segment corresponding to the analysis for the following flow curve.*

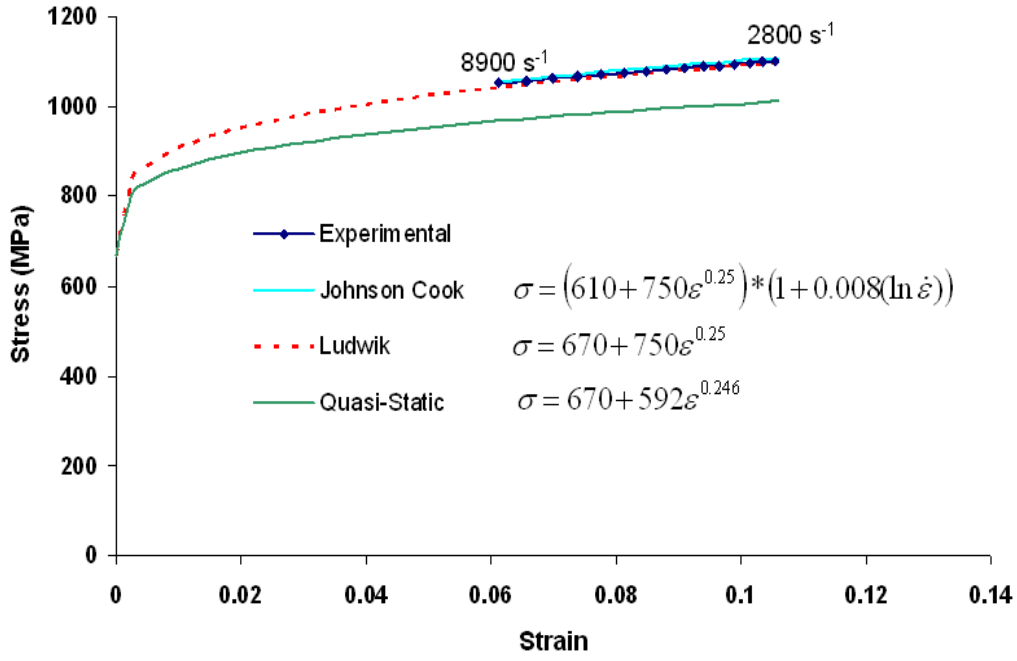

Figure 9: *Flow curves for AISI 4130 steel. Both Johnson-Cook and rate insensitive Ludwik models were fit to the experimental data with good results. Quasi-static data adapted from Park et al [13], where 1" gage length samples were tested in an Instron load frame at a strain rate of 10 $^{-3}$ s $^{-1}$.*

4 Conclusions

It is possible to accurately measure the high strain rate constitutive properties of ductile materials in tension with the ring expansion test. Accuracy and repeatability are ensured through the careful design and construction of actuators, and velocimetry fixtures, along with attention to overall system topology.

In the case of a ring expanding solely under its own momentum determining flow stress as a function of radial displacement is straightforward, provided that the experimental instrumentation is of high enough resolution. Establishing flow stress in cases of rings expanding under the influence of a time varying pressure and/or composite samples including a driver ring is less straightforward. Here detailed knowledge of the pressure variation with time is required for a full analysis.

Furthermore, it has been demonstrated that the same basic setup can be adapted to the expansion of many different materials through the use of Exploding Wire (EW) and Electro-Magnetic (EM) actuator technology. Also, Photon Doppler Velocimetry (PDV) has proved to be an indispensable tool in the development of the Fully Instrumented Ring Expansion (FIRE) system. Future revisions of the test will include the ability to perform testing at elevated temperatures and will also likely include modified ring geometries capable of testing situations other than simple tension. It is hoped that through these efforts the ring expansion test will become a standardized test methodology for probing the high rate response of materials.

References

[1] *ASTME, Wilson, F. W. ed.:* High Velocity Forming of Metals, Prentice-Hall International, London, England, 1964, pp. 148-151.

[2] *Zhang, H., Ravi-Chandar, K.:* "On the Dynamics of Necking and Fragmentation – I. Real-Time and Post-Mortem Observations in Al 6061-O", **Int. Journal of Fracture**, Vol. 142, pp. 183-217, 2006.

[3] *Hu, X., Daehn, G. S.*: "Effect of Velocity on Flow Localization in Tension", **Acta Materialia**, Vol. 44, No. 3, pp. 1021-1033, 1996.

[4] *Grady, D. E.*: Fragmentation of rings and shells: the legacy of N. F. Mott, pp. 153-197, **Springer**, New York, NY, 2006.

[5] *Stepanov, G. V., Babutskii, A. I.*: "Question of fracture of rings", Trans. from **Problemy Prochnosti**, No. 6, pp. 31-34, June, 1988.

[6] *Gourdin, W. H., Weinland, S. L., Boling, R. M.:* "Development of the electromagnetically launched expanding ring as a high-strain-rate test technique", **Review of Scientific Instruments**, Vol. 60, No. 3, pp. 427-432, March, 1989.

[7] *Strand, O. T., Goosman, D. R., Martinez, C., Whitworth, T. L., Kuhlow, W. W.: "*Compact system for high speed velocimetry using heterodyne techniques*"*, **Review of Scientific Instruments**, Vol. 77, No. 083108, pp. 1-8, 2006.

[8] *Landen, D., Satapathy, S., Surls, D.: "*Measurement of high-strain-rate adiabatic strength of conductors*"*, **IEEE Transactions on Magnetics**, Vol. 43, No. 1, January, 2007.

[9] *Johnson, J. R., Taber, G., Vivek, A., Zhang, Y., Golowin, S., Banik, K., Fenton, G., Daehn, G.:* "Coupling experiment and simulation in electromagnetic forming using Photon Doppler Velocimetry", **Steel Research International**, Vol. 80, No. 5, pp. 359-365, 2009.

[10] Johnson, J. R.: U.S. Provisional Patent Application No. 61,267,269.
[11] http://www.cadicompany.com/
[12] *Li, Z., Lambros, J.*: "Strain Rate Effects on the Thermomechanical Behavior of Polymers", **Int. Journal of Solids and Structures**, Vol. 38, pp. 3549-3562, 2001.
[13] *Park, L., Kim, H., Yoo, J., Lee, C., Park, K.:* "Tensile Failure of 4130 Steel Having Different Ultrafine Grained Structures", **Materials Science and Engineering A**, Vol. 527, pp. 645-651, 2010.

Construction of the Hill48 and Yld89 for Auto-body Steel Sheets considering the Strain Rate

C. S. Leea[1], G. H. Baea[1], S. B. Kima[1], Y. Loua[1], and H. Huha[1]

[1]Department of Mechanical Engineering, Korea Advanced Institute of Science and Technology, 335 Gwahangno, Daejeon, 305-701, Republic of Korea

Abstract

This paper deals with the anisotropic material properties and the initial yield locus considering the strain rate. Uni-axial tensile tests are performed with variation of the strain rate in order to obtain flow stress curves and the tensile properties. The R-values have been measured with a high speed camera by analyzing the deformation history during the tensile test. Anisotropy of auto-body steel sheets have been described by using Hill48 and Yld89 (Barlat89) yield functions according to the strain rate ranged from 0.001/sec to 100/sec. Hill48 and Yld89 yield loci of auto-body steel sheets at various strain rates have been constructed in order to visualize the initial yield state. The performance of two yield criteria is evaluated by comparing yield loci constructed in the principal stress plane. The initial yield locus becomes different from the static one when the strain rate is considered to describe the anisotropy of the steel sheets.

Keywords

Anisotropy, Strain Rate, Sheet Metal Forming, Yield Function, Auto-body Steel Sheets

1 Introduction

The sheet metal forming is an effective process widely used in many industries. The main concern of industries is to secure good formability at the higher forming speed in order to increase productivity of sheet metal parts. In sheet metal forming processes, the quality of deformed parts is influenced by many process parameters, such as the shape of the die, the shape and thickness of the initial blank, the material properties, the blank holding force, the friction, and so on. The sheet metal forming simulation has proven to be beneficial to reduce the time and cost at the initial stage of the tool design and for optimizing process parameters [1]. The deformation of steel sheets generally involves strain rate effects during the practical forming process. When the deformation of steel sheets is accelerated, the strain rate effect becomes important. Therefore, it is essential to calculate the final shape and deformation history of a product considering the strain rate effect in the forming process. However, the

change of the material properties has been seldom considered in the real forming analysis since it is difficult to measure the change of the material properties with experimental methods. Recently, it was demonstrated that the material properties can be changed according to the strain rate [2]. Among material parameters, the R-value and the yield stress have a significant effect on the initial anisotropic state of auto-body steel sheets. The initial anisotropic state has an effect on the amount of spring-back since it calculates the different residual stress and strain distribution after the forming process. Spring-back is a challenging issue in the sheet metal forming industry because of the assembly problem among formed parts. Therefore, the modeling of the anisotropic behavior of metal sheets can be one of the most important aspects in the simulation of sheet metal forming process. In order to precisely describe the initial anisotropic yield state of metal sheets, many anisotropic yield functions have been proposed such as Hill48 [3], Hill79 [4], Hill90 [5], Hill93 [6], Yld89 [7], Yld2000-2d [8], BBC2000 [9] and Yld2000-18p [10]. The order of anisotropic yield functions becomes higher to describe complicated plastic behavior of metal sheets such as aluminum alloy. This means that newly developed yield functions are formulated by using more variables from many kinds of experiments in order to obtain higher accuracy in the forming simulation [1]. However, the changes of the material properties according to the strain rate have not been considered in these yield functions.

This paper is concerned with the anisotropic material properties and the initial yield state considering the strain rate. Unit-axial tensile tests are performed with the variation of the strain rate ranged from 0.001/s to 100/s and tensile angle at intervals of 15° from 0° to 90° with respect to the rolling direction in order to obtain flow stress curves and the tensile properties. Hill48 is used to describe the anisotropy of two auto-body steel sheets, CQ and DP590. Yld89 is additionally selected to compare the initial yield state with Hill48. The anisotropy of steel sheets is evaluated based on experimental data according to the strain rate. Finally, the strain rate effect on the initial yield state is analyzed by comparing yield loci.

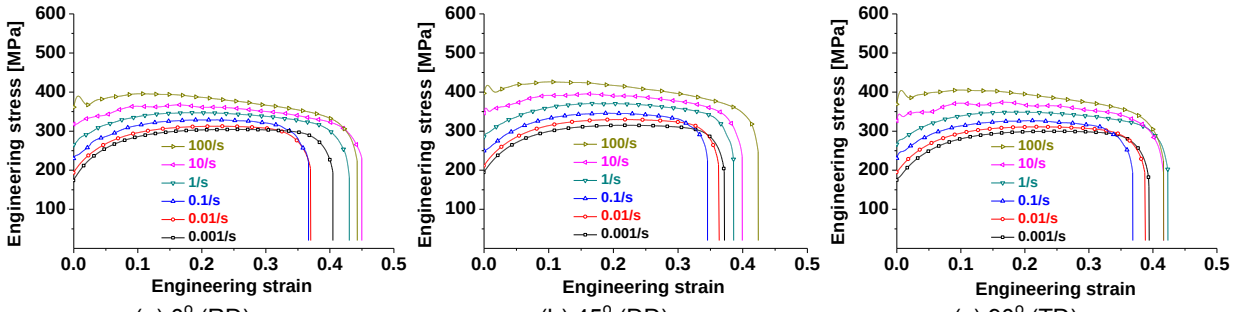

(a) 0° (RD) (b) 45° (DD) (c) 90° (TD)

***Figure 1**: Engineering stress-strain curves of CQ at various strain rates.*

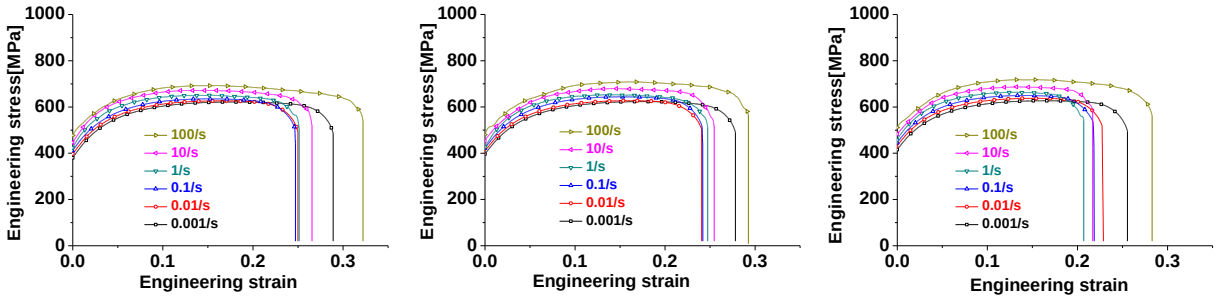

(a) 0° (RD) (b) 45° (DD) (c) 90° (TD)

***Figure 2**: Engineering stress-strain curves of DP590 at various strain rates.*

2 UNIAXIAL Tensile tests considering the strain rate

The most common mechanical test is the uni-axial tensile test to measure the material properties of sheet metals. Since the rate sensitivity is important for steel sheets, tests were performed with variation of the strain rate ranged from 0.001/sec to 100/sec, which is the common range in most practical forming process [1, 11]. INSTRON 5583 and HSMTM (High Speed Material Testing Machine) [12] were used to obtain tensile properties at various strain rates. Two typical auto-body steel sheets, CQ (Commercial Quality) and DP590 (Dual Phase), were selected in this research. The specimens were extracted at intervals of 15° from 0° (RD; rolling direction) to 90° (TD; transverse direction). The dimensions of a specimen for uni-axial tensile tests are adopted from the previous research [11]. Engineering stress-strain curves of the two steel sheets from uni-axial tensile tests for RD (rolling direction); DD (diagonal direction); and TD (transverse direction) are shown in FIGURE 1 and 2. (a) ~ (c).

3 Measurement of the R-value considering the Strain Rate

The plastic strain ratio, r, is defined as the incremental plastic strain in width, $d\varepsilon_w$, divided by the incremental plastic strain, $d\varepsilon_t$ in thickness, of a tested specimen during the tensile test. It is expressed as Eq. (1) on the assumption of the volume constancy:

$$r = \frac{d\varepsilon_w}{d\varepsilon_t} = \frac{-d\varepsilon_w}{d\varepsilon_l + d\varepsilon_w} \tag{1}$$

where $d\varepsilon_l$ is the increment of the plastic longitudinal strain [13].

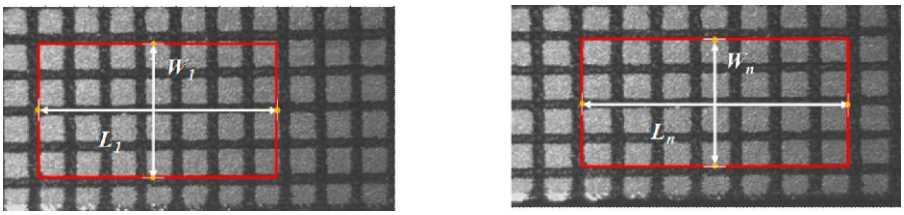

(a) Initial grids (b) Deformed grids (15% to the longitudinal direction)

***Figure 3**: Deformation of grids and measurement region in the gauge section at the strain rate of 100/sec.*

(a) INSTRON5583 (b) High Speed Material Testing Machine

***Figure 4**: Experimental setup of tensile testing apparatus with a high speed camera.*

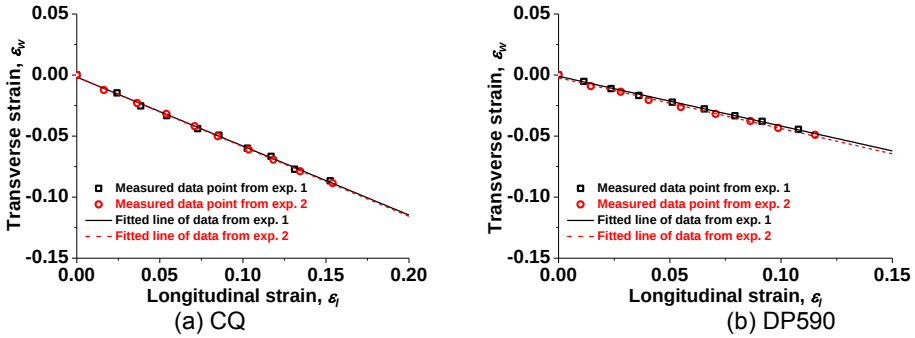

(a) CQ (b) DP590

***Figure 5**: Transverse strain vs. longitudinal strain and the fitted line along the RD at 100/s.*

In order to measure the deformation of steel sheets, square grids of 1*mm* by 1*mm* were marked in the gage section by the silk-screen. The longitudinal and transverse deformations were measured in the maximum broad region for minimizing a measurement error as shown in FIGURE 3. The R-values were measured with a high speed camera of Phantom V. 9.0 by analyzing the deformation history during the tensile test [14, 15]. FIGURE 4 shows an experimental setup of a tensile testing apparatus with a high speed camera. To obtain reliable R-values, the measurement range is limited to the necking instability strain of steel sheets. The longitudinal and transverse strains of CQ and DP590 were measured by longitudinally straining up to 15% and 12% corresponding to the uniform elongation respectively. The Eq. (1) can be rewritten as Eq. (2) based on the fitted slope of longitudinal and transverse strains.

$$d\varepsilon_l = \ln\left(\frac{L_n}{L_1}\right),\ d\varepsilon_w = \ln\left(\frac{W_n}{W_1}\right),\ Slope\ \ in\ \ FIGURE\ 5 = \frac{-r}{1+r} \tag{2}$$

Using the established measuring procedure as shown in FIGURE 5, linear relationships were observed in plots for ε_l *vs.* ε_w according to all strain rates and loading angles from RD [13]. The R-values were calculated by using an average slope obtained from the tensile tests. The initial yield stresses of the two steel sheets were determined using the method of 0.2% offset.

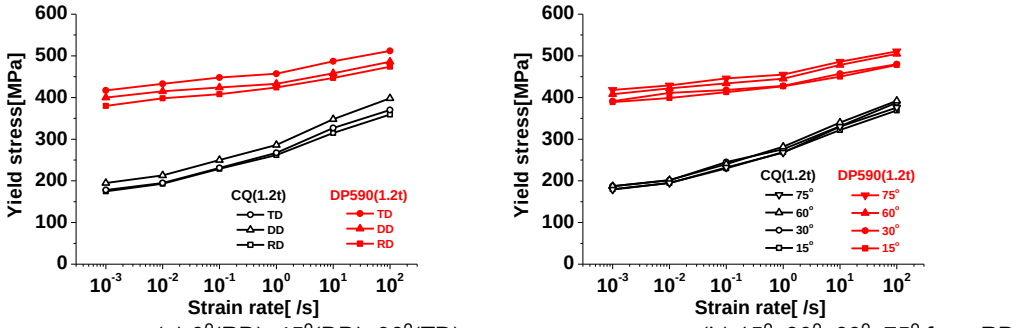

(a) 0°(RD), 45°(DD), 90°(TD) (b) 15°, 30°, 60°, 75° from RD

***Figure 6**: Rate sensitivity of yield stresses of CQ(1.2t) and DP590(1.2t).*

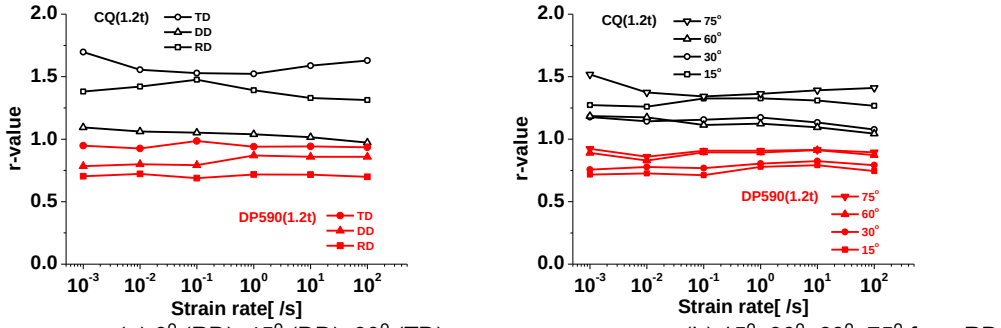

(a) 0° (RD), 45° (DD), 90° (TD) (b) 15°, 30°, 60°, 75° from RD

***Figure 7**: Rate sensitivity of r-values of CQ (1.2t) and DP590 (1.2t).*

4 Change of the Yield Stress and the R-value with respect to the Strain Rate

The yield stress increases as the strain rate increases for both auto-body steel sheets, and it is also observed that the R-value is globally more insensitive than yield stress according to the strain rate. However, the yield stress and the R-value of CQ are more sensitive to the strain rate effect than DP590 as shown in FIGURE 7 and 8. In previous research, it has been observed that the flow stress increases along with strain rate in several auto-body steels due to an abrupt increase of dislocation density obtained from TEM (Transmission Electron Microscopy), while the texture of a material observed by EBSD (Electron Backscattered Diffraction) [16] has little connection with strain rate effect.

5 Evaluation of Anisotropy according to the strain rate

A Hill48 quadratic yield criterion is basically used to describe anisotropy of two auto-body steel sheets. It has been widely used for simulations of forming processes of auto-body steel sheets due to the simplicity of its numerical formula and the low computing cost. It has been also known that Hill48 shows good performance to approximate anisotropy of auto-body steel sheets. Yld89 is additionally selected in order to evaluate the performance of Hill48 with the same experimental data (σ_0, r_0, r_{45}, r_{90}). The exponent value of Yld89 is six since the crystal structure of CQ and DP590 is BCC.

The uni-axial yield stress and the R-value were predicted from the Hill48 and Yld89 and were compared with the measured values of CQ and DP590 in FIGURE 8~11. The uni-axial yield stresses were normalized by yield stress at RD. The normalized yield stress at 0^o is always unity as a reference and calculated R-values at 0^o, 45^o, 90^o coincide with experimental data since they were used to calculate the anisotropic coefficients in Hill48 and Yld89. Figures show that Hill48 and Yld89 well represent anisotropy of the yield stress and the R-value at the given range of the strain rate for CQ and DP590. Moreover, it is observed that anisotropy of the R-value of CQ is relatively greater than that of DP590 as shown in FIGURE 12.

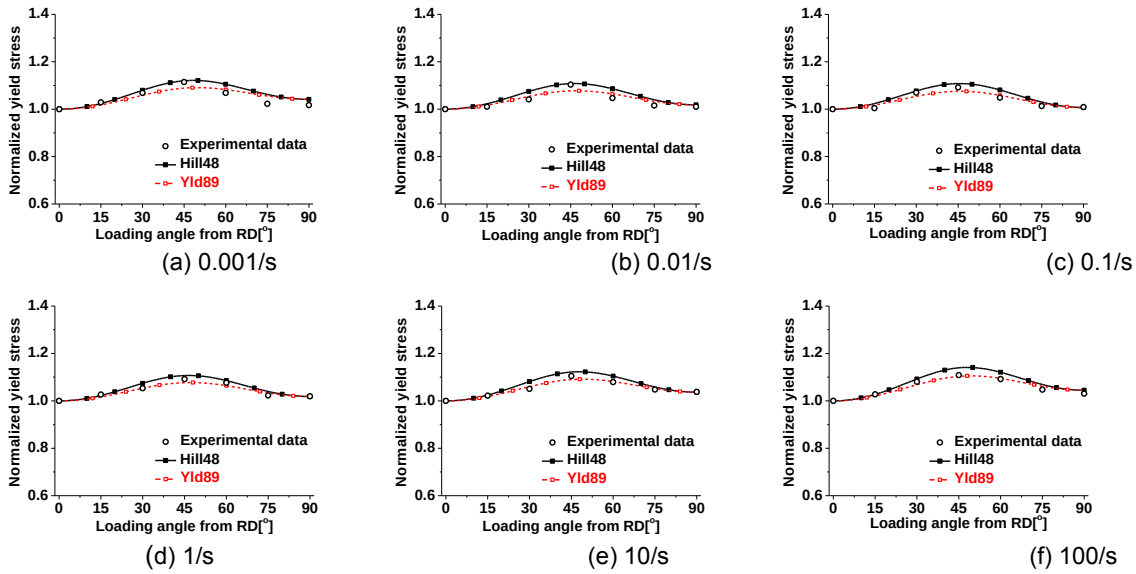

***Figure 8**: Normalized yield stress of CQ (1.2t) with variation of the loading angle from RD.*

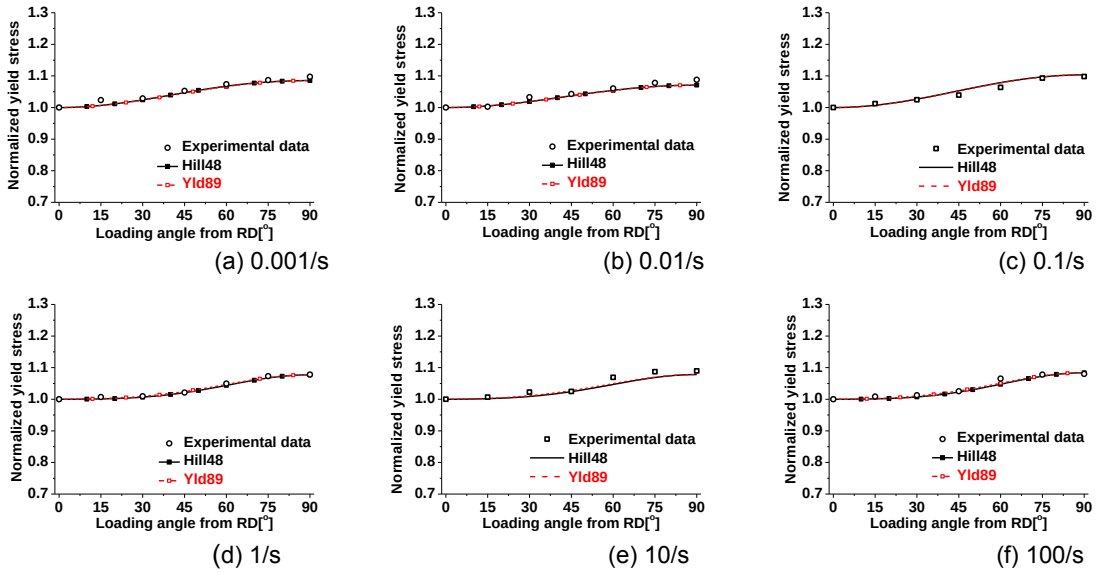

***Figure 9**: Normalized yield stress of DP590 (1.2t) with variation of the loading angle from RD.*

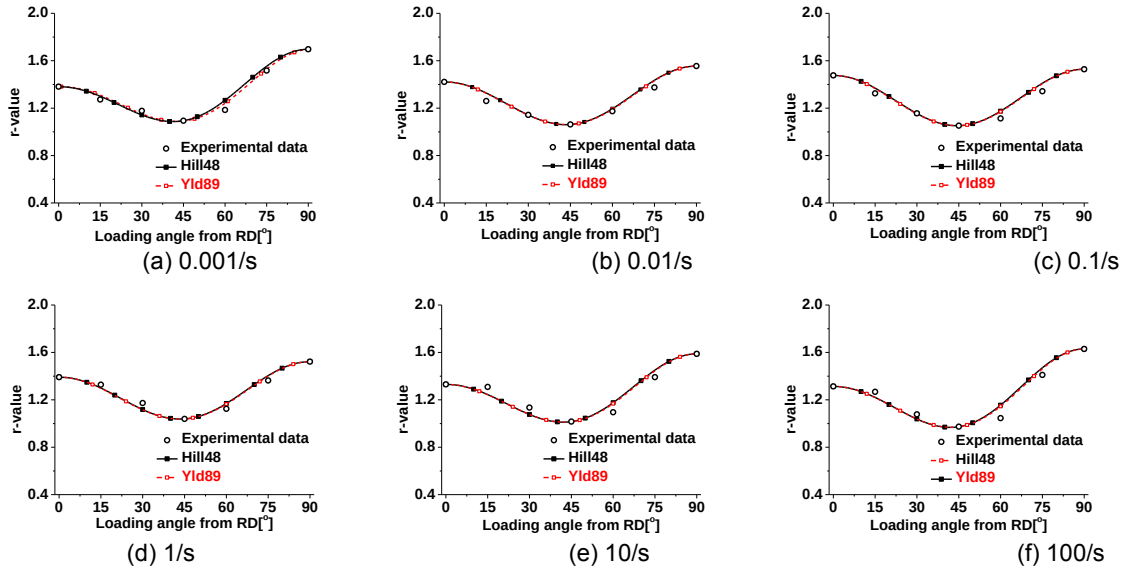

***Figure 10**: R-value of CQ (1.2t) with the variation of the loading angle from RD.*

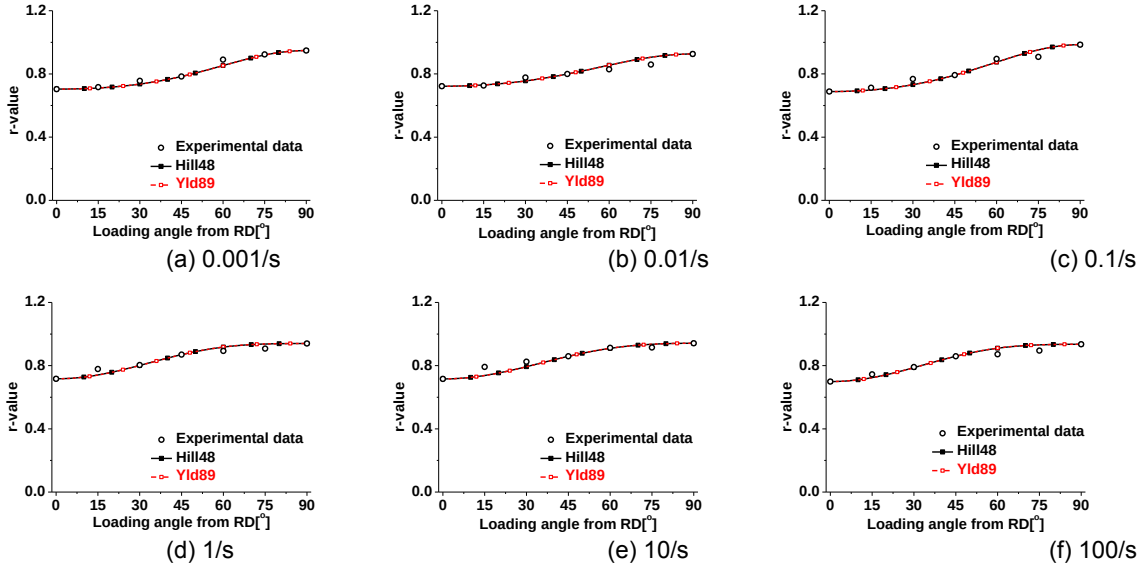

***Figure 11**: R-value of DP590 (1.2t) with the variation of the loading angle from RD.*

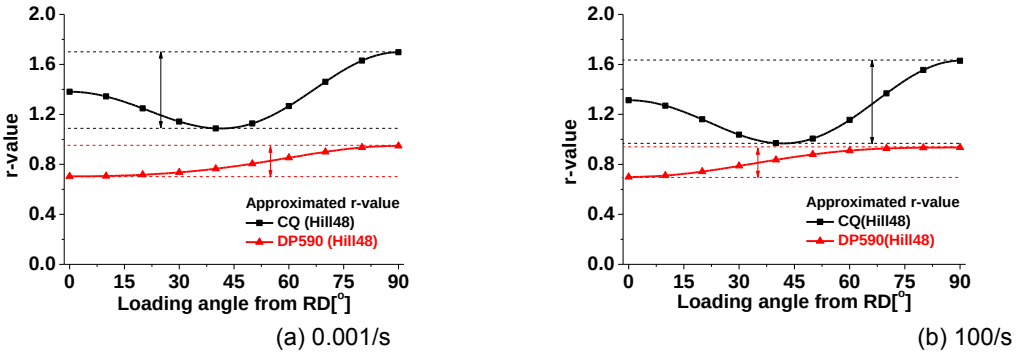

***Figure 12**: Comparison between approximated R-values of CQ and DP590 with the variation of the loading angle from RD.*

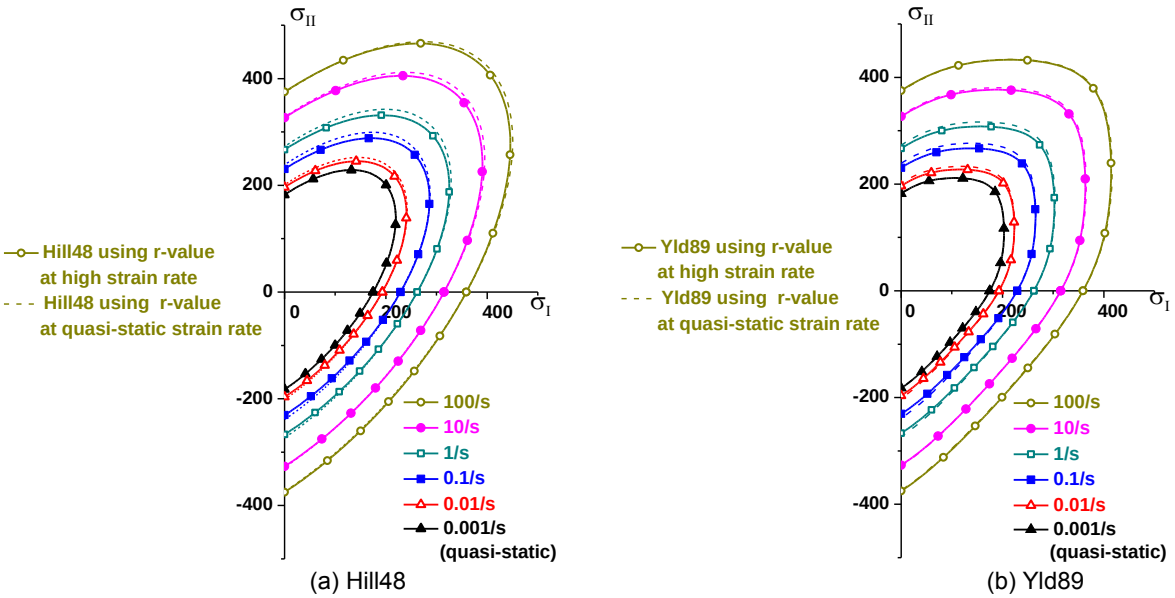

(a) Hill48 (b) Yld89

***Figure 13**: Yield loci of CQ at various strain rates.*

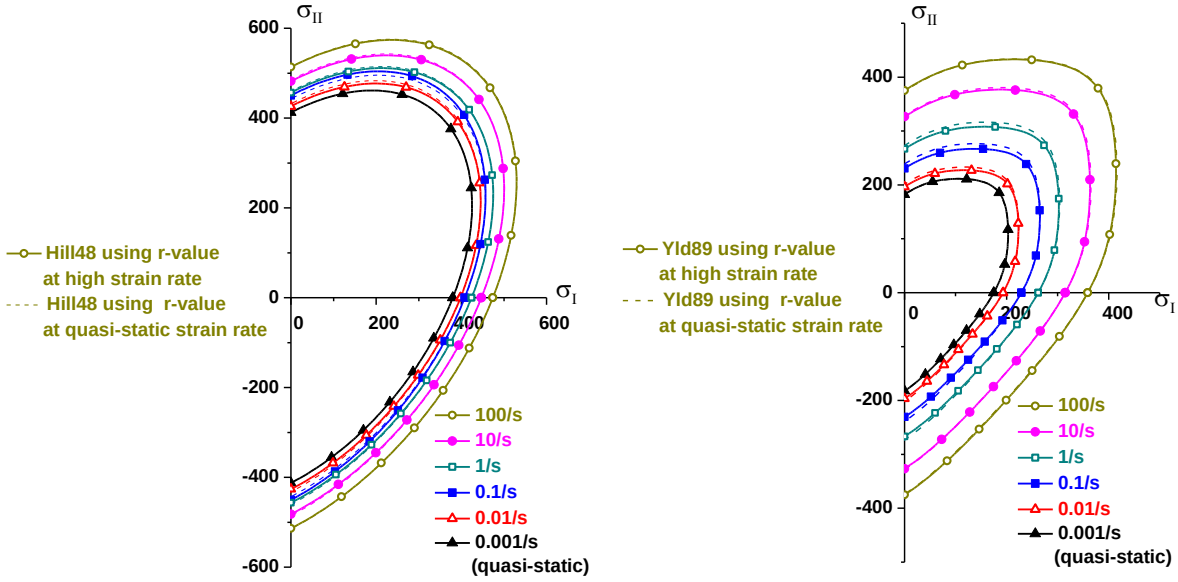

(a) Hill48 (b) Yld89

***Figure 14**: Yield loci of DP590 at various strain rates.*

6 Construction of Yield loci according to the strain rate

Assuming that principal axes of stress and anisotropy coincide with each other, Hill48 and Yld89 yield loci are able to be presented in the principal stress plane. This is an effective way to visualize the initial yield state of a material in the sheet metal forming process. Both yield loci can be constructed by using the yield stress and the R-value obtained from uni-axial tensile tests. The yield stress and the R-value influence the size and shape of a yield locus, respectively. Therefore, the initial yield state is determined by the combination of

those parameters. The yield loci of CQ and DP590 according to the strain rate are shown in FIGURE 13 and 14. As previously stated, the predicted yield stress can be evaluated in the uni-axial state. The predicted σ_{90} using Hill48 and Yld89 are deemed to be reasonable based on σ_0, r_0 and r_{90} in the principal stress plane. The performance of both yield functions is almost same at the uni-axial state, while two yield functions show slightly different behavior in the biaxial state. The different biaxial state is basically caused by the difference of the exponent values of yield functions which are two for Hill48 and 6 for Yld89 [17]. The Hill48 yield locus has a more rounded shape than the Yld89 yield locus. To evaluate accuracy of the two yield functions in the biaxial state, additional mechanical tests should be conducted in the equi-biaxial, plane strain, pure shear condition according to the strain rate.

In the figures, the solid line and the dotted line stand for yield loci using R-values at the corresponding strain rate and a constant R-value at quasi-static state. It shows that the initial yield states are different from the static one when the strain rate is considered to describe anisotropy of steel sheets. Since the R-value of DP590 is less sensitive to the strain rate effect than CQ, there was little deviation of the initial yield state in case of DP590.

7 Conclusions

This paper represents experimental results for the anisotropic material properties and the initial yield state considering the strain rate. Two auto-body steel sheets, CQ and DP590 are considered to demonstrate the change of the R-value and the yield stress. It is observed that the R-value is globally more insensitive than yield stress according to the strain rate. However, the yield stress and the R-value of CQ are more sensitive to the strain rate effect than DP590. Based on the experimental results, Hill48 and Yld89 are constructed to investigate the anisotropy of the yield stress and R-value at the given range of strain rate. The comparison between the measured data and the constructed ones shows that the R-value and the yield stress have some deviation from each other according to the loading angle and Hill48 and Yld89 have to be modified to accurately describe the initial yield state. The initial yield states are different from the static one when the strain rate is considered to describe anisotropy of steel sheets. Since the R-value of DP590 is less sensitive to the strain rate effect than CQ, there was little change of the initial yield state in case of DP590. In case of a sensitive metal sheet according to the strain rate, there is a need to describe initial yield state accurately considering the strain rate in the forming simulation.

References

[1] *H. Vegter, C.H.L.J. ten Horn, Y. An, E.H. Atzema, H.H. Pijlman, T.H. van den Boogaard and H. Huétink*, Characterization and modeling of the plastic material behavior and its application in sheet metal forming simulation, COMPLAS Ⅶ, ed. by E. Onate and D. R. J. Owen, Barcelona, 1-20 (2003).

[2] *H. Huh, J. H. Lim, and S. H. Park*, High speed tensile test of steel sheets for the stress-strain curve at the intermediate strain rate, Int. J. Automot. Techn. **10**, 195-204 (2009).

[3] *R. Hill*, A theory of a yielding and plastic flow of anisotropic metals, Proc. Roy. Soc. A **193**, 281-297 (1948).
[4] *R. Hill*, Theoretical plasticity of textured aggregates, Math. Proc. Camb. Phil. Soc. **85**, 179 191 (1979).
[5] *R. Hill*, Constitutive modeling of orthotropic plasticity in sheet metals, Int. J. Mech. Phys. Solids 3**8**, 405-419 (1990).
[6] *R. Hill*, A user-friendly theory of orthotropic plasticity in sheet metals, Int. J. Mech. Sci. **35**, 19-25 (1993).
[7] *F. Barlat and J. Lian*, Plastic Behavior and Stretch ability of sheet metals - Part I: a yield function for orthotropic sheets under plane stress conditions, Int. J. Plasticity **5**, 51-66 (1989).
[8] *F. Barlat, J. C. Brem, J. W. Yoon, K. Cheng, R. E. Dick, D. J. Lege, F. Pourboghrat, S. H. Choi, E. Chu*, Plane stress yield function for aluminum alloy sheets – Part 1: theory, Int. J. Plasticity **19**, 1297-1319 (2003).
[9] *D. Banabic, H. Aretz, D. S. Comsa, L. Paraianu*, An improved analytical description of orthotropy in metallic sheets, Int. J. Plasticity **21**, 493-512 (2005).
[10] *F. Barlat, H. Aretz, J. W. Yoon, M. E. Karabin, J. C. Brem, R. E. Dick*, Linear transformation based anisotropic yield functions, Int. J. Plasticity **21**, 1009-1039 (2005).
[11] *H. Huh, S. B. Kim, J. H. Song and J. H. Lim*, Dynamic tensile characteristics of TRIP-type and DP-type steel sheets for an auto-body, Int. J. Mech. Sci. **50**, 918~931 (2008).
[12] *J. H. Lim*, "Study on dynamic tensile tests of auto-body sheet at the intermediate strain rate for material constitutive equation", Ph.D. Thesis, KAIST, 2005.
[13] *Y. C. Liu*, On the Determination of Hill's Plastic Strain Ratio, Metall. Trans. A, **14A**, 2566 2567 (1983).
[14] *E. Parsons, M. C. Boyce and D. M. Parks*, An experimental investigation of the large-strain tensile behavior of neat and rubber-toughened polycarbonate, Polymer **45**, 2665-2684 (2004).
[15] *F. Laraba-Abbes, P. Ienny and R. Piques*, A new 'tailor-made' methodology for the mechanical behavior analysis of rubber-like materials: I. Kinematics measurements using a digital speckle extensometry, Polymer **44**, 807-820 (2003).
[16] *H. Huh, J.-H. Yoon, C.-G. Park, J.-S. Kang, M.-Y. Huh, H.-G. Kang*, Correlation of microscopic structures to the strain rate hardening of SPCC steel, Int. J. Mech. Sci. on line (2010).
[17] *W. F. Hosford*, On the crystallographic basis of yield criteria, Textures Microstruct. **26-27**, 479-493 (1996).

Author Index

Keyword Index